

364p

(NASA-CR-136726) PROJECT APOLLO. VOLUME  
2: DATA BOOK (General Electric Co.)  
364 p

N74-71534

Unclas  
28847

00/99

MISSILE AND SPACE  
VEHICLE  
DEPARTMENT

TO =  
By authority of  
Changed by L. Shirley  
CLASSIFICATION CHANGE  
~~CONFIDENTIAL~~  
E.O. 11652  
Date 11-16-73

# PROJECT APOLLO DATA BOOK VOLUME II

Available to NASA Offices and  
NASA Centers Only.

GENERAL  ELECTRIC

[REDACTED]

This document contains 361 numbered pages.  
Copy number 106 of 150 copies.

14 MARCH 1961

# **PROJECT APOLLO**

## **DATA BOOK**

### **VOLUME II**

*Prepared for:*

**National Aeronautics and Space Administration  
Space Task Group**

on contract NAS-5-302

**GENERAL  ELECTRIC**

**MISSILE AND SPACE VEHICLE DEPARTMENT**

*A Department Of The Defense Electronics Division*  
3198 Chestnut Street, Philadelphia 4, Penna.

[REDACTED]



## VOLUME II

### TABLE OF CONTENTS

Chapter	Page
VII FLIGHT MECHANICS	VII-1
1. Powered Ascent Trajectory	VII-1
2. Burnout Point Selection	VII-4
3. Sample Transit Trajectory	VII-7
4. Emergency Return Trajectories	VII-11
Introduction	VII-11
Discussion	VII-11
5. Velocity Increment for Lunar Orbit Entry	VII-17
6. Sample Lunar Orbit	VII-21
7. Re-entry Flight Mechanics	VII-25
Re-entry Corridor	VII-25
Extremal Trajectories	VII-26
Maneuverability and Landing Point Selectivity	VII-26
References	VII-27
 VIII NAVIGATION, CONTROL, AND GUIDANCE	 VIII-1
1. Introduction	VIII-1
2. Error Analysis	VIII-4
Estimate of Insertion Errors	VIII-4
Outbound Leg Mid-Course	VIII-6
Transition from Outbound Leg to Terminal Phase	VIII-15
Injection into Orbit Around the Moon	VIII-16
Transition from Lunar Orbit to Return Leg	VIII-17
Return Leg Mid-Course Velocity Corrections	VIII-18
Mid-Course Terminal Errors	VIII-24
Re-Entry Initial Condition Errors	VIII-25
Emergency Escape	VIII-25
3. Guidance Concepts	VIII-27
Solution of Equations of Motion	VIII-29
Time of Arrival Considerations	VIII-38
4. Mid-Course Navigation	VIII-39
System No. 1	VIII-39
System No. 2	VIII-90
Crew Functions	VIII-108
5. Lunar Terminal Phase	VIII-114
Introduction	VIII-114
Injection into Lunar Orbit	VIII-114
Orbiting Around the Moon	VIII-119
Ejection from Lunar Orbit	VIII-129

~~CONFIDENTIAL~~

## TABLE OF CONTENTS (Continued)

Chapter	Page
6. Re-entry Energy Management	VIII-131
Introduction	VIII-132
Re-entry System Description	VIII-132
Selection of Safe Flight Paths	VIII-135
Path Control System	VIII-136
Technique for Accomplishing Energy Management	VIII-138
Energy Management Trajectory Studies	VIII-149
7. Attitude Control	VIII-162
Propulsion Requirements	VIII-162
Infrared Horizon Sensing Systems	VIII-165
Sun Sensing Systems	VIII-170
8. Navigation, Control, and Guidance System Summary	VIII-172
 IX   AERODYNAMICS, THERMODYNAMICS & RE-ENTRY HEAT PROTECTION	 IX-1
1. Aerodynamics	IX-1
Introduction	IX-1
B-2 Configuration	IX-1
C-1 Configuration	IX-8
D-2 Configuration	IX-10
High L/D Glider	IX-19
High Attitude Glider	IX-19
Modified Lenticular Shape	IX-23
2. Thermodynamics and Materials	IX-29
External, Re-Entry Phase Heating	IX-29
External Boost Phase	IX-46
Internal Temperature During Boost and Re-Entry Phases	IX-48
Internal Temperature During Cislunar Phase	IX-48
 X    LANDING AND RECOVERY	 X-1
1. Landing Systems for Semi-Ballistic-Type Re-entry Vehicles	X-2
Problem Definition	X-2
The Recovery System	X-3
Other Advanced Retardation Devices	X-37
Landing Impact Attenuation	X-46
General List of References Employed	X-61
2. Landing Study for Glide-Type Re-entry Vehicle	X-64
List of References	X-68
3. Flotation System	X-69
General Description	X-69
4. Recovery Aid System	X-72
General Description	X-72
System Synthesis	X-73
System Design	X-78

~~CONFIDENTIAL~~



## LIST OF ILLUSTRATIONS

Figure		Page
VII-2-1	Range safety limits on Moon declination	VII-6
VII-2-2	Launch parameters for lunar missions	VII-6
VII-3-1	Circumlunar trajectory retrograde class	VII-8
VII-3-2	North-south miss distance	VII-9
VII-3-3	Conditions for $z = 0$	VII-10
VII-3-4	Launch time for $z = 0$	VII-10
VII-4-1	Typical transit trajectory	VII-13
VII-4-2	Emergency return trajectory	VII-13
VII-4-3	Emergency return orientation of $\Delta V$ vector for $\gamma_E = 5.0$ degrees	VII-14
VII-4-4	Emergency return re-entry velocity	VII-14
VII-4-5	Emergency return apogee altitude versus initial altitude	VII-15
VII-4-6	Time to re-entry versus initial altitude for various $\Delta V$ values	VII-15
VII-5-1	Approach velocity relative to the Moon versus altitude at the distance of closest approach	VII-18
VII-5-2	Velocity increment required to enter lunar orbit	VII-19
VII-6-1	Sample lunar satellite orbit orientation	VII-22
VII-6-2	X-y projection, lunar satellite orbit (first revolution)	VII-22
VII-6-3	Y-z projection, lunar satellite orbit (first revolution)	VII-23
VII-6-4	X-z projection, lunar satellite orbit (first revolution)	VII-23
VII-6-5	Lunar orbit altitude variation	VII-24
VII-7-1	Re-entry angular corridor	VII-28
VII-7-2	Virtual perigee altitude versus re-entry path angle for escape velocity	VII-29
VII-7-3	Angular re-entry corridor for supercircular entry, 8-g deceleration limit	VII-30
VII-7-4	Angular re-entry corridor for supercircular entry, 12-g deceleration limit	VII-30
VII-7-5	Angular re-entry corridor for supercircular entry, 6-g deceleration limit	VII-31
VII-7-6	Typical re-entry trajectories, B-2 configuration	VII-32
VII-7-7	Typical re-entry trajectories for C-1 configuration	VII-33
VII-7-8	Re-entry profiles for high-altitude vehicles	VII-34
VII-7-9	Re-entry profiles for high L/D vehicle	VII-35
VII-7-10	Trajectory characteristics (re-entry) for APOLLO B-2 configuration	VII-36
VII-7-11	Trajectory characteristics (re-entry) for APOLLO C-1 configuration	VII-37
VII-7-12	Re-entry time history for R-1 vehicle	VII-38
VII-7-13	Re-entry time history for R-1 vehicle	VII-39
VII-7-14	Re-entry time history for R-2 vehicle	VII-40
VII-7-15	Re-entry time history for R-2 vehicle	VII-41
VII-7-16	Re-entry time history for R-2 vehicle	VII-42
VII-7-17	Maximum theoretical maneuvering capability	VII-43

~~CONFIDENTIAL~~

## LIST OF ILLUSTRATIONS (Continued)

Figure		Page
VIII-2-1	Near-lunar position sensitivity to velocity	VIII-8
VIII-2-2	Sensitivity of lunar velocity perturbation to nominal velocity perturbations at time $t$	VIII-9
VIII-2-3	Velocity sensitivity to near-lunar position	VIII-10
VIII-2-4	Variation of lunar miss distance with time	VIII-13
VIII-2-5	Transition phase	VIII-15
VIII-2-6	Maximum allowable velocity magnitude error $ \Delta V $ , flight path angle error $ \Delta \gamma $ , and radial position error, $\Delta R$ , for 25 nmi re-entry perigee variation as a function of distance from Earth	VIII-20
VIII-2-7	Mid-course velocity increment, $\Delta V$ , required to null an initial perigee error of 700 nmi as function of radial distance from Earth	VIII-22
VIII-2-8	Vacuum perigee error vs range from Earth for 10 fps velocity error both parallel and perpendicular to the velocity and radial position error of 5 nmi	VIII-26
VIII-4-1	General block diagram, mid-course navigation	VIII-40
VIII-4-2	Platform alignment mode	VIII-42
VIII-4-3	Navigation fix mode	VIII-42
VIII-4-4	Two-planet triangulation geometry	VIII-44
VIII-4-5	Planet, star triangulation geometry	VIII-45
VIII-4-6	One-planet triangulation geometry	VIII-46
VIII-4-7	Two-planet triangulation analysis	VIII-48
VIII-4-8	Planet, star triangulation analysis	VIII-49
VIII-4-9	One-planet triangulation analysis	VIII-50
VIII-4-10	Mid-course navigation schematic	VIII-55
VIII-4-11	Guidance system correction mode	VIII-56
VIII-4-12	Satellite borne - star tracker	VIII-60
VIII-4-13	Outline drawing electronics	VIII-61
VIII-4-14	Functional block diagram - servo system	VIII-62
VIII-4-15	Vibrating-reed scanner	VIII-65
VIII-4-16	400-cycle error signals versus lateral image displacement	VIII-65
VIII-4-17	Relative amplitude of Star-presence signal (1600 cps) versus relative lateral image displacement	VIII-66
VIII-4-18	Relative amplitude of Star-presence signal versus reed amplitude	VIII-67
VIII-4-19	Magnitude of 400-cycle-error versus lateral image displacement with unequal reed amplitudes	VIII-68
VIII-4-20	Spectral response - S-4 surface	VIII-70
VIII-4-21	Partial open loop block diagram	VIII-80
VIII-4-22	Inner gimbal block diagram	VIII-82
VIII-4-23	Inner gimbal Bode diagram	VIII-83
VIII-4-24	Pointing mode - functional block diagram	VIII-84
VIII-4-25	Search signal mechanical block diagram	VIII-85
VIII-4-26	Star-presence circuit - functional block diagram	VIII-86

## LIST OF ILLUSTRATIONS (Continued)

Figure		Page
VIII-4-27	APOLLO functional block diagram — mid-course guidance, System no. 2	VIII-91
VIII-4-28	Primary measurements — cross-position error	VIII-99
VIII-4-29	Secondary constraints on measurement of the vertical	VIII-100
VIII-4-30	Cross-range position error	VIII-102
VIII-4-31	Altitude error using Earth diameter measurements	VIII-103
VIII-4-32	Altitude error using Moon diameter measurements	VIII-104
VIII-4-33	Altitude error using secondary measurements	VIII-105
VIII-4-34	Position error versus time	VIII-106
VIII-4-35	Typical lunar trajectory — retrograde motion	VIII-107
VIII-4-36	Velocity errors	VIII-109
VIII-5-1	Altitude error versus altitude	VIII-118
VIII-5-2	Scale drawing of orbit with apolune altitude of 1000 nmi and perilune altitude of 50 nmi	VIII-121
VIII-5-3	Altitude versus time for orbit with apolune altitude of 1000 nmi and perilune altitude of 50 nmi	VIII-121
VIII-5-4	Angle subtended by Moon versus time from orbit, with apolune altitude of 1000 nmi and perilune altitude of 50 nmi	VIII-122
VIII-5-5	Angular velocity of the radius vector versus time for orbit with apolune altitude of 1000 nmi and perilune altitude of 50 nmi	VIII-122
VIII-5-6	Radial velocity versus time for orbit with apolune altitude of 1000 nmi and perilune altitude of 50 nmi	VIII-123
VIII-5-7	Path velocity versus time for orbit with apolune altitude of 1000 nmi and perilune altitude of 50 nmi	VIII-123
VIII-5-8	Flight path angle (angle between path velocity and azimuth velocity) versus time for orbit with apolune altitude of 1000 nmi and perilune altitude of 50 nmi	VIII-124
VIII-5-9	Position of line of apsides versus time for orbit with apolune altitude of 921 nmi and perilune altitude of 57 nmi. Inclination of orbit plane of Moon's orbit is 11.3 degrees.	VIII-124
VIII-5-10	Inclination angle versus time for orbit with apolune altitude of 921 nmi and perilune altitude of 57 nmi. Inclination of orbit plane to plane of Moon's orbit is 11.3 degrees.	VIII-125
VIII-5-11	Position of line of nodes versus time for orbit with apolune altitude of 921 nmi and perilune altitude of 57 nmi. Inclination of orbit plane to plane of Moon's orbit is 11.3 degrees.	VIII-125
VIII-5-12	Eccentricity versus time for orbit with apolune altitude of 921 nmi and perilune altitude of 57 nmi. Inclination of orbit to plane of Moon's orbit is 11.3 degrees.	VIII-126
VIII-5-13	Lunar orbiting mode concept schematic	VIII-128
VIII-6-1	Re-entry system block diagram	VIII-133
VIII-6-2	Safe flight corridor boundaries	VIII-140
VIII-6-3	Maximum, minimum, and nominal range capability versus velocity	VIII-142

## LIST OF ILLUSTRATIONS (Continued)

Figure		Page
VIII-6-4	Altitude versus velocity for minimum range, B-2' configuration Runs 1 through 4	VIII-154
VIII-6-5	Altitude versus velocity for minimum range, B-2' configuration Runs 5 through 8	VIII-154
VIII-6-6	Altitude versus velocity for minimum range, B-2' configuration Runs 1 through 8	VIII-155
VIII-6-7	Altitude versus velocity for maximum range, B-2' configuration Runs 9 through 13	VIII-155
VIII-6-8	Altitude versus velocity for minimum range, B-2' configuration runs 9 through 13	VIII-156
VIII-6-9	Altitude versus velocity for maximum range, B-2' configuration Runs 14 through 18	VIII-156
VIII-6-10	Altitude versus velocity for maximum range, B-2' configuration Runs 14 through 18	VIII-157
VIII-6-11	Altitude versus velocity for minimum range, B-2' configuration Runs 19 through 22B	VIII-157
VIII-6-12	Altitude versus velocity for minimum range, B-2' configuration Runs 19 through 22B	VIII-158
VIII-6-13	Altitude versus velocity for minimum range, B-2' configuration Runs 23 through 26	VIII-158
VIII-6-14	Altitude versus velocity for minimum range, B-2' configuration Runs 23 through 26	VIII-159
VIII-6-15	Altitude versus velocity for minimum range, B-2' configuration Runs 27 through 29	VIII-159
VIII-6-16	Altitude versus velocity for minimum range, B-2' configuration Runs 27 through 29	VIII-160
VIII-6-17	Altitude versus velocity, banked at 45 degrees and unbanked, B-2" configuration	VIII-160
VIII-6-18	Altitude versus velocity, banked at 45 degrees and unbanked, B-2' configuration	VIII-161
IX-1-1	B-2 configuration	IX-2
IX-1-2	B-2 configuration — variation of lift coefficient with angle of attack (Newtonian)	IX-3
IX-1-3	B-2 configuration — variation of drag coefficient with angle of attack (Newtonian)	IX-4
IX-1-4	B-2 configuration — variation of lift-drag ratio with angle of attack (Newtonian)	IX-5
IX-1-5	B-2 configuration — variation of moment coefficient with angle of attack (Newtonian)	IX-6
IX-1-6	B-2 configuration — comparison of experimental and calculated variation of lift-drag ratio with angle of attack	IX-7
IX-1-7	C-1 configuration	IX-8

## LIST OF ILLUSTRATIONS (Continued)

Figure		Page
IX-1-8	C-1 configuration — variation of lift coefficient with angle of attack (hypersonic)	IX-9
IX-1-9	C-1 configuration — variation of drag coefficient with angle of attack	IX-9
IX-1-10	C-1 configuration — variation of lift-drag ratio with angle of attack (hypersonic)	IX-10
IX-1-11	Newtonian forebody lift-drag ratio for spherical segments	IX-11
IX-1-12	Variation of lift-drag ratio with afterbody radius and angle	IX-12
IX-1-13	D-2 configuration	IX-13
IX-1-14	D-2 configuration — variation of lift coefficient with angle of attack	IX-14
IX-1-15	D-2 configuration — variation of drag coefficient with angle of attack	IX-15
IX-1-16	D-2 configuration — variation of moment coefficient with angle of attack	IX-16
IX-1-17	D-2 coefficient — variation of lift-drag ratio with angle of attack	IX-17
IX-1-18	D-2 configuration — variation of lift coefficient versus Mach number	IX-18
IX-1-19	D-2 configuration — variation of the pitching moment versus Mach number	IX-18
IX-1-20	High L/D glider design	IX-20
IX-1-21	Hypersonic characteristics of the high L/D glider	IX-21
IX-1-22	High attitude configuration	IX-22
IX-1-23	Hypersonic longitudinal characteristics — high attitude glider	IX-23
IX-1-24	R-3 configuration re-entry vehicle	IX-24
IX-1-25	Hypersonic longitudinal characteristics — modified lenticular shape	IX-25
IX-1-26	Hypersonic lateral stability characteristics — fins folded	IX-26
IX-1-27	Modified lenticular shape — lateral aerodynamic center	IX-27
IX-1-28	Low-speed L/D comparison — clean configurations	IX-28
IX-2-1	C-1 configuration — total heat flux of the stagnation point, re-entry angle, $\Theta_E = 5.7$ degrees	IX-31
IX-2-2	C-1 configuration — total heat flux at selected stations*, re-entry angle, $\Theta_E = 5.7$ degrees	IX-31
IX-2-3	C-1 configuration — total heat flux at selected stations between windward and leeward stations, re-entry angle, $\Theta_E = 5.7$ degrees	IX-32
IX-2-4	C-1 configuration — total heat flux at the stagnation point, re-entry angle, $\Theta_E = 8.7$ degrees	IX-33
IX-2-5	C-1 configuration — total heat flux at selected stations, re-entry angle, $\Theta_E = 8.7$ degrees	IX-33
IX-2-6	C-1 configuration — total heat flux at selected stations between windward and leeward, re-entry angle, $\Theta_E = 8.7$ degrees	IX-34

~~CONFIDENTIAL~~

## LIST OF ILLUSTRATIONS (Continued)

Figure		Page
IX-2-7	B-2 configuration — effect of wall temperature on convective heat flux at the B-2 stagnation point, re-entry angle, $\Theta_E = 6$ degrees	IX-34
IX-2-8	B-2 configuration — effect of wall temperature on convective heat flux at the stagnation point, re-entry angle, $\Theta_E = 7.6$ degrees	IX-35
IX-2-9	C-1 configuration — effect of wall temperature on convective heat flux at the stagnation point, re-entry angle, $\Theta_E = 5.7$ degrees	IX-35
IX-2-10	C-1 configuration — effect of wall temperature on convective heat flux at the stagnation point, re-entry angle, $\Theta_E = 8.7$ degrees	IX-36
IX-2-11	Heats of ablation — phenolic/nylon	IX-37
IX-2-12	C-1 configuration — re-radiation equilibrium temperatures, re-entry angle, $\Theta_E = 5.7$ degrees, emissivity = 0.9	IX-40
IX-2-13	Typical ablation heat protection system	IX-42
IX-2-14	Composite graphite heat protection system	IX-42
IX-2-15	Graphite oxidation regimes	IX-46
IX-2-16	Heat flux during boost	IX-47
IX-2-17	Space vehicle temperature during lunar orbit	IX-50
IX-2-18	Radiator requirements — 3000 watts continuous internal heat	IX-52
X-1-1	Typical terminal trajectory — APOLLO. Equilibrium glide [ $C_L$ at $L/D$ max]	X-4
X-1-2	Drag ( $C_{DA}$ ) versus impact velocity	X-6
X-1-3	Opening force versus altitude—reefed parachute	X-7
X-1-4	System I—Terminal (retardation) trajectory. Payload weight = 10,000 pounds	X-13
X-1-5	System II—Terminal (retardation) trajectory. Payload weight = 7,000 pounds	X-14
X-1-6	System III—Terminal (retardation) trajectory. Payload weight = 7,000 pounds	X-15
X-1-7	System IVA—Terminal (retardation) trajectory. Payload weight = 5,000 pounds	X-16
X-1-8	System IVB—Terminal (retardation) trajectory. Payload weight = 5,000 pounds	X-17
X-1-19	System II and System III—Altitude versus retardation trajectory	X-18
X-1-10	System II versus System III—Comparison of altitude difference versus velocity along the terminal trajectory	X-19
X-1-11	System III—Altitude of first-stage deployment versus descent velocity at 15,000 feet	X-20

## LIST OF ILLUSTRATIONS (Continued)

Figure		Page
X-1-12	System III—Altitude of first-stage deployment versus terminal trajectory $V, q, g$	X-21
X-1-13	System II and System III—Altitude versus range	X-23
X-1-14	System III—Altitude of first-stage deployment versus $\Delta$ range (referenced to System III first-stage deployment at $h_{\max} = 68,000$ feet)	X-24
X-1-15	System III—Altitude of first-stage deployment versus $\Delta$ range (referenced to System II first-stage deployment at $h = 80,000$ feet)	X-25
X-1-16	System IVA and System IVB—Altitude versus range	X-26
X-1-17	System III—Trajectory tolerance effect, altitude versus range	X-28
X-1-18	Typical abort trajectory for parachute study	X-30
X-1-19	Typical abort trajectory for parachute study	X-30
X-1-20	Typical abort trajectory range including retardation	X-31
X-1-21	Typical recovery trajectories indicating the effects of a paraglider	X-33
X-1-22	Position corrections available utilizing a paraglider for lift augmentation equilibrium glide	X-33
X-1-23	Lift-drag augmentation required for maneuvering a ballistic-type re-entry vehicle	X-34
X-1-24	Paraglider area required for terminal maneuverability	X-35
X-1-25	Schematic of spiral descent maneuver	X-36
X-1-26	Spiral radius as a function of velocity, load factor = $3g$	X-38
X-1-27	Lift-drag maneuver ratio required for spiral descent; $3g$ maneuver equilibrium glide	X-39
X-1-28	Lift augmentation required to initiate spiral maneuver	X-39
X-1-29	Increment of area to be supplied by paraglider	X-40
X-1-30	Paraglider area required spiral maneuver	X-40
X-1-31	Drag area ( $C_D A$ ) versus final-stage canopy weight, other 'chutes	X-41
X-1-32	Supersonic spiked parachute configuration	X-42
X-1-33	Flexi-rotor weight versus payload weight. Flareout at $h=0$ .	X-47
X-1-34	Impact attenuation study	X-48
X-1-35	Landing bag performance, $\gamma = 10^4 \text{ ft}^2/\text{sec}^2$	X-50
X-1-36	Landing bag performance, $\gamma = 10^5 \text{ ft}^2/\text{sec}^2$	X-51
X-1-37	Landing bag performance, $\gamma = 5 \times 10^5 \text{ ft}^2/\text{sec}^2$	X-52
X-1-38	Landing bag performance, $\gamma = 10^6 \text{ ft}^2/\text{sec}^2$	X-53
X-1-39	Internal pressure differential across bag wall	X-54
X-1-40	Landing bag impact attenuation system, B-2 configuration	X-55
X-1-41	Landing bag impact attenuation and flotation	X-56
X-1-42	Retardation system weight versus impact velocity	X-58
X-1-43	Impact attenuation system weight versus impact velocities	X-59
X-1-44	Total landing plus recovery system weight versus impact velocity	X-60
X-2-1	Rate-of-sink criteria	X-65

~~CONFIDENTIAL~~

## LIST OF ILLUSTRATIONS (Continued)

Figure		Page
X-2-2	Velocity loss from flare initiation to touchdown	X-67
X-2-3	Low L/D landing analysis	X-67
X-2-4	L/D and approach speeds for acceptable landing characteristics	X-68
X-3-1	APOLLO flotation system	X-71
X-4-1	Schematic representation of major recovery phases	X-75
X-4-2	Block diagram of recovery aid system	X-79



## LIST OF TABLES

Table		Page
VIII-2-1	Total RMS Insertion Errors	VIII-5
VIII-2-2	Instrument Errors (Three Sigma)	VIII-6
VIII-2-3	Matrix Elements Relating Lunar Position and Velocity Variations to Insertion Errors	VIII-11
VIII-2-4	Three-Sigma Lunar Aimpoint Errors for Estimated Insertion Errors	VIII-11
VIII-2-5	Outbound Leg Mid-Course Corrections	VIII-12
VIII-2-6	Lunar Aimpoint Errors	VIII-14
VIII-2-7	Lunar Escape Sensitivities for "Figure-Eight" Return Trajectory	VIII-19
VIII-2-8	Representative Return Leg Mid-Course Corrections	VIII-23
VIII-2-9	Comparison of Effect of Velocity Measurement Errors	VIII-24
VIII-4-1	Stellar Magnitude — Luminous Flux	VIII-59
VIII-4-2	Weight Tabulation	VIII-75
VIII-4-3	Motor Characteristics — Inland Type T-2108B	VIII-78
VIII-7-1	Mark 3C TP Type Infrared Horizon Scanning System Performance Data	VIII-167
VIII-7-2	Nimbus Type, Infrared Horizon Scanning System Performance Data	VIII-168
VIII-7-3	Advent-Type Infrared Horizon Scanning System Performance Data	VIII-169
VIII-7-4	Performance Data Advent Coarse Sun Sensor	VIII-171
VIII-7-5	Performance Data Nimbus Fine Sun Sensor	VIII-171
VIII-8-1	Navigation, Control, and Guidance System Summary, System No. 1	VIII-173
VIII-8-2	Navigation, Control, and Guidance System Summary, System No. 2	VIII-174
IX-2-1	Heat Protection for APOLLO Vehicles	IX-38
X-1-1	Preliminary Descriptions of APOLLO Retardation Systems	X-8
X-1-2	Preliminary Data for ROR and Escape System	X-45
X-4-1	Phase/Recovery Aid Program	X-77



## **CHAPTER VII**

# **FLIGHT MECHANICS**

~~CONFIDENTIAL~~

## VII. FLIGHT MECHANICS

### 1. POWER ASCENT TRAJECTORY

The Saturn-powered ascent trajectory, required to place the APOLLO vehicle on its free-flight trajectory to the Moon, must be selected on the basis of a trade-off of several criteria. Some of the factors influencing the choice of a nominal Saturn trajectory are:

- Allowable APOLLO weight
- Tracking geometry
- Flexibility of firing schedules
- Abort and emergency return velocity requirements

These criteria will be discussed in the order listed and then a tentative selection of a nominal ascent trajectory, for study purposes, will be made.

The allowable gross weight of the APOLLO vehicle which can be boosted to the velocity required for the free-flight transit trajectory is a function of the burnout path angle, the firing azimuth, and the total energy of the transit trajectory. The largest Saturn payload capacity is achieved with a due east launch from Cape Canaveral with as low a path angle as practical for a given transit trajectory energy (which would define a transit trajectory to the Moon corresponding to a "figure 8" or "modified ellipse" circumlunar trajectory, for example). Plotting the Saturn burnout weight (empty third stage plus APOLLO) indicates that a path angle of about 1.5 degrees, corresponding very nearly to NASA's Case I, results in the maximum weight at escape velocity, since the available weight would be reduced at lower path angles because of increased drag during powered flight. In addition, these lower path angles, at the corresponding lower altitudes, result in larger drag losses during the free-flight coast up to an altitude of the order of 1,000,000 feet.

~~CONFIDENTIAL~~

~~CONFIDENTIAL~~

The ground-based tracking and communications require that the vehicle be visible from available or planned sites. The critical portion of the trajectory from the tracking point-of-view is the powered ascent and the first few thousand miles of altitude on the free-flight trajectory. The very shallow ascent trajectories require that the Earth-surface traces pass very nearly over the array of tracking sites. The tracking complex set up by the Atlantic Missile Range, which lies on an azimuth of about 106 degrees east of north, could serve as a tracking network for the APOLLO mission and allow launch azimuths to vary between approximately 105 and 108 degrees east of north.

The flexibility of firing schedules should also be considered in the selection of a nominal Saturn ascent trajectory. If a continuously powered ascent trajectory is chosen, it will have a fixed range to burnout. This would require that the launch azimuth be changed as the Moon's declination at close approach is varied. With a powered-ascent range of about 2160 miles, the allowable variation in accessible lunar declinations is limited to values between approximately -15 and -28.5 degrees. The launch azimuths required would vary from approximately 90 to 120 degrees for this declination variation, and thus require the use of ship-based tracking and communication networks. The locus of abort stations would also have to be shifted as the launch azimuth is changed. Once the APOLLO vehicle has reached an altitude of 8 to 10,000 miles, it could be tracked by the NASA deep-space net stations as planned.

The velocity increment required for abort during powered ascent, especially in the portion of the trajectory when the vehicle's velocity is between orbital and approximately escape, increases with positive instantaneous path angles. This should not be a limiting criterion for trajectories with final burnout path angles of five degrees or less since the APOLLO vehicle designed for the lunar orbit and return mission will have the "built-in" velocity capability of 6000 to 7000 feet/second which could be used to change the trajectory to one which leads to a satisfactory re-entry velocity vector.

On the basis of the preceding discussion of several criteria, the nominal Saturn-powered ascent trajectory for the APOLLO mission is chosen as Case III of the NASA Saturn Performance data report. This trajectory passes through a horizontal attitude as the velocity passes through orbital velocity at an altitude of about 650,000 feet. The third-stage engines could, therefore, be shut down at that point and the vehicle allowed to

~~CONFIDENTIAL~~

~~CONFIDENTIAL~~

coast in a circular orbit to adjust the latitude-longitude coordinates of the burnout point to reach the vicinity of the Moon at declinations varying between the maximum positive and negative values. After the appropriate coasting arc, the third stage engine would be re-started to gain the remaining required velocity. The burnout path angle for this case is approximately 3.0 degrees at an altitude of about 750,000 feet.

Some consideration is still being given to Saturn ascent trajectories which are defined by more shallow burnout path angles, because of the payload increase with decreasing angle. For example, the allowable Saturn payload increases by about 500 pounds as the burnout path angle is decreased from 3.0 degrees to a value of 1.6 degrees.

~~CONFIDENTIAL~~

~~CONFIDENTIAL~~

## 2. BURNOUT POINT SELECTION

The selection of the set of initial parameters for the free-flight transfer trajectory to the vicinity of the Moon can be accomplished by the use of spherical trigonometry. A computer program has been written to aid in the determination of these initial conditions for the "n-body" trajectory program. This program considers the launch point on a rotating Earth and also includes the in-plane range of the booster. The input values are the booster range and estimates of the in-plane transit angle from injection to the Moon and the free-flight time.

The output quantities are:

- Latitude and longitude at injection
- Declination and right ascension at injection
- Azimuth at both launch and injection - The program is set up to restrict azimuths which are within range safety limits.
- The components of velocity and position as well as launch time in a form which is compatible with the G-E "n-body" program.

Figure VII-2-1 presents the accessible declinations of the Moon as a function of the total in-plane transit angle, which is the sum of the powered range and the free-flight transit angle. As the total in-plane angle approaches 180 degrees the allowable lunar declination variation converges to 28.5 degrees, which is the maximum declination of the Moon during its 18.6-year period. The total in-plane angles appropriate to this study range upwards from 205 degrees, so that the range of accessible lunar declination widens out.

The latitude-longitude coordinates of the injection points for launch from Cape Canaveral are given in Figure VII-2-2 for an injection path angle of zero degrees. Also indicated on this graph are the range safety limit on launch azimuth and the declination limit of the Moon. The coordinates are also shown for ascent trajectories with various coasting ranges during interrupted burning phase.

~~CONFIDENTIAL~~

An interesting aspect of this graph shows that all launch azimuths are in a south-easterly direction because of the lunar declination limits and the characteristics of the booster (low injection angles and long ascent ranges).

The vehicle can be sent to the vicinity of the Moon over a narrow range of declinations by varying the launch azimuth. By varying the length of the coasting arc during powered ascent, the spread of lunar declinations which are accessible is increased considerably.

~~CONFIDENTIAL~~

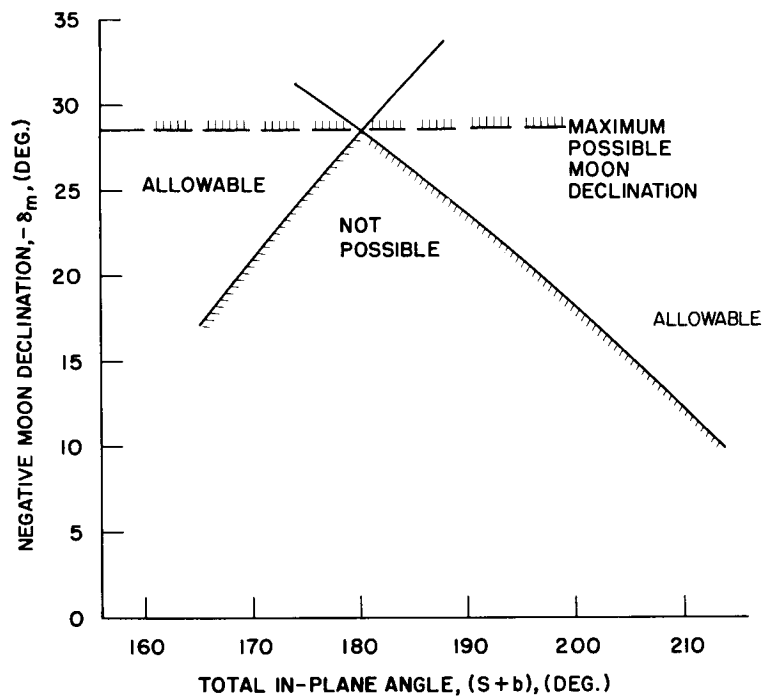


Figure VII-2-1. Range safety limits on Moon declination

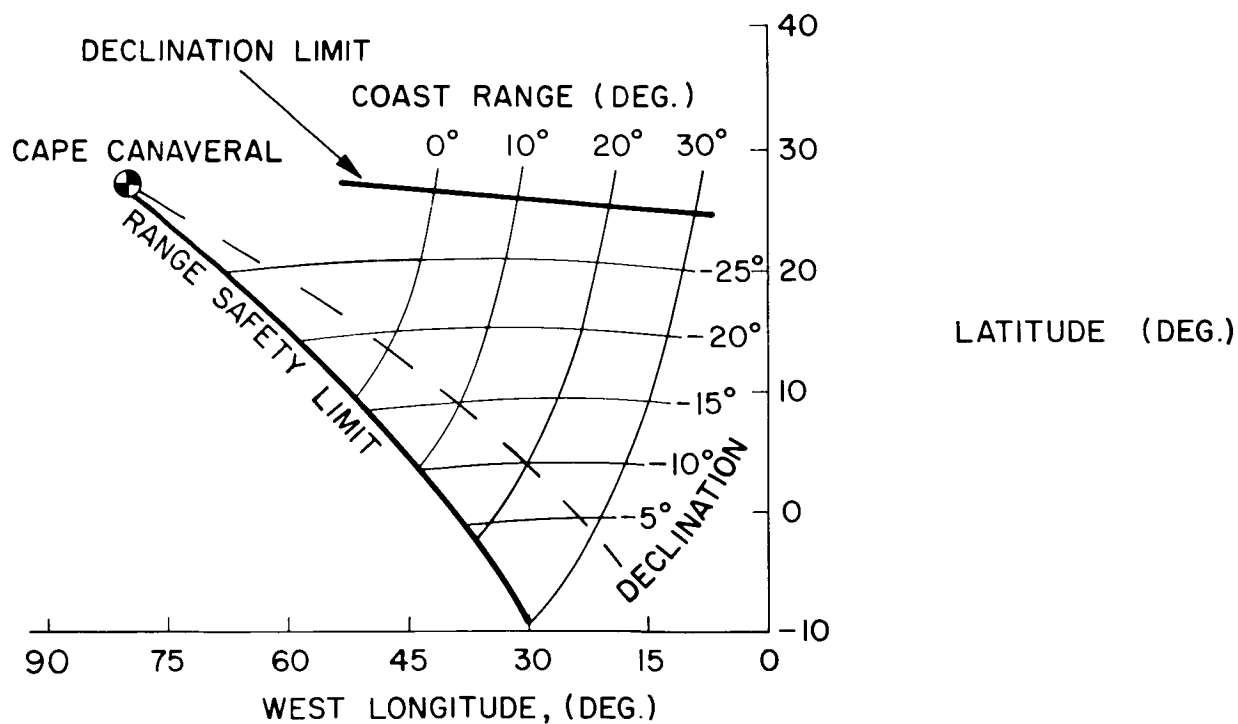


Figure VII-2-2. Launch parameters for lunar missions



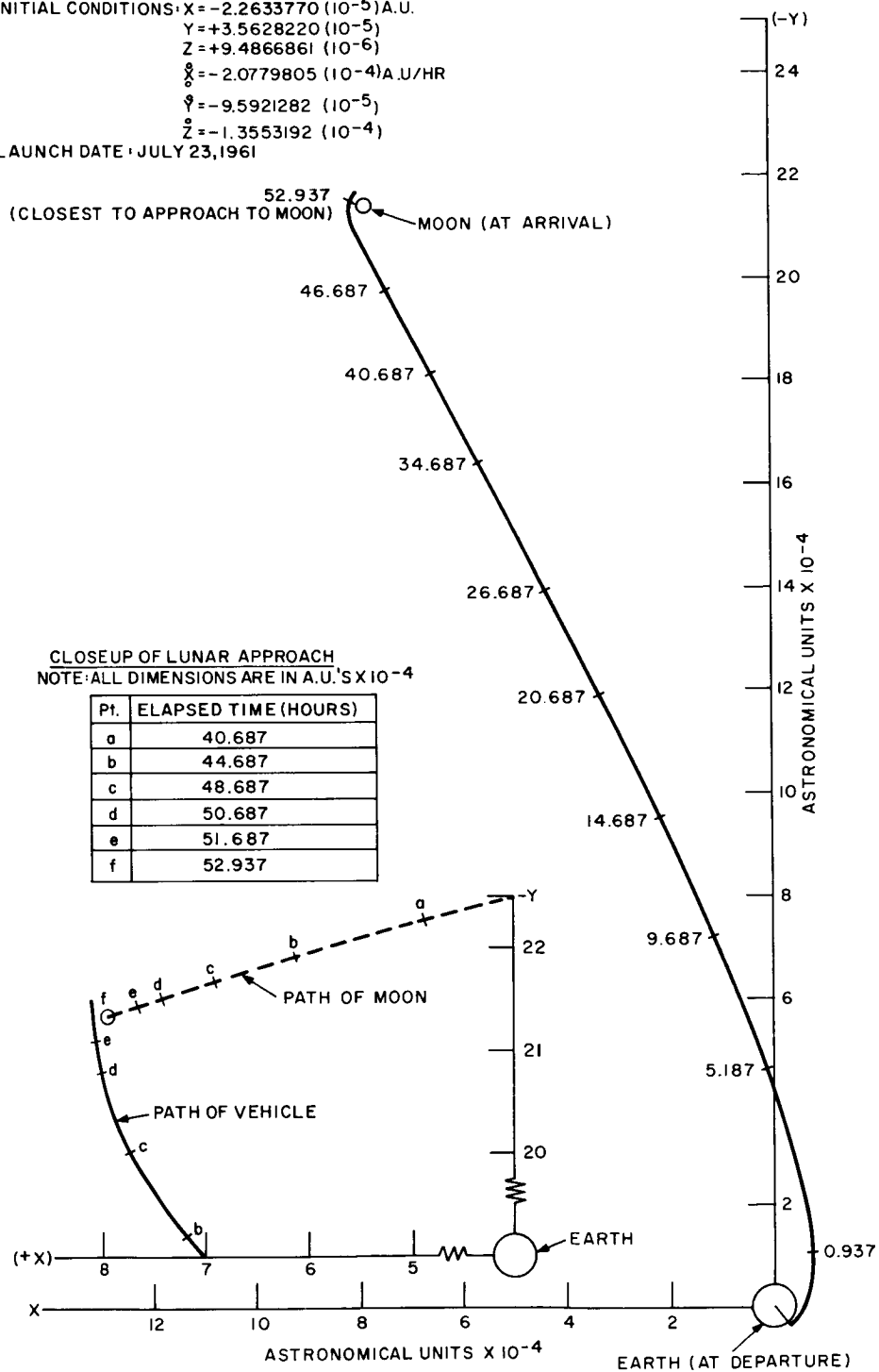
### 3. SAMPLE TRANSIT TRAJECTORY

A sample transfer trajectory from the Earth to the vicinity of the Moon is shown in an earth-equatorial projection in Figure VII-3-1. The initial velocity for this sample is 36,240 feet/second at an injection altitude of 60 miles and corresponds to a "modified ellipse" type of circumlunar trajectory with a closest approach to the Moon at an altitude of about 1050 statute miles. The Moon, whose declination at the point of close approach is -18 degrees, is about 70,000 miles below the x-y plane. The point of closest approach to the Moon is at a relative z-position of zero. The z-component of the vehicle's velocity, however, is not zero, so that the lunar orbital plane will be inclined relative to the Moon's equator.

The z-coordinate relative to the Moon at the point of closest approach is shown as a function of the azimuth at injection for various injection times in Figure VII-3-2. The point, labelled A-1, corresponds to the trajectory shown in Figure VII-3-1.

Figure VII-3-3 presents a cross plot of the data in Figure VII-3-2 to give the launch time-azimuth combinations for perilune to occur at a relative z value of zero. Figure VII-3-4 presents the corresponding close approach or perilune radius as a function of launch time. The portion of the curve above the band labelled "Moon" corresponds to trajectories which pass ahead of the Moon in its orbit and would lead to satellites orbits which are in retrograde motion. The portion of the curve below the band corresponds to trajectories which cross the lunar orbit after the Moon has passed and would result in orbits in direct motion.

INITIAL CONDITIONS:  $X = -2.2633770 (10^{-5})$  A.U.  
 $Y = +3.5628220 (10^{-5})$   
 $Z = +9.4866861 (10^{-6})$   
 $\dot{X} = -2.0779805 (10^{-4})$  A.U./HR  
 $\dot{Y} = -9.5921282 (10^{-5})$   
 $\dot{Z} = -1.3553192 (10^{-4})$   
 LAUNCH DATE: JULY 23, 1961



\* NOTE: NUMBERS ON TRAJECTORY INDICATE TIME ELAPSED (SINCE DEPARTURE FROM EARTH) IN HOURS

Figure VII-3-1. Circumlunar trajectory retrograde class\*

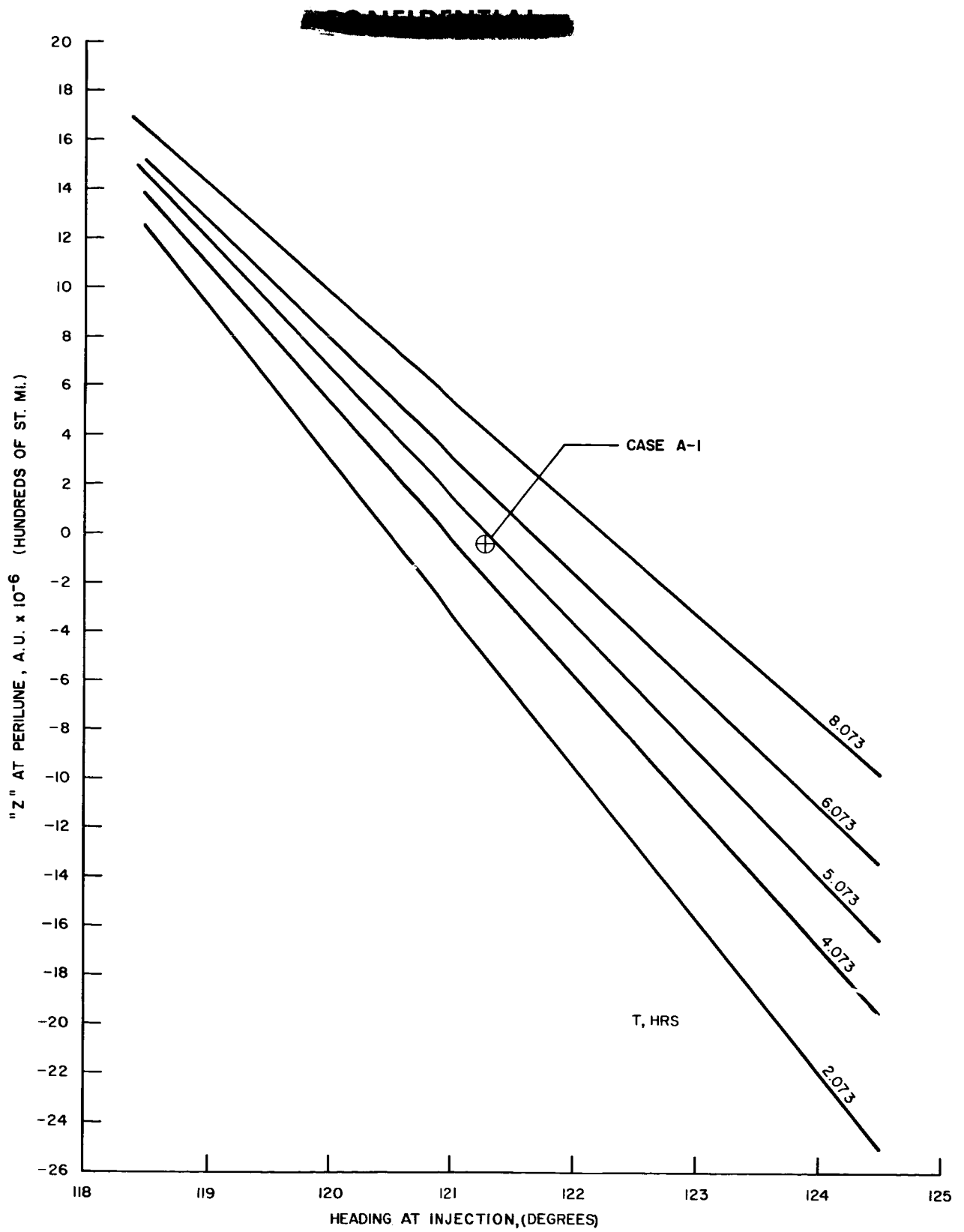


Figure VII-3-2. North-south miss distance

~~CONFIDENTIAL~~

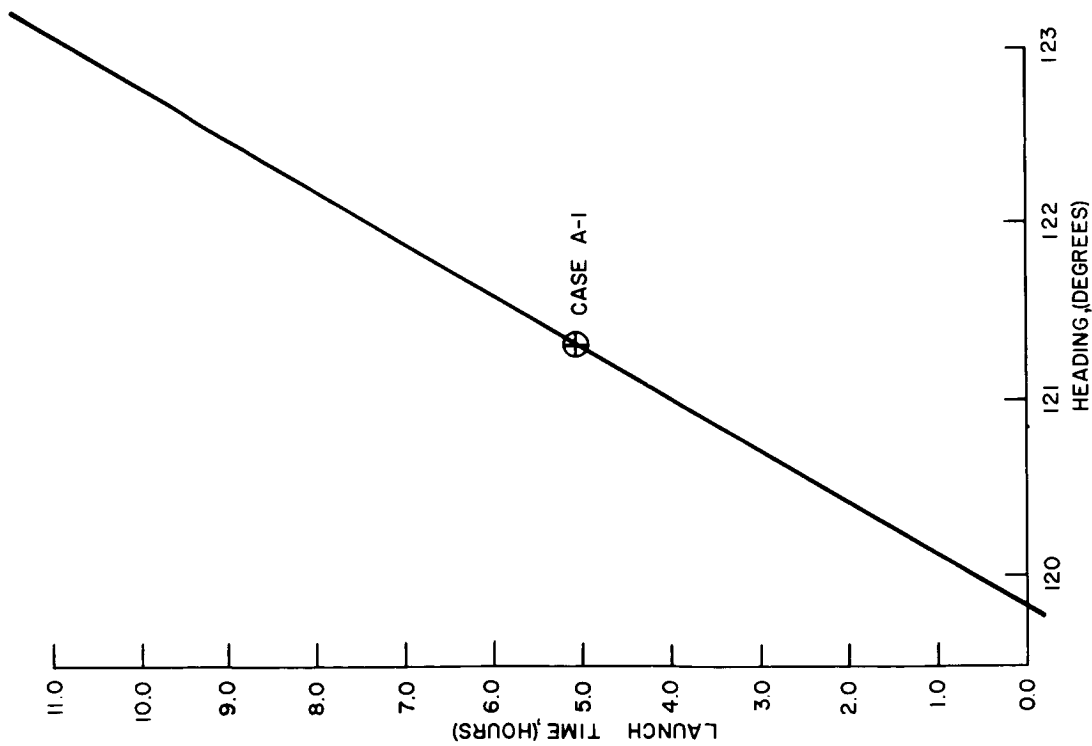


Figure VII-3-3. Conditions for  $z = 0$

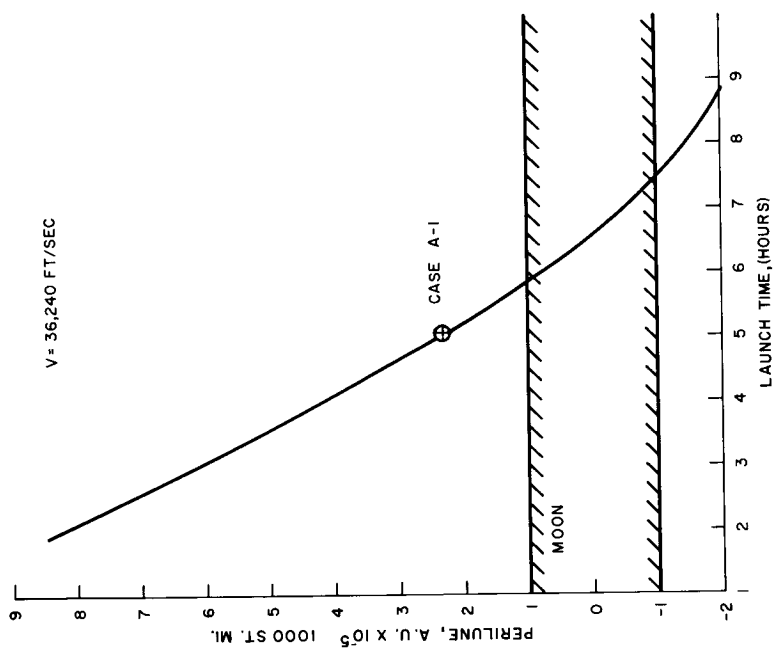


Figure VII-3-4. Launch time for  $z = 0$

~~CONFIDENTIAL~~

~~CONFIDENTIAL~~

#### 4. EMERGENCY RETURN TRAJECTORIES

##### INTRODUCTION

These paragraphs present some preliminary results of a study of "emergency return" trajectories. This term is used to differentiate trajectories which are initiated during the free-flight portion of the mission from "abort" trajectories which are initiated during the powered ascent phase. The aim of both the "abort" and "emergency return" trajectories is to shorten the mission duration and to place the vehicle on a trajectory which has an acceptable velocity — path-angle combination at the re-entry altitude of 400,000 feet.

Emergency return trajectories can be considered to be initiated during the three major trajectory phases of the APOLLO lunar orbit mission. These are: (1) outbound transfer trajectory, (2) lunar orbit phase, and (3) return trajectory phase. The present study is restricted to the outbound transfer phase of the mission.

It can be assumed that the velocity increments to be used to enter and leave the lunar orbit would be available for use in effecting an emergency return to Earth. The velocity increment used to enter the lunar orbit will be of the order of 3000 to 3500 ft/sec, depending on the transfer time, and the dis-orbit velocity increment is expected to be of the same order of magnitude. Thus, velocity increments as large as 6000 to 7000 ft/sec would be used to initiate the return trajectories.

In the case of the continuous circumlunar mission for APOLLO, a propulsion system with approximately this same velocity capability would have to be provided.

##### DISCUSSION

For the purposes of this study, the outbound transfer trajectory from the Earth to the Moon is approximated by an unperturbed elliptical orbit relative to an isolated earth. The instantaneous values of velocity and path angle for this trajectory are shown as a

~~CONFIDENTIAL~~

~~CONFIDENTIAL~~

function of altitude in Figure VII-4-1. Selected points on this trajectory ranging from an altitude of a few hundred miles to about 100,000 miles were used to initiate the emergency return trajectories by the addition of a velocity increment,  $\Delta V$ . The geometry of this vector addition is sketched in Figure VII-4-2. The vector velocity increment is defined by its magnitude  $\Delta V$  applied at an angle,  $\delta$ , relative to the initial velocity,  $V_o$ , as sketched. The positive sense of this angle is shown. The emergency return trajectory is defined by the resultant velocity,  $V_i$ , at an angle,  $\gamma_i$ , relative to the local horizontal.

After passing through apogee, at an altitude,  $h_a$ , (in most cases), the trajectory passes through the re-entry altitude of 400,000 feet with a velocity,  $V_e$ , at a path angle,  $\gamma_e$ . Figure VII-4-3 shows the angle  $\delta$  required for various  $\Delta V$ 's to return to re-entry altitude with a typical path angle of 5 degrees as a function of altitude. There is little shift of this angle with entry path angle for initial altitudes greater than about 5000 miles, indicating rather high sensitivities,  $\frac{\partial \gamma_e}{\partial \delta}$ , at these altitudes.

The corresponding re-entry velocity,  $V_e$ , is shown in Figure VII-4-4 for various increments. Also indicated on the graph are the values of escape and circular orbital velocities at re-entry altitude. The velocity corresponding to the nominal outbound trajectory at this altitude ( $\Delta V=0$ ) is approximately 36,150 ft/sec.

The apogee altitude, through which the return trajectory passes, is shown in Figure VII-4-5 as a function of initial altitude for various  $\Delta V$ 's. The line for  $h_o = h_a$ , corresponding to apogee of the return ellipse (see Figure VII-4-2) is also included. The locations of the peaks of the Van Allen radiation belts are indicated approximately along the apogee scale. Return trajectories initiated at altitudes from 100 to 5,000 miles by velocity increments from 6000 to 8000 ft/sec are seen to have apogees which lie between the peaks of the two radiation belts.

The flight time from the initial altitude to re-entry is shown in Figure VII-4-6 as a function of altitude for various velocity increments. The effect of re-entry path angle from 0 to 10 deg. is seen to be of the order of one hour or less. Returns initiated from altitudes above 10,000 miles with a velocity increment of 4000 ft/sec or less are seen to result in flight times of the order of one day or more.

~~CONFIDENTIAL~~

**CONFIDENTIAL**

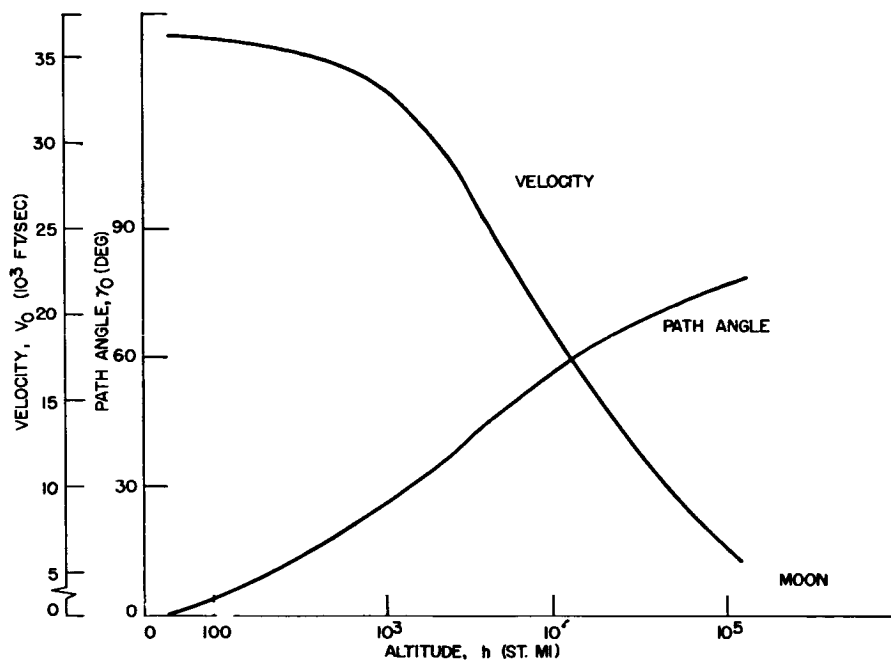


Figure VII-4-1. Typical transit trajectory

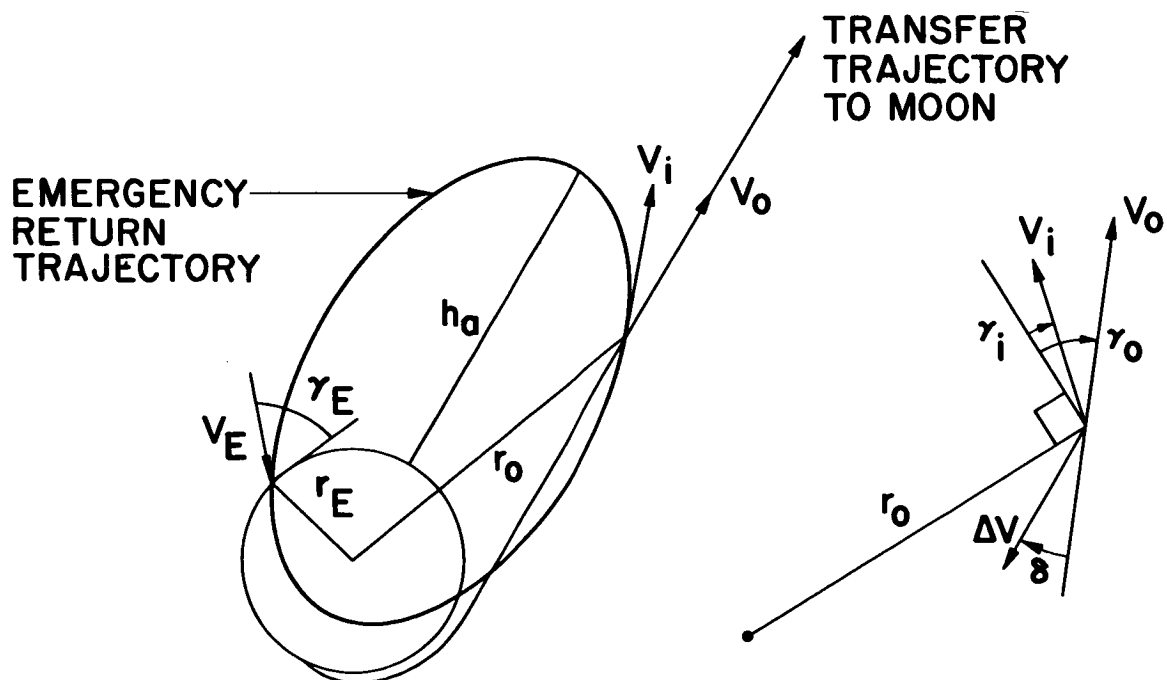


Figure VII-4-2. Emergency return trajectory

**CONFIDENTIAL**

~~CONFIDENTIAL~~

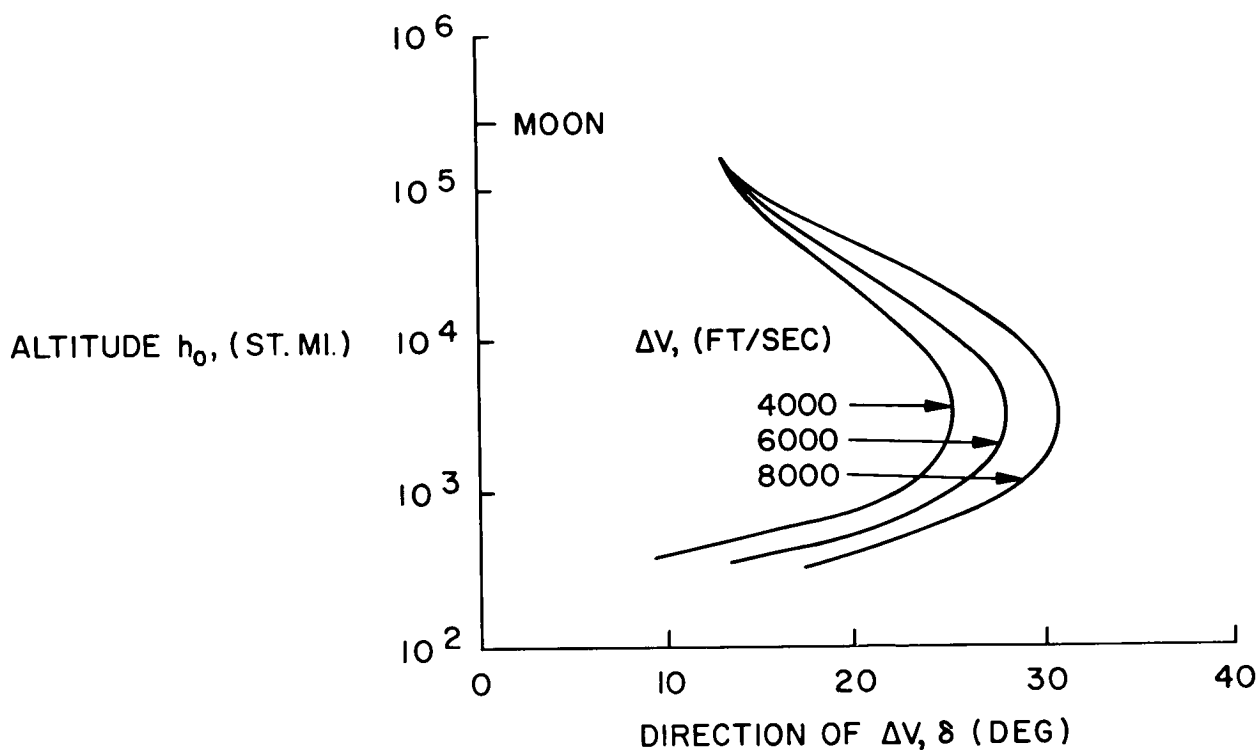


Figure VII-4-3. Emergency return orientation of  $\Delta V$  vector for  $\gamma_E = 5.0$  degrees

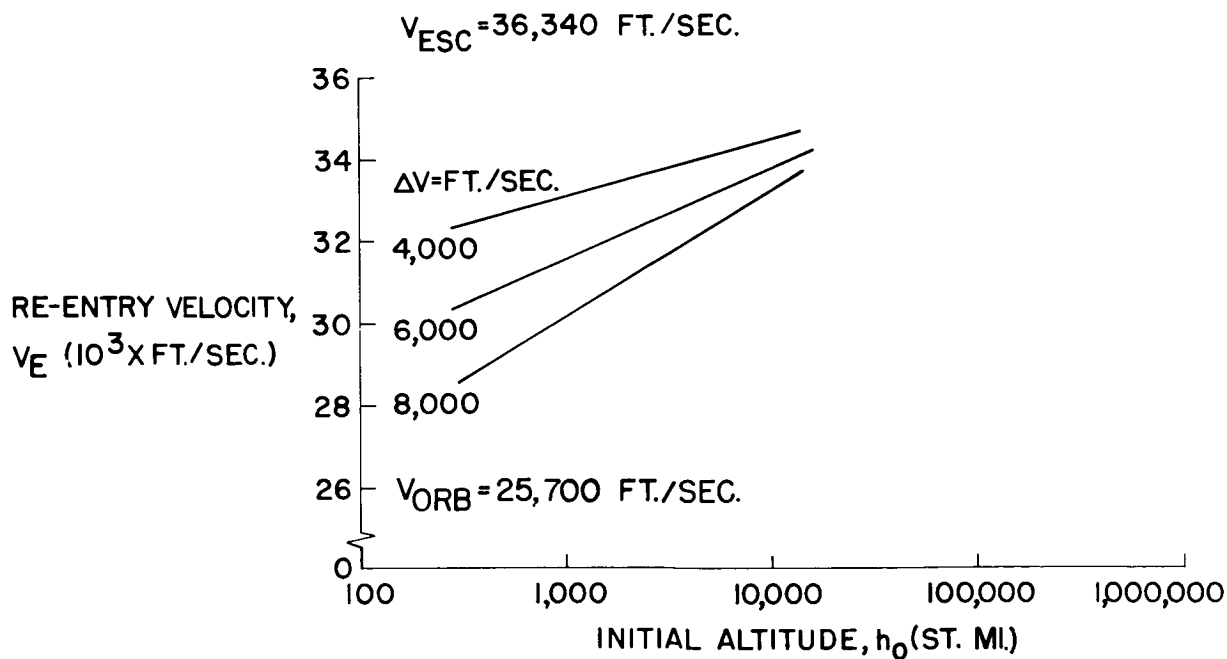


Figure VII-4-4. Emergency return re-entry velocity

~~CONFIDENTIAL~~



INITIAL ALTITUDE,  
 $h_0$  (ST. MI.)

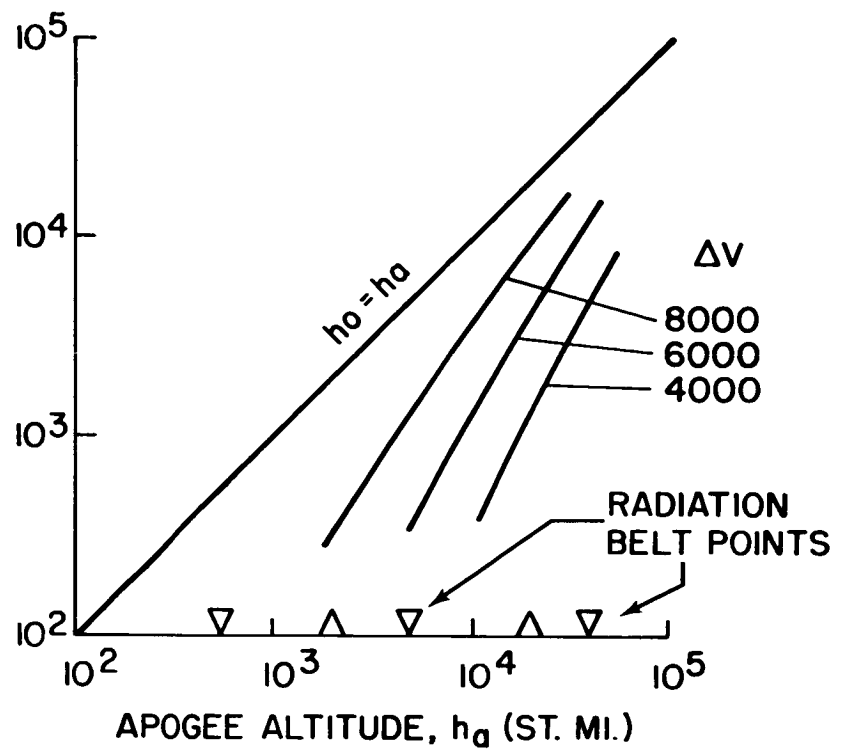


Figure VII-4-5. Emergency return apogee altitude versus initial altitude

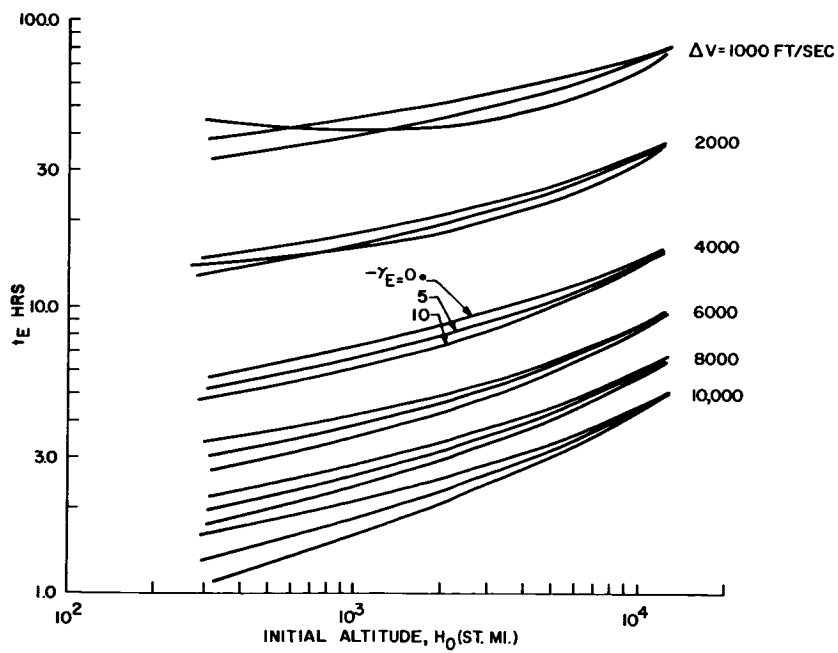


Figure VII-4-6. Time to re-entry versus initial altitude for various  $\Delta V$  values

~~CONFIDENTIAL~~

The information on the latitude-longitude coordinates of the re-entry point is not available for inclusion in this preliminary note. Since the Saturn launch azimuth will be in the range from 90 to 110 degrees east of north, however, the tangent latitudes of the Earth surface traces will be between 28 and about 35 degrees. The inclination of the plane of the return trajectory could be changed slightly by the use of a three-dimensional velocity increment to initiate the return trajectory. This feature has not been investigated as yet.

~~CONFIDENTIAL~~

## 5. VELOCITY INCREMENT FOR LUNAR ORBIT ENTRY

As it approaches the Moon from the Earth, the APOLLO vehicle's energy is hyperbolic relative to the Moon. Thus, a velocity increment must be applied to the vehicle at the appropriate altitude to reduce its velocity to a value which is less than the local escape velocity to allow it to be captured and remain in orbit around the Moon.

The magnitude of the required velocity increment is a function of both the burnout velocity at the Earth (or equivalent transit time) and also the altitude of the close approach, or perilune distance. It is assumed that the velocity increment will be applied when the vehicle is at perilune ( $\gamma = 0$  deg) and in a direction opposite to the velocity vector.

The "work statement" specifies that the lunar orbit be an ellipse with a maximum altitude, beyond the Moon, of 1000 to 2000 miles and a minimum altitude, on the near side, of 50 to 100 miles. The corresponding lunar orbital periods will range from three to five hours as a function of the average altitude.

The approach velocity as a function of the initial distance of closest approach is shown in Figure VII-5-1 for transfer trajectories with launch velocities typical of the two classes of trajectories. The corresponding flight times to the Moon are about 2.6 days and 3.0 days for the "modified ellipse" and "figure-8" trajectories, respectively.

Figure VII-5-2 presents the velocity increment required at the initial close approach altitudes of 1000 and 2000 in nmi to place the vehicle into elliptical orbits with perilune radii ranging from 0 to 100 nmi. Curves are given for transit trajectories corresponding to a "figure-8" as well as a "modified ellipse" case.

It can be seen that velocity increment of a fixed value can place the vehicle into lunar orbits of varying dimensions because of the slopes of the curves in Figure VII-5-2. For example, an increment of 3050 ft/sec can be used to establish orbits which range between altitude limits of 1000 and 35 nmi to 2000 and 85 nmi.

A final selection of the characteristics of the lunar orbit has not yet been made, pending the results of an analysis of the velocity increment required for exit from the lunar orbit for the return transfer trajectory to Earth.

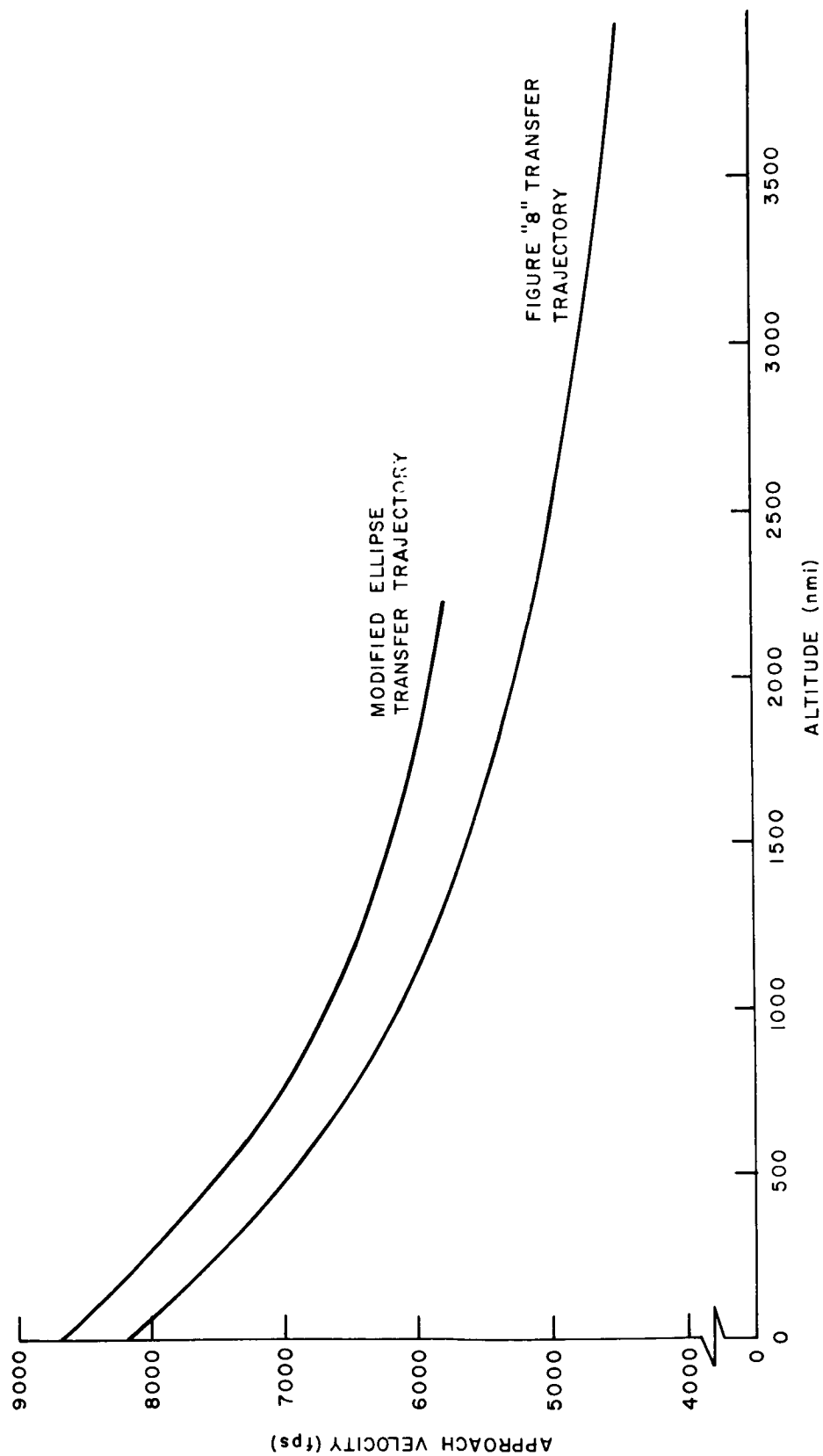


Figure VII-5-1. Approach velocity relative to the Moon versus altitude at the distance of closest approach

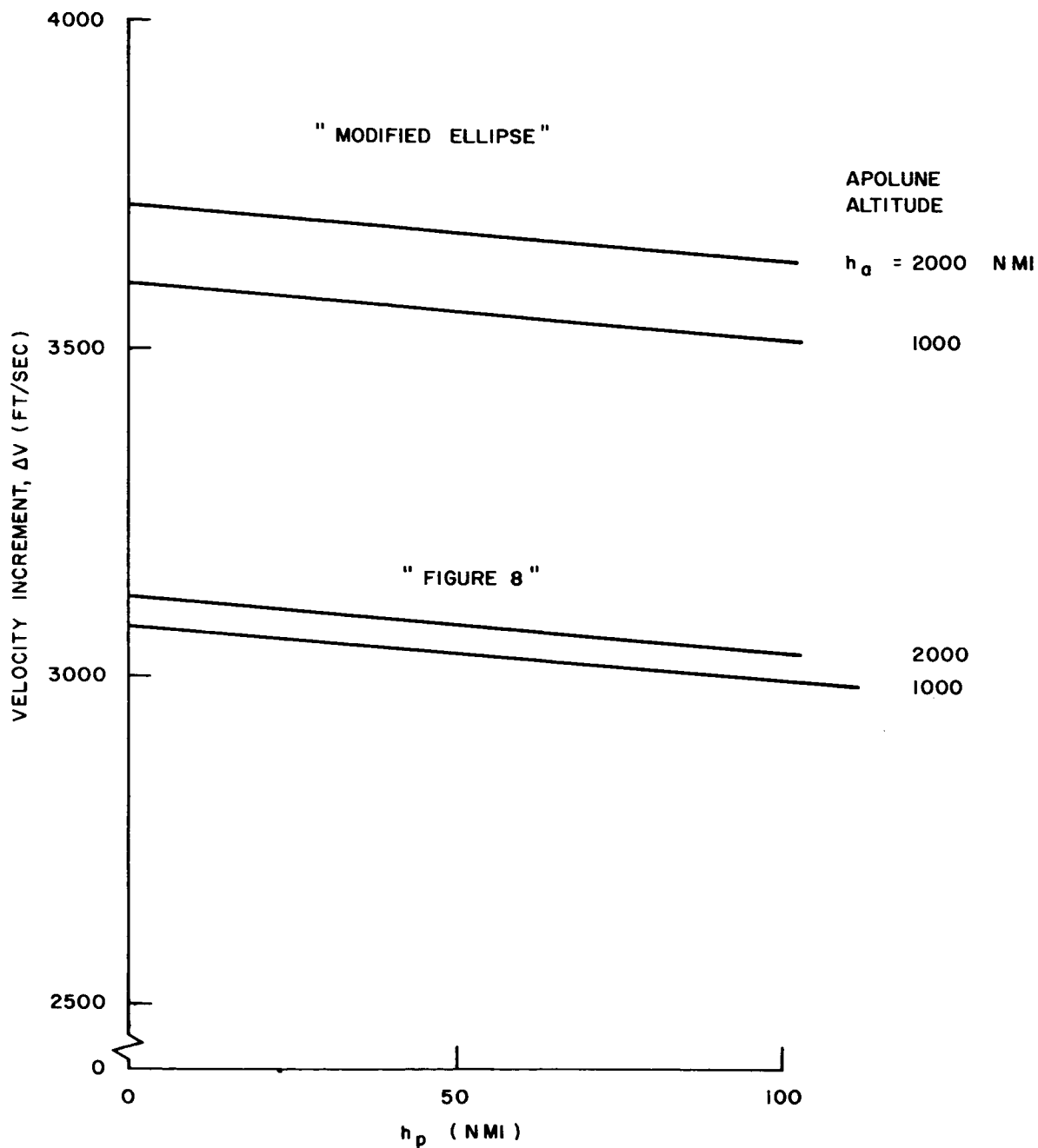


Figure VII-5-2. Velocity increment required to enter lunar orbit

~~CONFIDENTIAL~~

This return velocity increment, which must be investigated for each orbit during the expected stay time, must place the vehicle on a transfer trajectory which will return to an acceptable latitude-longitude point for re-entry and landing on the Earth.

~~CONFIDENTIAL~~

~~CONFIDENTIAL~~

## 6. SAMPLE LUNAR ORBIT

This section presents the results of a sample computation of a lunar satellite orbit which is derived from the transit trajectory described in Section 3 of this chapter. At the close approach distance of about 1050 miles, a velocity increment is added in the negative sense of the transit velocity vector relative to the Moon to establish an orbit with a perilune altitude of about 60 statute miles. Figure VII-6-1 presents a sketch showing the orientation of the satellite orbital plane relative to the Moon, and also the direction to the Earth. The line of nodes is also indicated.

Figures VII-6-2, VII-6-3, and VII-6-4 present the x-y, y-z, and x-z projections of the first revolution of the orbit. Figure VII-6-2 also shows the direction to the Earth at initiation of the orbit. The time at several points on the orbit is given in the table included in the figure.

The trajectory was computed with the G-E "n-body" program using a Moon-centered, Enke method. The computation extended to a time of three days to investigate, "experimentally", the behavior and stability of the lunar orbit. The Earth and Sun, which are located approximately in the direction of the perilune, can be seen to apparently decrease the semi-major axis (and hence the energy) of the orbit since both apolune and perilune are decreased. The apolune altitude is decreased by a distance of about eight miles while the perilune distance is decreased by five miles in the first three days of the orbit as shown in Figure VII-6-5.

~~CONFIDENTIAL~~

**CONFIDENTIAL**

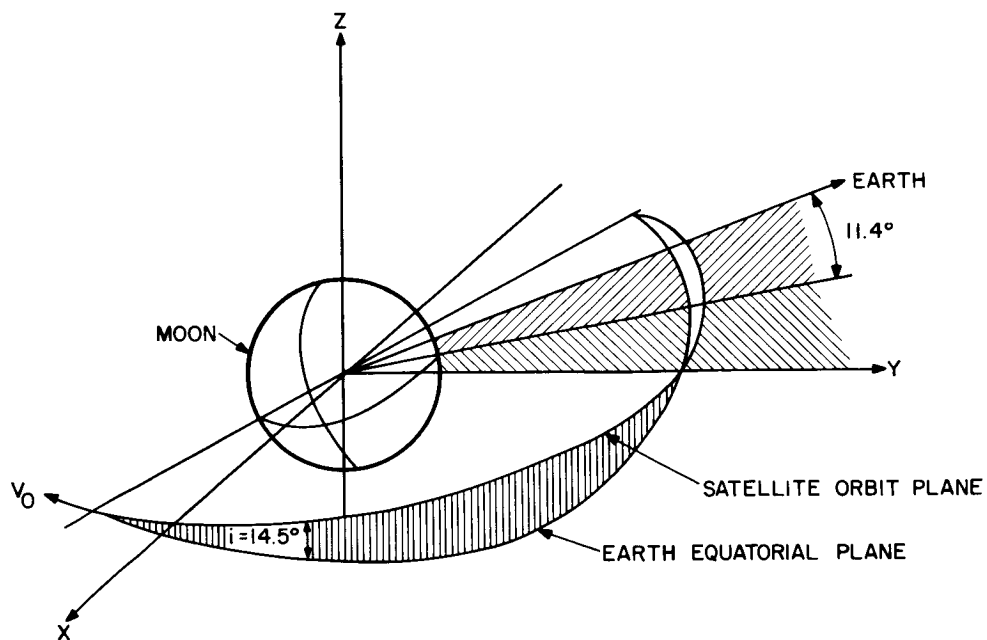


Figure VII-6-1. Sample lunar satellite orbit orientation

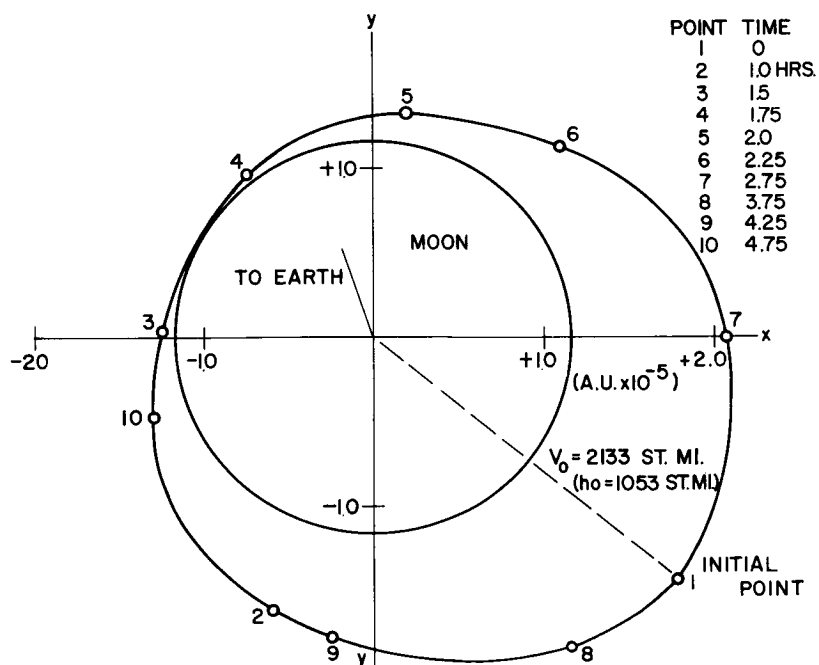


Figure VII-6-2. X-y projection, lunar satellite orbit (first revolution)

**CONFIDENTIAL**



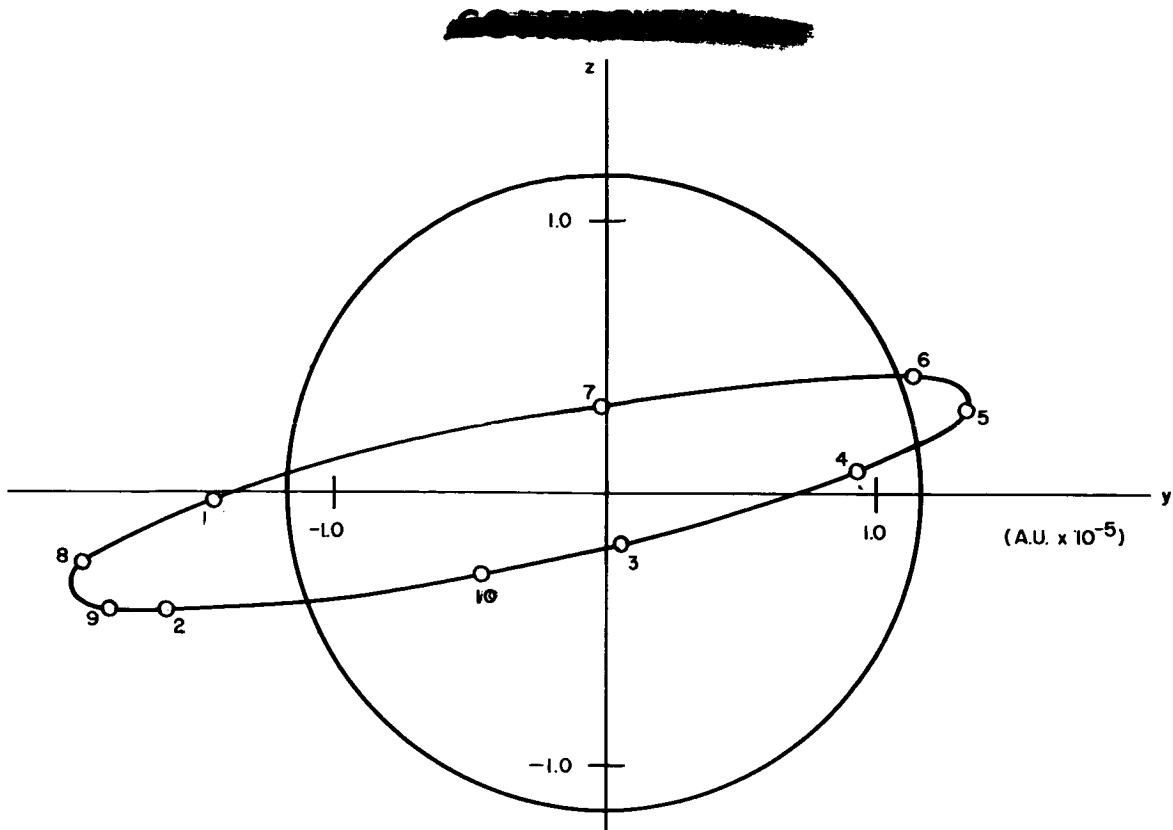


Figure VII-6-3. Y-z projection, lunar satellite orbit (first revolution)

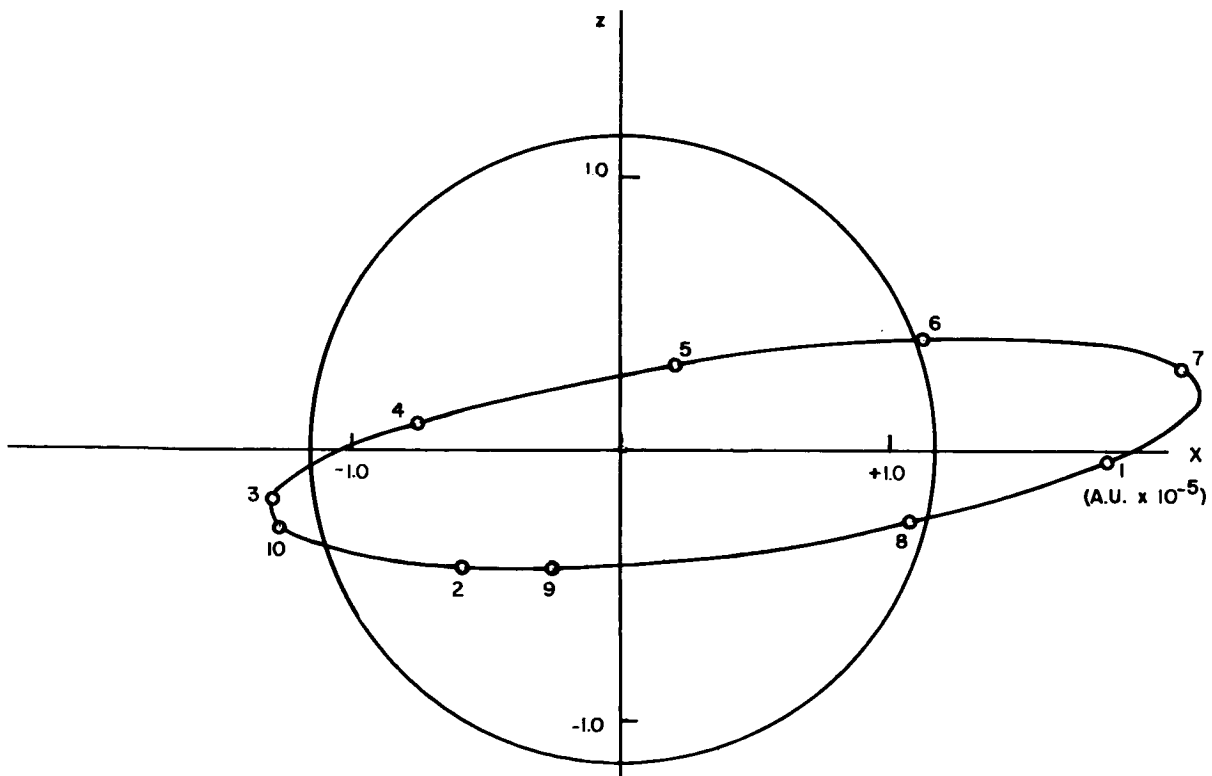


Figure VII-6-4. X-z projection, lunar satellite orbit (first revolution)

~~CONFIDENTIAL~~

~~CONFIDENTIAL~~

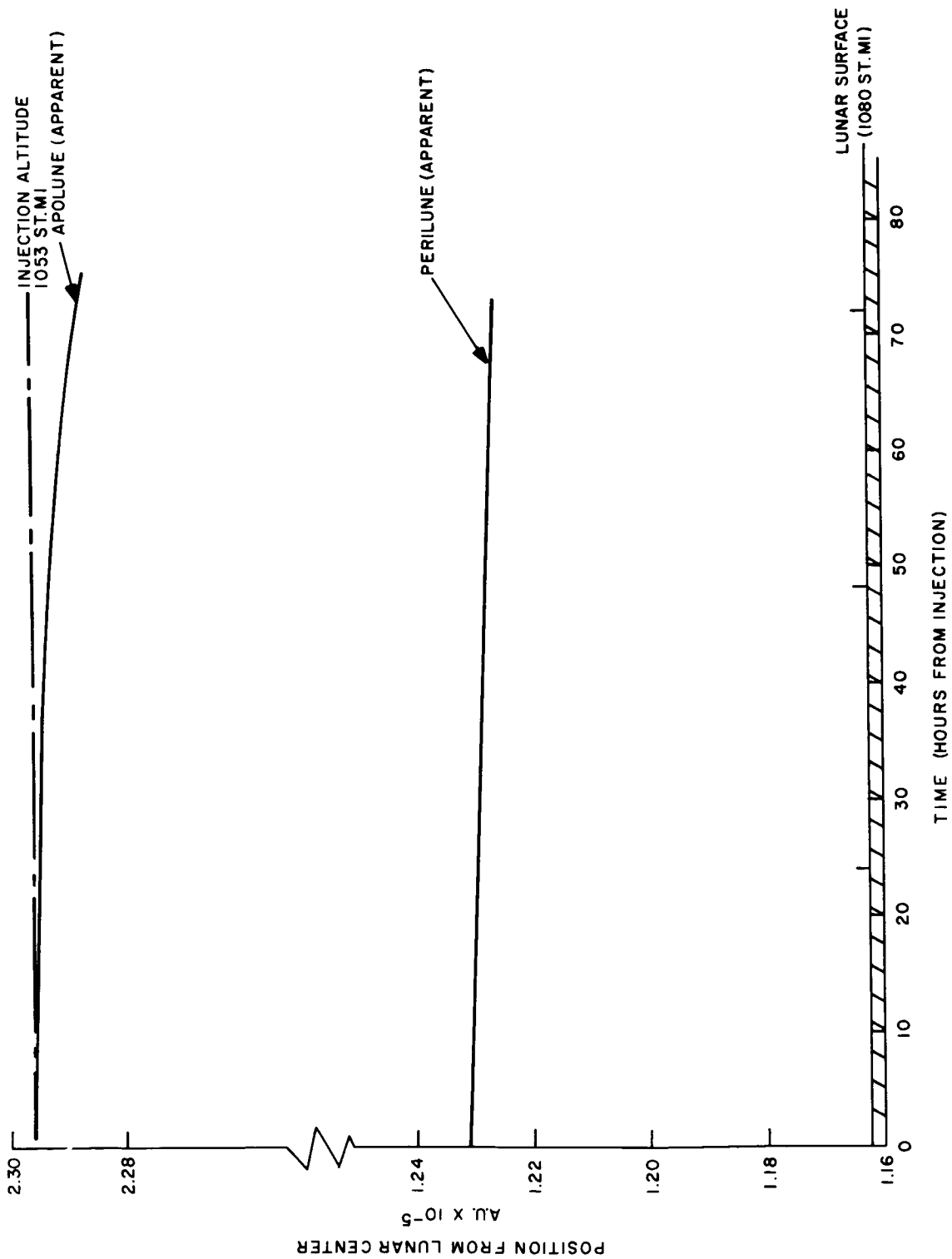


Figure VII-6-5. Lunar orbit altitude variation

~~CONFIDENTIAL~~

~~CONFIDENTIAL~~

## 7. RE-ENTRY FLIGHT MECHANICS

On the basis of the general studies reported in References 1 and 2, design trajectories and supplementary information for the various APOLLO study configurations has been generated and typical data are presented herein.

### RE-ENTRY CORRIDOR

From the upper portion of Figure VII-7-1, the maximum or undershoot path angle for 12g peak deceleration can be found for any lifting vehicle, if  $(L/D)_{MAX}$  and  $C_L$  at  $(L/D)_{MAX}$  are known, by entering the curves of  $L/D$ . The minimum or undershoot boundary for any configuration can be found, if  $-(W/C_L A)_{MIN}$  is known and the  $(L/D)$  corresponding to this is greater than one quarter, by entering the curve labeled "negative lift capture".

If, for some reason, it is not desirable to employ negative lift in pullout, the minimum path angle for shallow re-entry at positive  $(L/D)_{MAX}$  is given, the dashed curve labeled positive lift capture. Note that both capture limits are independent of the magnitude of  $(L/D)$ .

The lower portion of Figure VII-7-1 can be used to find the minimum and maximum re-entry angles for ballistic vehicles, it being necessary to know only  $W/C_D A$  in this case.

If the re-entry path angles for shallow and steep limits are known at 300,000 or 400,000 feet, Figure VII-7-2 allows determination of corresponding virtual perigee altitudes. The difference between the minimum and maximum perigee altitudes is often referred to as the "linear corridor" as opposed to the "angular corridor" associated with  $\gamma_E$ .

Figures VII-7-3, VII-7-4, and VII-7-5 extend the corridor variables for lifting vehicles of  $100 \text{ lb/ft}^2 W/C_L A$  to include re-entry velocity and allowable peak deceleration.

~~CONFIDENTIAL~~

## EXTREMAL TRAJECTORIES

Figures VII-7-6, VII-7-7, VII-7-8, and VII-7-9 are extremal trajectories for the B-2, C-1, R-3, and R-1 configurations, respectively, the corresponding L/D's being 0.25, 0.7, 0.7, 2.0 respectively. Load histories for the B-2 and C-1 configurations are given for 12g re-entries in Figures VII-7-10 and VII-7-11. These loads are within human tolerance limits, and above 6g levels for only 30-50 seconds. Note that these extremal trajectories represent three-sigma guidance errors, and more moderate loads would normally be encountered. Figures VII-7-12 and VII-7-13 are time histories of shallow and steep re-entries for the high L/D R-1 configuration. Note the extremely long flight times resulting from the high L/D. Figures VII-7-14 and VII-7-15 are similar trajectories for the high-altitude R-3 vehicle. For comparison purposes, a constant L/D trajectory is presented for the R-3 in Figure VII-7-16. This type of path control is simple but fairly inflexible, so that very accurate corridor entry is necessary.

## MANEUVERABILITY AND LANDING POINT SELECTIVITY

If, during the constant altitude path phase, the bank angle is appropriately modulated instead of the angle of attack, considerable cross-range maneuvering can be achieved to compensate for midcourse guidance and other error sources. For the B-2 and C-1 configurations, Figure VII-7-17 indicates the maximum theoretical maneuvering capabilities for shallow (positive lift capture) and steep (12g peak deceleration) where maneuvering is assumed to begin at the North Pole on a non-rotating Earth. The area covered in both steep and shallow re-entry may be considered to represent available or guaranteed coverage, and any landing point within the common coverage area would presumably be attainable with perfect mechanization or in-atmosphere energy management. Note that minimum range is not indicated here, and must be subtracted from the coverage area. Minimum range can be a relatively large factor for low L/D vehicles such as the B-2, but is of minor importance for moderate L/D configurations such as the C-1 or R-3. We see from Figure VII-7-17 that, with the B-2, maximum guaranteeable cross-range distance is only about 100 nmi, while the C-1 provides cross-range capability of almost 1000 nmi, and is thus considerably more attractive from this standpoint.

~~CONFIDENTIAL~~

~~CONFIDENTIAL~~

## REFERENCES

1. Galman, Barry A. "Direct Re-entry at Escape Velocity" American Astronautical Society Preprint 60-86, 1960.
2. Mandell, Donald S. "A Study of the Maneuvering Performance of Lifting Re-entry Vehicles" American Rocket Society Preprint 1555-60, 1960.

~~CONFIDENTIAL~~

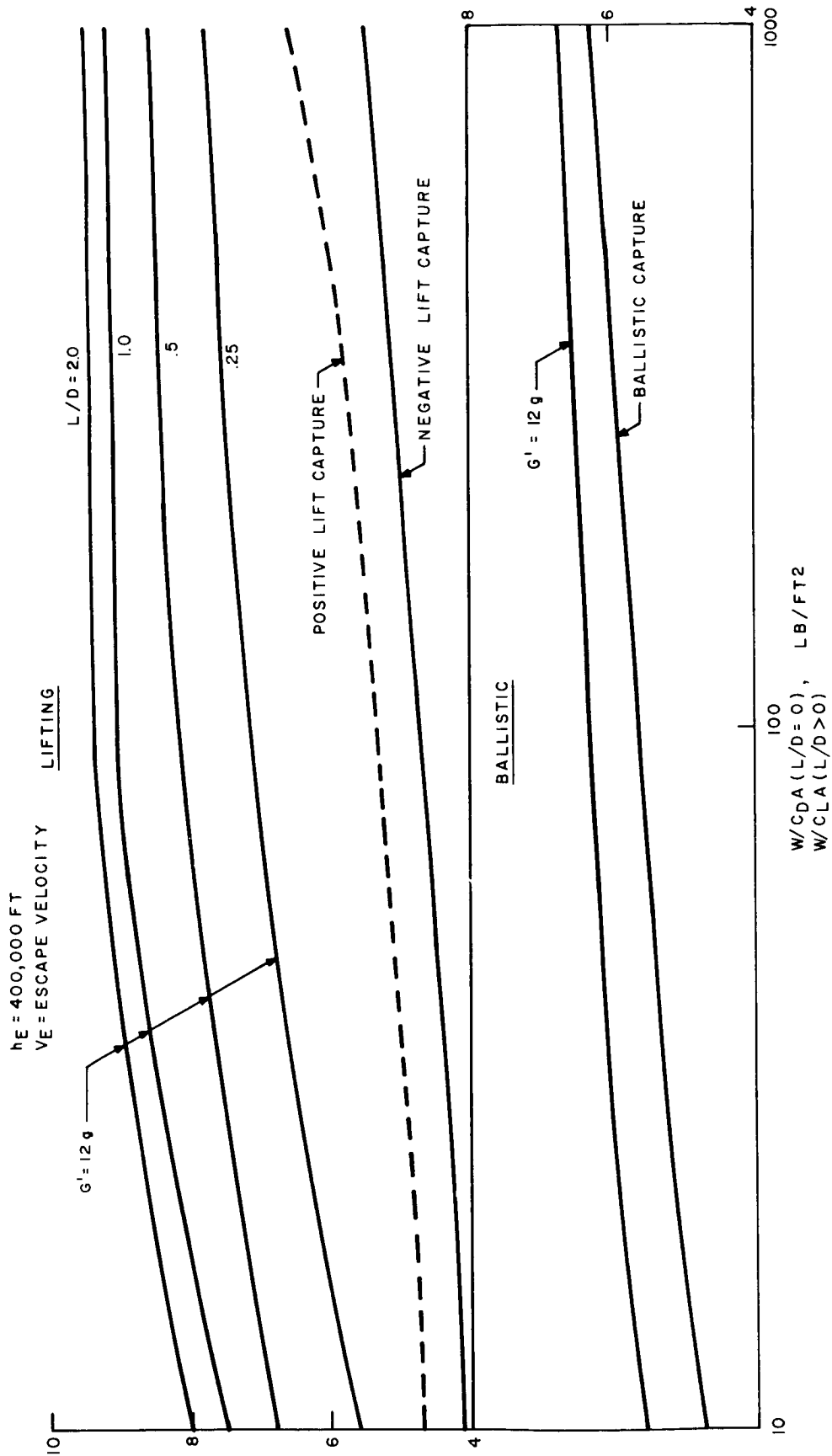


Figure VII-7-1. Re-entry angular corridor

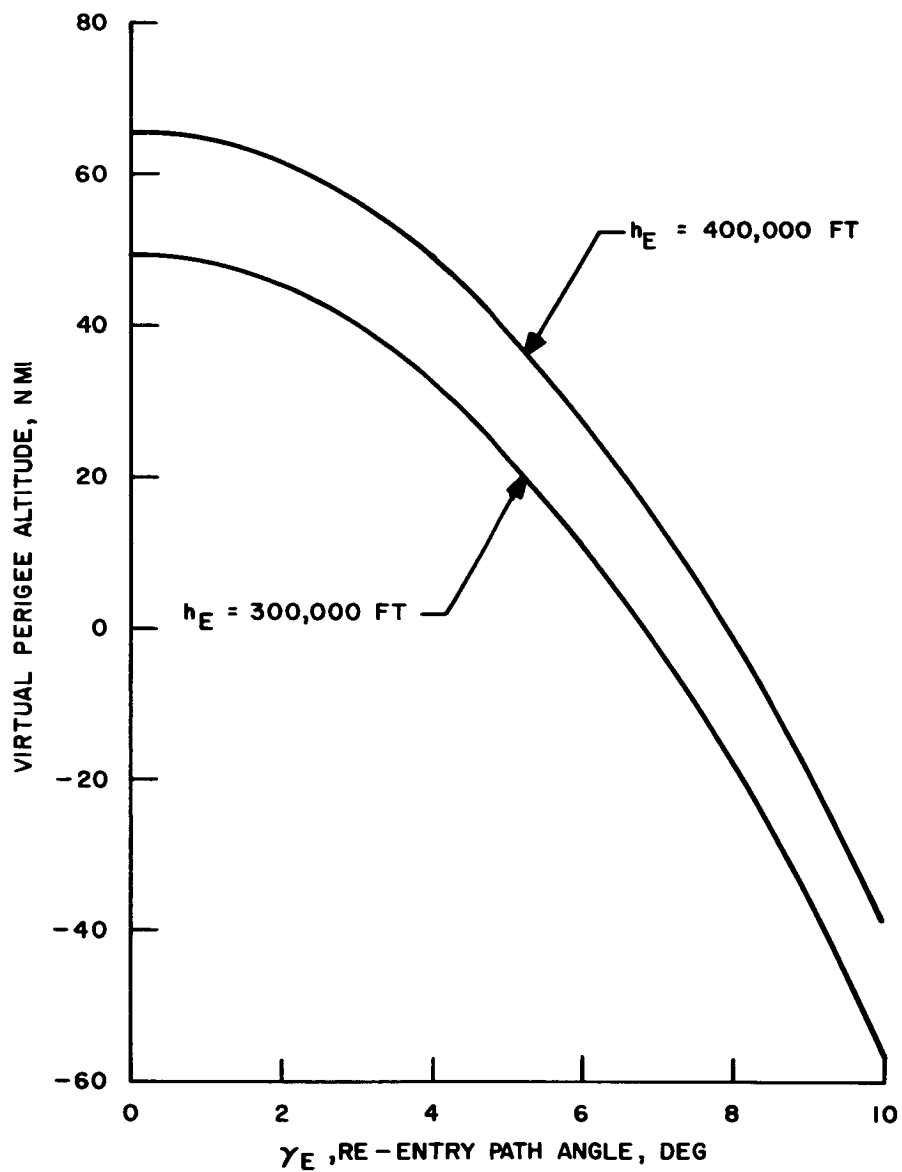


Figure VII-7-2. Virtual perigee altitude versus re-entry path angle for escape velocity

~~CONFIDENTIAL~~

**CONFIDENTIAL**

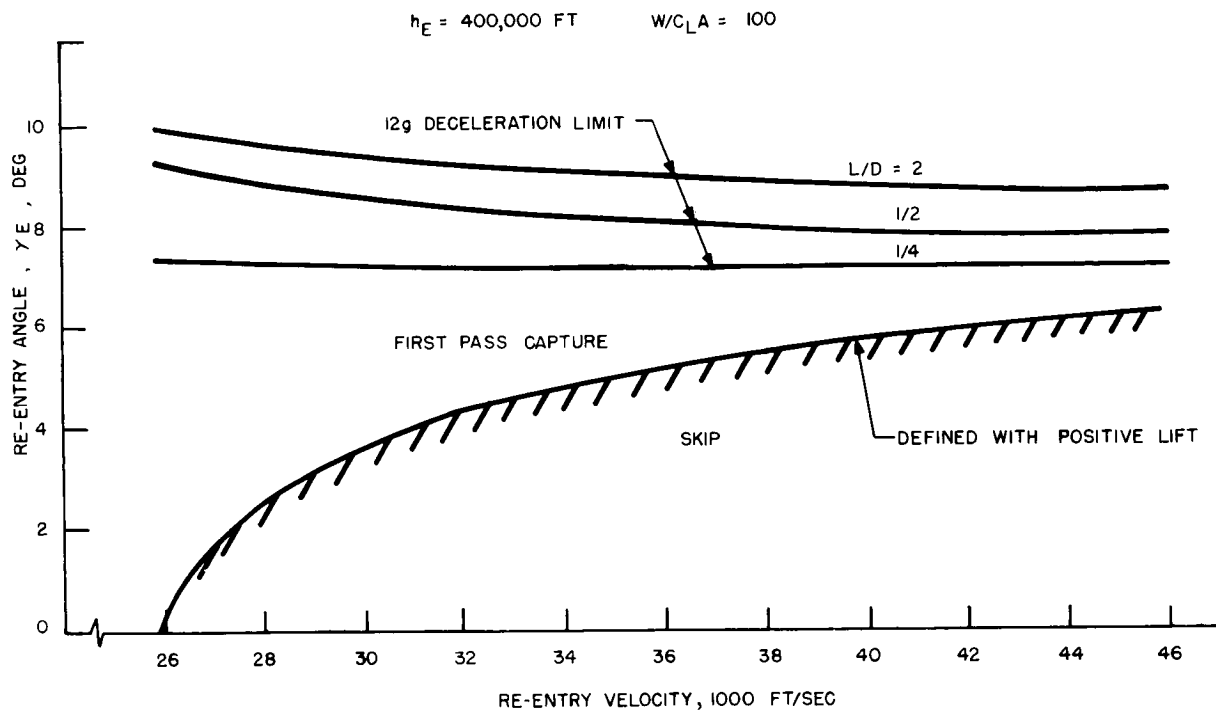


Figure VII-7-3. Angular re-entry corridor for supercircular entry, 8-g deceleration limit

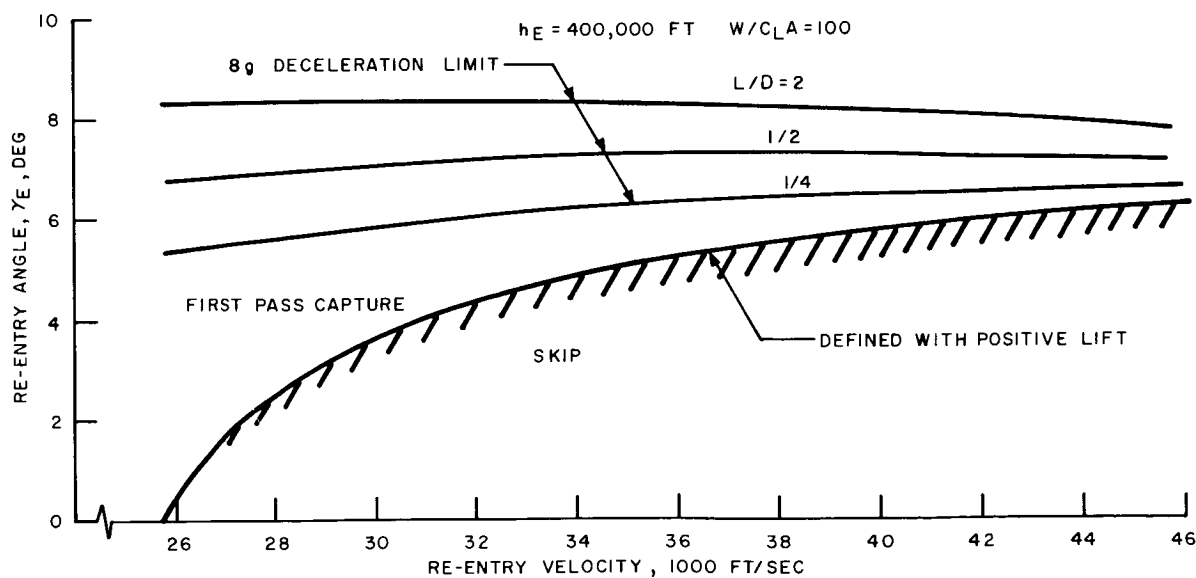


Figure VII-7-4. Angular re-entry corridor for supercircular entry, 12-g deceleration limit



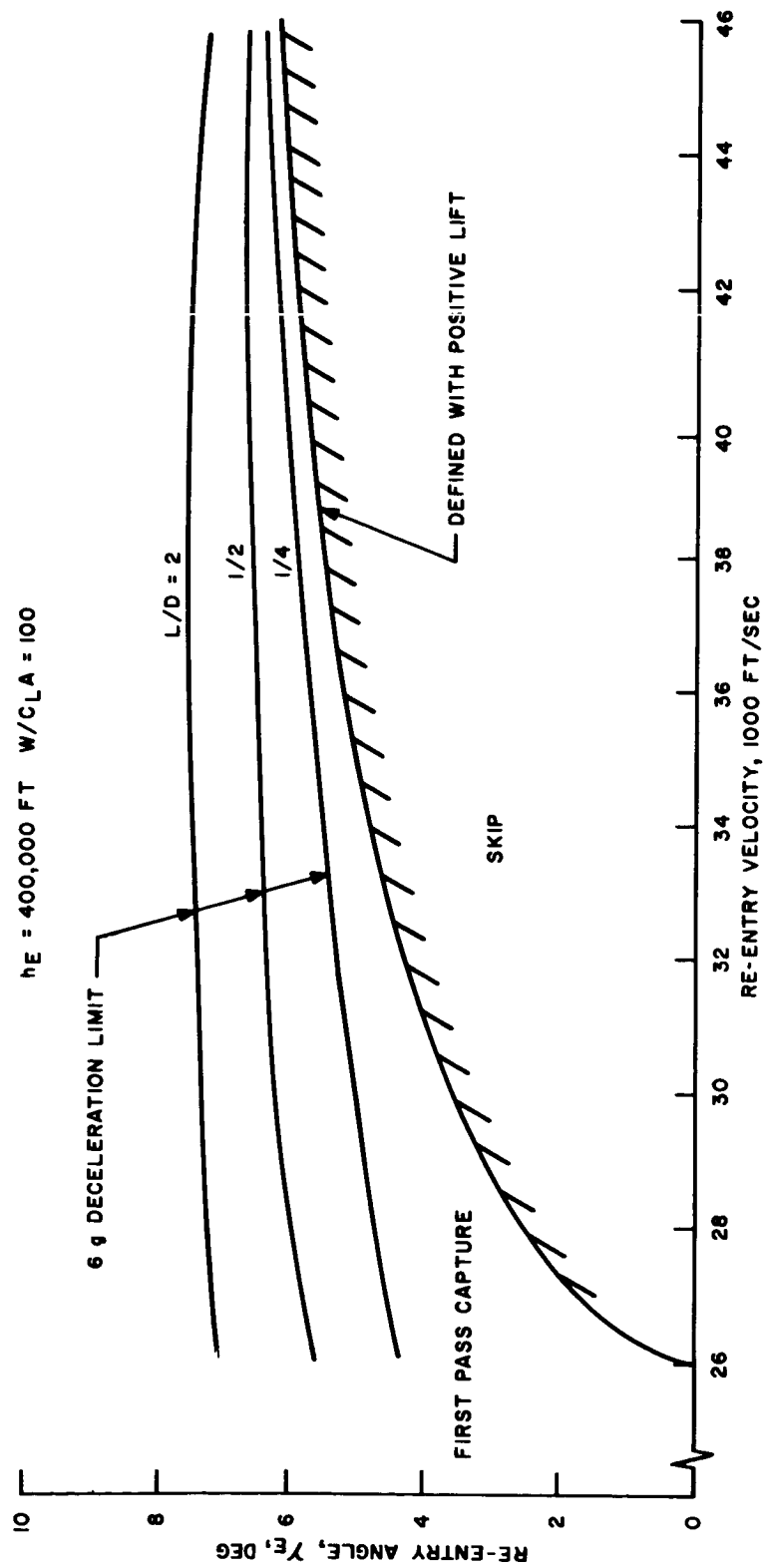


Figure VII-7-5. Angular re-entry corridor for supercircular entry, 6-g deceleration limit

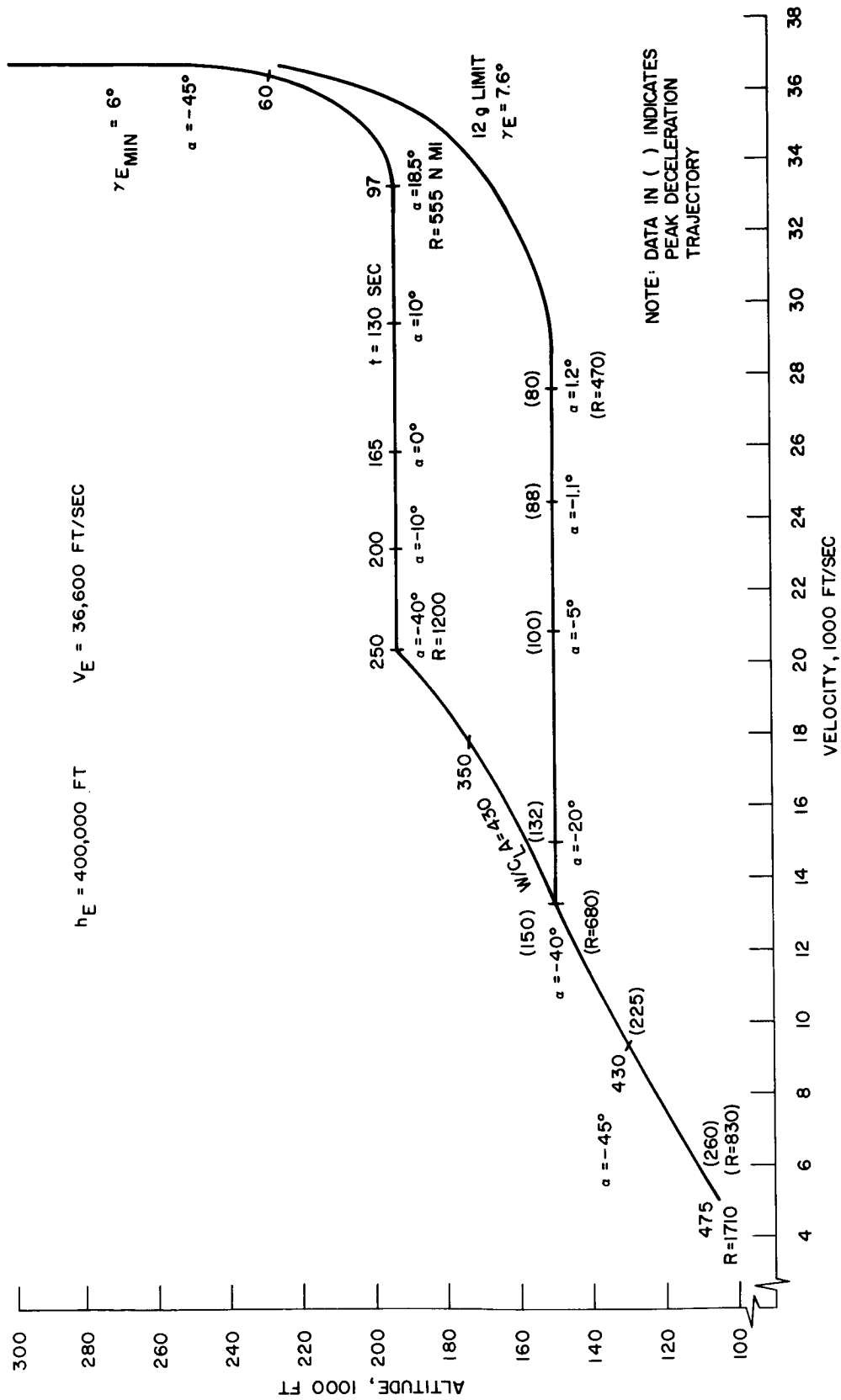


Figure VII-7-6. Typical re-entry trajectories, B-2 configuration

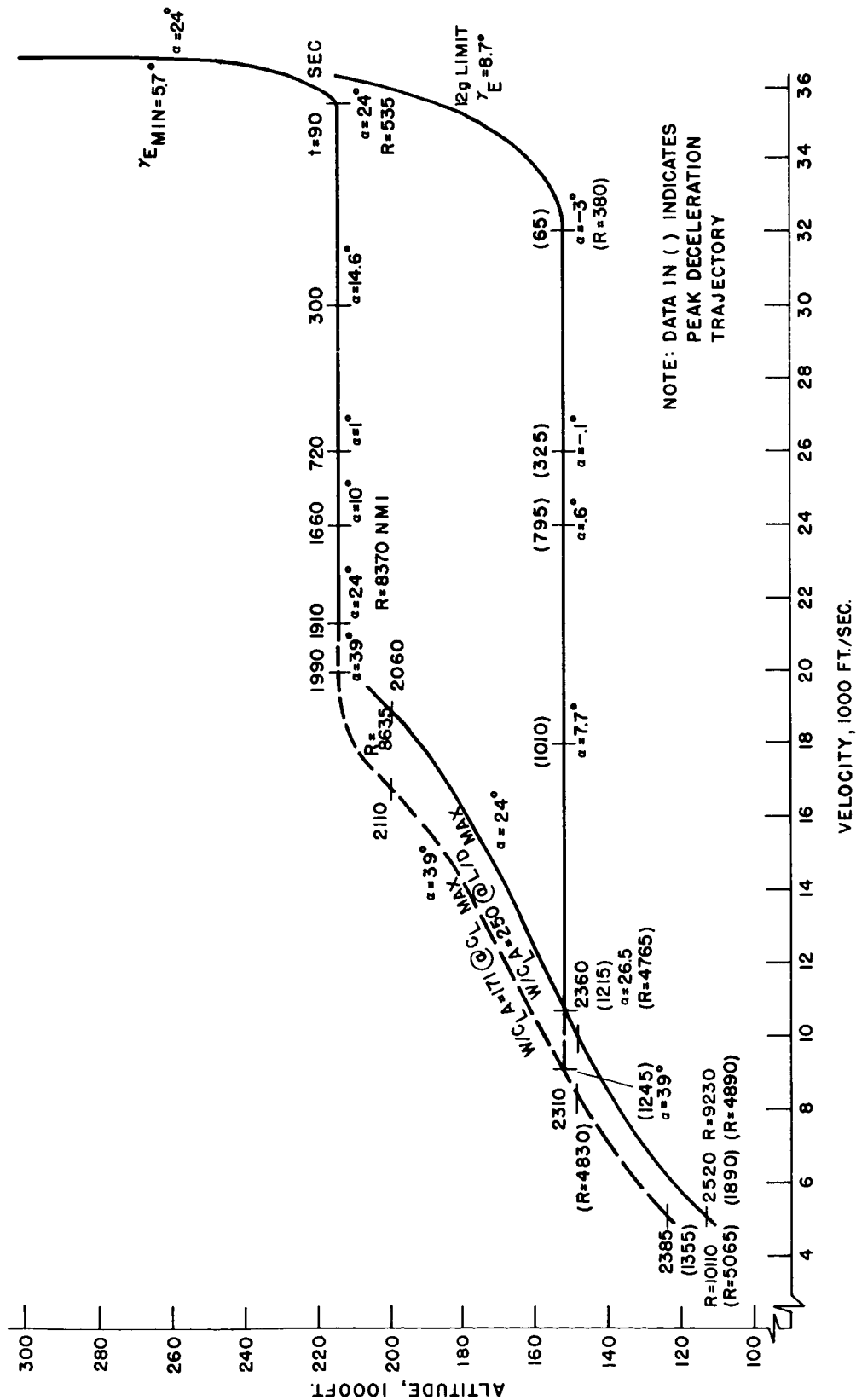


Figure VII-7-7. Typical re-entry trajectories for C-1 configuration

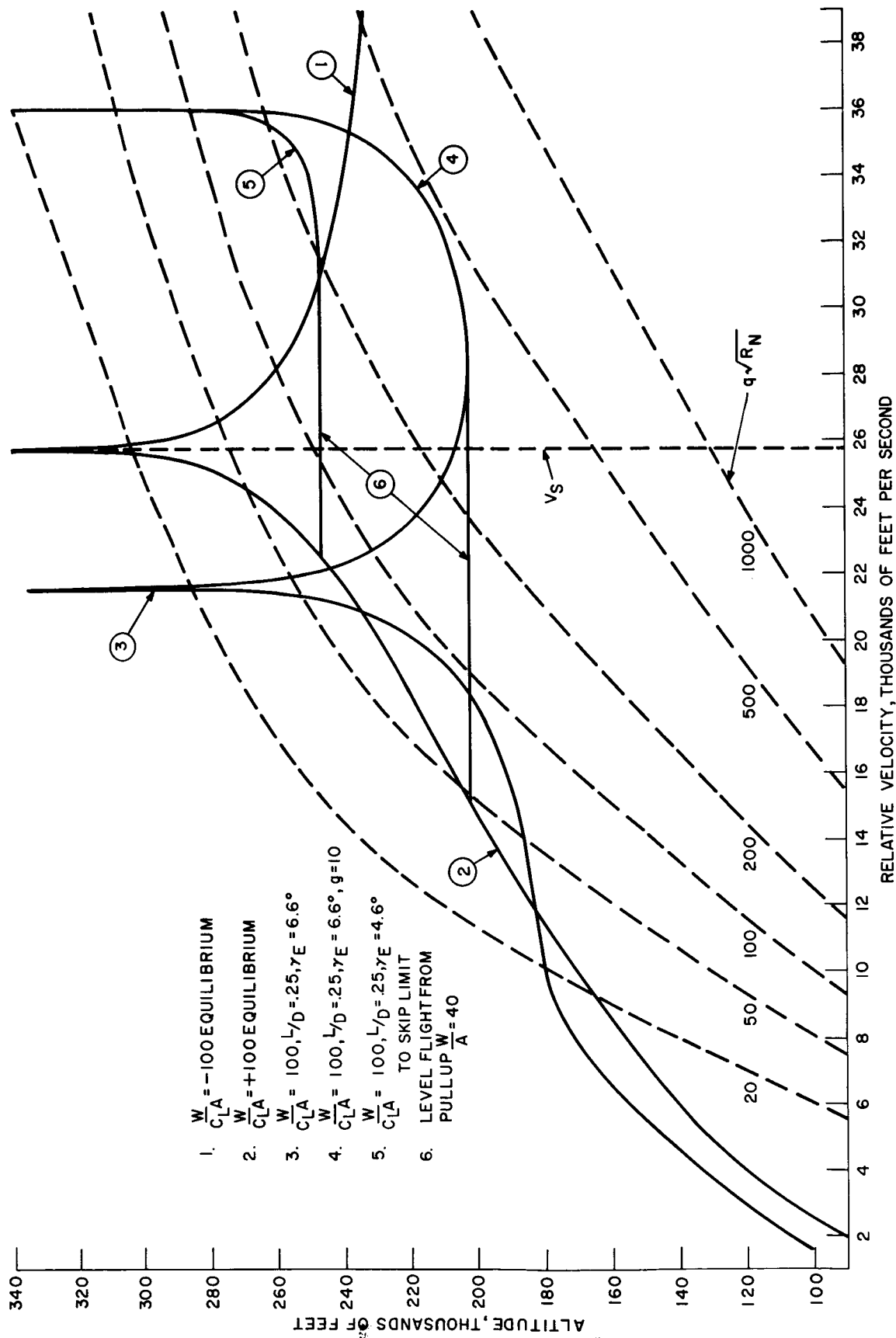


Figure VII-7-8. Re-entry profiles for high-altitude vehicles

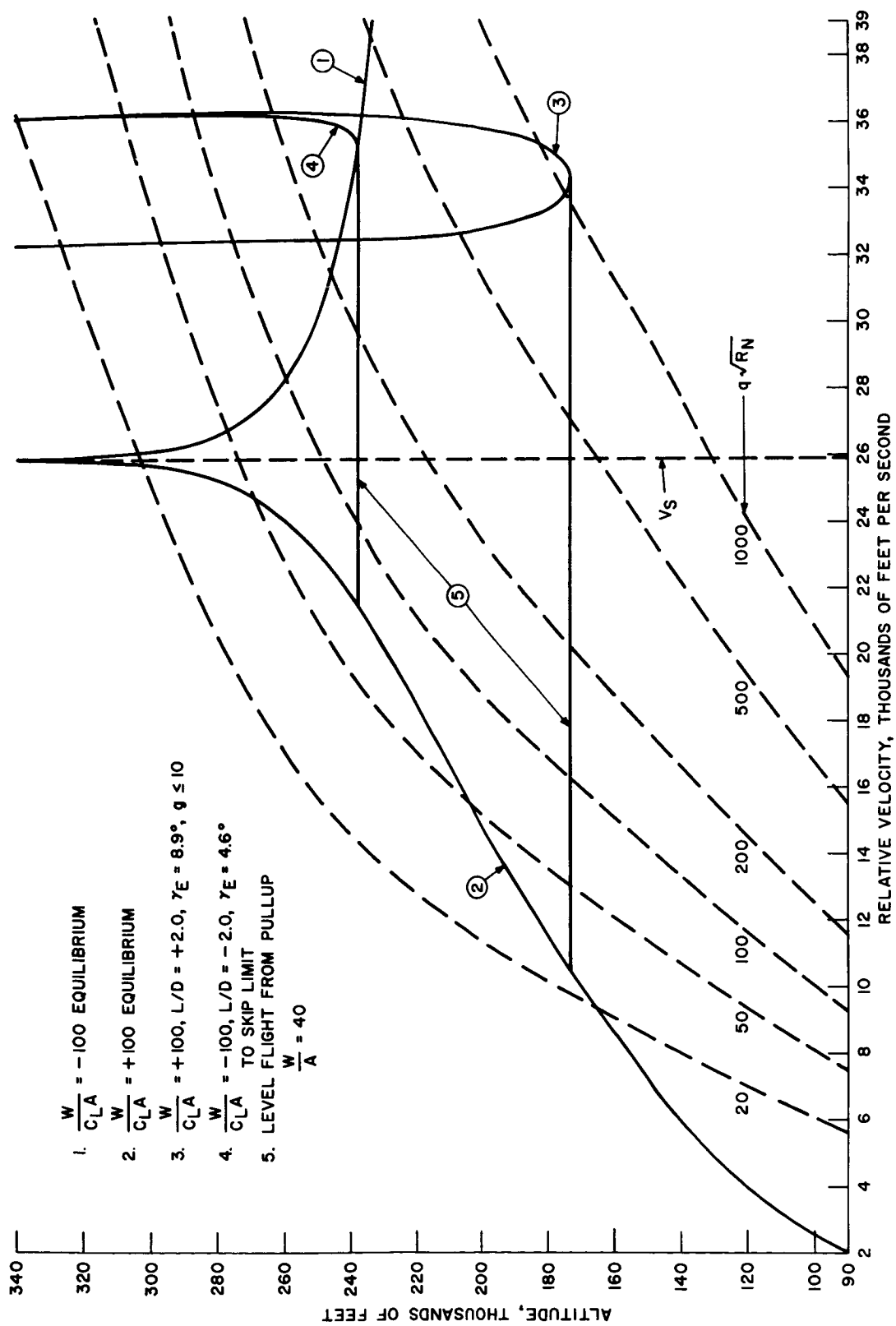


Figure VII-7-9. Re-entry profiles for high L/D vehicle

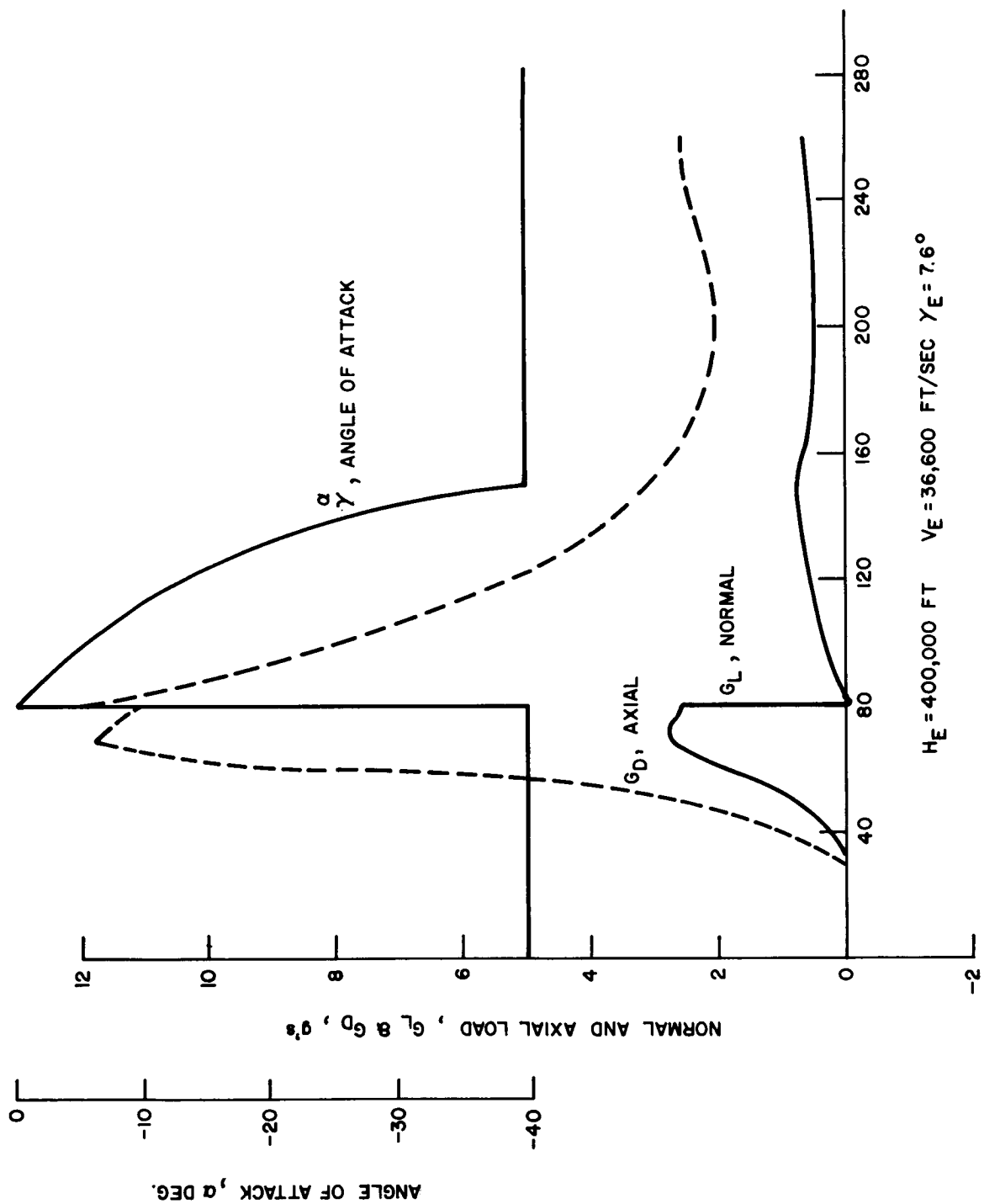


Figure VII-7-10. Trajectory characteristics (re-entry) for APOLLO B-2 configuration

$h_E = 400,000 \text{ FT}$     $V_E = 36,000 \text{ FT/SEC}$     $\gamma_E = 8.76$

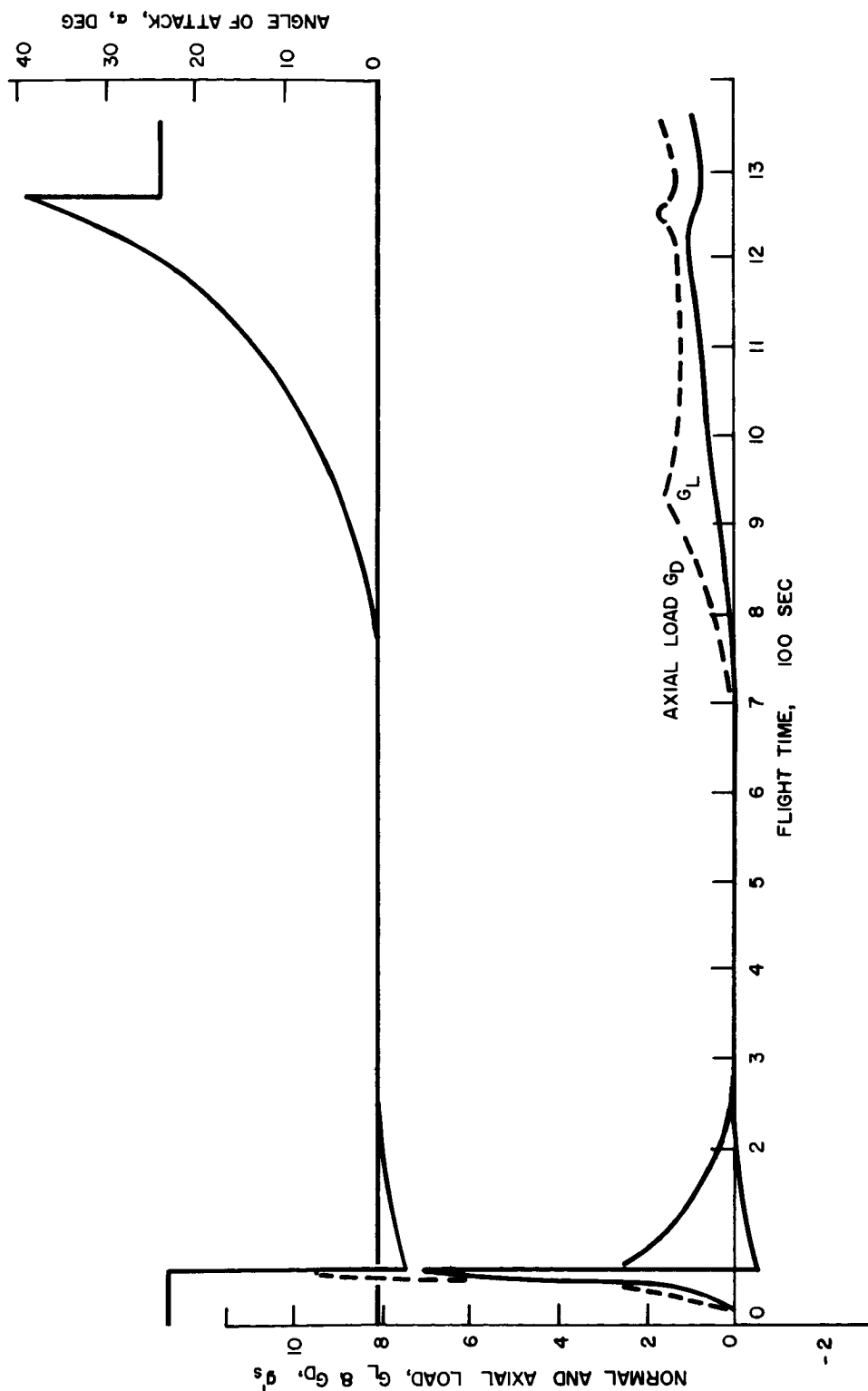


Figure VII-7-11. Trajectory characteristics (re-entry) for APOLLO C-1 configuration

CONFIDENTIAL

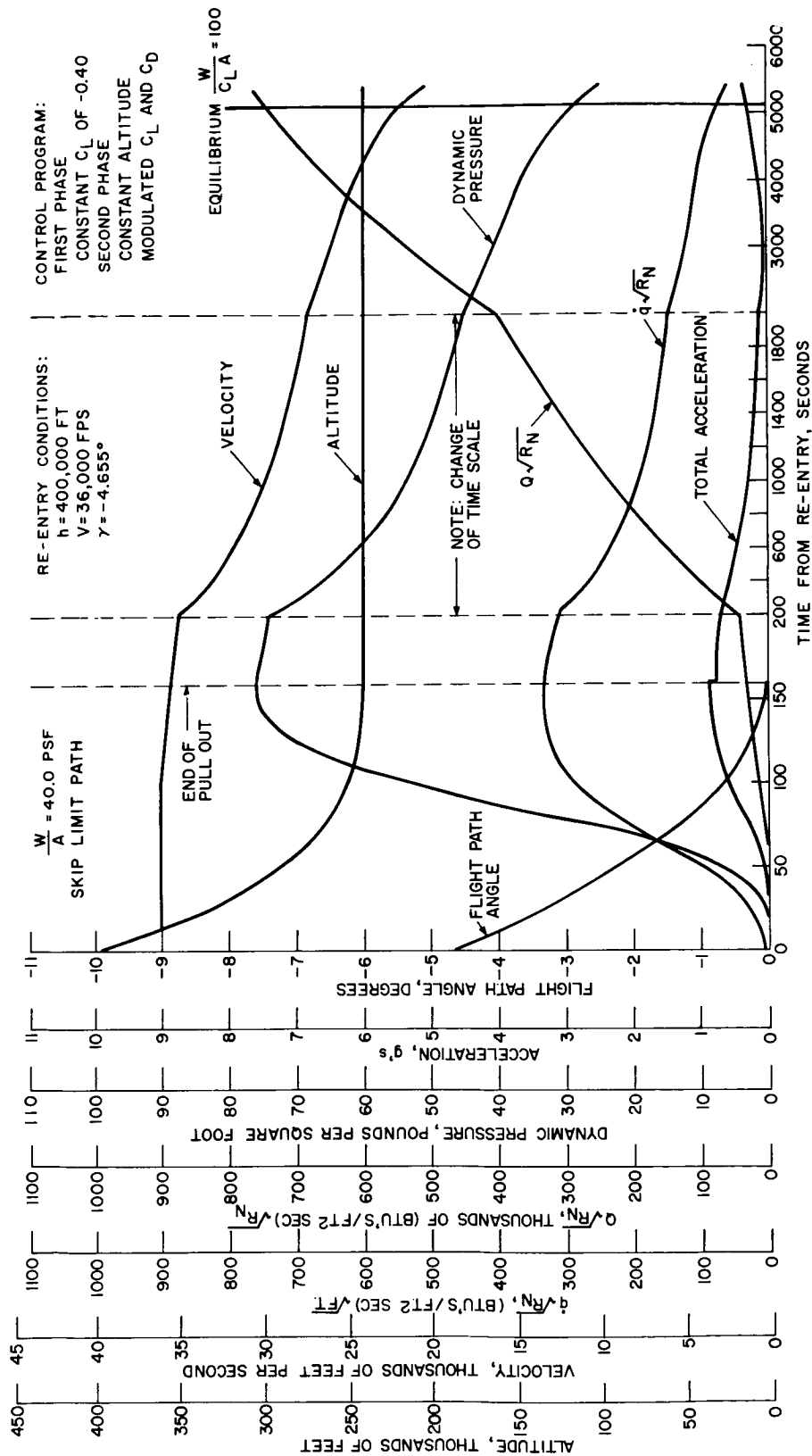
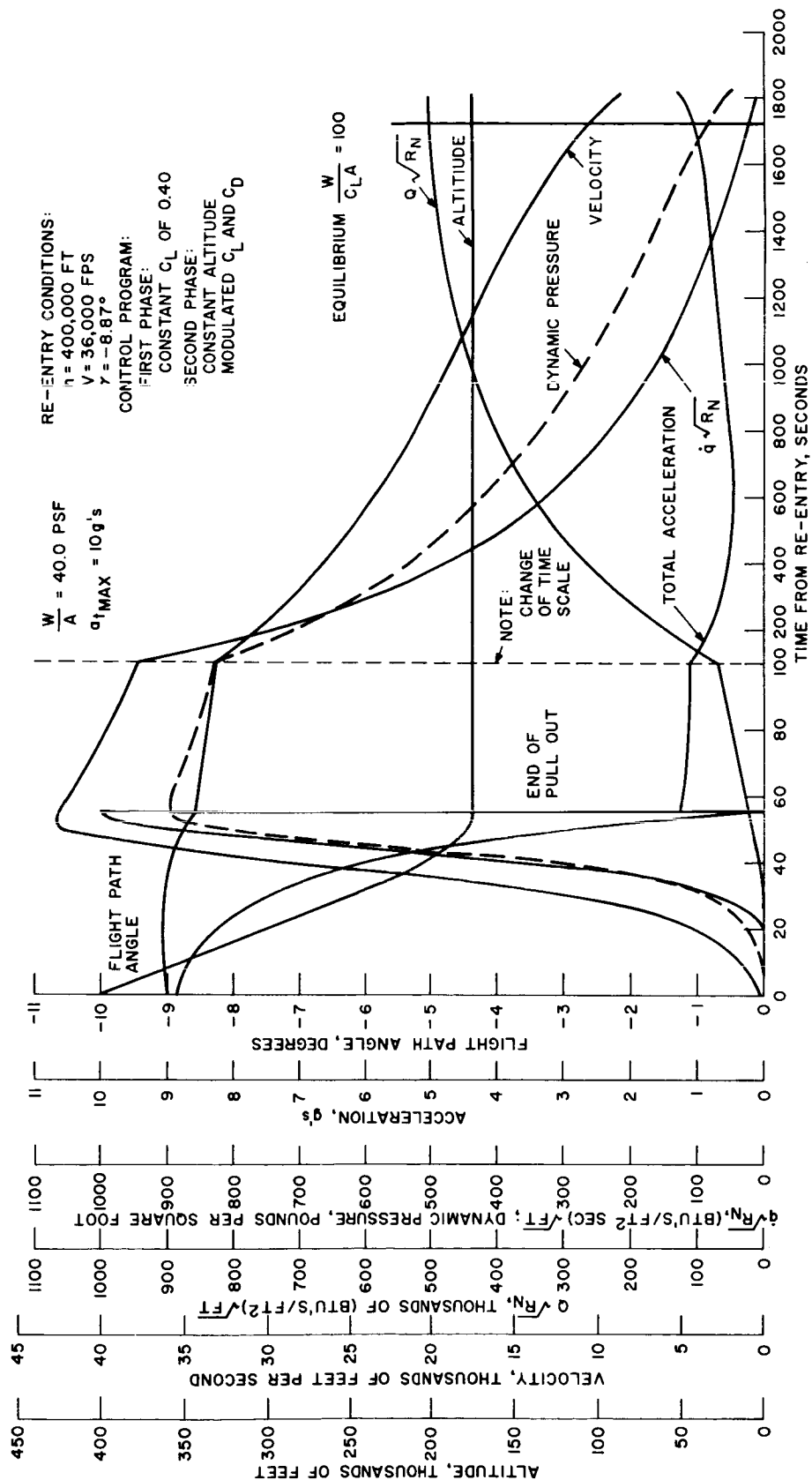


Figure VII-7-12. Re-entry time history for R-1 vehicle

CONFIDENTIAL



CONFIDENTIAL



CONFIDENTIAL

Figure VII-7-13. Re-entry time history for R-1 vehicle

CONFIDENTIAL

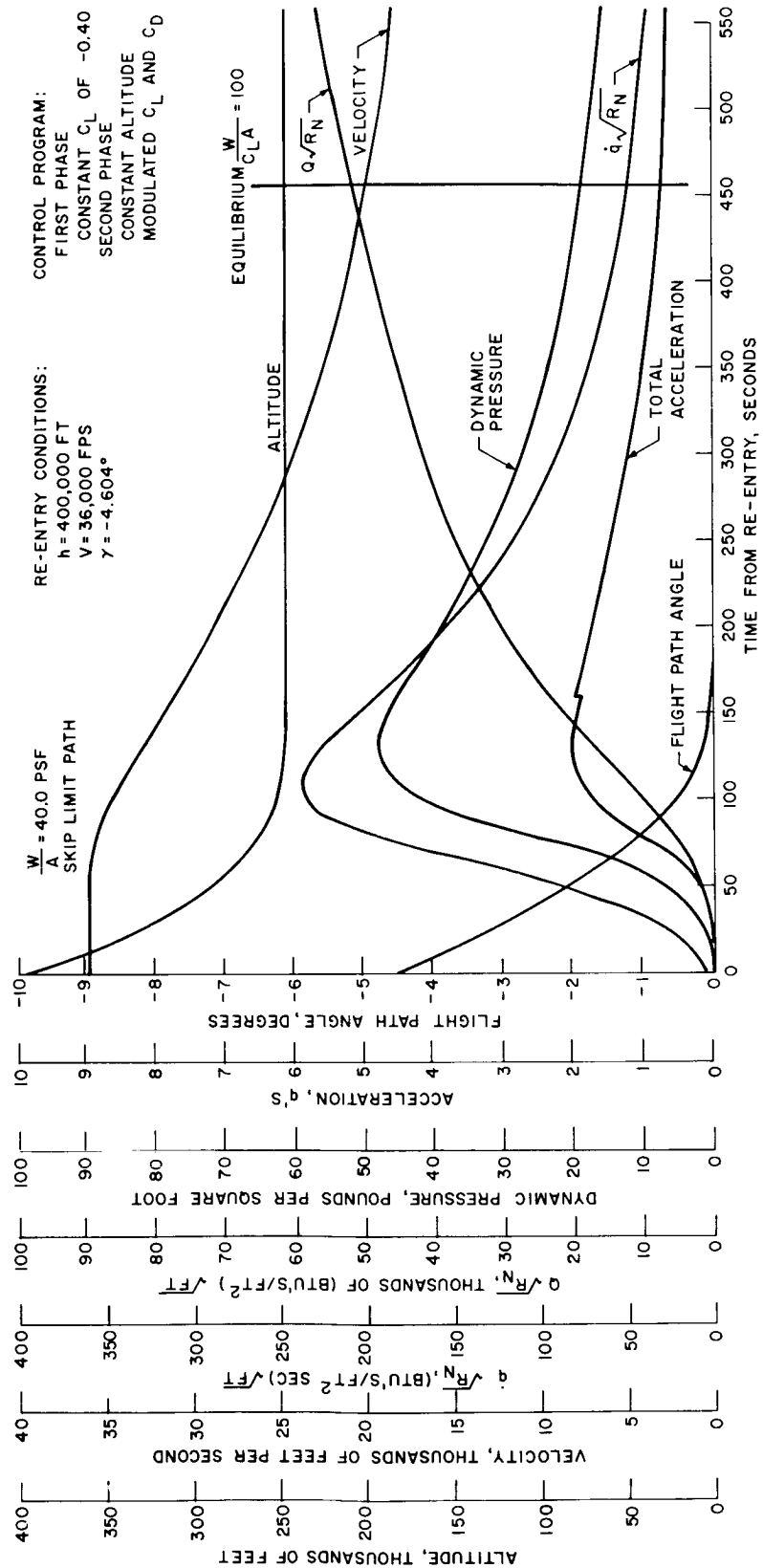


Figure VII-7-14. Re-entry time history for R-2 vehicle

CONFIDENTIAL

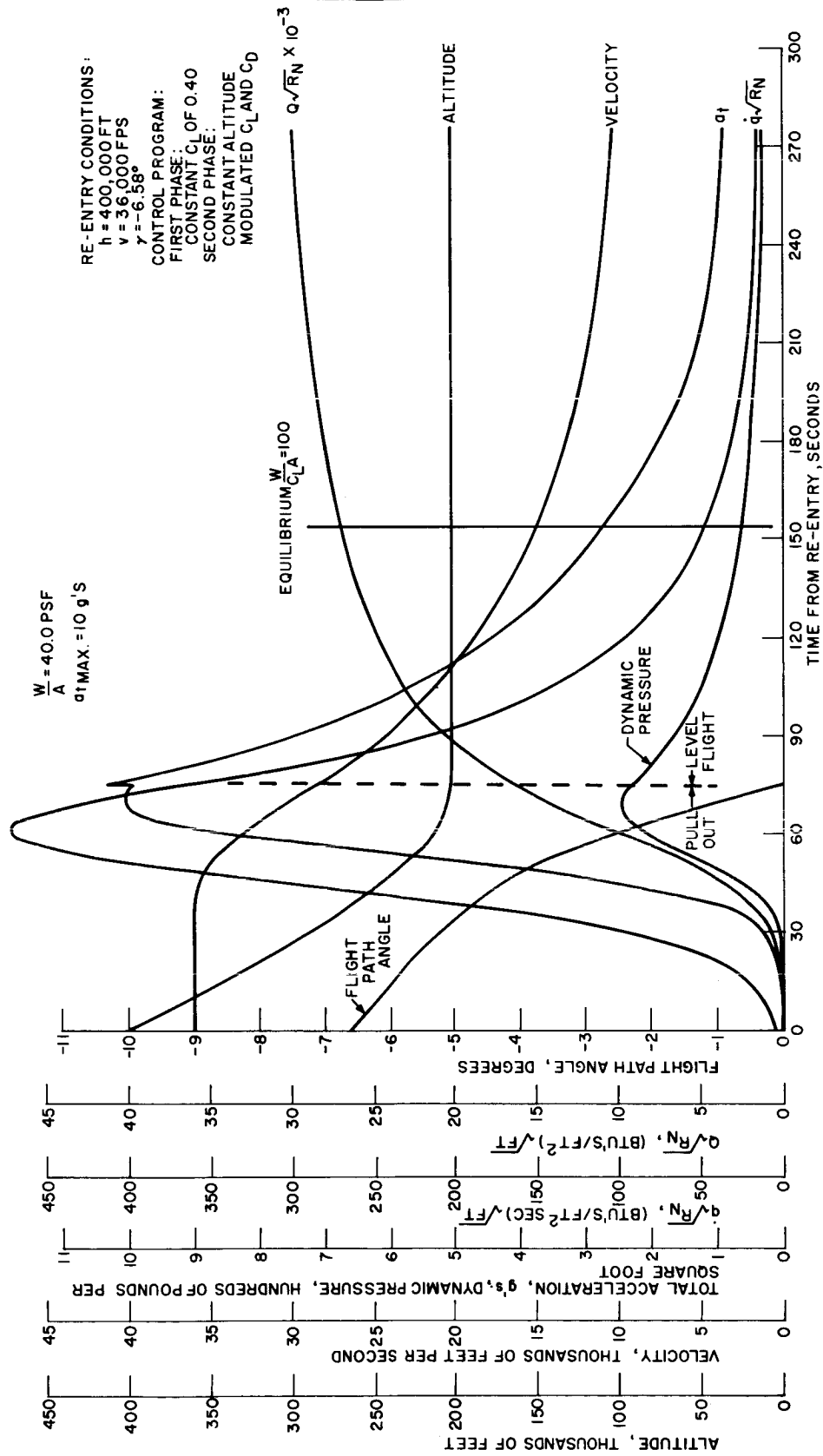


Figure VII-7-15. Re-entry time history for R-2 vehicle

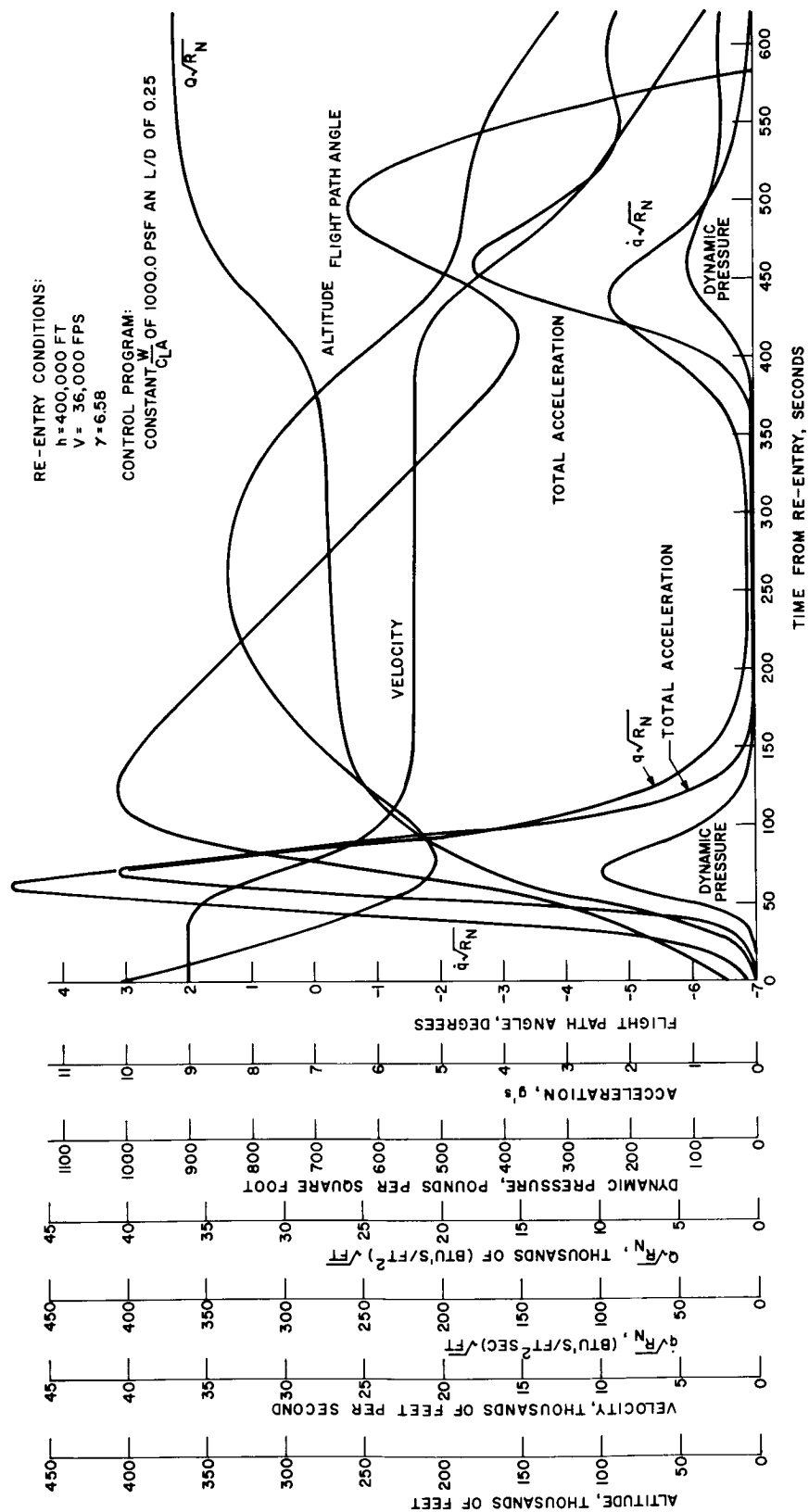


Figure VII-7-16. Re-entry time history for R-2 vehicle

~~CONFIDENTIAL~~

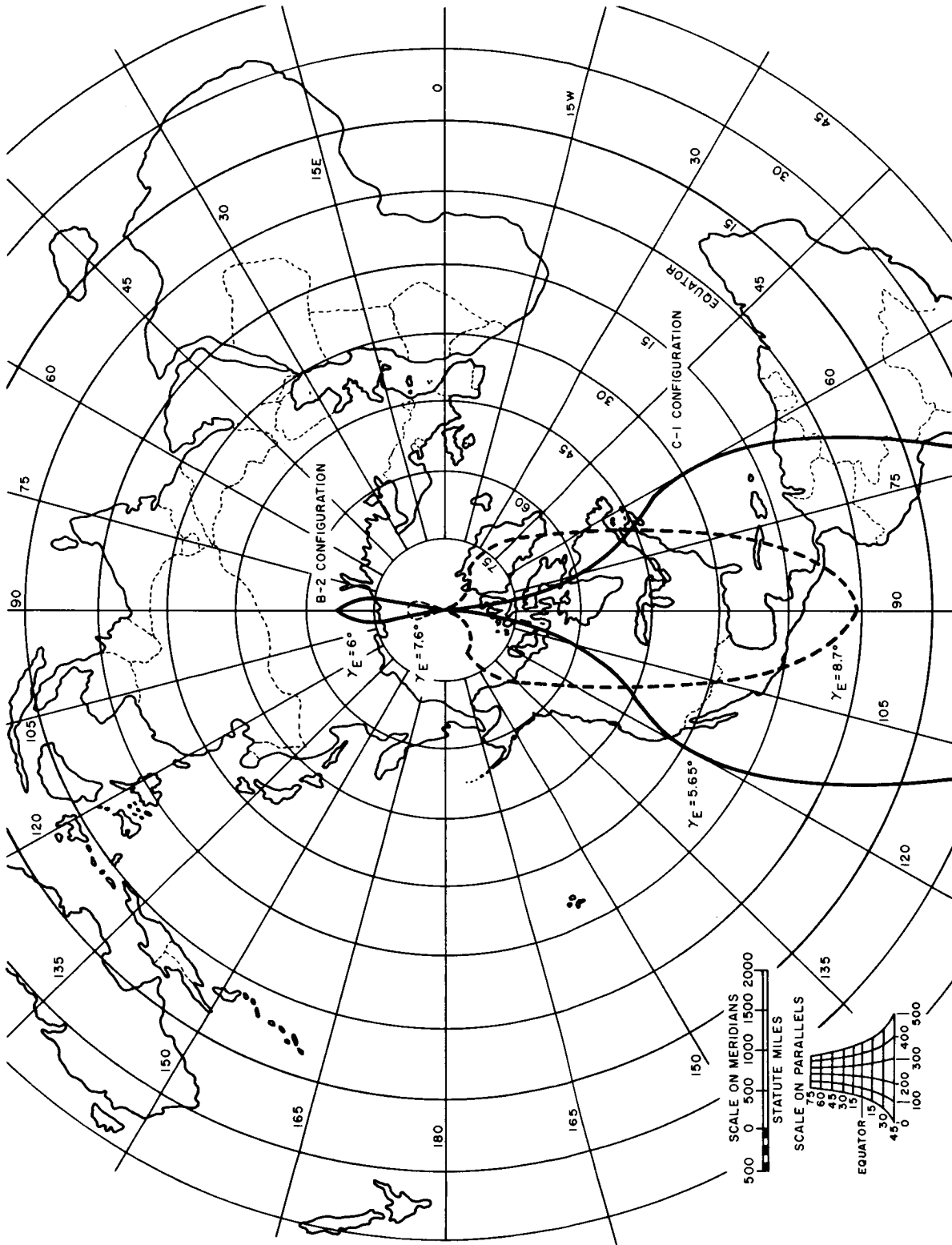


Figure VII-7-17. Maximum theoretical maneuvering capability

~~CONFIDENTIAL~~

~~CONFIDENTIAL~~

~~CONFIDENTIAL~~

## **CHAPTER VIII**

# **NAVIGATION, CONTROL, & GUIDANCE**

~~CONFIDENTIAL~~

## VIII. NAVIGATION, CONTROL, AND GUIDANCE

### 1. INTRODUCTION

The navigation and guidance problem can be divided into the following phases:

Launch

Mid-course — outgoing and return

Lunar orbit and return injection

Re-entry

Abort and emergency return

We are concerned with two aspects of launch guidance. In the first place, injection errors resulting from launch guidance errors must be corrected by the midcourse system. A preliminary estimate of injection errors is summarized in Tables VIII-2-1 and VIII-2-2 of Section VIII-2. This is based on our best estimate of launch guidance characteristics since information on Saturn guidance is presently not available. Component and alignment errors quoted there are based on actual component and flight tests on the Polaris guidance system. This estimate is considered to be conservative for the expected time of APOLLO launchings.

The other launch guidance consideration is the possibility of using part or all of the Saturn guidance equipment for APOLLO. Carrying this to the extreme, one navigation and guidance system could be used for the entire mission (including injection). In our work to date we have assumed completely separate systems. Since the Saturn will be used for a variety of missions, it seems desirable to avoid the difficult interface problem by designing the Saturn with a very reliable guidance system of not too high accuracy, and providing each payload vehicle with its own special guidance system. Thus, we have assumed that the APOLLO system must be capable of providing all required navigation and guidance, starting at separation.



~~CONFIDENTIAL~~

A major part of our effort to date has been directed toward the implementation of the midcourse navigation system, since preliminary analysis indicates that equipment satisfactory for midcourse navigation can also be used for lunar orbit and return injection measurements and for obtaining alignment and initial condition information required for navigation during the re-entry phase. This work has been directed toward selecting sensing equipment which can be used for making navigation fixes and determining how best to use this equipment in a midcourse navigation system. It was necessary to concentrate on equipment selection early in this study program in order to provide information to vehicle design personnel on size, weight, and desired location of components. The specifications on this equipment are based on an approximate error analysis described below. We are currently initiating more detailed analyses to provide better specification of equipment requirements and tradeoffs.

The other area which has received considerable attention is the re-entry management problem. In this case, equipment requirements are quite similar to those for re-entry from satellite orbits, a problem in which we have done considerable study. These include a study for WADD on Contract No. AF33(616)-6204 summarized in a report entitled "Manned Re-entry Vehicle Study", July 1960; re-entry studies for the Global Surveillance Satellite Study; and studies for MSVD's proposal on other Air Force reconnaissance satellites. The major problem in the re-entry system is the effect of post-orbital re-entry velocity on the control equations and techniques. We have concentrated, therefore, on an analog computer study to determine these control requirements and the amount of maneuvering possible with low  $L/D$  (of order 0.5) vehicles.

Much of our work to date has been concentrated in the area of automatic or semi-automatic systems. It is our present opinion that a partly automatic system is desirable for the APOLLO mission because of the requirements for taking large numbers of sightings on celestial bodies, relatively complex data processing, and accurate thrust vector control during large corrections. Our approach to designing such a system is to start with a completely automatic system, then determine what functions can be better performed by the crew. In the remaining part of the study more emphasis will be given to the role of the crew.

~~CONFIDENTIAL~~

Contributors to portions of this study include the Light Military Electronics and the Ordnance Departments of the General Electric Company.

~~CONFIDENTIAL~~

**CONFIDENTIAL**

## 2. ERROR ANALYSIS

The major phases of the over-all mission from insertion to landing may be indicated by the following list.

- Insertion to lunar trajectory
- Out-bound leg mid-course
- Transition from mid-course to lunar terminal
- Terminal phase retro-thrust
- Lunar orbit establishment
- Orbit escape thrust
- Transition to return leg mid-course
- Mid-course
- Transition from mid-course to re-entry
- Re-entry
- Landing
- Emergency escape

An error analysis is continuing in all phases and as yet is not completed.

The results presented in the following paragraphs give a preliminary estimate of the position and velocity accuracies and correction velocity requirements needed to successfully complete the entire mission.

### ESTIMATE OF INSERTION ERRORS

An estimate of RMS insertion errors for an inertial guidance system used for powered flight guidance is shown in Table VIII-2-1. Saturn C-2 reference powered flight trajectories were used. Table VIII-2-2 lists the instrument errors. These values are

**CONFIDENTIAL**

typical of the performance expected from inertial components. Instrument and alignment errors are considered to be the greatest source of error contributing to deviations from nominal conditions.

These values of insertion errors may be used to obtain a representative estimate of outgoing leg mid-course correction requirements.

TABLE VIII-2-1. TOTAL RMS INSERTION ERRORS

<u>Escape Trajectory</u>	<u>Velocity Error</u>			<u>Position Error</u>		
	<u>x</u> <u>ft</u>	<u>y</u> <u>ft</u>	<u>z</u> <u>ft</u>	<u><math>\dot{x}</math></u> <u>ft/sec</u>	<u><math>\dot{y}</math></u> <u>ft/sec</u>	<u><math>\dot{z}</math></u> <u>ft/sec</u>
Case I	1508	1520	2063	5.6	5.0	4.0
Case II	1495	1529	2091	5.6	5.0	4.0
Case III	1498	1539	2116	5.6	5.0	4.1
Case IV	1470	1548	2141	5.5	5.0	4.2

x - along local vertical

z - along local horizontal and in trajectory plane

y - out of trajectory plane - perpendicular to x, y

Further study of this problem indicates that:

(a) A platform realignment made by a stellar fix at 200,000 feet can reduce the burnout velocity error from 24 fps (3 $\sigma$ ) total velocity error to 6 fps. The stellar sight is good to 10 seconds.

(b) Best foreseeable ICBM components\* with 10 seconds of arc alignment (all axes) accuracy yields a three-sigma 8 fps velocity error

(c) If the system of (b) is corrected with a stellar fix, the velocity error can be reduced to 3 fps.

---

\* Gyros - 3 meru, 3 meru/g, 1 meru/g<sup>2</sup>  
 Accelerometers - 25 PPM, bias 0.05 cm/sec<sup>2</sup>  
 Alignment - 10 seconds all axes.

**TABLE VIII-2-2. INSTRUMENT ERRORS (THREE SIGMA)**

Initial Misalignment	
$x_0$ axis	30 seconds of arc
$y_0$ axis	90 seconds of arc
$z_0$ axis	30 seconds of arc
Constraint Drift	10 meru* (for all gyros)
Unbalance Drift	10 meru/g
Anisoelastic Drift	3 meru/g <sup>2</sup>
Vibration	1.5 meru/g <sup>2</sup>
Accelerometer Bias	0.03 cm/sec <sup>2</sup>
Accelerometer Scale Factor	4 x 10 <sup>-5</sup>
* 1 meru = 0.015 degrees/hr	
$x_0, y_0, z_0$ - Fixed at launch	

## OUTBOUND LEG MID-COURSE

Insertion errors produce deviations from the nominal aimpoint at the Moon. Mid-course and terminal velocity corrections are required to produce the desired accuracy of establishing orbits around the Moon.

A study is being conducted to obtain an estimate for the total velocity required and number of velocity corrections to achieve a desired terminal accuracy in the region of the Moon. At this point, a transition will be made to a navigation and guidance mode to place the vehicle in an orbit around the Moon.

The guidance concept employed for this study utilizes a fixed time-of-arrival technique. Velocity corrections are made such that the vehicle will arrive at a given nominal position vector fixed in inertial space with a given fixed total time-of-flight from, in this case, insertion into orbit. At the time-of-arrival velocity corrections can be made, if desirable, to place the vehicle on the nominal trajectory in position, velocity, and time correspondence.

~~CONFIDENTIAL~~

To obtain an estimate for representative velocity corrections, the aim point analyzed coincides with the nominal distance-of-closest approach at the Moon at the time of arrival. Sensitivity coefficients which relate perturbations in arrival position and velocity as functions of position and velocity perturbations at previous times can be determined (for fixed times-of-flight).

In general, the aim point (return to nominal conditions) may not be located at the distance-of-closest approach but at some previous point, a few hours removed, to allow adequate preparation for checking and cross-checking before either orbiting the Moon or continuing on a circumlunar flight. A reasonable number for such a point is two hours before the closest approach.

A matrix of sensitivity coefficients may be determined relating lunar position and velocity perturbations from nominal end conditions to position and velocity perturbations occurring earlier. Figures VIII-2-1 and VIII-2-2 each show three of the most important elements of the matrix as a function of time after insertion.

The Earth-centered coordinate reference used is such that the X axis points to 1950 Aries, Z axis to the North Pole, and the Y axis orthogonal to X and Z.

Figure VIII-2-1 shows the sensitivities relating position perturbations at the Moon for velocity deviations from nominal conditions as a function of time after insertion.

Figure VIII-2-2 shows the sensitivities relating velocity perturbations at the Moon for velocity deviations from nominal conditions.

Figure VIII-2-3 shows the sensitivities of velocity at time  $t$  to lunar position perturbations (inverse matrix of sensitivities of Figure VIII-2-1). Insufficient data is available to predict all portions of these curves so parts have been estimated.

These sensitivities may be used to indicate the effect of measurement errors and also the mid-course velocity corrections which must be made to correct for aimpoint errors.

The complete matrix relating insertion errors to aimpoint errors is given in Table VIII-2-3. The complete matrix is used to obtain initial aimpoint errors. After

~~CONFIDENTIAL~~

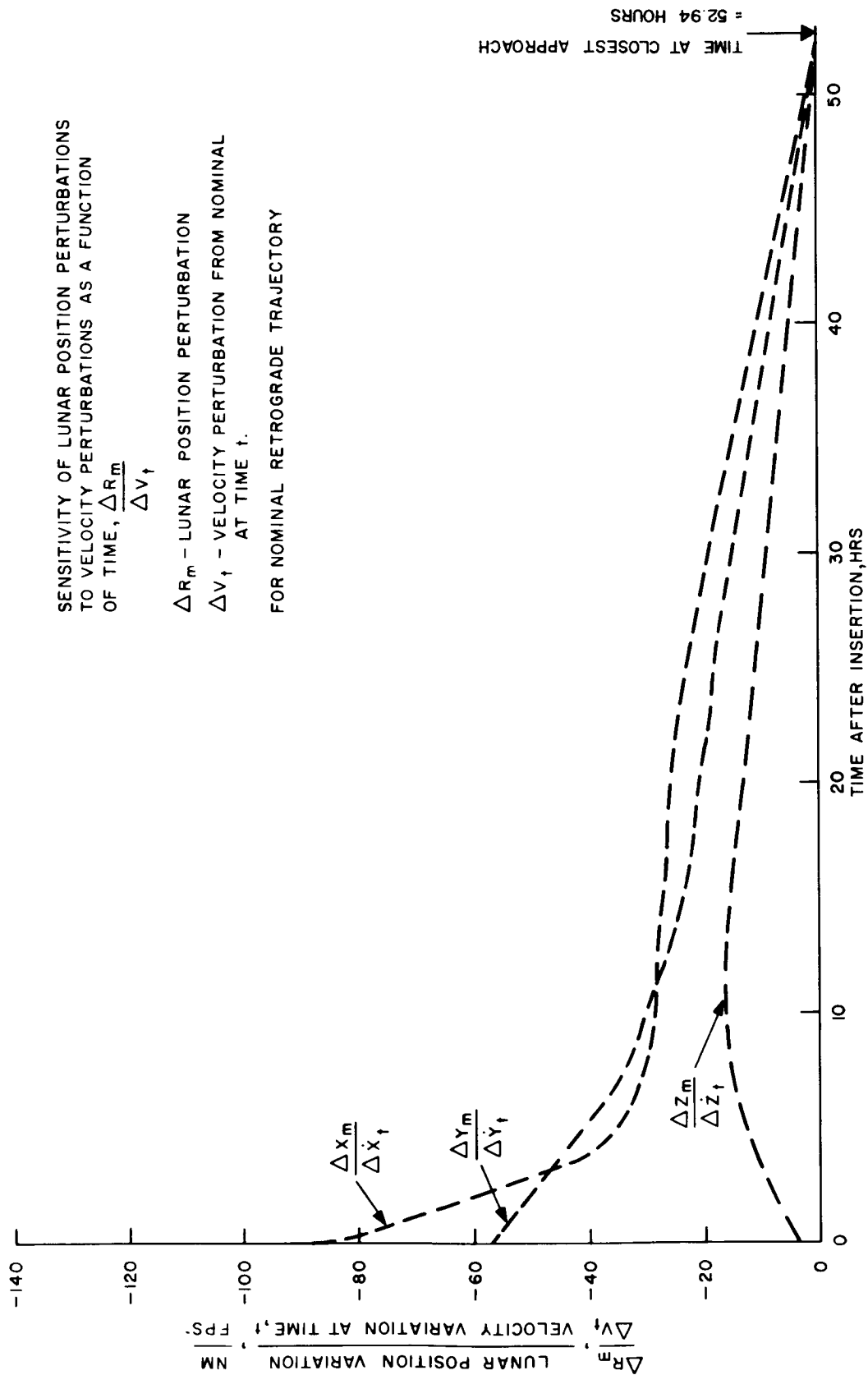
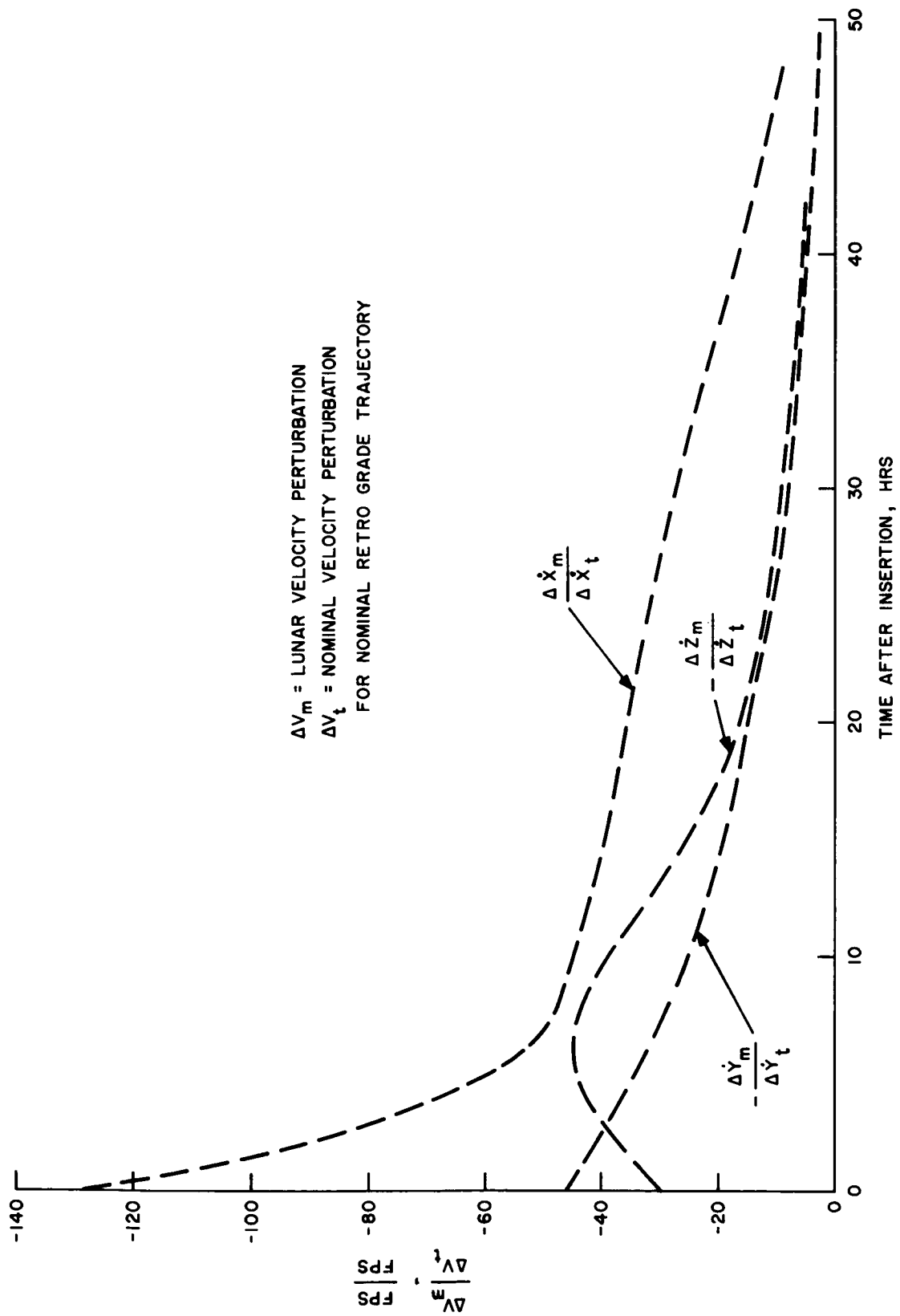


Figure VIII-2-1. Near-lunar position sensitivity to velocity

CONFIDENTIAL



CONFIDENTIAL

Figure VIII-2-2. Sensitivity of lunar velocity perturbations to nominal velocity perturbations at time t.



~~CONFIDENTIAL~~

SENSITIVITY OF MID-COURSE  
CORRECTION VELOCITY TO NULL  
LUNAR POSITION ERRORS  $\frac{\Delta V_t}{\Delta R_M}$

$\Delta R_M$ —LUNAR POSITION PERTURBATION  
 $\Delta V_t$ —VELOCITY PERTURBATION AT  
TIME  $t$   
FOR NOMINAL RETROGRADE  
TRAJECTORY

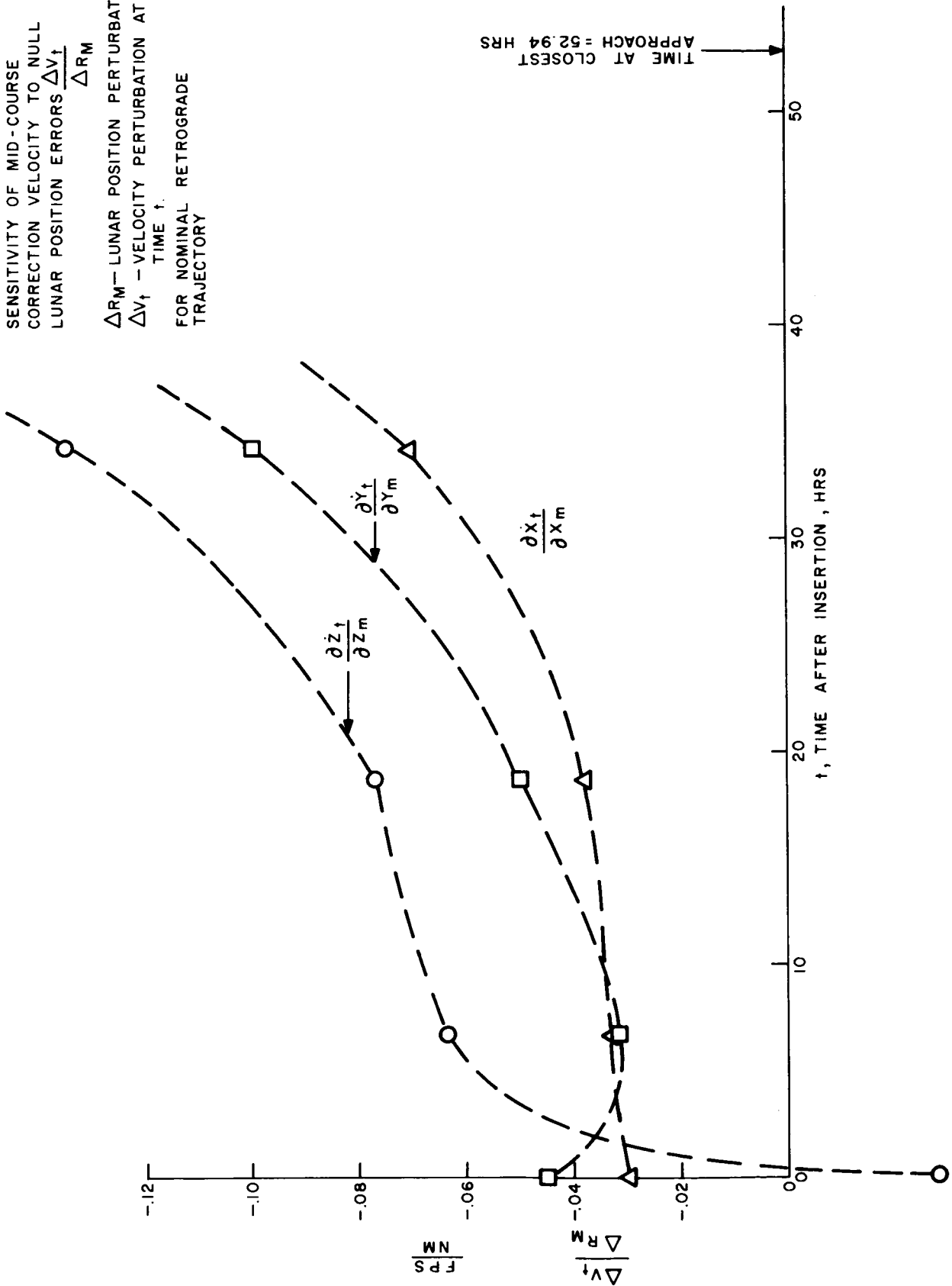


Figure VIII-2-3. Velocity sensitivity to near-lunar position

~~CONFIDENTIAL~~

~~CONFIDENTIAL~~

insertion position errors have a small effect and only velocity errors are considered for preliminary analysis.

Using the sensitivities given in Table VIII-2-3 and approximately the insertion errors of Table VIII-2-1 yields the results given in Table VIII 2-4 for initial aimpoint errors. The insertion errors used are 15 fps ( $3\sigma$ ) for velocity components and one nmi ( $3\sigma$ ) for position components.

TABLE VIII-2-3. MATRIX ELEMENTS RELATING LUNAR POSITION AND VELOCITY VARIATIONS TO INSERTION ERRORS

	$\Delta X_o$	$\Delta Y_o$	$\Delta Z_o$	$\Delta \dot{X}_o$	$\Delta \dot{Y}_o$	$\Delta \dot{Z}_o$
$\Delta X_M$	-335	421	56	-88	-24	-48
$\Delta Y_M$	-479	734	161	-136	-57	-85
$\Delta Z_M$	-260	341	103	-68	-25	-4
$\Delta \dot{X}_m$	-470	566	86	-125	-33	-68
$\Delta \dot{Y}_M$	387	-535	-123	116	46	71
$\Delta Z_M$	175	-200	-106	46	20	30

$\Delta X_o, \Delta Y_o, \Delta Z_o$	-	Position Errors at Insertion, nmi
$\Delta X_M, \Delta Y_M, \Delta Z_M$	-	Position Errors at Lunar Aimpoint, nmi
$\Delta \dot{X}_o, \Delta \dot{Y}_o, \Delta \dot{Z}_o$	-	Velocity Errors at Insertion, fps
$\Delta \dot{X}_M, \Delta \dot{Y}_M, \Delta \dot{Z}_M$	-	Velocity Errors at Lunar Aimpoint, fps

TABLE VIII-2-4. THREE-SIGMA LUNAR AIMPOINT ERRORS FOR ESTIMATED INSERTION ERRORS

$\Delta X$	1640 nmi
$\Delta Y$	2700 nmi
$\Delta Z$	1150 nmi
$\Delta \dot{X}$	1530 fps
$\Delta \dot{Y}$	2200 fps
$\Delta \dot{Z}$	930 fps

\* 15 fps for velocity components ( $3\sigma$ )  
1 nmi for position components ( $3\sigma$ )

~~CONFIDENTIAL~~

Studies are being conducted to determine the accuracy of measurement of position and velocity by on board systems. Preliminary estimates indicate that velocity may be measured to 10 fps or better over sufficient data smoothing intervals. Figure VIII-2-4 indicates the expected miss distance at the lunar aimpoint for a 10 fps velocity deviation from nominal conditions.

For analysis, a desired terminal accuracy at the Moon will be to achieve a miss distance of  $\pm 20$  nmi.

A representative mid-course correction sequence using the expected velocity uncertainty, desired terminal accuracy and insertion errors previously discussed is shown on Table VIII-2-5.

TABLE VIII-2-5. OUTBOUND LEG MID-COURSE CORRECTIONS

Time of Mid-Course Corrections (Hrs)	$\Delta V_X$ (ft/sec)	Mid-Course Velocity Corrections			Vector Result (ft/sec)
		$\Delta V_Y$ (ft/sec)	$\Delta V_Z$ (ft/sec)		
7	24	64	21		71
34	19	34	26		47
41	26	24	29		45
50	40	60	40		82

Velocity corrections are applied whenever the miss distance is at least twice as great as the miss distance due to measurement errors (including inaccuracies of 0.5 fps in providing the velocity correction). No attempt has been made, as yet, to determine an optimum sequence of corrections.

The results are obtained by assuming the measurement error to be always of the same polarity which yields some corrections which are worst possible and some which are not.

Table VIII-2-6 shows an estimate for the aimpoint errors at the nominal distance-of-closest approach to the lunar surface ( $\approx 1000$  miles). The  $\Delta Z$  error occurs approximately normal to the nominal orbital plane with respect to the Moon and represents a rotation of the arrival trajectory plane from the nominal of approximately 0.5 degree. The X-Y axes are rotated in the plane of the distance-of-closest approach by approximately 38 degrees.

~~CONFIDENTIAL~~

**CONFIDENTIAL**

TIME AT DISTANCE OF CLOSEST APPROACH = 52.94 HRS

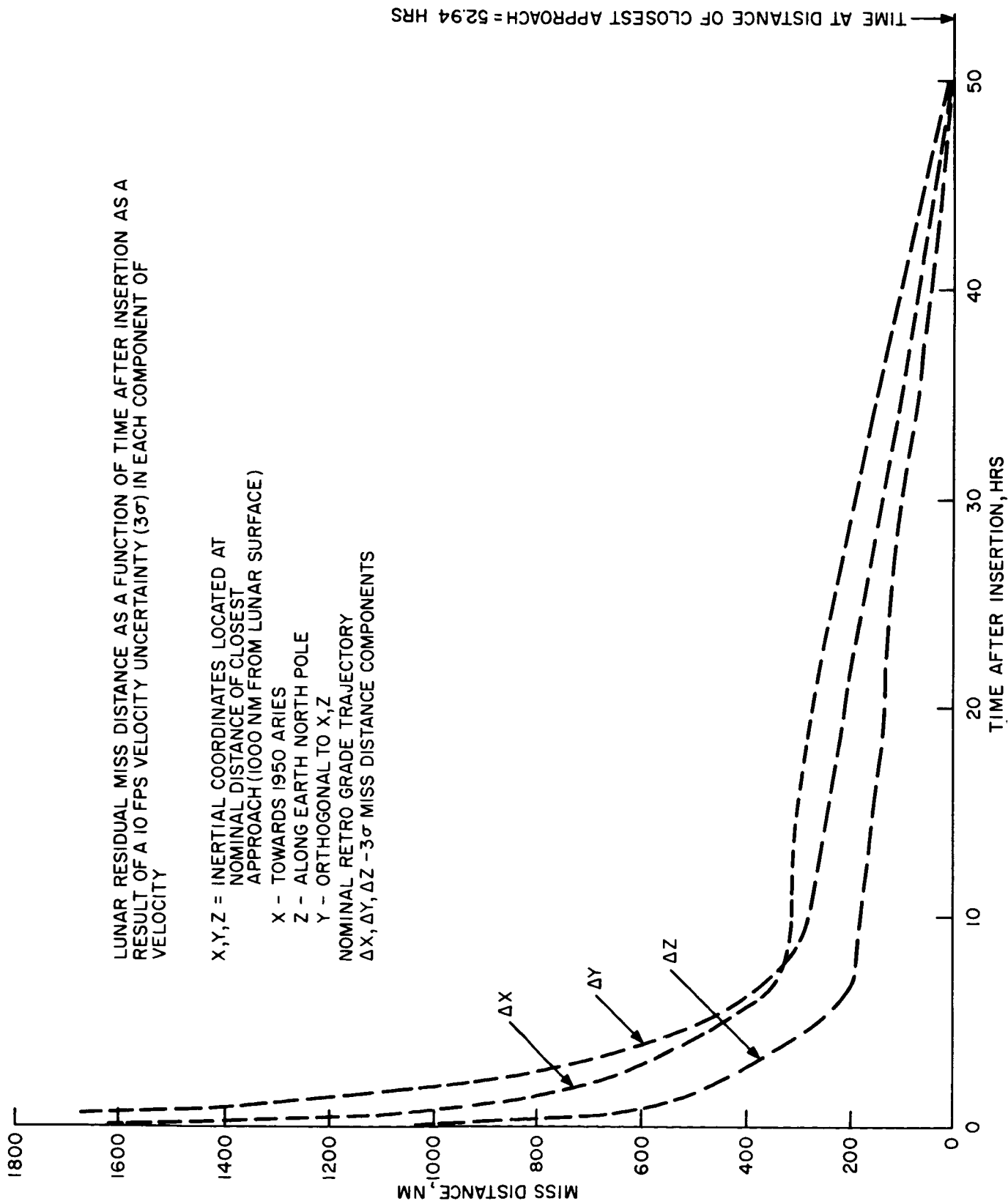


Figure VIII-2-4. Variation of lunar miss distance with time

~~CONFIDENTIAL~~

TABLE VIII-2-6. LUNAR AIMPOINT ERRORS

$\Delta X$	20 nmi
$\Delta Y$	10 nmi
$\Delta Z$	10 nmi
$\dot{\Delta X}$	110 fps
$\dot{\Delta Y}$	50 fps
$\dot{\Delta Z}$	50 fps

To establish an orbit about the Moon, thrust may be applied near the nominal distance-of-closest approach. At this time, the arrival velocity errors may be eliminated (to within measurement uncertainty) to return to approximately nominal conditions. A retro-velocity increment of at least 3000 fps is required to establish an orbit about the Moon. If, simultaneously, the velocity of arrival errors are eliminated vectorially, velocity requirements will be increased by several hundred feet per second.

In the more general case, the mid-course aimpoint may be several hours away from the distance-of-closest approach. The arrival velocity errors at this point will be corrected. The vehicle will thus be placed on the nominal computed trajectory at this point except for measurement errors. The nominal computed trajectory itself will be in error from the true trajectory because of uncertainties of physical parameters.

In general, it is anticipated that the foregoing results can be readily achieved. The effect of varying some of the parameters can be indicated in the following manner: If the insertion errors are increased, the first correction will be proportionately larger (at seven hours) but the remaining corrections will be the same. Thus, for errors combined in a RMS manner the total would tend to approach the first correction. If measurement accuracy is improved, the magnitude of first correction will remain essentially the same but subsequent corrections will be smaller in magnitude and fewer in number for a given terminal accuracy. The total velocity would approach that of the first correction.

If the same measurement errors and insertion errors pertain but the first correction is made earlier, the first correction will have a smaller value but the ensuing corrections would remain the same. The value of seven hours used was to allow sufficient smoothing of data before applying the first correction.

~~CONFIDENTIAL~~

~~CONFIDENTIAL~~

A total estimate of velocity corrections for the outgoing leg would be approximately 300 feet per second.

The foregoing results are based on a retrograde nominal trajectory (modified ellipse). The "Figure 8" nominal trajectory will be studied in more detail but it is not expected that mid-course velocity requirements will change significantly.

## TRANSITION FROM OUTBOUND LEG TO TERMINAL PHASE

The transition from the outbound leg to the terminal phase may be considered to occur where the last mid-course velocity correction is made prior to applying a retro-thrust to orbit the Moon for the nominal mission. The transition is demonstrated by reference to Figure VIII-2-5. At  $R_2$  a mid-course correction,  $C_1$ , is completed which places the vehicle nearly on the nominal trajectory. In this case,  $R_2$  would constitute the nominal aimpoint and velocity-of-arrival errors would be eliminated at this point. The vehicle would then arrive at  $R_1$  with residual velocity and position errors from nominal conditions as a result of errors existing at  $R_2$ . The distance  $R_2$  must be established such that the desired time delay before initiating the retro-thrust  $C_2$  at  $R_1$  is compatible with allowable arrival errors at  $R_1$ .

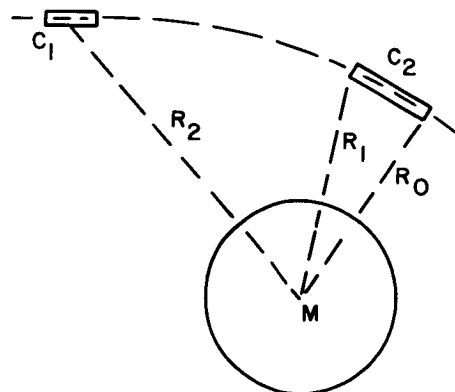


Figure VIII-2-5. Transition phase

From the results of previous investigation for outbound leg mid-course corrections the errors propagated to point  $R_1$  would be of the order of 20 miles in the three components

~~CONFIDENTIAL~~

~~CONFIDENTIAL~~

of position uncertainty and 30 fps in velocity components (for 10 fps measurement errors). The velocity errors may be eliminated simultaneously with the retro-thrust starting at  $R_1$  and terminating at  $R_0$ .

For the "modified ellipse" trajectory used,  $R_2$  would be about 20,000 miles for a two-hour time delay before reaching the nominal distance-of-closest approach at 53 hours.

## INJECTION INTO ORBIT AROUND THE MOON

An investigation of injection sensitivities was made in order to determine the effects of measurement inaccuracies. Since there are no critical requirements on a 1000 nmi circular orbit and the 50-100 nmi altitude perilune can be approached in steps which can be monitored, the results indicate that lunar orbit injection places no highly critical requirements on hardware unless a highly precise ( $\pm 1$  nmi perilune altitude tolerance) orbit must be achieved. Sensitivities for the case of first transferring to a circular orbit about the Moon at an altitude of 1000 nmi above the surface of the Moon are summarized below.

$$(a) \quad \frac{\partial h'}{\partial h_i} = 3 \text{ nmi/nmi}$$

where

$h_i$  = Injection altitude

$h'$  = Altitude 180 degrees from point of injection

$$(b) \quad \frac{\partial h'}{\partial \epsilon} = 25 \text{ nmi/degree}$$

where

$\epsilon$  = Angular error of incremental velocity vector with respect to the local horizontal in the plane of the orbit.

$$(c) \quad \frac{\partial h'}{\partial \nu_h} = 2 \text{ nmi/fps}$$

where

$\nu_h$  = horizontal velocity at injection point

~~CONFIDENTIAL~~

$$(d) \quad \frac{\partial \beta}{\partial \alpha} = 0.76 \text{ degree/degree}$$

where

$\alpha$  = angular error of incremental velocity vector with respect to the vehicle velocity vector in local horizontal plane

$\beta$  = Angle of orbital plane with respect to nominal plane determined by vehicle velocity vector.

After the circular orbit has been achieved by the application of a velocity decrement of about 2350 fps, additional incremental velocity corrections, which will total about 700 fps, can be made at the selected apolune position in order to bring the vehicle safely to a minimum altitude of 50 to 100 nmi. The sensitivity coefficients also change.

For example,

$$\frac{\partial h'}{\partial v_h} = 0.93 \text{ nmi/fps}$$

$$\frac{\partial h'}{\partial h_i} = 1.25 \text{ nmi/nmi}$$

when transferring directly from the circular orbit to the specified elliptical orbit.

In order to achieve a perilune altitude of 50 nmi with an RMS tolerance of one nmi, the error in velocity at the injection point must be less than 0.75 fps and the altitude error must be less than 0.56 nmi for the case where velocity and position errors contribute equally to the total error. The anticipated errors at the time of closest approach (10 fps in velocity and 5 nmi in altitude) would result in an RMS error of 11.2 nmi at perilune if a direct transfer from the hyperbolic approach trajectory to the elliptical orbit were made.

## TRANSITION FROM LUNAR ORBIT TO RETURN LEG

The transition from the lunar orbit phase to the return mid-course leg may be considered to occur at the escape thrust phase termination. Range and cross range position should

~~CONFIDENTIAL~~



~~CONFIDENTIAL~~

be known to 5 nmi or better for altitudes of 2000 nmi or less. It is estimated that velocity can be measured to 10 fps. Studies are still in progress to obtain more details for the accuracy of these measurements.

An escape velocity increment of the order of 3000 fps must be measured. With a stellar monitored reference accurate to 0.01 degrees ( $3\sigma$ ) or better and accelerometers with scale factor errors of  $1 \times 10^{-4}$  the velocity increment can be measured to better than 2 fps. Thrust tail-off uncertainties are expected to be  $\pm 0.5$  fps or less.

The foregoing results are also applicable to the retro-thrust accuracy for establishing the lunar orbit for the terminal retro-thrust phase.

## RETURN LEG MID-COURSE VELOCITY CORRECTIONS

To obtain an estimate for the return leg mid-course velocity correction requirements and expected re-entry accuracy, deviations are specified in terms of re-entry vacuum perigee variations about a nominal value. Allowable variation of perigee is approximately 40 nmi for a 0.5 L/D vehicle or  $\pm 1.5$  degree re-entry flight path angle at an altitude of 400,000 feet.

The same guidance concept is employed as for the out bound leg - i. e. a fixed time-of-flight to the aimpoint is considered. In this case, to achieve a nominal re-entry for landing at a given landing site, any variations in time-of-flight of the total mission from insertion (as the datum point\*) to landing must be made up.

The following estimate for mid-course correction velocity requirements uses data based on co-planar three-body trajectories and two-body data when the Earth's gravitational field is most significant.

---

\* Time-of-flight variations which occur during powered flight to insertion can be made up on the outgoing leg. For one engine failure, a variation of two minutes or less is expected. This variation can also be corrected by the boost guidance system as well.

~~CONFIDENTIAL~~

~~CONFIDENTIAL~~

## Vacuum Perigee Sensitivity of Lunar Escape Initial Conditions

Table VIII-2-7 shows the variation of vacuum re-entry perigee to variations of altitude and velocity magnitude at lunar escape for a "Figure-8" return trajectory. Time-of-flight errors of 0.03 hours/ft/sec are typical at this point.

TABLE VIII-2-7. LUNAR ESCAPE SENSITIVITIES FOR "FIGURE-EIGHT" RETURN TRAJECTORY

<u>Escape Lunar Altitude</u>	$\frac{-R_p}{R_m}$	$\frac{R_p}{V_m}$
(NM)	NM/NM	nm/ft-sec
1000	67	66
2000	32	62

$R_p$  = variation in re-entry vacuum perigee

$R_m$  = variation in lunar escape altitude

$V_m$  = variation in lunar escape velocity

To obtain a representative estimate for the return leg mid-course maneuver requirements we consider that escape altitude errors of 5 nmi ( $3\sigma$ ) and escape velocity errors of 10 fps ( $3\sigma$ ) can be achieved. The resulting vacuum perigee variation is 700 nmi ( $3\sigma$ ) for a 2000 nmi nominal escape. In addition, 15 minutes or less is expected as an initial time-of-flight error. This error accrues from time-of-flight errors for the outgoing leg mid-course phase and time errors occurring while in the lunar orbit (for seven days) from semi-major axis uncertainties. This error must be eliminated on the return leg.

## Allowable Velocity Vector Errors

Figure VIII-2-6 shows the allowable flight path angle variation  $|\gamma|$  velocity vector magnitude error  $\Delta V$  and radial position error  $\Delta R$  which results in a 25 nmi variation in vacuum perigee for each component of error. These sensitivities are shown as a function of distance from the Earth.

~~CONFIDENTIAL~~

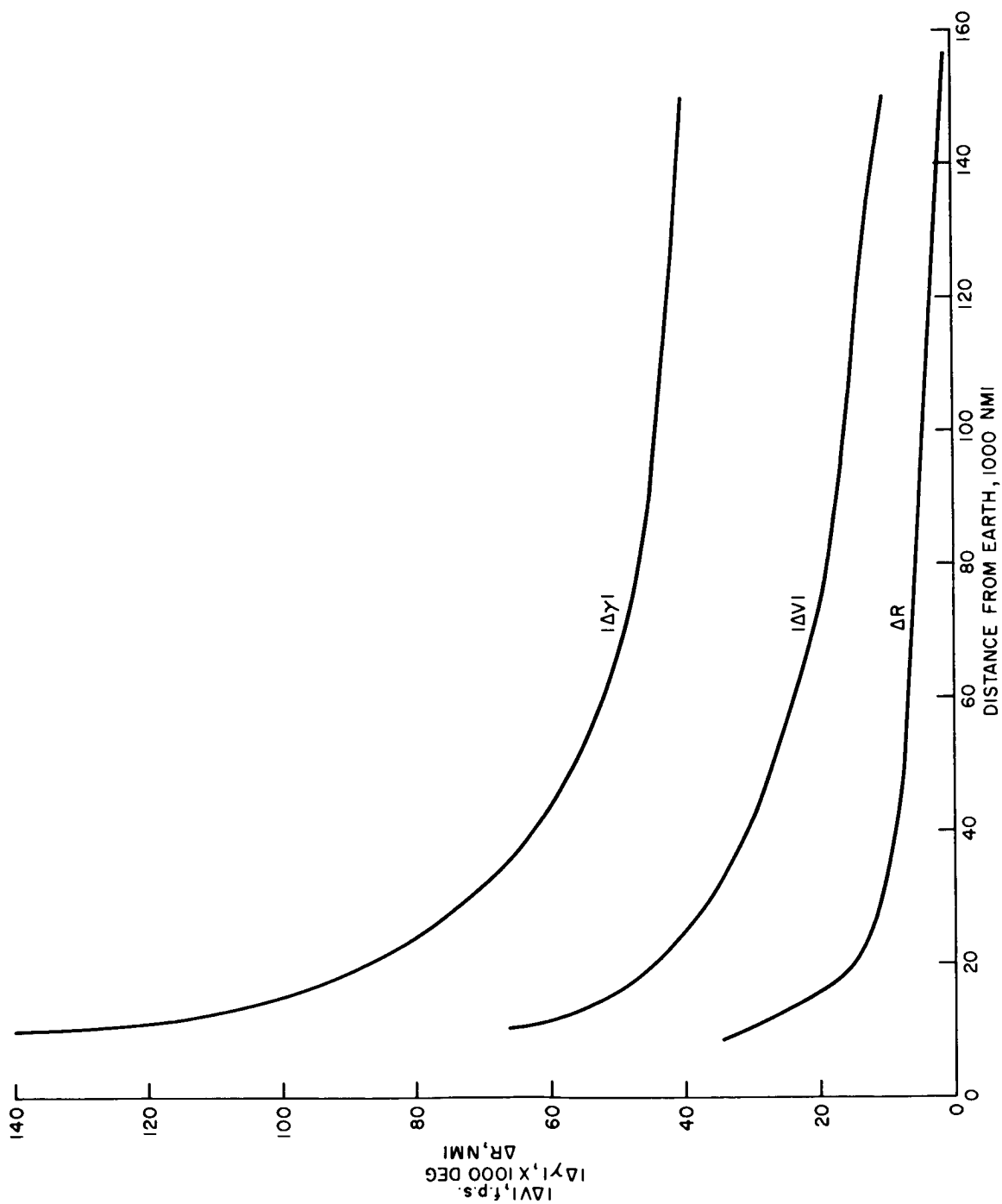


Figure VIII-2-6. Maximum allowable velocity magnitude error  $|\Delta V|$ , flight path angle error  $|\Delta \gamma|$ , and radial position error,  $\Delta R$ , for 25 nmi re-entry perigee variation as a function of distance from earth

~~CONFIDENTIAL~~

The eccentricity of the return leg orbit is 0.97 and the semi-major axis is 120,000 nmi in the region of the Earth where two body approximations apply.

### **Single Mid-course Velocity Correction Maneuver**

Figure VIII-2-7 shows the single velocity increment required to correct for an initial vacuum perigee variation of 700 nmi. The velocity increment requirement may be scaled linearly for any other desired initial perigee variation.

The velocity correction is applied in the optimum direction which is approximately perpendicular to the radius vector to the Earth to correct for perigee errors. Time of arrival errors are corrected independently of perigee error by corrections approximately along the radius vector.

### **Vacuum Perigee Variation as a Function of Representative Mid-course Velocity Measurement Error**

Figure VIII-2-6 shows the vacuum perigee error for a velocity measurement error of 10 fps ( $3\sigma$ ) and 5 nmi during the mid-course return flight. The curve is obtained from the results of Figure VIII-2-5 by combining the perigee error resulting from velocity magnitude and flight path angle errors in an RMS manner.

### **Return Leg Mid-course Velocity Correction Sequence**

A representative return leg correction sequence may be indicated in the following manner. A velocity correction will be made whenever the predicted perigee variation is at least twice as great as the perigee variation which would result from velocity uncertainties ( $3\sigma$ ).

We will apply this criterion for an initial perigee variation of 700 nmi( $3\sigma$ ) as indicated previously and consider that velocity measurement uncertainty of 10 fps ( $3\sigma$ ) will exist whenever a correction is made (the corrections must be spaced in time such that sufficient data smoothing time is available between corrections).

Table VIII-2-8 summarizes the results of the return leg mid-course maneuvers. It is seen that the total maneuver requires 87 fps ( $3\sigma$ ) and the vacuum perigee error is

~~CONFIDENTIAL~~

~~CONFIDENTIAL~~

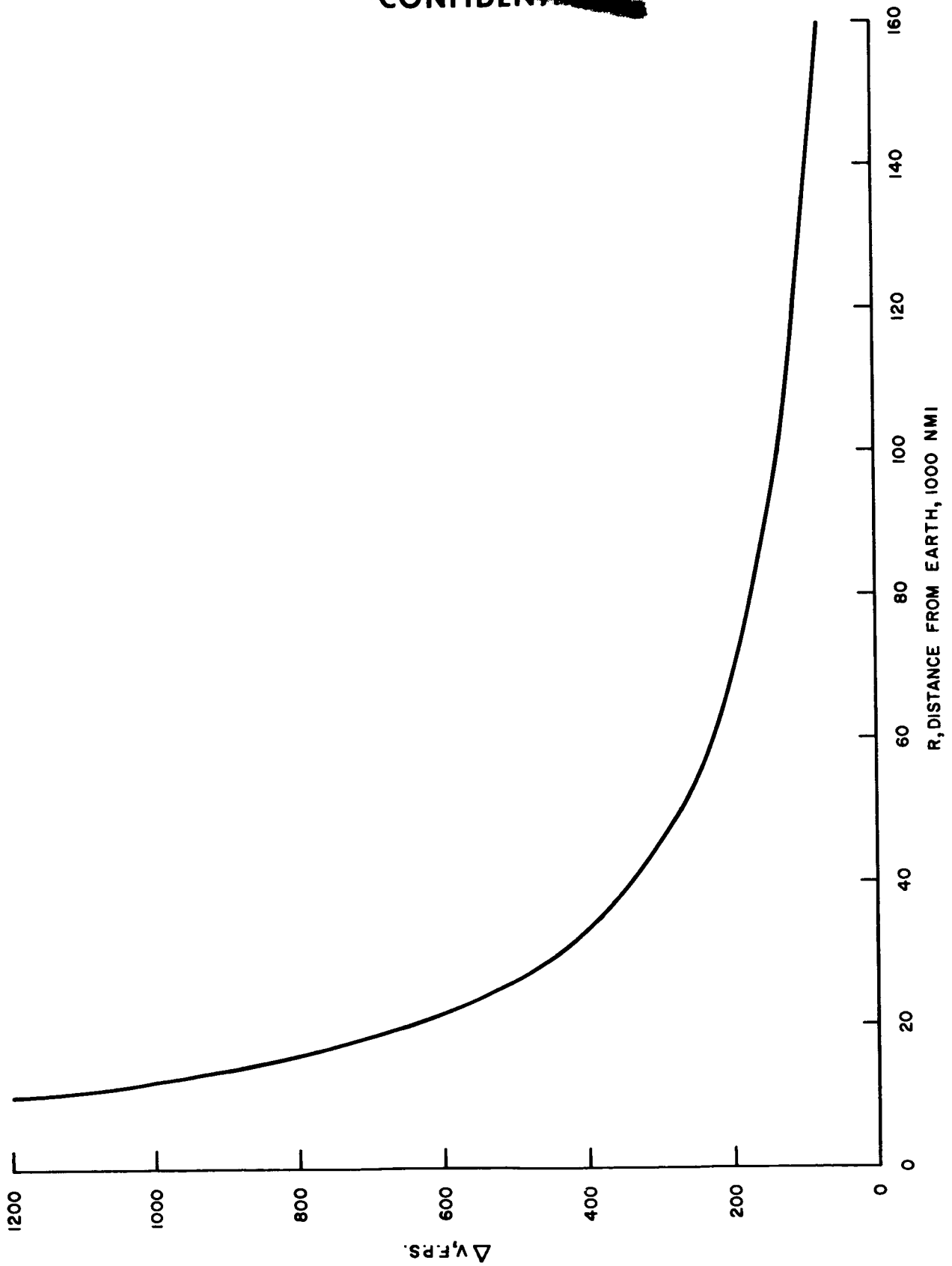


Figure VIII-2-7. Mid-course velocity increment,  $\Delta V$ , required to null an initial perigee error of 700 nmi as function of radial distance from Earth

~~CONFIDENTIAL~~

~~CONFIDENTIAL~~

12 nmi ( $3\sigma$ ) at the last correction 20,000 nmi from the Earth center. The expected variation in re-entry flight path angle is approximately 1.5 degrees. If the last correction occurred at 10,000 miles the perigee error would be 8 nmi.

For the fixed time-of-arrival concept, velocity-of-arrival deviations will have to be corrected at the nominal aimpoint. Studies are not yet complete to obtain this estimate.

TABLE VIII-2-8. REPRESENTATIVE RETURN LEG MID-COURSE CORRECTIONS

<u>Distance from Earth when Correction Made</u>	<u>Magnitude of Correction</u>	<u>Residual Perigee Error</u>
(1000 nmi)	(ft/sec)	(nmi)
210	0	700
200	56	250
150	16	125
100	54	62
50	18	20
20	<u>30</u>	12
Total	174	
	87 ( $3\sigma$ )	

The effect of improved accuracy of mid-course measurements or larger errors at escape may be indicated in the following manner.

If the mid-course data processing and velocity-to-be gained system can determine and make velocity corrections to  $\pm 1$  fps accuracy after escape the first mid-course correction at 200,000 miles from the earth would require the same velocity increment as before but the resulting vacuum perigee error would be  $\pm 17$  nmi. One more correction at 50,000 miles of 30 fps would yield a 3 nmi perigee error. The total velocity correction would be 86 fps. Thus only two corrections are required and resulting accuracy is greatly improved. (These results neglect the errors due to uncertainties in physical constants.)

~~CONFIDENTIAL~~

~~CONFIDENTIAL~~

If the escape velocity error is increased by a factor of five to 50 fps and mid-course measurement accuracy is unchanged, the first correction would be 200 fps as compared to 56 fps and the remaining corrections would be unchanged. Table VIII-2-9 summarizes the results.

TABLE VIII-2-9. COMPARISON OF EFFECT OF VELOCITY MEASUREMENT ERRORS

Mid-course Velocity Measurement Error (ft/sec)	Escape Velocity Error (ft/sec)	Number of Corrections	Total Velocity Correction (ft/sec)	Residual Error nmi
10	10	5	175	12
1	10	2	86	3.0
10	50	5	320	12

## MID-COURSE TERMINAL ERRORS

The mid-course guidance system will establish a variation of vacuum perigee of less than  $\pm 12$  nmi for a final mid-course correction made at 20,000 nmi from the center of the Earth. For this perigee variation, the re-entry angle variation at 400,000 feet will be less than  $\pm 0.75$  degrees.

Studies are still being made for the re-entry phase, but an estimate of the expected initial condition errors at re-entry altitude can be made.

The angular in-plane error about the nominal re-entry point is approximately two times the re-entry angle variation for near parabolic orbits. This error corresponds to less than  $\pm 100$  nmi on the Earth's surface.

The out-of-plane errors are related by

$$A_f = \sin \theta B_i + \cos \theta A_i$$

$$B_f = -\cos \theta B_i + \sin \theta A_i$$

~~CONFIDENTIAL~~

~~CONFIDENTIAL~~

Where

$A_f$  = final out-of-plane angular error

$B_f$  = final out-of-plane velocity vector angle error

$A_i$  = initial out-of-plane angular error

$B_i$  = initial out-of-plane velocity vector angular error

$\theta$  = true anomaly between initial and final position

For a 10 fps velocity error at 20,000 nmi, horizontal velocity component of 7000 fps,  $\theta$  approximately equal to 130 degrees, and a position error of 5 nmi; the resulting error in out-of-plane position is  $\pm 5$  nmi. Time-of-flight errors to the re-entry point will be one minute or less. The resulting maximum cross range position error will be  $\pm 15$  miles or less (for the maximum case of a polar return).

## RE-ENTRY INITIAL CONDITION ERRORS

Studies are in progress to determine the expected landing dispersion. As a preliminary estimate, the on-board navigation system will be able to establish position at re-entry altitude to better than 5 nmi ( $3\sigma$ ) and velocity to better than 10 fps ( $3\sigma$ ). Expected accuracy will be better than 10 nmi for a time-of-flight of 1000 seconds from re-entry to landing and a maximum down-range variation from re-entry to landing of 2000 miles.

## EMERGENCY ESCAPE

Studies are being made to determine the regions after insertion in which a successful return to Earth may be accomplished for an abort from the nominal mission.

It is anticipated that mid-course corrections will be needed and required accuracies will be similar to those for the nominal lunar mission to at least successfully re-enter and, if possible, to land at a pre-selected landing site.

~~CONFIDENTIAL~~



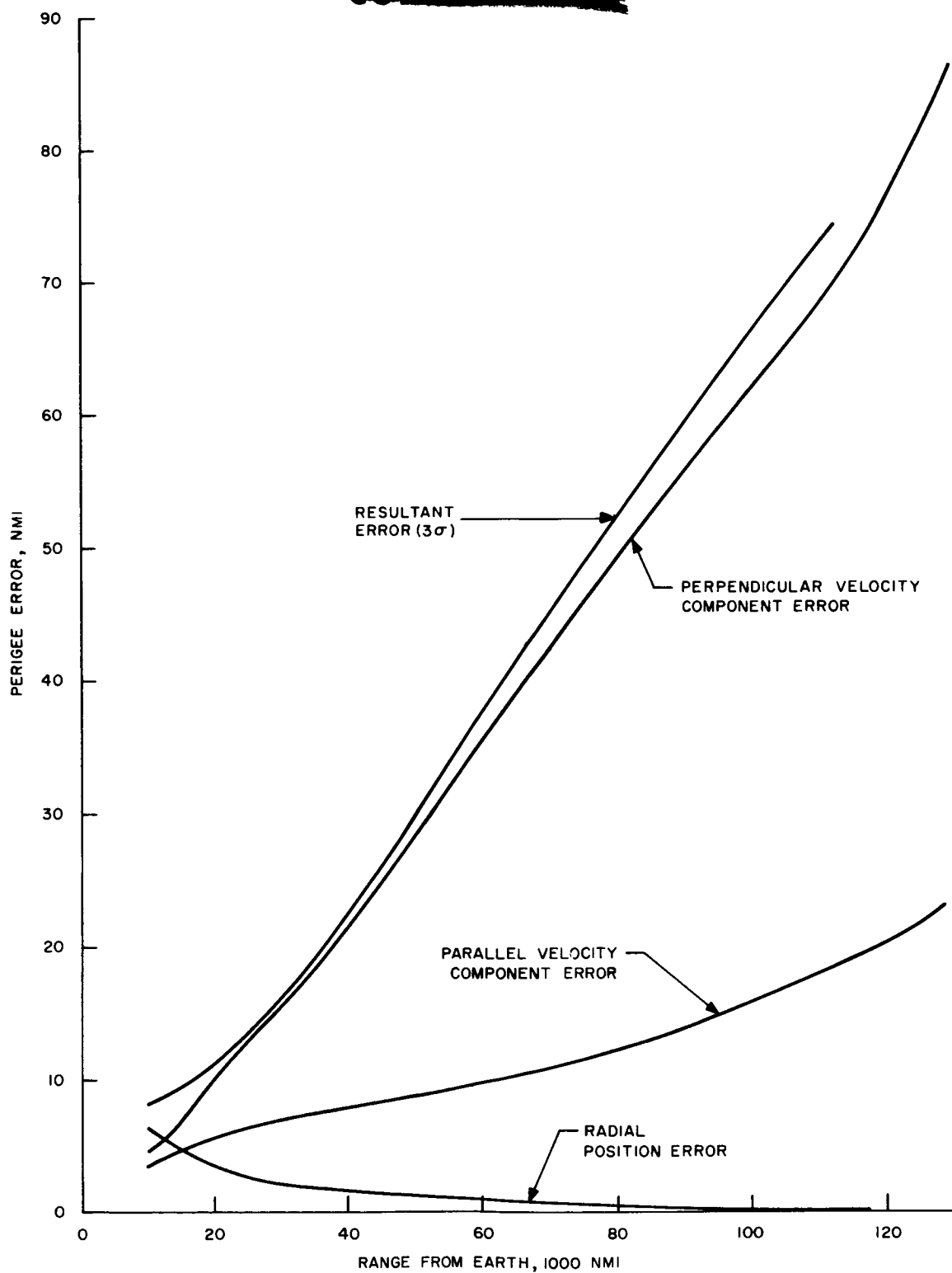


Figure VIII-2-8. Vacuum perigee error vs range from Earth for 10 fps velocity error both parallel and perpendicular to the velocity and radial position error of 5 nmi

~~CONFIDENTIAL~~

### 3. GUIDANCE CONCEPTS

Midcourse guidance techniques fall into two categories. The first of these, usually called implicit guidance, makes use of a precomputed, stored trajectory which is used as a nominal trajectory. After each position fix, the deviation of the vehicle from the nominal is computed and the required velocity correction is computed using error matrices. These matrices are precomputed for the nominal trajectory and stored in the computer memory. The second, or explicit, technique depends on the computer to provide velocity corrections from observed positional information and knowledge of the required astronomical constants only.

The implicit technique involves less arithmetical operations than the explicit technique. However, since trajectory information and error matrices must be stored for every position at which it is desired to compute a correction, the memory requirement becomes quite large. Although these requirements would probably not be excessive for only one nominal trajectory, the necessity of providing for a large number of emergency return trajectories precludes the use of this technique exclusively, at least for abort or emergency return conditions. In addition, for engine-out failure the lunar nominal trajectory may also be severely perturbed. The problem of achieving the proper initial conditions to follow a precomputed return trajectory after orbiting the moon seems formidable, especially if a large number of passes around the moon is contemplated. This method, however, is being studied further.

For the above reasons, an explicit guidance technique is desirable. Any explicit technique consists of two operations. Using the observed position and velocity as initial conditions, the trajectory is computed and the miss distance from the target point determined. The desired velocity correction is then computed using error coefficients as in the implicit scheme. Several methods are possible for the trajectory computation. A highly accurate program to integrate the differential equations of motion, such as the Cowell, Encke or multiple two-body methods, can be used.

CONFIDENTIAL

The sequence of operations for an explicit guidance scheme is as follows:

1. Several sets of observations are made over a period of a few hours. From these smoothed measurements, the position and velocity of the vehicle at a particular time,  $t_0$ , can be computed. For best accuracy, this time should be near the middle of the interval during which the observations are being made.
2. With the computed position and velocity at  $t_0$  as initial conditions, a trajectory computation is made, giving position and velocity at two times,  $t_1$  and  $t_2$ , where  $t_1$  is the time at which the velocity correction will be made and  $t_2$  is the desired time of arrival at the aim point.  $t_1$  should be chosen so as to allow sufficient time for all necessary computations prior to correction.
3. The expected miss vector,  $\vec{\gamma}_m$ , is obtained by subtracting the position at the aim point from the predicted vehicle position at  $t = t_2$ .
4. Three trajectories are now computed using the position and velocity at  $t_1$  as initial conditions, perturbing one component of velocity at a time. For each trajectory, the three components of the difference in position at  $t_2$  between this trajectory and the unperturbed trajectory are obtained. These nine quantities are the elements of the error matrix  $A$ .
5. A trial velocity correction is obtained from the relation:  $\vec{\Delta V} = A^{-1} \vec{\gamma}_m$ , where  $A^{-1}$  is the inverse of  $A$ .
6. A new trajectory is computed using  $\vec{V}_1 + \vec{\Delta V}$  as the initial velocity at  $t_1$ .
7. The last two steps are repeated until the miss vector has been reduced to a sufficiently small value.
8. The final value at  $\vec{\Delta V}$  is stored until  $t_1$  at which time the indicated velocity correction is made.

The amount of computation for the above procedure required may be found to be excessive, either because the computer needed is too large or because the computation time is too long. It may be possible to relieve the burden on the computer by storing error matrices which are computed for a nominal trajectory. If the actual trajectory does not deviate too far from this nominal, the nominal trajectory error coefficients may be usable.

~~CONFIDENTIAL~~

The computer requirements can be still further eased by breaking the trajectory computation down into the two-body computations, one with respect to the Earth and the other with respect to the Moon. (This is the so-called "patched conic" technique.)

Any errors in the trajectory computation will result in errors in the velocity correction. Since these errors will have to be corrected for at a later time, more propellant will be required. This indicates a tradeoff involving computer weight versus propellant weight.

An alternative approach consists of guiding the vehicle to an aim point outside the "sphere of influence" of the Moon, transforming to moon coordinates and continue by guiding to the required distance of closest approach to the Moon.

Each part of this trajectory would be close to a two-body trajectory, the first an ellipse with the Earth at one focus and the second a hyperbola with the Moon at one focus. The error coefficients could then be computed analytically from the well-known two-body formulae. The return trip would be accomplished by applying this method in reverse. This method requires less computation than those described earlier; however, it may be necessary to make a fairly large velocity correction after reaching the first aim point.

A guidance scheme which is only approximate should still be adequate for the job if the inherent errors in the method are sufficiently less than the instrumentation errors.

## SOLUTION OF EQUATIONS OF MOTION

The equation of motion of a body of zero mass in a coordinate system centered at a mass point  $M_K$  and subject to the gravitation attraction at  $n$  mass points is:

$$\ddot{\vec{R}}_K = -K^2 (M_K + m) \frac{\vec{R}_K}{R_K^3} - K^2 \sum_{\substack{i=1 \\ j \neq K}}^n M_j \left[ \frac{\vec{R}_i}{R_i^3} - \frac{\vec{R}_{Kj}}{R_{Kj}^3} \right] \quad (1)$$

where  $R_K$  is the position vector of  $m$  with respect to  $M_K$ , and  $R_j$  and  $R_{Kj}$  are the position vectors of  $m$  and  $M_K$  with respect to  $M_j$ . In order to integrate this equation it is necessary to know:

~~CONFIDENTIAL~~

~~CONFIDENTIAL~~

- (1) The initial position and velocity of  $m$
- (2) The positions of the  $M_j$ 's with respect to  $M_K$  as functions of time.

Three of the most suitable methods which are available for the solution of this equation are the Cowell method, the Encke method, and the multiple two-body method.

### Cowell Method

The Cowell method consists of integrating Equation (1) directly using some method of numerical integration such as the Runge-Kutta.

### Encke Method

The Encke method consists of computing the perturbations of  $m$  from the conic trajectory it would follow if  $M_K$  were the only attracting body. This conic trajectory is given by:

$$\ddot{\vec{F}}_K = -K^2 (M_K + m) \frac{\vec{F}_K}{F_K^3} \quad (2)$$

for which an analytic solution can easily be obtained. Subtracting  $F_K$  from Equation (1) we have

$$\ddot{\vec{\rho}} = -K^2 (M_K + m) \left( \frac{\vec{R}_K}{R_K^3} - \frac{\vec{F}_K}{F_K^3} \right) - K^2 \sum_{\substack{j=1 \\ j \neq K}}^n M_j \left[ \frac{\vec{R}_j}{R_j^3} - \frac{\vec{R}_{Kj}}{R_{Kj}^3} \right] \quad (3)$$

where:  $\vec{\rho} = \vec{R}_K - \vec{F}_K$

Equation (3) is integrated numerically and the result added to the two body solution  $F_K$  to find  $R_K$ . The advantage of this method is that the quantity integrated changes more slowly than in the Cowell method, allowing the use of a longer integration interval. The advantage over the Cowell method is particularly marked when the disturbing potentials are small.

~~CONFIDENTIAL~~

~~CONFIDENTIAL~~

If the perturbation is small, the quantity

$$\left( \frac{\vec{R}_K}{R_K^3} - \frac{\vec{F}_K}{F_K^3} \right)$$

represents the difference between two nearly equal quantities, which is undesirable for computation. This difficulty can be overcome by expanding this quantity as follows:

$$\frac{R_K}{R_K^3} - \frac{F_K}{F_K^3} = \frac{1}{F_K^3} (f q r_i - \sigma_i) \quad -i = 1, 2, 3 \quad (4)$$

where:

$$f q = 3 q - \frac{3 \cdot 5}{2!} q^2 + \frac{3 \cdot 5 \cdot 7}{3!} q^3 - \dots$$

and:

$$q = \frac{1}{F_K^2} \sum_{i=1}^3 \sigma_i \left( \gamma_i + \frac{1}{2} \sigma_i \right)$$

The  $\gamma_i$  are the three components of  $\vec{F}_K$  and the  $\sigma_i$  are the three components of  $\vec{\rho}$  in a rectangular coordinate system.

If  $\vec{R}_K$  is small compared with  $\vec{R}_{Kj}$ , the same situation exists with the term

$$\frac{\vec{R}_j}{R_j^3} - \frac{\vec{R}_{Kj}}{R_{Kj}^3}$$

In this case the same transformation can be used, except that now the  $\gamma_i$  are components of  $\vec{R}_{Kj}$  and the  $\sigma_i$  are components of  $\vec{R}_j - \vec{R}_{Kj} = \vec{R}_K$ . This transformation is useful only if

$$\frac{|\vec{\rho}|}{|\vec{R}_K|} \text{ or } \frac{|\vec{R}_K|}{|\vec{R}_{Kj}|}$$

~~CONFIDENTIAL~~

~~CONFIDENTIAL~~

is small (e.g., less than 0.1) since the series for  $f_q$  converges slowly if  $q$  is too large.  $\rho$  can be kept small by finding a new two body trajectory whenever  $\rho$  exceeds a predetermined amount. This process is known as rectification. It can be seen that the necessity for computing two body solutions, together with the transformations described above, result in considerably more mathematical operations than the Cowell method, so that the Encke method is preferable only if the perturbations are small and a large number of integration steps can be made between rectifications.

### Multiple Two-Body Method

This method is similar to the Encke method in that it computes the perturbations of  $m$  from a conic trajectory. It differs from the Encke by avoiding the use of numerical integration altogether. Instead, the perturbations are obtained by a superposition of two body solutions around the various perturbing bodies. The method is developed as follows:

Let

$$\vec{\phi}_K(t) = \vec{F}_K(t) + \sum_{\substack{j=1 \\ j \neq K}}^n \left[ F_j(t) - F_{Kj}(t) \right] \quad (5)$$

where, as before:

$$\ddot{\vec{F}}_K = -K^2 (M_K + m) \frac{\vec{F}_K(t)}{F_K^3(t)}$$

with initial conditions

$$\vec{F}_K(t_0) = \vec{R}_K(t_0), \quad \dot{\vec{F}}_K(t_0) = \dot{\vec{R}}_K(t_0).$$

Also

$$\ddot{\vec{F}}_j(t) = -K^2 M_j \frac{\vec{F}_j(t)}{F_j^3(t)}$$

with initial conditions:

$$\vec{F}_j(t_0) = \vec{R}_j(t_0), \quad \dot{\vec{F}}_j(t_0) = \dot{\vec{R}}_j(t_0)$$

~~CONFIDENTIAL~~

~~CONFIDENTIAL~~

and

$$\ddot{\vec{F}}_{Kj}(t_0) = -K^2 M_j \frac{\vec{F}_{Kj}(t)}{F_{Kj}^3(t)}$$

with initial conditions:

$$\vec{F}_{Kj}(t_0) = \vec{R}_{Kj}(t_0), \quad \dot{\vec{F}}_{Kj}(t_0) = \dot{\vec{R}}_{Kj}(t_0)$$

The vectors  $\vec{F}$  are solutions to two body problems, which can be computed easily.

Now define:

$$\vec{\rho}(t) = \vec{R}_K(t) - \vec{\phi}(t) \quad (6)$$

We have:

$$\ddot{\vec{\phi}}(t) = \ddot{\vec{F}}_K(t) + \sum_{\substack{j=1 \\ j \neq K}}^n \ddot{\vec{F}}_j(t) - \ddot{\vec{F}}_{Kj}(t)$$

$$\ddot{\vec{\phi}}(t) = -K^2 (M_K + m) \frac{\vec{F}_K(t)}{F_K^3(t)} - K^2 \sum_{\substack{j=1 \\ j \neq K}}^n M_j \left[ \frac{\vec{F}_j(t)}{F_j^3(t)} - \frac{\vec{F}_{Kj}(t)}{F_{Kj}^3(t)} \right] \quad (7)$$

$$\therefore \vec{\phi}(t_0) = \vec{R}_K(t_0) \quad \text{from the initial conditions.}$$

and

$$\therefore \ddot{\vec{\rho}}(t_0) = \ddot{\vec{R}}_K(t_0) - \ddot{\vec{\phi}}(t_0) = 0$$

Differentiating  $\ddot{\vec{\phi}}(t)$  and  $\ddot{\vec{R}}(t)$  and evaluating at  $t = t_0$

gives

$$\vec{\phi}(t_0) = \vec{R}_K(t_0)$$

$$\therefore \ddot{\vec{\rho}}(t_0) = 0$$

If  $\vec{\rho}(t)$  is expanded in a Taylor series, we have

$$\vec{\rho}(t_0 + \Delta t) = \vec{\rho}(t_0) + \dot{\vec{\rho}}(t_0) \Delta t + \ddot{\vec{\rho}}(t_0) \frac{(\Delta t)^2}{2!} + \dots \quad (8)$$

~~CONFIDENTIAL~~



~~CONFIDENTIAL~~

since

$$\ddot{\vec{p}}(t_0) = \ddot{\vec{p}}(t_0) = 0$$

Now

$$\vec{p}(t_0) = \vec{R}_K(t_0) - \vec{\phi}_K(t_0) = \sum_{\substack{j=1 \\ j \neq K}}^n \left[ \vec{F}_j(t_0) - \vec{F}_{Kj}(t_0) \right] = -(n-1) \vec{F}_K(t_0) = -(n-1) \vec{R}_K(t_0) \quad (9)$$

Similarly,

$$\dot{\vec{p}}(t_0) = -(n-1) \dot{\vec{R}}_K(t_0) \quad (10)$$

$$\therefore \vec{R}_K(t + \Delta t) = \vec{p}(t + \Delta t) + \vec{\phi}(t + \Delta t) = \vec{p}(t_0) + \dot{\vec{p}}(t_0)\Delta t + \dots + \vec{\phi}(t + \Delta t)$$

$$= -(n-1) \vec{R}_K(t_0) - (n-1) \Delta t \dot{\vec{R}}_K(t_0) + \vec{F}_K(t_0 + \Delta t) +$$

$$\sum_{\substack{j=1 \\ j \neq K}}^n \left[ \vec{F}_j(t_0 + \Delta t) - \vec{F}_{Kj}(t_0 + \Delta t) \right] + \ddot{\vec{p}}(t_0) \frac{(\Delta t)^4}{4!} + (\text{Terms in } (\Delta t)^5 \text{ and higher}) \quad (11)$$

Also

$$\begin{aligned} \dot{\vec{R}}(t + \Delta t) &= \dot{\vec{p}}(t_0 + \Delta t) + \dot{\vec{\phi}}(t_0 + \Delta t) \\ &= -(n-1) \dot{\vec{R}}_K(t_0) + \dot{\vec{F}}_K(t_0 + \Delta t) + \sum_{\substack{j=1 \\ j \neq K}}^n \left[ \dot{\vec{F}}_j(t_0 + \Delta t) - \dot{\vec{F}}_{Kj}(t_0 + \Delta t) \right] + \\ &\quad + \ddot{\vec{p}}(t_0) \frac{(\Delta t)^3}{3!} + (\text{Terms in } (\Delta t)^4 \text{ and higher}) \end{aligned} \quad (12)$$

If we now neglect the terms containing  $\ddot{\vec{p}}(t_0)$  and higher derivatives we have approximate solutions for the position and velocity at time  $(t_0 + \Delta t)$ . We continue by taking these quantities as initial conditions and repeating the procedure.

$\ddot{\vec{p}}(t_0)$  can be obtained by differentiating  $\ddot{\vec{p}}(t)$  twice, substituting from eq. (1) and evaluating at  $t_0$  as before. We can now use this term in eq. (11) and (12) to give improved accuracy. The expression for  $\ddot{\vec{p}}(t_0)$  is quite lengthy, however, and the increased computation may not be warranted.

~~CONFIDENTIAL~~

~~CONFIDENTIAL~~

Although the amount of computation per step is considerably greater than in the Encke method, a larger interval may be used.

All of these methods require the positions of the attracting bodies as functions of time. In addition, the multiple two-body method requires the velocities of these bodies as well.

Both the Encke and the multiple two-body methods require solutions to the two body problem.

The procedure for obtaining this solution is as follows:

Given  $\vec{r}_0$  and  $\dot{\vec{r}}_0$  at time  $t_0$

$$\frac{1}{a} = \frac{2}{r_0} - \frac{|\dot{\vec{r}}_0|^2}{\mu} \quad \text{where } \mu = K^2 M_K \quad (1)$$

$$N = \sqrt{\frac{\mu}{|a|^3}} \quad (2)$$

If  $a > 0$ , the path is elliptic, if  $a < 0$  the path is hyperbolic.

Elliptic

$$e = \left[ \left( 1 - \frac{r_0}{a} \right)^2 + \frac{(\vec{r}_0 \cdot \dot{\vec{r}}_0)^2}{\mu a} \right]^{1/2}$$

$$E_0 = \tan^{-1} \frac{\vec{r}_0 \cdot \dot{\vec{r}}_0}{\sqrt{\mu a} \left( 1 - \frac{r_0}{a} \right)}$$

$$\vec{p} = \frac{\vec{r}_0 \cos E_0}{r_0} - \dot{\vec{r}}_0 \sqrt{\frac{a}{\mu}} \sin E_0$$

Hyperbolic

$$e = \left[ \left( 1 - \frac{r_0}{a} \right)^2 - \frac{(\vec{r}_0 \cdot \dot{\vec{r}}_0)^2}{\mu |a|} \right]^{1/2} \quad (3)$$

$$F_0 = \log \left[ \frac{1}{e} \left( 1 - \frac{r_0}{a} + \frac{\vec{r}_0 \cdot \dot{\vec{r}}_0}{\mu |a|} \right) \right] \quad (4)$$

$$\vec{p} = \frac{\vec{r}_0 \cosh F_0}{r_0} - \dot{\vec{r}}_0 \sqrt{\frac{|a|}{\mu}} \sinh F_0 \quad (5)$$

~~CONFIDENTIAL~~

~~CONFIDENTIAL~~

<u>Elliptic</u>	<u>Hyperbolic</u>
$\vec{Q} = \frac{1}{\sqrt{1-e^2}} \left[ \dot{\vec{r}}_0 \sqrt{\frac{a}{\mu}} (\cos E_0 - e) + \frac{\vec{r}_0 \sin E_0}{r_0} \right]$	$\vec{Q} = \frac{1}{\sqrt{e^2-1}} \left[ \dot{\vec{r}}_0 \sqrt{\frac{ a }{\mu}} (e - \cosh F_0) + \frac{\vec{r}_0 \sinh F_0}{r_0} \right] \quad (6)$

$$M_0 = E_0 - e \sin E_0$$

$$M_0 = e \sinh F_0 - F_0 \quad (7)$$

At any time,  $t$

$$M = M_0 + N(t-t_0)$$

$$M = M_0 + N(t-t_0) \quad (8)$$

$$M = E - e \sin E$$

$$M = e \sinh F - F \quad (9)$$

$$X_w = a (\cos E - e)$$

$$X_w = a (\cosh F - e) \quad (10)$$

$$Y_w = a \sqrt{1-e^2} \sin E$$

$$Y_w = a \sqrt{e^2-1} \quad (11)$$

$$\dot{X}_w = -\sqrt{\frac{\mu}{a}} \frac{\sin E}{1-e \cos E}$$

$$X_w = -\sqrt{\frac{\mu}{|a|}} \frac{\sinh F}{e \cosh F - 1} \quad (12)$$

$$\dot{Y}_w = \sqrt{\frac{\mu}{a}} \sqrt{1-e^2} \frac{\cos E}{1-e \cos E}$$

$$\dot{Y}_w = \sqrt{\frac{\mu}{|a|}} \sqrt{e^2-1} \frac{\cosh F}{e \cosh F - 1} \quad (13)$$

The position and velocity at time  $t$  are now obtained from:

$$\vec{r} = X_w \vec{P} + Y_w \vec{Q} \quad (14)$$

$$\dot{\vec{r}} = \dot{X}_w \vec{P} + \dot{Y}_w \vec{Q} \quad (15)$$

Note: Equation (9) is a transcendental equation and must be solved by iteration or power series techniques to obtain  $E$  (or  $F$ ).

~~CONFIDENTIAL~~

~~CONFIDENTIAL~~

## PRINCIPAL NOTATIONS

$a$	semi major axis
$E$	eccentric anomaly
$e$	eccentricity
$F$	hyperbolic equivalent of eccentric anomaly
$\vec{F}_j, K$	vectors defining conic (two body) trajectories
$K$	Gaussian constant
$M_K$	mass of central body
$M_j$	mass at perturbing bodies
$m$	mass at perturbed body (vehicle)
$N$	mean motion
$\vec{P}$	unit vector in direction of periapsis
$\vec{Q}$	unit vector in orbit plane at right angles to $\vec{P}$
$\left. \begin{array}{l} \vec{R}_K, \\ \vec{R}_j, \\ \vec{R}_{Kj} \\ \vec{r} \end{array} \right\}$	position vectors
$r_i$	rectangular components of $\vec{F}_K$
$t$	time
$\Delta t$	time interval
$X_w$	component of $\vec{r}$ in $\vec{P}$ direction
$Y_w$	component of $\vec{r}$ in $\vec{Q}$ direction
$\vec{\rho}$	perturbation vector
$\sigma_i$	rectangular components of $\vec{\rho}$
$\mu$	gravitation field constant
$o$	subscript - indicates initial condition

~~CONFIDENTIAL~~

~~CONFIDENTIAL~~

## TIME OF ARRIVAL CONSIDERATIONS

A fixed time-of-arrival navigation method has received preliminary attention. As indicated in MIT Report R-283\*, for variable time-of-arrival navigation the total mid-course velocity corrections may be reduced over that required for fixed time-of-arrival navigation. However, if the arrival velocity must also be corrected, then it is not necessarily true that, for the technique proposed, the total velocity, including mid-course and arrival corrections, is less. The total velocity increment itself must be minimized.

---

\* "A comparison of Fixed and Variable Time of Arrival Navigation for Interplanetary Flight", R. H. Battin, May 1960

~~CONFIDENTIAL~~

~~CONFIDENTIAL~~

#### 4. MID-COURSE NAVIGATION

A general block diagram illustrating the required elements of the mid-course navigation system is shown in Figure VIII-4-1. Navigation measurements are obtained from sightings on the Earth, Moon and other celestial bodies. This information is fed into the data processing computer where it is used to determine position fixes. By taking a large number of such fixes and smoothing the data the position and velocity of the vehicle are determined with sufficient accuracy to be used for guidance. The guidance computer then uses this information to calculate a velocity correction  $V_g$ . The vehicle is oriented to point the correction engine in the proper direction. The rocket is then fired until the velocity increment, as measured by the accelerometers on the inertial measurement unit; equals  $V_g$ . This same inertial measurement unit is used for re-entry navigation.

In investigating methods of implementing a semi-automatic mid-course navigation system an attempt has been made to utilize proven hardware, or hardware currently under development for other programs, wherever possible. In particular several schemes using the astrotrackers currently being built for the attitude control system for the Orbiting Astronomical Observatory are being investigated. One of these is described below as system No. 1. The astrotracker is described in Section VIII-4B. An alternative approach based on the use of the electrostatic gyro currently under development by the General Electric Company is described as system No. 2. Although it is believed that this system is somewhat further in the future as far as proven hardware is concerned, it possesses a number of advantages in size, weight, and performance of equipment. It will be seen from the following discussion that the only basic difference between the two systems is in the equipment for making navigation measurements.

##### SYSTEM NO. 1

The following is a brief description of a mid-course navigation system using astrotrackers similar to those now being designed for attitude control of the Orbiting Astronomical Observatory. This application requires modifications of these astrotrackers

~~CONFIDENTIAL~~

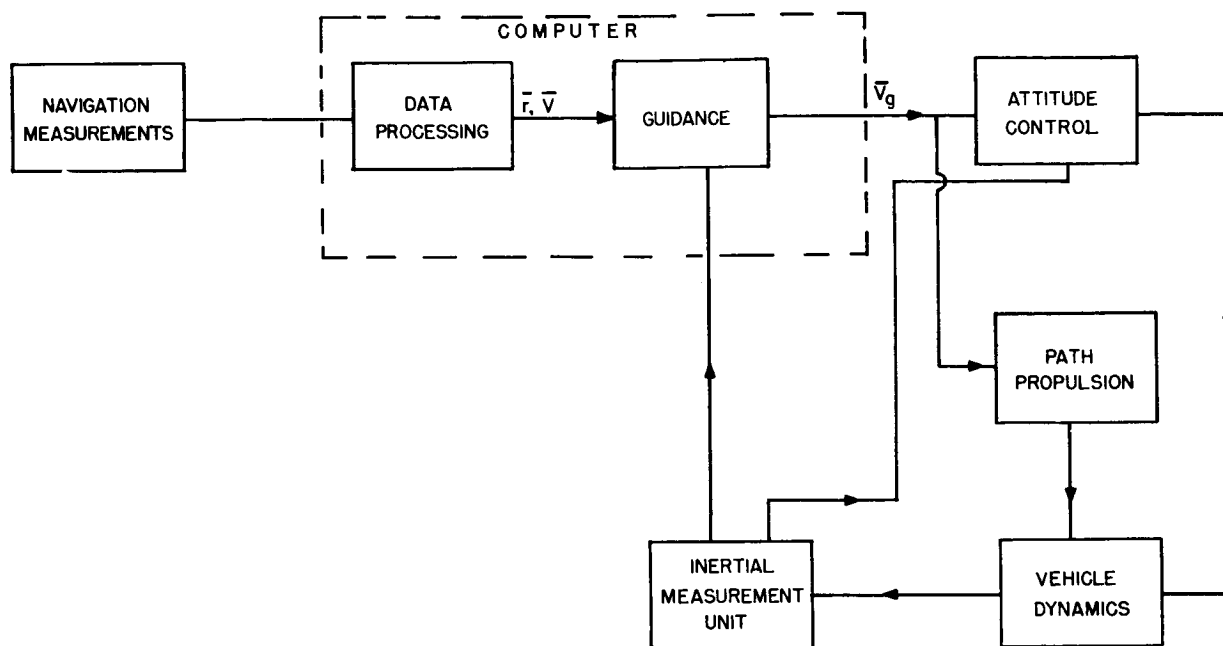


Figure VIII-4-1. General Block diagram, mid-course navigation

to provide more accurate digital readouts and the capability of measuring the vertical to and the angle subtended by the Earth and Moon.

Navigation measurements are made by three astrotrackers, mounted on a stabilized platform, which measure angles between the Earth, Moon and stars and the angles subtended by the Earth and Moon. This is accomplished through a dome in the nose of the mission module. The tracker platform is stabilized by slaving it to the inertial guidance platform in the re-entry vehicle. A stabilized base is required because of the finite time required to fix on the Earth or Moon. With this scheme, simultaneous measurements of the three angles can be achieved which simplifies the required data processing.

### Inertial Platform Alignment

Because of gyro drift, the alignment of the inertial platform must be checked prior to each correction. This is accomplished by two star trackers fixed to the inertial platform. These relatively simple trackers can be mounted on the platform without changing its external size or appreciably increasing its weight. Star fixes are made through

~~CONFIDENTIAL~~

a small window in the re-entry vehicle and a optical path to the outside. System operation during platform realignment is illustrated in Figure VIII-4-2. Using estimated gimbal angles the vehicle is reoriented so the window points in the direction of one star. The astrotracker error signals are then nulled by torquing two of the gyros, which aligns the platform about two axes. The third axis is aligned in a similar manner using a second star approximately at right angles to the first.

Two alternative approaches to platform alignment are presently being considered, both of which allow use of information from the navigational astrotrackers. The problem in this case is the unknown misalignment between the bases of the two platforms. One approach includes an optical system for transmitting alignment information. The other approach is to design the inertial platform so it can be manually carried from the re-entry vehicle and mounted close to the tracker platform. With either of these approaches the need for a window in the re-entry vehicle is eliminated and attitude control propulsion requirements are somewhat reduced. Also, the solar collector is not turned away from the sun during platform alignment.

### **Mid-Course Navigation Fixes**

Operation of the system in the navigation fix mode is illustrated in Figure VIII-4-3. Navigation fixes are obtained from the three astrotrackers mounted on the tracker platform. When it is decided to take a series of navigation fixes the trackers are pointed approximately in the correct direction either by manual control or automatically from programmer signals. While taking fixes the astrotrackers will be locked on the Earth, Moon and a selected star. Each astrotracker is mounted in two gimbals with digital readouts on each axis. These gimbal angles are simultaneously read into the computer at periodic intervals where the data is processed to produce accurate values of position and velocity, as described below. To achieve the required data accuracy it is necessary to take a large number of such fixes over an appreciable time interval. This procedure of taking simultaneous angle readouts at equal time intervals considerably simplifies the data processing problem. The accurate fix data is then used to calculate the velocity correction,  $\bar{V}_g$ , in the guidance computer, as discussed in Section VIII-3.



~~CONFIDENTIAL~~

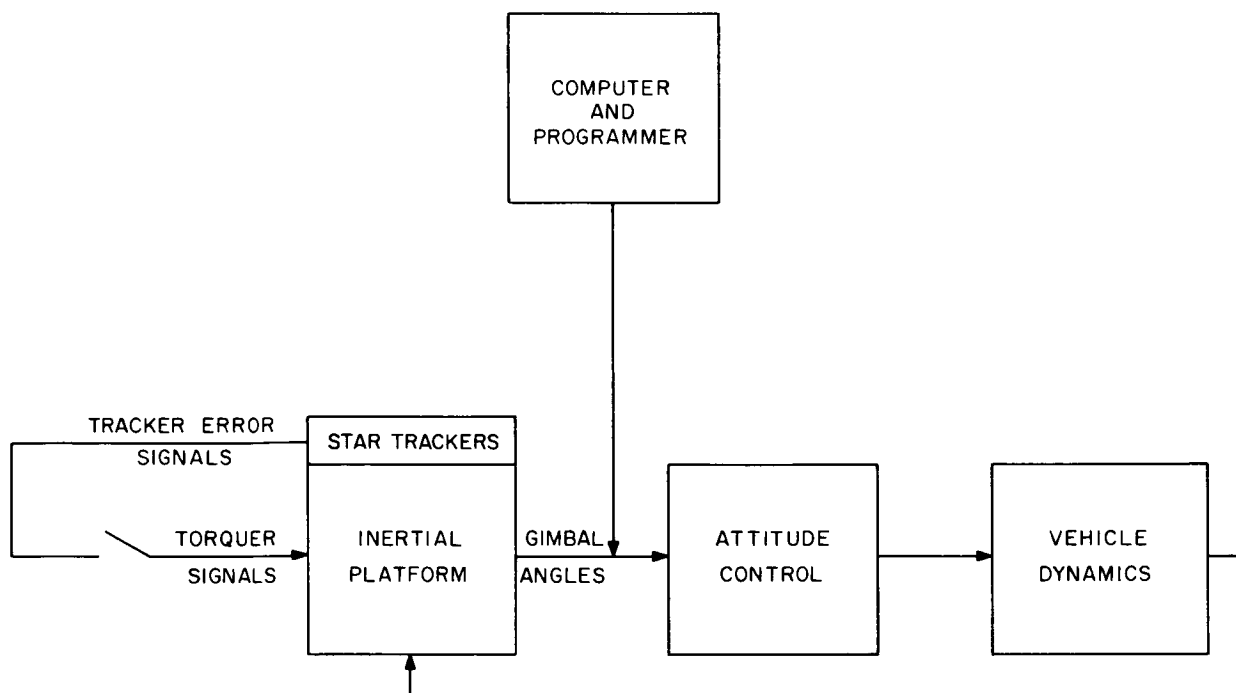


Figure VIII-4-2. Platform alignment mode

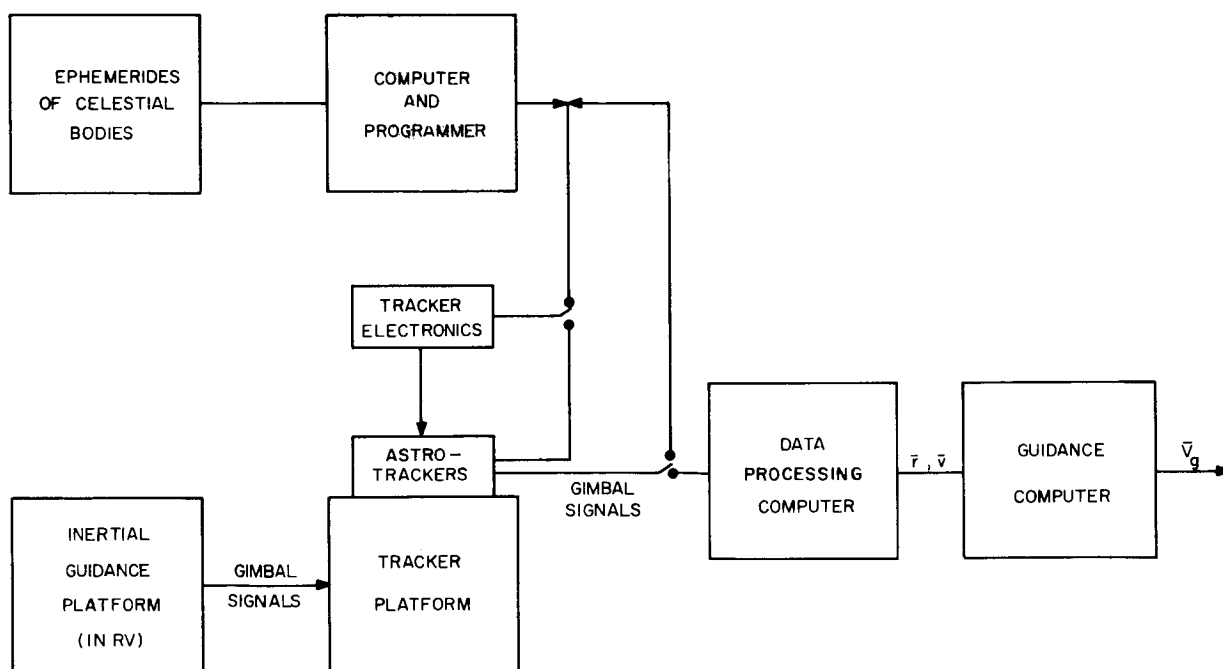


Figure VIII-4-3. Navigation fix mode

~~CONFIDENTIAL~~

~~CONFIDENTIAL~~

Earth and Moon tracking is accomplished by tracking the periphery of the body. The data so obtained is used to determine the line to the center of these bodies. This same data can be used to determine the angular diameter of these bodies which is used as a measure of range when the vehicle is close to either the Earth or Moon. The astrotrackers are mounted on a stabilized platform because tracking the Earth or Moon periphery requires about 1 or 2 seconds and it is necessary that the tracker bases be stabilized during this period. It is not necessary that the attitude of the platform in inertial space be precisely known. Thus, it is feasible to obtain this stabilization by slaving the tracker platform to the inertial platform in the re-entry vehicle. The possibility of body-mounting these trackers is also being investigated. This could be done either by accurately stabilizing the vehicle rates while measurements are being taken, or by measuring these rates and compensating for them in the computation of the direction of the vertical.

The problem of vehicle contained navigation in cis-lunar space requires that both position and velocity be known. Position gives knowledge of the vehicle's present location. The combination of position and velocity information allows the prediction of vehicle location and velocity at a future time through trajectory calculations. Roughly, for a lunar mission a knowledge of position to  $<12$  mi and velocity to  $<10$  ft/sec is desired.

The measurement of position in three dimensional space can be accomplished through a knowledge of celestial distances and angles. A knowledge of the location of the celestial bodies and the stars as a function of time in the proper reference frame is implied.

The direct measurement of velocity with the desired accuracy is not possible at this time. The various methods available do not possess the necessary accuracy. The doppler shift of stellar spectral absorption lines can yield velocity to no more than two significant figures. The aberration of starlight would yield a similar accuracy. Doppler radar techniques yield velocity with about 0.5 percent accuracy depending upon antenna pointing accuracy and the surface characteristics of the planet.

The most feasible method of velocity determination is to establish velocity indirectly from the position data and time.

[REDACTED]

To obtain the desired accuracy in both position and velocity requires data smoothing to remove as much as possible the effects of the random errors in measurement.

The ensuing discussion centers on the measurement of position from celestial angles and distances and the determination of velocity from this information.

### Position Measurement

Three basic types of measurement are available to a vehicle mounted system:

- (1) The angle between two planets
- (2) The angle between a star and a planet
- (3) The angle subtended by a planet of known diameter

### Geometrical Interpretation

One method of viewing these various measurements is to consider the restraint each imposes on vehicle location.

#### (1) ANGLE BETWEEN TWO PLANETS

The angle between two planets whose separation distance is known locates the vehicle on the surface of revolution of an arc of a circle rotated about the line between the two planets and is commonly called a spheroid. This can be established from Figure VIII-4-4 below:

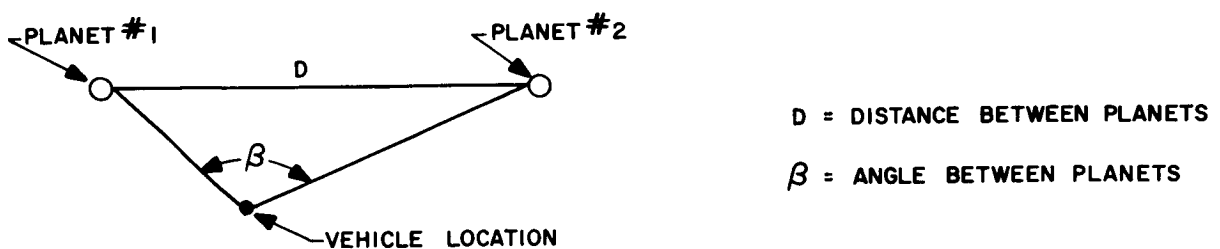


Figure VIII-4-4. Two-planet triangulation geometry

~~CONFIDENTIAL~~

and the axiom: given an arc of a circle subtended by a chord — the angle between the lines from a point on the arc to the intersection points of the chord and arc is a constant.

In two dimensions, the vehicle must lie on the arc of the circle. In three dimensions, it must lie on the surface generated by the revolution of the circle arc about the chord. If one planet is located at the origin of a coordinate system and the second planet on the X axis, the equation of the spheroid is as follows:

$$X^2 + Y^2 + Z^2 + D (\tan \beta \sqrt{Z^2 + Y^2} - X) = 0 \quad (1)$$

## (2) ANGLE BETWEEN A STAR AND A PLANET

The angle between a star and a planet locates the vehicle on the surface of revolution of the line between the planet and vehicle about the line from the planet to the star. This is a cone with apex at the planet whose cone angle is twice the angle between the star and the planet. This can be established by the diagram shown in Figure VIII-4-5.

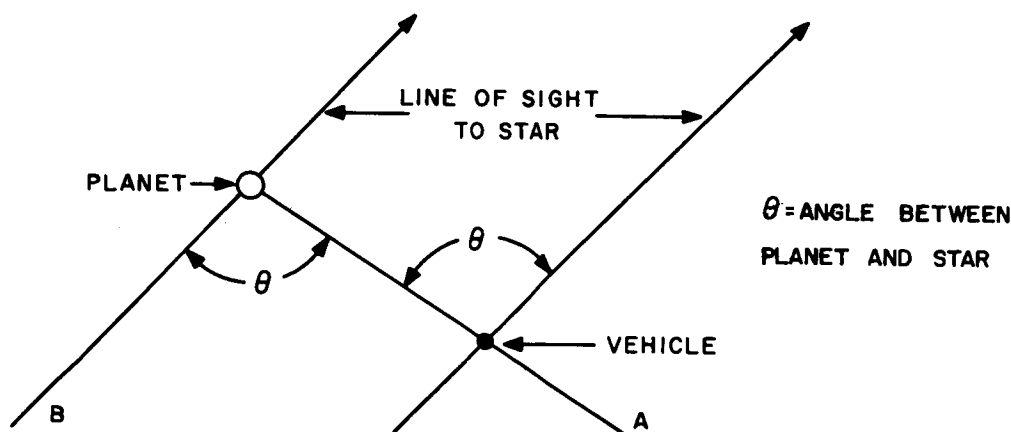


Figure VIII-4-5. Planet, star triangulation geometry

In two dimensions, the vehicle lies on the line A. In three, it lies on the surface generated by the rotation of A about B.

If the planet is located at the origin of a coordinate system and the star on the X axis, the equation of the cone is as follows:

$$Y^2 + Z^2 = X^2 \tan^2 \theta \quad (2)$$

~~CONFIDENTIAL~~

~~CONFIDENTIAL~~

### (3) ANGLE SUBTENDED BY A PLANET

The angle subtended by a planet of known diameter locates the vehicle on the surface of a sphere whose origin is at the planet center. This can be established by the diagram shown in Figure VIII-4-6.

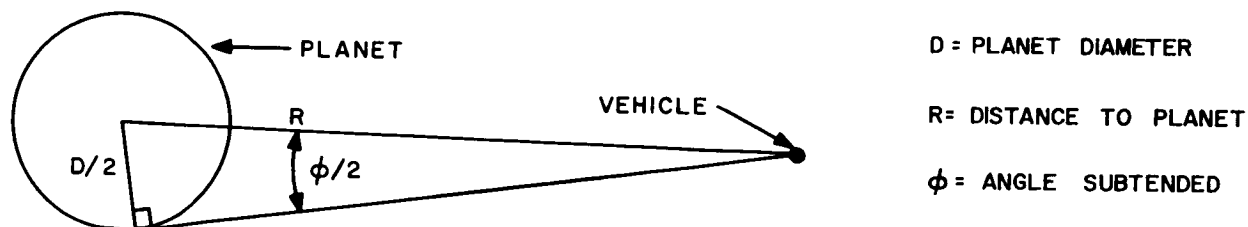


Figure VIII-4-6. One-planet triangulation geometry

The measurement of  $\phi$  establishes  $R$ .  $R$ , in turn, is the radius of a sphere whose center is at the planet center.

In two dimensions, the vehicle is located on a circle of radius  $R$  about the planet. In three dimensions, the vehicle is located on a sphere of radius  $R$  about the planet. If the origin of a coordinate system is located at the planet center, the equation of the sphere is as follows:

$$X^2 + Y^2 + Z^2 = \frac{D^2}{4 \sin^2 \phi/2} \quad (3)$$

The determination of position is, geometrically, the intersection point of three surfaces. The intersection of two surfaces, establishes a line in space and the third surface a point. It should be noted that an ambiguity arises because the equations involved are second order with two solutions in common. This ambiguity can be resolved by knowledge of the approximate position of the vehicle.

Equations (1), (2), and (3) allow an insight into the geometrical nature of the position fix. In addition, a feel for the sensitivity characteristics can be established.

~~CONFIDENTIAL~~

## Sensitivity

Using the first term of a Taylor series expansion of the three measurement techniques shows that, in general, the sensitivity of the position fix to angular measurement errors is directly proportional to the distance term involved, i.e. the distance between the two planets or the distance from the vehicle to a planet. Since the nearest planet to the Earth-Moon space is in the order of 80 or greater times the distance from the Earth and Moon, it is very desirable to limit the bodies involved to those in cis-lunar space.

An ideal measurement system which causes the intersection of the three surfaces to be orthogonal will generate the following sensitivities at mid-course. (These decrease as we approach the Earth or Moon).

$$\frac{\partial Y}{\partial B} = 1.25 \text{ nmi/sec}$$

nmi = nautical miles

$$\frac{\partial Z}{\partial \theta_1} = 0.65 \text{ nmi/sec}$$

sec = angular measure

$$\frac{\partial X}{\partial \theta_2} = 0.65 \text{ nmi/sec}$$

These numbers create a feel for the sensitivities. However, the practicalities of the situation will not allow this ideal situation and a practical scheme will probably allow the sensitivity in the direction in line with the Earth and Moon to increase, because an orthogonal restraint cannot be established in this direction.

Additional insight into the position fix problem can be obtained from the general vector equations for the various geometrical shapes referred to a common coordinate system.

The angle between two planets can be analyzed from the diagram shown in Figure VIII-4-7.

~~CONFIDENTIAL~~

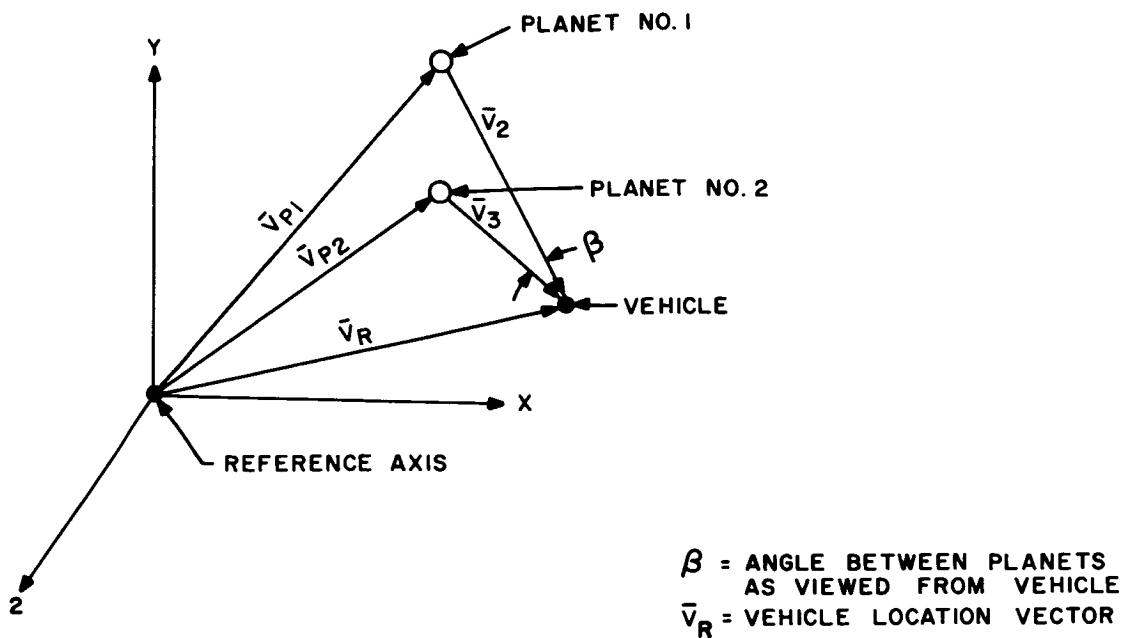


Figure VIII-4-7. Two-planet triangulation analysis

In Vector notation:

$$(\bar{V}_R - \bar{V}_{P2}) \cdot (\bar{V}_R - \bar{V}_{P3}) = |\bar{V}_R - \bar{V}_{P2}| |\bar{V}_R - \bar{V}_{P3}| \cos \beta$$

or in X Y Z coordinates

$$(X_r - X_{p2})(X_r - X_{p3}) + (Y_r - Y_{p2})(Y_r - Y_{p3}) + (Z_r - Z_{p2})(Z_r - Z_{p3}) = \cos \beta \sqrt{(X_r - X_{p2})^2 + (Y_r - Y_{p2})^2 + (Z_r - Z_{p2})^2} \sqrt{(X_r - X_{p3})^2 + (Y_r - Y_{p3})^2 + (Z_r - Z_{p3})^2}$$

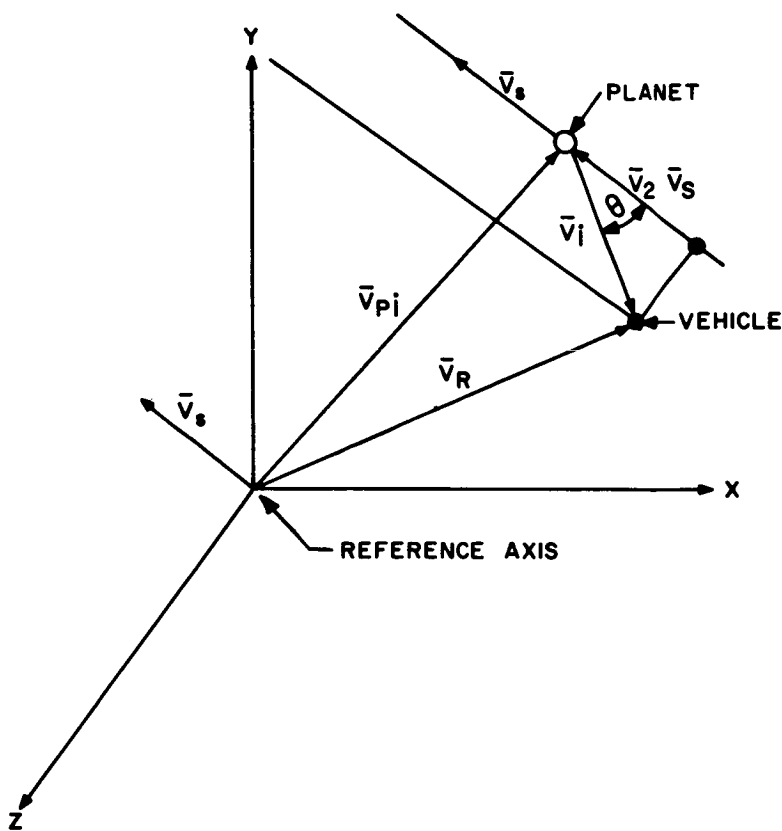
where

$$\sqrt{(X_r - X_{p2})^2 + (Y_r - Y_{p2})^2 + (Z_r - Z_{p2})^2} = |\bar{V}_2|$$

$$\sqrt{(X_r - X_{p3})^2 + (Y_r - Y_{p3})^2 + (Z_r - Z_{p3})^2} = |\bar{V}_3|$$

The angle between a Star and a planet can be analyzed from the diagram shown in Figure VIII-4-8.

~~CONFIDENTIAL~~



$\vec{V}_s$  = UNIT VECTOR IN DIRECTION OF STAR  
 $\theta$  = ANGLE BETWEEN PLANET AND STAR VIEWED FROM VEHICLE  
 $V_R$  = VEHICLE LOCATION VECTOR

Figure VIII-4-8. Planet, star triangulation analysis

In vector notation:

$$(\vec{V}_R - \vec{V}_{pi}) \cdot \vec{V}_s = |\vec{V}_R - \vec{V}_{pi}| \cos \theta$$

or in X Y Z coordinates:

$$(X_R - X_{pi}) X_S + (Y_R - Y_{pi}) Y_S + (Z_R - Z_{pi}) Z_S =$$

$$\cos \theta \sqrt{(X_R - X_{pi})^2 + (Y_R - Y_{pi})^2 + (Z_R - Z_{pi})^2}$$

Note that  $\sqrt{(X_R - X_{pi})^2 + (Y_R - Y_{pi})^2 + (Z_R - Z_{pi})^2} = |V_i|$

The angle subtended by a planet can be analyzed from the diagram shown in Figure VIII-4-9.

~~CONFIDENTIAL~~



~~CONFIDENTIAL~~

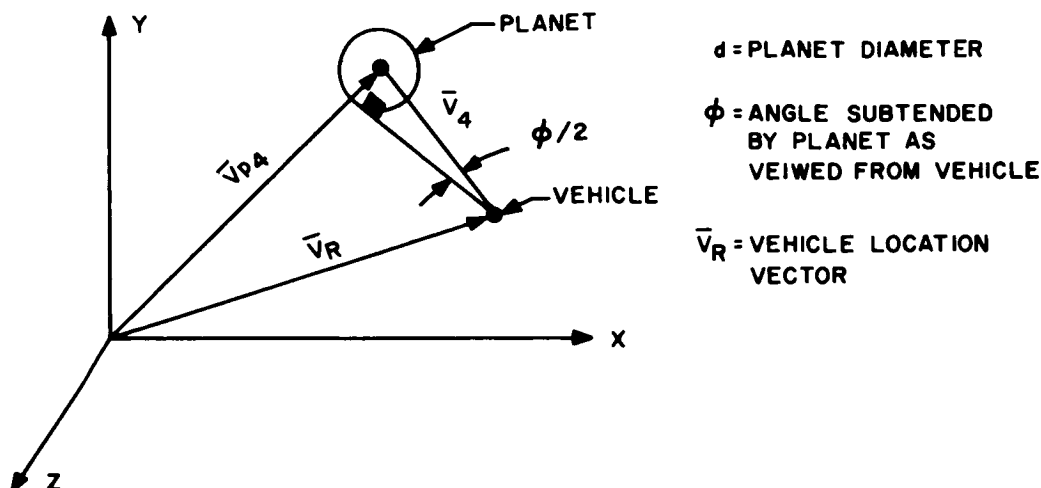


Figure VIII-4-9. One-planet triangulation analysis

In vector notation:

$$\left| \bar{V}_R - \bar{V}_{p_4} \right| = \frac{D}{2 \sin \phi/2}$$

or in X Y Z coordinates:

$$\sqrt{(X_R - X_{p_4})^2 + (Y_R - Y_{p_4})^2 + (Z_R - Z_{p_4})^2} = \frac{D}{2 \sin \phi/2}$$

Note that  $\sqrt{(X_R - X_{p_4})^2 + (Y_R - Y_{p_4})^2 + (Z_R - Z_{p_4})^2} = |V_4|$

The position fix in the reference coordinate system is the simultaneous solution of three equations of the type just mentioned. The measurement scheme should minimize the sensitivity to errors. These three equations can be differentiated and used in conjunction with the particular trajectory concerned to establish error sensitivities. The selection of the particular bodies to be used for measurement depends very much on the trajectory. The following schemes appear promising:

where:  $\Delta_e$  = angle subtended by the Earth      subscripts 1, 2 = different Stars  
 $\Delta_M$  = angle subtended by the Moon  
 $P_E S$  = angle between line to Earth and line to star  
 $P_M S$  = angle between line to Moon and line to star  
 $P_M P_E$  = angle between line to Earth and line to Moon

~~CONFIDENTIAL~~

$$\begin{array}{l}
 \triangle_{e, P_E S_1 P_E S_2} \\
 \triangle_{e, P_E S, P_M S} \\
 \triangle_{e, P_M P_E, P_e S} \\
 P_M P_E, P_E S_1 P_E S_2
 \end{array}$$

$$\begin{array}{l}
 \triangle_{M, P_M S_1 P_M S_2} \\
 \triangle_{M, P_M S, P_E S} \\
 \triangle_{M, P_M P_E, P_M S} \\
 P_M P_e, P_M S_1 P_M S_2
 \end{array}$$

These were chosen considering the criteria of using the closest body as often as possible. A cislunar flight trajectory will determine the optimum measurement combination. Differentiation of the positional equations will yield an error sensitivity matrix as shown below

$$\begin{array}{|c|} \hline \Delta X \\ \hline \\ \hline \Delta Y \\ \hline \\ \hline \Delta Z \\ \hline \end{array} = \begin{array}{|ccc|} \hline \frac{\partial X}{\partial a_1} & \frac{\partial X}{\partial a_2} & \frac{\partial X}{\partial a_3} \\ \hline \frac{\partial Y}{\partial a_1} & \frac{\partial Y}{\partial a_2} & \frac{\partial Y}{\partial a_3} \\ \hline \frac{\partial Z}{\partial a_1} & \frac{\partial Z}{\partial a_2} & \frac{\partial Z}{\partial a_3} \\ \hline \end{array} \cdot \begin{array}{|c|} \hline \Delta a_1 \\ \hline \\ \hline \Delta a_2 \\ \hline \\ \hline \Delta a_3 \\ \hline \end{array}$$

This matrix must be generated for the out bound leg, lunar orbit, and the return leg. In all probability, the reference coordinate system will be an Earth-centered non-rotating system with one axis pointing toward the first point of Aries. A knowledge of all planet and Star locations concerned is inherent in this calculation.

### Accuracy of Measurements

Various effects must be considered in establishing a position fix. These are:

Aberration of Star light

Proper motion of Stars

Parallax of Stars

Instrument uncertainty

Time measurement uncertainty

~~CONFIDENTIAL~~

~~CONFIDENTIAL~~

Star ephemeris information contains the aberration effect due to earth motion. For use of this information for inter-lunar flight, a correction must be added for aberration due to vehicle motion relative to the earth. This correction can be precomputed based on a knowledge of the trajectory. The amount of angular displacement is given by  $\Theta = \arctan V/C$  where V is the component of the vehicle velocity perpendicular to the line of sight to the star. This effect can be as high as 8 seconds error if not accounted for.

Proper motion of the stars can be neglected for a trip of 15 days duration as the effect is much less than 1 second angular shift.

Motion within cis-lunar space for 15 days does not produce sufficient parallax effect to be accounted for.

Instrument uncertainty most certainly must be taken into account. Extreme care must be exercised to eliminate bias errors and to account for systematic errors. Random error will be discussed in the following pages.

Time will be measured to 1 part in  $10^6$ . This for a 15 day trip represents an error in time of 1.3 seconds. A 1.3 second error is not significant to travel in cis-lunar space.

### Instrument Accuracy

Star Tracker Studies have indicated that a random ( $3\sigma$ ) instrument error of 10 seconds of arc is not unreasonable. This will be the principle error when tracking a star. When tracking the center of a visibly large body, uncertainties in the geometry of the body will create additional error. Part of this error, in all probability, will not be random during any reasonable period of data taking and must be considered a bias error. A portion of this error will be systematic and can be removed. It is estimated that the unpredictable - non random - bias error will be in the order of 15 seconds arc ( $3\sigma$ ).

If we consider the total error in the instrument as 25 seconds ( $3\sigma$ ) and utilize the ideal sensitivities on 2 foregoing pages, the following are the position errors:

$$\Delta X = 16.4 \text{ nmi}$$

$$\Delta Y = 31.2 \text{ nmi}$$

$$\Delta Z = 16.4 \text{ nmi}$$

~~CONFIDENTIAL~~

~~CONFIDENTIAL~~

Two fifths of this error is random, indicating that improvement in accuracy can be obtained with data smoothing techniques to the limit of the bias error with an infinite number of samples.

### Smoothing of Data

Improvement in the accuracy of the data can be accomplished by sampling the position angles over a period of time and using this information to obtain the smoothed result whose accuracy increases as the number of samples increase.

The mathematical expression to be minimized in the least squares approach is

$$\sum_{i=1}^M \frac{(X_i - X(a, t))^2}{G^2(N_i)}$$

Where  $X_i$  = sample  
 $X(a, t)$  = curve to be fitted to data  
 $G^2(N_i)$  = variance of measurement  
 $t$  = time  
 $a$  = curve parameters

The minimization of this expression with respect to "a" produces the most probable value of the vehicle position  $X(a, t)$ . The particular function to be fitted to the data must make the most use of the available knowledge of the vehicle trajectory. Thus, the function will be the best approximation of the segment of the vehicle trajectory thought to exist during the sample period. The actual trajectory will not vary to a great degree from this and thus the order of the curve will probably be correct. The variance of the probable position of the vehicle will be a function of the variance of the position measurements.

If it is assumed that the samples taken are uncorrelated, that the matrix shown on a foregoing page is diagonal, and that a least-squares data-smoothing technique fitting a second order curve to the data is used, it is possible to make certain very simple

~~CONFIDENTIAL~~

~~CONFIDENTIAL~~

statements concerning the accuracy of the smoothed position information and the implied velocity which allow a feel for the problem.

$$\text{Var} \left( \hat{Y} (I) \right) = A^2 \left[ \left( \underline{Gm}'^2 \right) + \frac{9}{I} \left( \underline{Gn}'^2 \right) \right]$$

where:

$$\text{Var} \left( \hat{Y} (I) \right) = \text{the variance of the estimate of position}$$

$$\left( \underline{Gm}' \right)^2 = \text{the bias variance of the angular measurement}$$

$$\left( \underline{Gn}' \right)^2 = \text{the instrument variance of the angular measurement.}$$

$$A = \frac{\partial Y}{\partial \phi}, \text{ where } \phi \text{ is the angle concerned.}$$

$$I = \text{Total number of samples.}$$

And

$$\text{Var} \left( \hat{Y} (I) \right) = A^2 \frac{192 \underline{Gn}'^2}{T^2 I}$$

where:

$$T = \text{the total time interval of taking samples.}$$

The above equations apply to the end of the fitting interval. The variance of the velocity estimate is in the order of 15 times more accurate at the middle of the interval.

To obtain 10 feet/sec velocity accuracy ( $3 \sigma$ ) with an instrument which has a  $3 \sigma$  error of 10 seconds with a 1/2 minute sampling period requires a sample time of approximately 1 hour 40 minutes with 200 samples involved. The resulting position accuracy with a 15 mile ( $3 \sigma$ ) bias error is approximately 16 miles ( $3 \sigma$ ).

Thus it is seen that it is reasonable to expect a sufficiently accurate position and velocity fix with a reasonable sampling time and sampling rate with an instrument which is within the state of the art in the near future (three to five years). Extreme care, however, must be exercised in choosing the bodies to be measured for a particular trajectory. In addition, the characteristics of the instrument must be accurately established.

~~CONFIDENTIAL~~

~~CONFIDENTIAL~~

The particular technique used in smoothing data is subject to many considerations. The method of maximum likelihood has advantages for establishing the most probable value of position. In essence it consists of choosing those values of the parameters for which the likelihood function is a maximum. This function is defined as the probability density of the data sample. This particular technique reduces to the weighted least squares technique when the particular samples are uncorrelated and their distribution is normal. The maximum likelihood technique will be investigated further.

#### THE POSITION FIX

Once the most probable location of the vehicle is established, the position must be extrapolated ahead in time in order that trajectory calculations be made and processed to obtain a velocity correction. Since the accuracy of the position fix is greatest at the midpoint of the interval of the sample, this information will be used in the explicit calculation of trajectory to obtain an extrapolated position and velocity. Pictorially, in Figure VIII-4-10:

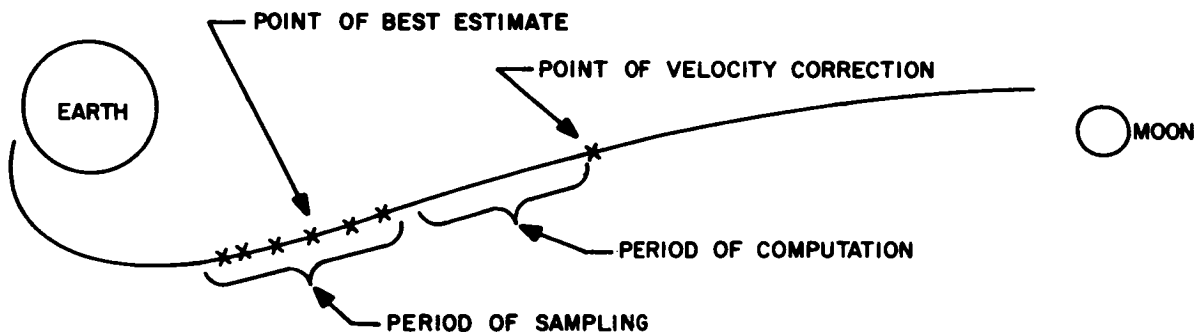


Figure VIII-4-10 - Mid-course Navigation Schematic

#### GUIDANCE CORRECTIONS

System operation during guidance correction is illustrated in Figure VIII-4-11. The required correction is computed in the guidance computer in the form

$$\bar{V}_{gc} = \bar{X} V_{gxc} + \bar{Y} V_{gyc} + \bar{Z} V_{gzc} \quad (1)$$

~~CONFIDENTIAL~~

where  $\bar{X}$ ,  $\bar{Y}$ ,  $\bar{Z}$ , is the coordinate system to which the inertial platform axes are aligned. A coordinate system  $\bar{X}$ ,  $\bar{Y}$ ,  $\bar{Z}$ , fixed to the vector  $V_{gc}$  is related to  $\bar{X}$ ,  $\bar{Y}$ ,  $\bar{Z}$  through the direction cosine matrix

$$\begin{vmatrix} \bar{X}_1 \\ \bar{Y}_1 \\ \bar{Z}_1 \end{vmatrix} = \begin{vmatrix} \alpha_X & \alpha_Y & \alpha_Z \\ \beta_X & \beta_Y & \beta_Z \\ \gamma_X & \gamma_Y & \gamma_Z \end{vmatrix} \begin{vmatrix} \bar{X} \\ \bar{Y} \\ \bar{Z} \end{vmatrix} \quad (2)$$

where

$$\alpha_X = \frac{V_{gxc}}{V_{gc}} ; \quad \alpha_Y = \frac{V_{gyc}}{V_{gc}} ; \quad \alpha_Z = \frac{V_{gzc}}{V_{gc}} \quad (3)$$

The other six elements of the matrix can be determined from  $\alpha_X$ ,  $\alpha_Y$ ,  $\alpha_Z$ , as can the inertial platform gimbal angles with the selected engine or combination of engines pointing nominally in the  $\bar{V}_{gc}$  direction. These are used in conjunction with the attitude control system to orient the vehicle to the proper attitude or making the correction.

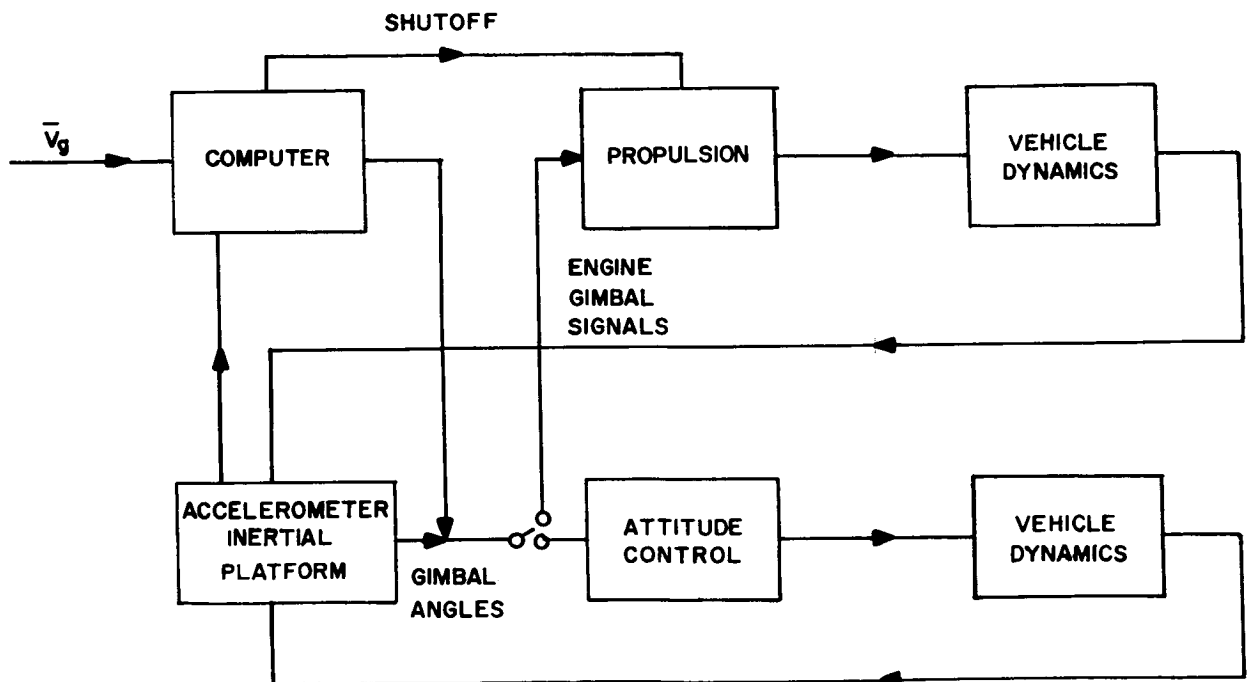


Figure VIII-4-11. Guidance System Correction Mode

~~CONFIDENTIAL~~

After the start of correction the velocity to be gained is

$$\bar{V}_g = \bar{X}_1 (V_{gc} - V_{ax_1}) - \bar{Y}_1 V_{ay_1} - \bar{Z}_1 V_{az_1} \quad (4)$$

where

$$V_{ax_1} = \int (a_{tx}^{\alpha} x + a_{ty}^{\alpha} y + a_{tz}^{\alpha} z) dt \quad (5)$$

$$V_{ay_1} = \int (a_{tx}^{\beta} x + a_{ty}^{\beta} y + a_{tz}^{\beta} z) dt \quad (6)$$

$$V_{az_1} = \int (a_{tx}^{\gamma} x + a_{ty}^{\gamma} y + a_{tz}^{\gamma} z) dt \quad (7)$$

During application of corrective thrust, attitude about two vehicle axes is controlled by varying the gimbal angles of the correction engines, to achieve thrust vector control. This is accomplished by adding to the above calculated platform gimbal angles the small angles

$$\delta \Theta_y = K V_{az_1} \quad (8)$$

$$\delta \Theta_z = K V_{ay_1} \quad (9)$$

and using the error signals to control engine orientation. The engine is cut off when

$$V_{ax_1} = V_{gc} \quad (10)$$

### Astrotracker

A precision star tracker is required to perform two important functions in modern satellites and space probes: determination and control of vehicle attitude (attitude control); and determination of the vehicle position (astronavigation). The tracker proper is common to each system. They differ basically in their processing of the positional information generated (in the case of the tracker described herein, gimbal angles). An attitude control system customarily operates closed-loop, the closed loop being operated by positioning the vehicle (e.g. with momentum packages). In an astronavigational system, it is customarily used open-loop, the information being fed to a computer.

~~CONFIDENTIAL~~



~~CONFIDENTIAL~~

As stated previously, the tracker proper is basically the same for either system. The basic tracker design described in this discussion is inherently applicable for either type system, but was designed specifically to meet Specification No. A-3629 for a satellite-borne Star tracker issued by NASA - Ames, Moffet Field, California, dated 1/17/61. At pertinent points in the description of the basic tracker, the modifications specifically needed to meet the navigational requirements of an APOLLO mission will be specified. Table VIII-4-1 gives the luminous fluxes for the various star magnitudes to be considered in this discussion.

## DETAILED DESCRIPTION OF SYSTEM

### Optical System

The optical system chosen is a Cassegranian system with spherical mirrors and a Maksutov-Bouwers corrector plate, all with concentric spherical surfaces (see Figure VIII-4-12). The radii of the menisci and their separation have been chosen to produce an effective focal length of 24 inches, yet allow the complete system, including scanner, photodetector, gimbals, etc., to be packaged with the major dimension no more than 12 inches. The telescope diameter at the entrance aperture is 3.2 inches, expanding down the tube to a diameter of 3.35 inches at the second meniscus, which gives an effective aperture of 3-inch diameter. A condensing lens is included behind the focal plane to refocus the image on the photosensitive surface. A corrector plate (not shown in Figure VIII-4-12) will be incorporated to correct the spherical aberration introduced by the optically-ground dome which permits the telescope to perform inside an hermetically-sealed container.

Foremost among the reasons for choosing a reflective system over a refractive one is the savings in weight and size. Our experience with an early design of a tracker designed about a refractive telescope with a 12-inch focal length and a 3-inch aperture has shown that this design has inherent weight and size problems. A compact design such as this results in large weight savings in designing a gimbal and housing structure which is capable of achieving and maintaining the required alignment accuracies.

A second major advantage is inherent to this optical system because of the uniformity of each optical element. Unlike a refractive element of varying thickness, the menisci

~~CONFIDENTIAL~~

TABLE VIII-4-1. STELLAR MAGNITUDE — LUMINOUS FLUX

Stellar Visual Magnitude ( $m_v$ )	Luminous Flux	
	(a) (lumen/cm <sup>2</sup> )	(b) (watts/cm <sup>2</sup> —see Note 2)
-5	$2.43 \times 10^{-8}$ lumen/cm <sup>2</sup>	$3.57 \times 10^{-11}$ watts/cm <sup>2</sup>
-4	$9.67 \times 10^{-9}$	$1.42 \times 10^{-11}$
-3	$3.85 \times 10^{-9}$	$5.66 \times 10^{-12}$
-2	$1.53 \times 10^{-9}$	$2.25 \times 10^{-12}$
-1	$6.10 \times 10^{-10}$	$8.97 \times 10^{-13}$
0	$2.43 \times 10^{-10}$ *	$3.57 \times 10^{-13}$
1	$9.67 \times 10^{-11}$	$1.42 \times 10^{-13}$
2	$3.85 \times 10^{-11}$	$5.66 \times 10^{-14}$
3	$1.53 \times 10^{-11}$	$2.25 \times 10^{-14}$
4	$6.10 \times 10^{-12}$	$8.97 \times 10^{-15}$
5	$2.43 \times 10^{-12}$	$3.57 \times 10^{-15}$
6	$9.67 \times 10^{-13}$	$1.42 \times 10^{-15}$
7	$3.85 \times 10^{-13}$	$5.66 \times 10^{-16}$
8	$1.53 \times 10^{-13}$	$2.25 \times 10^{-16}$
9	$6.10 \times 10^{-14}$	$8.97 \times 10^{-17}$

Note 1: To extend table, remember that an increase (or decrease) of 5 magnitudes divides (or multiplies) the flux by 100.

Note 2: Flux in watts/cm<sup>2</sup> calculated for light at the wave length of maximum visibility (5550A), where 1 lumen =  $1.47 \times 10^{-3}$  watts.

\*Reference: C. W. Allen, "Astrophysical Quantities", University of London Athlone Press, London (1955), page 24.

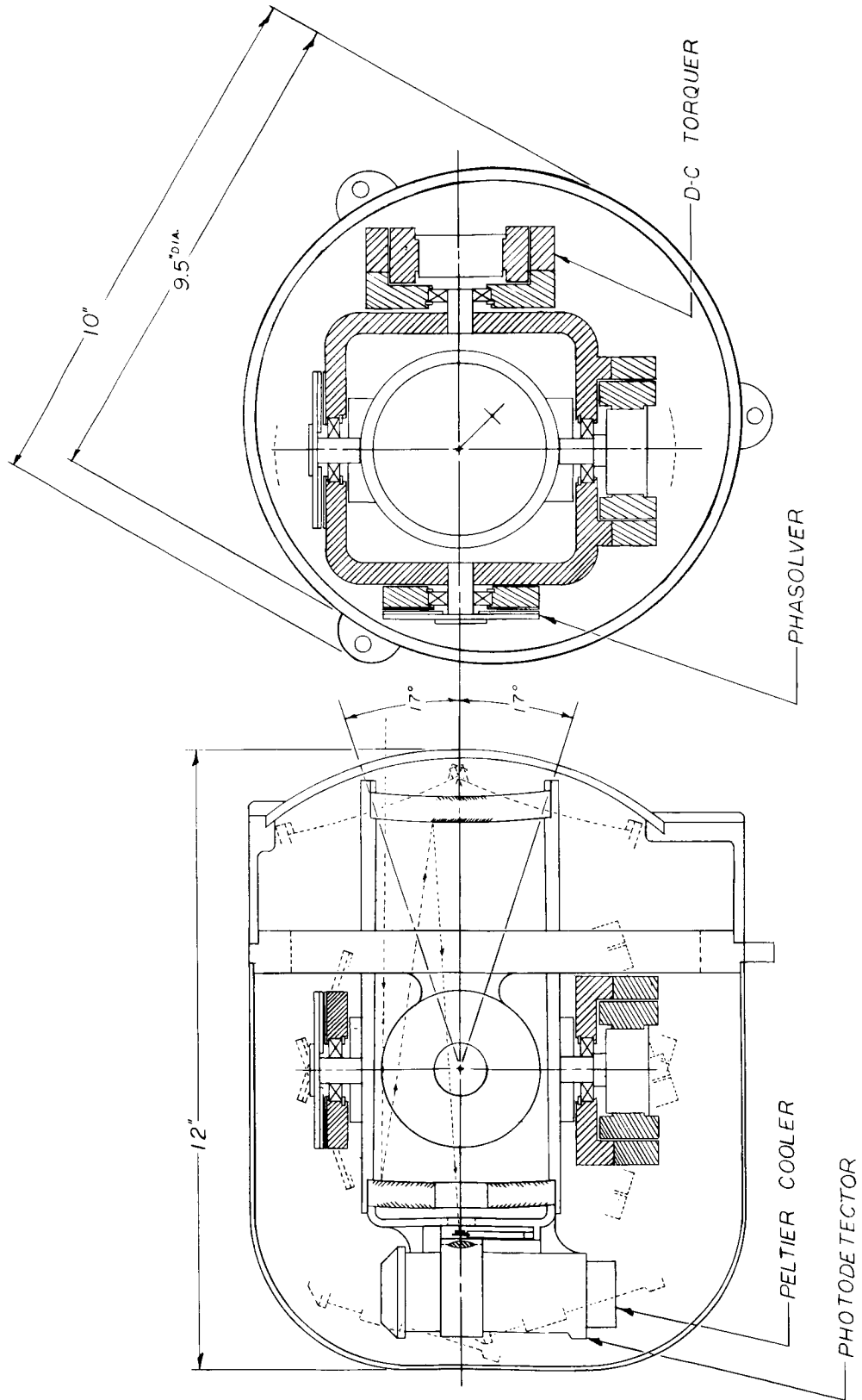


Figure VIII-4-12. Satellite borne - Star tracker

~~CONFIDENTIAL~~

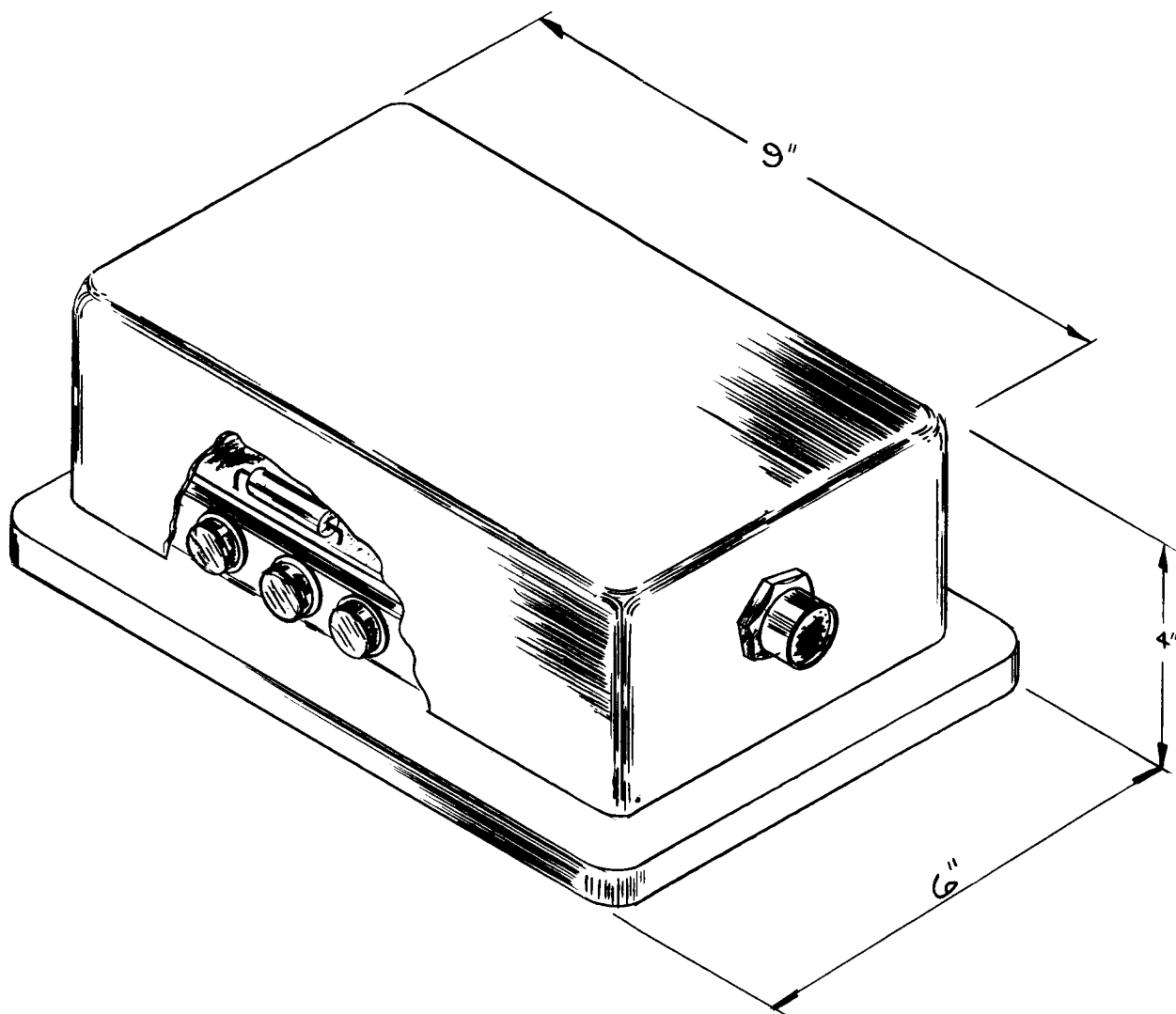


Figure VIII-4-13. Outline drawing—electronics

~~CONFIDENTIAL~~

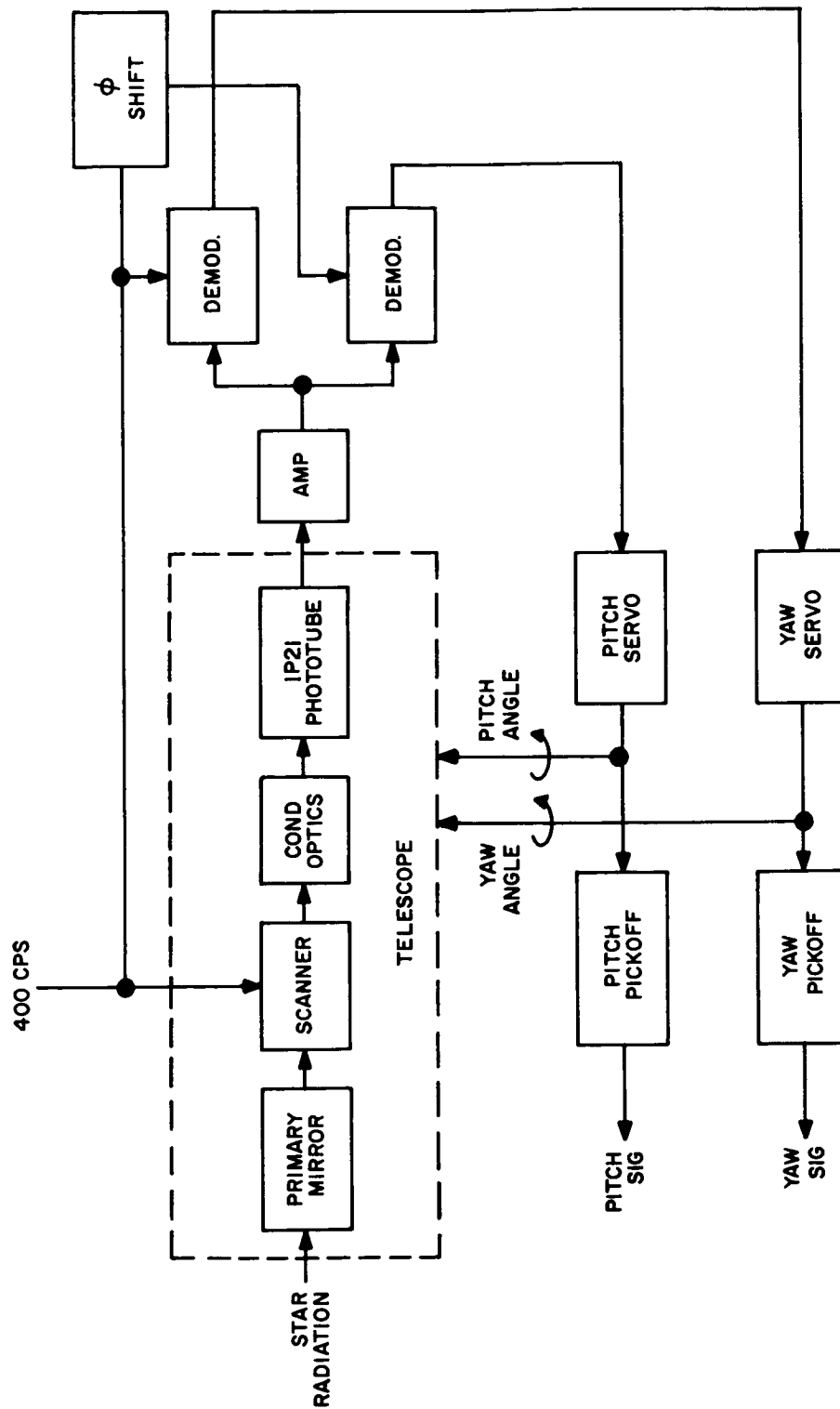


Figure VIII-4-14. Functional block diagram — servo system

~~CONFIDENTIAL~~

will be much more stable when subjected to temperature changes. The rear surface of the principal mirror will be rough-polished, and aluminized like the front surface, virtually eliminating any mechanical distortion because of non-uniform temperature gradients.

Another advantage of this optical system is that it is virtually achromatic. With only a simple change from glass to quartz (the dome, partially coated meniscus, and the photomultiplier window), the system can be used in the ultraviolet region. Finally; of course, there are the simplicity and low-cost advantages of a spherical system.

Critics of such a system will cite obscuration and spherical aberration as its inherent weaknesses. However, it is seen that only a slight increase in objective diameter (3 inches to 3.2 inches) is required to retain a 3-inch aperture. By utilizing the Maksutov design, by properly choosing the radii of the menisci, their separation, and by selecting the proper glass, the spherical aberration can be kept to a satisfactory level of less than one minute of arc. This would be reduced for the APOLLO tracker. The glass used in the system will be a non-browning glass for use in a nuclear radiation environment.

An effective aperture of three inches was selected for the Ames tracker to gather enough light from a 6th-magnitude star to give a signal-to-noise ratio of 1:1 when the star image is five seconds off axis. When redesigned for APOLLO, this telescope diameter could be reduced somewhat as a much brighter star could be selected (e.g. a 2nd-magnitude star would have 40 times the luminous flux of a 6th-magnitude star). This will be expanded in a later Section.

### Scanner

The purpose of the scanner is to develop an optical signal which indicates the tracking error between the target Star's image and the optical axis. This optical signal is detected by a photomultiplier and fed into a servo system which realigns the telescope to reduce this tracking error. When the star is centered on the optical axis, the scanner also provides a presence signal which indicates star presence and star magnitude.

~~CONFIDENTIAL~~

~~CONFIDENTIAL~~

The scanner, shown in Figure VIII-4-15, develops the required signals in the following manner. Two cantilevered reeds are mounted in the focal plane at right angles to one another and parallel to the pitch and yaw gimbal axes. At the free end of each reed is mounted an opaque scanner plate with a slotted aperture along the neutral axis of the reed. The reeds are arranged so that in the rest position the two slots cross at the optical axis, forming a square aperture in the focal plane of the telescope. The two reeds are caused to vibrate with equal frequencies and amplitudes, and a relative phase difference of 90 degrees, so that the square aperture is translated in a circular path about the optical axis as a center. The radius of this circular path (which equals the amplitude of vibration of the reeds), is maintained at a value such that a star image centered on the optical axis will appear four times per cycle, once in each corner of the square aperture. The resulting output signal contains a strong component at the fourth harmonic of the frequency of vibration, and contains no component at the fundamental frequency. This fourth harmonic is the presence signal, which indicates star-presence and star magnitude. When the star image is off the optical axis, the output signal contains a greatly-reduced fourth harmonic component (presence signal) and a component at the fundamental frequency, its amplitude increasing with increasing lateral displacement of the image. This fundamental is the tracking error signal: its magnitude is a function of the magnitude of the error; its phase is a measure of the direction of the error about the roll axis. This error signal can be resolved into cosine and sine components and used as inputs to the pitch and yaw servo control motors. As the reeds will be driven at 400 cps, the "error" and "presence" signals will be 400 and 1600 cps, respectively.

Figure VIII-4-16 gives the magnitude of the fundamental frequency signal as a function of the relative lateral displacement of the star image (actually, the ratio of lateral displacement to aperture width). Figure VIII-4-17 shows the magnitude of the fourth harmonic signal (star-presence signal) as a function of the relative lateral image displacement. This signal is sharply peaked at the zero-error position.

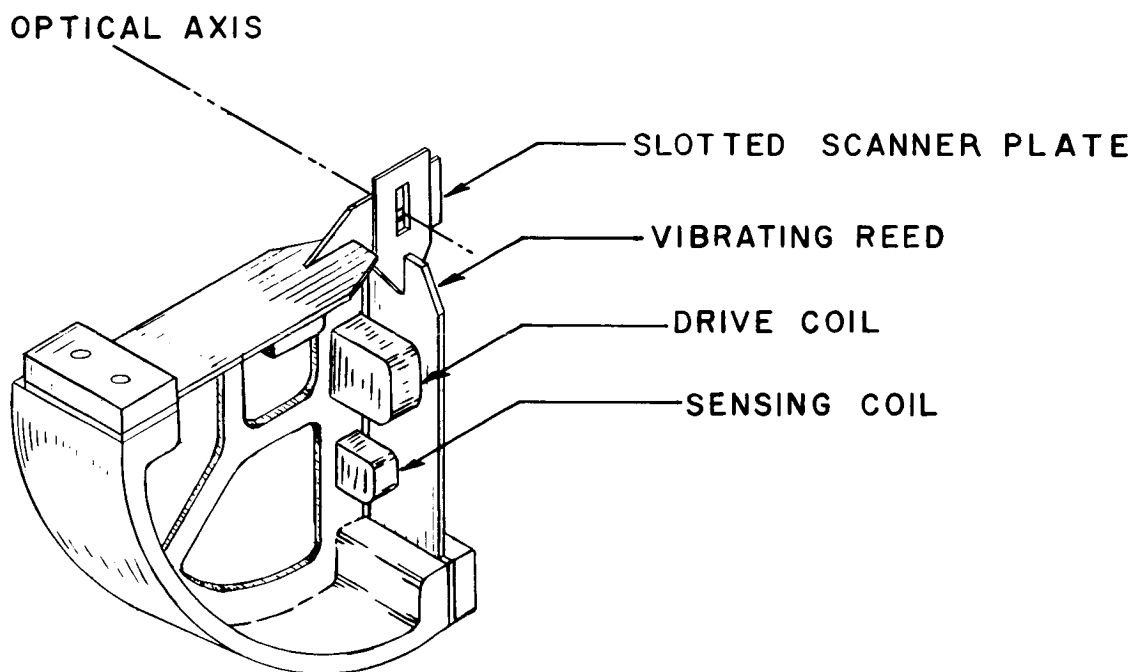


Figure VIII-4-15. Vibrating-reed scanner

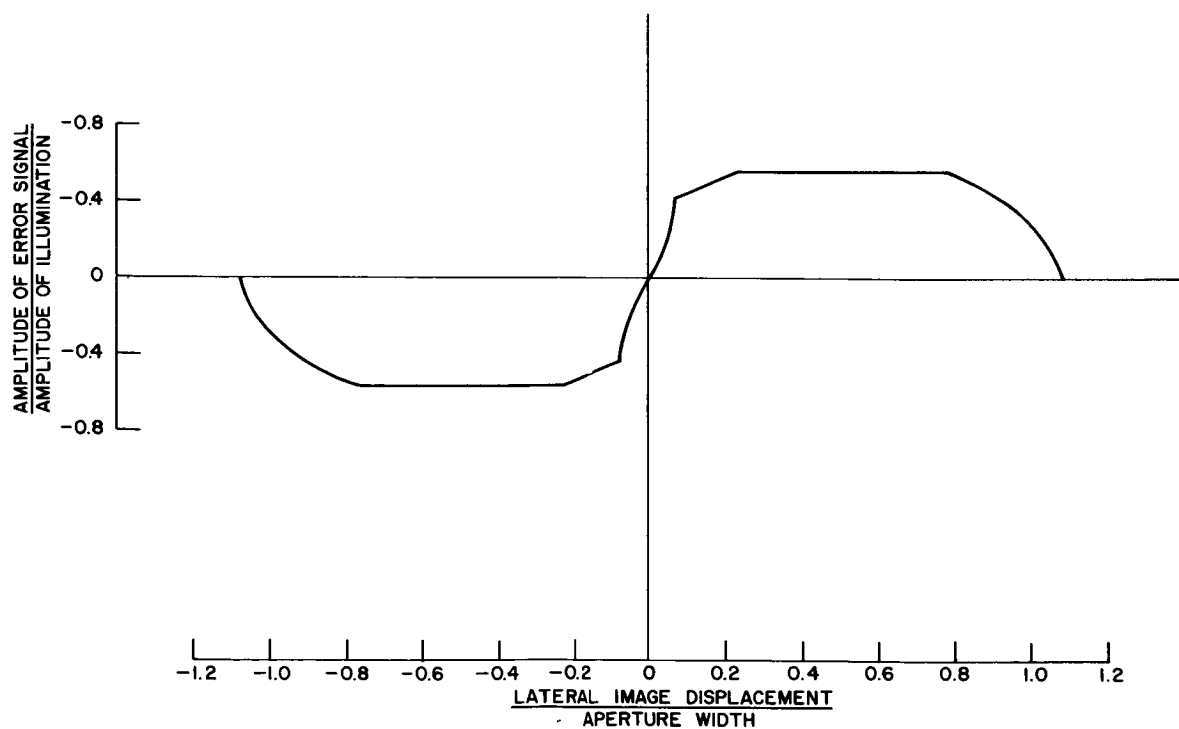


Figure VIII-4-16. 400-cycle error signals versus lateral image displacement



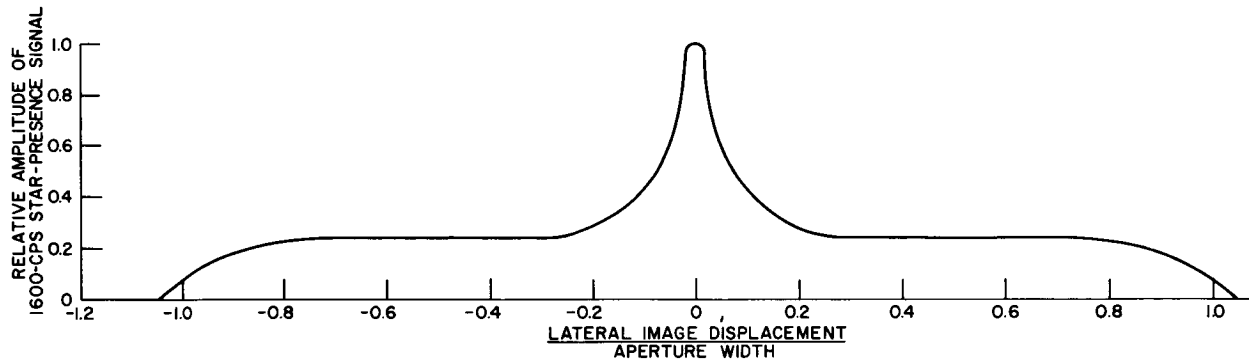
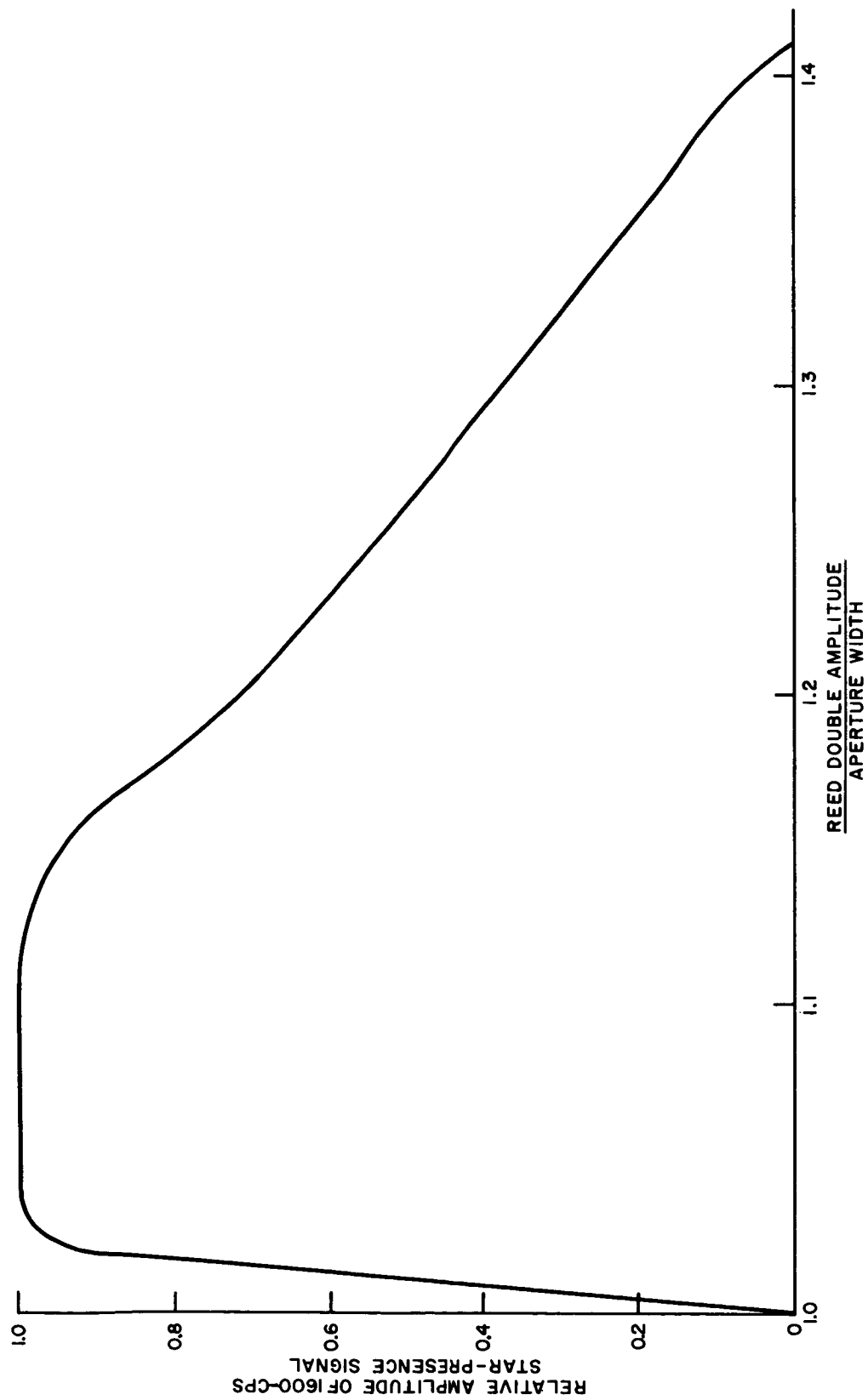


Figure VIII-4-17. Relative amplitude of Star-presence signal (1600 cps) versus relative lateral image displacement

During manufacture the two reeds are matched to have exactly the same resonant frequency. Each reed is excited by an electromagnetic drive coil, its drive current being maintained at the resonant frequency by feedback from the reed's motion. This feedback requires use of a magnetic pickoff coil which senses the motion of one of the two reeds, designated as the master reed. This ensures that the reeds are excited at resonance, resulting in close control of amplitude and phase of vibration, with a minimum of exciting force and of power consumption. Permanent-magnet flux biasing is provided to avoid the frequency-doubling effect of the alternating flux acting on the magnetic reed material. The excitation system will be designed to maintain the reeds' vibrations within the required tolerances, as have been determined by studies of changes in the output signal resulting from variations in the parameters of the reeds' vibrations. Output waveforms have been determined for the following conditions of vibration: varying amplitude of one reed; varying amplitudes of both reeds together; varying phase lag between reeds; and varying initial position of each reed. Some of these results are presented in Figures VIII-4-18 and VIII-4-19. Figure VIII-4-18 shows the effect of

~~CONFIDENTIAL~~



~~CONFIDENTIAL~~

Figure VIII-4-18. Relative amplitude of Star-presence signal versus reed amplitude

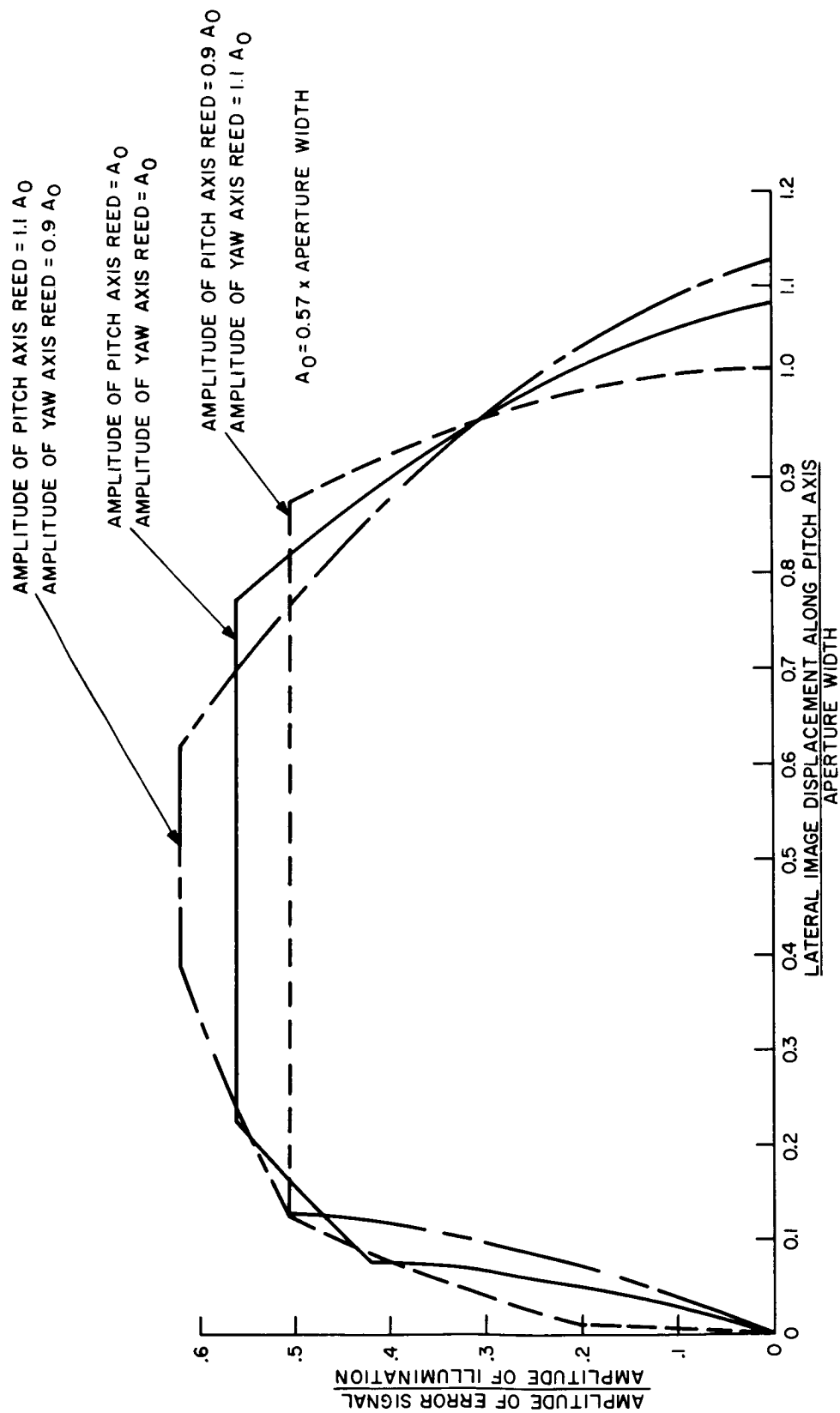


Figure VIII-4-19. Magnitude of 400-cycle-error signal versus lateral image displacement with unequal reed amplitudes

~~CONFIDENTIAL~~

variations of both reed amplitudes on the magnitude of the star-presence signal. This is equivalent to varying the radius of the circular path of the square aperture. Figure VIII-4-19 shows the effect on the error signal of a 10-percent increase in the amplitude of one reed coupled with a 10-percent decrease in the amplitude of the other.

In summary, it can be said that the scanner of this proposed system has good sensitivity to tracking error, is compact, light in weight, and requires less than 0.5 watts total power for operation. The use of vibration reeds eliminates mechanical friction and wear in the scanner and dissipates very little energy. It will have an indefinitely long operating life time.

#### Photodetector

Several studies have been made of possible photodetectors for use in star trackers. These studies have shown that each of the three main types of detectors — photomultipliers, phototransistors, and vidicons — has particular features that make them desirable for a given system. However, of the three, the photomultiplier is generally the highest developed and proven, and specifically it will insure that the proposed tracker meets the specified sensitivity, weight, and power requirements simultaneously.

Among photomultipliers, the RCA 1P21 has been chosen because of its all-around proven performance. The ITT Type FW-118 (S11 surface) has definite advantages (such as reduced dark current, increased gain), but its increased weight (by a factor of almost 4) and size, increased voltage required, the decreased photosensitive area available and inherent mounting problems have outweighed the advantages. The 1P21 has an S-4 spectral response (Figure VIII-4-20), which peaks at the blue end of the spectrum. It should be noted here that the achromatic reflective system allows maximum use of the S-4 response characteristic in the near ultraviolet region.

To calculate the maximum signal-to-noise ratio (S/N) for a 6th-magnitude Star, the following assumptions were made:

The maximum radiation received from the star background (from stars of greater than 6th-magnitude) is  $12 \times 10^{-9}$  stilb (lumen/cm<sup>2</sup>/steradian). This value was obtained from Table 61, p. 125, of Astrophysical Quantities, by C. W. Allen, corrected to above the atmosphere.

~~CONFIDENTIAL~~

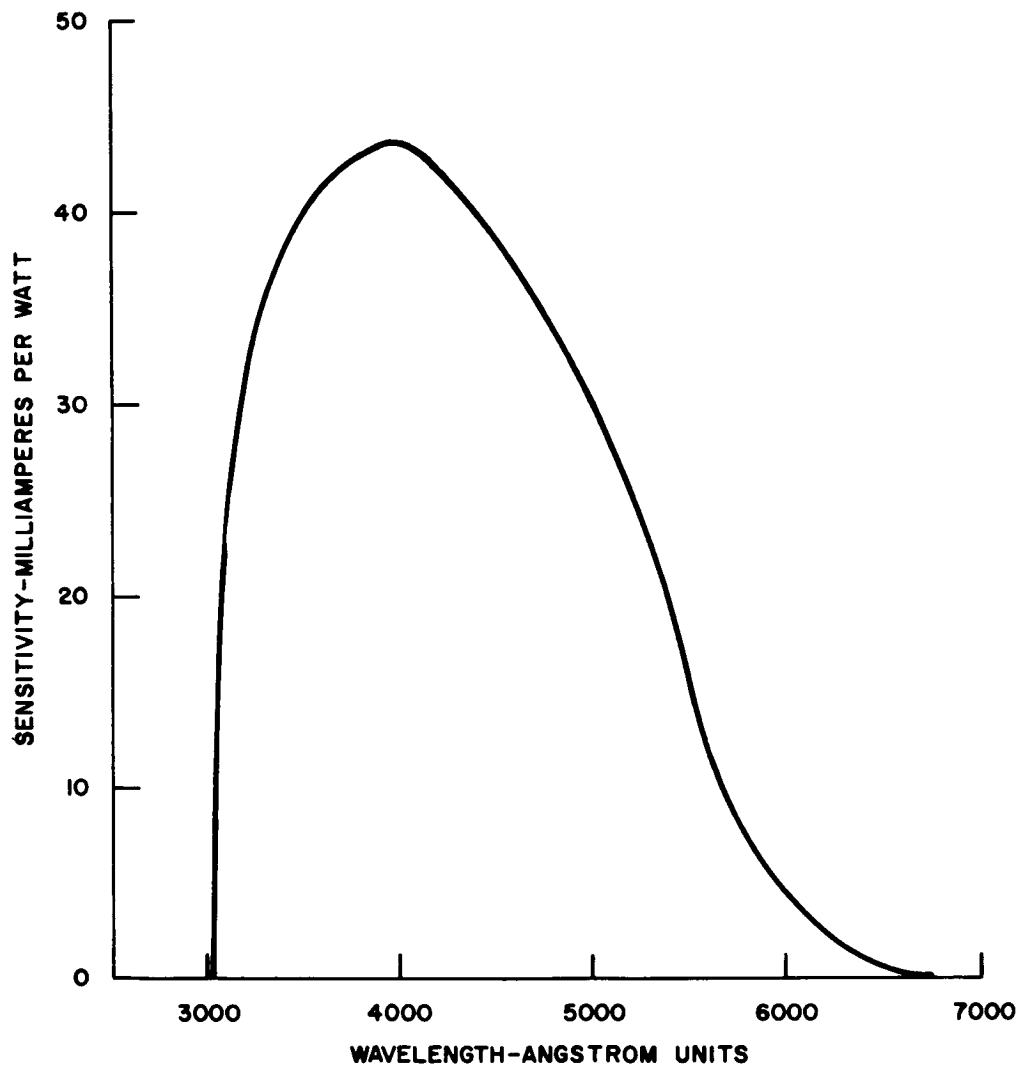


Figure VIII-4-20. Spectral response — S-4 surface

~~CONFIDENTIAL~~

The spectral distribution of the typical 6th-magnitude star is such that the S-4 surface response is about 100  $\mu$  amps per lumen.

The spectral distribution of the background noise is such that the S-4 surface response is about 40  $\mu$  amps per lumen.

The optical efficiency of our system is 80 percent.

The optical energy,  $L_s$ , received by the telescope from a 6th-magnitude Star (see Table VIII-4-1) is

$$L_s = \epsilon \cdot E_s \cdot A.$$

where

$$\epsilon = \text{optical efficiency} = 0.8$$

$$E_s = \text{luminous flux of 6th-magnitude Star}$$

$$= 9.67 \times 10^{-13} \text{ lumen/cm}^2. \text{ (Table VIII-4-1)}$$

$$A = \text{Effective aperture} = \frac{9\pi}{4} \text{ in}^2$$

Substituting, we have

$$L_s = 3.5 \times 10^{-11} \text{ lumen}$$

Our peak-to-peak photomultiplier signal current ( $I_{sm}$ ) is thus (See above):

$$I_{sm} = 3.5 \times 10^{-9} \mu \text{ amp}$$

The background noise flux reaching the photomultiplier is (for long focal length):

$$L_b = \epsilon \cdot \pi \sin^2 \alpha \cdot B \cdot A_a$$

~~CONFIDENTIAL~~

~~CONFIDENTIAL~~

where

$$\epsilon = \text{optical efficiency} = 0.8$$

$$B = \text{Background brightness}$$

$$= 12 \times 10^{-9} \text{ lumen/cm}^2/\text{steradian (See page VIII-71)}$$

$$\pi \sin^2 \alpha = \text{solid angle subtended by entrance aperture at focal plane.}$$

$$= \pi \left( \frac{D}{2f} \right)^2 = \pi \left( \frac{3}{48} \right)^2$$

$$= \frac{\pi}{256} \text{ steradian}$$

$$A_a = \text{area of reed aperture}$$

$$= 3 \times 10^{-4} \text{ ft}^2$$

Substituting, we have

$$L_b \approx 3.2 \times 10^{-11} \text{ lumen}$$

Our photomultiplier current due to background noise ( $I_b$ ) is thus (See page VIII-71):

$$I_b = 1.3 \times 10^{-9} \mu \text{ amp}$$

This is almost an order of magnitude greater than the equivalent anode dark current, which can be kept to  $5 \times 10^{-10}$  lumens by selection. This dark current is a function of temperature, becoming a significant addition to the value  $I_b$  at temperatures above 50 C. A thermoelectric cooler is also included in the design (Figure VIII-4-12) to insure that the photomultiplier temperature is kept at or below 50 C.

The mean square noise,  $I_N^2$ , in a bandwidth  $\Delta f = 1 \text{ cps}$  is:

$$I_N^2 = 2 e (I_b + I_{so})$$

~~CONFIDENTIAL~~

~~CONFIDENTIAL~~

where

$e$  = electronic charge, coulombs

$I_{so}$  = steady state component of signal =  $1.2 \times 10^{-9}$   $\mu$  amp

Thus

$$I_N^2 = 8 \times 10^{-34} (\text{amp})^2$$

Our RMS signal can be shown to be

$$\begin{aligned} I_s(\text{rms}) &= \frac{2 \times .88 I_{sm}}{\pi \sqrt{2}} \\ &= 13.8 \times 10^{-10} \mu \text{ amp} \end{aligned}$$

Thus, our signal-to-noise ratio (S/N) is:

$$\begin{aligned} S/N &= \frac{13.8 \times 10^{-16}}{\sqrt{8 \times 10^{-17}}} \\ &\approx 60 \end{aligned}$$

It will be necessary in our accuracy analysis (Section, "Accuracy Considerations") to know the distance off-axis we must move before S/N becomes 1. The value,  $I_s'$  of the signal current needed (assuming  $I_b$  = constant) is:

$$I_s' = I_N$$

Therefore:

$$I_s' = .017 I_s$$

This value and its significance will be expanded later in "Accuracy Considerations".

~~CONFIDENTIAL~~



~~CONFIDENTIAL~~

For use in the APOLLO mission the AGC system described for the general tracker system (see page VIII-85) would be removed so that the signal would be significantly larger, (by a factor of 40). This would increase the signal-to-noise ratio with the star off axis to over 400, and reduce the fraction of maximum signal needed for  $S/N = 1$  to  $I_s' = 0.00025 I_s$ .

#### Mechanical Configuration

The mechanical structure is shown in Figure VIII-4-12. The gimbal configuration is a conventional two-axis system. Each axis has a d c torque-motor drive, an angular readout device, and sliprings. The telescope is mounted on the inner gimbal axis, with the scanner, photodetector, and thermoelectric cooler mounted directly to it. Some electronics, (not shown in Figure VIII-4-12) are mounted judiciously on both the gimbals and the structure to counterbalance the gimbal system.

The prime structural member consists of a mounting ring which is integral with the outer gimbal trunnion and the mounting ears. The close proximity of the mounting surface to the trunnion provides maximum rigidity with minimum weight. Aluminum alloys are used extensively to maintain the total tracker weight (including electronics) to twenty pounds or less.

Table VIII-4-2 lists the weights of the tracker elements for the 6th-magnitude tracker. These individual weights would be slightly reduced in the APOLLO version. In addition, if such trackers were to be used in an already sealed unit with its own dome, the weights of individual viewing domes, mounts and covers (Table VIII-4-2) could be eliminated. Also, a reduction in electronic complexity (and thus weight) could be effected for a tracker design with such a specific purpose.

The unit is made to be hermetically sealed with slightly over 1 atmosphere of a dry nitrogen-helium mixture, so that any minute leakage over several months on the shelf will be to the atmosphere, thus excluding any oxygen, moisture, or other contaminants. A desiccant is provided to insure that a low moisture level is maintained. The sealing technique utilized wherever possible in the final version is welding, the most reliable possible method. The glass-to-metal joints will be mechanically clamped and epoxy sealed.

~~CONFIDENTIAL~~

TABLE VIII-4-2. WEIGHT TABULATION

<u>Component</u>	<u>Weight (Pounds)</u>
Ring, Mounting	2.55
Gimbal, outer	2.0
Gimbal, inner including telescope and lenses	1.9
D-C Torquers 2 @ 0.875	1.75
Phasolvers (Angular Pickoffs) 2 @ 0.2	0.4
Dome, Viewing	1.5
Mount, Dome	1.0
Cover, Rear	1.4
Photodetector and Shield	1.0
Thermoelectric Cooler	0.5
Scanner	0.7
<hr/>	
Tracker Assembly	14.7
Electronics Package	5.3
<hr/>	
Star Tracker Total	20.0

~~CONFIDENTIAL~~

~~CONFIDENTIAL~~

### Gimbal Pickoff Devices

The angular positions of the two gimbals must be measured with an accuracy of two seconds of arc to attain the system accuracy of ten seconds desired for APOLLO. It presently seems that this accuracy can be achieved with the Phasolver. A concerted test program is now underway to evaluate the Telecomputing Corporation Phasolver to determine its suitability for this system.

The Phasolver is a two-speed (electrical) transducer which produces (at each "speed") an electrical output which is of constant amplitude, its phase being a unique function of position. The output can be supplied in digital or analog form. The inherent accuracy of the Phasolver is better than one second of arc, and has already demonstrated on accuracy and repeatability of better than six seconds of arc in the Askania cinetheodolite at Edwards Rocket Base.

### Servo System

The star tracker is required to operate in three basic modes:

- a. The track mode, where the telescope is made to follow the apparent motion of a star. The position of the star is then determined by the electrical readout of the gimbal transducers.
- b. The pointing mode, where gimbal angles are determined by command from external transducers such as a resolver.
- c. The search mode, where the telescope is required to follow a spiral pattern from the zero position to a full 30 degree field.

Each of these modes has different requirements as far as the servos driving the gimbals is concerned. The search mode may be considered as a slowly varying external command and thus the servo operation will be essentially the same as in the pointing mode. This will be explained later.

After the star light has been modulated by the scanner and detected by the photomultiplier, the electrical star signal consists of rectangular pulses. The fundamental or 400-cycle signal is proportional to the error and is phase-sensitive to determine

~~CONFIDENTIAL~~

~~CONFIDENTIAL~~

the direction of the error. The fourth harmonic or 1600-cycle component is strongest when the error is zero and is therefore used as an indication of the star-presence. The two desired components are separated by passing the photomultiplier output into two narrow-band amplifiers tuned to 400 cps and 1600 cps. Along with each component there exists a certain amount of noise generated in the photomultiplier which happens to be in the band-pass region of the narrow-band amplifier. The 400-cycle signal (along with the noise) is phase-split into two components: an in-phase and a quadrature signal. Each of the components is now in phase (or 180 degrees out of phase) with one of the two vibrating reeds. The pitch signal, for example, is now demodulated phase sensitively so as to remove the 400-cycle signal and give us only the modulation frequencies produced by the star motion plus the noise. The problem is now one of servo design and the details will follow. The general approach, however, will be to amplify the d-c signal from the demodulator or discriminator and drive the torque motor so as to reduce the error. The use of the 1600-cps star-presence signal will be explained later.

Of the total accuracy of the star tracker of ten arc seconds, two arc seconds are allotted to each servo. Restating this, the servo must maintain the error between the optical axis and the line of sight to the star to less than two arc seconds under all tracking rates (to 36 degrees per minute). The gain required to restrict the error to two arc seconds is considerably less than that required because of the friction torque at the output shaft.

Direct-drive torque motors are used in this application for the following reasons:

- a. The inherent backlash of the gearing required by two-phase motors is eliminated.
- b. The inertia is all located on the same shaft, which allows the power dissipation for satellite motion to be a minimum. When gears are used, the motor inertia is on a higher-speed shaft than the load and works to expose the tendency of the load to stay fixed in inertial space.
- c. A more efficient motor is possible by using d.c. rather than a.c.  
(Remember that at these low speeds no brush problem exists.)

- ~~CONFIDENTIAL~~
- d. The driving power may be obtained directly from the battery power source without requiring conversion as would a-c motors. A recognized disadvantage is the absence of the high gain contributed by the gear ratio of an a-c drive. Past experience has shown that this may be overcome as can be attested to by several very successful direct-drive applications designed and built by the General Electric Company, (e.g., Atlas Radar tracker, Tartar missile director, and Polaris Guidance gimbal and accelerometer servos). The mechanical design will be such that a friction torque of no more than 0.02 lb-ft is predicted. An Inland Motor catalogue T-2108B has been selected. This motor has a peak torque of 0.31 lb-ft, giving adequate surplus torque to accelerate the load. Actually, a larger motor would reduce the power requirements at the expense of increased size and weight. The size selected is felt to be a reasonable compromise. Table VIII-4-3 lists its characteristics.

TABLE VIII-4-3. MOTOR CHARACTERISTICS — INLAND TYPE T-2108B

Peak torque, lb-ft	0.31
Volts at peak torque stalled at 25 C	25.6
Back EMF, volts/rad/sec	0.34
Amperes at peak torque	1.24
Torque constant, lb-ft/amp	0.25
D-c resistance at 25 C, ohms	20.6
Self-inductance, henries	0.020
Friction, lb-ft	0.0078
Rotor inertia, Slug ft <sup>2</sup>	0.0002
Weight, lb	0.875

From the mechanical design of the telescope and gimbals, the inertias are found to be as follows:

$$\text{Inner } J_{\text{in}} = 0.013 \text{ slug-ft}^2$$

$$\text{Outer } J_o = 0.018 \text{ slug-ft}^2$$

~~CONFIDENTIAL~~

Computing the inertial time constants, we have:

$$\text{Inner } T_m = \frac{1}{\omega_m} = \frac{JR}{K_v K_t} = \frac{(0.013)(20.6)}{(0.34)(0.25)} = 3.06 = \frac{1}{0.33}$$

$$\text{Outer } T_m = \frac{1}{\omega_m} = \frac{JR}{K_v K_t} = \frac{(0.018)(20.6)}{(0.34)(0.25)} = 4.36 = \frac{1}{0.23}$$

To calculate the servo gain, we first see from the accuracy specifications to be given that the servo error permitted is two seconds, and that from the mechanical design of the tracker a friction and unbalance torque = 0.02 lb-ft is expected. From Figure VIII-4-21 (A) we can see that when  $\Theta_i = 0$ ,  $\Theta = e$ . Now when the block diagram of Figure VIII-4-21 (A) is rearranged

$$\frac{T_D}{e} = \frac{K K_t}{R} \text{ results}$$

Solving for the unknown gain K gives

$$K = \frac{T_D R}{e K_t} = \frac{(0.02)(20.6)}{(2)(0.25)} = .823 \text{ volts/sec}$$

$$K = 1.7 \times 10^5 \text{ volts/rad}$$

Now rearranging the block diagram in Figure VIII-4-21 (A) gives Figure VIII-4-21 (B). From Figure VIII-4-21 (B) the steady-state gain of the servo open loop is:

$$\frac{K}{K_v} = \frac{1.7 \times 10^5 \text{ volts/rad}}{0.34 \text{ volts/rad/sec}} = 5 \times 10^5 \text{ sec}^{-1}$$

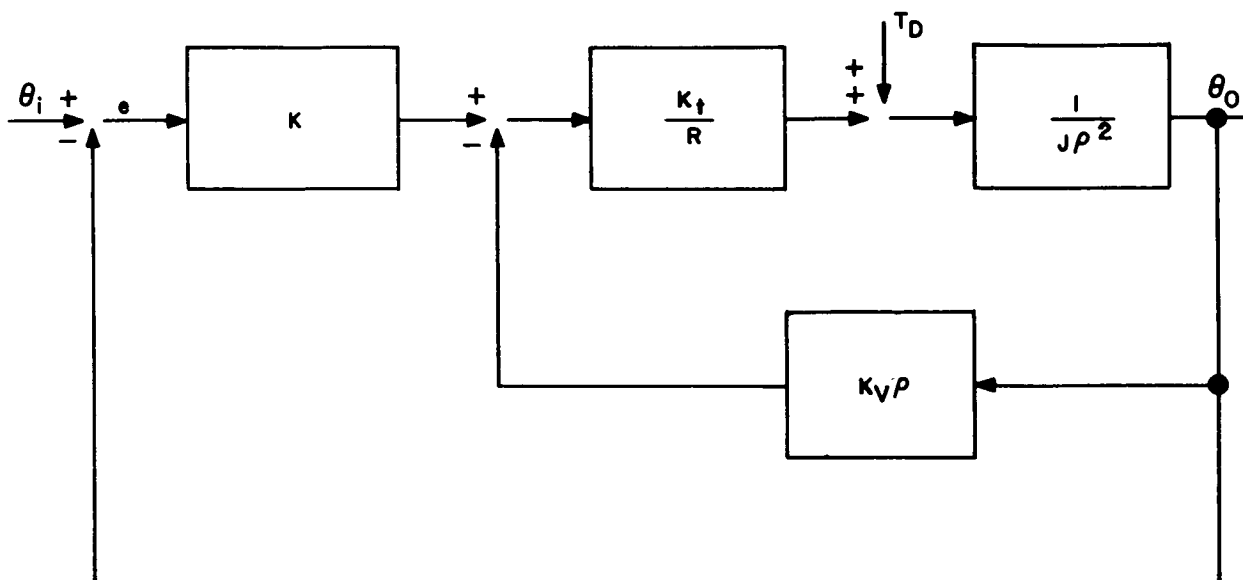
$$\frac{K}{K_v} = 114 \text{ db/sec}$$

The motor will be driven from a low-impedance source with an output impedance of less than an ohm. Thus,

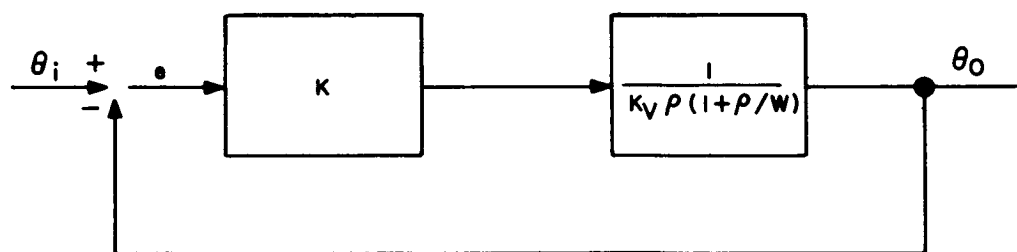
$$\omega_L = R/L = \frac{20.6}{0.020} = 1030 \text{ rad/sec}$$

~~CONFIDENTIAL~~

~~CONFIDENTIAL~~



(A)



(B)

$T_D$  = TORQUE DISTURBANCE AT LOAD SHAFT  
 $\theta_o$  = OUTPUT POSITION  
 $\theta_i$  = INPUT POSITION  
 $e$  = ERROR

Figure VIII-4-21. Partial open loop block diagram

~~CONFIDENTIAL~~

~~CONFIDENTIAL~~

The complete servo block diagram of the inner gimbal is given in Figure VIII-4-22, and the corresponding Bode diagram in Figure VIII-4-23. Since the outer gimbal inertial time constant is only slightly different from the inner it can be expected that the same electronics can be used for both.

The pointing mode is shown in the functional diagram of Figure VIII-4-24. Here it is seen that pitch and yaw commands as set by the shafts of the respective transmitters will cause the servos to slew to the designated gimbal angles. The servo design is basically the same as that of the track mode. Although only a one-speed system is shown (as would be the case with a resolver) a two-speed system would be used with a phasolver. The phasolver is favored here both because of its increased accuracy and its great reduction in weight. This has a marked effect on the size and weight of the over-all star tracker.

The telescope of the tracker will be driven in a spiral pattern until the desired celestial body is brought into the field of view of the optics. A spiral pattern is chosen, for it will initially search the area closest to the reference axes. The radial width of the field of view determines the radius of each spiral in the search pattern. There will be some overlapping of the areas searched in successive loops of the spiral to insure the condition that a celestial body will be in the field of view long enough to allow the acquisition circuitry to operate. The time to search a given area is dependent upon the size of the field of the optics and the time for the acquisition circuitry to operate. When these two parameters are optimized it is then desired to drive the telescope at the maximum rate possible to achieve the shortest search time. To accomplish this objective, the angular velocity of the telescope line-of-sight about the roll axis must vary non-linearly with time. A mechanism to generate the necessary pitch and azimuth signals (Figure VIII-4-25) will consist of a synchronous motor driving a mechanical linkage which will rotate a resolver with the desired speed variation. The two outputs from the resolver are 90 degrees out of phase, and will be used to drive the pitch and azimuth gimbals. Rigid requirements as to size, weight, accuracy, and reliability will be designed into the mechanism.

~~CONFIDENTIAL~~



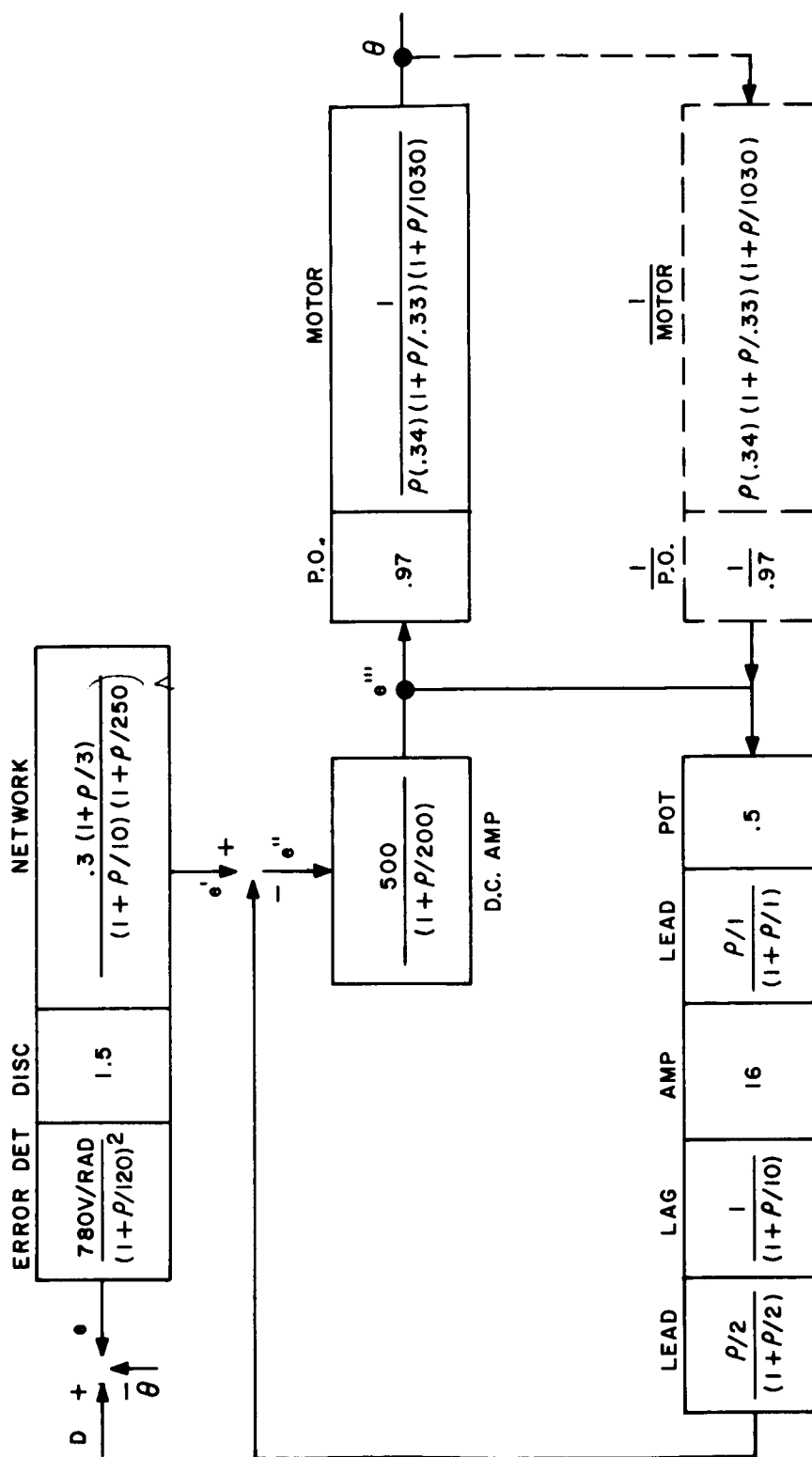


Figure VIII-4-22. Inner gimbal block diagram

CONFIDENTIAL

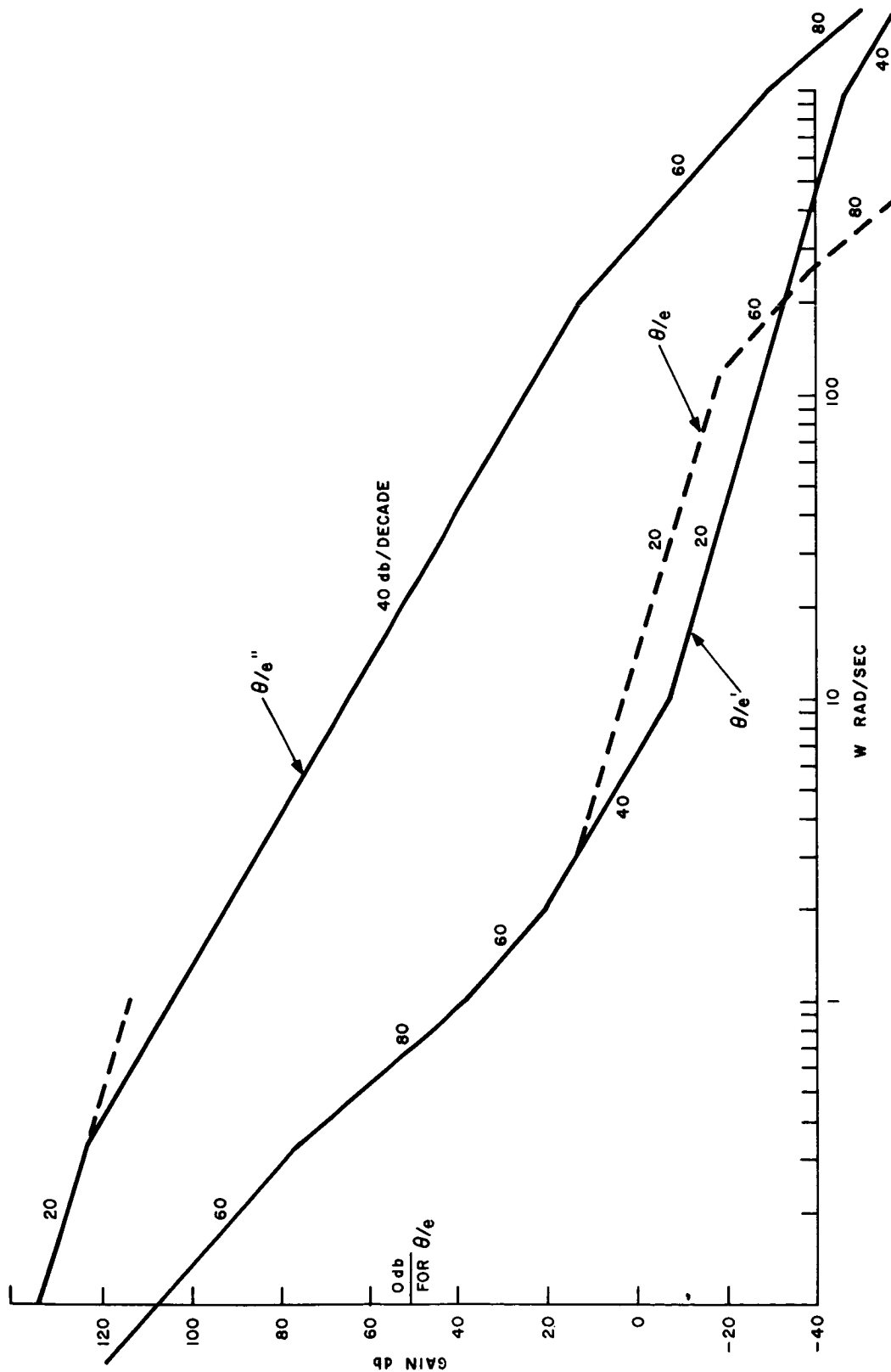


Figure VIII-4-23. Inner gimbal Bode diagram

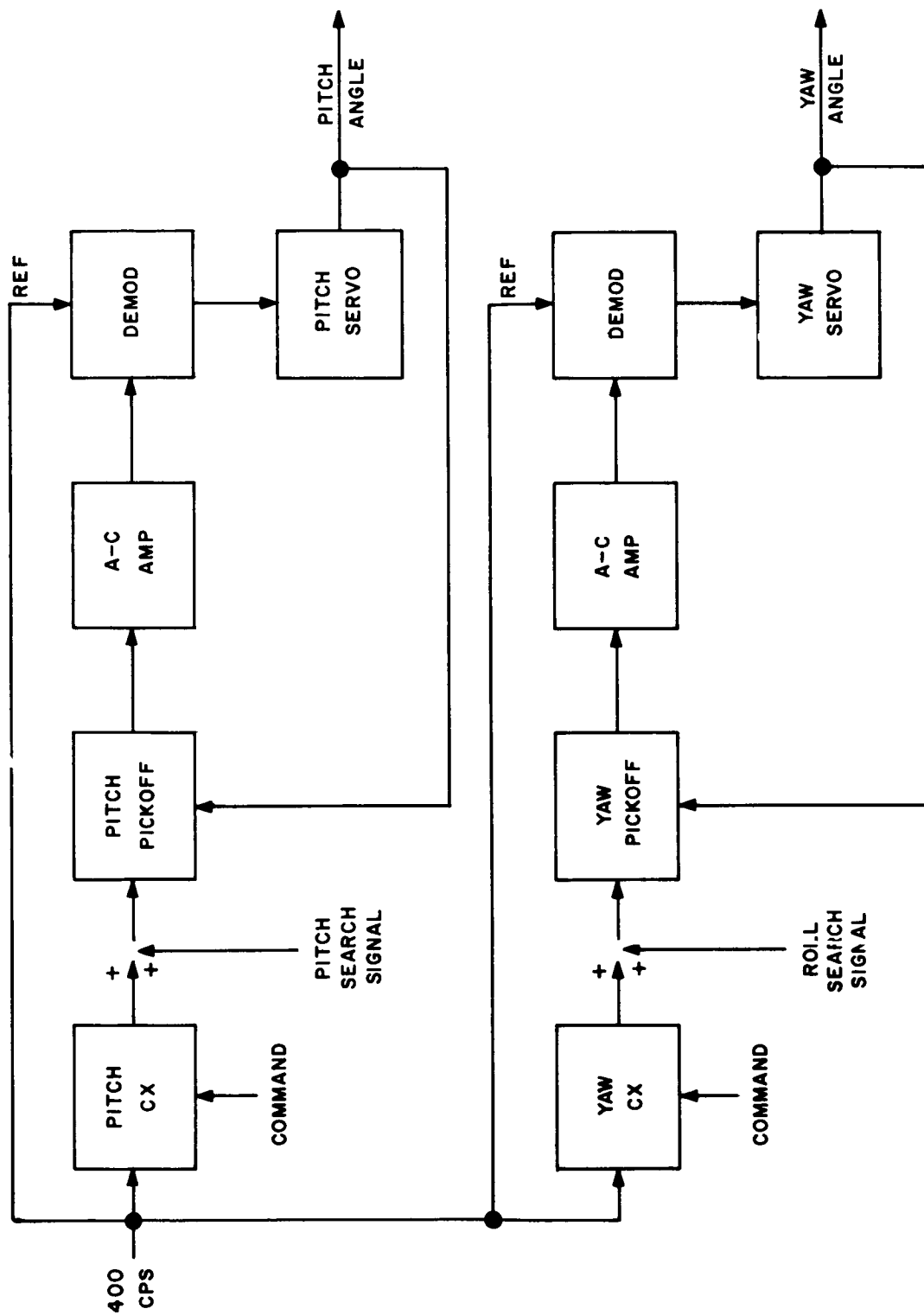


Figure VIII-4-24. Pointing mode — functional block diagram

~~CONFIDENTIAL~~

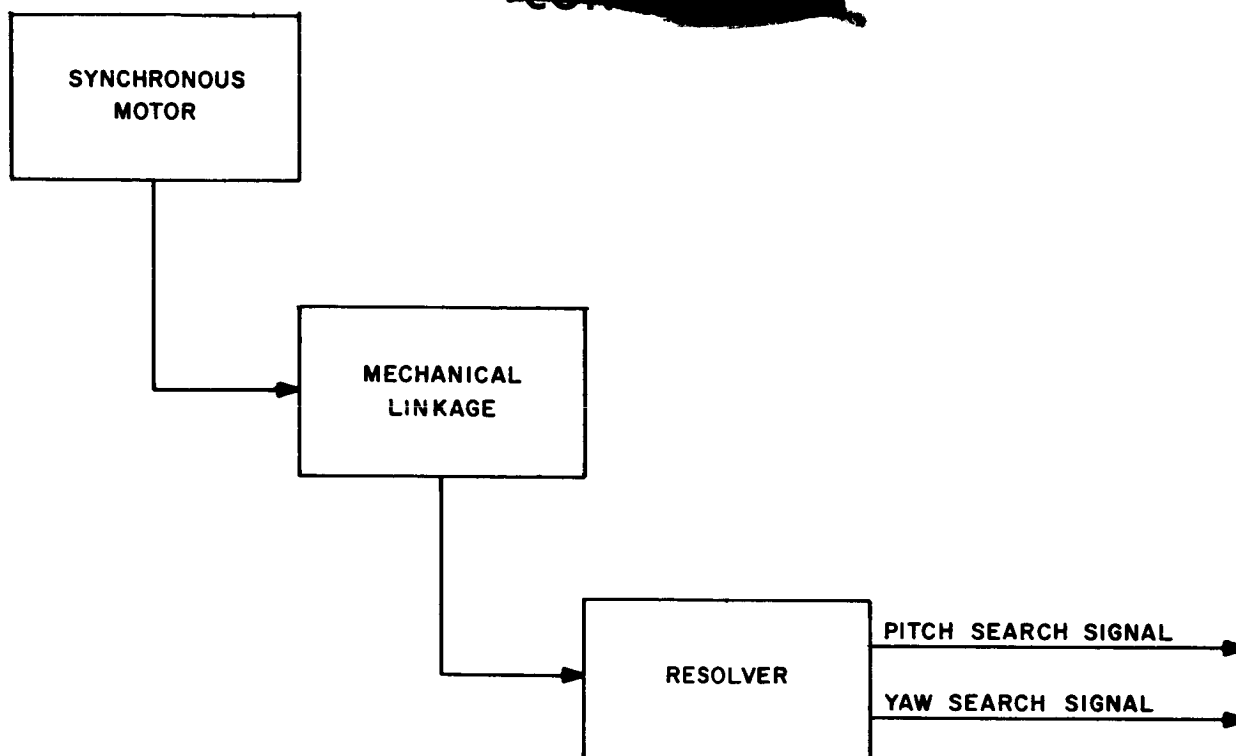


Figure VIII-4-25. Search signal mechanical block diagram

The star-presence circuit is shown in Figure VIII-4-26 and is explained as follows. Both the 1600-cycle and 400-cycle signals as they come from the narrow-band amplifiers contain considerable noise. In order to eliminate this, a broad-band amplifier is used to amplify the preamplifier output by the same amount as the narrow-band amplifiers increase the 400- and 1600-cycle components. This broad-band signal is now rectified and subtracted from the rectified 400- and 1600-cycle signals. In this way, the noise channel may be adjusted to just cancel the noise which is at the output of the narrow-band amplifiers. Now when a star is present, the increase at the output of the detectors will be entirely due to the star. The 1600-cycle signal is not used alone, since for large errors, or when the star is toward the edge of the field of view, where the 1600-cycle signal is low, the increase in output will be small. A nearly constant signal is obtained by adding both the 400- and 1600-cycle signals, and this is used as an indication that the search is to stop.

This presence signal is also sent to the high-voltage power supply so as to reduce the range of the photomultiplier output change over the wide range of star intensities. The

~~CONFIDENTIAL~~

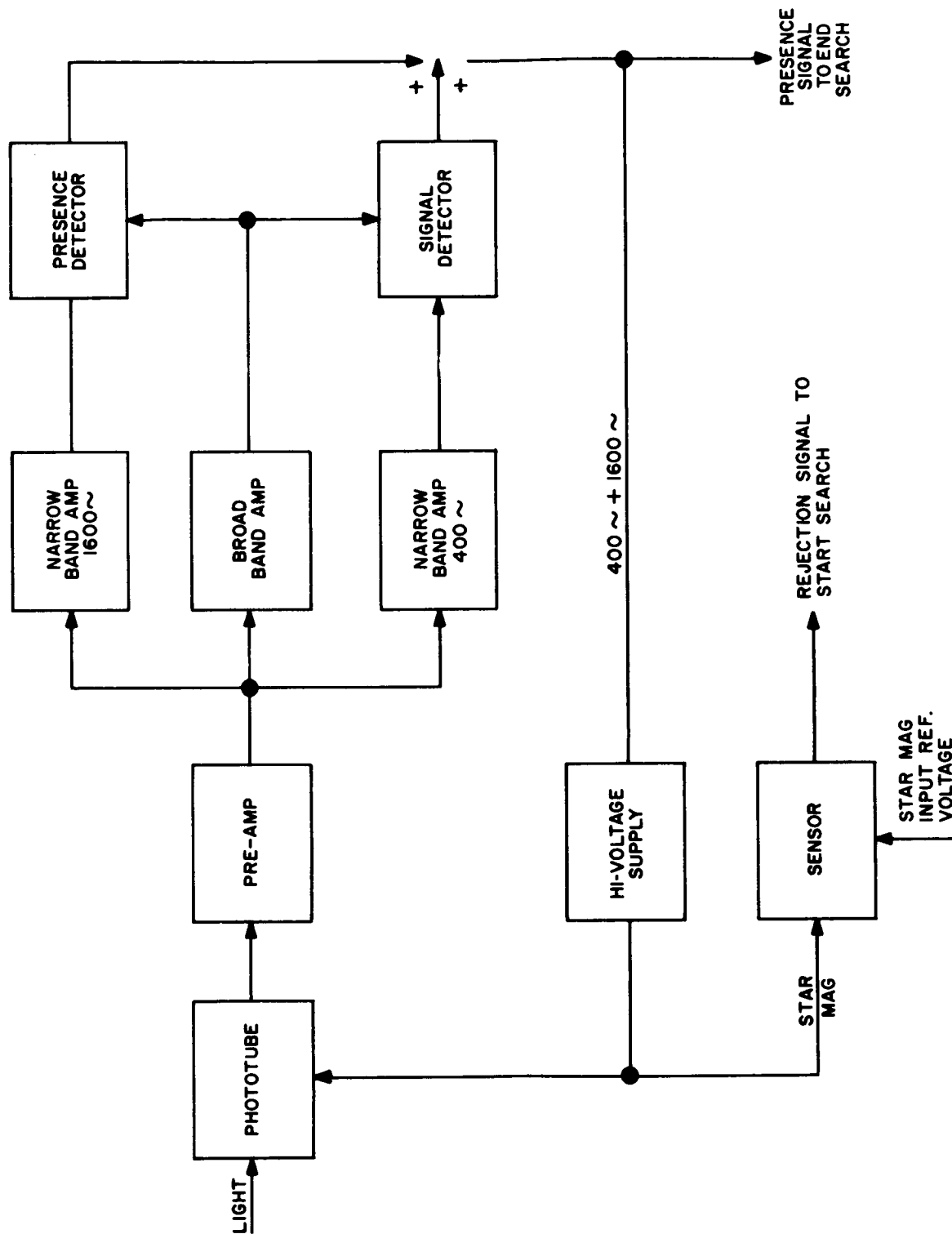


Figure VIII-4-26. Star-presence circuit — functional block diagram

~~CONFIDENTIAL~~

amount of automatic gain control can be used as an indication of star magnitude. The measured star magnitude is compared with the reference star magnitude and if they are not equal to within a half magnitude, the search is resumed.

The average power required when in operation is 10 watts.

#### Accuracy Considerations

The principal source of error in earlier models of star trackers has been from in the gimbal readout transducer. Recent indications, however, have been that the Phasolver (Telecomputing Corporation) has the capability of indicating angles with an accuracy better than one second of arc. It is relatively light in weight and has suitable mounting dimensions. The basic information from the unit is analogue; however, the usable information can be easily digitized. A maximum pickoff error of two seconds will be allowed.

The next important error is introduced as an uncertainty in the null position of the telescope position servo. As the input information (signal) is decreased with respect to spurious or random inputs (noise) the signal which is necessary to align the telescope eventually becomes lost in the noise. The signal-to-noise ratio analysis has shown that with a 2nd-magnitude star being tracked away from the galactic equator, the signal-to-noise ratio is 400:1 when the star is at the outer extremity of the field of view. The signal-to-noise ratio will be reduced to 1:1 when the telescope is less than one second of arc off axis. The noise calculated was that due to random fluctuations of the individual charges in the main stream of current. Since it is random and the distribution is not frequency-dependent, it can not be predicted.

The signal-to-noise ratio is an indication of the probability that the star may be detected. The detection, therefore, can be spoken of only on a statistical-basis. The signal-to-noise ratio of 400:1 shows that there is an extremely good chance of detecting a 6th-magnitude star in the mean sky. These calculations of a 400:1 S/N show that the 3.2-inch telescope, without AGC, is overdesigned for a 2nd-magnitude star. A study of tradeoffs will be made for the optimum telescope diameter (and thus weight and size), instantaneous field-of-view, and S/N to be used to keep this error to 2 seconds of arc.

~~CONFIDENTIAL~~

~~CONFIDENTIAL~~

The optical window will be formed in a manner which will compensate for the dishing effect which occurs with flat plates having a finite pressure difference across the faces. It will also be ground such that the wedge effect of the glass when combined with the error in compensation will be less than  $\pm 2$  seconds of arc.

The principal sources of error in the telescope are found in the opto-mechanical alignment, optical surface and coating defects, stray-light baffling defects, and null shifts due to temperature changes. Using extremely precise theodolites and a precision turntable the optical alignment of the telescope can be set to  $\pm 1$  second of arc with respect to the case.

Optical surface and coating defects combined with stray-light inputs will be minimized by good design practices and the use of highly reliable workmanship. Emissive paints and coatings will be used wherever possible to help thermal gradients to a minimum. These errors will be held to  $\pm 1$  second of arc.

Additional errors can arise from non-orthogonality of the gimbals' axes to the optical axis and random errors due to ball bearings and flexing of mechanical parts. These errors will be kept to  $\pm 2$  seconds of arc under any condition of gimbal error and telescope position.

The gain of the telescope loop and the stiction on the gimbals will be controlled to give a maximum "hang-off" error of  $\pm 2$  seconds of arc.

The total system error is therefore:

1. Angular transducer	$\pm 2$ seconds of arc
2. Signal-to-noise error ( $S/N = 1$ )	$\pm 2$ seconds of arc
3. Optical window	$\pm 2$ seconds of arc
4. Telescope errors	$\pm 2$ seconds of arc
5. Servo error	$\pm 2$ seconds of arc
Maximum Possible Error	$\pm 10$ seconds of arc
RSS Error	$\pm 5$ seconds of arc

~~CONFIDENTIAL~~

~~CONFIDENTIAL~~

### Disc Scanner

Parallel design studies are presently underway for a disc (Earth/Moon) scanner. One promising approach is to utilize the narrow field-of-view Star tracker to track around the illuminated circular edge of the disc. It is hoped that a high degree of accuracy will be obtained by keeping the instantaneous field-of-view small. A comparison design study for a separate disc scanner is also underway. The most promising system will be selected upon completion of these studies.

~~CONFIDENTIAL~~

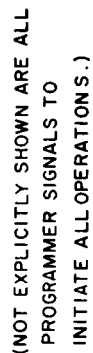


## SYSTEM NO. 2

The simplified diagram in Figure VIII-4-27 shows the basic functional relationship of the components for midcourse guidance. These components consist of optical and IR sensing systems, inertial systems, and computational equipment.

In this system, the primary external inputs come from a small field of view tracker and a horizon scanner capable of sensing the Earth and Moon horizon. The purpose of the small field of view tracker is to determine lines to stars, whereas the purpose of the horizon scanner is to achieve verticality measurements to the Earth and Moon and range measurements by virtue of planet diameter measurements. Further discussion of these external sensing instruments is discussed later. Other possible means of combining these two instruments into one basic, sensing instrument is also discussed. Figure VIII-4-27 shows that the basic external sensing instruments are placed on a two-gimballed platform having limited freedom of motion. The primary purpose of this platform is to provide base motion isolation. This permits fine tracking alignment of the IR and optical sensors without requiring extraordinarily precise attitude control of the entire vehicle as would be required if the instruments were body-mounted. Also on the platform is an electrostatic gyro package consisting of two electrostatic gyros. The purpose of the electrostatic gyros is threefold: first, they provide a basic reference for acquisition of optical sightings; second, they provide a means of accurately measuring and providing a digital output for traverse angles between sightings and finally, they provide a precise inertial reference for use during the corrective thrust intervals.

We will now describe in brief the operation of the functional block diagram as shown in Figure VIII-4-27. On the left side of the diagram we see a programmer which is, in effect, part of the digital computer. Inputs to the programmer come from the crew; they come also from a timer and other inputs may be from position information as computed in other portions of the computer. This position information may be, for example, range. The programmer box which also includes certain storage elements for acquisition purposes provides the basic inputs to all the various operational functions of the system to initiate the various sensing computational and correction actions.



VIII - 91/VIII - 92

~~CONFIDENTIAL~~

The initial function of the guidance system will occur in a condition of fixed gimbals. That is to say, the locking mechanism indicated on the block diagram will be engaged to precisely fix the two gimbal platforms relative to the vehicle. At that time, a signal is sent from the programmer to give command for direction cosines for the initial stellar acquisition. These command direction cosines are sent through the appropriate switching as shown to the comparator circuit and resolver. Here these direction cosines are compared with the direction cosines coming directly from the electrostatic gyro system. In the usual case the acquisition direction cosines will differ from the true direction cosines being read out from the electrostatic gyro and this will serve as a command input to the attitude control system for initial acquisition. This is accomplished in a comparator circuit and resolver. The resolving function transforms the attitude error into body system coordinates to give pitch, yaw and perhaps roll commands to the attitude control system. The attitude control system controls the vehicle rotational dynamics until such time as the small field of view tracker is within the field of view of the star to be acquired.

At this time, the gimbal locks are disengaged so as to provide fine control of alignment of the optical system by means of the gimbal drive. The small field of view tracker provides an input to the gimbal drive to center the image from the small field of view tracker. The gimbal drives rotate the two gimbals until such time as the small field of view tracker is acquired precisely. It is anticipated that the star sighting can be taken to better than five seconds of arc. When the small field of view tracker has precisely acquired the star, a lock-on signal is transmitted to the gyro readout gate. This is an indication that the electrostatic gyro readout should be operated. The star sighting provides a basic input alignment of the gyros. This alignment, however, is done in a gyro reset function and is an alignment which takes place digitally. No physical torquing of a gyro is required. The entire realignment of the gyro is based on star tracking information but the reset operation is performed by computational procedure in the digital computer.

The procedure described above is performed again for another star. The other star should be more or less orthogonal to the first. Two star sightings are sufficient to provide resetting of the gyro periodically.

~~CONFIDENTIAL~~

~~CONFIDENTIAL~~

The electrostatic gyro provides a highly stable inertial reference which requires only very infrequent resetting with information from the star tracker. All subsequent sightings to the Earth and to the Moon are accomplished by comparing the verticality as sensed by the horizon scanner to the inertial reference. In accomplishing these sightings to the Moon or Earth vertical, the horizon scanner provides inputs to the gimbal drive much as the small field of view tracker did previously. This allows precise lock-on of the horizon scanner to the Earth or the Moon vertical. As previously, the gimbal drive provides precise orientation control of the horizon scanner. The vehicle attitude control provides gross corrections of the attitude. In order to accomplish this the gimbals are provided with stop switches. These stop switches sense when the gimbals are approaching the limits of their allowable travel. When this occurs, signals are set to the pitch or yaw vehicle attitude control channels. In this way, the entire vehicle is torqued through angles to back-off the gimbal angles.

In the operation to sense the verticality and diameter of the Earth or Moon, the vehicle attitude is commanded to rotate through gross angles for acquisition of the Moon or the Earth. These signals come once again from the programmer and are compared with the true attitude as determined by the electrostatic gyro readout. This is very similar to the operation of the star tracker acquisition. Once the Earth or the Moon has been acquired, the gimbal locks are released to allow fine control of the gimbals for precise alignment to the Earth or Moon verticality.

When the horizon scanner has achieved precise vertical alignment, a lock-on signal is set to the gyro readout gate to indicate that the gyro should be read directly. This gyro readout information then becomes a primary input to the position computation operation.

Another piece of information coming from the horizon scanner is the horizon diameter. This information also flows directly to the position computation. The basic inputs to the position computation are then the horizon diameter measurements of the Earth and the Moon and the direction cosines of the vertical to the Earth and the Moon relative to inertial or stellar space.

~~CONFIDENTIAL~~

~~CONFIDENTIAL~~

The upper right-hand portion of Figure VIII-4-27 shows a very simplified concept of how the explicit guidance system might look. In the box marked "Position Computation" the basic information from the platform and sensing system is smoothed to provide the best inputs to the computation of the position. Position as computed based on these inputs is functions of stored inputs of the Earth-Moon system. These stored inputs consist of constants and ephemerides of the solar system. Based on the position computations, there are computed also the vehicle ephemerides. This is, in effect, a prediction computation of the future dynamic history of the vehicle. This likewise is based on the Earth-Moon storage system. The computed ephemerides of the vehicle are compared with the commanded ephemerides coming from the programmer. These commanded ephemerides may either be for the primary mission or for the abort mission. The ephemeris of the vehicle may be described in many ways but it will consist of at least six elements. These may be, for example, three positional and three velocity elements. The computed vehicle ephemerides are compared with commanded vehicle ephemeris which results in ephemeris error. This ephemeris error will in general be described by a  $6 \times 1$  matrix. Parallel with computing the vehicle ephemeris there are also computed velocity sensitivity coefficients. These velocity sensitivity coefficients compute the sensitivity to the vehicle ephemeris as determined by velocity changes or corrective velocity inputs to the system. These velocity sensitivity coefficients when operating on the ephemeris error matrix will in general provide an indication of velocity correction. This velocity correction is that which is required to achieve the commanded vehicle ephemeris.

Based on these navigation measurements, a velocity correction is calculated in the guidance computer. The corrective velocity increment will have a magnitude and a direction. The magnitude of the velocity increment will provide the primary input to the corrective thrust to be commanded by the main propulsion engine. The time of initiating this correction will be determined by a signal from the programmer. The main corrective engine thrust will then provide a basic path input to the vehicle dynamics. This in turn will be sensed by a three-accelerometer package. It is anticipated that these accelerometers will be body-mounted and will be of the pulse re-set type to give a digital readout of the corrective impulse. During this thrusting period, the gimbal locks will be engaged so that the electrostatic gyro will provide a direct indication of the direction of corrective thrust.

~~CONFIDENTIAL~~

The true direction of the thrust and the magnitude of the thrust will be computed based on the outputs of the three accelerometers resolved through the appropriate angles coming from the electrostatic gyro package. This will result in a corrective velocity magnitude signal which provides the cut-off signal to the main corrective engine. It also provides the indication of the direction of the corrective thrust. This is the true direction of the thrust and it takes into consideration misalignment of the engine thrust. This is compared to the desired or commanded direction cosines as computed from the velocity correction computation. The error between these two signals is used to control the orientation of the gimballed correction engines as described previously.

Before concluding this section, some further discussion of the platform will be made. It is anticipated that the platform will have the freedom of motion in the order of 7 degrees in two axes. This appears to be about the maximum perturbation which would accrue to the vehicle due to a maximum disturbance originated by motion of the crew in the vehicle. Stated another way, it appears that the inertia of the vehicle itself would be sufficient to stabilize the vehicle to within about 7 degrees in the presence of maximum crew disturbances. Furthermore, the 7 degree type of freedom is consistent with a simplified look-out window configuration.

It is noted at this time that it appears promising to accomplish both the star tracking acquisition problem as well as the Earth-Moon verticality and diameter measurements with a small field view tracker. This would represent an alternative to using both a small field tracker and a horizon scanner of the more conventional type. Further discussion of this possibility is presented later in this report.

### **Position and Velocity Determination for the Lunar Mission**

The fundamental measurements available in the system under consideration for the purpose of generating position and velocity data are the tracking of the Earth and lunar verticals (lines-of-sight) and Earth and Moon diameter measurements. These are position measurements which are inherently incapable of providing instantaneous velocity data. However when the vehicle is in free-fall and the vehicle dynamics are

~~CONFIDENTIAL~~

approximately known, it is possible to use various data processing and smoothing criteria for generating velocity information when data is taken over a sufficiently long period of time.

One technique for obtaining velocity information is to fit a free-fall trajectory to elements of position data taken at widely separated points on the trajectory. Once the elements of the trajectory are determined, the velocity and position of the vehicle may theoretically be computed for all time as long as the vehicle remains in a free-fall path. Deviations from the theoretical path propagate rapidly with time, however, since all perturbing forces on the vehicle are not known (i.e. solar radiation pressure, uncertainty in gravitational forces due to inaccurate physical constants, etc.). Therefore it is necessary periodically to update the information by incorporating additional data as it is taken.

When data is taken over very long periods of time, it is necessary to compute an accurate vehicle ephemeris in order to perform the smoothing computations. These methods will be described in some of our later work on "long period" smoothing. Our immediate objective is to study the feasibility of "short period" smoothing.

Short-period smoothing is defined as the smoothing of data over time periods that are small enough so that the parameters being measured may be adequately represented by a finite polynomial in time. If the measured parameters may be represented as a quadratic in time (second order fit) of the form

$$\Theta(t) = a_0 + a_1 t + \frac{a_2 t^2}{2} \quad (1)$$

and if each sample of data,  $\Theta_1$ , is corrupted by noise such that,

$$\Theta_i = |\Theta|_i + M + N_i \quad (2)$$

where  $|\Theta|_i$  is the true value,  $M$  is a bias error of zero mean and variance  $\sigma_m^2$ , and  $N$  is a sampling error which is uncorrelated from sample to sample, and has a zero mean and variance  $\sigma_n^2$ , then the variance of  $\hat{\Theta}$ , the best estimate of  $\Theta$ , at the end of the sampling interval is,

~~CONFIDENTIAL~~

~~CONFIDENTIAL~~

$$\mu_{\hat{\Theta}}^2 = \sigma_{\hat{\Theta}}^2 = \sigma_m^2 + \frac{9}{I} \sigma_n^2 \quad (3)$$

the velocity variance is,

$$\mu_{\dot{\hat{\Theta}}}^2 = \sigma_{\dot{\hat{\Theta}}}^2 = 192 \frac{\sigma_n^2}{T^2 I} \quad (4)$$

and the variance between position and velocity is,

$$\mu_{\hat{\Theta}, \dot{\hat{\Theta}}} = 36 \frac{\sigma_n^2}{T I} \quad (5)$$

where  $I$  is the total number of measurements taken at time intervals  $\Delta t$  apart, and  $T = I\Delta t$ , is the total time of observation.

From these results it may be seen that no amount of smoothing will remove the effect of a bias error from a smoothed parameter. Adequate amounts of data, and a sufficiently long smoothing time permit the generation of velocity data with a small velocity variance. However, the position and velocity data obtained is correlated and introduces data handling problems when it is used to compute velocity corrections and other pertinent parameters.

A bias error is typically introduced into Earth-Moon tracker measurements due to uncertainties in cloud cover and terrain, if the observation time is short enough so that the effect on the measurements is the same from sample to sample, even though the magnitude is normally distributed with zero mean. If the observation period is long enough to permit one or more Earth rotations during the sampling period, then the effect of cloud cover and terrain will tend to be random with time and would no longer introduce a bias error. This, however, would not fall into the realm of short-period measurements.

~~CONFIDENTIAL~~



~~CONFIDENTIAL~~

## Position Determination

The primary source of position data is obtained by tracking the vertical to the nearest celestial body. In cis-lunar space this is either the Earth or the Moon. Assuming that the position of either the Earth or Moon is known, the cross-position uncertainty,  $\delta r_c$  in spaceship location due to an angular error  $\sigma_{\hat{\theta}}$  in locating

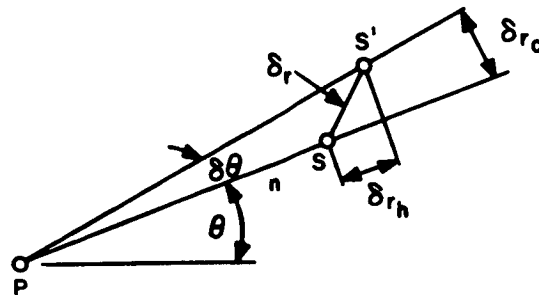


Figure VIII-4-28. Primary measurements—cross-position error

the vertical (see Figure VIII-4-28) is

$$\delta r_c = r \sigma_{\hat{\theta}}$$

and is always normal to the line-of-sight S-P. For a given angular measurement error, the cross-position error is always smallest for the nearest body sighted and these measurements are defined as primary measurements, since they place the strongest constraints upon spaceship location. Since the vertical is located in two dimensions (azimuth and elevation) the cross-position constraint is applicable to two dimensions and only range or altitude remains undefined.

Those measurements which place a constraint upon altitude are defined as secondary measurements. Included among these are Earth and Moon diameter measurements and tracking the vertical to secondary bodies (those other than the nearest body). As shown by Figure VIII-4-29 if  $\delta r' = \sigma_{\hat{\theta}} r'$   $r'$  is the cross-range position error of a

~~CONFIDENTIAL~~

~~CONFIDENTIAL~~

secondary measurement, its effective constraint in the vertical direction relative to the primary body, P, is approximately,

$$\delta r_H \approx \frac{\sigma_{\hat{\theta}}' r'}{\sin \beta} \quad (7)$$

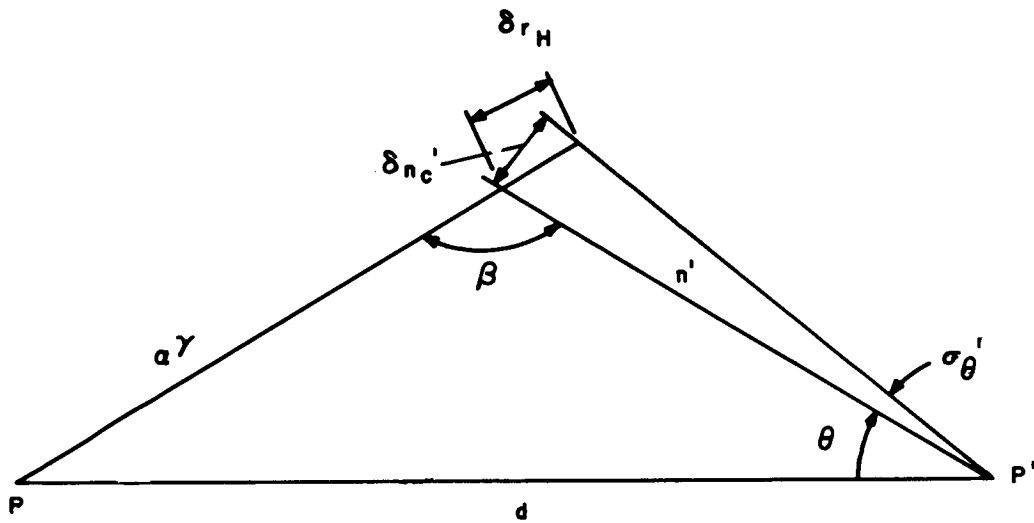


Figure VIII-4-29. Secondary constraints on measurement of the vertical

If we assume that the rms uncertainty in the altitude of the horizon due to cloud cover and terrain is two miles, it may be shown that the bias error introduced into the angular measurements varies inversely with range, and that the variance of the bias error may be expressed as,

$$\sigma_m^2 = \frac{K^2}{r^2} \quad (8)$$

(For the 2-mile uncertainty, the rms angular bias error at an altitude of 300 miles is 0.1 degrees).

~~CONFIDENTIAL~~

~~CONFIDENTIAL~~

If we assume that the noise component of the angular measurements, due to signal noise and servo error, has an rms value of 8 seconds, then the cross-position error as a function of range is shown by Figure VIII-4-30. It may be seen that for short/period smoothing, that the cross-position error component due to bias error is constant at 2 miles (since  $\sigma_m = K/r$ ) and no amount of smoothing can remove it. Smoothing, however, significantly reduces the position error due to the random noise component at long range. At short range the bias error is so predominant that something is not particularly useful for position measurements.

The corresponding altitude errors using Earth and Moon diameter measurements are shown by Figures VIII-4-31 and VIII-4-32. Similar comments apply to the significance of redundant data. At long range, however, the magnitude of the error becomes so large that even for a large amount of redundant data, diameter measurements no longer provide useful data. This is shown more clearly by Figure VIII-4-33 which shows the altitude error for Earth and Moon diameter measurements, superposed upon a plot of the altitude error obtained from secondary vertical measurements. It may be seen that except when the separation angle  $B$  approaches 0 degrees or 180 degrees ( $\sin \beta \rightarrow 0$ ), corresponding to the condition where the space vehicle, Earth, and the Moon, fall on a line, that secondary vertical measurements are significantly superior to diameter measurements except at very short ranges.

Figure VIII-4-34 shows the cross-range, altitude and spherical probable error of position as a function of time for the typical lunar trajectory shown by Figure VIII-4-35. It may be seen that the spherical probable error of position is of the order of five miles in the midcourse regime of flight if the measurements are limited to short period smoothing. We expect that for long period smoothing, that the bias introduced by cloud cover and terrain may be treated as a random error and permit a significant reduction in position error.

The break shown in the curves corresponds to the singularity that is introduced when the Earth, Moon and space vehicle fall on a line and no altitude information can be obtained using secondary vertical measurements. If primary measurements are taken, they will still provide useful data for inclusion into a long period smoothing criterion for predicting position at any point on the trajectory.

~~CONFIDENTIAL~~

~~CONFIDENTIAL~~

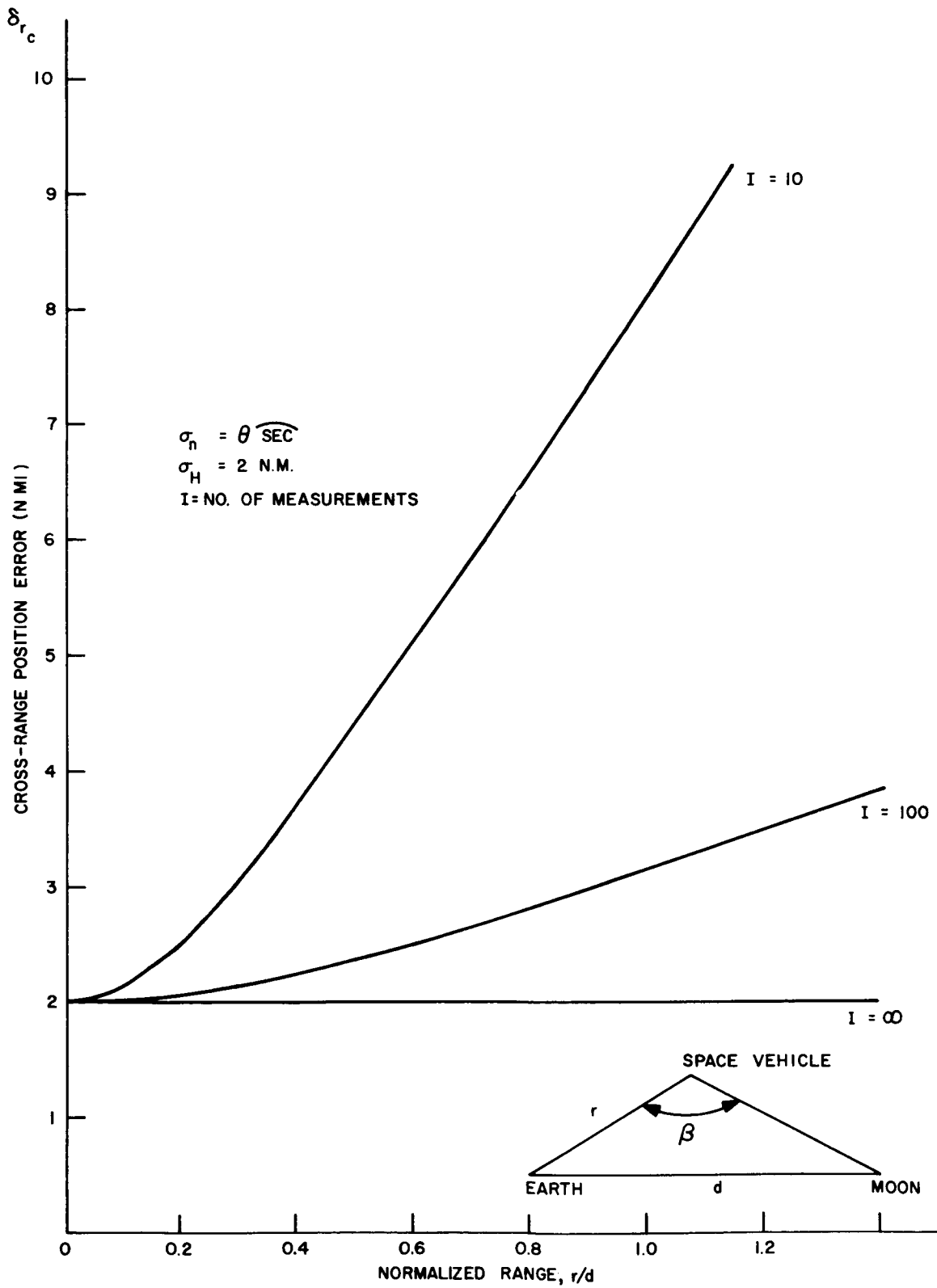


Figure VIII-4-30. Cross-range position error

~~CONFIDENTIAL~~

~~CONFIDENTIAL~~

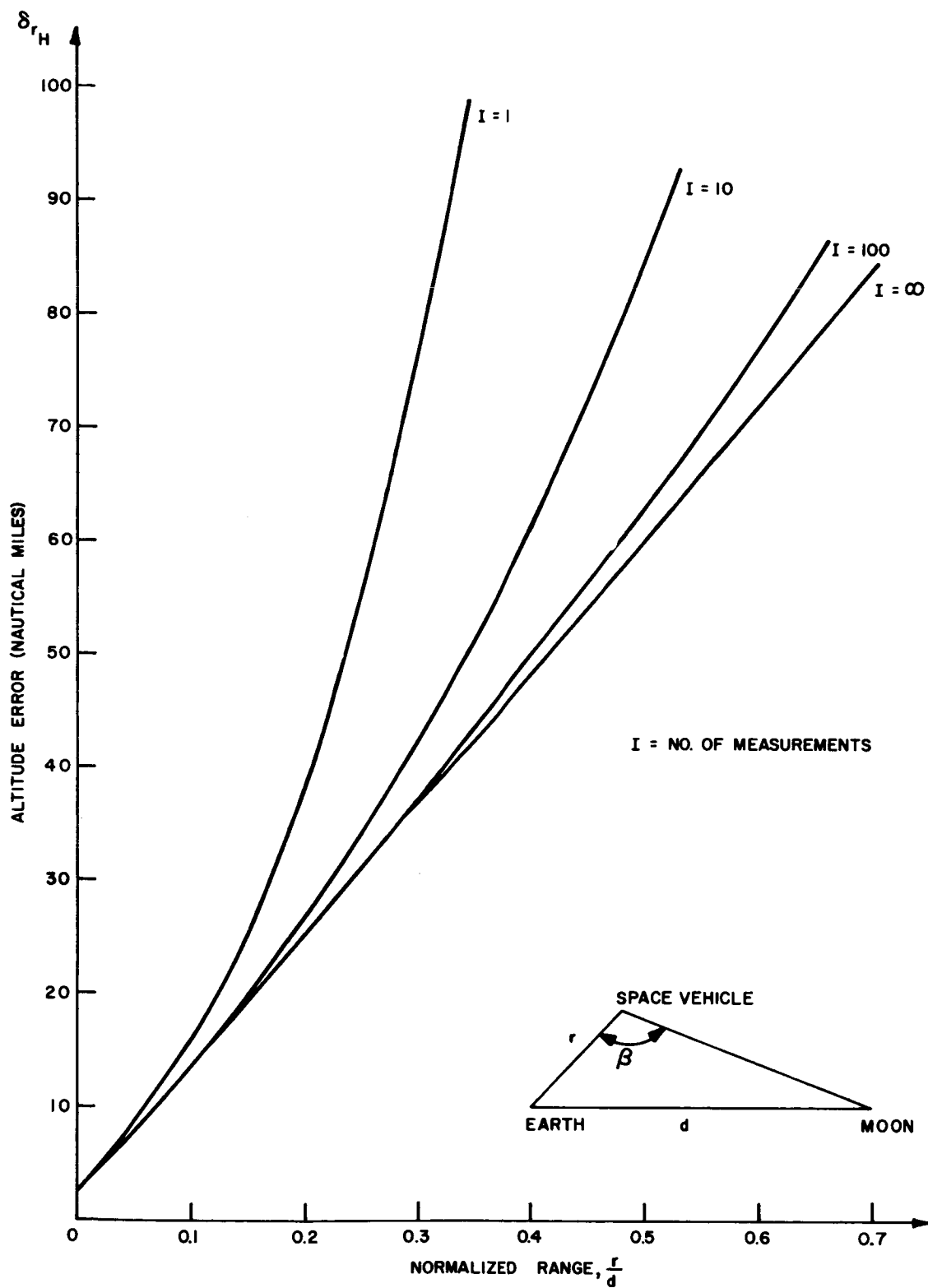


Figure VIII-4-31. Altitude error using Earth diameter measurements

\* ~~CONFIDENTIAL~~

~~CONFIDENTIAL~~

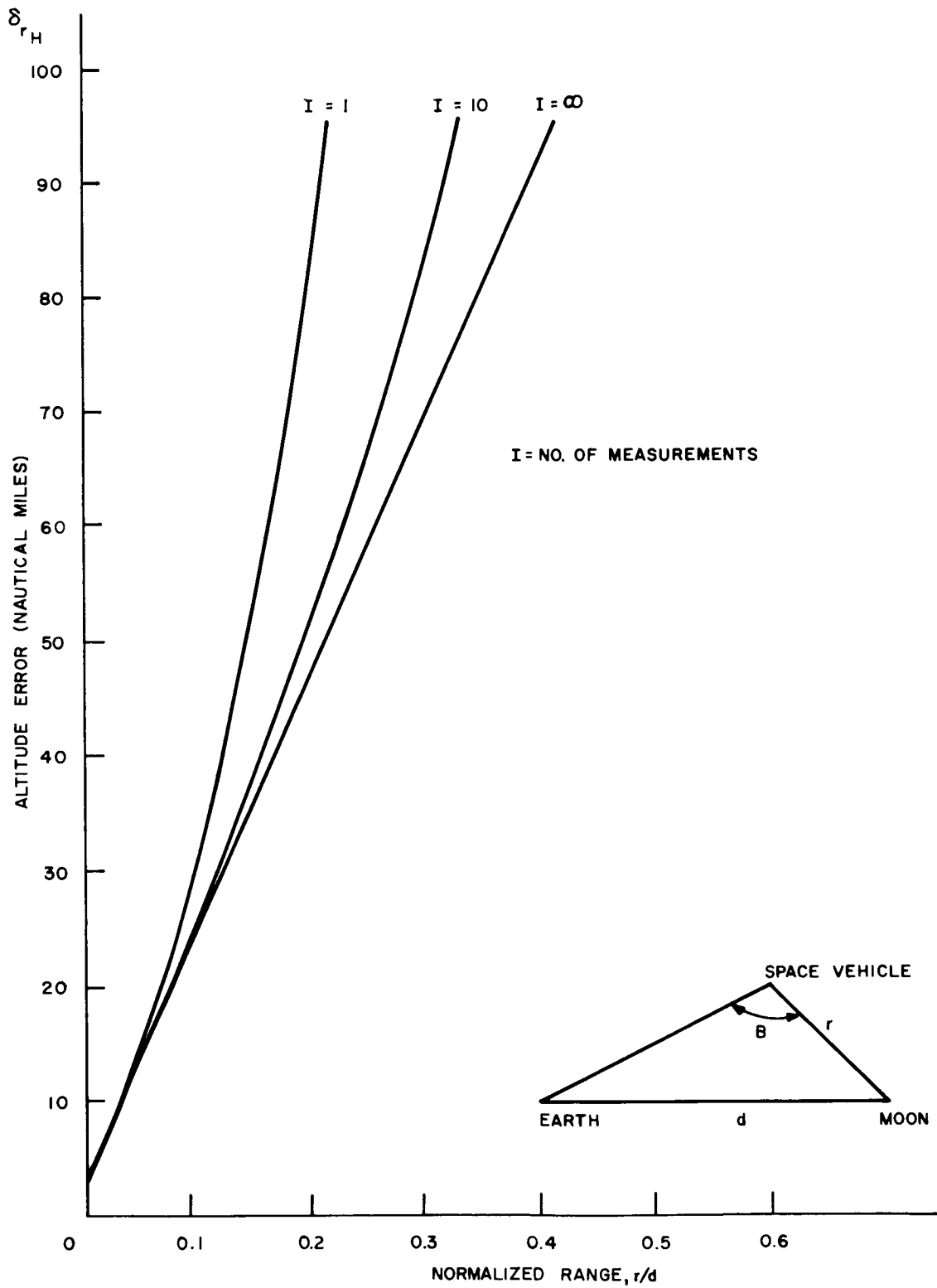


Figure VIII-4-32. Altitude error using Moon diameter measurements

~~CONFIDENTIAL~~

~~CONFIDENTIAL~~

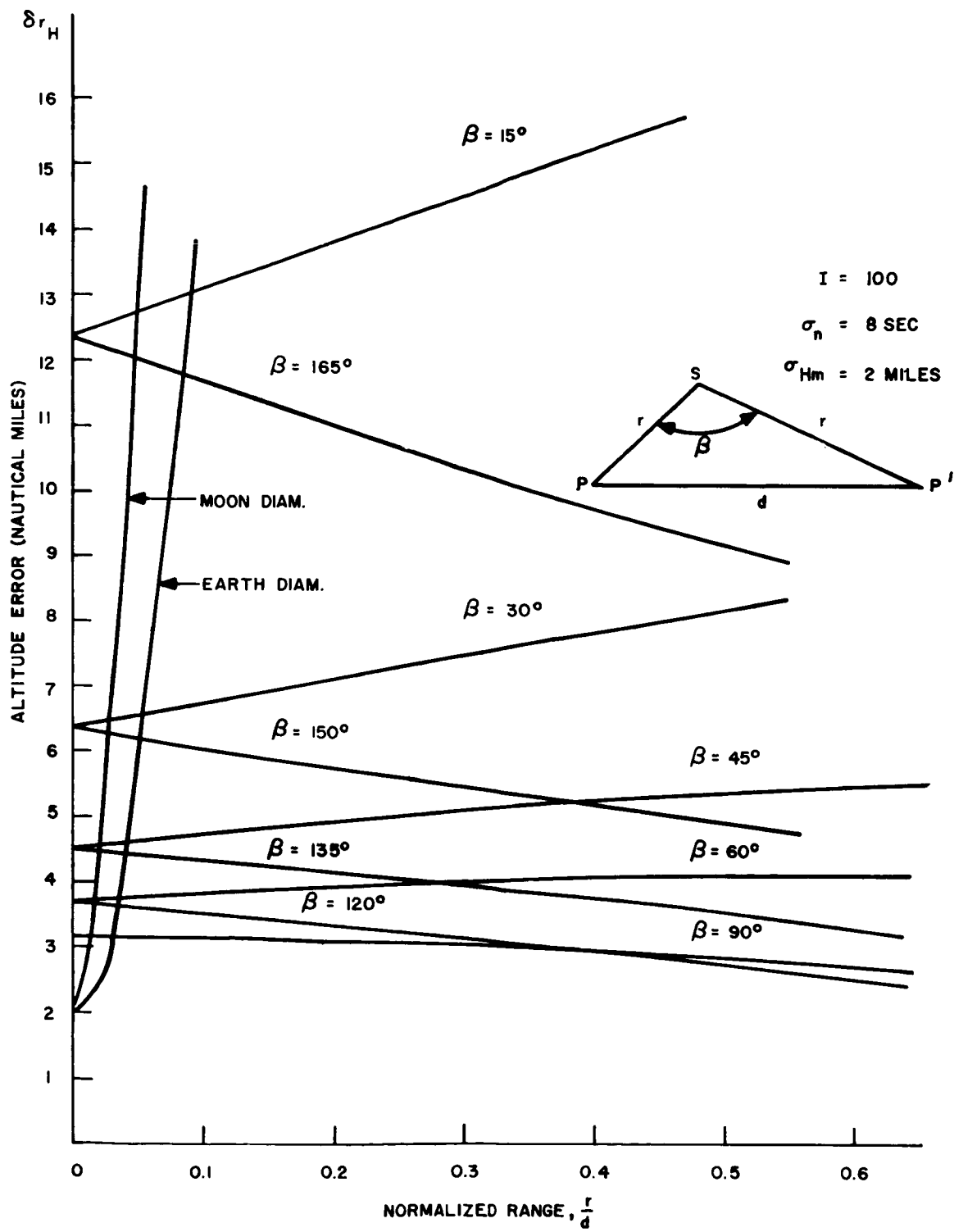


Figure VIII-4-33. Altitude error using secondary measurements

~~CONFIDENTIAL~~

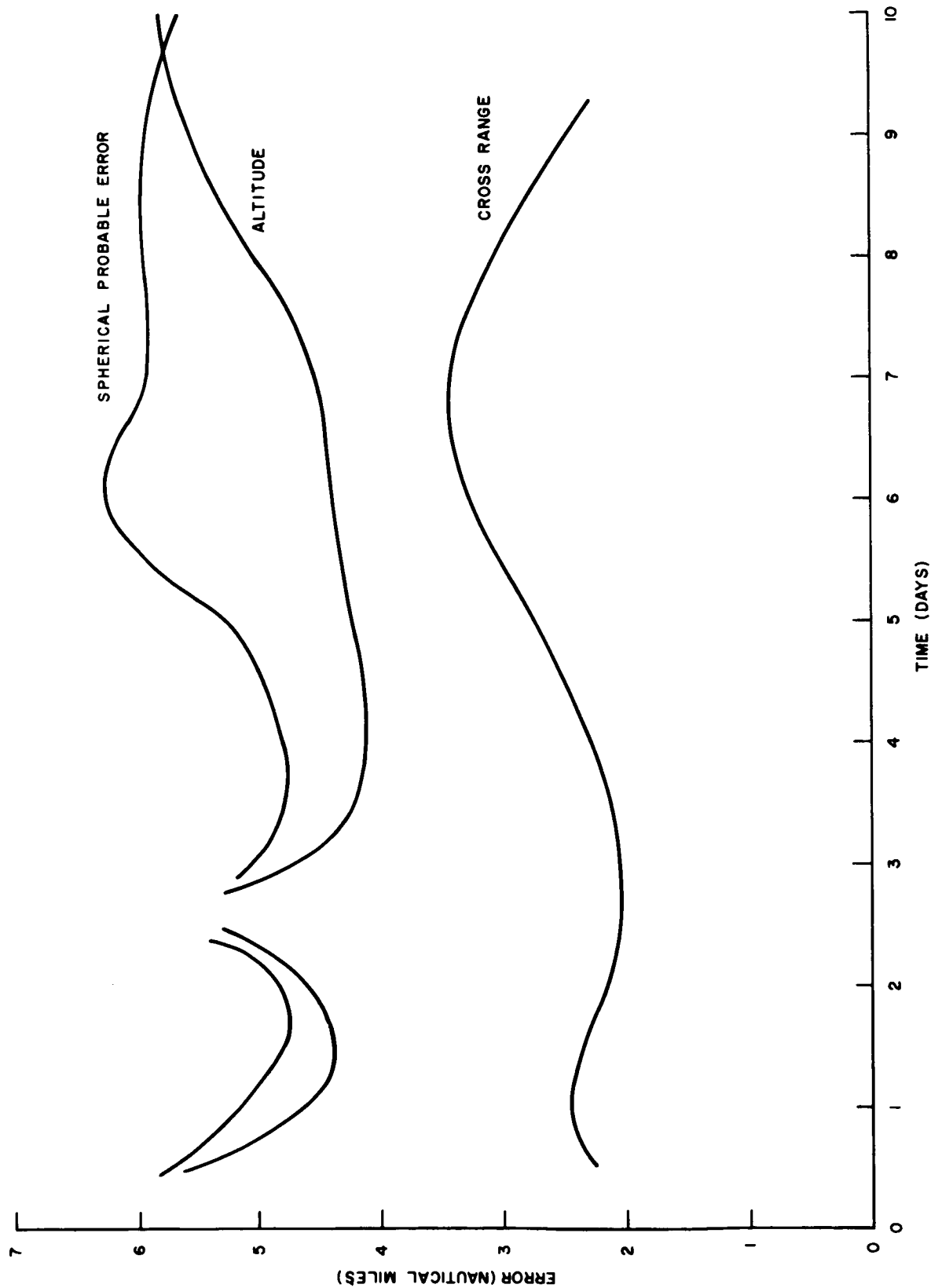


Figure VIII-4-34. Position error versus time





## Velocity Measurements

Velocity data may be obtained from the short-period smoothing criterion by evaluating the  $a_1$  coefficient of a second order fit to the position data. Again the velocity information may be generally resolved into cross-axis and vertical components. The results are shown by Figure VIII-4-36 for 100 measurements taken over a 20-minute smoothing period.

Since bias errors have no effect on the velocity variance, additional data or longer smoothing times may be used to improve upon the results shown by Figure VIII-4-36. The 100 measurements and 20-minute smoothing time were chosen as a representative example. For these values the resulting velocity error turns out to be relatively large. Therefore significant increases in data rate or smoothing times would be necessary in order to generate good velocity data. The most significant improvement would be obtained by increasing the smoothing time. However, the validity of a second order fit to the data for smoothing times greater than 20 minutes would have to be established.

## CREW FUNCTIONS

It is desirable that the mid-course navigation system operate semi-automatically because of the requirements for a large number of accurate measurements, complicated data processing computations, and accurate thrust vector control during corrections. However, mission reliability, and particularly the probability of safe return of the crew, is enhanced by proper utilization of the crew as part of the navigation and control system. The usual approach to this type of problem is to start with a completely automatic system, then determine what functions are best performed by the crew. The systems described in previous sections are automatic and could be programmed and controlled entirely by the digital computer. The next step then is to determine what functions it is desirable to perform manually.

In general, the primary function of the crew is that of monitoring and over-all command of the mission. At any time, the crew will make the decision as to how to proceed. In the case of automatic equipment, the crew will initiate operation of this equipment

~~CONFIDENTIAL~~

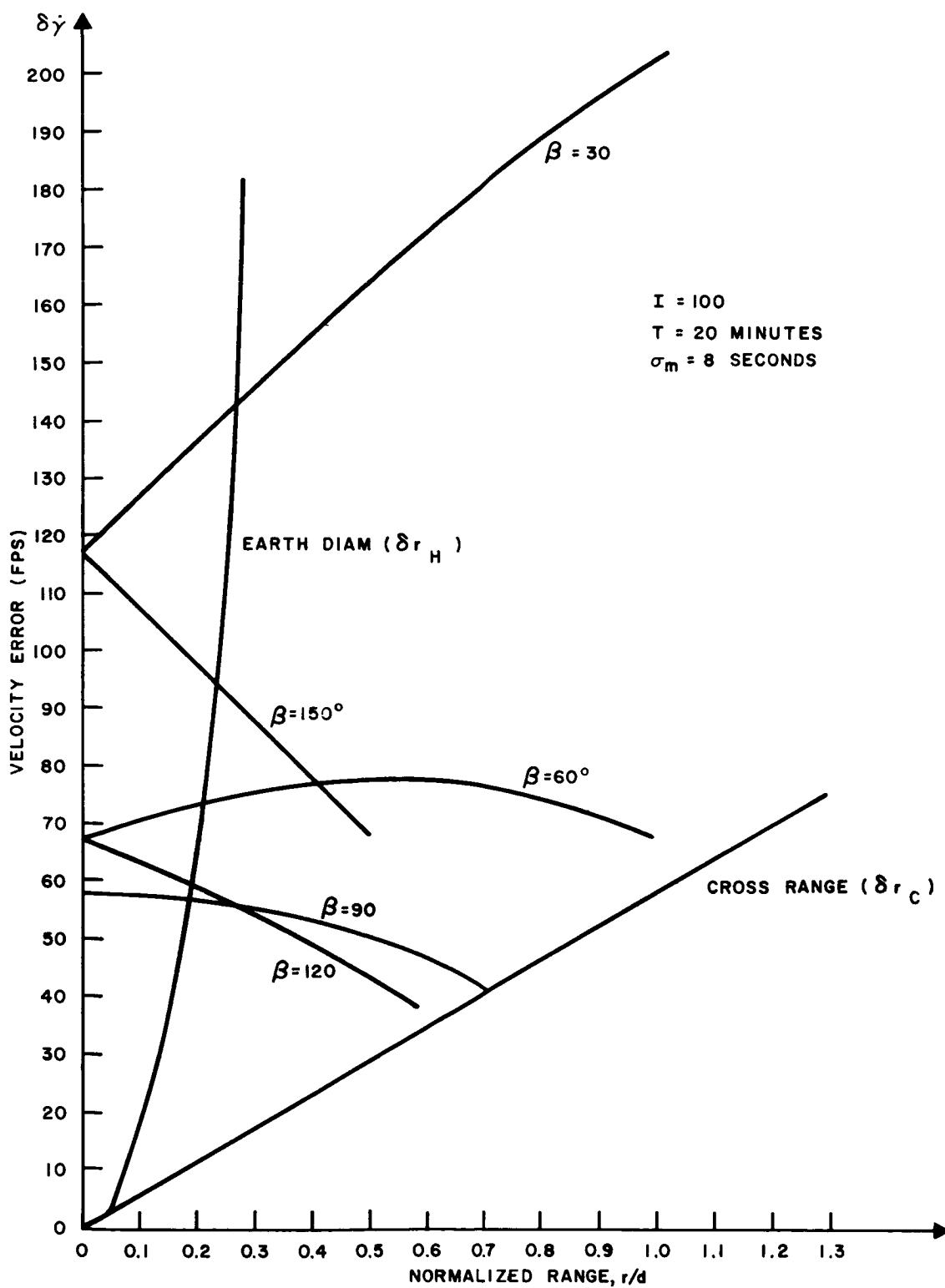


Figure VIII-4-36. Velocity errors

~~CONFIDENTIAL~~

~~CONFIDENTIAL~~

and maintain override control. In addition, they will manually perform certain control operations which do not require high precision or extended periods of concentrated effort. Finally, in case of failure of the automatic equipment, the crew will be provided with completely manual backup equipment for taking fixes and performing computations.

The question of crew functions in navigation and control has been studied only briefly to date, but will be studied more extensively in the remainder of the program. Thus the following list of navigation and control crew functions is not necessarily a complete one but merely gives an indication of our present ideas.

Monitoring and Mission Command:

1. Decision to make corrections
2. Decision to return to Earth (emergency)
3. Decision to go into lunar orbit
4. Decision to eject from lunar orbit

Manual Control Functions:

1. Gross attitude changes for platform alignment and path corrections.
2. Gross orientation of astrotrackers
3. Initiation of correction — manual override of shut-down
4. Control of solar collector angle in lunar orbit
5. Manual fix taking
6. Manual computation
7. Re-entry flight control

Performance of these functions will require certain displays and controls, such as

1. Vehicle attitude angles and rates
2. Present estimated miss distance (and rate)

~~CONFIDENTIAL~~

~~CONFIDENTIAL~~

3. Estimated miss distance resulting from correction now.
4. Fuel energy management.
5. Velocity correction
6. Attitude controller
7. Re-entry energy management
8. Re-entry flight controller
9. Solar collector attitude
10. Solar collector controller

In case of failure of the automatic equipment, apparatus will be supplied for taking fixes manually. The following paragraphs summarize our work to date in this area.

Manual cislunar navigation seems feasible using near conventional theodolites, cameras and/or telescopes. Techniques such as the measurement of the angle subtended between two near-celestial bodies (e.g. Earth and Moon), between a near body and a star or the angular diameter of a new body, as used by automatic devices such as astrotrackers or horizon sensors, may be duplicated manually. In addition, lines of position may be determined by the observation of occultations of a star or a planet by the Moon or a planet. The coincident observation of two occultations will give a position in space or a single occultation may be augmented by a stadiometric reading.

Theodolites such as the Wild T3 may be used to  $\pm 2$ -second instrument accuracy when measuring subtended angles between the center of a disc and a star. The precision bubble vertical reference provided with many instruments has, of course, no application in a weightless environment.

To use the instrument to obtain a navigation fix, it is suggested that the theodolite be mounted to a gimbaled stable reference to insure base motion isolation. Using accepted procedures of plunging and swinging the theodolite telescope to eliminate divided circle errors, a proficient operator may take one "fix" in one minute. A base motion drift rate of 0.01 degrees/hour for a 1-minute duration will contribute an additional  $\pm 0.6$  seconds error.

~~CONFIDENTIAL~~

**CONFIDENTIAL**

For vehicle attitude determination, the theodolite would be body mounted to the vehicle. This may be accomplished by caging the base motion isolation platform provided for navigation fixes.

The angle between two points in the heavens may also be determined photographically or xerographically. Using a 205-inch focal length optical system would give 1000 seconds of arc/inch scale factor on a plate. An engine dividing machine can be used to measure the image to 0.001 inches or an equivalent 1 second of arc.

An aperture of six inches, and using an ultra-rapid plate, would require one second duration exposures of the Moon. A camera position drift rate of 0.6 degrees/hour, for a one-second duration would contribute the same 0.6 second of arc error as in the case of the Theodolite. The shorter viewing time, therefore, lessens considerably the requirements for base motion isolation.

Conventional liquid processing techniques can be mechanized to space vehicle manipulation. The Polaroid-Land process or dry process xerographic techniques may also find application.

Perhaps the simplest methods of manual navigation to implement would be the occultation technique. Merely stellar, lunar and planet ephemeris tables, a telescope, a chronometer, and provision for manual input of position information, would be required.

The technique appears particularly valuable when objects are occluded by the Moon, because of the sharpness with which this effect occurs due to the lack of atmosphere. In general, the use of lunar occultations would require the following conditions to be realized:

1. The object being occluded would have to be identified and its positional coordinates known.
2. The position of the occluding body would be necessary to enable computation to be made with respect to the occluding edge.
3. To utilize a position fix to generate a line rather than a cylinder, the position or the lunar horizon at which the occlusion occurred should be known.

**CONFIDENTIAL**

~~CONFIDENTIAL~~

These conditions are sufficient to establish the vehicle on a line of position which is directed toward the occluded object, and tangent to the occluding object at a specific point. If the position of this line is precomputed, any deviations from previously computed values would indicate errors having the following characteristics:

1. Initial uncertainties in the position of the occluded or occluding body would be equivalent to an error in the indicated position in a direction normal to the line of position.
2. Deviations in the horizon of the occluding body or the exact time of the occlusion would generate an error in position normal to the line of position, and in the direction of the velocity normal to this line.
3. Deviations in the position on horizon where the occlusion occurs would be equivalent to an error in position normal to the line of position and in a direction parallel to the horizon at that point.

From these observations, no indications of range to the occluding body are obtained from a single observation. However, if multiple measurements are made, deviations in the relative observed time will contain range information when referred to a reference path and its velocity components.

Assuming that the occlusion can be sensed, and the point on the horizon where the occlusion occurs is known, a planet diameter or range measurement is not needed to establish a line of position. However, if it is desirable to locate the position along the line of position, a range or planet diameter measurement is needed unless use is made of multiple observations.

~~CONFIDENTIAL~~

~~CONFIDENTIAL~~

## 5. LUNAR TERMINAL PHASE

### INTRODUCTION

The lunar terminal phase of the APOLLO mission consists of the following three phases:

1. Injection of the vehicle into a suitable orbit around the Moon from the hyperbolic approach trajectory.
2. Orbiting around the Moon for a period of time up to a maximum time of seven days.
3. Ejection from the lunar orbit into an appropriate return trajectory.

In order to accomplish each of these phases, the following three aspects of each phase must be considered:

1. Basic trajectory studies in the vicinity of the Moon.
2. Navigation, guidance and control concepts.
3. Implementation of the navigation, guidance and control concepts.

The work accomplished in these areas will be summarized at this time.

### INJECTION INTO LUNAR ORBIT

#### General

As the APOLLO vehicle approaches the Moon, it is essentially on a free-fall trajectory which will return the vehicle to the Earth if only small mid-course guidance corrections are made. It is at this time in the mission that the astronauts on board must decide whether or not to go into orbit around the Moon. If the decision is made to go into orbit, the conservative approach will be to go into a near-circular orbit first and then



~~CONFIDENTIAL~~

modify the orbit, in one or more steps, so that the final minimum altitude of 50 nautical miles (nmi) is achieved. The details of injection will depend upon hardware accuracy considerations.

The objective is to achieve an elliptical orbit with a maximum altitude above the surface of the Moon of 1000 to 2000 nmi and a minimum altitude of 50 to 100 nmi. Such orbits have periods in the range of three to five hours. The minimum altitude must be in the vicinity of the portion of the surface of the Moon which is closest to the Earth. In order to minimize fuel consumption for injection into an orbit with a minimum altitude of 50 nmi, the point of closest approach to the surface of the Moon should be 1000 nmi on the farthest side of the Moon with respect to the Earth. At the point of closest approach, retro-thrust is applied in order to reduce the vehicle velocity to that required for a circular orbit about the Moon with an altitude of 1000 nmi. Continuous altitude measurements with respect to the Moon then can be made and additional thrust applications at a selected injection point will appropriately reduce the velocity at the point so that the corresponding minimum altitude point will move toward the desired 50 nmi perilune. There is theoretically no fuel weight penalty associated with this incremental approach to the desired elliptical orbit. If additional requirements are placed on the orientation of the plane of the orbit with respect to the Moon, the latitude of the point of closest approach should be controlled by means of the mid-course guidance corrections and the inclination of the plane about the radius vector at the point of closest approach can be controlled by the orientation of the injection velocity increment.

#### CONCEPTS-INJECTION PHASE

The point of closest approach to the Moon is the most efficient point for injection into an orbit around the Moon. This is true since a given velocity change results in the greatest energy change when the velocity is maximum and this occurs at the point of closest approach.

Injection into the elliptical orbit should be made in two or more steps for the following reasons:

1. Orbits can be achieved which will require less fuel than does the ultimate elliptical orbit. For instance, circular 1000-nmi orbit requires a velocity

~~CONFIDENTIAL~~

~~CONFIDENTIAL~~

decrement of about 2350 feet per second (fps) whereas the 1000 nmi apolune and 50 nmi perilune orbit requires about 3050 fps, or 700 fps more. These figures are based on the "figure 8" data given in Chapter VII. The decision to consume the additional fuel required to go into and out of the ultimate elliptical orbit can be made after the vehicle is in orbit around the Moon.

2. Approaching the minimum perilune altitude in steps will permit better control of perilune altitude since resulting orbital elements can be more accurately measured prior to the time at which final corrections are made.
3. If the transfer includes a circular orbit, the line of apsides can be adjusted conveniently if desired.
4. This is the conservative approach from the safety point of view.

If the inclination of the resulting orbit about the radius vector of the point of closest approach must be adjusted in order to meet observational or ejection requirements, this must be done at the time of injection to minimize fuel consumption. Small plane changes can be accomplished by proper retro-thrust orientation with essentially no fuel penalty.

Mid-course navigation and guidance information can be used to predict the time and location of the point of closest approach and calculate the required vector velocity decrement for entering a specific orbit around the Moon. However, equipment required for measuring orbital elements while in orbit around the Moon may provide more accurate measurements at short ranges which can be used to make more accurate predictions. If this is the case, and if time permits, the measurements made with respect to the Moon should be used to calculate the velocity decrement and corresponding time for orbit injection.

The transition from mid-course to terminal measurement techniques is being studied at the present time.

Chapter VII shows how velocity decrement requirements vary with apolune and perilune altitudes. This information is required when making the decision as to whether to make a mid-course correction or use the additional fuel which would be required when going into a specified elliptical orbit at a high altitude because of

~~CONFIDENTIAL~~

~~CONFIDENTIAL~~

mid-course guidance errors. In these circumstances, it may be desirable to change the perilune altitude. The minimum velocity increment requirement for a given transfer trajectory applies to the case in which the injection altitude is 1000 nmi and the perilune altitude is 100 nmi. However, Chapter VII indicates that the variations in velocity decrement with altitude of closest approach and perilune altitude are relatively small for the ranges considered in the case of the "Figure 8" trajectory.

#### IMPLEMENTATION - INJECTION PHASE

As the vehicle approaches the Moon, measurements with respect to the Moon can be made with increasing accuracy. The basic information which is required is as follows:

1. Range information, i.e., the distance between the vehicle and the center of the Moon.
2. Line-of-sight motion information, i.e., the motion in space of the line connecting the vehicle and the center of the Moon.

Two basic approaches for obtaining this information involve passive systems using optical or infrared horizon sensing schemes and active systems using radar techniques. Investigations of both of these approaches are continuing. However, some remarks are pertinent at this time.

When in close proximity to the Moon, the subtended angle of the Moon increases to 140 degrees at an altitude of 50 nmi. Mid-course disc trackers will not be able to accommodate large subtended angles. There is also the problem of partial illumination of the Moon's surface. Under these circumstances, the use of IR sensors for establishing the local vertical and measuring altitude is quite attractive. Within about one year, it is expected that sensors with sufficient sensitivity to operate on the dark side of the moon will be available. This development will be an outgrowth of the three generations of infrared horizon sensing systems which have already been manufactured, tested and flown by General Electric's Missile and Space Vehicle Department to control the attitude of space vehicles. Thus there will be no restriction on when these measurements can be made. Figure VIII-5-1 shows the expected altitude error as a function of range. It is expected that these sensors will be capable of measuring subtended angle with an accuracy approaching 0.01 degrees. Range rate information could be derived from range

~~CONFIDENTIAL~~

~~CONFIDENTIAL~~

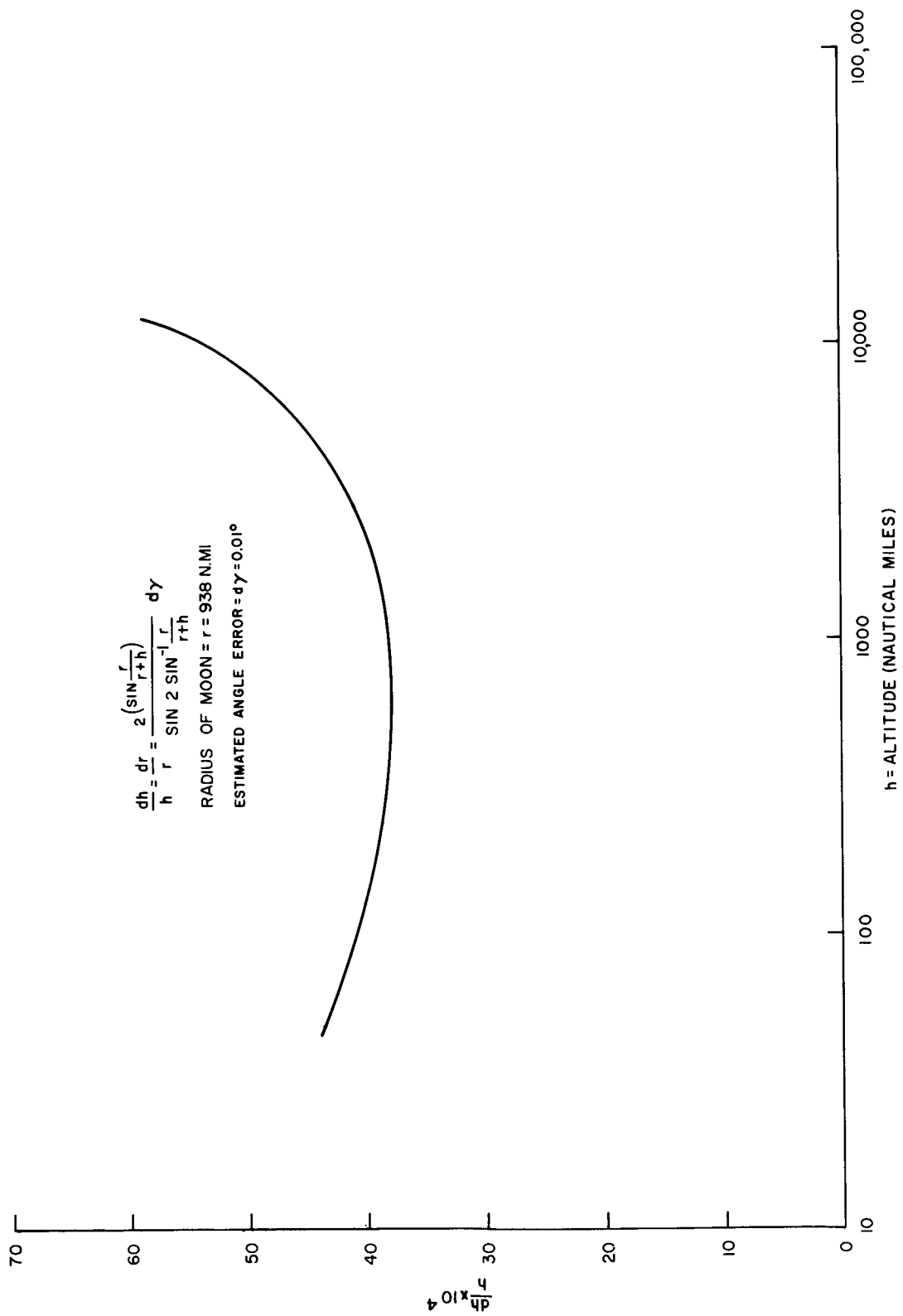


Figure VIII-5-1. Altitude error versus altitude

~~CONFIDENTIAL~~

~~CONFIDENTIAL~~

versus time information, but the resulting accuracy as a function of smoothing time must be investigated. Further discussion of IR horizon scanners is given in Section VIII-7.

A high-altitude radar, capable of operating at ranges of approximately 10,000 nmi, is also being considered for this application. This equipment is much heavier (95 pounds) than the IR sensor equipment and power requirements (625 watts) are also much higher. Since the beamwidth is less than the subtended angle of the Moon at these altitudes, additional problems relating to accuracy are introduced. Accuracies in the range of 1/2 to 1 percent are reasonable at these altitude ranges. Range-rate information can also be derived from this range versus time information, but the doppler radar approach is also being considered as a possible method for obtaining range rate information.

The computer will calculate the required vector velocity decrement, along with the corresponding injection time, which will place the vehicle in a suitable orbit about the Moon. Prior to the time of injection, the vehicle will be oriented with respect to the inertial platform such that the appropriate engine (or engines) is properly aligned with respect to inertial space in accordance with the computed vector velocity decrement orientation requirement. The continuous change of vehicle velocity occurring during the thrusting period will be monitored by integrating accelerometers which will terminate thrust when the computed total velocity change has been achieved.

## **ORBITING AROUND THE MOON**

### **General**

When retro-thrust has been applied at the point of closest approach, the vehicle enters an orbit around the Moon. The elements of the resulting orbit in space must be determined so that information will be available for making orbit modification and orbit ejection calculations. The following comments apply to this phase of the mission:

- (1) The origin of the measurement reference system is changed to the center of the Moon. This affects data processing.

~~CONFIDENTIAL~~

- ~~CONFIDENTIAL~~
- (2) It is difficult to determine accurately the local vertical with respect to the Moon at low altitudes.
  - (3) The vehicle position is changing quite rapidly with respect to the Moon, i.e. 360 degrees in 3 to 5 hours. This also influences the processing of data, especially with respect to the smoothing of data.

### **Orbit Characteristics**

Certain characteristics of an orbit are of particular interest when designing a navigation, guidance and control system for an orbiting vehicle. These characteristics have been determined for an orbit around the Moon with a maximum altitude of 1000 nmi and a minimum altitude of 50 nmi, and are displayed in Figures VIII-5-2 to VIII-5-8, inclusive.

An n-body computer program, using the Encke method, was run in order to obtain information on the stability of an orbit around the Moon which has an apolune altitude of approximately 1000 nmi and a perilune altitude of approximately 50 nmi. The program includes the effects of Earth perturbations but assumes a spherical Moon. The information obtained covered a real-time period of 150 hours which approximately corresponds to the maximum orbiting time for the APOLLO mission. The variations with time of various orbital elements for this sample case are displayed in Figure VIII-5-9 to Figure VIII-5-12 inclusive.

An examination of these results indicates that the orbit is quite stable. The element showing the greatest change during the period of 150 hours is the position of the line of apsides which moves through an angle of approximately  $1\frac{1}{4}$  degrees.

This example indicates that it is reasonable to expect to be able to predict position and velocity with respect to time at least one to two orbits after the orbital elements have been measured. This simplifies the problem of calculating the conditions for ejection from the lunar orbit.

### **Concepts - Orbiting Around the Moon**

When the vehicle is orbiting around the Moon, measurements must be made in order to determine the elements of the orbit. There are three major classical methods for

~~CONFIDENTIAL~~

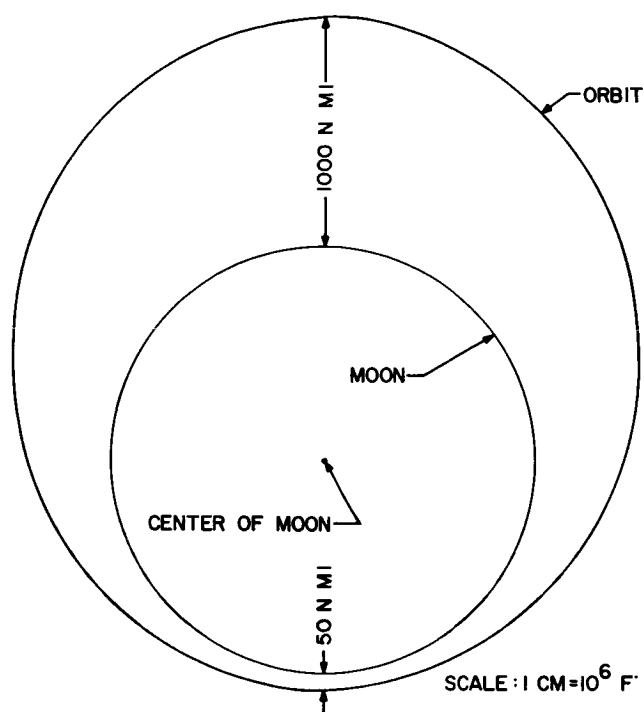


Figure VIII-5-2. Scale drawing of orbit with apolune altitude of 1000 nmi and perilune altitude of 50 nmi

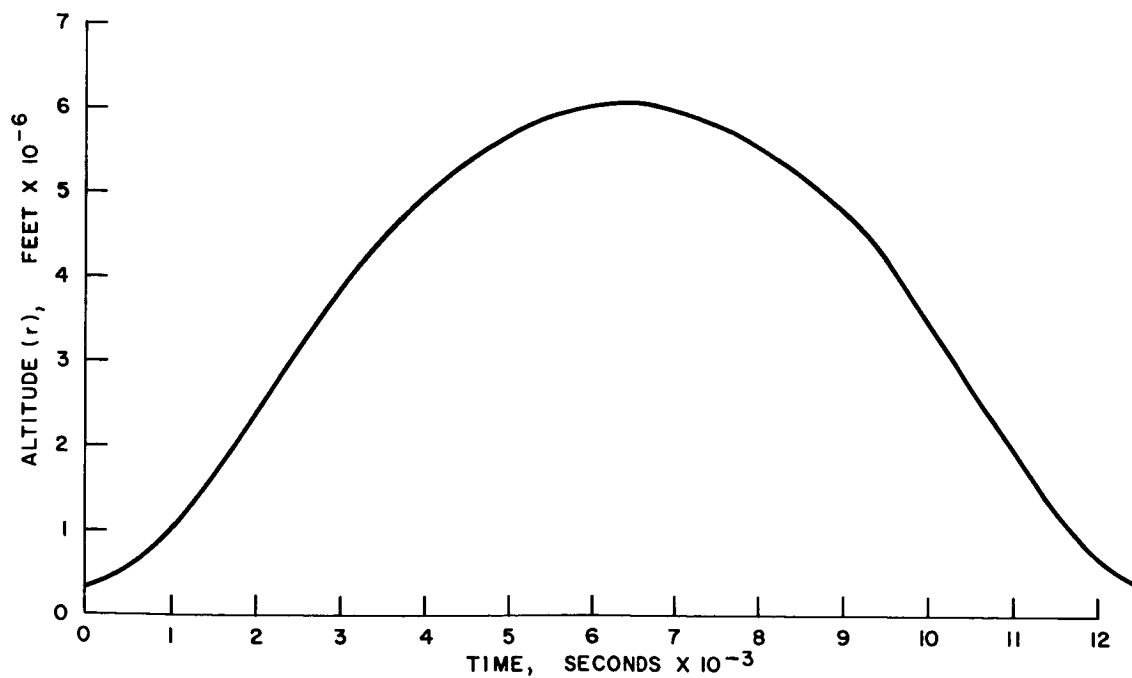


Figure VIII-5-3. Altitude versus time for orbit with apolune altitude of 1000 nmi and perilune altitude of 50 nmi

~~CONFIDENTIAL~~

~~CONFIDENTIAL~~

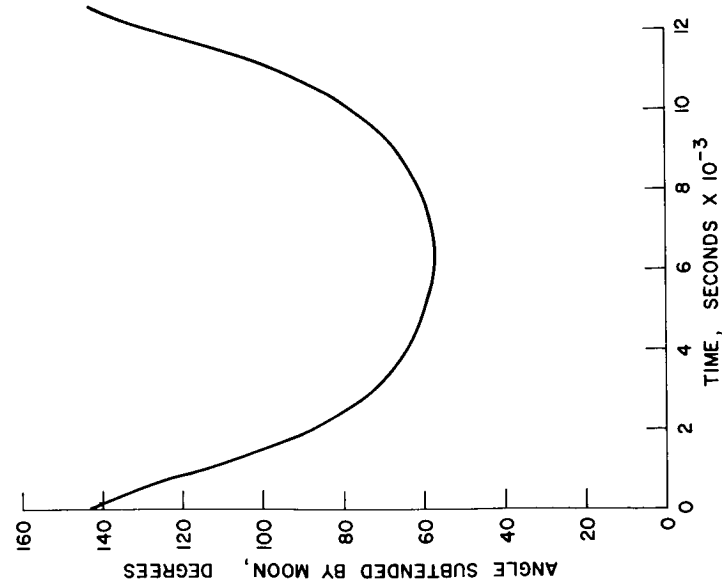


Figure VIII-5-4. Angle subtended by Moon versus time from orbit, with apolune altitude of 1000 nmi and perilune altitude of 50 nmi

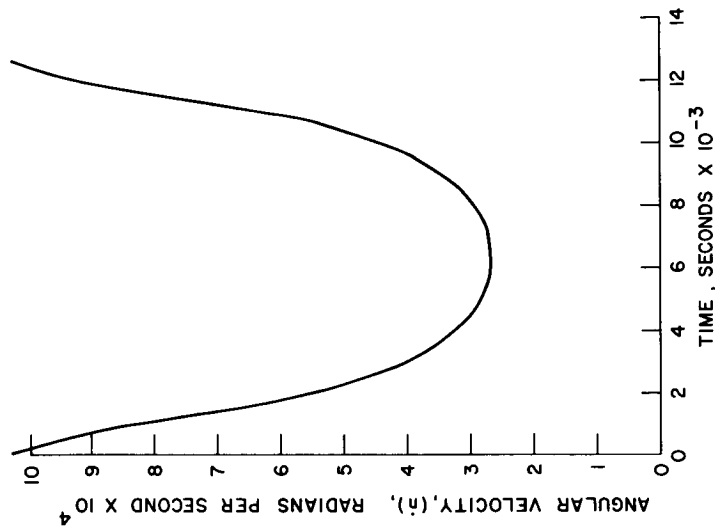


Figure VIII-5-5. Angular velocity of the radius vector versus time for orbit with apolune altitude of 1000 nmi and perilune altitude of 50 nmi

~~CONFIDENTIAL~~



~~CONFIDENTIAL~~

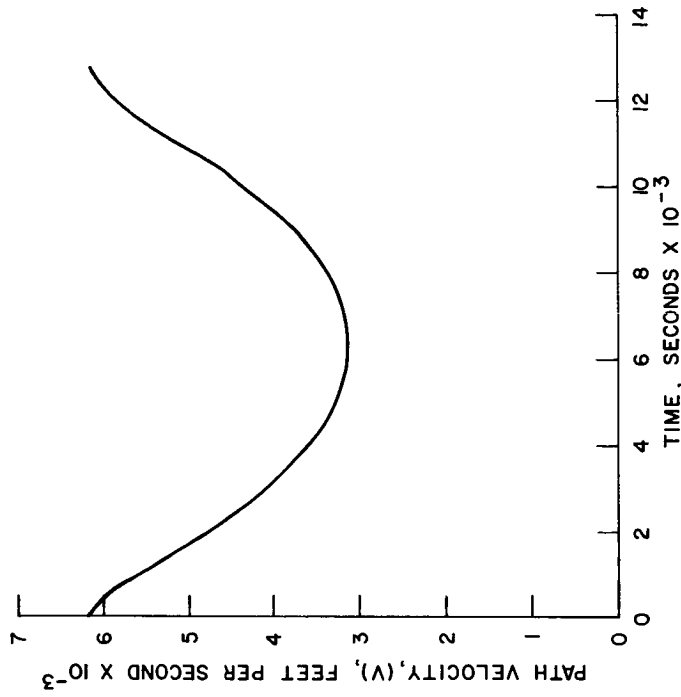


Figure VIII-5-7. Path velocity versus time for orbit with apolune altitude of 1000 nmi and perilune altitude of 50 nmi

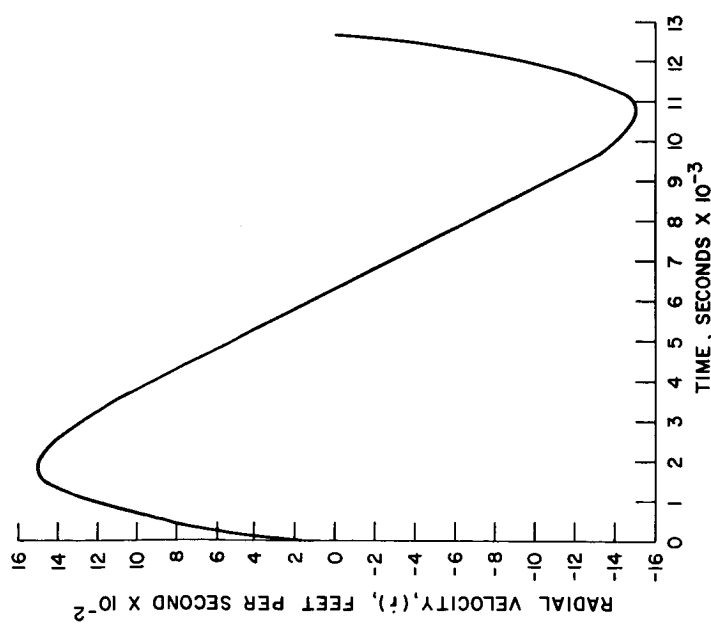


Figure VIII-5-6. Radial velocity versus time for orbit with apolune altitude of 1000 nmi and perilune altitude of 50 nmi

~~CONFIDENTIAL~~

**CONFIDENTIAL**

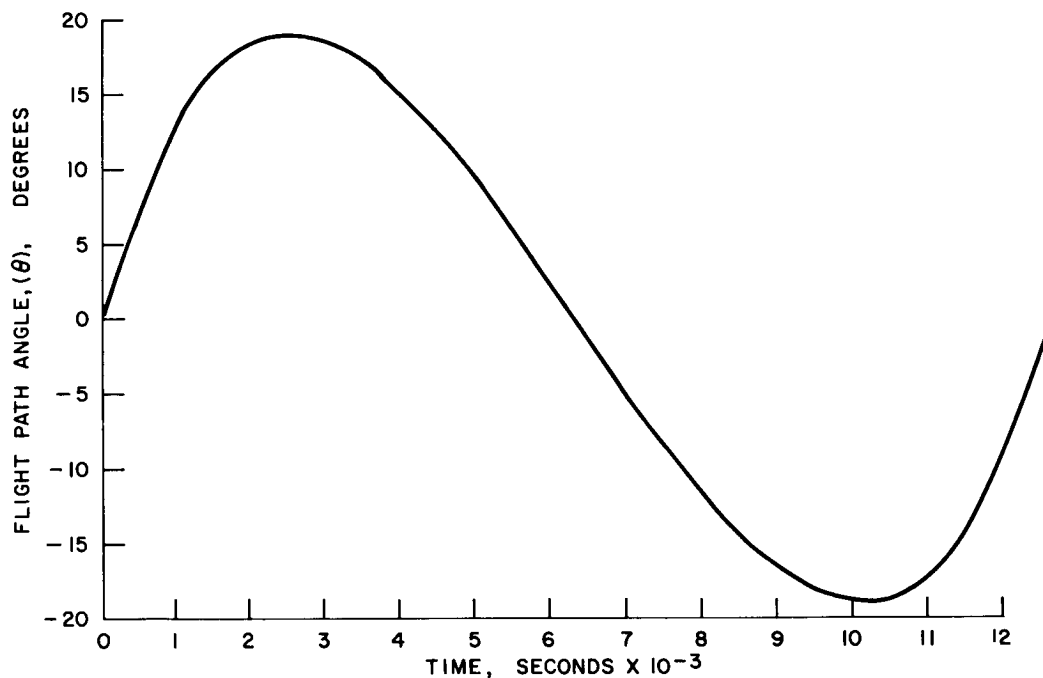


Figure VIII-5-8. Flight path angle (angle between path velocity and azimuth velocity) versus time for orbit with apolune altitude of 1000 nmi and perilune altitude of 50 nmi

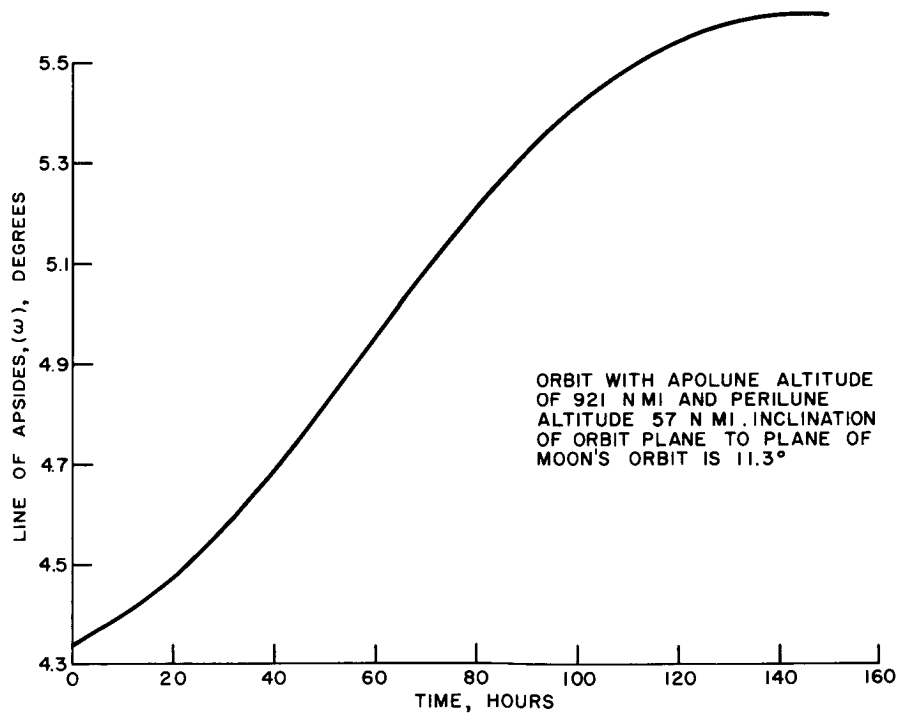


Figure VIII-5-9. Position of line of apses versus time for orbit with apolune altitude of 921 nmi and perilune altitude of 57 nmi. Inclination of orbit plane of Moon's orbit is 11.3 degrees

~~CONFIDENTIAL~~

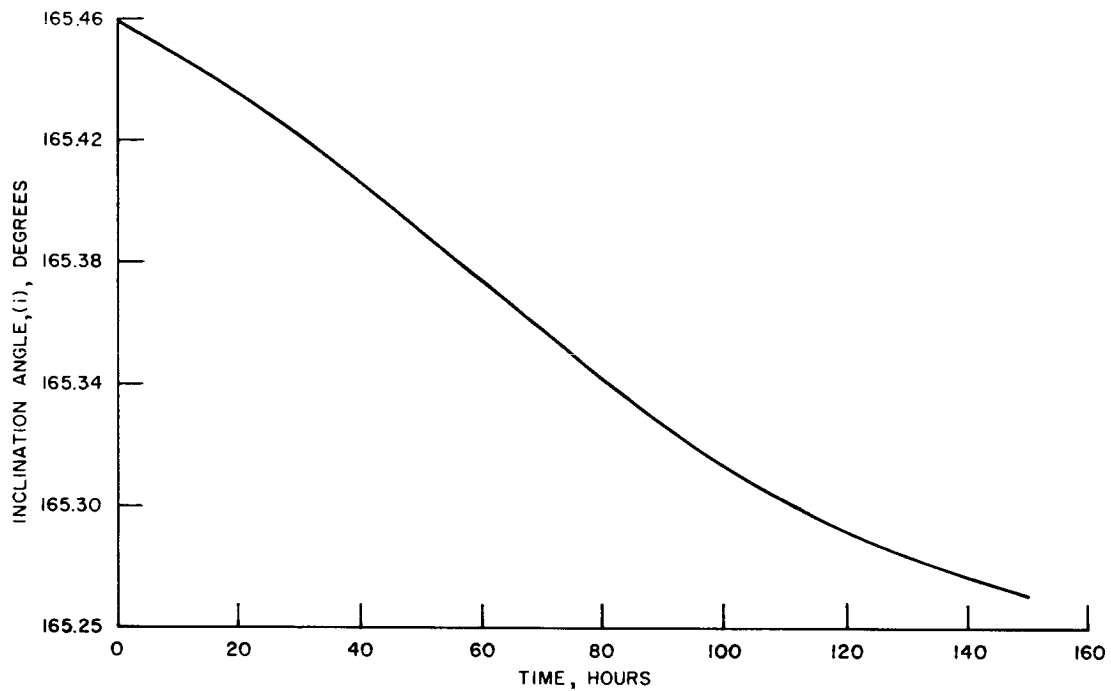


Figure VIII-5-10. Inclination angle versus time for orbit with apolune altitude of 921 nmi and perilune altitude of 57 nmi. Inclination of orbit plane to plane of Moon's orbit is 11.3 degrees

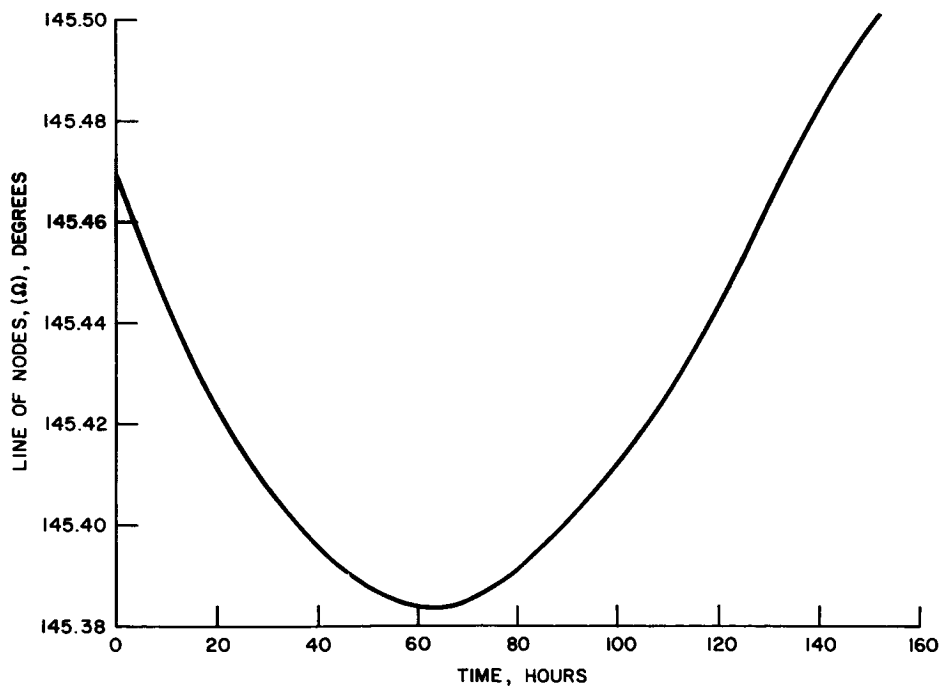


Figure VIII-5-11. Position of line of nodes versus time for orbit with apolune altitude of 921 nmi and perilune altitude of 57 nmi. Inclination of orbit plane to plane of Moon's orbit is 11.3 degrees

~~CONFIDENTIAL~~

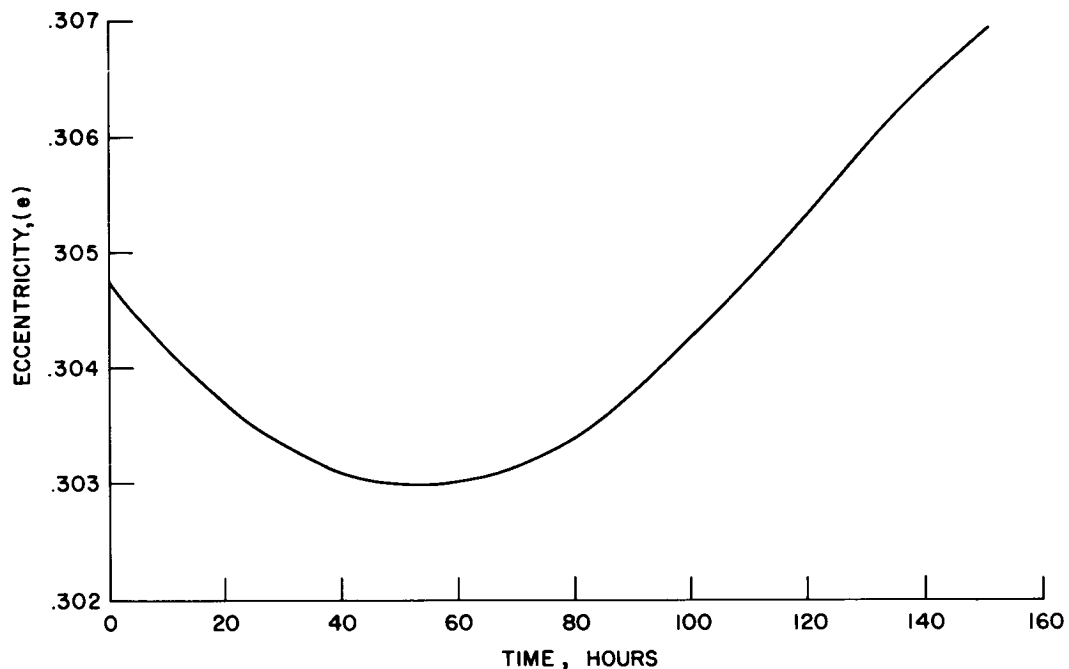


Figure VIII-5-12. Eccentricity versus time for orbit with apolune altitude of 921 nmi and perilune altitude of 57 nmi. Inclination of orbit to plane of Moon's orbit is 11.3 degrees

determining the elements of an orbit from measurements in the simple two-body case. These are:

- (1) Measure vector position and vector velocity at a given instant of time.
- (2) Measure three vector positions and the time at which one of the measurements was taken.
- (3) Measure two vector positions and the time at which each measurement was taken.

These are listed in the order of increasing computational difficulty. If the computer is capable of calculating orbits for an explicit guidance method, the third approach listed becomes a stronger contender.

Because of measurement errors, not one of the classical methods can be used in its simplest form. It will be necessary, therefore, to take a number of readings over a period of time and use appropriate smoothing techniques to improve the accuracy with

~~CONFIDENTIAL~~

which the orbital elements are determined. It is proposed at this time to make the following measurements simultaneously over a period of time:

- (1) The elevation angles of two stars, i.e. the angle measured at the vehicle between the line-of-sight to a star and the local vertical with respect to the Moon.
- (2) The altitude of the vehicle with respect to the Moon.

The two star elevations generate two cones of position loci with respect to the center of the Moon. Since the cones can intersect along two common elements, one intersection can be disregarded by having an approximate knowledge of vehicle position. The altitude information locates vehicle position along the line of intersection with respect to the Moon.

A possible implementation of this concept is described in the next section.

### **Implementation — Orbiting Around The Moon**

A possible implementation for the concept discussed under the foregoing approach is shown in block diagram form in Figure VIII-5-13. The basic philosophy here is to utilize the navigation, guidance and control implementation of the midcourse phase to the greatest extent possible.

Basically, vehicle-fixed infrared horizon sensors are used to establish the local vertical and measure altitude with respect to the Moon. The platform is caged to the vehicle so that the astrotrackers mounted on the platform can measure the angle between selected stars and the local vertical. Measurements with respect to two stars are made. Attitude error signals are used to correct for errors in vehicle position with respect to the local vertical and all readings are made simultaneously and continuously during a specific period of time. These data are smoothed and combined with Moon and star position information and sidereal time in the computer so that the ejection velocity increment and the corresponding time of ejection can be computed. The astrotrackers are initially oriented either automatically or manually with respect to the selected two stars. After acquisition, the astrotracker is switched to the automatic tracking mode of operation so that the tracker will be continuously aligned with the line-of-sight to the star. The most opportune time during an orbit can be selected for

~~CONFIDENTIAL~~



Figure VIII-5-13. Lunar orbiting mode concept schematic

~~CONFIDENTIAL~~

making the measurements since the infrared sensors will provide local vertical and altitude information even with respect to the dark side of the Moon.

Other possible approaches for obtaining orbital element information are being considered. The use of radar techniques for obtaining range and velocity information is being investigated, especially since radar equipment may be required in order to establish initial re-entry conditions with sufficient accuracy. Manual map-matching and optical angle-measurement techniques might also be used as a back-up for the automatic approach described previously in this Section.

## **EJECTION FROM LUNAR ORBIT**

### **General**

When the elements of the orbit have been established from measurements, it is probable that any orbit which would be considered as nominal is sufficiently stable so that vector position and vector velocity with respect to time can be predicted accurately for at least one orbit. The computer must be capable of solving for the required vector velocity increment and the corresponding time for ejection from the orbit around the Moon to a suitable return trajectory for each orbit. Ejection time is important since the vehicle must arrive at the Earth at the proper time. The velocity increment required for ejection should also be minimized in order to minimize fuel consumption. Accuracy of ejection is also important since return mid-course velocity corrections must also be minimized because of fuel consumption.

### **Concepts and Implementation for Ejection**

The computer will be capable of calculating the required vector velocity increment, and the corresponding ejection time, which will place the vehicle on a suitable return trajectory with the minimum expenditure of fuel. This information will be calculated for at least one or two future orbits. Prior to the selected time for ejection, the vehicle will be oriented with respect to the inertial platform such that the appropriate engine is properly aligned with respect to inertial space. The calculated vector velocity increment when added to the vehicle's velocity vector, will place the vehicle on a

~~CONFIDENTIAL~~

~~CONFIDENTIAL~~

suitable return trajectory. The velocity increment will be monitored by integrating accelerometers which will turn the engine off when the computed velocity change has been accomplished. Ejection errors will be compensated for during the mid-course return phase. There are no requirements for additional equipment for the ejection phase.



~~CONFIDENTIAL~~

## 6. RE-ENTRY ENERGY MANAGEMENT

One of the objectives of the APOLLO mission is that the vehicle return to some pre-selected landing area. In order to accomplish this task within some acceptable error limit, it is necessary to have on board the vehicle an energy-management system which serves to close control loops to effect range and cross range maneuvering.

Maneuvering capability is required as a result of tolerances in the range from re-entry to the landing area, tolerances in the re-entry path angle, atmospheric variations, and variations in aerodynamic characteristics. The approach considered here was to investigate the range maneuvering capability for various re-entry path angles. If the vehicle re-enters with a steep path angle, the nominal range capability is reduced whereas, for shallow re-entry path angles, the nominal range capability is increased. Therefore, to achieve a single preselected landing area, the vehicle must be capable of extending range beyond nominal for steep angles and obtaining ranges less than nominal for shallow angles.

For a single nominal landing area, the permissible re-entry path angle tolerances is a function of the vehicle's aerodynamic characteristics. That is, the capability of the vehicle must be compatible with the accuracy of the midcourse guidance system. If this compatibility does not exist, then the landing area must be selected as a function of the re-entry path angle which, of course, implies multiple landing points.

Another point worth mentioning is that the required range from re-entry to landing area is established once the vehicle has been selected. Therefore, given a vehicle and a landing area, the midcourse guidance system must not only establish the correct re-entry angle, but must also control the re-entry position. For vehicles flying trajectories perpendicular to the Earth's axis, range is controlled by varying in-orbit time of flight, whereas for trajectories which are coplaner with the Earth's axis, cross range is controlled by varying time of flight.

Effort has been directed towards obtaining a path control concept. The results of this investigation indicate that the attitude control loop should operate to achieve commanded

~~CONFIDENTIAL~~

**CONFIDENTIAL**

levels of dynamic pressure where dynamic pressure indication is obtained from an accelerometer.

The instrumentation problem has not been investigated yet, but the major blocks have been defined. There appears to be no major problem insofar as re-entry instrumentation is concerned. The techniques for accomplishing energy management have been considered, at least in a fundamental form, and will be presented in the sub-section titled "Techniques for Accomplishing Energy Management" starting on page VIII-138.

## **INTRODUCTION**

The problem of developing guidance concepts for the APOLLO mission during operation within the Earth's atmosphere was initially divided into two specific tasks. The first task was concerned with developing methods for controlling the vehicle to fly pre-selected flight paths which basically involves the selection of the parameter(s) used to close the feedback loop. The second task involves the determination of the maneuvering capability and the flight paths which must be flown in order to achieve maximum maneuvering capability.

The development of the energy management system for the APOLLO vehicle encompasses the combining of these two tasks into a single system wherein the range and cross-range to go, which are obtained from the navigation system, result in the selection of the proper flight path. The selected flight path is then commanded by the pilot control or the automatic path control system. The path control commands will be accomplished through control of the angle of attack, or pitch angle, which causes variations in the lift force. Thus, except in an emergency manual mode, the commands (manual or automatic) will be sent to a flight control system (autopilot). The general form of the re-entry control system is shown in Figure VIII-6-1.

## **RE-ENTRY SYSTEM DESCRIPTION**

The block diagram of Figure VIII-6-1 shows the major subsystems required by the energy management system and the flow of information between the subsystems. The

**CONFIDENTIAL**

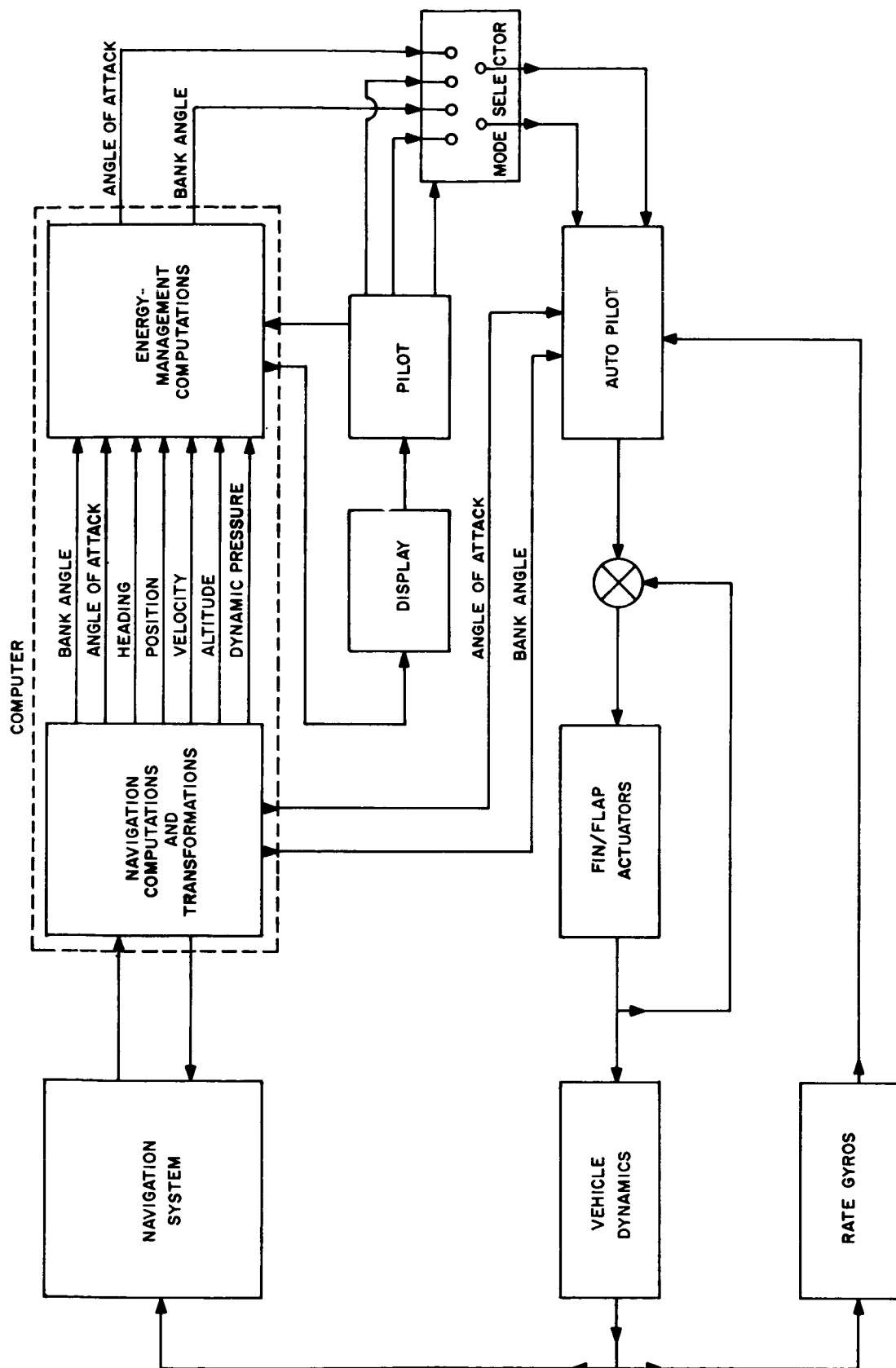


Figure VIII-6-1 Re-entry system block diagram

~~CONFIDENTIAL~~

navigation system makes use of the inertial platform and supporting equipment included in the midcourse guidance system. The computer is intended to be part of the digital computer used in other phases of the flight.

Since the vehicle's position and heading must be known, the navigation system is required to measure the velocity changes and vehicle attitude angles. The computer will process this information and transform the position, velocity and heading into earth coordinates as required for the energy management computations. The computer is also required to continuously compute the vehicle's bank angle, angle of attack, altitude, and dynamic pressure. The energy management section of the computer will compute the appropriate angle of attack and bank angle command necessary to fly that path which will satisfy both range control and vehicle safety requirements. The computer must be digital since many of the parameters computed vary over a wide dynamic range, while demanding a high degree of accuracy such as range to the target and altitude velocity path control.

The outputs of the energy management section are of two distinct forms. One is direct attitude commands (bank angle and angle of attack) to the autopilot. These commands are channeled through the pilot controlled mode selector which permits the pilot override capabilities, if necessary. Other outputs will be used to drive indicators and generate graphic displays. Indicators in the form of flashing lights or similar devices inform the pilot of malfunctions, while needle-dial type indicators monitor the variations in such important parameters as heating rates, g-loading, and altitude rates, and will indicate when corrective action must be taken by the pilot. Graphic displays presented on oscilloscopes can indicate, for example, predicted vehicle landing point and the various target positions with respect to this landing point. The vehicle's maneuvering capability is superimposed on this display, thus permitting the pilot to select the landing site. Also, the trajectory of the vehicle in the atmosphere can be presented to the pilot via an altitude-velocity display upon which safe flight corridors are superimposed. Should the vehicle approach the limits of this corridor or exhibit any unusual phenomena, the pilot will be aided in determining if corrective action is required to maintain the safety of the vehicle. If so, he can then over-ride the system via the mode selection switch and command the proper angle of attack or bank angle commands.

~~CONFIDENTIAL~~

[REDACTED]

The energy management computations for angle of attack and bank will include the necessary prediction or lead compensation and damping required for long-term path control stabilization. The autopilot will contain the compensation and damping required for short-term vehicle stabilization.

The error signal for flap actuation is generated within the autopilot by comparing the angle of attack and bank angle commands with the actual angles as computed in the navigation computation section. The rate gyros provide attitude rate information for the autopilot.

## SELECTION OF SAFE FLIGHT PATHS

The selection of flight paths which are considered safe for the vehicle and passengers was constrained to lie within bounds of (1) a maximum g limit, 7 to 12 g, for purposes of early study, and (2) the equilibrium maximum lift coefficient line.

If the vehicle exceeds limits of 2, it cannot generate sufficient negative lift to counteract the centrifugal force and, thus, it will perform a "skip" maneuver. The GE study has adopted the limitation that this situation is to be avoided, since the vehicle will skip out of the atmosphere and all aerodynamic control will be lost. The range traversed and time spent out of the atmosphere are extremely sensitive to the path angle and velocity at which the vehicle leaves the atmosphere; the conditions for the next re-entry are determined solely by the conditions at the previous skip. It was found that a low L/D vehicle ( $L/D \approx 0.25$ ) re-entering at a relatively steep angle will exhibit large range variations for small re-entry angle variations when the skip maneuver carries the vehicle above the maximum lift coefficient line. For variations in re-entry angle about a seven-degree re-entry, there is approximately 900 nmi of range change per degree variation in re-entry angle. The one important fact is that the majority of this range difference is acquired while the vehicle is in the stall condition while above the maximum lift coefficient line, which means the range difference is acquired when aerodynamic control is non-existent. Also, as the re-entry angle becomes shallower, this difference in range becomes much larger per degree of re-entry angle variation, while the majority of the difference is still acquired when aerodynamic control does not exist.

~~CONFIDENTIAL~~

Unlike sub-orbital-speed flight where holding a constant angle of attack results in a damped oscillation about the equilibrium glide trajectory, flight at super-orbital speed requires precise, constantly varying, angle of attack control in order to fly any prescribed path. If one were to hold a constant angle of attack, the vehicle will either climb or dive, depending upon initial conditions. That is, super-orbital flight presents an unstable situation with respect to angle of attack control.

## PATH CONTROL SYSTEM

To achieve path control, then, it is necessary to have available information representing altitude, altitude rate, path angle, density, or dynamic pressure, any one of which can be used in a control system to effect flight along some prescribed path.

Since ionization prevents the use of a radar altimeter, and also since angle of attack control presumes knowledge of the local vertical, an inertial guidance system is required and represents the only known method for obtaining any of the aforementioned parameters. If path angle is known accurately, it follows that altitude rate is also accurate since the velocity computation is good. In this case, the altitude information should be relatively good, but it may have some constant offset error.

We could, thus, use an altitude command control system using altitude rate for damping wherein a nominal altitude program is followed. Range control would be obtained by commanding variations from the nominal altitude. Since the drag coefficient is fairly constant with angle of attack for the vehicle studied, flying at different attitude results in a different dynamic pressure, thus causing variations in the rate of change of velocity.

However, this approach has its disadvantages in that the vertical channel of an inertial guidance system is unstable, and thus the altitude rate and altitude computations may assume rather large errors. Therefore, other methods of path control must be considered.

It seems much more desirable to control path with a parameter which is measured rather than one which is computed. For example, dynamic pressure appears to be an excellent control parameter since it causes drag forces or g loading, generates lift

[REDACTED]

and is a function of altitude or density and velocity. Controlling with dynamic pressure would make the system independent of altitude density variations which is quite desirable.

Because the flight path angles are quite small, an accelerometer whose input axis is horizontal and in the direction of flight will be a good indication of the deceleration due to drag, which can be expressed as the product of a constant times  $q C_D$  where  $q$  is dynamic pressure and  $C_D$  is drag coefficient. The coefficient of drag can vary with angle of attack, Mach Number and Reynolds number. For blunt shaped bodies, there is negligible variation in  $C_D$  with Mach number, less than two percent for the D-2 configuration, down to Mach 1. Reynolds number affects  $C_D$  only above 200,000 feet, but its effect varies also with angle of attack. Up to the altitude of 280,000 feet, the  $C_D$  varies by a factor of two for relatively blunt vehicles, thus it becomes necessary to store a number of  $C_D$  vs angle of attack curves, for use at the various altitudes up to maximum of about 260,000 feet. During the range control phase, the vehicle is not expected to go above this altitude. About 75 percent change in  $C_D$  can be expected over this altitude range so that storage of five curves, each containing a 15 percent difference in  $C_D$  results in maximum errors of 7.5 percent when computing  $q$  which is near the maximum dynamic pressure measurement error limit. Further studies into error allotments will have to be made before the number of stored curves is determined.

Narrow, point-shaped vehicles and flared vehicles exhibit variations in  $C_D$  due to Mach number variations as well as with Reynolds numbers, thus the problem of determining  $C_D$  is complicated somewhat. A separate family of Reynolds numbers curves for  $C_D$  versus angle of attack will be required for each range of Mach numbers causing significant changes in  $C_D$ . The total number of curves required cannot be determined until the  $C_D$  versus Mach number variation for a particular vehicle is assessed.

It appears, then, that we should control the flight path by using the accelerometer output as the controlled variable. The desired paths and path variation commands will be expressed in terms of desired accelerometer outputs and the error signal plus the rate of change of the error will control angle of attack or pitch angle. These variations in path angles are required in order to change the expected vehicle to equal the

[REDACTED]

**CONFIDENTIAL**

range to go to the target. The amount of path variation (or change in accelerometer output) is a function of both the velocity and instantaneous value of  $q$ . This information may have to be stored in the control system, via a computer most likely.

This type of control system, without the range loop closed around it, was programmed on the analog computer. Variations in paths were commanded and the system works quite well except when large step function commands are inserted at super orbital velocities. If the commands required ascending to altitudes just below the equilibrium maximum lift coefficient line, the path angle often becomes so large that even when maximum negative lift is commanded, the vehicle is committed to go outside the flight corridor, making control impossible until such time as the vehicle returns to the sensible atmosphere, which may be some considerable time later. However, for any given value of dynamic pressure,  $q$ , and velocity, there is a maximum time rate of changes of  $q$ , ( $\dot{q}_m$ ), below which proper angle of attack commands can control the vehicle within the flight corridor; but above which, maximum negative lift is not enough to maintain the vehicle in the flight corridor. Both  $q$  and velocity could be programmed into the control system such that when the  $\dot{q}_m$  is approached, maximum negative lift would be commanded as an override regardless of any other command. A stored program system could be used where the rate of change of the accelerometer output (actually a measure of  $q$ ) is limited, possibly as a function of the error in  $q$  and velocity or, as a function of  $q$  and velocity. Another possibility is a predictive control system wherein we would predict that unless the angle of attack is changed now, path control capability will be lost.

## **TECHNIQUE FOR ACCOMPLISHING ENERGY MANAGEMENT**

When considering the techniques for energy management, certain restrictions imposed on the vehicle limit the extremes of permissible flight paths. As mentioned previously, these include  $g$  loading, heating, and aerodynamic stability. Heating and  $g$  loading will limit the lower boundaries of a flight path while aerodynamic stability limits the upper boundary.

When the re-entry velocity is greater than orbital velocity, angle of attack control is unstable since, when holding a constant angle of attack, the vehicle will either dive or

**CONFIDENTIAL**



~~CONFIDENTIAL~~

climb depending on the initial conditions. Care must be taken to prevent the vehicle from diving too deeply into the denser atmosphere where g loading and heating rates limitations will be exceeded. Aerodynamic control will be lost if the vehicle is permitted to skip above the equilibrium maximum lift-coefficient line.

Below orbital velocity, however, the angle of attack loop is stable, and flying equilibrium glide paths, as defined by constant angles of attack, appear very desirable. To attain equilibrium glide conditions, it is only necessary to damp out the altitude oscillations and then fly at a constant angle of attack. Variations in the lift coefficient with Mach and Reynolds Numbers will result in the vehicle's flying various equilibrium glide paths but since the change in lift coefficient with these parameters is smooth, the resultant transitions from one equilibrium glide path to another will be smooth. By limiting the upper and lower angles of attack, one can generate a safe flight corridor that observes all the flight path restrictions. By flying various equilibrium glide paths within the corridor which are defined by various angles of attack, the range may be altered. See Figure VIII-6-2, "Equilibrium flight corridor boundaries".

The existence of these safe flight corridors is very important to the operation of the re-entry vehicle. The width of the corridor is a good indication of how much safety factor the vehicle has, but it is not necessarily indicative of the range-change capability, since this depends on the slope of the lift-to-drag curve. By defining the safe flight corridor in terms of equilibrium glide paths, the vehicle can be controlled to fly within the flight corridor by using only angle of attack and altitude rate.

Above orbital velocity, the foregoing does not hold true; thus, angle of attack programs cannot be used, and other modes such as constant dynamic pressure or constant altitude path will be flown. This study has considered these two in terms of implementation and concludes that constant dynamic pressure would be the better control parameter, thus constant dynamic pressure ( $q$ ) flight paths will be considered here. Once again, the lower limits of the constant  $q$  flight path are dictated by the heating rates and g loading limits. The upper limit is restricted by maximum equilibrium glide line, above which aerodynamic control is lost. By flying various constant  $q$ 's, the range may be altered. Needless to say, though not controlled explicitly, the angle of attack control is used to vary and maintain the constant  $q$  flight paths.

**CONFIDENTIAL**

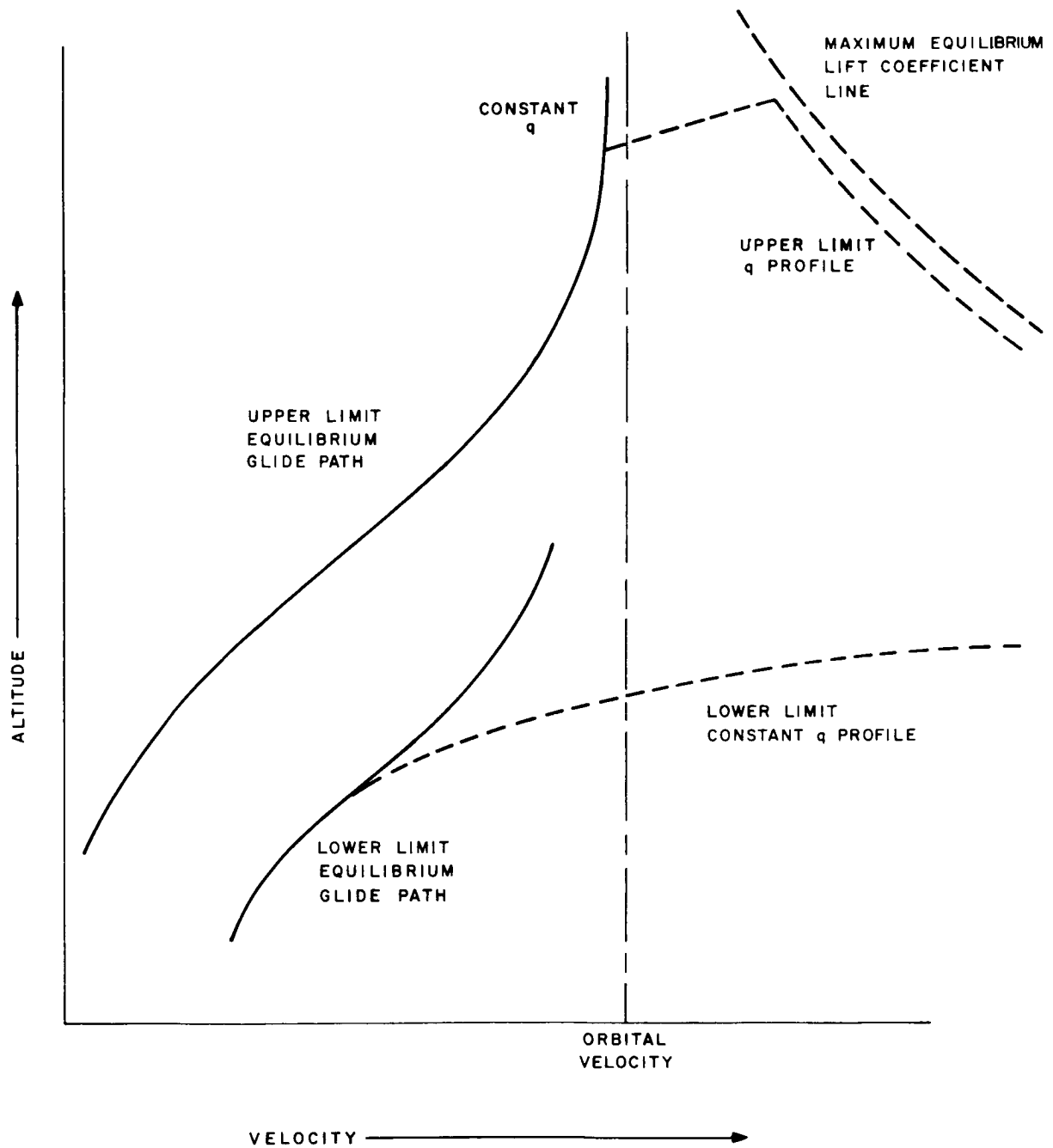


Figure VIII-6-2. Safe flight corridor boundaries

**CONFIDENTIAL**

~~CONFIDENTIAL~~

## Range Control

The range control loop will be discussed first, after which the added complications of cross range control will be considered.

When flying constant angle of attack equilibrium glide paths, the range the vehicles will go is directly proportional to the lift to drag ratio ( $L/D$ ) and velocity. Since  $L/D$  is a function of Mach and Reynolds numbers and of angle of attack, it is possible to obtain a program of range versus velocity for any angle of attack program. The procedure, then, is to obtain a plot of range versus velocity for a vehicle flying an angle of attack program consistent with the upper limit of the safe flight corridor and then obtain a like plot for the lower limit of the safe flight corridor. The two plots will be similar to the solid line curves of Figure VIII-6-3 "Range Capability versus Velocity". The range and velocity referred to are inertially measured; that is, referenced to a non-rotating earth. Now, by carefully considering the  $L/D$  curves, an angle of attack program can be devised which will, when followed, yield a range-versus-velocity curve which will be very nearly midway between the maximum and minimum capability. A digital computer can be programmed to yield the nominal angle of attack program quite readily. This mean range is referred to as range can go nominally ( $R_{CGN}$ ). The purpose of the range control loop is to attempt to make the range to go to the target equal to  $R_{CGN}$ , the reason for which will be shown later on. Ideally, then, once the two ranges are equal, no further range errors should result.

Above orbital velocity, analogous information can be obtained for range-versus-velocity for a vehicle flying the upper limit of the safe flight corridor and for one flying the lower limit of the safe flight corridor. The boundaries of safe flight corridor may not necessarily be a fixed constant  $q$  throughout the entire super-orbital velocity regime, but rather a  $q$ -versus-velocity program. Once again, the nominal  $q$  versus velocity program can be devised which will yield a range ( $R_{CGN}$ ) versus velocity curve which will be midway between the maximum and minimum capability. See Figure VIII-6-2, broken lines.

The final shape on the upper limit of the flight corridor has not yet been defined exactly, except that it must be below the maximum equilibrium lift coefficient line. At orbital velocity, this line peaks at some extremely high altitudes; therefore, the command on

~~CONFIDENTIAL~~

~~CONFIDENTIAL~~

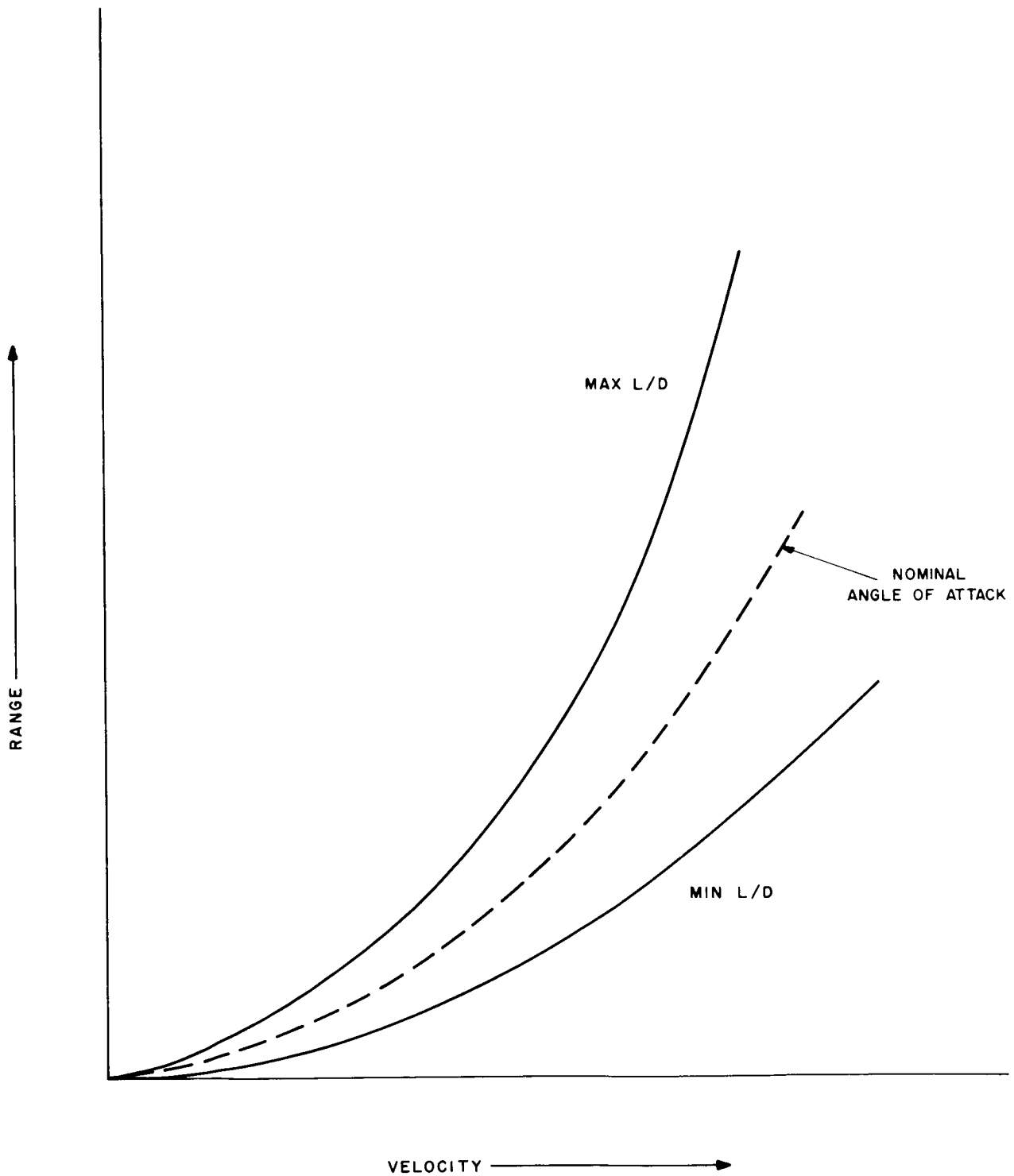


Figure VIII-6-3. Maximum, minimum, and nominal range capability versus velocity

~~CONFIDENTIAL~~

~~CONFIDENTIAL~~

the upper boundary will be one which "blends-in" with the upper limit of the safe flight corridor at about 24,000 feet/sec. There is a small area above this  $q$  line where safe flight corridors are theoretically possible but not advisable, since the safe margin is reduced considerably. If the extra capability available above the constant  $q$  line (shown in Figure VIII-6-2) is required in an emergency, the pilot could override the system and manually command the system to exceed the  $q$  limit.

The range control loops will operate in the following manner: For large range errors (a range error exists when the range to go to the target is not equal to the  $R_{CGN}$  as defined by the nominal  $q$  (or angle of attack) versus velocity program) the vehicle via the angle of attack loop depending on whether range must be gained or lost; i.e. the range control loop is saturated. When the range error has been reduced below some smaller threshold value (probably between 25 - 100 nmi depending on velocity), proportional control is used to gradually bring the vehicle back on to the nominal flight path. The purpose of saturating the range control loop is to reduce the range error as quickly as possible and get the vehicle back on the nominal flight path, the only path from which maximum range change capability can be obtained in order to overcome any errors which may appear later in flight. These errors that may appear later in flight include uncertainties in the expected aerodynamic coefficient, atmospheric density variations, local winds, etc.

The control system just described here was deemed much more satisfactory than a control system which looks at the range to go to the target and then decides what flight path would, ideally, (if flown all the way) result in arriving at the target (landing area). This system, in effect, computes or determines in some other manner a trajectory or flight path that is not centered about the maximum range change capability and the uncertainties listed above can result in insufficient reserve capability for overcoming the resulting errors in range.

For example, suppose the computed distance to the target requires almost, but not quite, the maximum range capability of the vehicle. The control system which saturates the angle of attack command and flies along the boundary of safe flight corridor will eventually remove all the range error and return to the nominal flight path, providing maximum range change capability for variations in expected conditions near the target, such as the local winds,  $C_D$  and  $C_L$  variations, etc. The system which attempts to

~~CONFIDENTIAL~~

~~CONFIDENTIAL~~

compute the proper flight path will fly a path that will be just below the boundary of the safe flight corridor. If errors, due to variations in those unexpected conditions listed above, result in the distance travelled to be less than expected, then range capability must be extended.

The vehicle flying the path just below the flight corridor boundary will be hard pressed to extend range any farther since it is nearly at the limit already, whereas the vehicle which has reduced all the error as soon as possible has a greater capability for correcting these unexpected errors. Thus, a range control system which attempts to make the  $R_{CGN}$  equal the range to the target manages its energy much more effectively than a system which tries to compute the proper flight path to reduce the range error. This system is more effective, since full use is made of the range-change capabilities at the high velocities. In effect, it attempts to maintain the target in the center of the range maneuvering capability.

### **Cross-Range Control**

It is very unlikely that the re-entry vehicle will be heading in the proper direction to land on the target when it re-enters, especially in a polar re-entry when the target position is very sensitive to time of flight errors. Thus, it becomes necessary for the vehicle to be able to re-orient its heading of after re-entry.

### **Effects of Banking**

Angle of attack, or pitch, control alters the range in the vertical plane of flight, but cannot effect range changes perpendicular to the flight plane. Some method of rotating either the lift or drag vectors out of flight plane must be employed. Angles of yaw can be generated by rotating the vehicle in the horizontal plane, in which case a component of drag and a body side force component is generated perpendicular to the path direction. Or, the vehicle can be rolled, or banked, which will produce a component of lift perpendicular to the flight direction. Since 180-degree banking is required to invert the lift vector, banking will also be used to obtain that component of force, perpendicular to the vertical flight plane, required to change the path heading and generate cross components of range.

~~CONFIDENTIAL~~

[REDACTED]

Due to this banking maneuver, the component of lift force in the vertical plane is reduced by the cosine of the bank angle, and the vehicle will fly at a lower altitude than if it were not banked. Therefore, when flying angle of attack programs below orbital velocity, in order to constrain the vehicle to fly within the safe flight corridor limits, the minimum allowable angle of attack,  $\alpha_{\min}$ , should be multiplied by the secant of the bank angle, assuming the lift coefficient nearly linear in the vicinity of  $\alpha_{\min}$ . This has the effect of increasing the lift so that the vehicle will not fly lower than the bottom of the safe flight corridor. Furthermore, if the vehicle is flying in a banked attitude at its maximum angle of attack it will not be at the top of the safe flight corridor; therefore, the bank angle has the effect of shrinking the safe flight corridor. This has the effect also of reducing the range change capability and implies the nominal angle of attack program is no longer in the middle of the maximum and minimum capability.

The foregoing considerations will also apply when flying the dynamic pressure versus velocity profiles. The lower boundary on the flight corridor can be maintained although the corresponding angles of attack, negative for superorbital velocities, will have to be increased. The maximum equilibrium lift coefficient line will be effectively lowered according to the magnitude of the bank angle. The corresponding restriction that the vehicle remain below this lowered line is still imposed on the vehicle.

When flying a constant  $q$  line, unbanked, at superorbital velocities, the coefficient of lift, and therefore angle of attack, must be continually varied in order to produce just enough negative lift to balance the difference between centrifugal and weight forces. At orbital velocity, zero angle of attack is required since the centrifugal and weight forces are equal and lift is not required. Maximum negative lift is required at the maximum velocity since centrifugal force has its maximum at this velocity. Thus, the angle of attack, or better, the lift force, will decrease from some maximum to zero during flight through superorbital velocities.

Since maximum cross-range distances are produced when a banked vehicle flies at maximum  $L/D$ , the angle of attack may be held constant and the vehicle bank angle varied in such a manner as to produce just enough vertical lift to balance the forces. All excess lift capability is applied perpendicular to the path direction for use in obtaining as much cross range as possible. This is the most efficient use of vehicle

~~CONFIDENTIAL~~

capabilities. As orbital velocity is reached, the vehicle will have completed a 90-degree roll maneuver such that all lift is applied in the cross range direction. There remains no vertical component of lift since none is required. Each value of constant  $q$  desired while banking will generate a different bank angle versus velocity profile. Thus, if large increases in range are desired, a high-altitude, low- $q$  path will be required. The low  $q$  requires larger vertical components of lift to maintain equilibrium of vertical forces, but much longer times of banked flight result. If range decreases are required, then, high- $q$  paths are flown, smaller vertical components of lift are required, the bank angle is increased but shorter times of flight result. For zero range errors, a nominal  $q$  is flown, and a nominal bank versus velocity program is flown. Since the bank angle profile is dependent on the  $q$  path, it may be necessary to generate three banking-velocity profiles, one each for maximum  $q$ , minimum  $q$  and nominal  $q$ . As will be shown later, each profile requires the following associated information:

1. Down range can go, banked, versus velocity
2. Cross range can go, banked, versus velocity
3. Change in heading angle, banked, versus velocity

Below orbital velocity, the angle of attack loop is stable and the dependence of bank angle on vertical lift component is no longer required. Thus, it is proposed to generate one angle of attack versus velocity profile based on one fixed bank angle, somewhere between 30 and 45 degrees. Any increases in bank angle above 45 degrees does not generate any more cross range capability, but serves only to decrease the down range capability of the vehicle.

As mentioned previously, banking the vehicle causes the safe flight corridor to contract, thereby reducing the range change capability. Thus, the band of  $L/D$  ratios available through variations in angle of attack are different from those available when the vehicle is not banked. The nominal angle of attack profile representing the mean  $L/D$  values will be generated for, say 45-degree banking. Once again, it is necessary to generate the range, cross range and change in heading versus velocity for banked conditions. This information will be combined with that generated from the constant  $q$  banked profiles to produce one composite set of curves, which will yield the total range, cross range and heading angle change versus velocity when banked first according to the  $q$  versus velocity program and the constant bank at 45 degrees.

~~CONFIDENTIAL~~



~~CONFIDENTIAL~~

## Theory of Operation

Since the range control loop operates in a fairly straightforward manner, it would seem best to eliminate the cross range errors as quickly as possible and reduce the problem to one of simple range control.

The operation of the cross-range loop, in its simplest form, could be one which commands banking as long as the heading is in error, or as long as cross range errors exist. Once the cross-range errors are eliminated, the vehicle is unbanked and the problem is now one of range control. There is one serious shortcoming to this scheme, however, in that the range control problem has been completely ignored while banking. It is distinctly possible that insufficient range change capability is present when the vehicle unbanks. It becomes necessary to know well beforehand the velocity at which the cross-range error is eliminated and the distance from the point of unbank to the target.

The energy management system has at its command the following information:

1. Instantaneous distance in range and cross range to the target.
2. Instantaneous velocity.
3. Range can go nominally unbanked as a function of velocity.
4. Range, cross range, and change in heading angle versus velocity when banked.

The theory of operation is as follows. An unbank point is chosen for some small velocity and from the range and cross range can go versus velocity while banked, the position of the vehicle with respect to the target at the unbank velocity can be determined. The heading the vehicle should have in order to be flying directly toward the target is determined from the relative positions at unbank.

From the change in heading angle versus velocity information, together with the initial (present) heading, vehicle heading at unbank can be computed and compared with the required heading. If the headings are not the same, a new unbank point is chosen and the process, or computations, are repeated. The polarity of the differences in the heading angles indicates whether the unbank velocity should be increased or decreased.

~~CONFIDENTIAL~~

~~CONFIDENTIAL~~

When the proper unbank point is found, the range to the target is computed and compared to the range can go nominally, unbanked, at the unbank velocity. If there are range errors, the flight path is altered immediately such that a path along the appropriate boundary of the safe flight corridor is flown.

Since the range, cross range and change in heading angle versus velocity information was obtained using a nominal banking trajectory during the period of constant angle of attack control, the predicted unbank point will be in error. However, the unbank point is continually being computed and, as the vehicle velocity approaches the unbank velocity, the inaccuracy is gradually reduced until the unbank velocity is reached, at which time the vehicle is heading toward the target. Note that as the vehicle moves along the flight path, the prediction is constantly up-dated, consequently it has no dependence on past history. This discussion ignores rotating earth and air mass velocities. Nominal time of flight information can be generated as a function of velocity when both banked and unbanked. This is, then, used to predict future target position. These considerations were purposely ignored to keep the discussion as simple as possible.

### **Stored Versus Explicit Computations**

Explicit type control systems, wherein the complete equations of motion are continually solved in order to determine the range errors and necessary corrections, possess no inherent advantage over the stored reference trajectory type system proposed herein. Whatever can be computed in-flight can be computed beforehand to just as good an accuracy, and then stored in the energy management computer.

Since many of the parameters, such as atmospheric density, local winds, and aerodynamic characteristics vary in an unpredictable manner, it becomes difficult to compute with any degree of accuracy the vehicle's future glide trajectory. These variations will be handled by the control system when they are recognized, recognition being in the form of range errors.

The stored system requires continual computation of range errors and the necessary transformation from the stored information, such as range, cross range, and change in heading into the appropriate Earth-centered coordinate system. Also, the effects of rotating earth and air mass velocity must be considered. The additional computations

~~CONFIDENTIAL~~

~~CONFIDENTIAL~~

required by an explicit computation system could lead to prohibitively long computation cycles. Although computation times have not been specifically considered, the maximum allowable time would seem to be around one computation every five seconds. Further studies, including implementation considerations, are required to determine if either system has a clear-cut advantage over the other.

## ENERGY MANAGEMENT TRAJECTORY STUDIES

In order to assess the required capabilities for the energy management path control subsystem, a series of analog computer runs were made in order to determine the performance envelope for two typical re-entry vehicles under study, the B-2' configuration and the B-2'' configuration. Typical results are presented in Figures VII-6-4 through VII-6-18. The important aspects under scrutiny in the analysis of these results were:

1. Minimum range capability at shallow re-entries;
2. Maximum range capabilities at steep re-entries;
3. Range change capabilities for various re-entry angles;
4. Time of flight considerations; and,
5. Effects of deceleration limits.

The limitations and/or assumptions discussed in the preceding section also apply here. For typical restriction of these runs, it was assumed that 7 g deceleration could be withstood for up to three minutes, and that peak decelerations up to 12 g could be withstood for short durations of time. During re-entry, both positive and negative lift was assumed permissible; thus, shallow path angle re-entries employed negative lift when attempting to minimize range and positive lift is employed when attempting to increase range. Positive lift is always used for the steep path angle re-entries in order to limit the peak deceleration.

The following ground rules were set up for these runs: minimum range would be obtained by flying a constant maximum-g deceleration line as soon as possible after pull-out for steep re-entries and as quickly as the vehicle could be forced down to the

~~CONFIDENTIAL~~

~~CONFIDENTIAL~~

maximum g line, using the negative lift, for shallow re-entries. Maximum range was obtained by flying as close as possible to the maximum  $C_L$  equilibrium line after pull-out.

The control system used for maintaining constant q worked well once the vehicle approached the maximum g line; thus, maximum negative or positive lift (depending on path re-entry angle) was used from the beginning of the run until the maximum g line was approached, at which time the constant q control system was switched in. In programming the constant  $W/C_L A$  control system for maximum range, it was discovered, by plotting that value of q, corresponding to the  $W/C_L A$  points, versus velocity, that the plot is nearly a straight line, i.e.  $q = K_1 V - V_g$ . The dynamic pressure, q, approaches zero as V approaches  $V_g$ , therefore the origin is translated along "V" axis by  $V_g$ . It was this control system which illustrated the fact that limiting of some sort is required to prevent the vehicle from overshooting the maximum  $C_L$  equilibrium line. Observe run No. 11, Figure VIII-6-7, for example. Positive lift was employed until pullout at which time the control system was switched in. Maximum (or nearly maximum) negative lift was commanded by the control system as the vehicle followed the constant  $W/C_L A$  line. If positive lift had not been removed at this point, the path angle would have begun to build up such, that by employing even maximum negative some short time later (a few seconds) not enough lift can be generated to decrease the rate of ascent sufficiently to maintain the vehicle below the maximum  $C_L$  equilibrium line. The vehicle would have eventually travelled outside the sensible atmosphere due to the predominant centrifugal force over the combined weight and lift forces. This is also the reason for flying slightly below the maximum equilibrium line; so that a safety factor is maintained in the event of errors in the system, such as measurements of q,  $\dot{q}$  or velocity.

Figures VIII-4 through 18 present the altitude versus velocity trajectories and the corresponding range versus velocity plots. Figures VIII-6-4 to 8 (runs 1-13) refer to nominal  $C_D$  and  $C_L$  for the B-2'' configuration while Figures VIII-6-9 to 16 (runs 14-29) refer to B-2'' configuration. Each run was performed in two sections, the first part including the altitude from 400,000 feet to 260,000 feet, and the second from 260,000 feet down to approximately 140,000 feet. Only the second part is shown on these Figures (VIII-6-4 through 18). Since there is such a small change in velocity in going from 400K

~~CONFIDENTIAL~~

[REDACTED]

to 260 K feet, the altitude versus velocity plot is simply a vertical line, and, therefore, is not shown. For this reason, the range versus velocity plots include only the range from 260,000 feet on down to the end of the run. Since the range covered in descending from 400 K to 260 K feet is not included on these plots, these ranges have been tabulated on the altitude versus velocity plots under the column "ΔR". The range under the column "Range, nmi." is the range covered from 260,000 feet down to 140,000, the lower limit for which the computer was scaled. The velocity at the end of the runs will not be the same for the maximum and minimum range runs, since the velocity, at 140 K feet for the maximum  $C_L$  equilibrium line is less than the velocity at 140 K feet for 7 g. Therefore, in comparing range capabilities, it is wiser to go to the range versus velocity curves and use a common velocity as a reference for ending the runs, say 16,000 fps. Under the heading "g limit" the numbers 12 g or 7 g indicate the maximum deceleration in g permitted. For example, run 2,  $\gamma_E = 4.5$  degrees employed negative lift well down into the atmosphere in order to get the vehicle into dense enough air to generate the required dynamic pressure,  $q$ . Eventually positive lift is used to pull out and get the vehicle up to 7-g limit. In run 1, however, positive lift is switched in, via the constant  $q$  control system, at a higher altitude such that 7 g is also the peak deceleration. A range difference of about 26 nmi is observed. Since g limitations have not been fixed, it was decided to investigate both possibilities (7 and 12 g) for the shallower re-entries. (Steeper re-entries always pull more than 7 g even with positive lift used from re-entry through pull-out.) It should be pointed out that constant dynamic pressure lines were flown, not actually constant G lines. This can be justified in the following manner. First of all  $C_D$  is relatively constant, about 1.2. Also  $L/D = 0.23$  maximum, or less. Looking again at the equation describing deceleration, G:

$$G = \sqrt{L^2 + D^2}$$

for  $\frac{L}{D} = 0.23$

$$L = 0.23 D$$

~~CONFIDENTIAL~~

Therefore,

$$\begin{aligned} G &= \sqrt{(.23D)^2 + D^2} \\ &= \sqrt{1.053 D^2} \\ G &= 1.025 D \end{aligned}$$

There is 2.5 percent error when the lift is ignored.

Now, since  $D = q C_D A$

where  $\frac{W}{A} = 100$

$$q = \frac{G (100)}{C_D}$$

for a 12 g limit and  $C_D$  of 1.23,  $q = 1000$  lbs per sq ft.

Thus, a constant  $q$  of 1000 lbs per sq ft is satisfactory for simulating a constant  $g$  line. A similar derivation applies for the 7-g line where  $q$  comes out to be about 585 lbs per sq ft. For those runs where  $L/D = 0.46$ , the difference between  $g$  and drag is about 10 percent.

Note that, on the minimum range runs, the ordinate, altitude  $\times 10^{-3}$  feet includes the altitude span from 140 K to 240 K feet, while for maximum range runs, the ordinate spans the range of altitudes from 160 K to 260 K feet. The scaling along the ordinate of the range versus velocity curves also varies according to the range capabilities for the particular runs presented. Figures VIII-6-17 and 18 show the effect of banking the vehicle on both the trajectory and the range capabilities. A six-degree path angle at re-entry and 45 degree bank starting at 260,000 feet is shown, where maximum range and cross range is sought. Notice on the altitude/velocity plot that banking causes the vehicle to pull out at lower altitudes. This is the result of decreased vertical component of lift when the vehicle is banked. At 45 degree banked, the vertical lift is decreased by 30 percent. Looking at the range versus velocity, Figure VIII-6-18, it is seen that only 42 nmi of cross range is attained while the range is only 800 nmi. Unbanked, the range

~~CONFIDENTIAL~~

~~CONFIDENTIAL~~

was 1170 nmi. Thus, 370 nmi down range are lost at a gain of 42 nmi cross range. This is not to say that 42 miles is maximum cross range capability; however, it does give an indication of relative effects on the down range capability.

~~CONFIDENTIAL~~

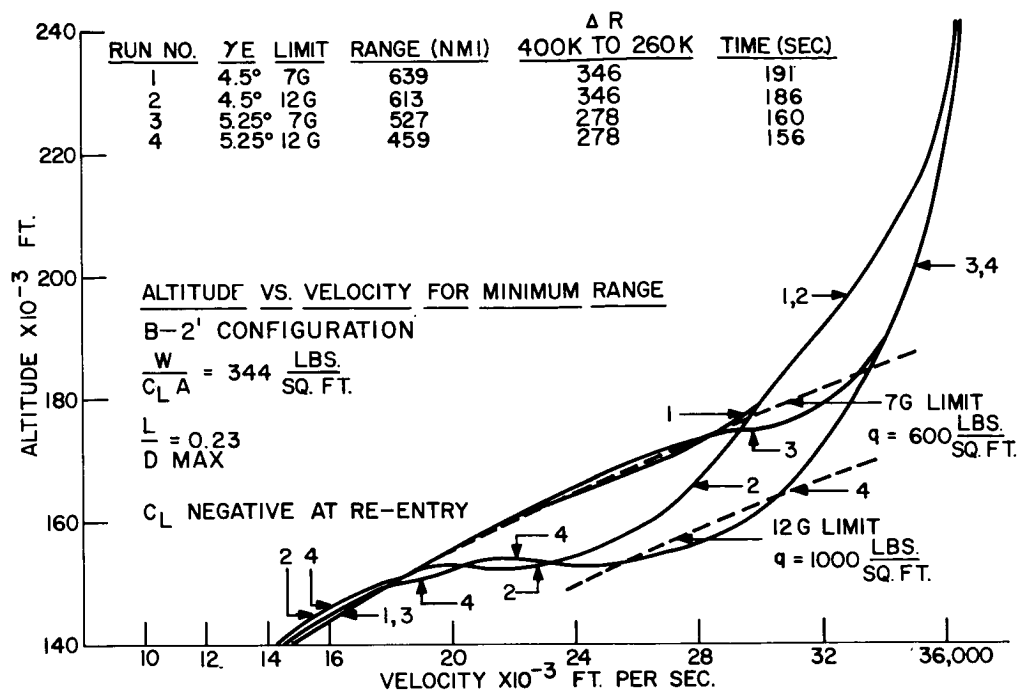


Figure VIII-6-4. Altitude versus velocity for minimum range, B-2' configuration Runs 1 through 4

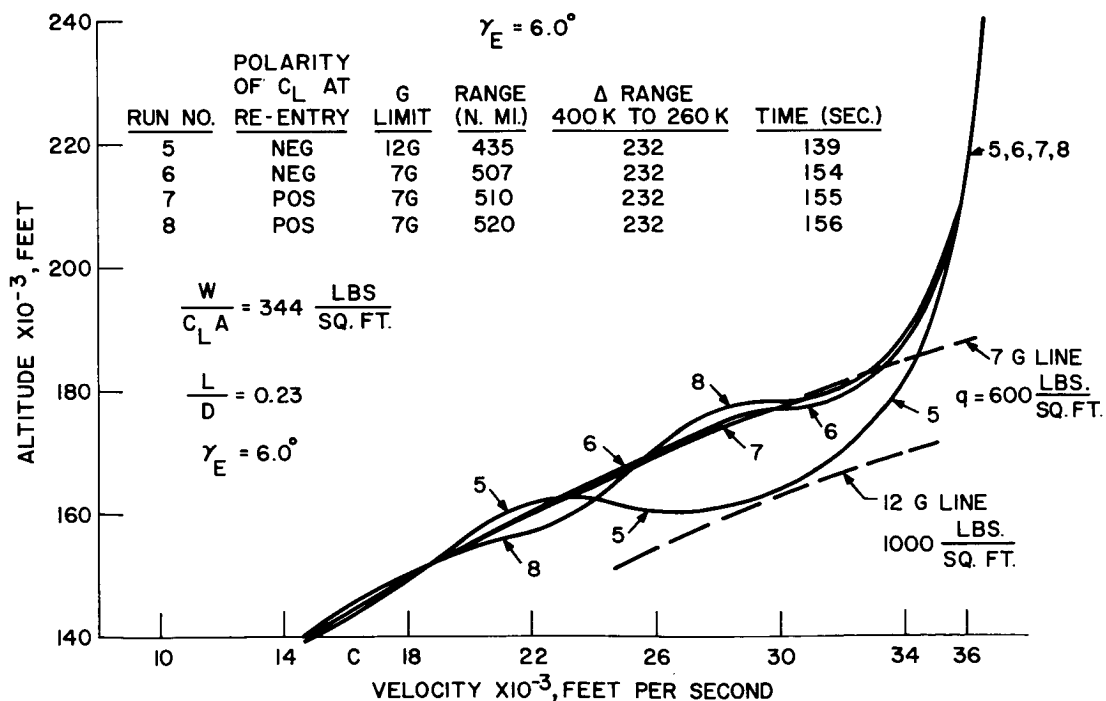


Figure VIII-6-5. Altitude versus velocity for minimum range, B-2' configuration Runs 5 through 8



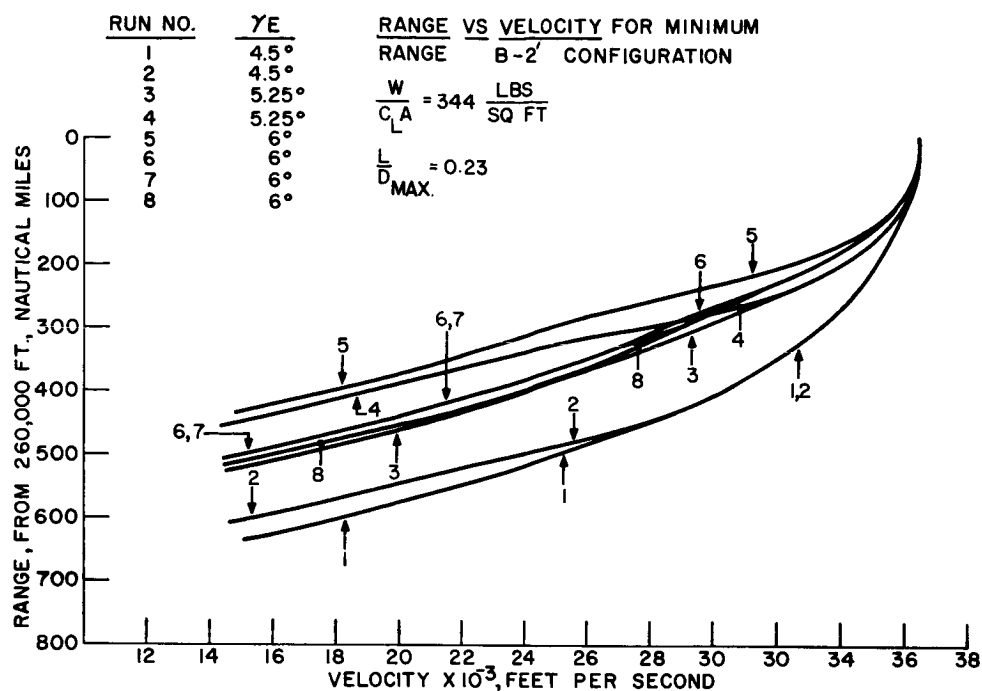


Figure VIII-6-6. Altitude versus velocity for minimum range, B-2' configuration Runs 1 through 8

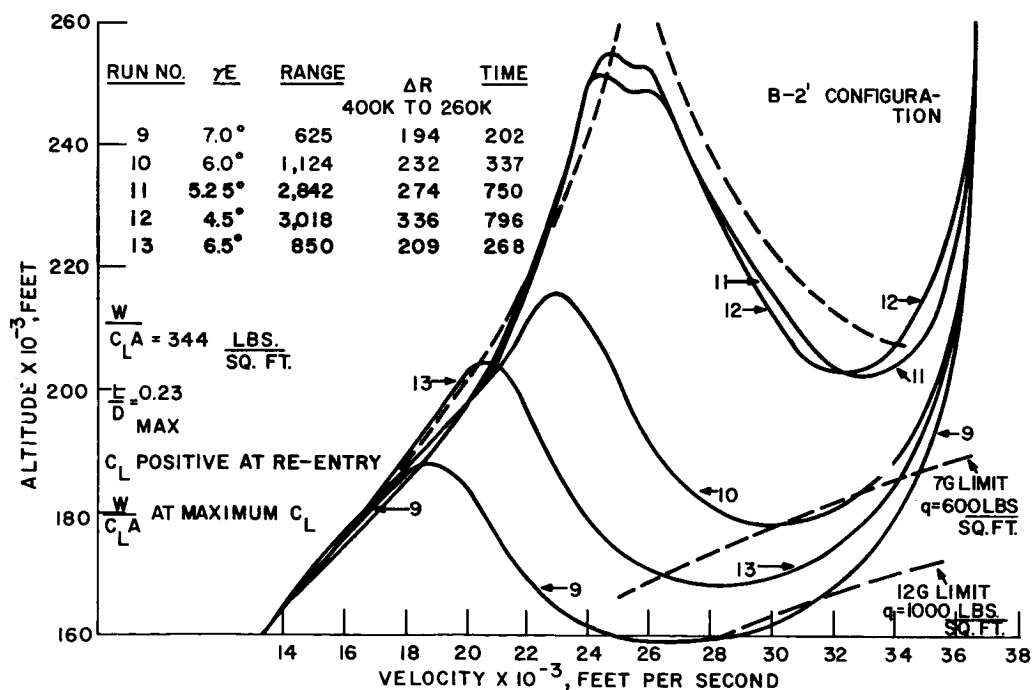


Figure VIII-6-7. Altitude versus velocity for maximum range, B-2' configuration Runs 9 through 13

**CONFIDENTIAL**

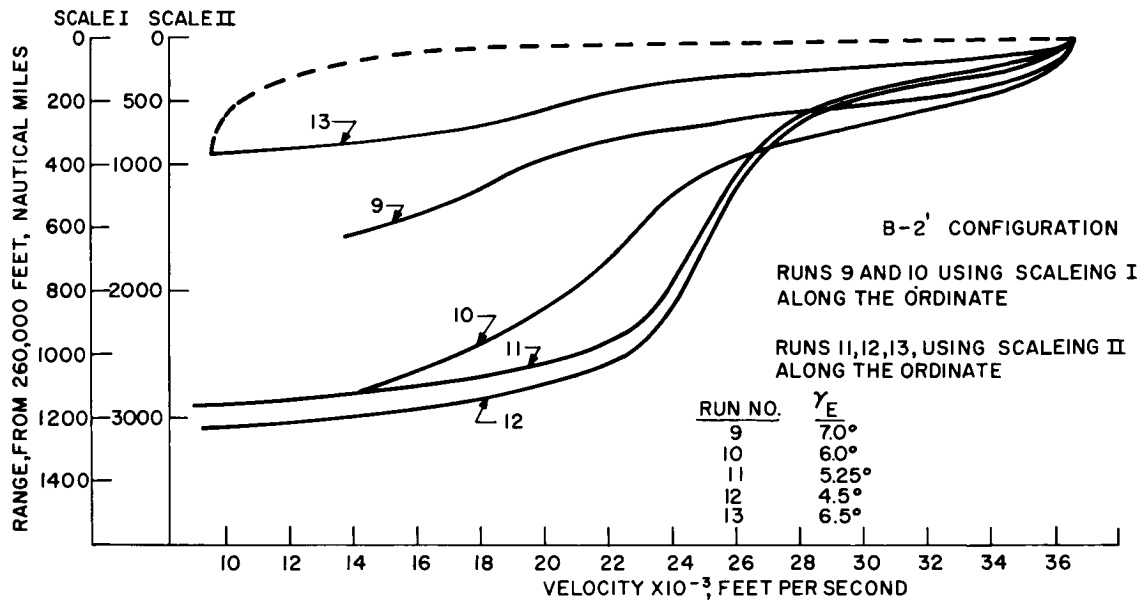


Figure VIII-6-8. Altitude versus velocity for minimum range, B-2' configuration Runs 9 through 13

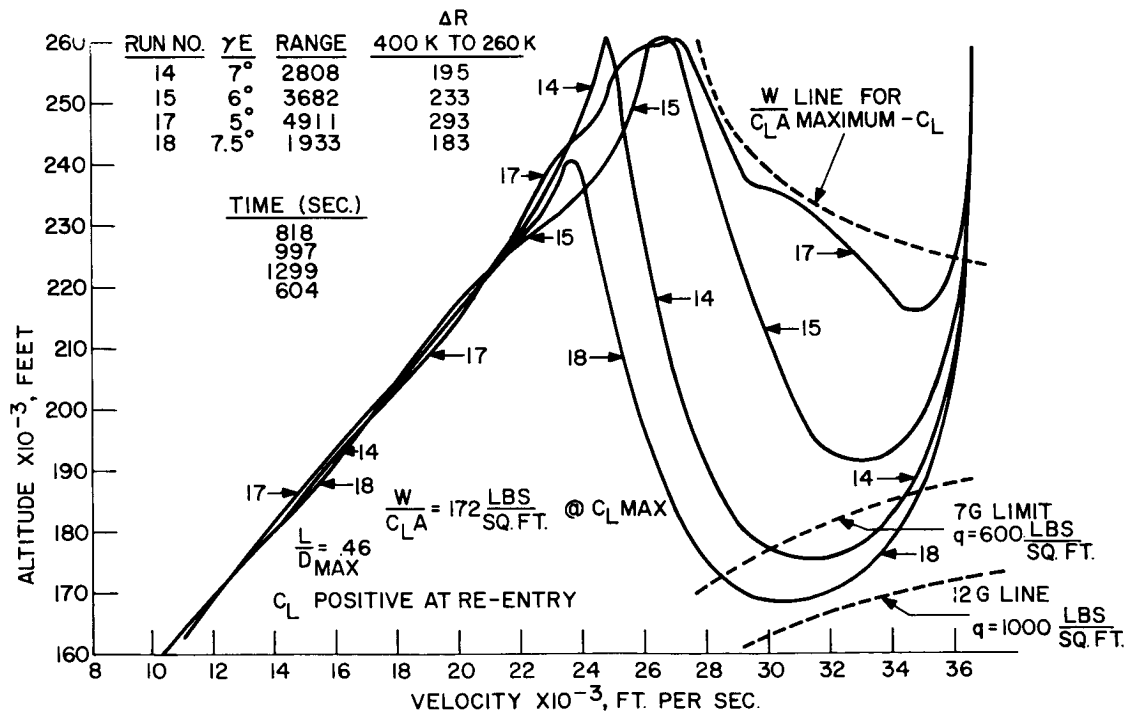


Figure VIII-6-9. Altitude versus velocity for maximum range, B-2'' configuration Runs 14 through 18

**CONFIDENTIAL**

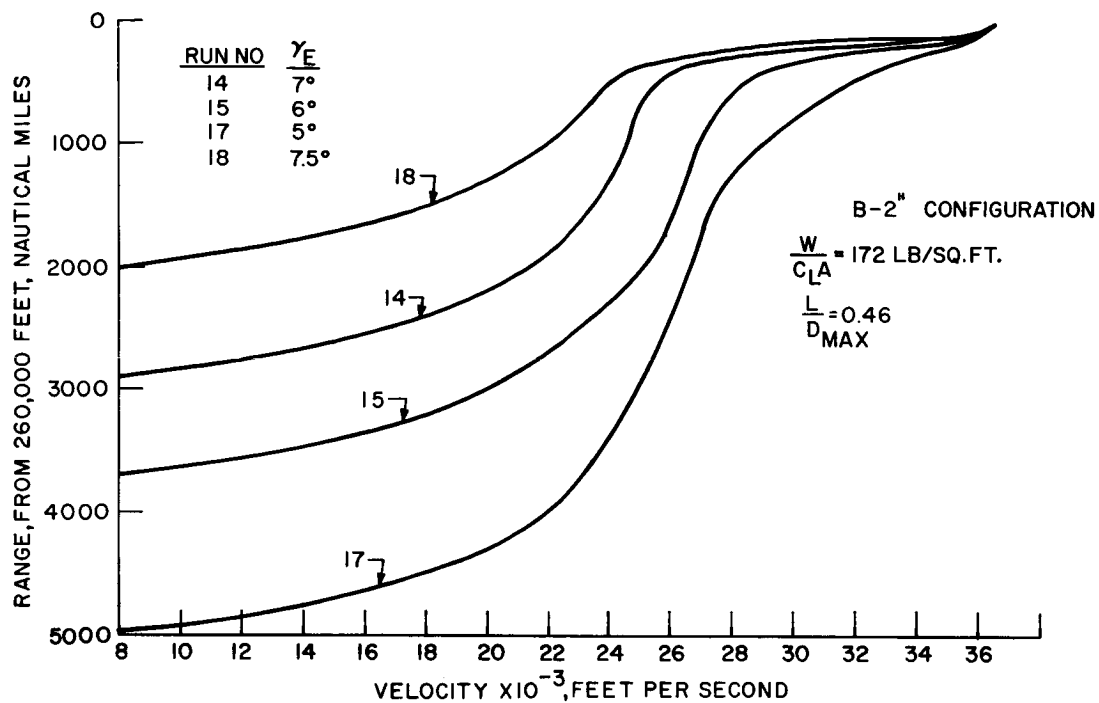


Figure VIII-6-10. Altitude versus velocity for maximum range, B-2'' configuration Runs 14 through 18

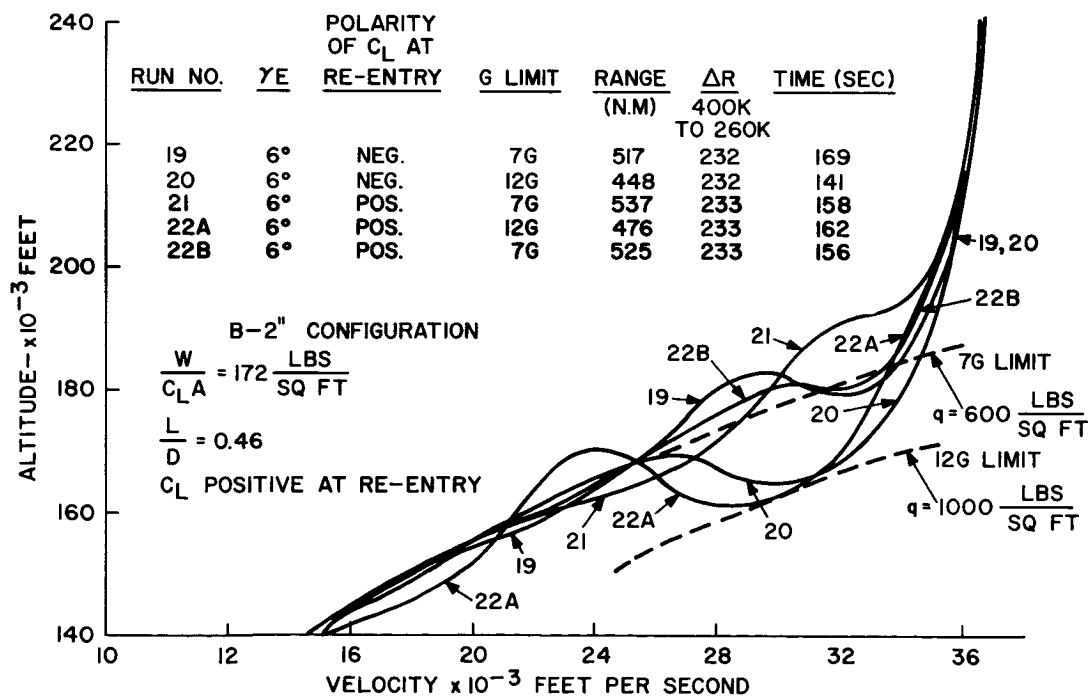


Figure VIII-6-11. Altitude versus velocity for minimum range, B-2'' configuration Runs 19 through 22B

~~CONFIDENTIAL~~

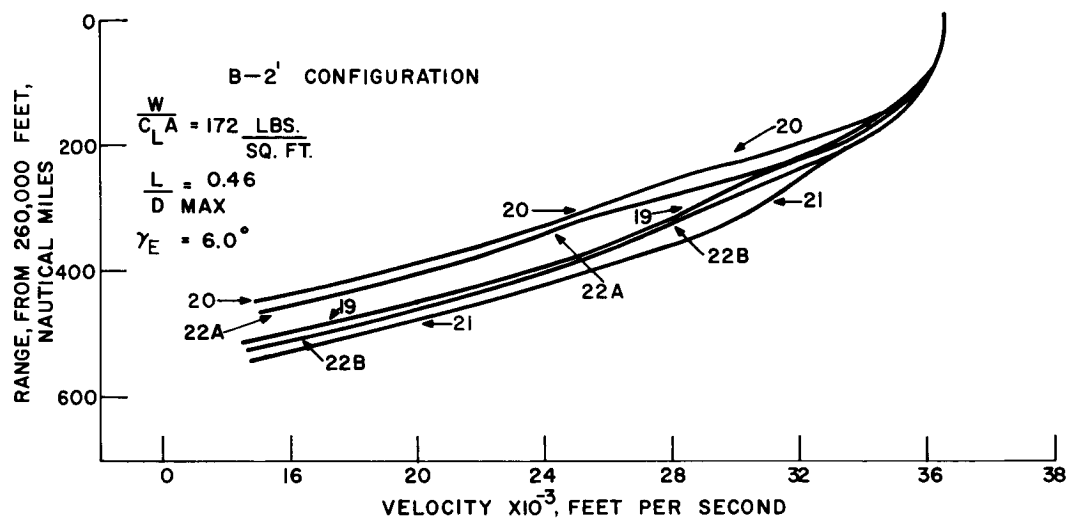


Figure VIII-6-12. Altitude versus velocity for minimum range, B-2'' configuration Runs 19 through 22B

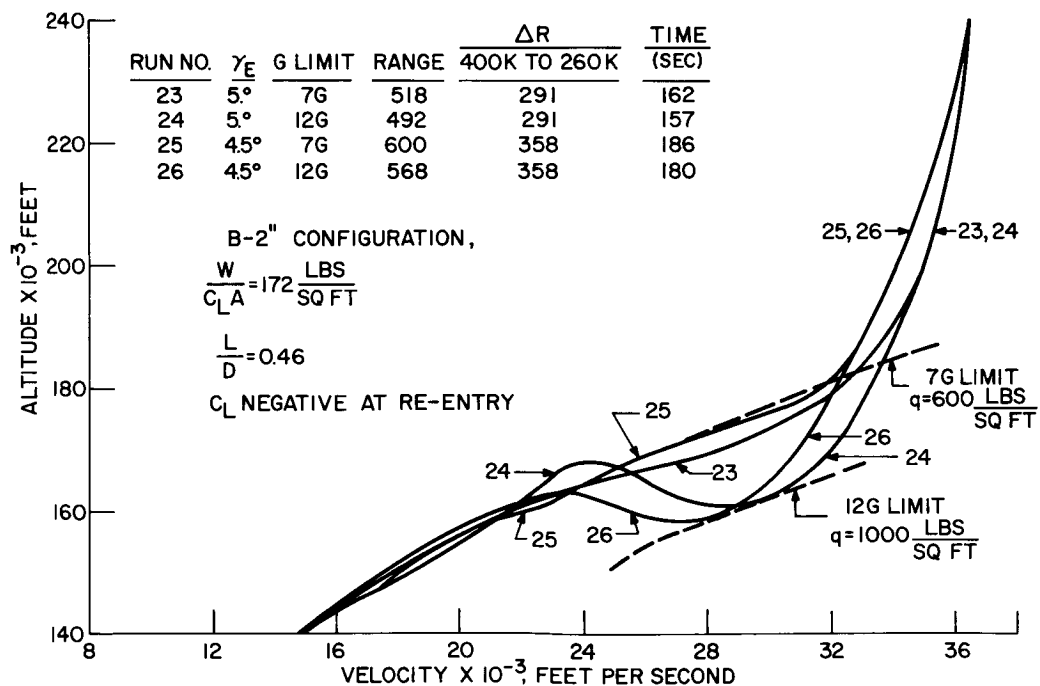


Figure VIII-6-13. Altitude versus velocity for minimum range, B-2'' configuration Runs 23 through 26

~~CONFIDENTIAL~~

**CONFIDENTIAL**

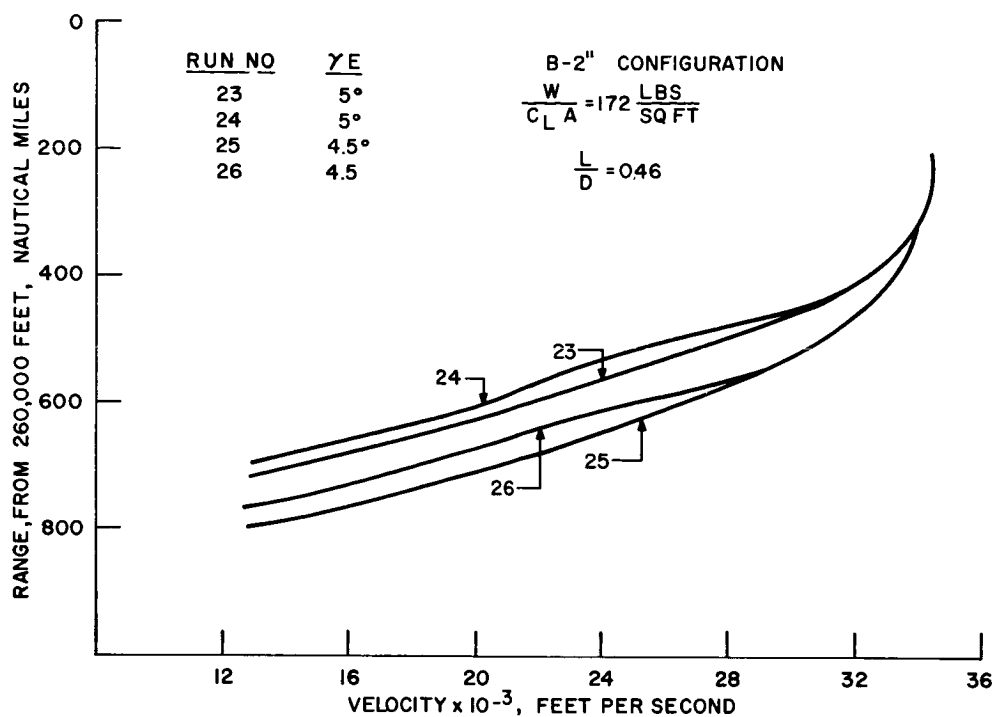


Figure VIII-6-14. Altitude versus velocity for minimum range, B-2'' configuration Runs 23 through 26

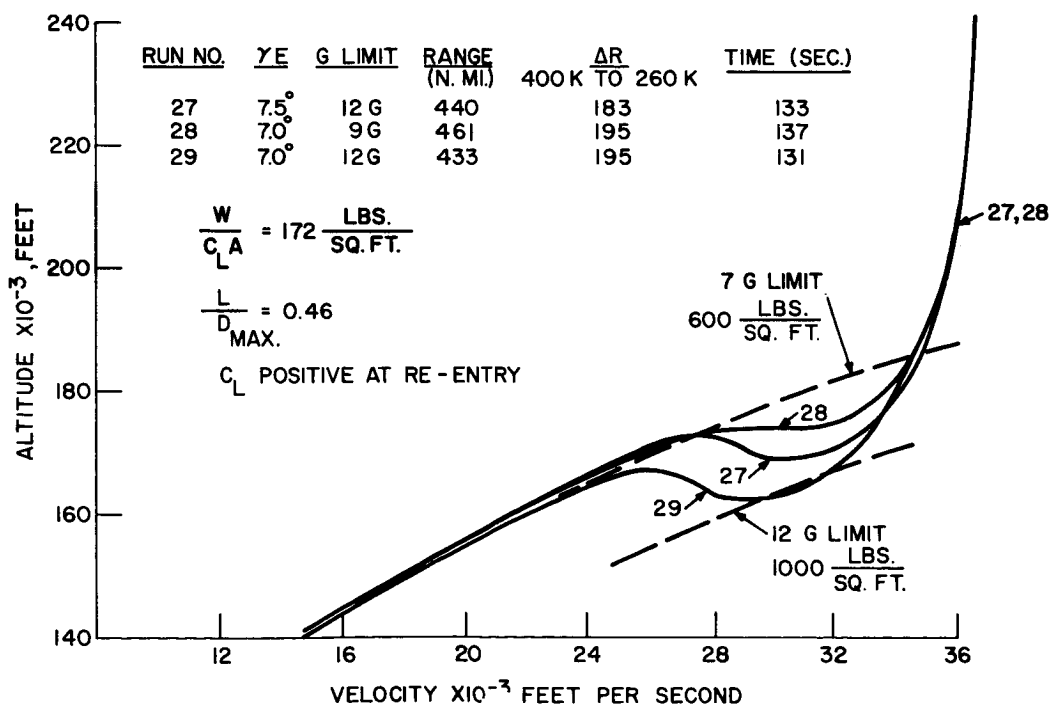


Figure VIII-6-15. Altitude versus velocity for minimum range, B-2'' configuration Runs 27 through 29

**CONFIDENTIAL**

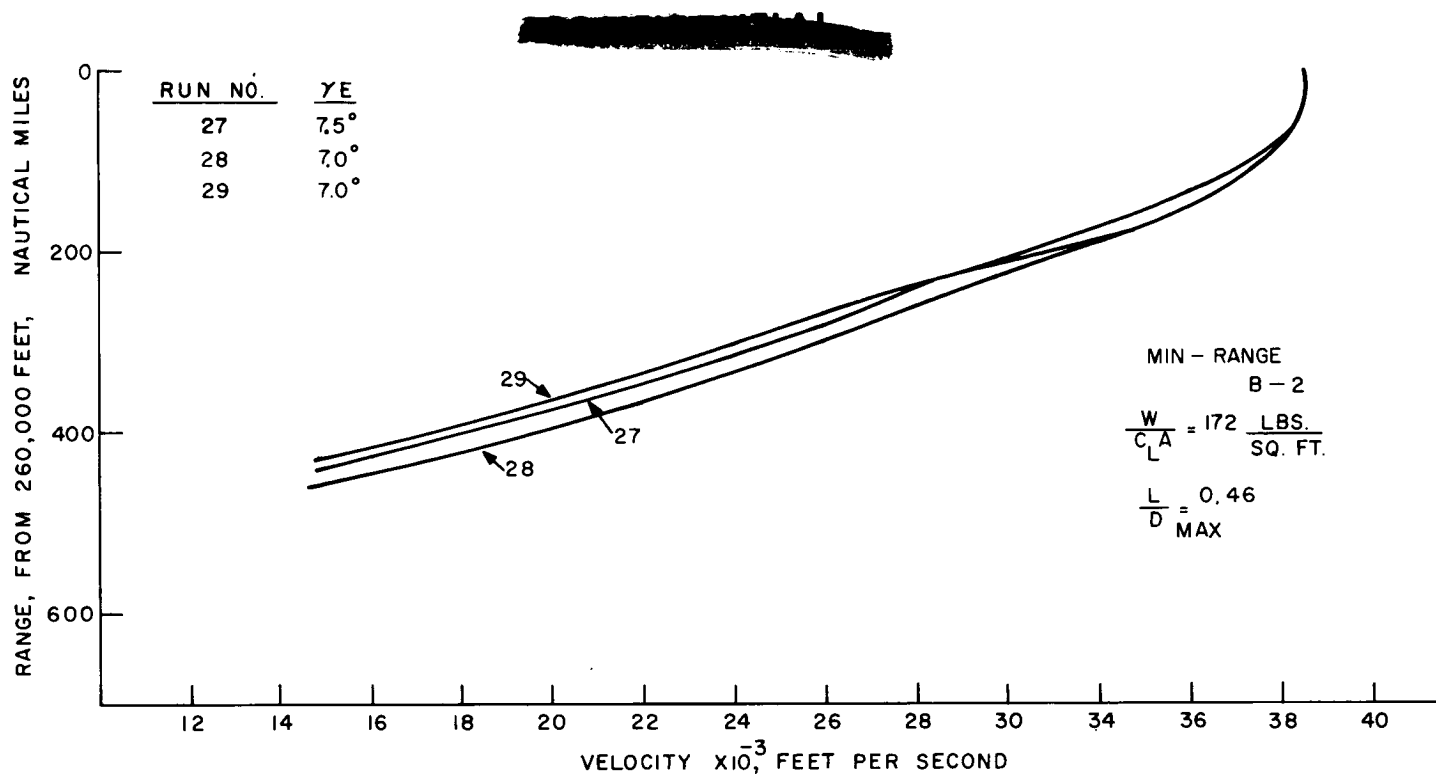


Figure VIII-6-16. Altitude versus velocity for minimum range, B-2'' configuration Runs 27 through 29

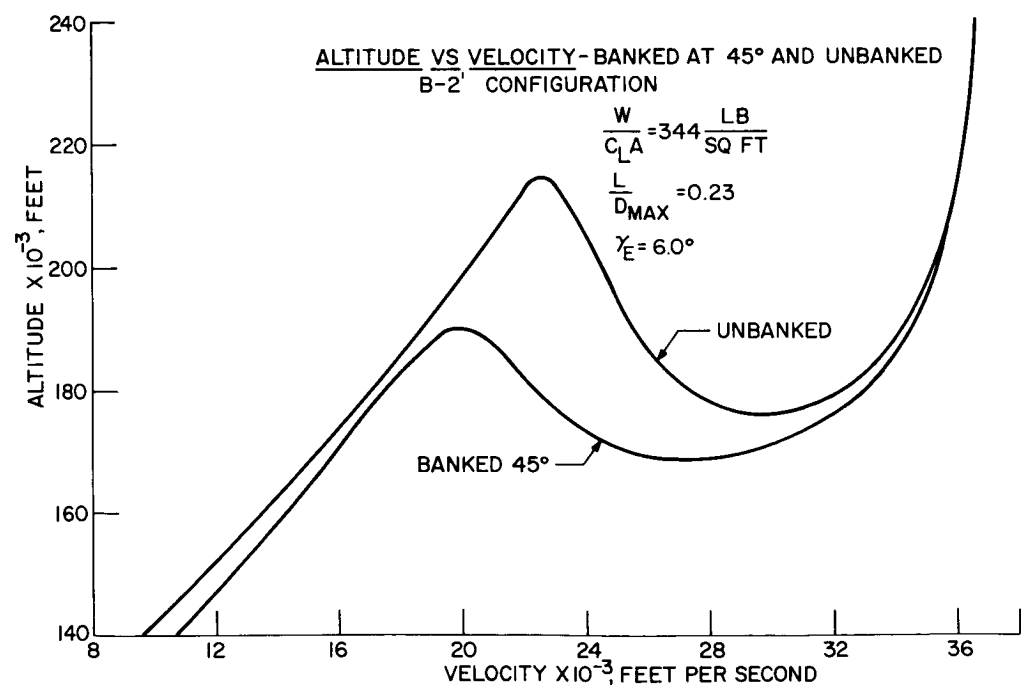


Figure VIII-6-17. Altitude versus velocity, banked at 45 degrees and unbanked, B-2'' configuration

**CONFIDENTIAL**

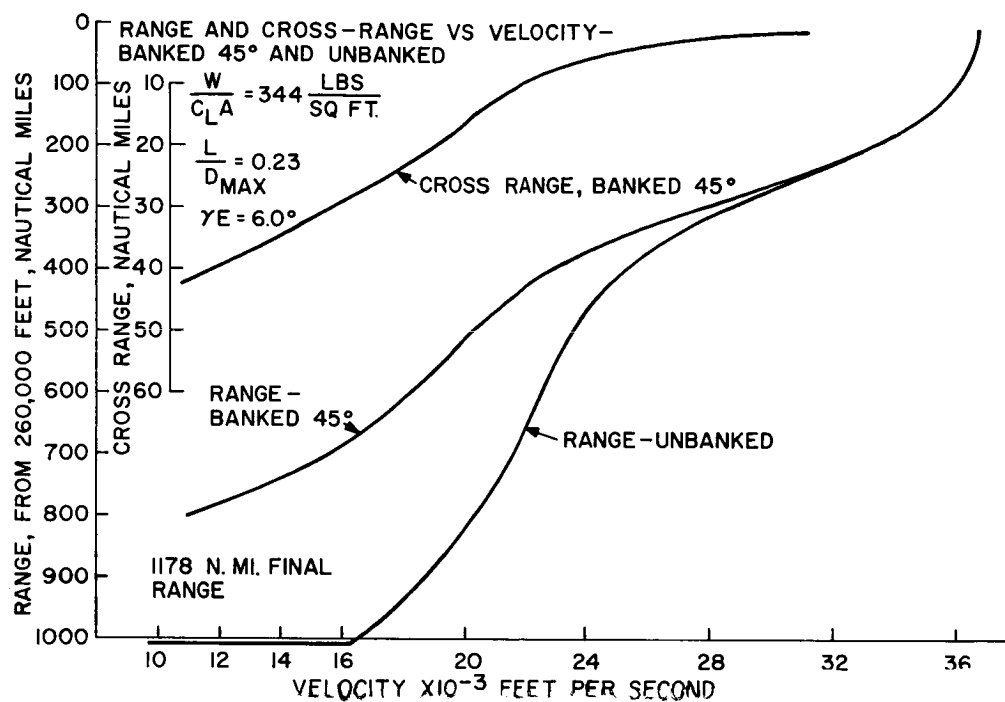


Figure VIII-6-18. Altitude versus velocity, banked at 45 degrees and unbanked, B-2' configuration

**CONFIDENTIAL**

~~CONFIDENTIAL~~

## 7. ATTITUDE CONTROL

The attitude control problem is one of relatively straightforward design. Furthermore, the detailed design of the attitude control system, in particular the use of propulsion versus momentum devices for applying torques to the vehicle, is intimately related to the design of the navigation and guidance system. The following is an estimate of attitude control requirements assuming only an on-off jet attitude control.

When the inertial platform alignment is being checked, all three axes are controlled from the inertial platform gimbal signals plus manual or automatic computer commands. At other times the attitude control system points the solar collector at the Sun. In this case, two axes are controlled by Sun sensor signals and the third by a signal from one inertial platform gimbal angle. During the lunar orbiting phase, two axes are controlled by signals from the body-fixed IR sensors to keep one vehicle axis aligned to the local vertical. The third axis is again controlled by a Sun sensor. For this phase of operation, the solar collector must also be rotated about one axis to keep it aligned to the Sun.

## PROPULSION REQUIREMENTS

As pointed out previously, the path correction engines are gimballed and thus the attitude-control jets are not required to overcome the misalignment torques of these engines. The nozzle thrusts are, therefore, determined by the angular rates at separation. Assuming an angular rate of 3 degrees/sec, a control acceleration of 0.1 degrees/sec<sup>2</sup> should be adequate. For a pitch and yaw moment of inertia of 30,000 slug-ft<sup>2</sup>, this leads to torques of about 50 lb-ft. which can be obtained with a pair of 3-lb thrust nozzles separated by 18 ft (Note that four nozzles are required about each axis to provide torques in both directions). Since the roll moment of inertia is roughly half that in pitch and yaw, the roll nozzle thrusts would only need to be 1.5 lb.

~~CONFIDENTIAL~~



~~CONFIDENTIAL~~

In order to realign the inertial guidance platform, the vehicle must be rotated so that certain stars can be seen through the window in the re-entry vehicle. At most this requires three 180-degree rotations, and that we make these rotations as rapidly as possible with the available torque. The time required for each 180-degree rotation is then 59 second and the impulse required for three rotations is  $3 \times 6 \times 59 = 1060$  lb-sec. Assuming we require ten such realignments, the total impulse is 10600 lb-sec.

Throughout most of the flight the system is in a deadband oscillation. For a control acceleration of about  $0.1 \text{ degree/sec}^2$  and estimated pickup and dropout propulsion delays of 20 milliseconds, the average limit cycle rate will depend primarily on the threshold of the rate gyros. Taking this as  $0.05 \text{ degree/sec}$  (a value easily obtained) and assuming a  $\pm 10$  degree deadband, corrections are made, on the average, every 400 seconds. Each correction requires an impulse of

$$I = 2 \times \frac{.05}{57.3} \times \frac{30000}{9} = 5.8 \text{ lb-sec}$$

The total impulse in 14 days is then

$$I = 5.8 \times \frac{14 \times 24 \times 3600}{400} = 17,600 \text{ lb-sec}$$

Since the roll thrusts are half those of pitch and yaw, we multiply this number by 2.5 to get a total of 44000 lb-sec for the three channels.

Compared to these numbers, the impulse required to keep one axis of the vehicle aligned to the local vertical during lunar orbiting is quite negligible. The angular change required is equal to the difference between true and mean anomaly which is given approximately by

$$\Delta \Theta = 2e \sin 2nt$$

where  $e$  is the eccentricity and  $n$  the mean motion. The angular acceleration is

$$\ddot{\Theta} = 8 en^2 \sin 2nt$$

and the angular impulse per orbit is

$$\text{Ang. Imp.} = 32 en^2 I \int_0^{\frac{\pi}{2n}} \sin 2nt \, dt = 32 en I$$

~~CONFIDENTIAL~~

~~CONFIDENTIAL~~

For the specified lunar orbit  $e = 1/3$  and  $n = \frac{2\pi}{3 \times 3600} = \frac{1}{1800}$  rad/sec

Thus, for eight days and eight orbits per day, the total impulse required would be

$$\text{Imp.} = \frac{32}{3} \left( \frac{1}{1800} \right) \left( \frac{30000}{9} \right) \times 64 = 1260 \text{ lb-sec}$$

Attitude control impulse is also required to rotate the vehicle about the local vertical to keep the solar collector pointed toward the sun. This is of the same order of magnitude as that required to keep the vehicle aligned to the vertical.

Adding these figures we get a total impulse requirement of approximately 60000 lb-sec. For a specific impulse of 300 sec the corresponding propellant weight is 200 lb. The attitude control system design will be further studied to determine what weight saving can be achieved through the use of momentum torquing devices.

The above analysis applies to the mid-course navigation scheme described in Section VIII-4 as System No. 1. The total impulse required for system No. 2 would be somewhat higher due to the necessity of rotating the vehicle to take fixes.

Attitude control propulsion is also required for roll control of the re-entry vehicle. Angle of attack control is achieved by a single controllable flap. Thus in order to provide pitch up and pitch down maneuvers as well as cross-range maneuvers in both directions, it is necessary to properly orient the vehicle in roll, which is accomplished by four roll nozzles.

A maximum roll maneuver required is a 180 degree roll in 10 seconds. For a roll moment of inertia of 860 slug-ft<sup>2</sup>, this requires a torque of about 110 lb-ft. On the re-entry vehicle this can be achieved by pairs of nozzles of 18 lb thrust, since the separation between them is about six-ft. The roll torque due to misalignment of the flap is considerably less than this. It is estimated that flap misalignment will be on the order of 0.1 degree. For typical force on the flap of about 1000 lbs, which results in a roll torque of  $\frac{0.1}{57.3} \times 1000 \times 4.5 = 7.5$  lb-ft.

The impulse required to make each 180 degree rotation is  $2 \times 18 \times 10 = 360$  lb-sec. Assuming that five such orientation changes are required during re-entry we get a total of 1800 lb-sec. The maximum re-entry time of flight is about 2000 seconds.

**CONFIDENTIAL**

Thus the impulse required to overcome aerodynamic roll torque is  $\frac{7.5}{3} \times 2000 = 5000$  lb-sec. the total impulse required for re-entry roll control, then, is approximately 7000 lb-sec.

The following two sub-sections give a brief description of the present state of development of the MSVD IR horizon sensors and Sun. Sensors which would be used for attitude control as described above.

## **INFRARED HORIZON SENSING SYSTEMS**

Three generations of horizon sensing systems have been manufactured, tested, and flown by GE/MSVD to control the attitude of space vehicles. See Tables VIII-7-1,2, and 3.

The first was a fixed field of view (18 degrees) detector. A long, thin bolometer element was placed in the image plane of a germanium lens. The dimensions of the bolometer corresponded to 18 degrees by 4 degrees of the image plane. A Nipkow reticle sequentially scanned segments down the length of the bolometer. By comparing the radiation from the sky or the earth with that from the reticle a horizon position was determined. Three such sensors were used with each system. The accuracy was about  $\pm 2$  degrees, the weight 5 lbs each, and power about 5 watts. This system was flown on G-E re-entry vehicles.

The second generation sensors also flown on re-entry vehicles, used a 2 degree x 4 degree aperture bolometer immersed in germanium at the image plane. A prism lens rotated to scan a cone having a 90 degree apex angle. The temperatures of the Earth and space were converted to rectangular electrical pulses. These and a reference signal associated with the reference axis on the vehicle were converted, by means of an analogue computer, with a signal proportional to the angular difference between the reference line and the geophysical local vertical. The accuracy of these sensors was  $\pm 1$  degree, the weight 7 lbs and the power 5 watts. Two were required for each system, one on each of two axes.

The third and most recent development was designed for and flown on a high-altitude rocket program in September - November 1960. The basic system was similar to the

**CONFIDENTIAL**

~~CONFIDENTIAL~~

second design (Mark 3CT system) but digital data processing was employed. The size was reduced, the measured laboratory accuracy was between 0.1 degree and 0.2 degree; the weight 5.8 lbs each, and the power 4 watts for the scanner and 9 watts for the associated computer. Two units were required, one mounted on each of two axes.

Sensors presently being designed for the Advent and Nimbus programs will incorporate several design improvements allowing for satisfactory operation at altitudes of up to 20,000 nautical miles. These are being designed for long life performance. The Advent model will use rotating reflecting mirrors for radiation concentration in place of the germanium lens.

Recent investigations indicate that filtering below  $8\ \mu$  and detecting radiation out to 20 to  $40\ \mu$  will permit the use of infrared sensors for Moon dark side tracking. Studies also indicate operation is feasible at altitudes basically greater than even the Advent application.

~~CONFIDENTIAL~~

~~CONFIDENTIAL~~

TABLE VIII-7-1. MARK 3C TP TYPE INFRARED HORIZON SCANNING  
SYSTEM PERFORMANCE DATA

Parts/System	2 scanners, 2 horizon attitude computers
Type Scan:	90 deg apex angle, conical scan
Detector:	Thermistor bolometer; 2 deg by 4 deg field of view, 1.5 ms time constant.
Scan Rate:	30 cps
Application:	Two scanners required to provide control signals to establish the local vertical. Scanners are mounted so that scan axes are perpendicular, i. e. parallel to pitch and roll axes.
Output:	$1 \pm 0.1$ volts (dc)/deg error, Output is limited at 10 deg error.
Frequency Response:	1 cps.
Accuracy:	0.2 deg.
Spectral Sensitivity:	3 - 11 $\mu$
Size:	scanner - 50 cu in; computer - 100 cu in
Weight:	2.5 pounds - scanner; 3.3 pounds - computer
Power Consumption:	4 watts - scanner; 9 watts - computer

~~CONFIDENTIAL~~

TABLE VIII-7-2. NIMBUS TYPE, INFRARED HORIZON SCANNING SYSTEM  
PERFORMANCE DATA

Parts/System:	2 scanners, 2 amplifiers, 1 horizon attitude computer
Type Scan:	90 deg apex angle, conical scan
Detector:	Thermistor bolometer; 2 deg by 4 deg field of view; 1.2 ms time constant.
Scan Rate:	30 cps.
Application:	Two scanners required to provide control signals to establish the local vertical. Scanners are mounted so that scan axes are parallel opposing i.e. in opposite directions along the roll axis.
Output:	$0.50 \pm 0.1$ volts (dc)/deg error. Output is limited at 30-deg error.
Frequency Response:	1 cps
Accuracy:	0.2 deg
Spectral Sensitivity:	Cut in at 8 microns, peak at 10 microns.
Size:	(4.5 inch dia by 3.3 inch long) (Each scanner)
Weight:	15 pounds (2 scanners, 2 amplifiers, 1 computer)
Power Consumption:	18 watts (2 scanners, 2 amplifiers. 1 computer)

~~CONFIDENTIAL~~

**CONFIDENTIAL**

**TABLE VIII-7-3. ADVENT TYPE INFRARED HORIZON SCANNING SYSTEM  
PERFORMANCE DATA**

<b>Parts/System:</b>	2 Scanners, 2 Horizon Attitude Computers
<b>Type Scan:</b>	360 deg. rotational scan; 230 degrees sector viewed; 90° actual sector.
<b>Detector:</b>	Thermistor bolometer; 2 deg by 2 deg field of view, 1.2 ms time constant.
<b>Scan Rate:</b>	24 cps.
<b>Application:</b>	Two scanners required to provide control signals to establish the local vertical. Scanners are mounted so that scan planes are perpendicular; i.e. parallel to pitch and roll axes.
<b>Output:</b>	0.32 ± 0.03 volt (dc)/deg. error. Output of scanner is one deg. phase shift of earth pulse to reference pulse per degree error.
<b>Frequency Response:</b>	2 cps
<b>Accuracy:</b>	0.1 deg.
<b>Spectral Sensitivity:</b>	13 to 26 microns
<b>Size:</b>	7 inch dia by 11 inch (Scanner) 6" x 4" x 9-3/4" (computer)
<b>Weight:</b>	8-1/2 pounds (Scanner) 6 lb. (computer)
<b>Power Consumption:</b>	12-1/2 watts (Scanner) 10 watts (computer)

**CONFIDENTIAL**

~~CONFIDENTIAL~~

## SUN SENSING SYSTEMS

Sun sensing systems were flown on Mark 2, Mod IE vehicles (1959) and their outputs were used to control successfully one axis of the vehicle. The sensor and its successive developments are static devices and have no moving parts.

The sensors which were flight tested successfully consisted essentially of a housing, a slit opening and two lead sulfide detectors. The slit was shaped to compensate for the daily variations of the sun with respect to the vehicle and to cast a narrow ray of sunlight at right angles to the two detectors. The oppositely-biased detectors were separated by an angular distance equal to the width of the ray. Vehicle motion about the axis being controlled resulted in a motion of the sun's ray across the detectors. Electronic circuits converted the output signal from the detectors to produce a voltage proportional to the angular position error. The pneumatic control system torqued the vehicle to a position to null the sensor output signal. The weight of these sensing systems were approximately 5 lbs, the accuracy 2 degrees, and the power 3 watts.

Sun sensors presently under development for the Advent and Nimbus program use solar voltaic cells and operate passive null detectors. No input electrical power is required. A number of cells are arranged in such pattern that if their angular position with reference to the sun is changed a voltage will be generated proportional to the deviation angle. The field of view is specified by the intended application and mounting positions on the vehicle. For a given solar azimuth angle the output is constant for solar elevation angles of  $\pm 45$  degrees. The approximate weight of these sensors is 3 lbs; the reproducibility of the calibration transfer function is  $\pm 0.1$  degrees. These particular sensors are being designed for continuous operation for three-year life. Redundant features have been included in the design to assure high reliability. See Tables VIII-7-4 and 5.

~~CONFIDENTIAL~~



~~CONFIDENTIAL~~

TABLE VIII-7-4. PERFORMANCE DATA  
ADVENT COARSE SUN SENSOR

Detector:	Photovoltaic cells
Application:	Four units mounted to provide complete spherical coverage.
Output:	$0.001 \pm$ volts (dc) deg deviation
Precision:	0.5 deg.
Size:	6.5 inch dia by 2.9 inch per sensor (2 units)
Weight:	3 lbs per sensor (2 units) 6 lbs total
Power Consumption:	None

TABLE VIII-7-5. PERFORMANCE DATA  
NIMBUS FINE SUN SENSOR

Detector:	Photovoltaic cells
Application:	One unit mounted to provide solar azimuth angle for telemetry.
Output:	$0.0015 \pm$ volts (dc)/deg. error.
Precision:	0.1 deg.
Size:	4 inches by 4 inches by 3 inches
Weight:	0.85 lb
Power Consumption:	None

~~CONFIDENTIAL~~

~~CONFIDENTIAL~~

## 8. NAVIGATION, GUIDANCE, AND CONTROL SYSTEM SUMMARY

A list of the equipment which comprises Navigation, Guidance, and Control System No.1, along with weight and power requirement information, is presented in Table VIII-8-1. A similar list for Navigation, Guidance, and Control System No. 2 is presented in Table VIII-8-2.

Some additional remarks with respect to some of the entries in these tables are pertinent.

(a) The auxiliary navigation equipment has not been defined at this time. The 25 pounds allocated allows for equipment such as a sextant theodolite or camera which the astronauts can use to obtain backup navigation information manually. This question is discussed in section VIII-4C.

(b) The estimate for display equipment weight includes only that used for displaying navigation, guidance, and control information. The weight estimate made for the total life support subsystem includes this equipment, but the estimate is listed here for the sake of completeness.

(c) Navigation aids at the present time include only a radar beacon which is carried in the APOLLO vehicle in order to make it possible to obtain backup vehicle position information. A study to determine feasibility of using Earth satellites as navigation aids is being initiated.

(d) A radar altimeter is included in the list at the present time in order to assure the availability of accurate altitude information prior to re-entry. The same equipment would also be used to measure altitude above the lunar surface when the vehicle is in the vicinity of the Moon. However, further study may indicate that this equipment is not required, since it may be possible to obtain initial re-entry conditions with sufficient accuracy by means of midcourse navigation equipment. Altitude measurements with respect to the Moon can be made by means of the IR sensors which can measure the angle subtended by the Moon. A radar set will, of course, be required for other possible APOLLO missions, such as lunar landing and satellite rendezvous, although the requirements are different in each case.

~~CONFIDENTIAL~~

~~CONFIDENTIAL~~

TABLE VIII-8-1. NAVIGATION, CONTROL, AND GUIDANCE SYSTEM  
SUMMARY, SYSTEM NO. 1

	Weight, lbs	Power, watts	Remarks
Inertial Platform & Electronics	40	200	Includes accelerometers & fixed startrackers
Tracker Platform & (am- pers-and) Electronics	45	100	Includes astrotrackers
Computer	50	100	
Attitude Control	260	150	Electronics, Rate Gyros, Valves and Tubing
Re-entry Flight Control	75	200	Flap Actuator, autopilot amplifier, roll jet system
IR Sensor & Electronics	13	15	Body Fixed, 2 Required
Aux. Nav. Equipment	25		
Display Equipment	100		
Navigation Aids	25	30	Radar Beacon for Backup Guidance
Radar Altimeter	50	300	May be required for Lunar Terminal & Re-entry Fix
Total System Weight	695		

~~CONFIDENTIAL~~

~~CONFIDENTIAL~~

TABLE VIII-8-2. NAVIGATION, CONTROL, AND GUIDANCE SYSTEM  
SUMMARY, SYSTEM NO. 2

	Weight, pounds	Power, watts	Remarks
Platform	6	1	Two gimbal platform with gimbal drive
Star Tracker	5	Low	
Earth/Moon Horizon Tracker	9	6 (inter)	Two vidicons
Gyro Package	10	2 (cont.) 2.5 (inter)	Includes 2 gyros and amplifiers
Accelerometer Package	1.2	Low	Includes 3 accelerometers
Computer	50	100	
Attitude Control	260	150	Electronics, rate gyros, valves, tubing, momentum package
Re-entry Flight Control	75	200	Hydraulic actuators, autopilot amplifiers
Manual Navigation Equip.	25		
IR Sensor & Electronics	13	15	Body fixed, 2 required
Navigation Aids	25	30	Radar Beacon for Backup Guidance
Radar Altimeter	50	300	May be required for lunar terminal and re-entry fix
Display Equipment	100		
Electronics	13	4 (cont) 1 (inter)	Includes digital input-output equipment, accelerometer and gimbal drive amplifiers

Total System Weight      655

~~CONFIDENTIAL~~

~~CONFIDENTIAL~~

**CHAPTER IX**

**AERODYNAMICS, THERMODYNAMICS  
& RE-ENTRY HEAT PROTECTION**

~~CONFIDENTIAL~~

~~CONFIDENTIAL~~

## IX. AERODYNAMICS, THERMODYNAMICS, AND RE-ENTRY HEAT PROTECTION

### 1. AERODYNAMICS

#### INTRODUCTION

A variety of aerodynamic shapes, covering the range from ballistic through glide vehicles, has been studied and their basic aerodynamic characteristics (including trim capabilities) are discussed here. The trimmed condition for the ballistic vehicles was achieved with the use of chin flaps or movable fins.

#### B-2 CONFIGURATION

This semi-ballistic vehicle is shown in Figure IX-1-1. Its longitudinal aerodynamic characteristics at hypersonic speeds as computed by modified Newtonian theory are presented in Figures IX-1-2 through IX-1-5, inc. Trimmed lift-to-drag ratio in the order of 0.24 at approximately  $\alpha = -30$  degrees is achieved using the flap deflected to an angle of 90 degrees with respect to the free stream. The lift-curve slope for this basic vehicle is negative, and positive  $(L/D)$  is achieved with the vehicle flying at negative angles of attack. Because of  $-C_{L\alpha}$  associated with this shape and the position of the center gravity for stable flight, the flap lift will augment the body lift; hence, increasing the  $(L/D)$ . The B-2 configuration is stable over the entire flight Mach number range and is dynamically stable above  $M \approx 1.1$ . A low amplitude limit cycle oscillation is expected to develop at  $M < 1.1$ . This, however, is of little or no significance, inasmuch as the B-2 vehicle will be recovered by parachute or some other deceleration device, which will be deployed at high transonic or low supersonic speeds.

Cross-range maneuver for the B-2 vehicle is accomplished by rolling and pitching the vehicle, so that the flight path is displaced in the lateral direction. The rolling motions are accomplished by jets and pitch (in the yaw plane) by the chin flap.

~~CONFIDENTIAL~~

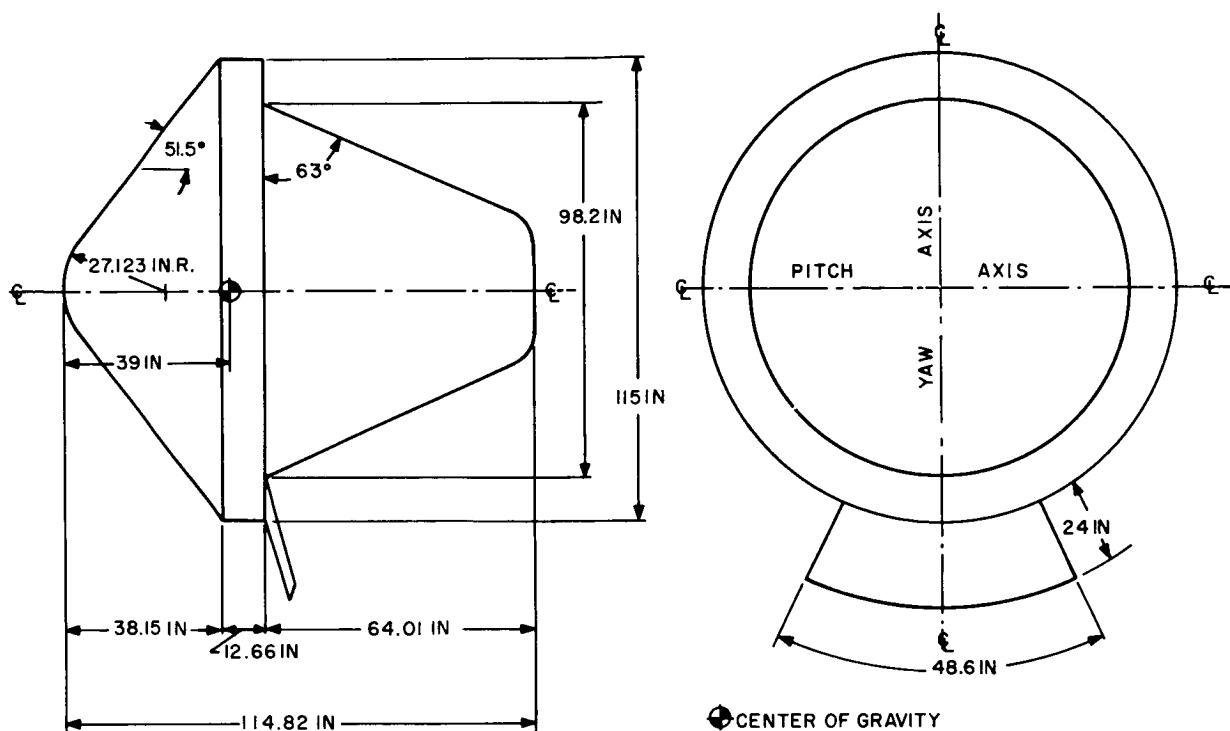


Figure IX-1-1. B-2 configuration

A comparison of small-scale experimental data obtained on the B-2 configuration in the GE/MSVD 6-inch Shock Tunnel at a full stream Mach number of 12.4 [ Reynolds number =  $2.8 \times (10)^5$  based on maximum diameter ] is shown in Figure IX-1-6. Reasonably good agreement between experimental results and Newtonian predictions is observed for the body alone and body with chin flap.

~~CONFIDENTIAL~~

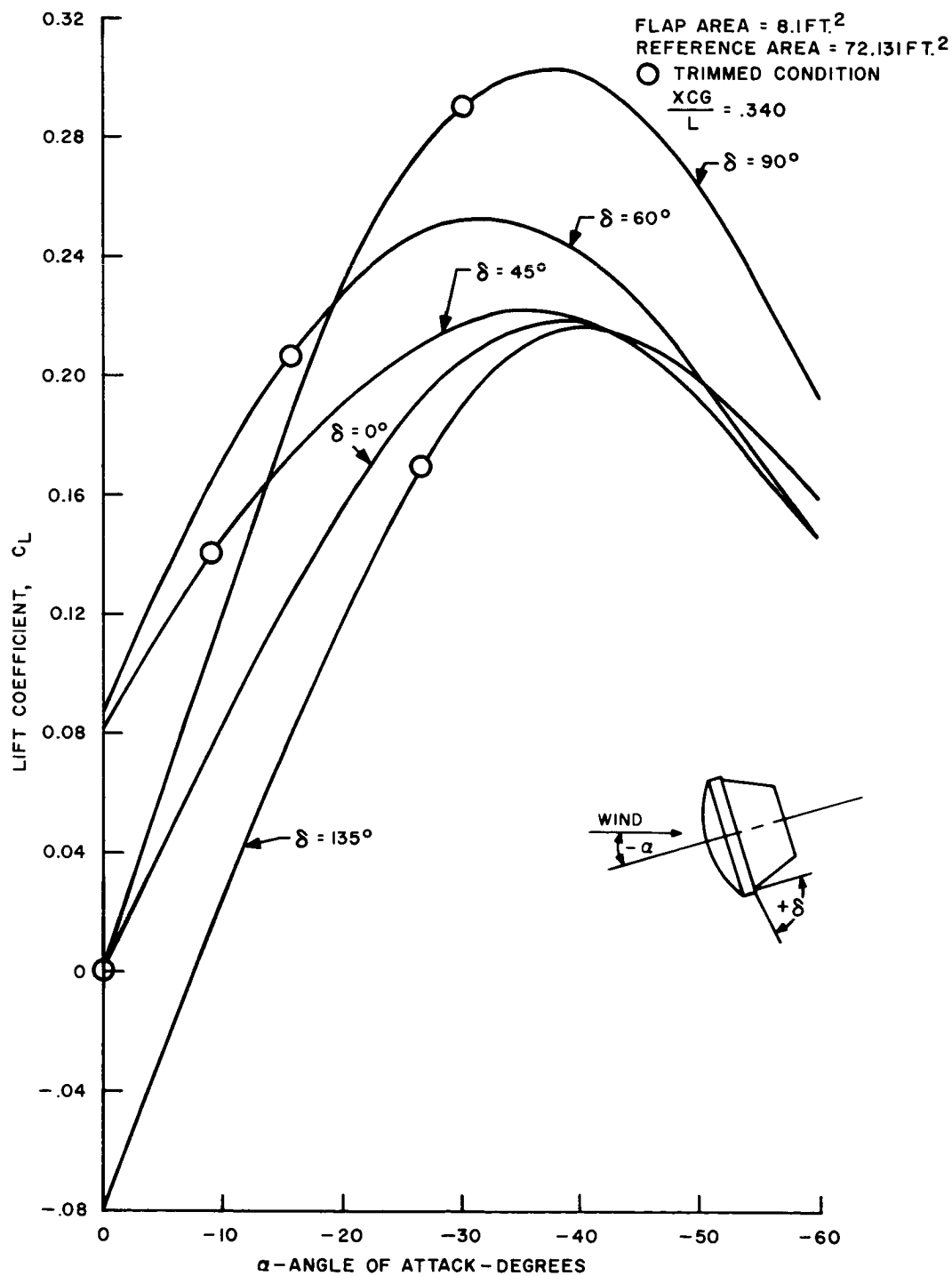


Figure IX-1-2. B-2 configuration — variation of lift coefficient with angle of attack (Newtonian)



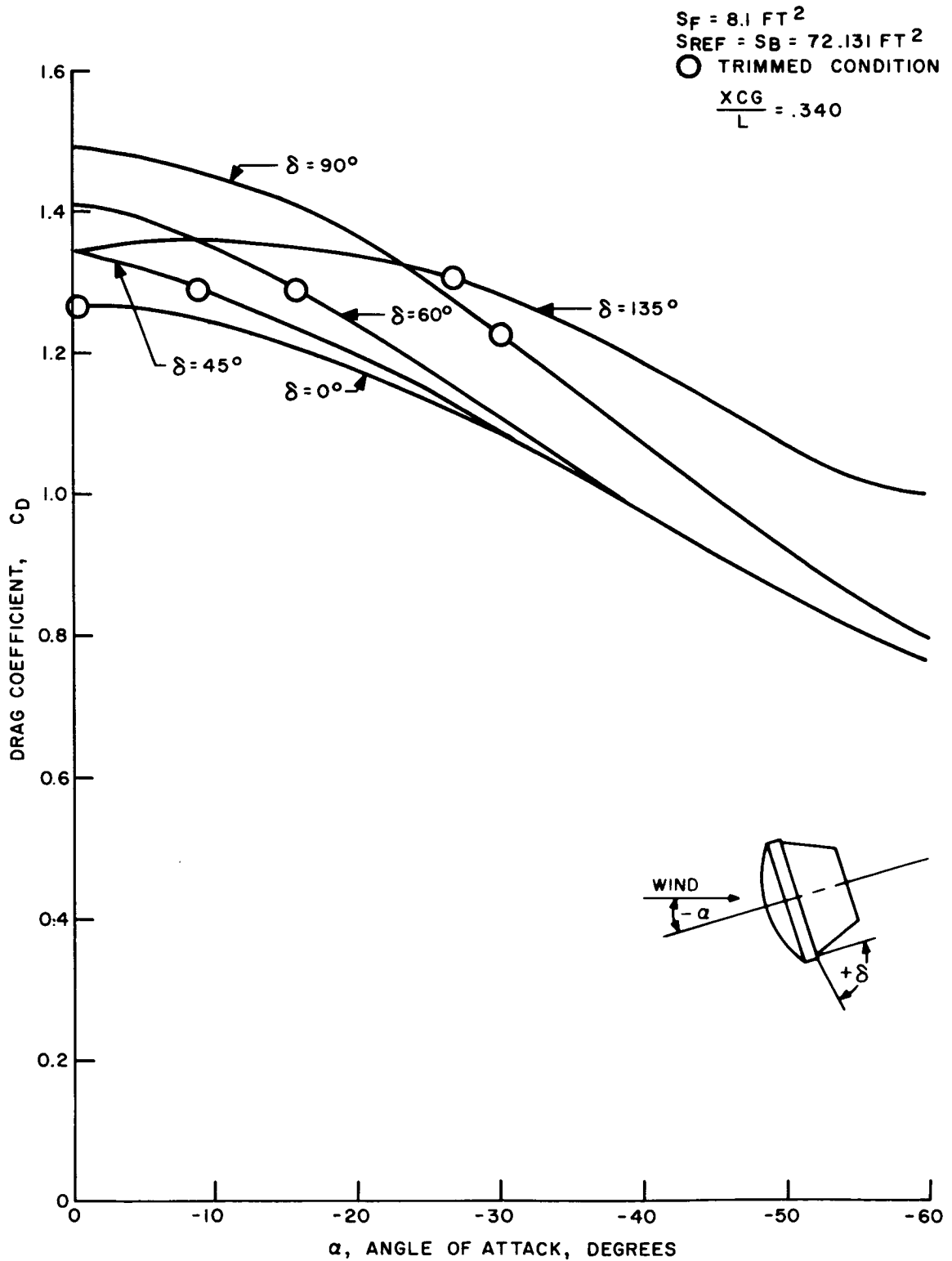


Figure IX-1-3. B-2 configuration — variation of drag coefficient with angle of attack (Newtonian)

~~CONFIDENTIAL~~

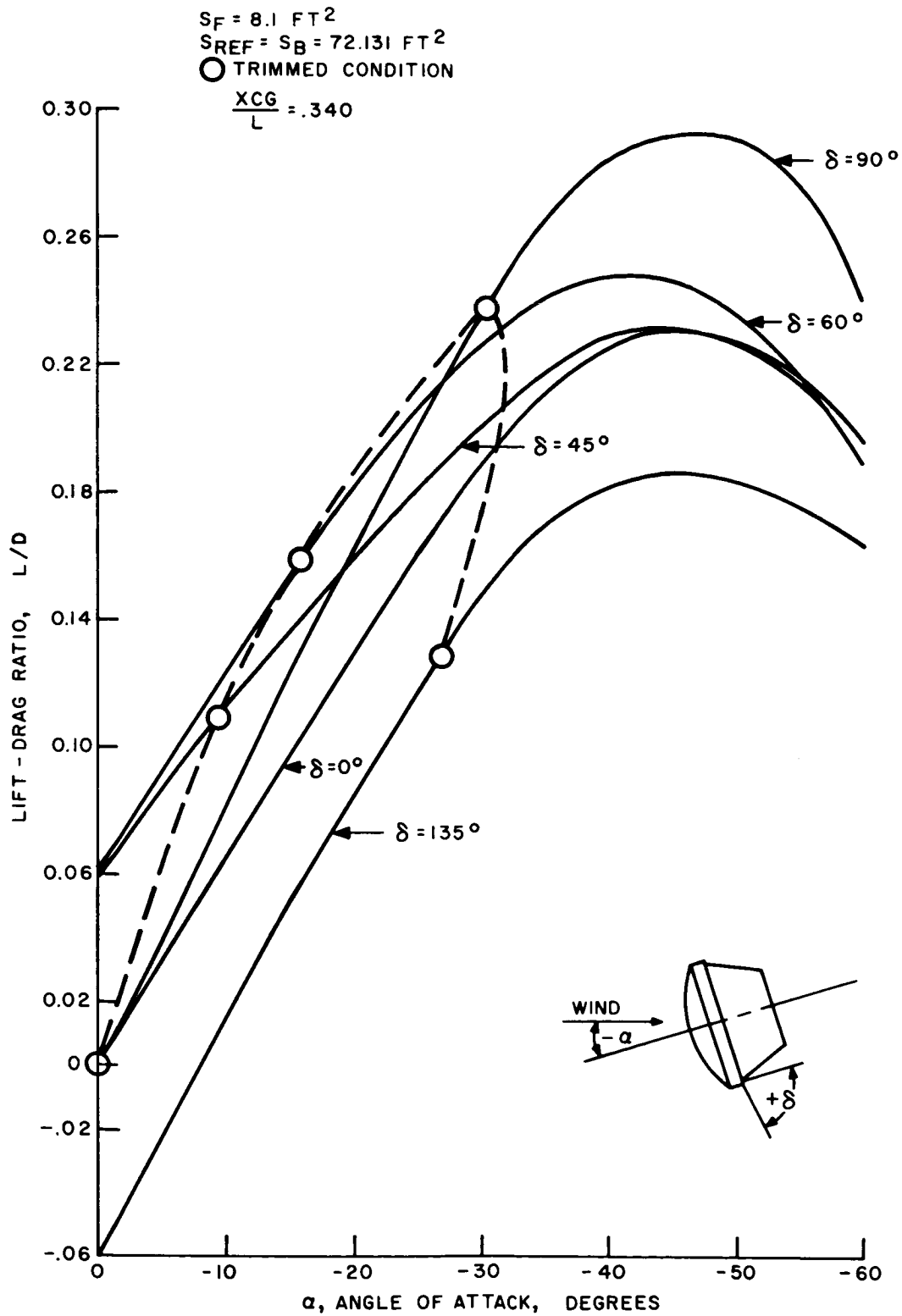


Figure IX-1-4. B-2 configuration — variation of lift-drage ratio with angle of attack (Newtonian)

~~CONFIDENTIAL~~

~~CONFIDENTIAL~~

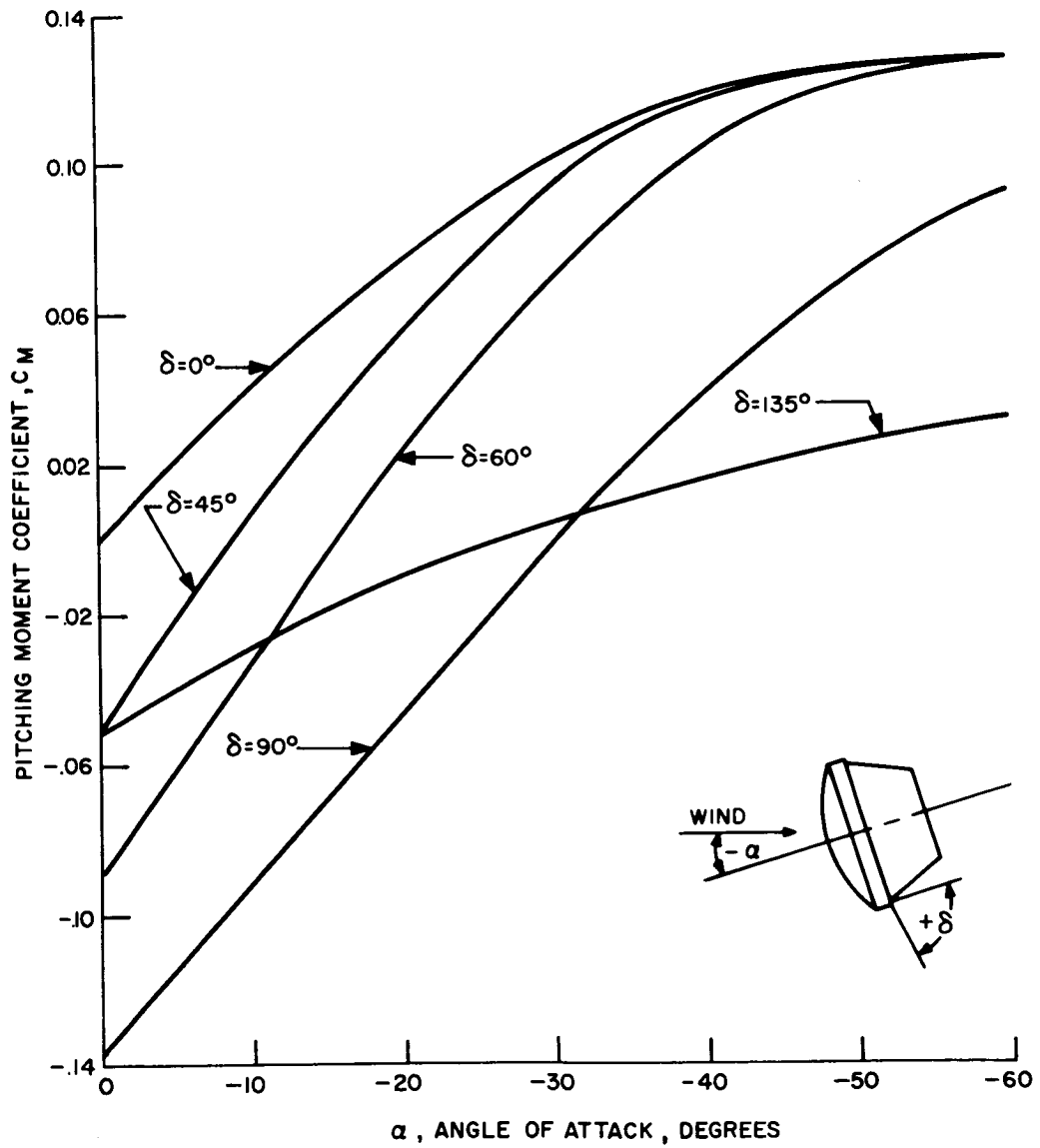


Figure IX-1-5. B-2 configuration — variation of moment coefficient with angle of attack (Newtonian)

~~CONFIDENTIAL~~

~~CONFIDENTIAL~~

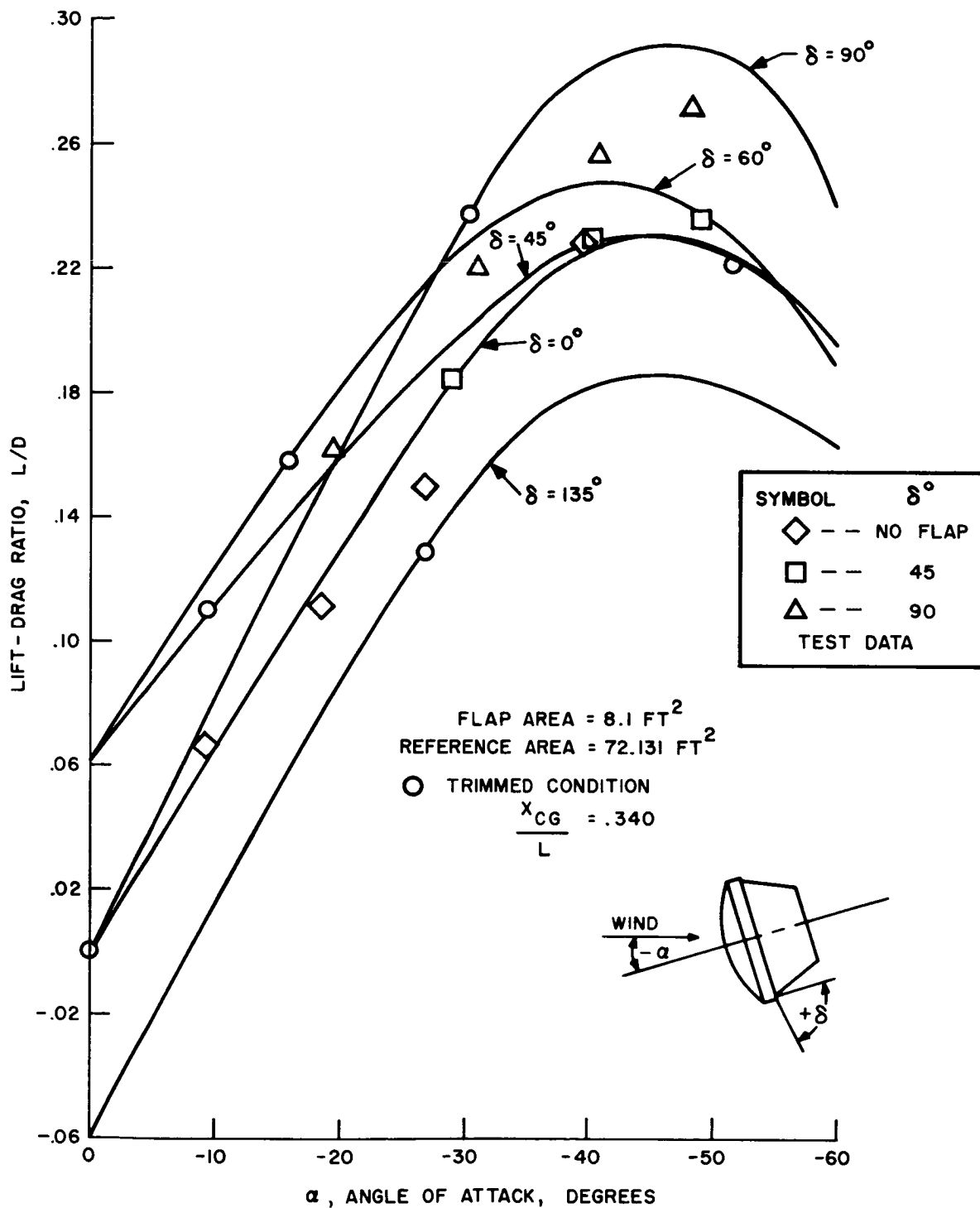


Figure IX-1-6. B-2 configuration — comparison of experimental and calculated variation of lift-drag ratio with angle of attack

~~CONFIDENTIAL~~

## C-1 CONFIGURATION

For this vehicle, shown in Figure IX-1-7, the static longitudinal aerodynamic characteristics and center of pressure variation with angle of attack were obtained from experiments performed in the GE/MSVD 6-inch shock tunnel at Mach number equal to 12.4. Trimmed  $(L/D)_{\max}$  in the order 0.73 at approximately  $\alpha = 23$  degrees is achieved by deflecting the all-movable horizontal control surfaces at negative angle of attack relative to the free stream. The hypersonic trimmed  $C_L$ ,  $C_{D3}$  and  $L/D$  for the basic C-1 vehicle with cruciform, swept control fins deflected at  $\delta = 0$ ,  $-15$  degrees and  $-30$  degrees are given in Figures IX-1-8 through IX-1-10, inclusive.

Directional and lateral control for this vehicle are achieved by deflecting the upper surfaces in unison and the horizontal surfaces differentially. However, additional theoretical and experimental verification of cross-coupling effects on the directional and lateral characteristics of the C-1 vehicle are necessary.

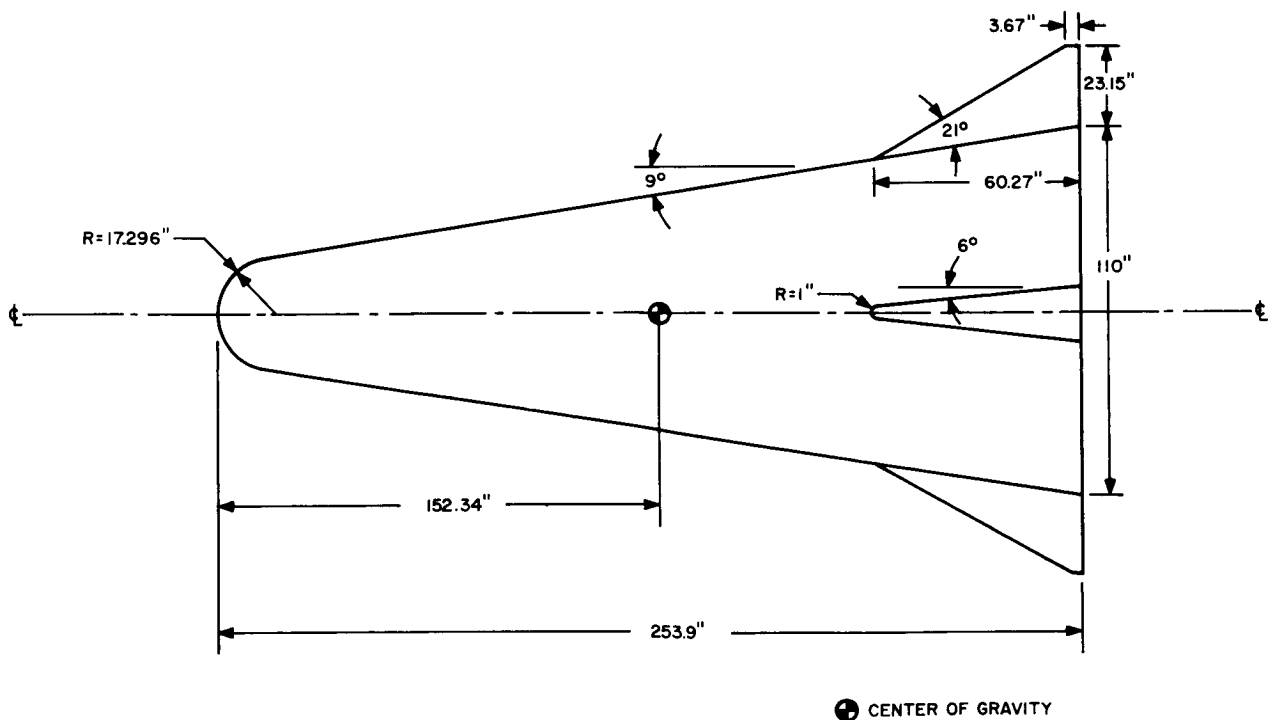


Figure IX-1-7. C-1 configuration

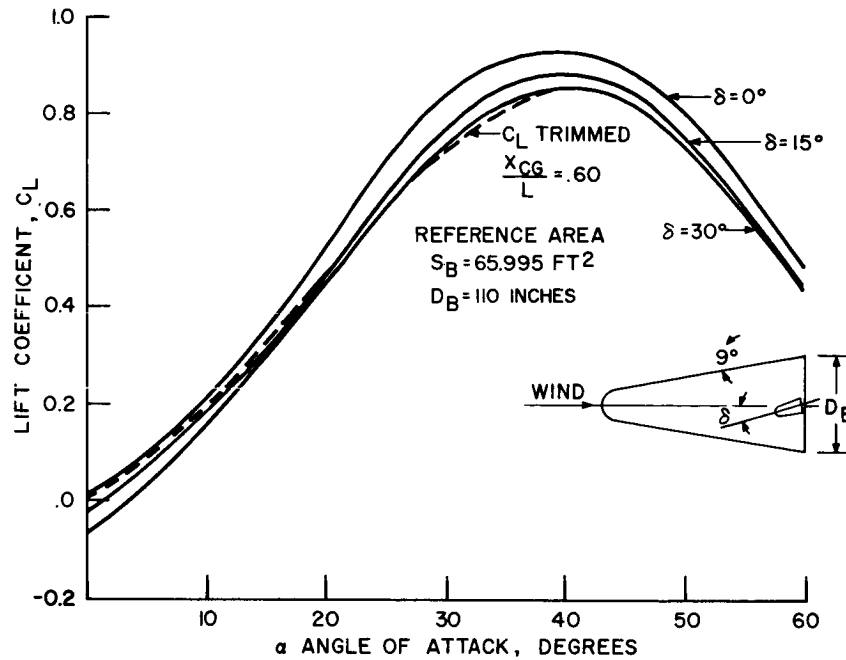


Figure IX-1-8. C-1 configuration — variation of lift coefficient with angle of attack (hypersonic)

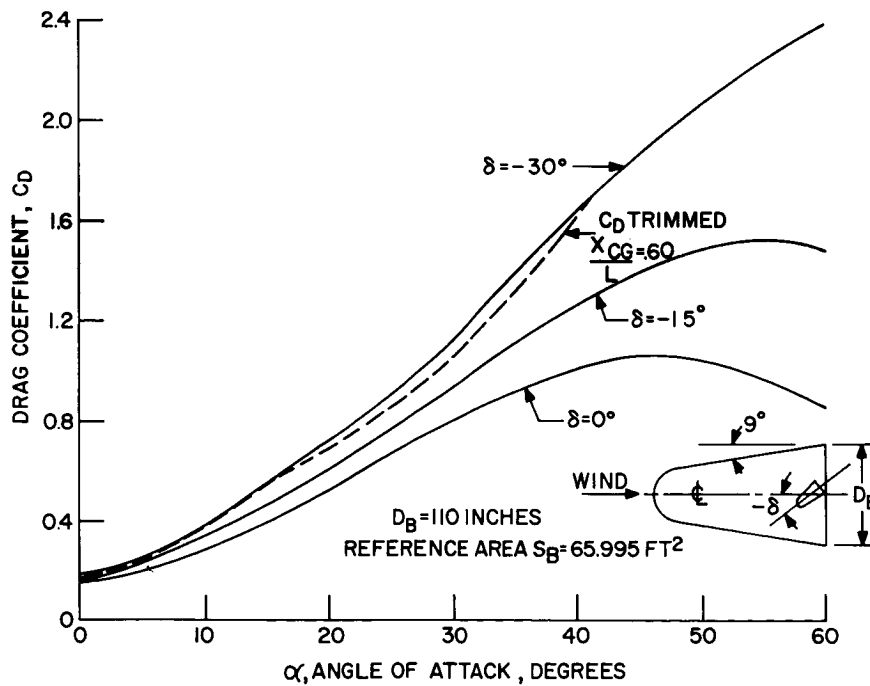


Figure IX-1-9. C-1 configuration — variation of drag coefficient with angle of attack

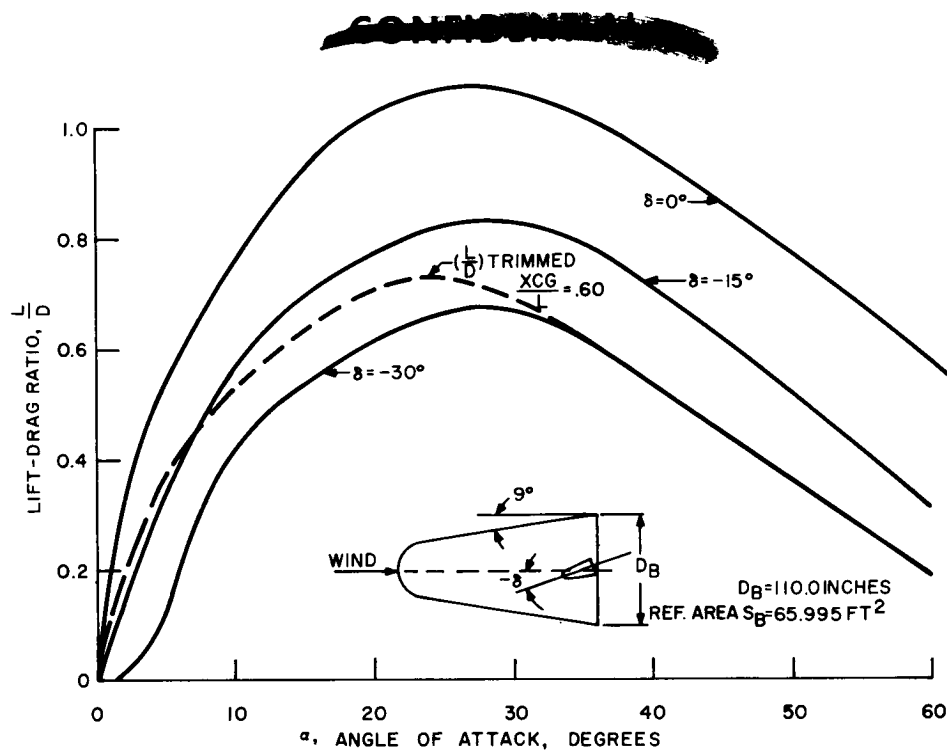


Figure IX-1-10. C-1 configuration — variation of lift-drag ratio with angle of attack (hypersonic)

## D-2 CONFIGURATION

The D configurations were derived from parametric studies of the variation of hypersonic lift-to-drag ratio with angle of attack, for various spherical segments using modified inviscid Newtonian theory. Figure IX-1-11 shows that decreasing the angle between the slope of the segment at its outer edge and the horizontal (thus, approaching the aerodynamically efficient flat plate) results in an increase in  $(L/D)$  for a given angle of attack. A similar parametric study on the effect of afterbody cone angle and afterbody blunting was performed using several forebodies. The results of that study are presented in Figure IX-1-12. From this illustration it is observed that further gains in maximum  $(L/D)$  may be realized by increasing the afterbody cone angle for a given afterbody radius.

The heating problem and consequent high heat protection requirement forced a compromise away from the ideal flat plate solution to a forebody comprised of a 77 degree segment. This makes some allowance for boundary layer buildup, and provides a better load structure.

~~CONFIDENTIAL~~

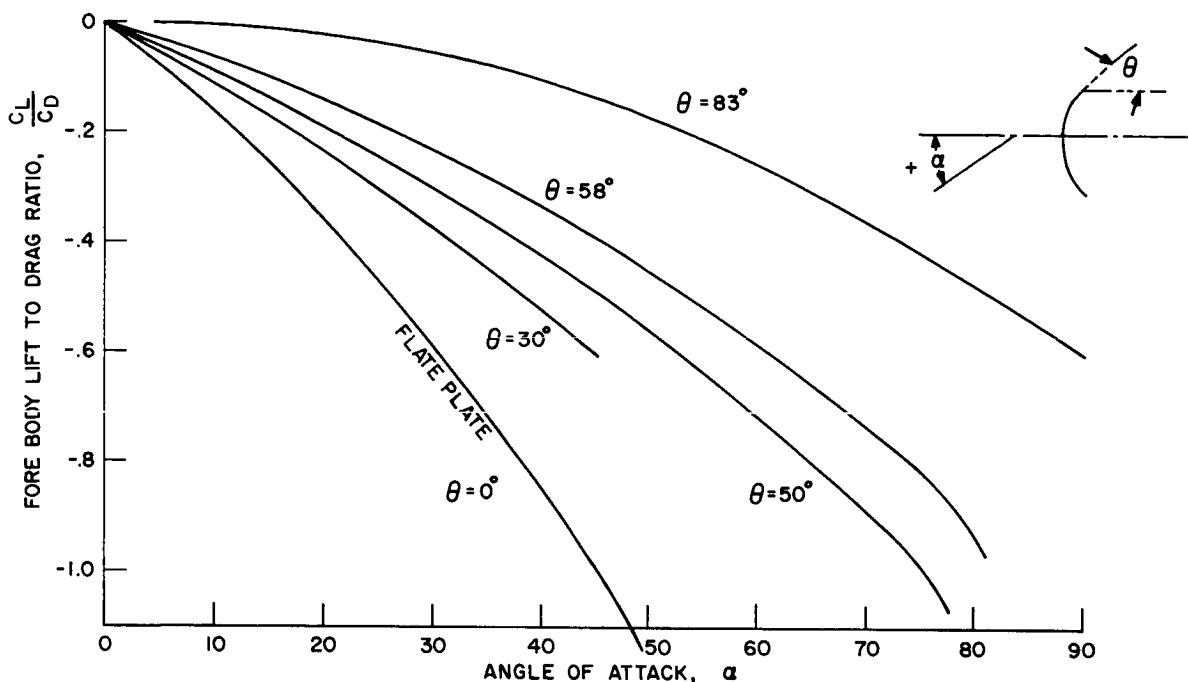


Figure IX-1-11. Newtonian forebody lift-drag ratio for spherical segments.

Combining results of Figures IX-1-11 and IX-1-12 with the trade-offs between the volumetric and packaging requirements led to the present shape for the D-2 configuration shown in Figure IX-1-13.

The longitudinal aerodynamic characteristics for the D-2 configuration (Figures IX-1-14 through IX-1-16, inclusive) were computed for the basic body and body with chin flap configuration. The D-2 vehicle has a negative lift curve slope over the entire Mach number range, Figure IX-1-17. Deflecting the chin flap up to  $\delta = 90$  degrees, will further increase the configuration lift, yielding higher L/D values. The trimmed L/D ratio for the D-2 vehicle with chin flap deflected, is given in Figure IX-1-18 and is shown to develop a trimmed  $(L/D)_{\max} \approx 0.59$  at  $\alpha = -40$  degrees with the flap deflected between 90 and 135 degrees.

With a center of gravity at  $\left(\frac{X_{CG}}{D_B}\right) = 0.273$ , the vehicle is predicted to be statically stable (Figure IX-1-19) throughout its flight Mach number range at angles of attack encompassing that for  $(L/D)_{\max}$ . Dynamic damping problems at supersonic and hypersonic speeds are expected to be encountered. The severity of this problem is under

~~CONFIDENTIAL~~



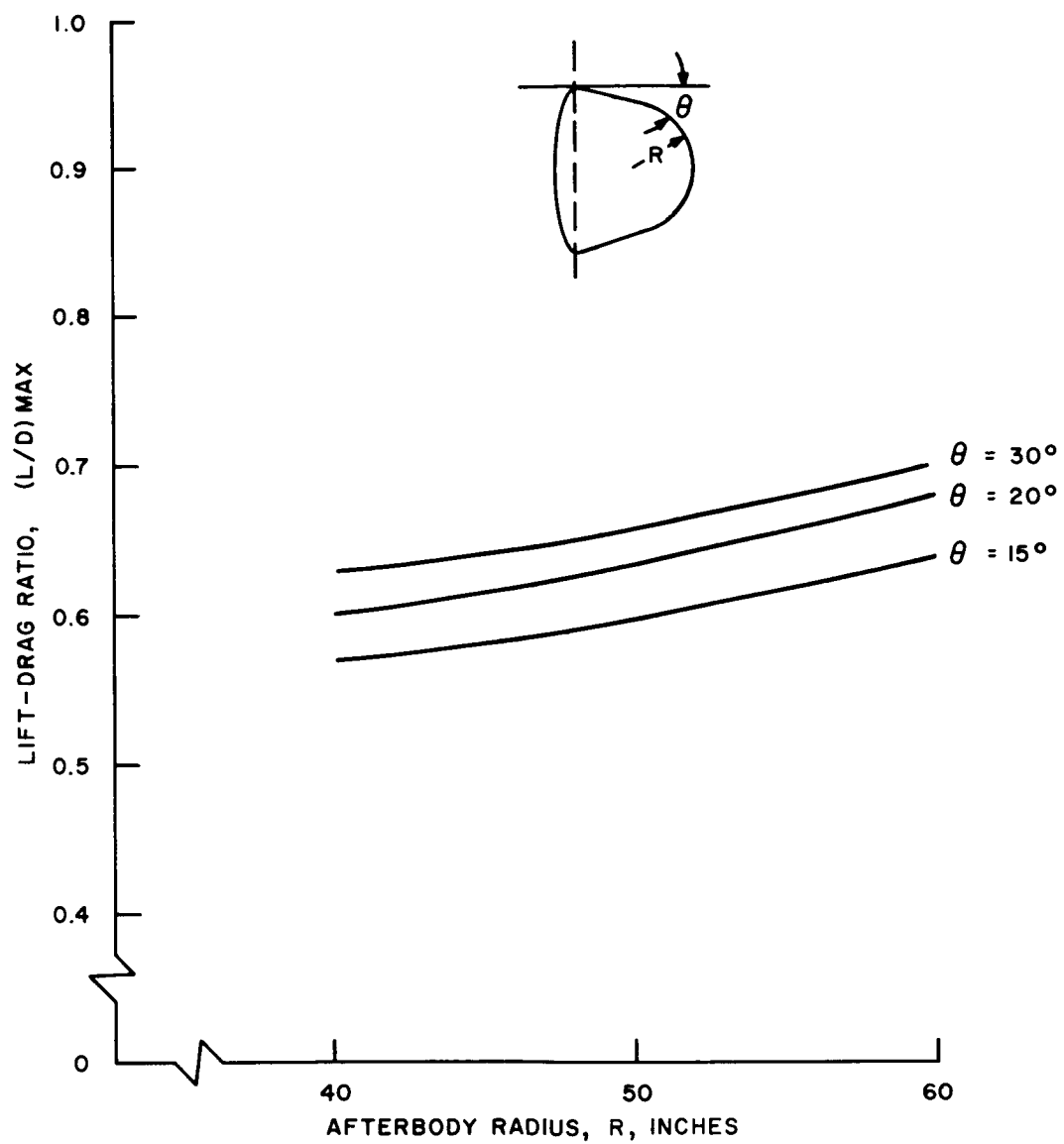


Figure IX-1-12. Variation of lift-drag ratio with afterbody radius and angle

~~CONFIDENTIAL~~

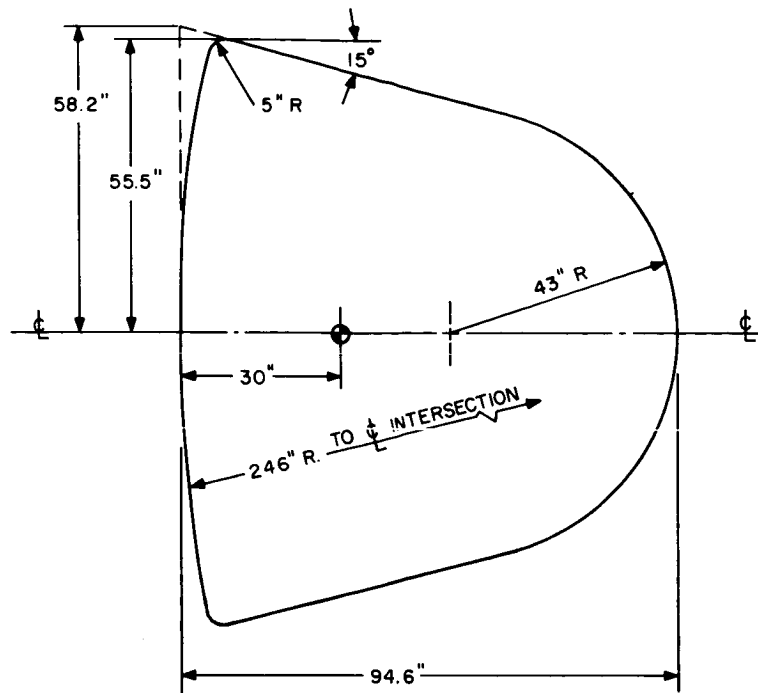


Figure IX-1-13. D-2 configuration

study. Previous experience on ballistic missiles indicates that afterbody shaping, alteration of the forebody-afterbody junction radius, and alterations in center of gravity position can resolve the problem, if it arises. At transonic speeds, the recovery system is deployed and this stability problem is, therefore, not encountered.

Lateral maneuvering for this vehicle is achieved by banking and pitching the vehicle, using reaction jets and the chin flap, respectively.

~~CONFIDENTIAL~~

~~CONFIDENTIAL~~

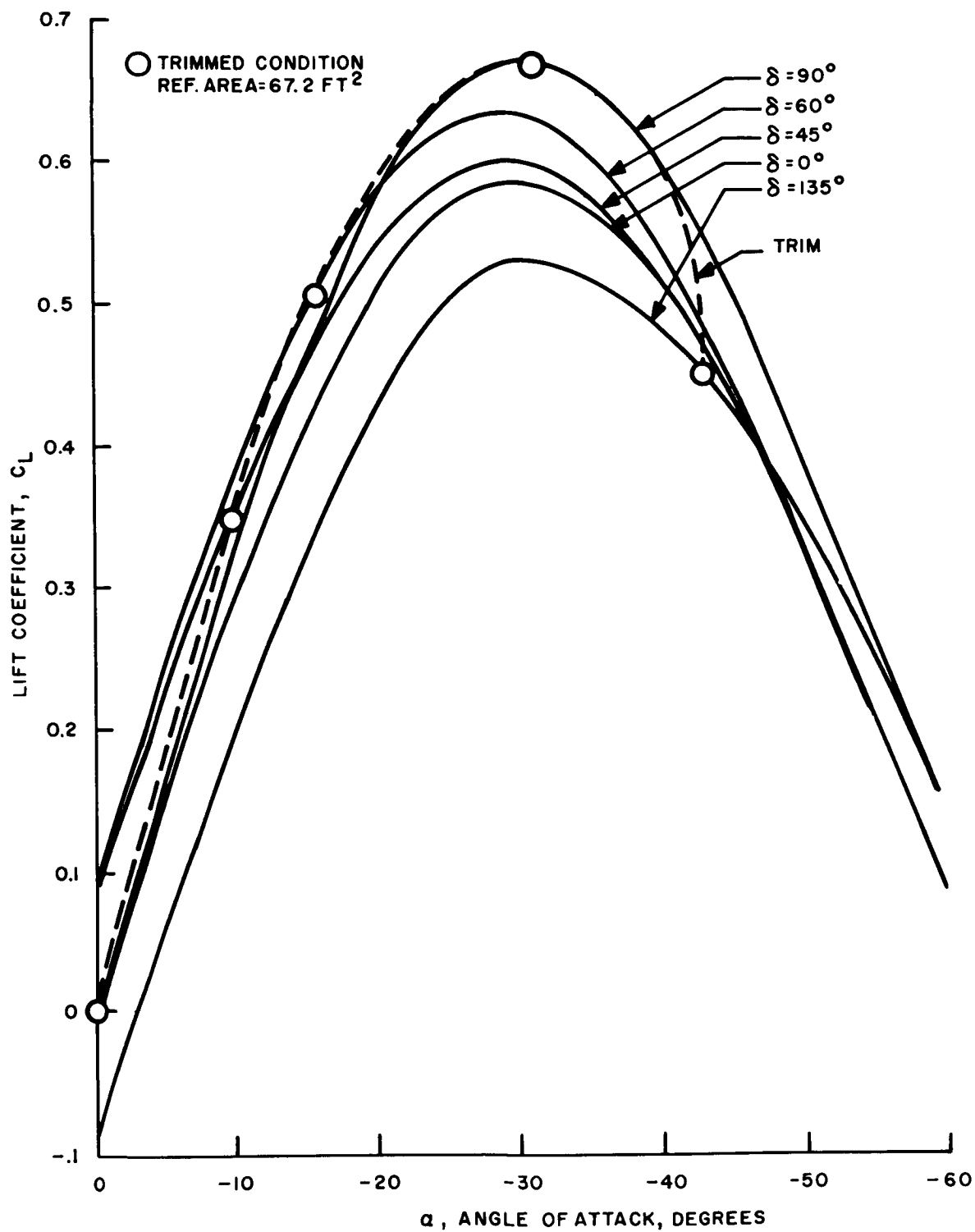


Figure IX-1-14. D-2 configuration — variation of lift coefficient with angle of attack

~~CONFIDENTIAL~~

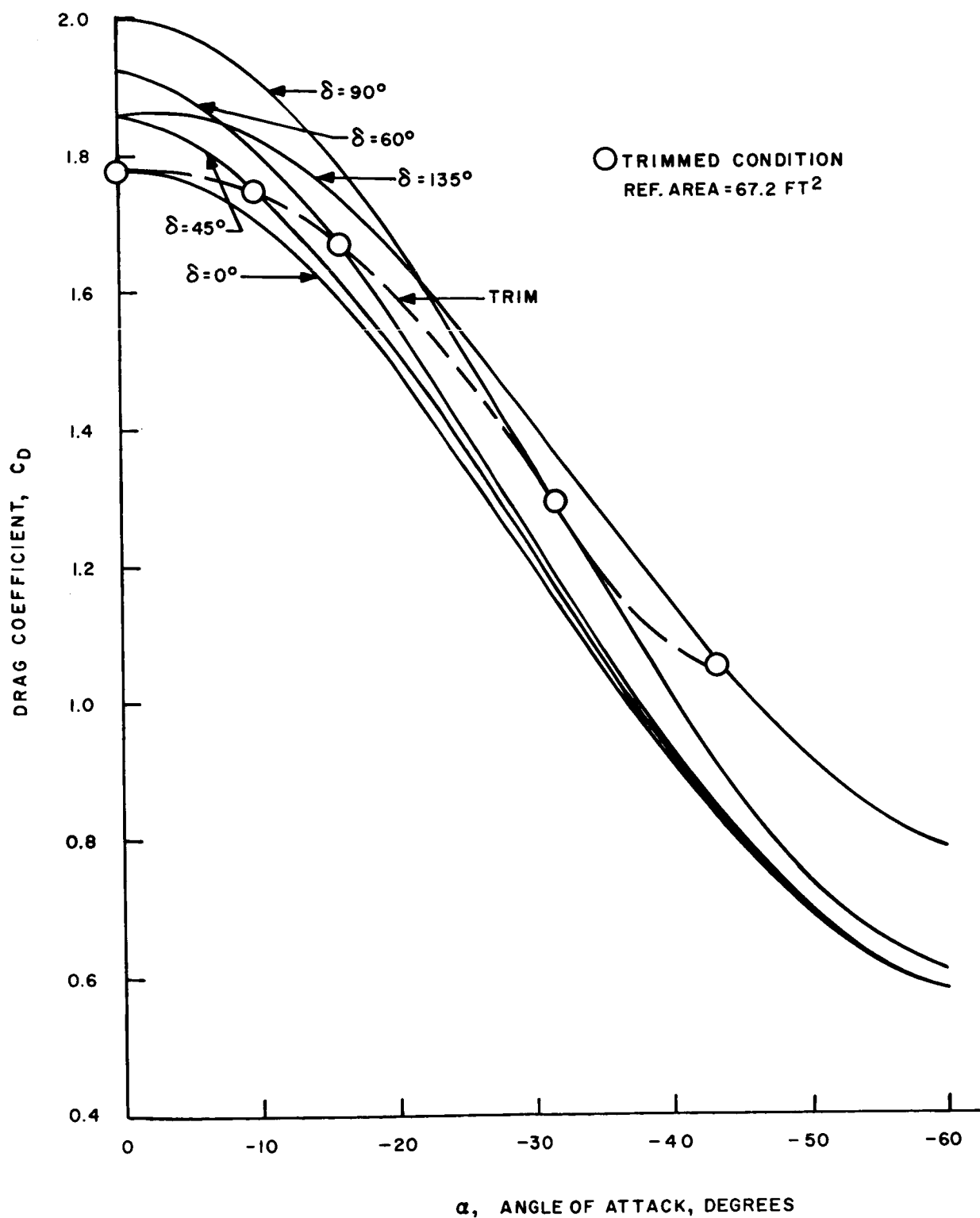


Figure IX-1-15. D-2 configuration — variation of drag coefficient with angle of attack

~~CONFIDENTIAL~~

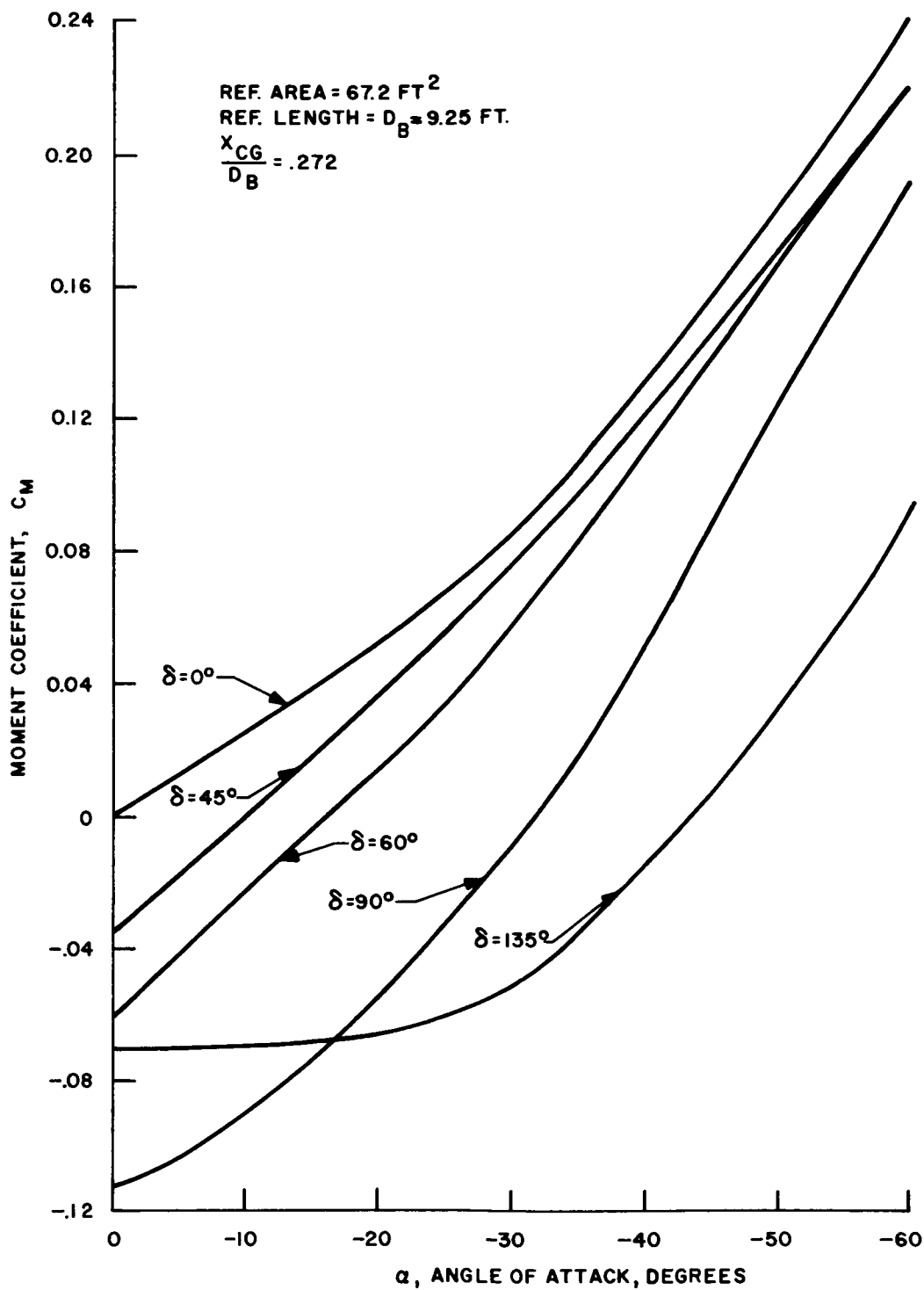


Figure IX-1-16. D-2 configuration — variation of moment coefficient with angle of attack

~~CONFIDENTIAL~~

~~CONFIDENTIAL~~

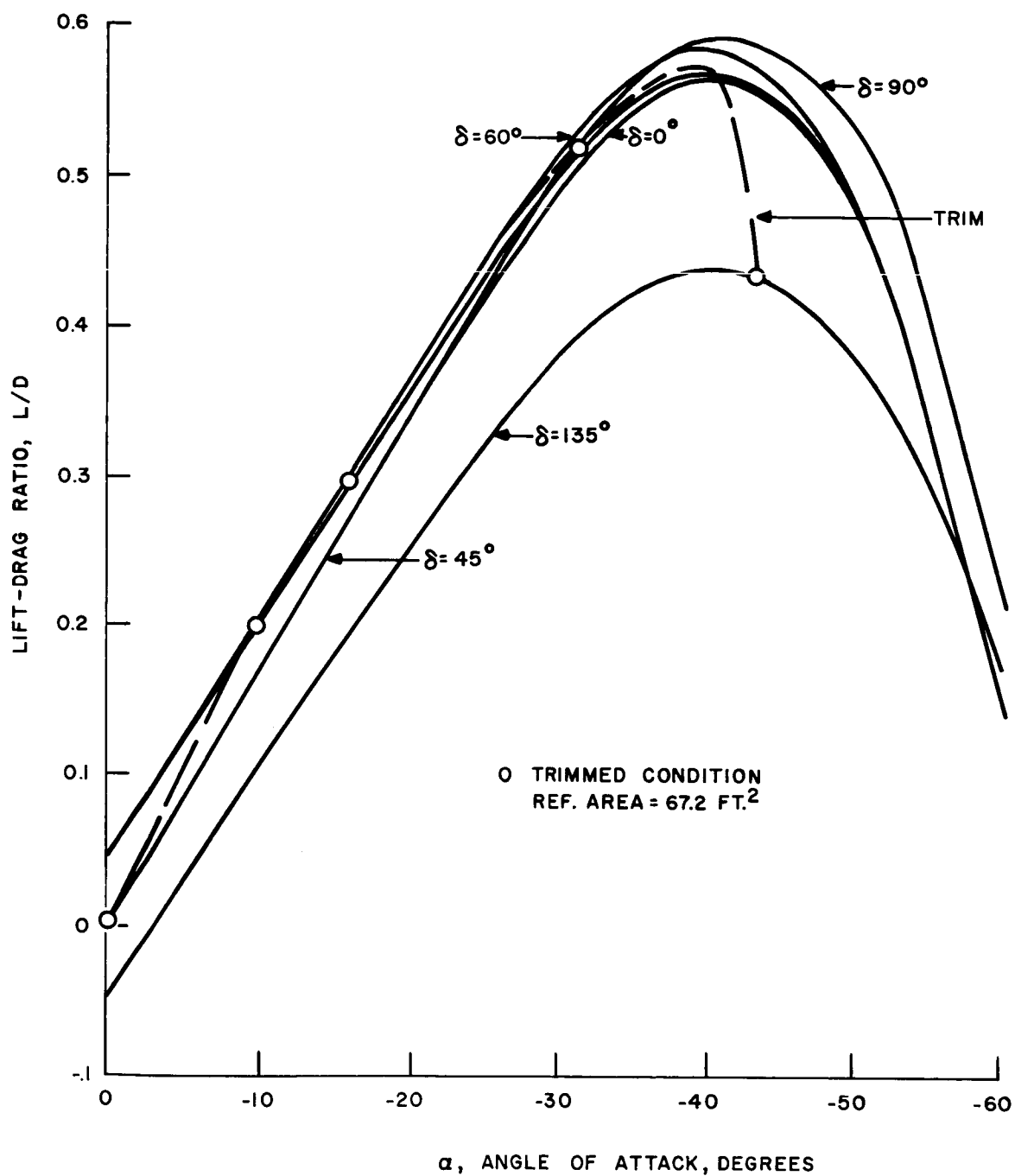


Figure IX-1-17. D-2 coefficient — variation of lift-drag ratio with angle of attack

~~CONFIDENTIAL~~

~~CONFIDENTIAL~~

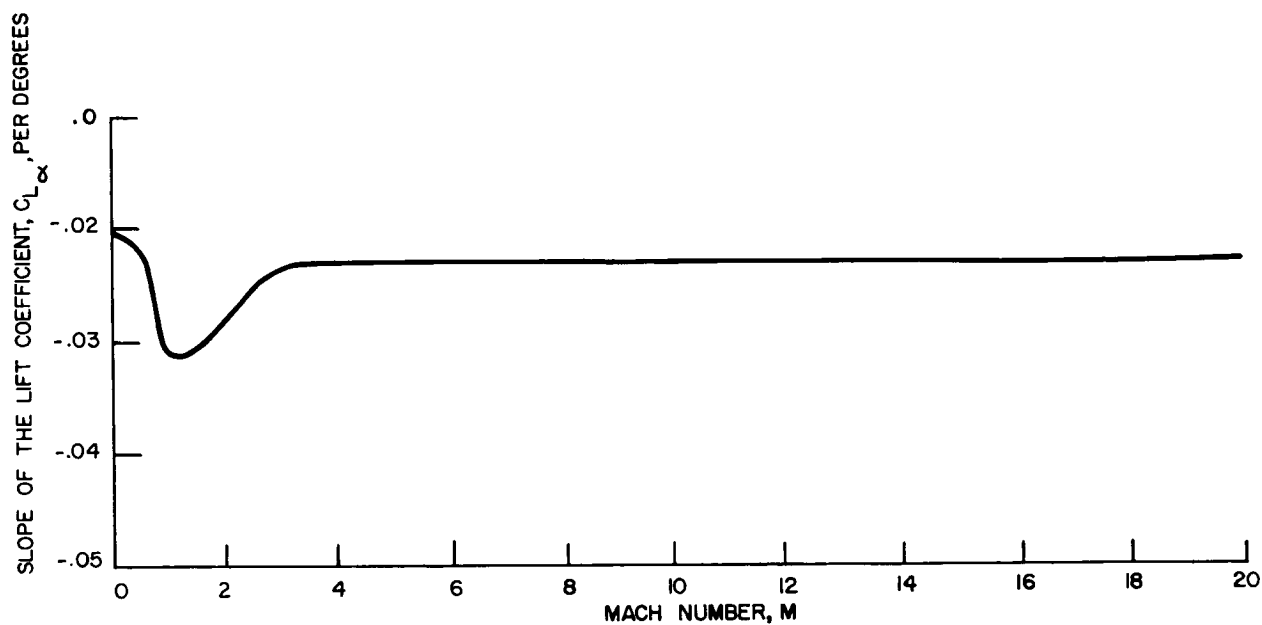


Figure IX-1-18. D-2 configuration — variation of lift coefficient versus Mach number

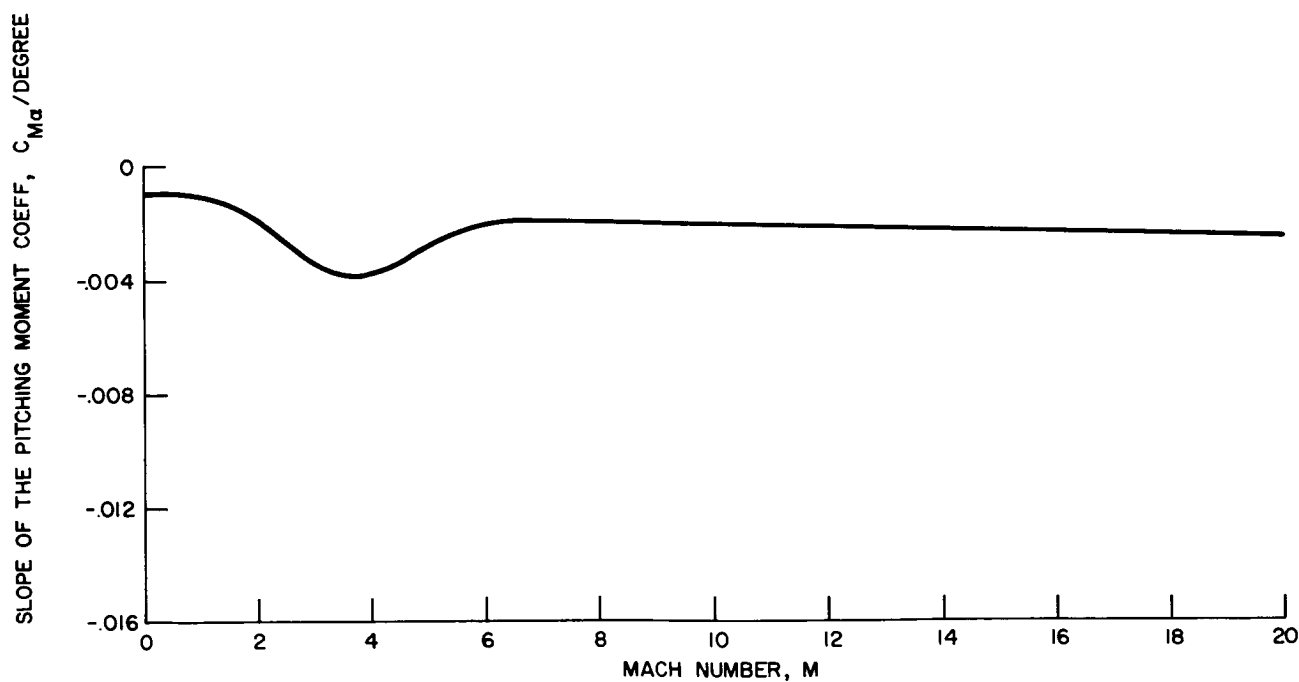


Figure IX-1-19. D-2 configuration — variation of the pitching moment versus Mach number

~~CONFIDENTIAL~~



## HIGH L/D GLIDER

The high L/D glider design shown in Figure IX-1-20 is intended to exploit to the greatest extent the advantages of a high L/D in providing a large re-entry angle for a given "g" limit and high lateral maneuvering capability. This design is to re-enter and glide hypersonically at attitudes between that for maximum L/D and that for maximum  $C_L$ ; it will approach and land at attitudes approximately at and below that for maximum L/D. The hypersonic maximum (L/D) is estimated to be 2.0 with maximum  $C_L$  approaching 0.7. The subsonic maximum (L/D) is estimated at 4.4 clean, and 3.8 with landing gear down.

A reaction engine system will provide attitude control during the very low density phases of re-entry. The elevons will provide longitudinal and roll control during atmospheric re-entry. The rudders will provide directional trim and damping and, in addition, will be extended outward during hypersonic glide to augment the basic directional stability.

The estimated static longitudinal characteristics for the high L/D glider at hypersonic and subsonic speeds is presented in Figure IX-1-21.

## HIGH ATTITUDE GLIDER

In the high-attitude glider design, such as that presented in Figure IX-1-22, it is intended to provide a configuration capable of equilibrium hypersonic glide but which also exposes the least surface (bottom only) to the critical super-orbital re-entry heating. This design is to re-enter and glide hypersonically at attitudes approximately between that for  $C_{L_{max}}$  and 80 degrees; at lower hypersonic or supersonic speeds, it will trim to lower attitudes (less than for maximum  $C_L$ ) and will approach for landing at  $(L/D)_{max}$ . As in the previous case, a wing loading of about 40 lb/ft was specified. The hypersonic maximum (L/D) is estimated to be about 1.5, but in the high-attitude condition the maximum usable (L/D) will be about 0.7. The subsonic maximum (L/D) is predicted to be 4.7 clean, and 4.0 with landing gear down.



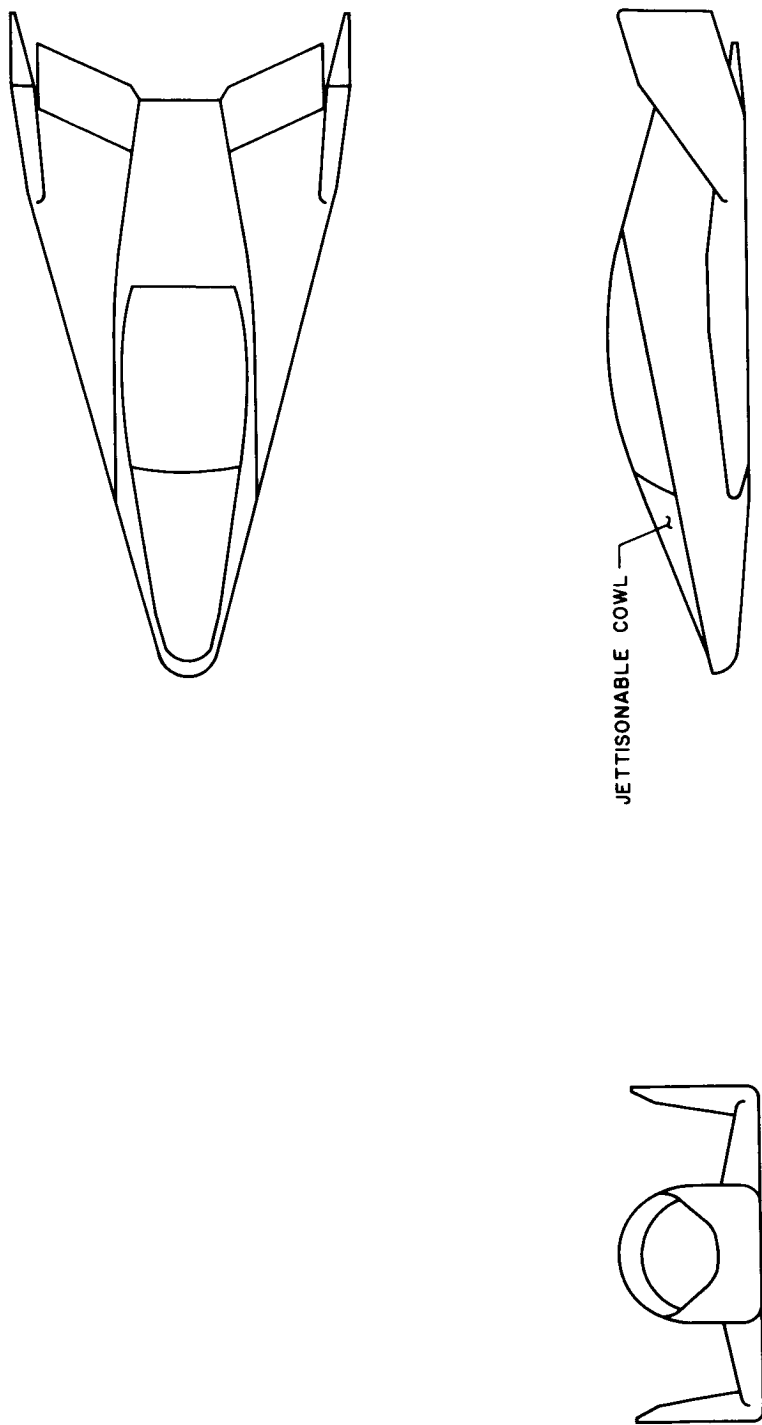


Figure IX-1-20. High L/D glider design

~~CONFIDENTIAL~~

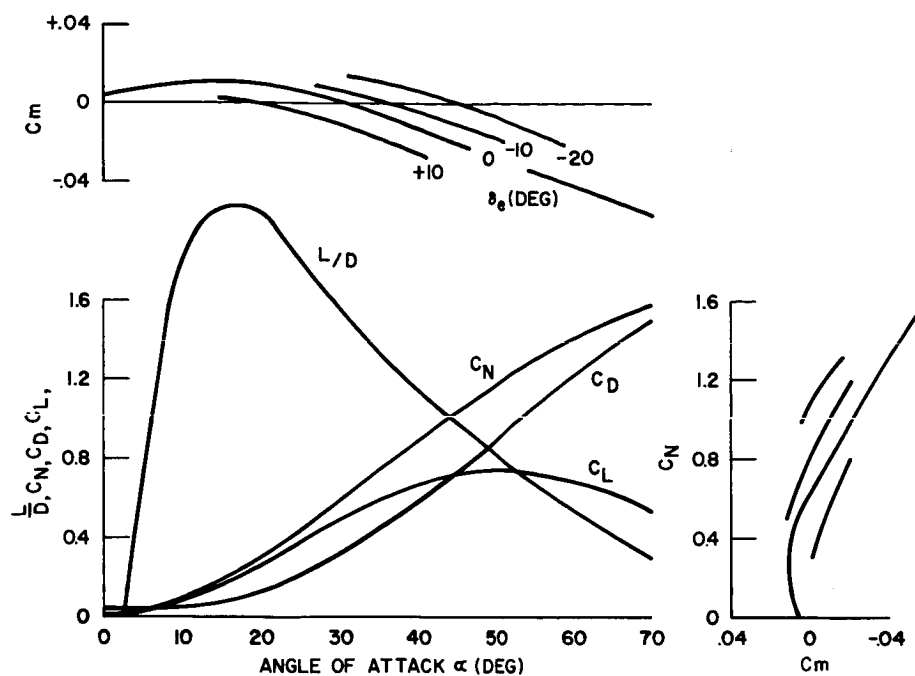


Figure IX-1-21. Hypersonic characteristics of the high L/D glider

During super-orbital re-entry, the vertical fins are folded in to relieve the heating on these surfaces. At suborbital glide conditions the vertical fins are tilted slightly outward to provide directional stability. At lower hypersonic and supersonic speeds, these fins may be tilted further out to assist in trimming to lower attitudes. At subsonic speeds, they are tilted to approximately 45 degrees to augment the normally marginal subsonic stability of such configurations.

The estimated static longitudinal characteristics for the high-attitude glide are shown in Figure IX-1-23.

~~CONFIDENTIAL~~

~~CONFIDENTIAL~~

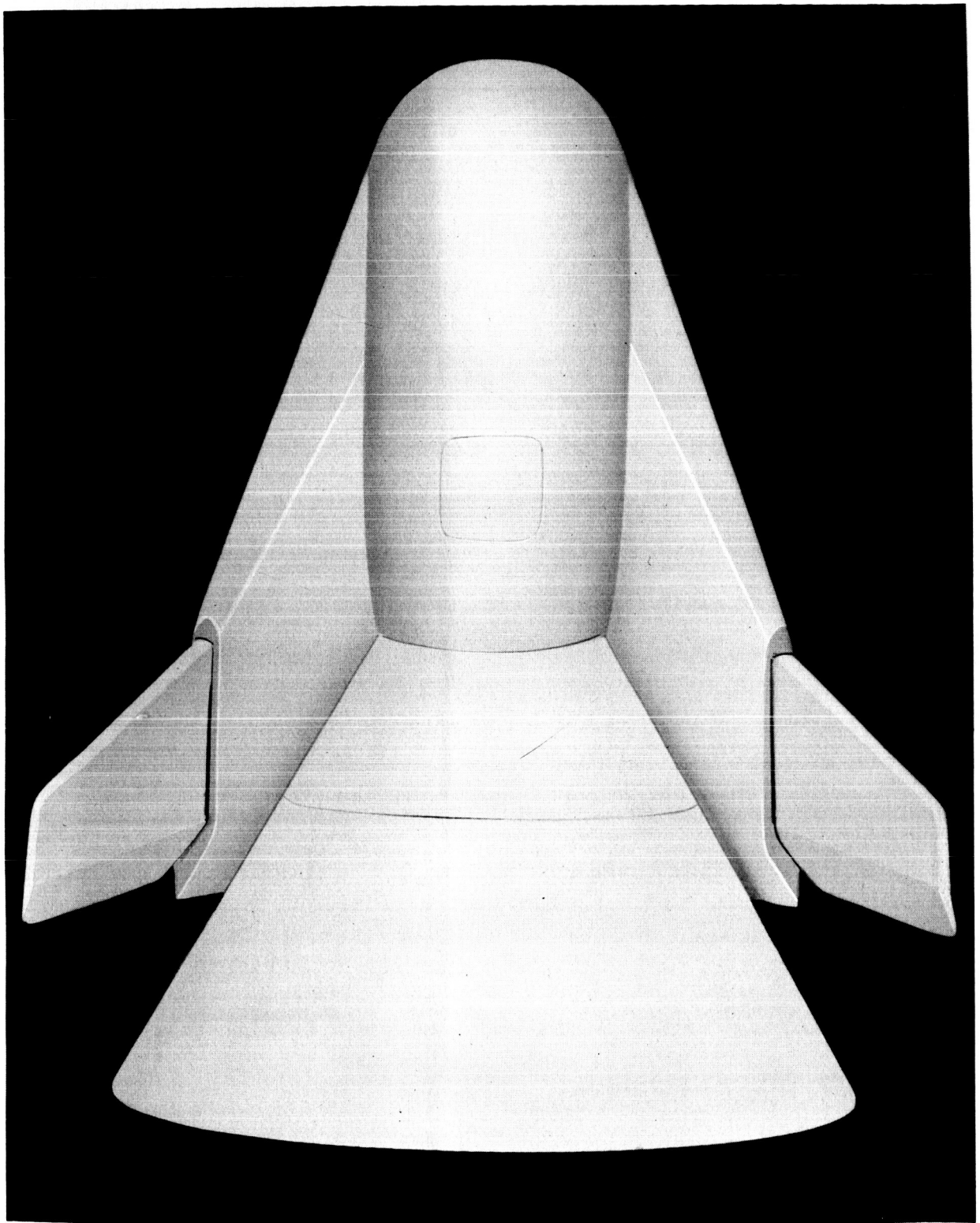


Figure IX-1-22. High attitude configuration

~~CONFIDENTIAL~~

~~CONFIDENTIAL~~

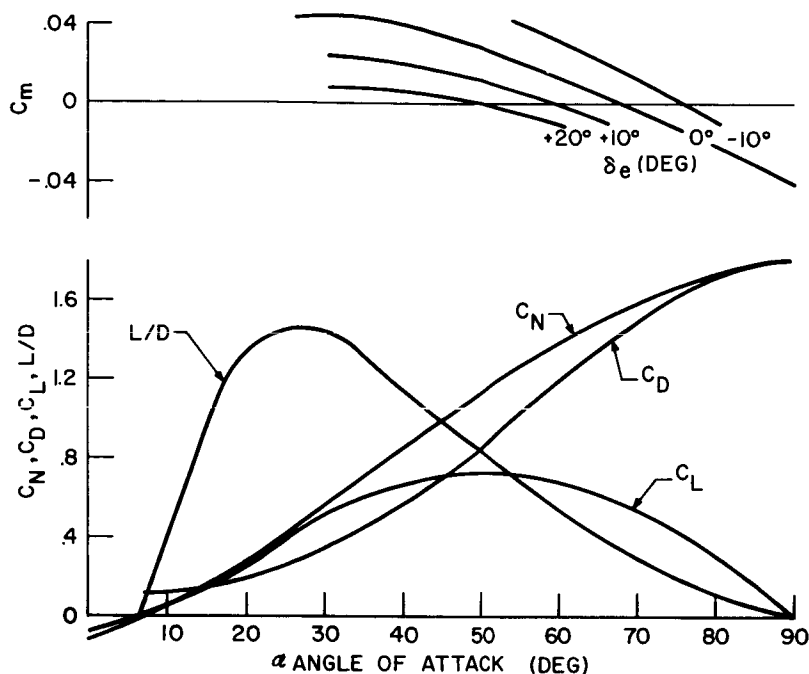


Figure IX-1-23. Hypersonic longitudinal characteristics — high altitude glider

## MODIFIED LENTICULAR SHAPE

The modified lenticular vehicle, shown in Figure IX-1-24, is intended to provide a compact, minimum lifting surface, and minimum volume configuration. This is a high attitude re-entry configuration which has approximately the same flight modes as the preceding configuration. It will re-enter hypersonically at attitudes above that for maximum  $C_L$  using a controllable range of  $L/D$  between 0 and 0.6 to widen its re-entry corridor. Additional range corrections can be obtained by rolling the vehicle about the wind vector to produce desired net side-range adjustments. At supersonic speeds, the vehicle may make use of the higher ( $L/D$ ) ratios available at attitudes below that for maximum  $C_L$ .

The vertical fins are folded on top of the vehicle during the high attitude super-orbital portion of re-entry, to avoid overheating of these surfaces. In this configuration, directional stability is obtained from the large radius of curvature of the leading edge and from the aft sides of the body which are skewed with respect to the body axes so

~~CONFIDENTIAL~~

~~CONFIDENTIAL~~

DATA -

WING AREA (LESS ELEVONS)	127.7-SQ. FT.
VERTICAL FIN AREA	12.2-SQ. FT. (EACH)
RUDDER AREA	3.6-SQ. FT. (EACH)
PYLON AREA	7.8-SQ. FT. (EACH)
ELEVON AREA	6.9-SQ. FT. (EACH)

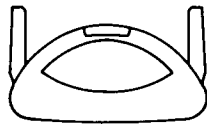
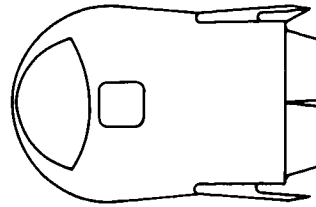


Figure IX-1-24. R-3 configuration re-entry vehicle

that they will be effective in the lateral direction. At suborbital speeds, when the danger of overheating has diminished, the fins are folded out to a near vertical position to provide additional directional stability and trim capabilities as well. The rudder surfaces can be used to supplement the elevon control capability when the fins are in the tilted-out position.

The basic hypersonic longitudinal characteristics for the modified lenticular shape are presented in Figure IX-1-25 and were obtained using modified Newtonian theory. The lateral characteristics are given in Figure IX-1-26 and IX-1-27.

The variation of landing (L/D) ratio with angle of attack for all three glide configurations is shown in Figure IX-1-28.

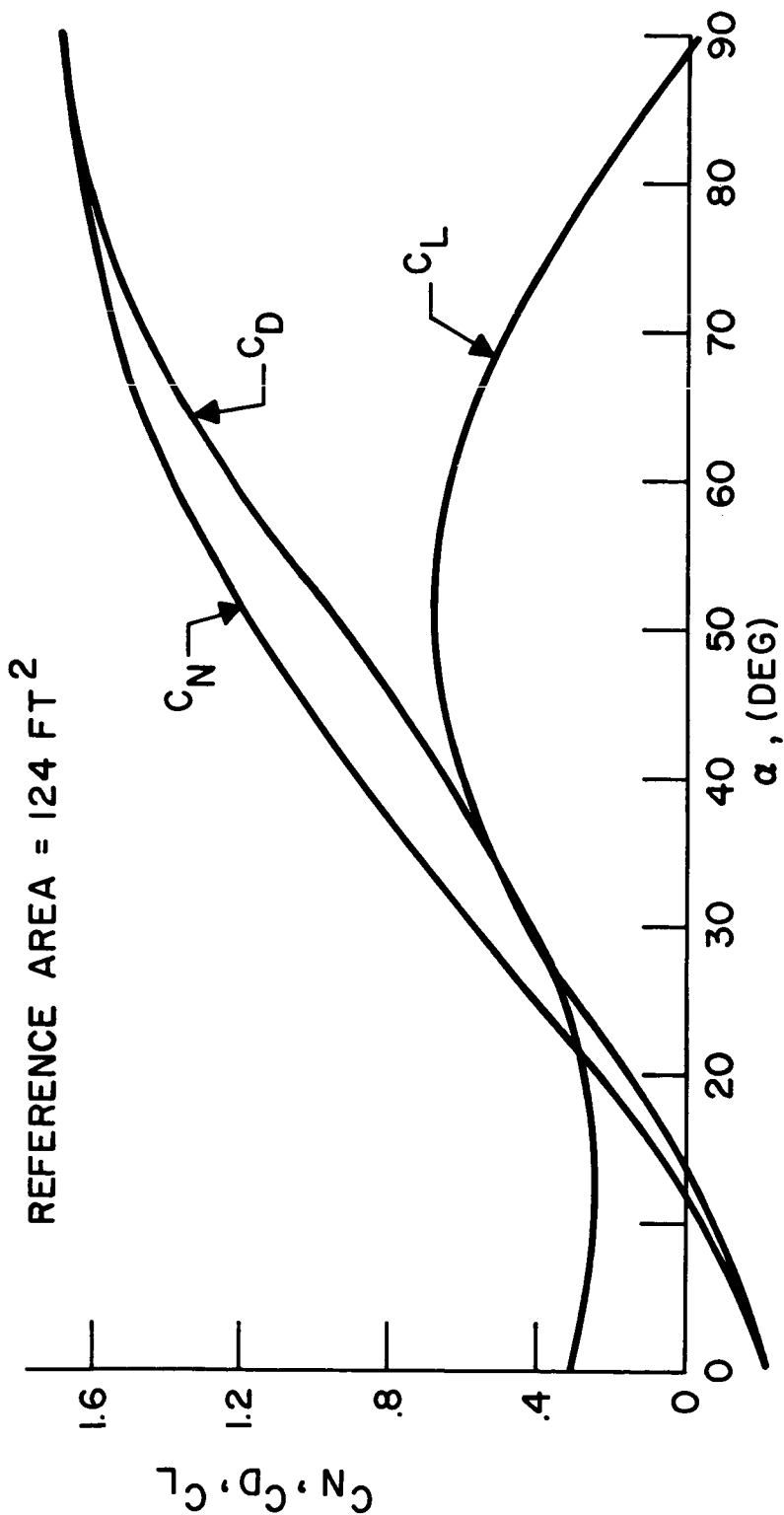
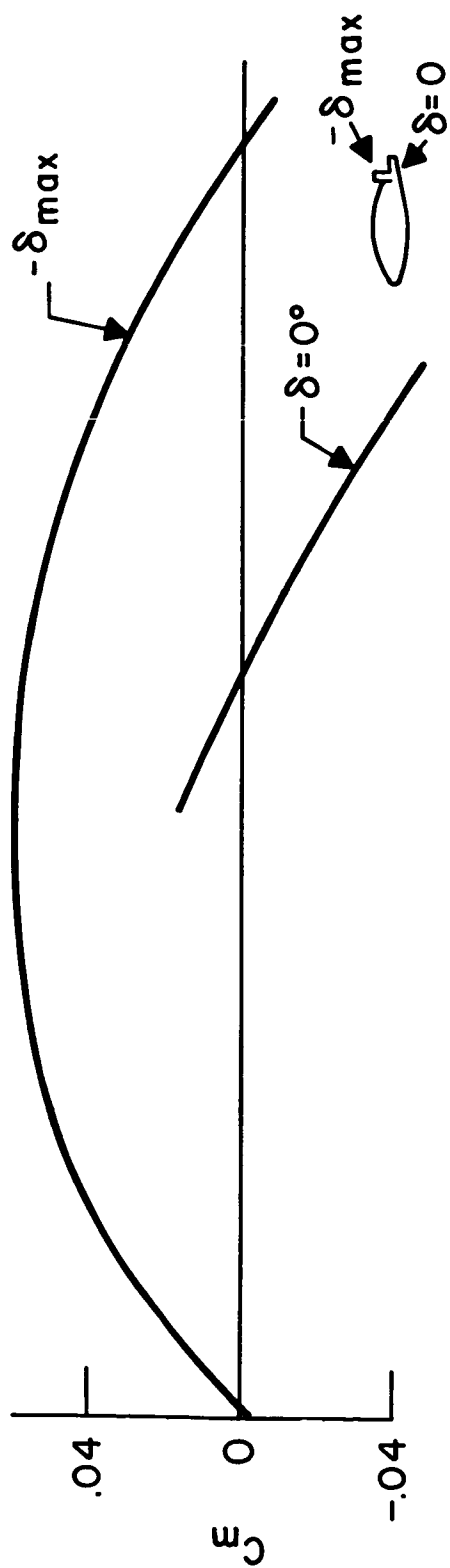
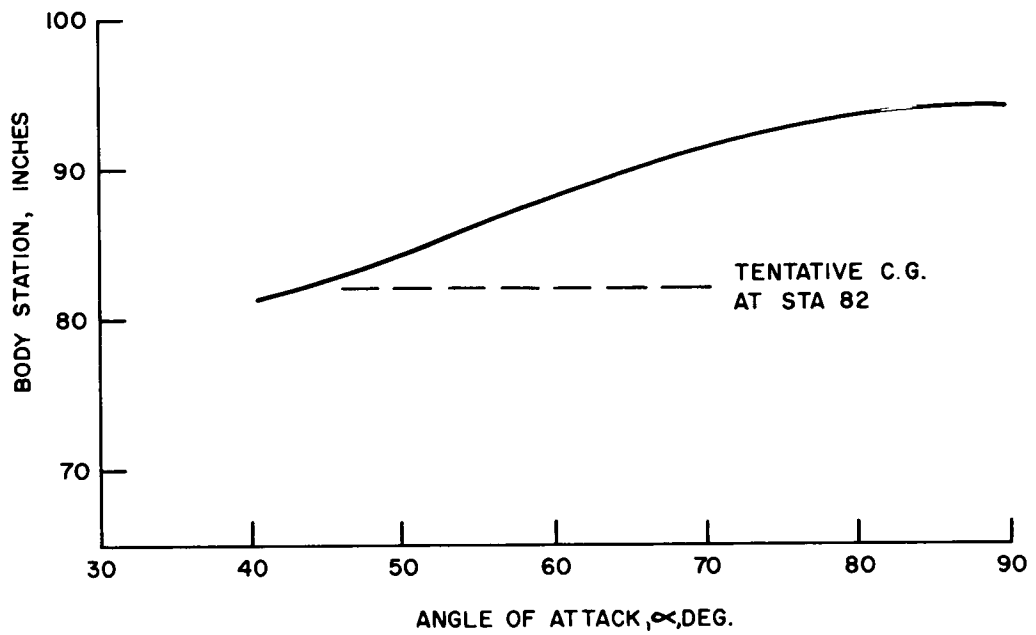


Figure IX-1-25. Hypersonic longitudinal characteristics — modified lenticular shape

~~CONFIDENTIAL~~

### LATERAL AERODYNAMIC CENTER



### SIDE FORCE DERIVATIVE

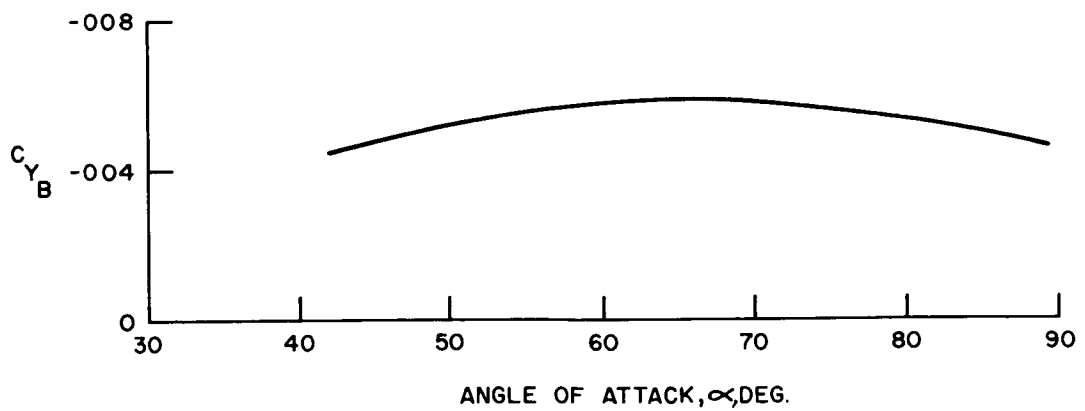


Figure IX-1-26. Hypersonic lateral stability characteristics — fins folded

~~CONFIDENTIAL~~

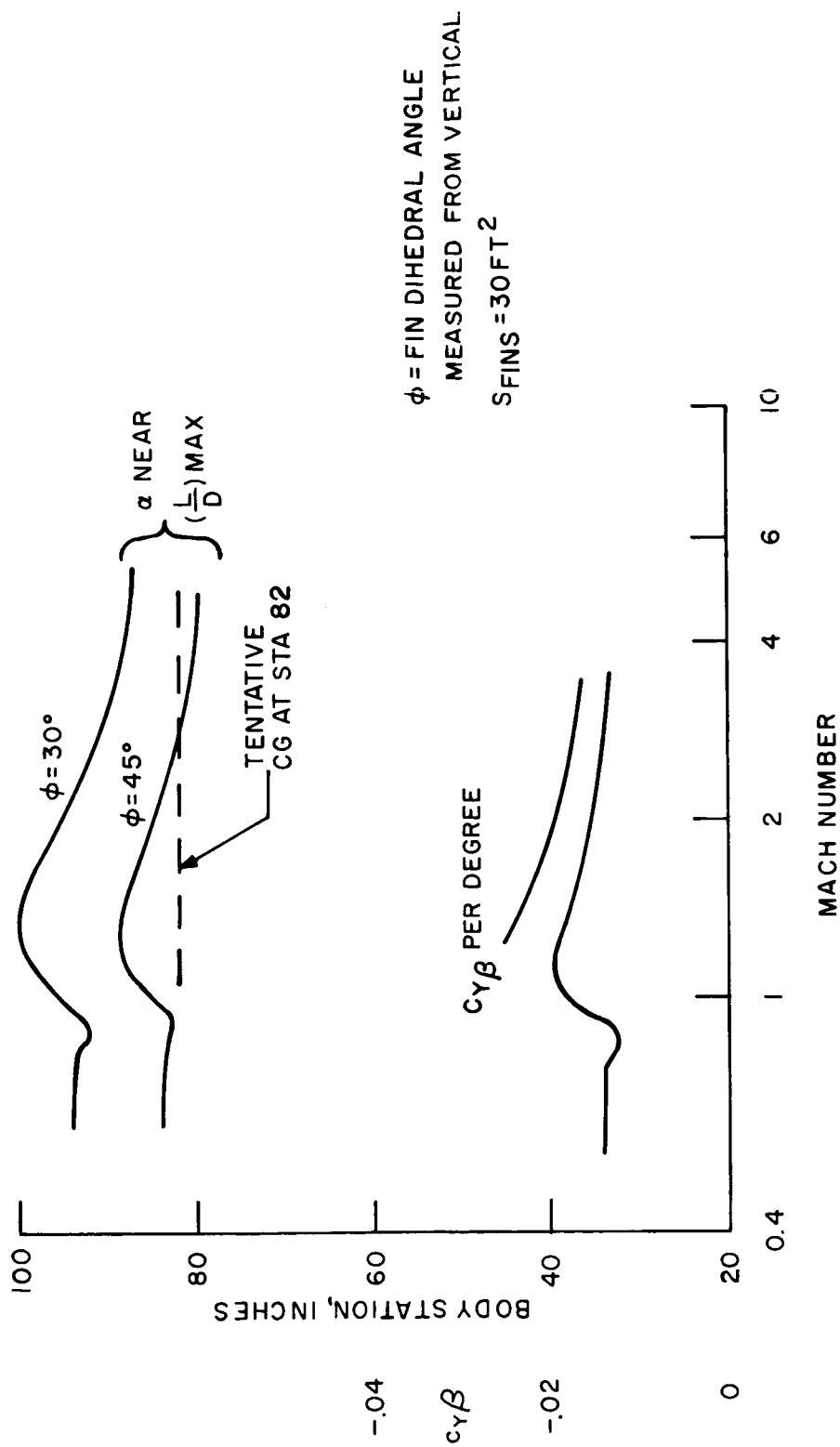


Figure IX-1-27. Modified lenticular shape — lateral aerodynamic center



~~CONFIDENTIAL~~

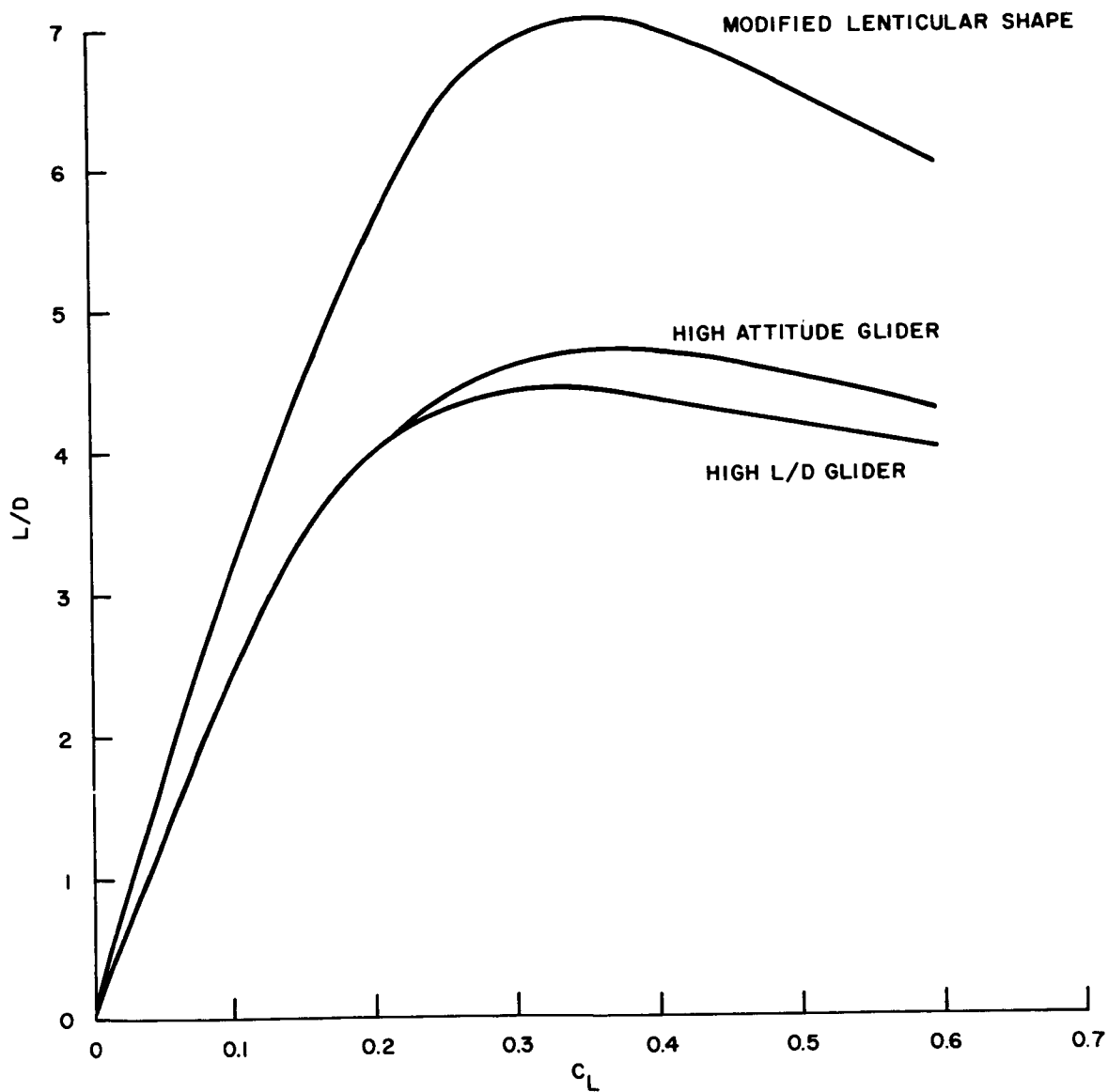


Figure IX-1-28. Low-speed  $L/D$  comparison — clean configurations

~~CONFIDENTIAL~~

## 2. THERMODYNAMICS AND MATERIALS

### EXTERNAL, RE-ENTRY PHASE HEATING

#### Heat Inputs

Convective and hot gas radiative heat fluxes have been calculated for two configurations, C-1 and B-2. The heating laws used are the same as those used by the Missile and Space Vehicle Department in ballistic missile re-entry vehicle studies and satellite re-entry vehicle studies. These laws have been established as adequate up to  $M_\infty = 25$  by calorimetry data from the Mk 2 re-entry vehicle program, and up  $M_\infty = 30$  by inference from the successful re-entry of several Discoverer capsules. The air properties used are extrapolations of values published by Logan and Treanor of Cornell Aeronautical Laboratories. Differences in heat fluxes calculated by Missile and Space Vehicle Department equations, and using extrapolations of the Logan and Treanor values, as contrasted to Moeckel and Weston values, are believed to be less than 30 percent.

Convective heat fluxes have been calculated using equations for axisymmetric bodies at zero angle of attack and then applying a correction factor to account for the effect of angle of attack on the windward and leeward meridians. These corrections are obtained directly from the theory of Vaglio-Laurin. The heating on the meridian midway between windward and leeward is assumed to be equal to the uncorrected zero angle of attack values for the axisymmetric body, a Newtonian assumption.

Transition has been assumed to occur at a local Reynolds number of 150,000, based on edge of boundary layer values and wetted length measured from the stagnation point. Qualitatively, for configuration C-1, with re-entry angle  $\Theta_E = 5.7$  degrees, the flow is entirely laminar during heating; for re-entry angle  $\Theta_E = 8.7$  degrees, the flow is all laminar on the front half of the cone and turbulent over the aft-half during more than half of the heating. For configuration B-2, the flow is laminar over the major portion of the forebody during heating.

~~CONFIDENTIAL~~

Time-integrated hot gas radiation amounts to less than 10 percent of the convective input for configuration C-1 and less than 15 percent of the convective input for configuration B-2.

To date no calculations have been made on the interference effects which flaps or fins will have on the heating of the basic vehicle.

Figure IX-2-1 through IX-2-6, inclusive, show calculated heat fluxes to a 4000-degree R wall corrected for angle of attack.

The effect of wall temperature on heat input at zero angle of attack is illustrated on Figures IX-2-7 through IX-2-10, inclusive.

### **Heat Protection Systems Requirements**

Three types of heat protection systems have been considered for the APOLLO semi-ballistic vehicles: graphite, ablation, and re-radiation. Table IX-2-1 breaks down the typical distribution of heat protection material for the C-1 configuration for two re-entry angles, 5.7 and 8.7 degrees, and for the B-2 configuration for re-entry angles of 6 and 7 degrees.

For the graphite shield, Table IX-2-1 shows required thicknesses of graphite heat protection systems and their calculated oxidation. The oxidation in laminar heating has been calculated by the technique of Scala and Nolan, assuming conservatively, that the process is always diffusion controlled. The additional graphite required for keeping the backface temperature below 2000 degrees R has been estimated based on previous studies made on the Dynasoar vehicle. 2000 degrees R has been selected as the maximum temperature which the structural attachments to the graphite can tolerate. The minimum commercial graphite thickness which can be manufactured in large sections is 0.19 inch. Backing the graphite is an addition thickness of low density insulation which serves to drop the temperature to a maximum of 960 degrees R.

~~CONFIDENTIAL~~

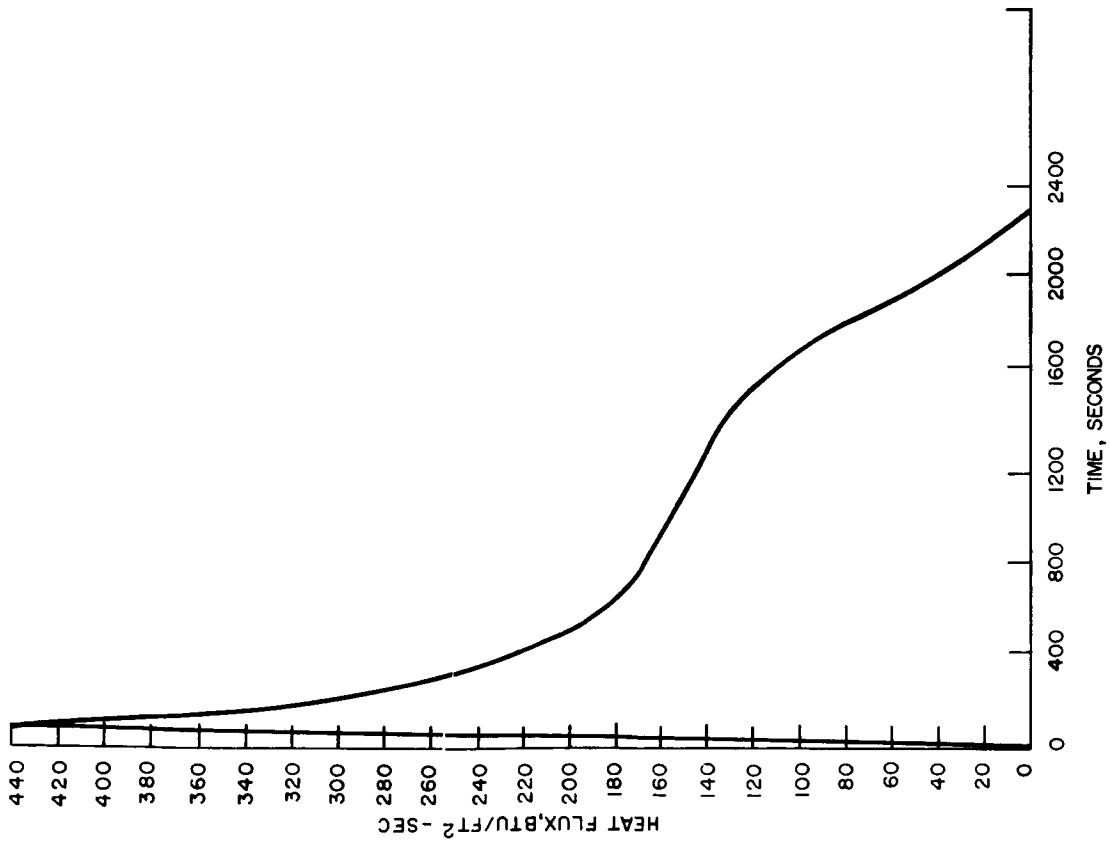


Figure IX-2-1. C-1 configuration -- total heat flux of the stagnation point, re-entry angle,  $\Theta_E = 5.7$  degrees

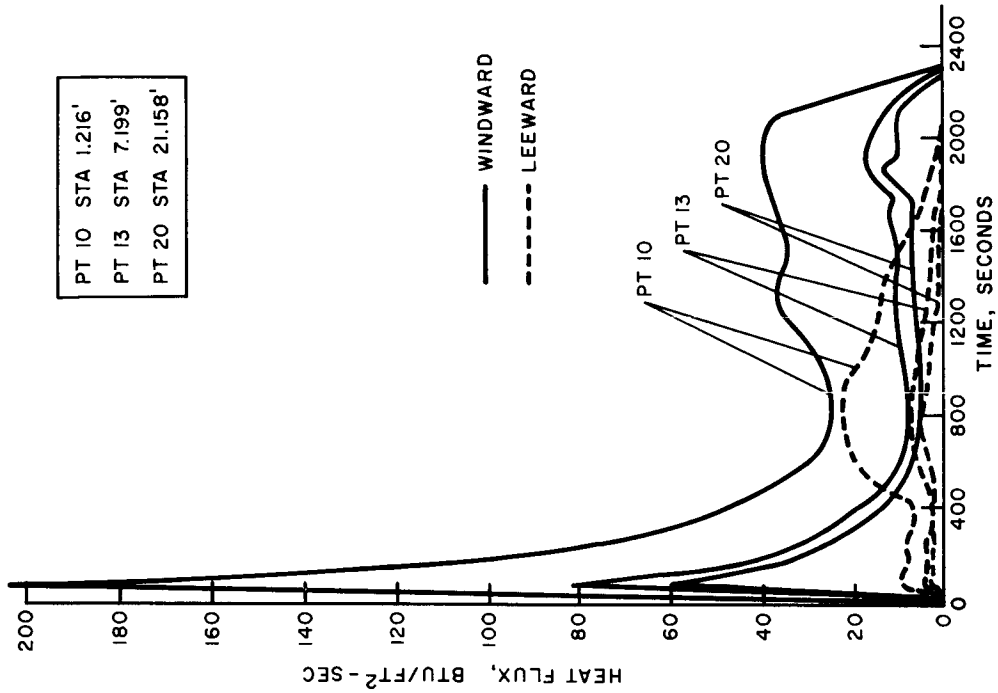


Figure IX-2-2. C-1 configuration -- total heat flux at selected stations\*, re-entry angle,  $\Theta_E = 5.7$  degrees

~~CONFIDENTIAL~~

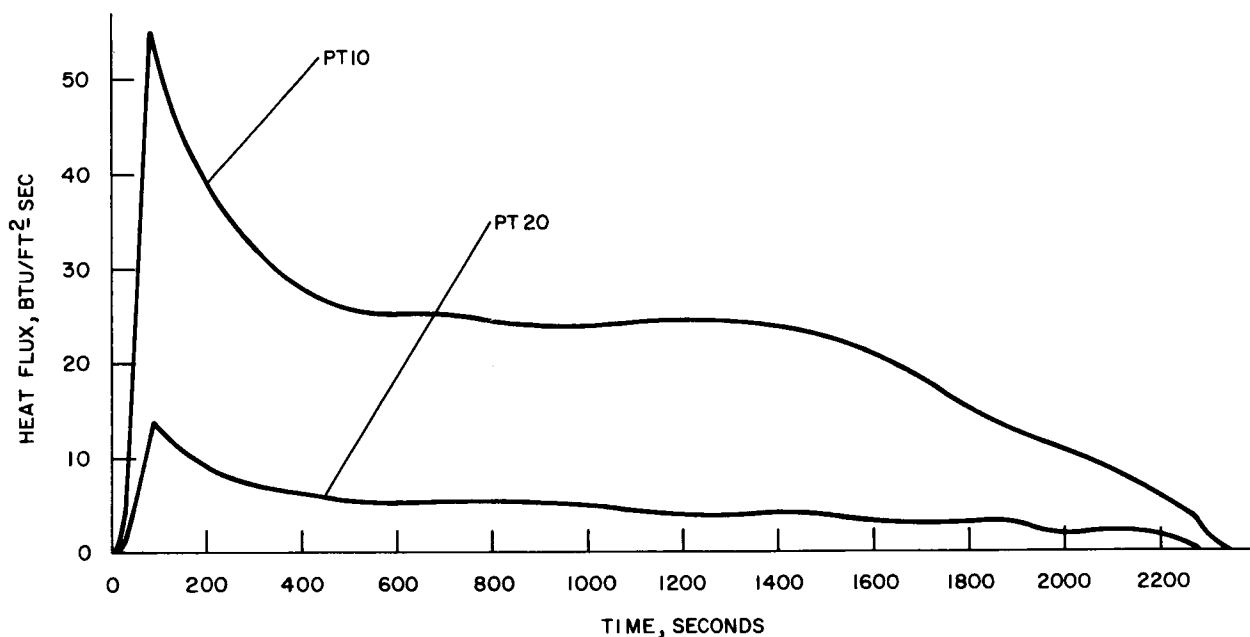


Figure IX-2-3. C-1 configuration — total heat flux at selected stations between windward and leeward stations, re-entry angle,  $\Theta_E = 5.7$  degrees

Using phenolic/nylon as the ablation material, the required thickness of an ablation system has been calculated. The material ablated and charred has been obtained assuming an effective heat of degradation equal to 5000 Btu/lb, where the effective heat of deg-

$$\text{radiation} = \frac{\int \dot{q}_{\text{CONV}}_{4000^{\circ}\text{R}} dt + \int \dot{q}_{\text{HGR}} dt}{\rho (X \text{ ablated} + X \text{ CHARRED})}$$

$\dot{q}_{\text{CONV}}$  = convective heat flux                       $\rho$  = density of material

$\dot{q}_{\text{HGR}}$  = radiative heat flux                       $X$  = thickness

The heat input is based upon an assumed wall temperature, based on flight experience, of 4000 degrees R and an emissivity of 0. Figure IX-2-11 shows some data for a typical ablation material.

The flight test data obtained at the relatively low enthalpies of ballistic missile flight indicate that the calculated design value of 5000 Btu/lb is reasonable for preliminary estimates of phenolic-nylon ablation and char at the higher enthalpy operational range of re-entry at near-escape velocity.

~~CONFIDENTIAL~~

CONFIDENTIAL

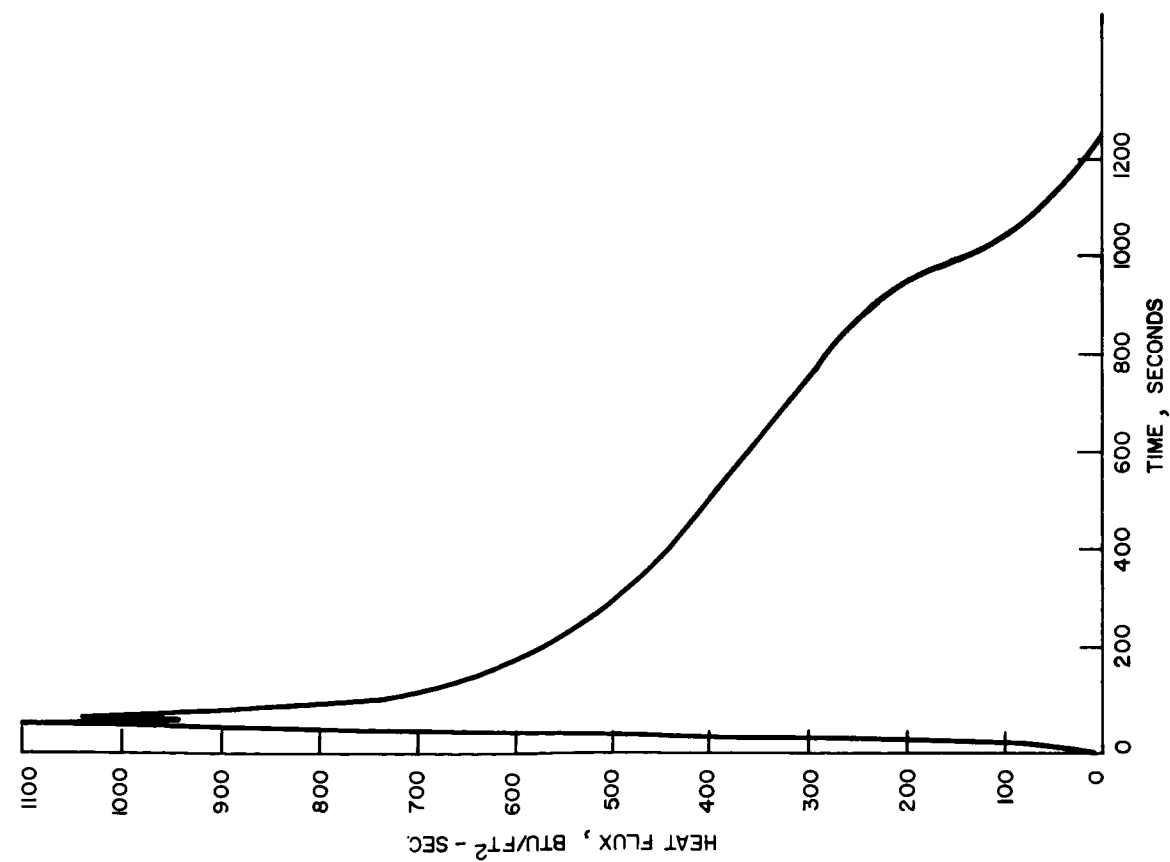


Figure IX-2-4. C-1 configuration — total heat flux at the stagnation point, re-entry angle,  $\Theta_E = 8.7$  degrees

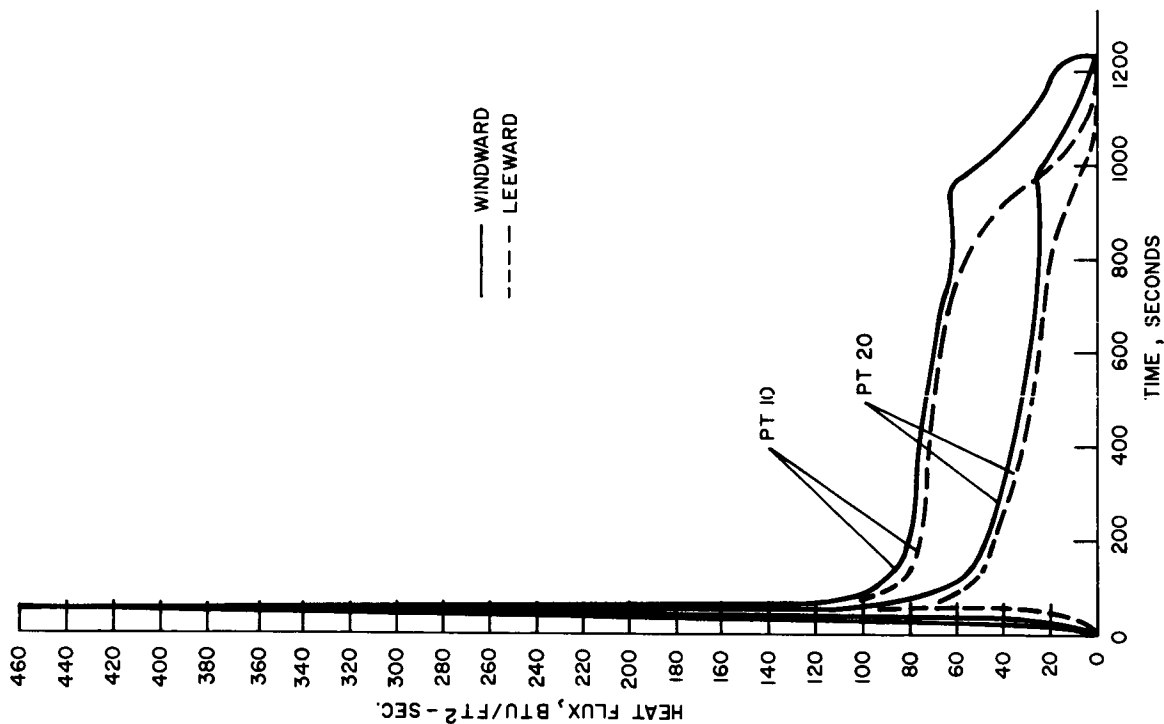


Figure IX-2-5. C-1 configuration — total heat flux at selected stations, re-entry angle,  $\Theta_E = 3.7$  degrees

CONFIDENTIAL

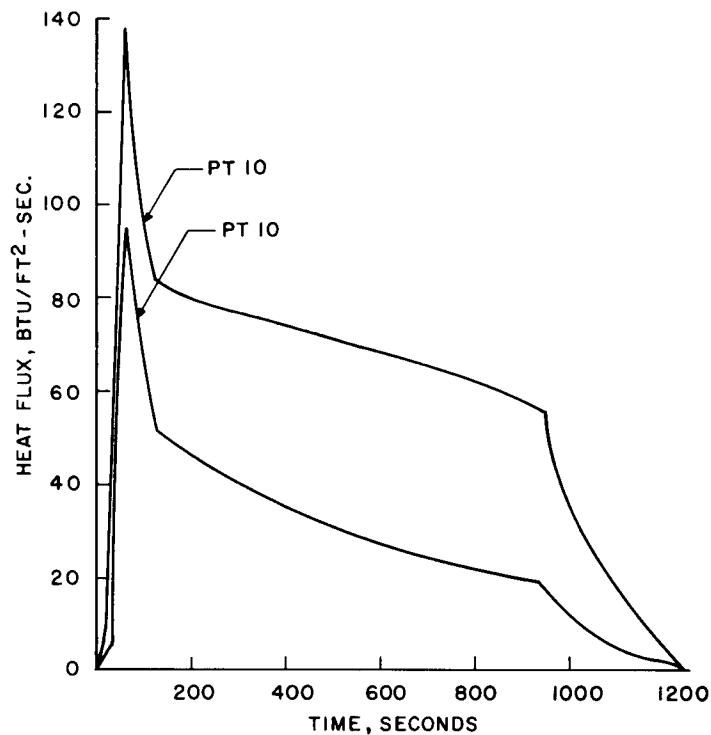


Figure IX-2-6. C-1 configuration — total heat flux at selected stations between windward and leeward, re-entry angle,  $\Theta_E = 8.7$  degrees

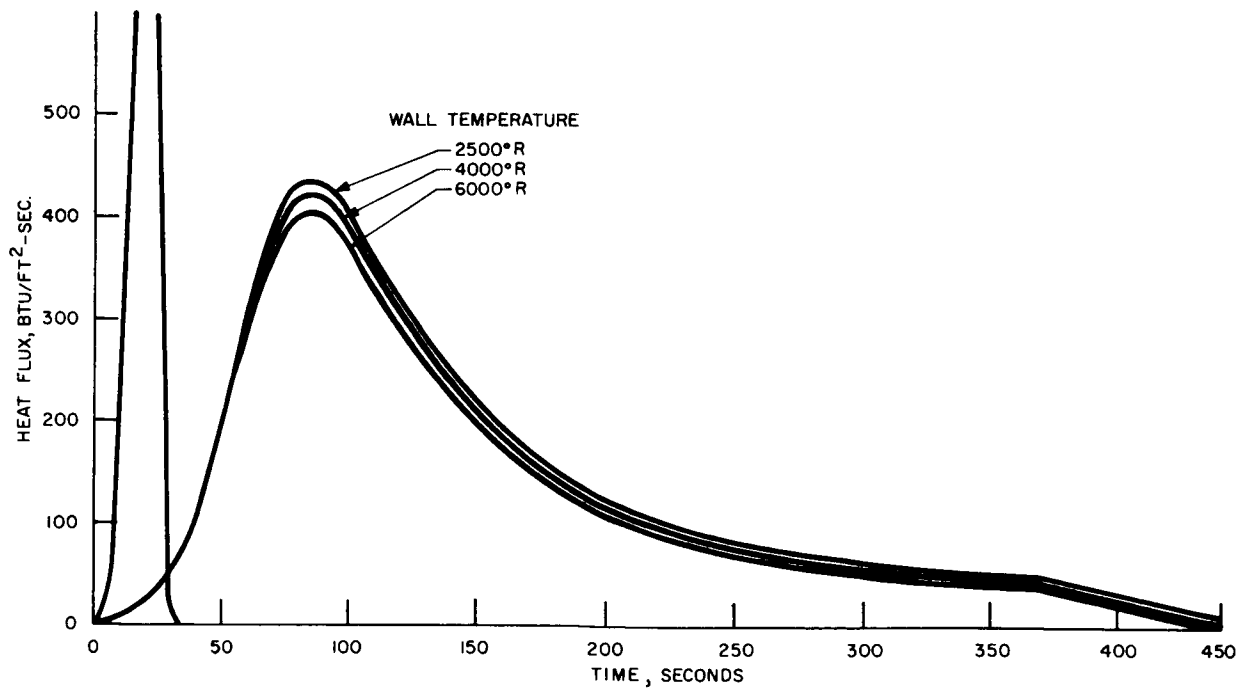


Figure IX-2-7. B-2 configuration — effect of wall temperature on convective heat flux at the B-2 stagnation point, re-entry angle,  $\Theta_E = 6$  degrees

~~CONFIDENTIAL~~

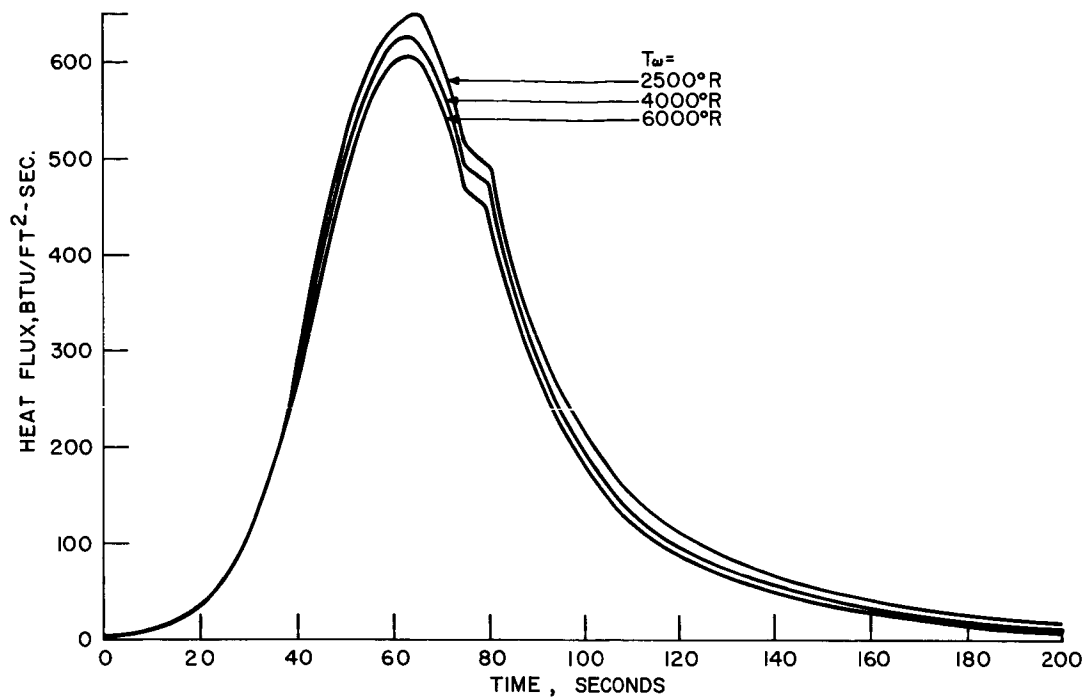


Figure IX-2-8. B-2 configuration — effect of wall temperature on convective heat flux at the stagnation point, re-entry angle,  $\Theta_E = 7.6$  degrees

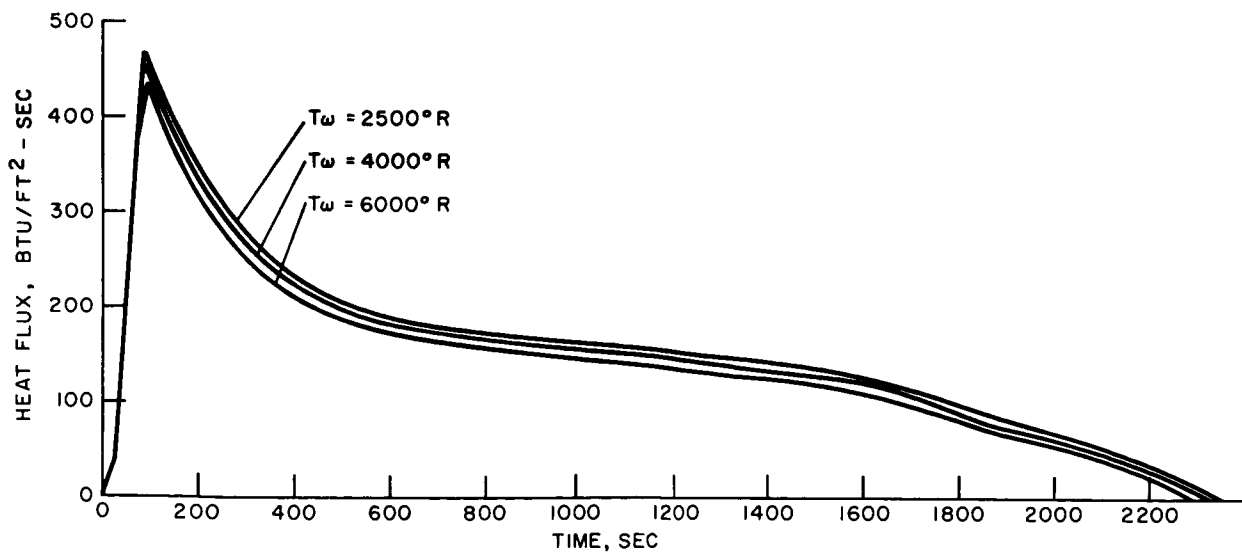


Figure IX-2-9. C-1 configuration — effect of wall temperature on convective heat flux at the stagnation point, re-entry angle,  $\Theta_E = 5.7$  degrees

~~CONFIDENTIAL~~



~~CONFIDENTIAL~~

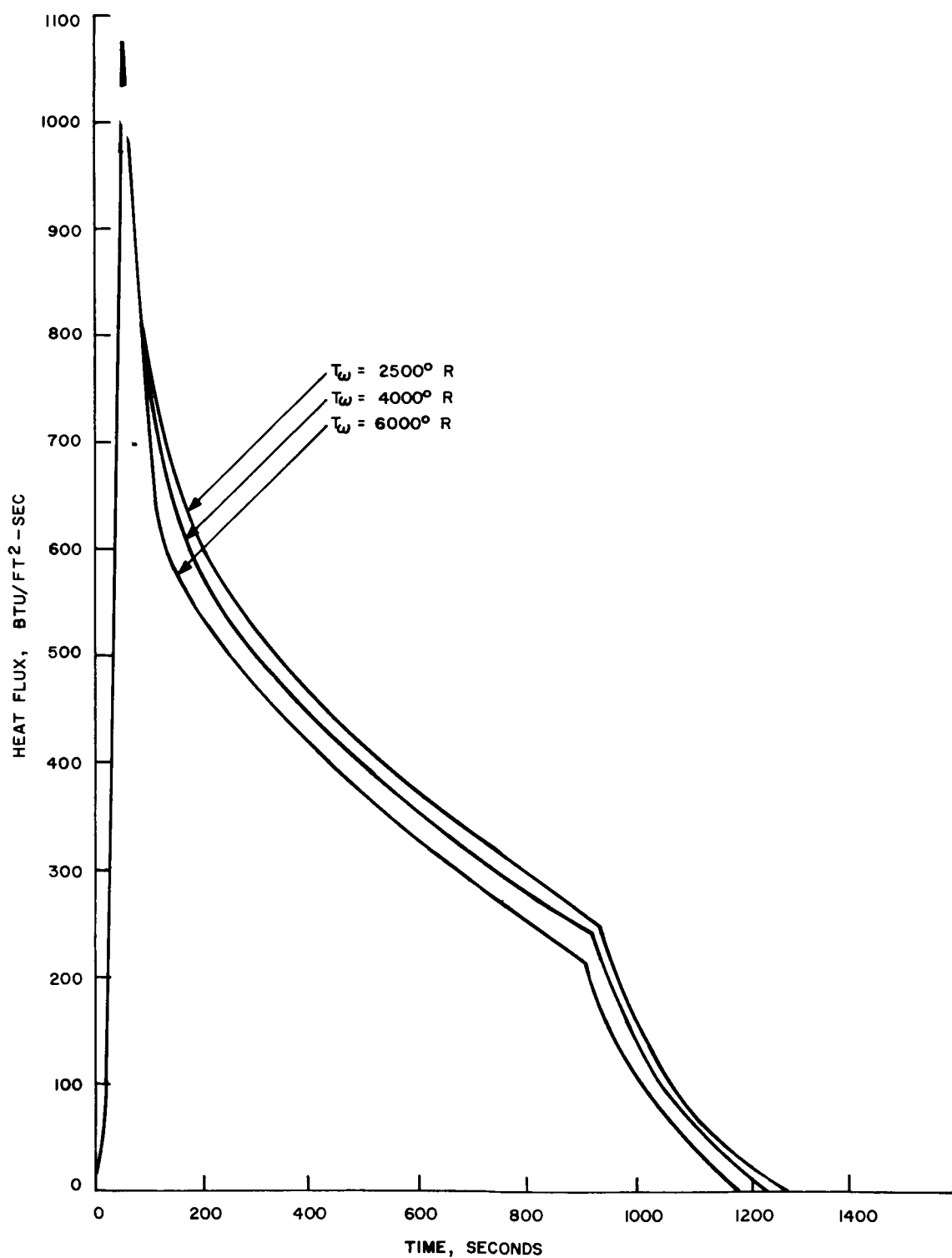


Figure IX-2-10. C-1 configuration — effect of wall temperature on convective heat flux at the stagnation point, re-entry angle,  $\Theta_E = 8.7$  degrees

~~CONFIDENTIAL~~

~~CONFIDENTIAL~~

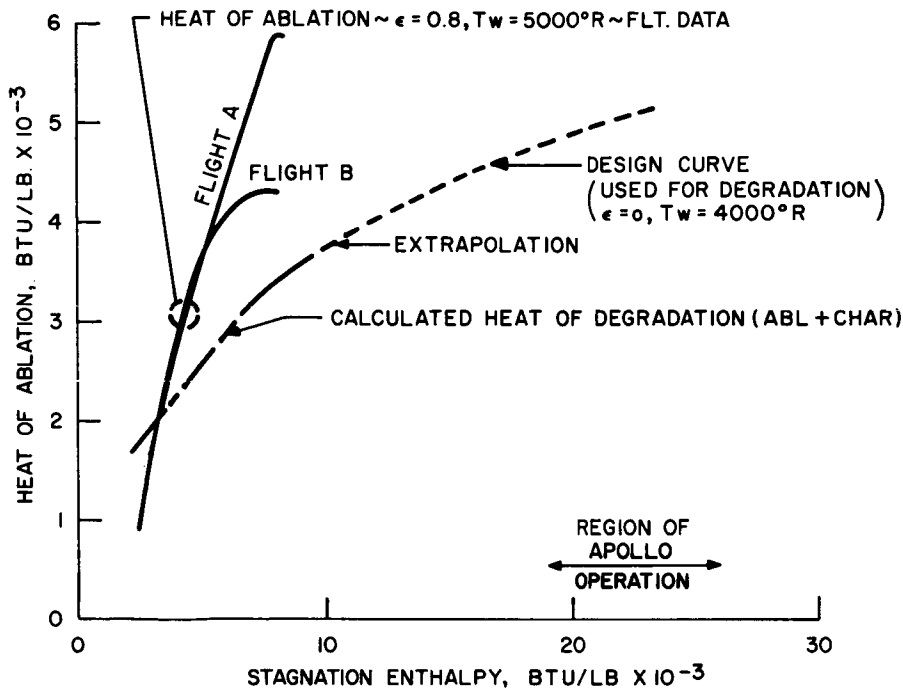


Figure IX-2-11. Heats of ablation — phenolic/nylon

The additional virgin plastic needed as insulation to limit the backface temperature to 960 degrees is estimated by means of a Groeber-type chart. Table IX-2-1 shows the thickness requirements for this type of system.

Because of the long times encountered and the resultant large time-integrated heat inputs, re-radiation cooled systems are attractive. Figure IX-2-12 shows re-radiation equilibrium temperatures as a function of time for body stations where the re-radiation cooled structure may be applicable. Potential materials are the refractory metals such as niobium, molybdenum, and moly-tungsten alloy. A possible current state of the art high temperature, high strength alloy is Rene' 41. The refractory metals, in general, require a suitable coating to prevent oxidation during their long time exposure to air at elevated temperature.

The technique or combination of techniques chosen for surface protection depends upon the magnitude and duration of the heating and

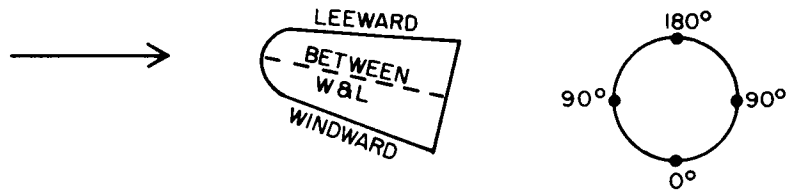
~~CONFIDENTIAL~~

~~CONFIDENTIAL~~

TABLE IX-2-1. HEAT PROTECTION FOR APOLLO VEHICLES  
FOR C-1 CONFIGURATION

		Phenolic-Nylon Shield Thicknesses Req'd to Maintain* 960°R Back Face					
		Windward (0°)		Between W & L (90°)		Leeward (180°)	
	Station	Amt. Ablated + Char	Insula- tion	Amt. Ablated + Char	Insula- tion	Amt. Ablated + Char	Insula- tion
$\Theta_E = 5.7^\circ$	0'	—	—	—	—	—	—
	1.216"	2.72"	0.55"	1.63"	0.71"	0.77"	0.81"
	7.199"	1.30"	0.69"	0.66"	0.82"	0.32"	0.96"
	21.158"	0.80"	0.80"	0.34"	0.94"	0.18"	1.05"
$\Theta_E = 8.7^\circ$	0'	—	—	—	—	—	—
	1.216'	2.82"	0.49"	2.30"	0.50"	2.04"	0.51"
	7.199'	1.92"	0.50"	1.36"	0.51"	1.08"	0.53"
	21.158'	1.54"	0.51"	1.12"	0.53"	0.90"	0.56"

\* At impact



$\Theta_E = 5.7^\circ$	Graphite					
			Insulation			
	Station	Amount Oxidized	Commercial	Pyrolytic	Low Density	
	0'	0.41"	0.19"	0.2"	7"	
	1,216'	0.12"	0.13"	0.15"	7"	
	7,199'	0.07"	0.12"	0.1"	7"	
	21,158'	0.05"	0.14"	0.1"	7"	
	$\Theta_E = 8.7^\circ$	0'	0.55"	0.20"	0.2"	5"
		1,216'	0.15"	0.15"	0.15"	5"
		7,199'	0.11"	0.08"	0.1"	5"
21,158'		0.08"	0.11"	0.1"	5"	

~~CONFIDENTIAL~~

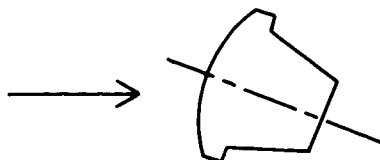
~~CONFIDENTIAL~~

TABLE IX-2-1. HEAT PROTECTION FOR APOLLO VEHICLES  
(Continued)

FOR B-2' CONFIGURATION

	Section	Graphite		Low Density Ins.	Phenolic-Nylon
		Commercial	Pyrolytic		
$\Theta_E = 6.0^\circ$	Entire Forebody	0.19"	0.05"	3.6"	1.4"
	Cylinder	0.19"	0.05"	3.6"	0.6"
		Phenolic-Nylon	Columbium	Low Density Ins.	
	Afterbody	0.15"	Min. Thick.	3.6"	0.5"

	Section	Graphite		Low Density Ins.	Phenolic-Nylon
		Commercial	Pyrolytic		
$\Theta_E = 7.6^\circ$	Entire Forebody	0.19"	0.05"	2.8"	1.3"
	Cylinder	0.19"	0.05"	2.8"	0.6"
		Phenolic-Nylon	Columbium	Low Density Ins.	
	Afterbody	0.15"	Min. Thick.	2.8"	0.5"



~~CONFIDENTIAL~~

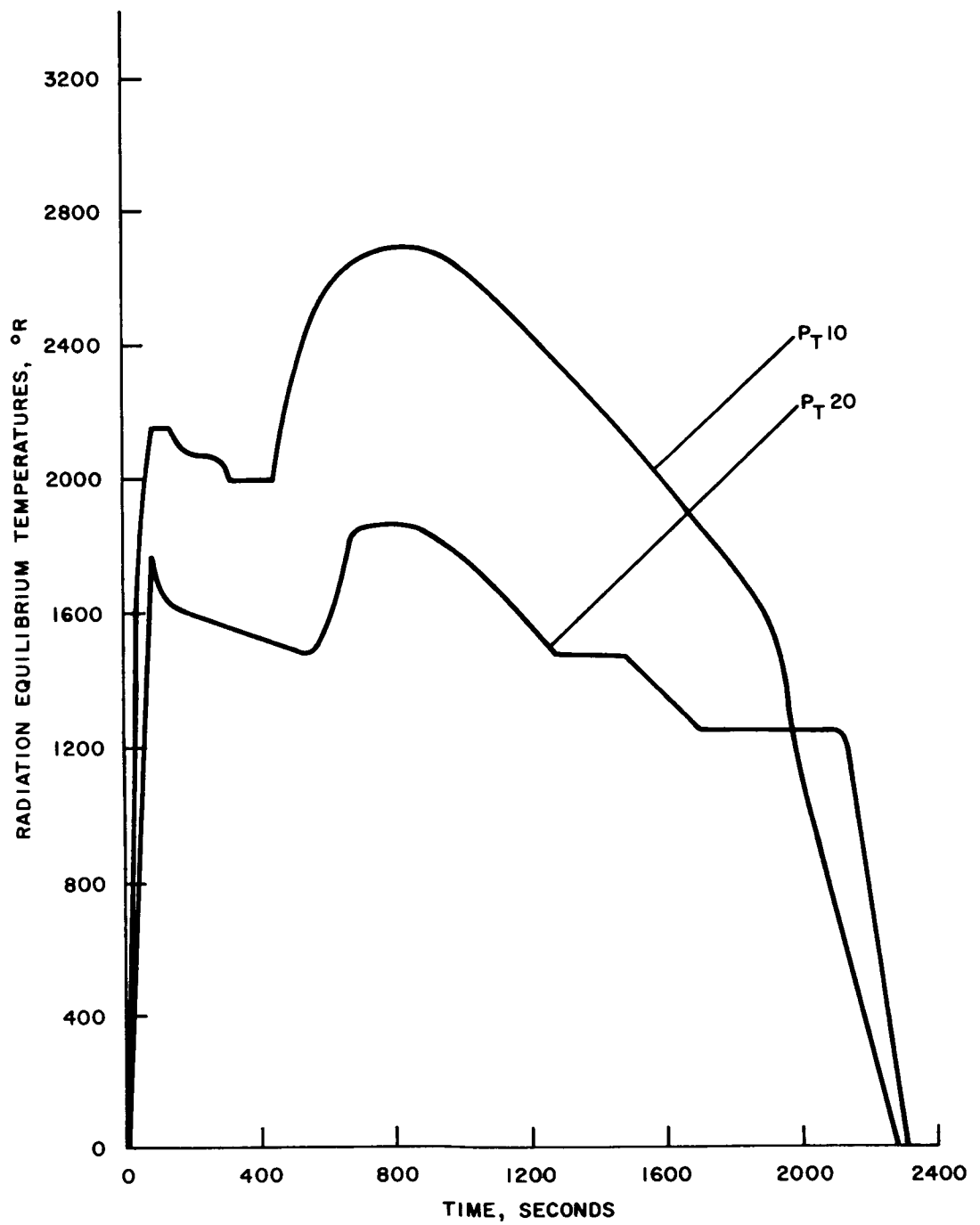


Figure IX-2-12. C-1 configuration — re-radiation equilibrium temperatures, re-entry angle,  $\Theta_E = 5.7$  degrees, emissivity = 0.9

~~CONFIDENTIAL~~

on the design limitations. For the APOLLO design, weight is a prime consideration and the final choice of the heat protection systems will be based upon optimization of the efficiency of the surface-protection technique, i. e., heat absorption per unit weight. The heating rates and total heat load for the APOLLO nominal re-entry trajectories lie between the ballistic and glide re-entry regimes, since the vehicle has both lift and an initial re-entry angle. This immediately suggests the utilization of a combined ablation-radiation heat protection system. Near the end of the return flight from the Moon, the APOLLO vehicle will have accelerated to velocities in the neighborhood of 36,000 feet-per-second which imposes a severe initial requirement on the heat absorption system. When one considers an ablation system, consideration must be given to the distortion which will take place at the stagnation region and its effect upon the aerodynamic control of the re-entry vehicle during the remainder of the trajectory. Figures IX-2-13 and IX-2-14 illustrate two possible heat protection systems for the nose cap section of the vehicle.

The phenolic/nylon nose cap design will act as a combined ablation-re-radiation-insulation system. During the initial re-entry period in which peak heating rates are encountered, the phenolic/nylon will act as an efficient heat-absorption system. For the remainder of the trajectory, the char formed at the surface should act as an efficient re-radiator since the emissivity of carbon is approximately 0.80. The uncharred phenolic/nylon which remains would serve as insulation to the vehicle internal support structure. As mentioned previously, distortions of the initial vehicle and char loss due to shear stress may outweigh the advantages of this single-material heat-absorption system. The ablation calculations utilized to predict the phenolic/nylon thicknesses were based upon the method of Scala. (1)

Figure IX-2-14 illustrates a composite heat-absorption system utilizing commercial graphite, pyrolytic graphite, and a low-density insulation.

The low oxidation rate of graphite (2) assures a minimum distortion of the initial nose cap shape. The pyrolytic graphite liner acts as an excellent insulator but must be backed by an additional low-density insulation (micro quartz) since the deposition thickness of pyrolytic graphite is limited at the present time. (3, 4) The graphite

~~CONFIDENTIAL~~

~~CONFIDENTIAL~~

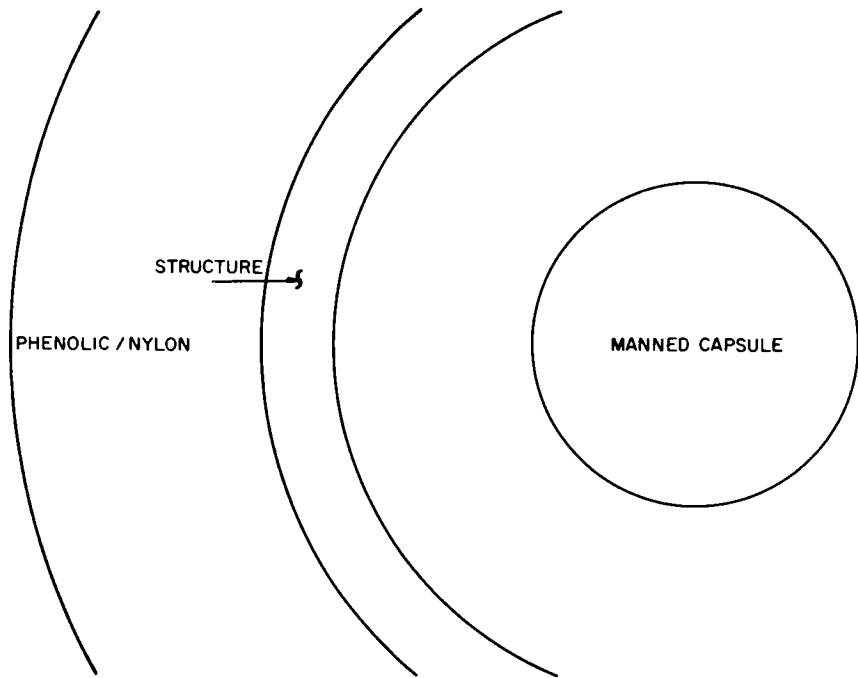


Figure IX-2-13. Typical ablation heat protection system

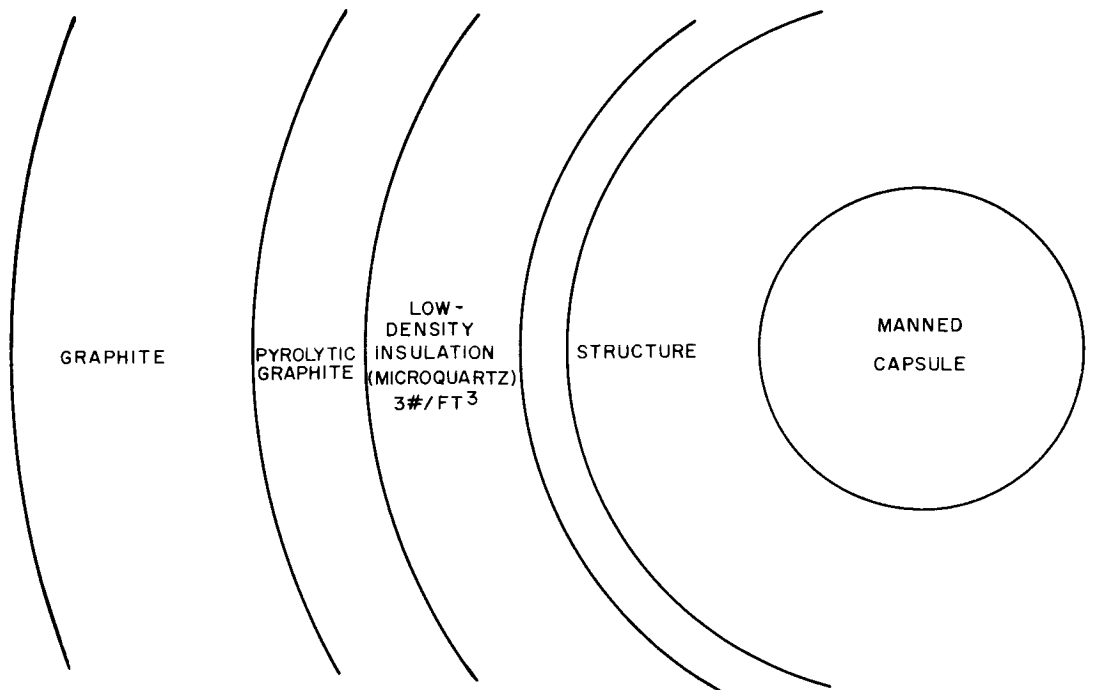


Figure IX-2-14. Composite graphite heat protection system

~~CONFIDENTIAL~~

~~CONFIDENTIAL~~

oxidation calculations for the APOLLO trajectory were based upon the method of Scala and Nolan. (5) Appendix "A" reviews the oxidation mechanism of graphite.

Another interesting possibility would be the utilization of a phenolic nylon/graphite composite where the highest efficiency of each heat absorption system would be utilized. For regions of the vehicle which are exposed to less severe heating rates and total heat load, coated molybdenum or columbium may be utilized.

Phenolic/nylon has been used for the heat protection system as a conservative initial design criterion. Significant increases in efficiency are possible with the use of General Electric Century series plastics or graphite.

## REFERENCES

- (1) Scala, S. M., "A Study of Hypersonic Abation", Tenth Int. Astro. Federation Congress, (1959).
- (2) Nolan, E. J., Scala, S. M., "Aerothermodynamic Feasibility of Graphite for Hypersonic Glide Vehicles", General Electric TIS R60SD425, August, 1960.
- (3) "Pyrolytic Graphite Preliminary Design Data", General Electric Company, Metallurgical Products Department.
- (4) Diefendorf, R. J., "Preparation and Properties of Pyrolytic Graphite", General Electric Report No. 60-RL-2572M.
- (5) See Reference (2).

~~CONFIDENTIAL~~



~~CONFIDENTIAL~~

## Appendix 'A' — Analysis Of Graphite Oxidation Process (A-1)

### CHEMICAL OXIDATION OF GRAPHITE

In an investigation of the behavior of graphite during re-entry, one requires data on the nature and extent of the chemical reactions between carbon and the primary products of dissociated air, including atomic and molecular oxygen and nitrogen. The reaction between carbon and oxygen produces both CO and CO<sub>2</sub>. A number of different mechanisms are possible and these include the following:

1. The formation of both CO and CO<sub>2</sub> is a surface reaction between C<sub>(s)</sub> and O<sub>2</sub> or O.
2. The formation of CO<sub>2</sub> from C<sub>(s)</sub> and O<sub>2</sub> and O at the surface, followed by the dissociation of CO<sub>2</sub> to CO, O<sub>2</sub> and O in the gas phase, or reduction of CO<sub>2</sub> to CO at the surface.
3. The formation of CO at the surface from C<sub>(s)</sub> and O<sub>2</sub> or O, or C<sub>(s)</sub> and CO<sub>2</sub>, the CO being oxidized to CO<sub>2</sub> in the gas phase.

Fortunately both the mass transfer and heat transfer at the surface can be predicted without specifying the specific oxidation mechanism.

It is commonly accepted that the manner in which the oxidation of graphite proceeds depends on the type of graphite, the environmental conditions (e.g., the pressure, temperature, velocity, and composition of the stream), the surface temperature; and at high surface temperatures, on the geometry of the model. The temperature at which a measurable mass loss first occurs, is called the threshold temperature (1000-1800 degrees R) and is not a constant but depends on the partial pressure of the reacting gas at the surface.

At low surface temperatures, the mass loss increases rapidly with surface temperature, and the ablation rate is limited by the speed of the chemical processes, including absorption, reaction, and desorption.

(A-1) Scala, S. M. "The Ablation of Graphite in Dissociated Air" (to be published).

~~CONFIDENTIAL~~

~~CONFIDENTIAL~~

At somewhat higher temperatures (1400-3200 degrees R), the speed of the chemical processes is comparable to the rate at which fresh reactant is brought to the surface and the products of reaction are removed by convection and diffusion. Therefore, the over-all process is in a transition regime, where the speed of the over-all oxidation process is limited by the presence of two resistances in series, one chemical and the second gas dynamic.

At temperatures above 3200 degrees R, the chemical oxidation processes are overshadowed by the gas dynamic processes. In this diffusion-controlled regime, the mass loss is relatively insensitive to the surface temperature.

Eventually, when the surface temperature is sufficiently high (5500-8000 degrees R), the sublimation rate of carbon atoms and molecules can exceed the surface oxidation rate, and these species are then present in the gas phase. These regimes are illustrated in Figure IX-2-15.

The predicted graphite surface temperatures and stagnation pressures indicated that the graphite oxidation would take place for the most part in the diffusion-controlled regime for the APOLLO trajectories considered. In the diffusion-controlled regime, it has been found that the mass loss for an axially-symmetric graphite body can be correlated in the form:

$$\frac{(\dot{m}_w) \sqrt{R_B}}{\sqrt{P_e}} = 6.2 \times 10^{-3} \frac{\text{lb}}{\text{ft}^{3/2} \text{ sec (atm)}^{1/2}}$$

where  $\dot{m}_w$  = rate of mass loss,  $R_B$  = nose radius,  $P_e$  = stagnation pressure.

This equation was used to predict the graphite erosion for the APOLLO vehicle.

~~CONFIDENTIAL~~

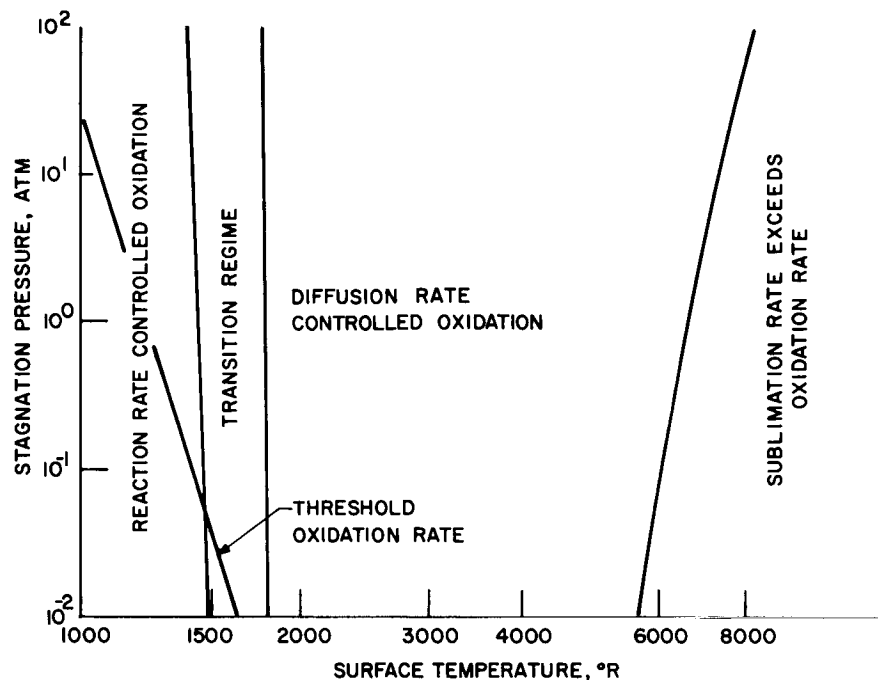


Figure IX-2-15. Graphite oxidation regimes

## EXTERNAL BOOST PHASE

### Heat Inputs

Aerodynamic heat fluxes have been calculated for the boost phase as shown in Figure IX-2-16 using trajectory 3 of the typical APOLLO launch trajectoring furnished by NASA.

### Heat Protection Systems

Due to the relatively low flux values and the short time of flight in the boost regime, a 0.030 in. coating of epoxy polysulfide over the wetted area has been considered as a conservative first approximation.

~~CONFIDENTIAL~~

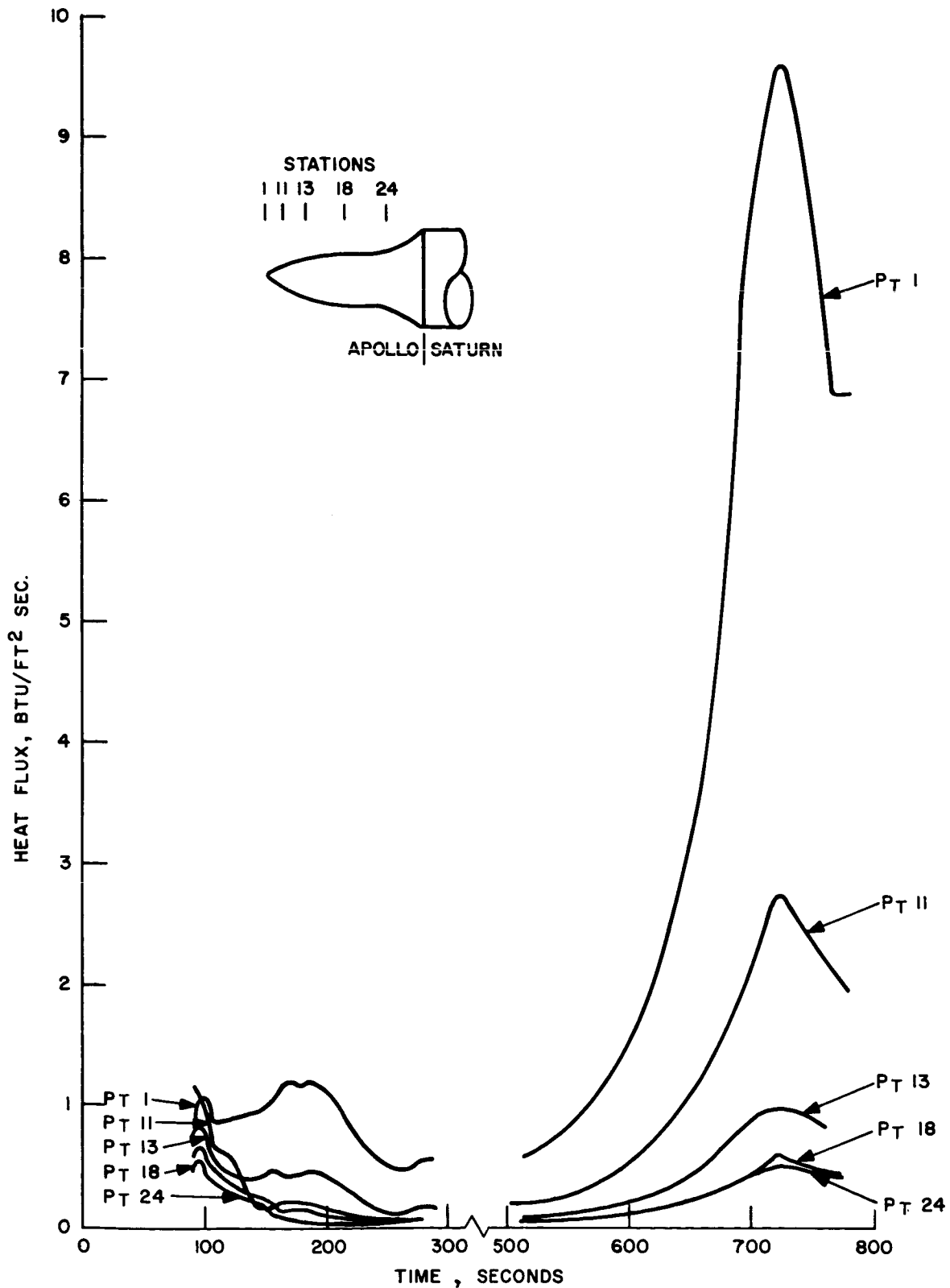


Figure IX-2-16. Heat flux during boost

~~CONFIDENTIAL~~

~~CONFIDENTIAL~~

## INTERNAL TEMPERATURE DURING BOOST AND RE-ENTRY PHASES

An analog computer program for determining the transient temperature characteristics of the compartments during boost and re-entry has been written and is now being programmed.

Preliminary estimates indicate no significant problems in maintaining the crew compartment internal wall temperature below 90F.

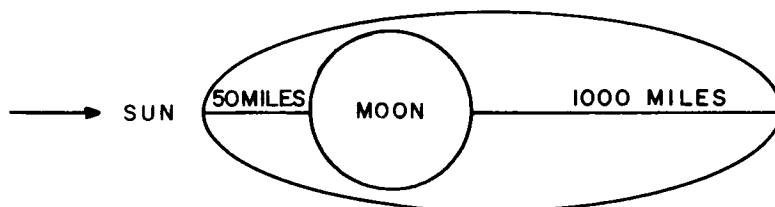
## INTERNAL TEMPERATURE DURING CISLUNAR PHASE

### Radiator

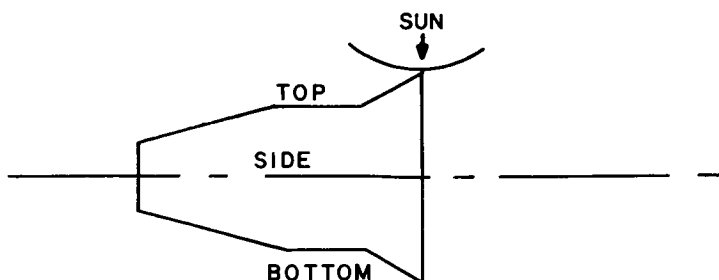
During the cislunar phase, the space vehicle will be oriented to the Sun. Consequently, large areas of the vehicle will be available for efficient use as radiator surfaces, i.e., low equivalent sink temperatures.

During the lunar orbit, however, the problem of finding a suitable location for the radiator is more difficult. This is because the Moon emits large amounts of energy in the same low-temperature spectrum as the radiator hence the radiator cannot be coated to block the incoming radiation.

To investigate this problem, a severe lunar orbit was examined. The orbit was approximated as follows:



the space vehicle was oriented to the Sun at all times as shown



~~CONFIDENTIAL~~

~~CONFIDENTIAL~~

The equivalent sink temperatures for the top, bottom, and sides of the vehicle are shown in Figure IX-2-17 versus time in orbit, where 0 time is at the apolune. The top was considered to have been coated with a material which resulted in an absorptivity to emissivity ratio of  $\alpha/\epsilon = 0.18$  in the solar spectrum, while the sides and bottom were assumed to have an emissivity of  $\epsilon = 0.9$  in the lunar reflected spectrum.

The internal heat dissipation was considered conservatively to be 3000 watts continuous for this investigation. However, the power system must store energy during exposure to sunlight for use during the shade passage. Based on using fuel cells for energy storage and including their waste heat in the internal heat dissipation gives a radiator requirement curve as shown in Figure IX-2-18.

By placing the radiators on each side there is more than enough area available to dissipate the internal heat during the maximum load, which occurs when the radiator sink temperature is approximately 0 degrees R. However, during passage of the vehicle over the sub solar point there is not sufficient area to dissipate the internal heat. This condition is alleviated considerably by the fact that the maximum sink temperature does not occur at the same time for the two sides.

Several solutions might be considered:

- a. Change the lunar trajectory so that the vehicle does not pass over the sub solar point during perigee.
- b. Incline the lunar trajectory so that the vehicle does not pass over the sub solar point at all.
- c. Raise minimum altitude to  $\approx 1000$  miles.
- d. Put additional radiator on top surface.
- e. Use thermal capacity during the short time the radiator is deficient.

In the event that evaporant is carried for re-entry dissipation, the use of the evaporant for thermal storage appears the most feasible. About 35 pounds of  $H_2O$  would be sufficient.

~~CONFIDENTIAL~~

~~CONFIDENTIAL~~

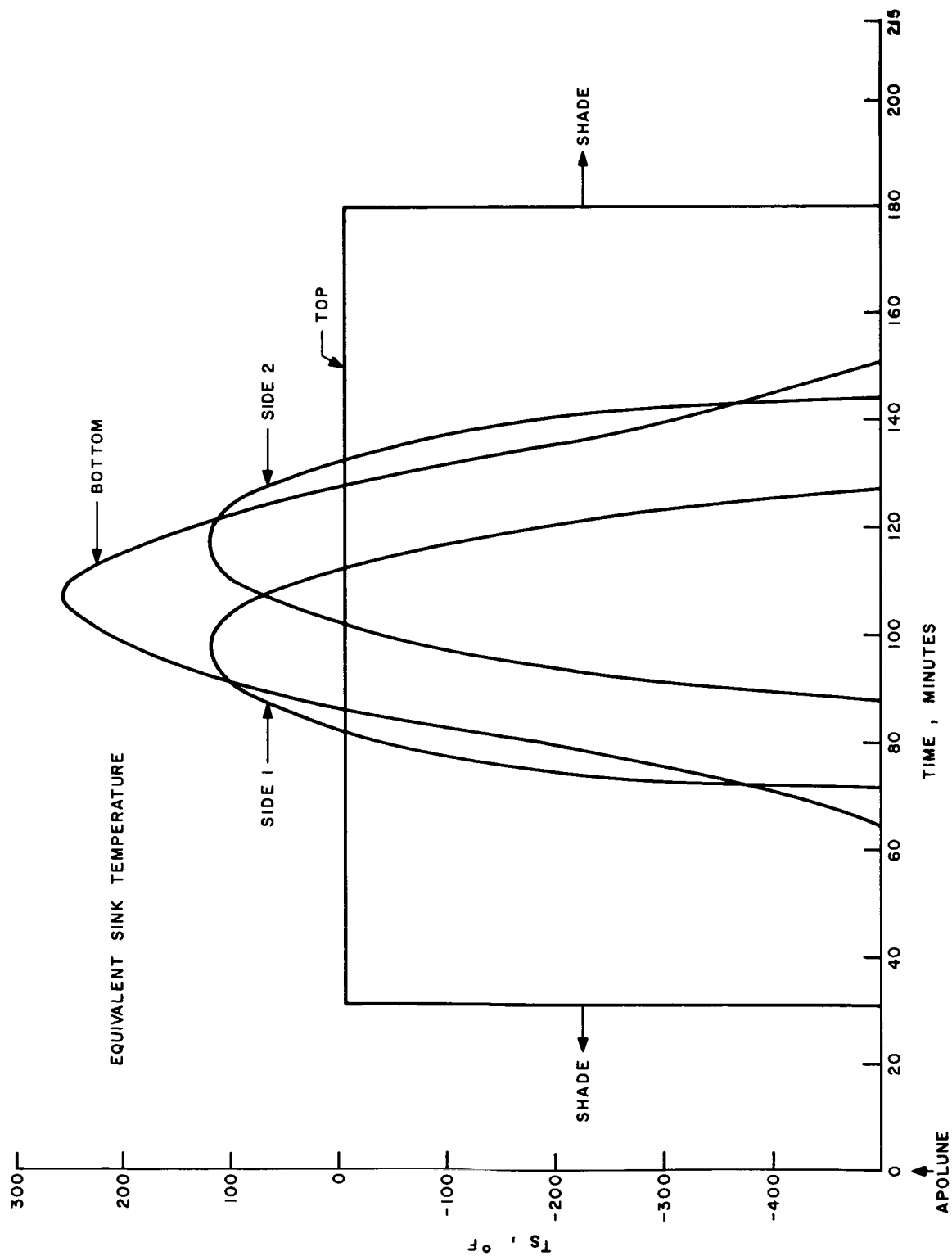


Figure IX-2-17. Space vehicle temperature during lunar orbit

~~CONFIDENTIAL~~

~~CONFIDENTIAL~~

The radiators are presently envisioned as being tubes integral with the exterior skin. Optimization studies are under way considering tube size, spacing, and arrangement from the weight and meteorite damage viewpoints.

~~CONFIDENTIAL~~



~~CONFIDENTIAL~~

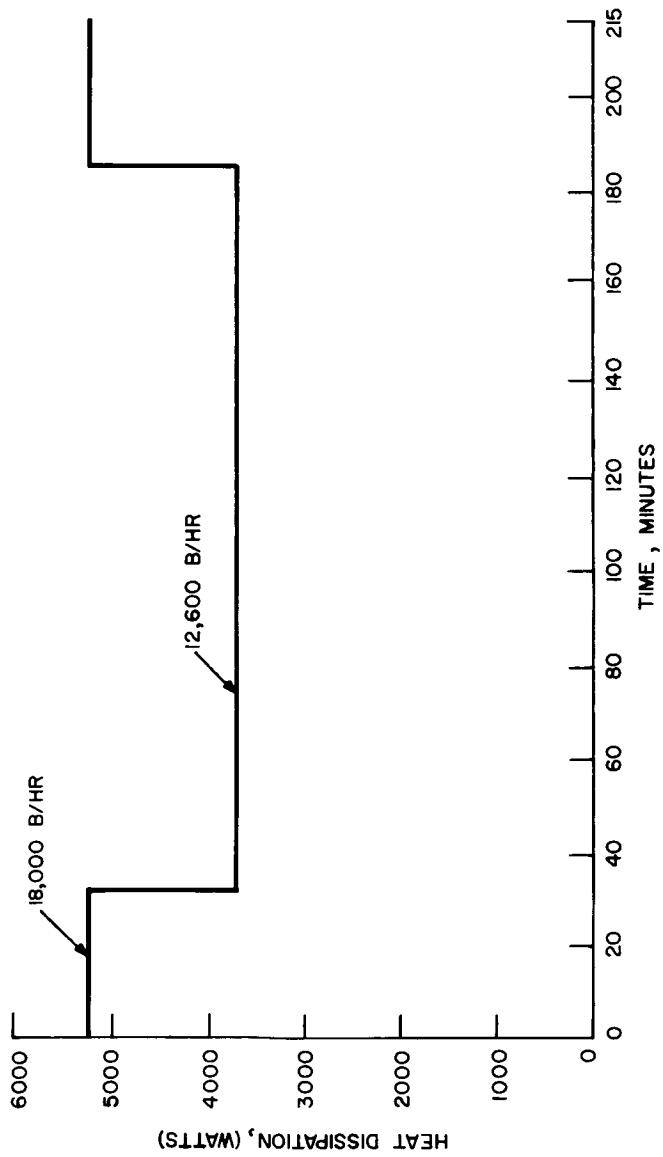


Figure IX-2-18. Radiator requirements — 3000 watts continuous internal heat

~~CONFIDENTIAL~~



## **CHAPTER X**

# **LANDING & RECOVERY**



~~CONFIDENTIAL~~

## X. LANDING AND RECOVERY

The material presented in this chapter represents a comprehensive review of the study performed to date on the landing and recovery system for the APOLLO vehicle. The presentation is divided into 4 major areas of consideration:

1. Landing Systems for Semi-Ballistic-type Re-entry Vehicles.
2. Landing Systems for Glide-type Re-entry Vehicles.
3. Flotation
4. Recovery Aid System

This division is made on the basis that landing system designs for the two types of vehicles used employ significantly different techniques, due to their inherently different configurational designs and re-entry flight paths.

The investigation includes the analysis of various design approaches, trade-off curves between varying degrees of performance and the requirements for such performance, a review of special problem areas (e.g. abort) and, in certain instances, a discussion of some "newer"-type devices that may be applicable to the APOLLO system.

The results of the study clearly indicate that a feasible landing and recovery system design concept is within the current "state-of-the-art" technology, and that further optimization of a system in terms of performance, reliability and weight savings can be accomplished with foreseeable "state-of-the-art" extensions.

~~CONFIDENTIAL~~

# 1. LANDING SYSTEMS FOR SEMI-BALLISTIC-TYPE RE-ENTRY VEHICLES

## PROBLEM DEFINITION

The recovery of ballistic-type re-entry vehicles has been successfully accomplished on a number of occasions in the RVX-1, RVX-2 and Discoverer Programs. Recently, Project Mercury joined the ranks of successful re-entry recovery, demonstrating that manned-capsule recovery is but a short time off. It is quite important to note that all of these vehicles used a straight-forward parachute approach to the solution of the retardation problem. However, it is equally important to remember that all of these programs involve mission profiles and system specifications that are considerably less stringent than those of Project APOLLO. Nevertheless, considerable insight into the solution of the landing and recovery problem for APOLLO can be gained by treating the recovery-flight phase as a straight-forward retardation problem. This approach, however, must be tempered with the following four facts:

1. The recovered payload weight will be two to three times greater than any of the aforementioned vehicles; and considering the lunar mission profile, may involve terminal flight environments much more severe than those previously encountered.
2. Point landing requirements and the possibility of large tolerances on the terminal portion of the re-entry trajectory point to the need for consideration of terminal maneuverability (possibly during the recovery phase).
3. Since human lives are at stake, fail-safe abort capability is a must for any practical system design.
4. Proper consideration of impact attenuation designs must be given when the terminal (final) retardation system is designed.

Using this line of reasoning, then, in conjunction with due consideration for the over-all system specifications has resulted in the following list of preliminary Landing and Recovery System Design Specifications:

~~CONFIDENTIAL~~

1. Recoverable payload weight — 5000 to 15,000 pounds. (To date, most consideration has been given to 5000, 7000, and 10,000 pound re-entry vehicles.)
2. Vertical descent velocity not to exceed 100 fps. (To date, the range of 25 to 35 fps has received the most attention.)
3. Axial loads not to exceed 12 g's in steady state or 20 g's in transient; lateral loads not to exceed 3 g's in steady state or 6 g's in transient.
4. Landing and Recovery System to be applicable in both normal and abort mission situation (i.e. avoid use of separate systems for abort and normal mission.)
5. Maximum Recovery System weight (exclusive of abort escape system) not to exceed 10 percent of total vehicle weight. (To date, recovery system weights on the order of four to six percent of total vehicle weight has evolved.)
6. "Point" Landing area to be a 20-mile square.
7. System reliability to be exceptional; thus dictating the use of proven concepts, or design techniques that are amenable to thorough experimental verification within current or projected testing capabilities (either ground or in flight).

These specifications, then, essentially define the landing and recovery problem and provide a set of working bounds within which the design analysis must function.

## THE RECOVERY SYSTEM

### Terminal Trajectory Conditions

The terminal portion of the re-entry trajectory (i.e. the portion from which recovery system actuation must take place) can, for purposes of this study, be considered as the equilibrium glide of the vehicle along a path corresponding to a  $C_L @ (L/D)_{max}$ . The vehicle will, during this phase, reach some selected altitude-velocity condition along the trajectory where actuation of the recovery system will occur. A typical nominal equilibrium glide case used in this study is presented in Figure X-1-1.

In the following section, the trajectory of Figure X-1-1 is used to formulate the analysis of the retardation system design.

~~CONFIDENTIAL~~

~~CONFIDENTIAL~~

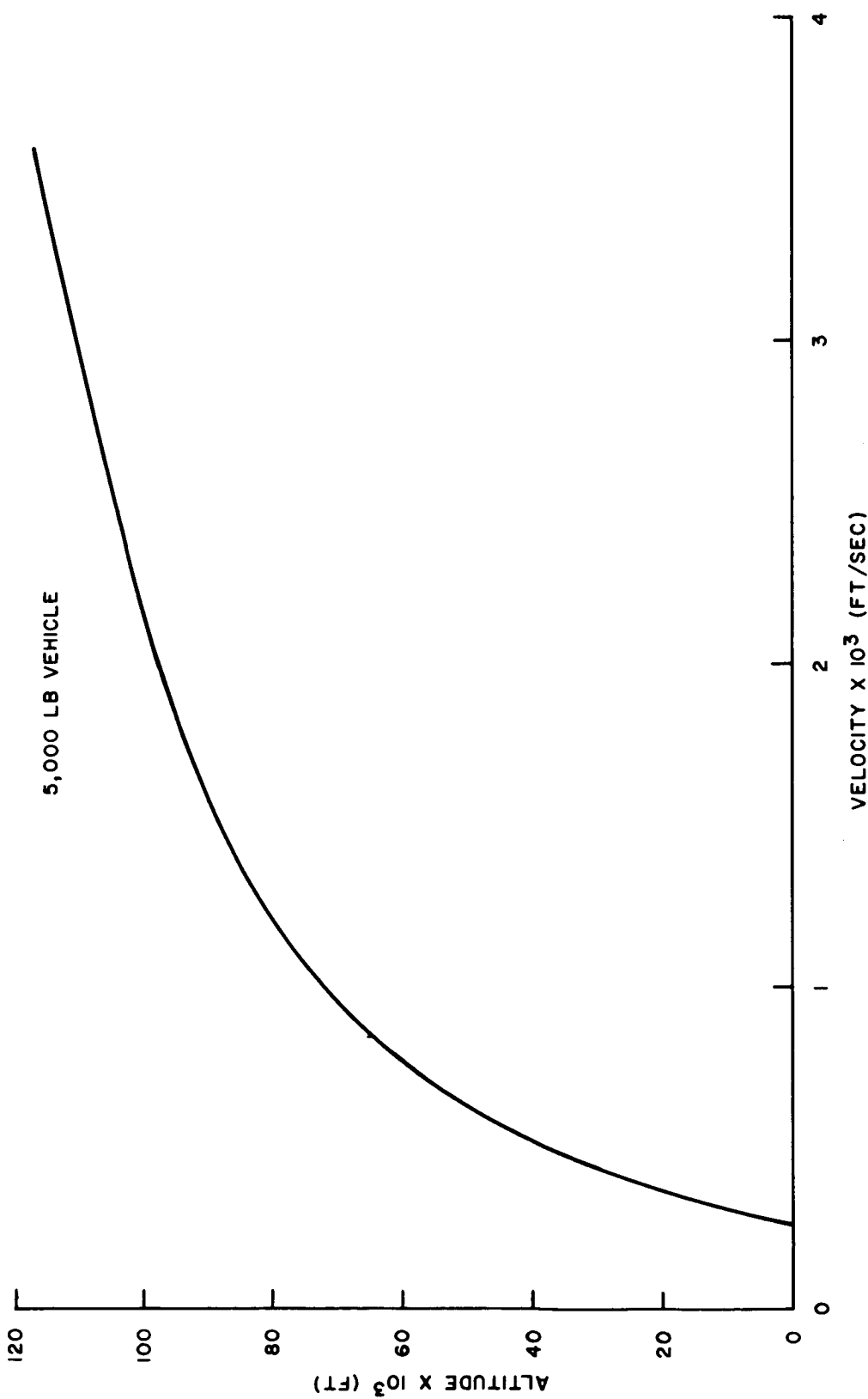


Figure X-1-1. Typical terminal trajectory — APOLLO. Equilibrium glide [ $C_L$  at  $L/D$  max]

~~CONFIDENTIAL~~

~~CONFIDENTIAL~~

Tolerances on the nominal trajectory of Figure X-1-1 have been arbitrarily assumed at  $h \pm 20\%$  (other parameters constant) as the type of error that could be encountered. (Obviously,  $h$ ,  $V$  and  $\gamma$  will all vary for any given error in the re-entry trajectory, and this condition is chosen merely to be representative). The effects of this tolerance, especially on range, have been determined for the recovery portion of the trajectory, and are discussed in a subsequent Section.

## The Retardation System

A rather straight-forward approach to a simple recovery system solution can be taken by considering the use of fairly conventional retardation devices. The equilibrium glide trajectory of Figure X-1-1, which is indicative of a typical flight path for a vehicle like the B-2, indicates that severe environments for retardation actuation will not be a problem. At altitudes as high as 80,000 feet, the Mach number is down to 2.4, and the vehicle is within a current "state-of-the-art" regime in regard to the type of devices that are available. The recovered payload weight, however, is large; values of 10,000, 7,000, and 5000 pounds have been chosen as realistic figures for this weight, and design calculations for representative retardation systems described in later paragraphs are based on these figures. With these large weights, multi-stage retardation systems become necessary in order to achieve a velocity decrease for final-stage deployment, and hence a tolerable snatch and shock load force. Such weights also necessitate large final stage drag areas ( $C_D A$ ) and Figure X-1-2 shows that this  $C_D A$  for a 5,000-pound payload can be as high as 7,000 square feet for an equilibrium descent velocity at impact ( $V_T$ ) of 25 fps. For large  $C_D A$  values, large retardation devices are required, possibly in cluster form. Suffice it to say that weight considerations certainly advise the use of inflatable devices in this final stage, self inflating if possible. At the present time, parachutes still appear to be an optimum selection, and it is certainly reasonable to say that parachutes approach an optimum selection for the early retardation stages also, if other factors do not indicate otherwise (e.g. Mach number or chute instability effects).

Neglecting for the moment considerations of terminal maneuverability and abort, and concentrating only upon payload weight, re-entry trajectory, tolerable  $g$  conditions, and impact velocity requirements, one can immediately pursue the design of a practical

~~CONFIDENTIAL~~

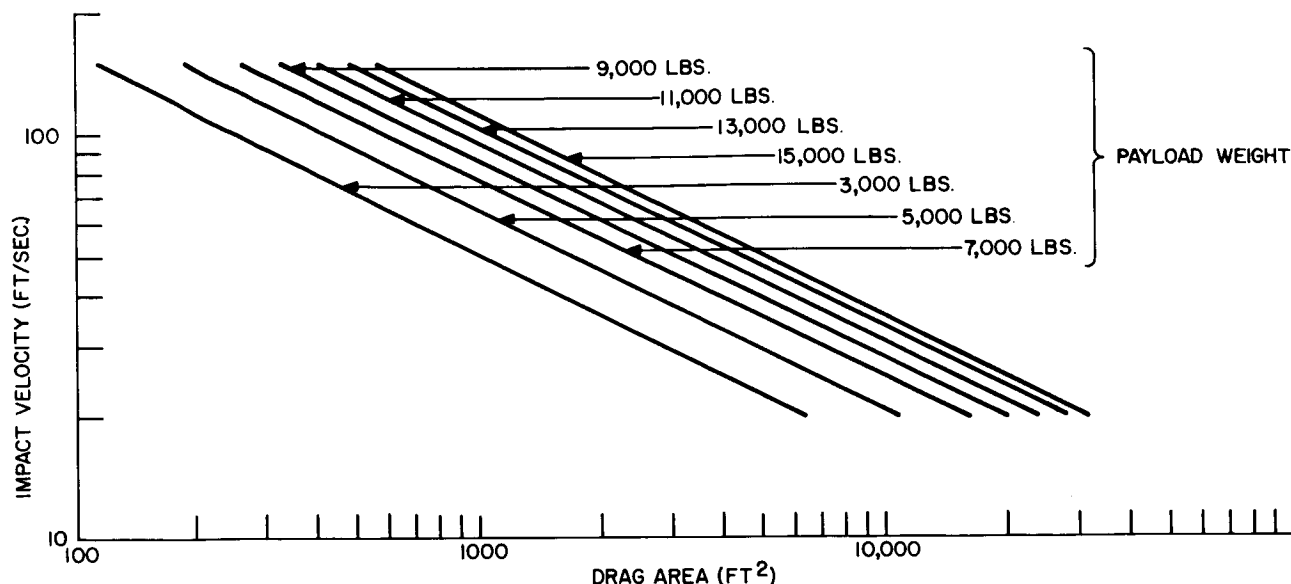


Figure X-1-2. Drag area ( $C_D A$ ) versus impact velocity

retardation system. Five such retardation systems have been devised for the terminal  $h - V$  profile given in Figure X-1-10. A resume of pertinent data for each of these systems is given in Table X-1-1. In line with early vehicle design concepts, the payload weights were limited to the 5000 pound, 7000 pound and 10,000 pound cases. Terminal velocities at  $h = 0$  were held to the 25 - 30 fps category, since early estimates of the optimum impact attenuation plus retardation system weight appeared to be located at the lower end of  $V_t$  scale (calculation of Figure X-1-16 later proved this to be true). Two 2-chute, 3-stage systems and one 2-chute plus inflatable cone, 4-stage system were chosen for investigation over a fairly wide range of deployment conditions. (System I, III and II of Table X-1-1 respectively.) The latter system was chosen with the intent that an additional deceleration stage at the beginning could well serve to reduce any serious or marginal  $g$  limit situations that may arise on a 2-chute system, and likewise produce a significant velocity reduction during first stage retardation at very little expense in altitude. An analysis of these variations for the three systems and their effect on such parameters as range (as measured from some pre-selected, fixed point of projection on the Earth) is given in subsequent paragraphs of this Section.



(Also, the interjection of a maneuvering device between the first and second stages of System II is presented in a later Section of this Chapter.

Two systems (IVA and IVB) represent modification of System III in which the systems have been scaled to apply to a payload weight of 5000 pounds. It can be seen from Table I that the difference between System IVA and IVB is in the size of the ribbon chute used as a first stage (25 feet  $D_0$  for System IVA and 16 feet  $D_0$  for System IVB).

After calculating the trajectory for System IVA it was observed that the deceleration loads, Figure X-1-3, upon deployment of the first stage were larger than the 9 g limit (without shock factor). Therefore, a trajectory was calculated for a System (IVB) having a first stage of a size which would reduce the deployment g loading below the 9 g limit but would still have a tolerable velocity at  $h = 15,000$  feet where the second stage is deployed. The g limit would also limit first stage deployment altitude for System IVB to, 58,000 feet  $> h > 25,000$  feet.

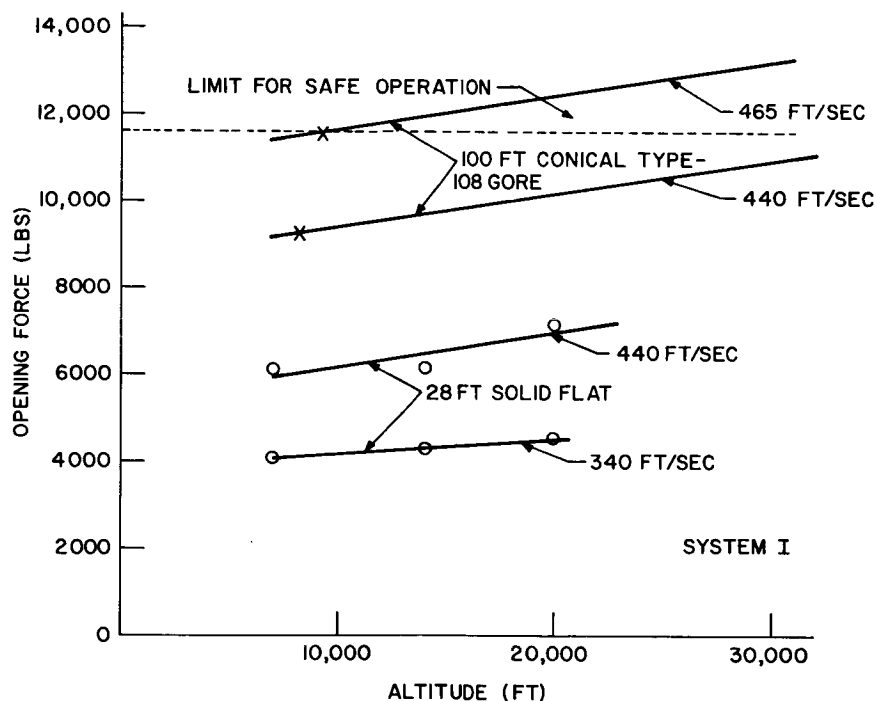


Figure X-1-3. Opening force versus altitude—reefed parachute

**CONFIDENTIAL**

TABLE X-1-1. PRELIMINARY DESCRIPTIONS OF APOLLO  
RETARDATION SYSTEMS

System I. 3 Stage — 2 Chute, Payload weight = 10,000 pounds

Stage and Description	Deployment Conditions	$D_o$ (ft)	$C_{D_o}$	Approx. Wt.-Total (lbs.)	Packing Volume (in <sup>3</sup> )	$V_t$ (fps)
Pilot Chute- Guide Surface	Prior to 1st Stage	3	0.7	1	50	--
1-Ribbon Chute—Fully Open	$h = 60,000$ ft $V = 1250$ fps	12	0.35(super- sonic) 0.50(sub- sonic)	50 (1000 lb ribbon)	5000	--
2-100 ft conical type -108 gore (three each)— reefed	$h = 30,000$ ft $V = 456$ fps	6.4 each	---	600	12,400	--
3-Same as 2— fully open	$h = 27,388$ ft $V = 218$ fps	100 each	0.7(in cluster)	Same Sys- tem as #2 above	Same Sys- tem as #2 above	25

System II. 4 Stage — 1 Cone + 2 Chute, Payload weight = 7,000 pounds

Pilot Chute- Guide Surface	Prior to 1st Stage	3	0.7	1	50	--
1-Inflatable Cone — 90°	$h = 80,000$ ft $V = 2400$ fps	0.88 Body Dia.	1.0(super- sonic)	10(estimate)	---	--
2-Ribbon Chute—Fully Open	$h = 75,565$ ft $V = 1367$ fps	25	0.35(super- sonic) 0.50(sub- sonic)	30 (300 lb. ribbon)	2500	--
3—See Note						
4-77 ft. conical type -108 gore (two each)— fully open	$h = 15,000$ ft $V = 182$ fps	77	0.7(in cluster)	265	~10,000	30

NOTE: Reefing required in this stage, but preliminary analysis of System II and III did not include reefing.

~~CONFIDENTIAL~~

TABLE X-1-1. PRELIMINARY DESCRIPTIONS OF APOLLO  
RETARDATION SYSTEMS (Continued)

System III. 3 Stage — 2 Chute, Payload weight = 7,000 pounds

Stage and Description	Deployment Conditions	$D_o$ (ft)	$C_{D_o}$	Approx. Wt.-Total (lbs.)	Packing Volume (in <sup>3</sup> )	$V_t$ (fps)
Pilot Chute- Guide Surface	Prior to 1st Stage	3	0.7	1	50	--
1-Ribbon Chute—fully open	h = 58,000 ft V = 1183 fps	25	0.35(super- sonic) 0.50(sub- sonic)	30 (300 lb. ribbon)	2500	--
2-See Note						
3-77 ft.conical type — 108 gore (two each)— fully open	h = 15,000 ft V = 182 fps	77	0.7(in cluster)	265	~10,000	30

System IVA. 3 Stage — 2 Chute, Payload weight = 5000 pounds

Pilot Chute- Guide Surface	Prior to 1st Stage	3	0.7	1	50	--
1-Ribbon Chute— Fully Open	h = 58,000 ft V = 1183 fps	25	0.35(super- sonic) 0.50(sub- sonic)	30 (100 lb. ribbon)	3000	--
2-65 ft.conical (two each) reefed	h = 15,000 ft V = 140 fps	7 ft each	--	202	7000	--
3-Same as 2 fully open	h = 14,260 ft V = 117 fps	65 ft each	0.7(in cluster)	202	7000	30

NOTE: Reefing required in this stage, but preliminary analysis of System II and III did not include reefing.

~~CONFIDENTIAL~~

~~CONFIDENTIAL~~

TABLE X-1-1. PRELIMINARY DESCRIPTIONS OF APOLLO  
RETARDATION SYSTEMS (Continued)

System IVB. 3 Stage — 2 Chute, Payload weight = 5000 pounds

Stage and Description	Deployment Conditions	$D_o$ (ft)	$C_{D_o}$	Approx. Wt.-Total (lbs.)	Packing Volume (in <sup>3</sup> )	$V_t$ (fps)
Pilot Chute- Guide Surface	Prior to 1st Stage	3	0.7	1	50	--
1-Ribbon Chute Fully Open	h = 58,000 ft V = 1183 fps	16	0.35(super- sonic) 0.5(sub- sonic)	10	1200	--
2-65 ft. conical (two each) reefed	h = 15,000 ft V = 178 fps	7 ft each	---	202	7000	--
3-Same as 2 fully open	h = 13,750 ft V = 114 fps	65 ft each	0.7(in cluster)	202	7000	30

NOTE: Reefing required in this stage, but preliminary analysis of System II and III did not include reefing.

~~CONFIDENTIAL~~

~~CONFIDENTIAL~~

By way of illustration, the design philosophy for System I is now reviewed to demonstrate the various design problems that are being considered in the study. For this case, a 10,000 payload impacting at  $V_t = 25$  fps was selected. This combination requires a final stage  $C_D A$  of 13,500 square feet. A review of available "hardware" indicated that a 100 foot diameter conical type — 108 gore parachute, arranged in a cluster of three, would meet this  $C_D A$  requirement with some margin to spare ( $C_D A$  of this arrangement  $\approx 16,000$  square feet). It is felt that this type of chute is a very reliable selection since it has already been extensively tested with 10,000 payloads. For similar values of  $C_D A$ , this particular chute is also considered to be a substantial improvement over the standard G-11 solid flat parachute since it is some 20 percent lighter, and has a packed volume approximately 35 percent less than that of the G-11. With this selection of the conical — 108 gore parachute as the final stage, it then became a question of determining the ideal deployment conditions for the final stage in light of the axial g limitations on the vehicle, the opening shock forces on the parachutes, and the forces required to pull the chute from the vehicle. In regard to axial g limits and opening shock forces, it was immediately obvious that a reefed second stage would be required on these large 100 foot chutes. Opening shock data, presented in Figure X-1-3, was examined to locate a suitable altitude for reefed opening. This was done by establishing the slope of the  $F_{\max}$  vs  $h$  line @  $V = \text{constant}$  from 28 foot Solid Flat parachute data. With data at 10,000 feet on the 100-foot chutes (X), lines of equal slope through these points were established. At 10,000 feet, speeds in excess of 465 fps produced failures on the 100-foot reefed chute, hence an  $F_{\max} = 11,600$  pounds was chosen as an operating limit. At 440 fps, the curves indicated that safe operation could take place at  $h > 30,000$  feet, and the arbitrary condition of  $h = 30,000$  feet was selected for reefed opening. Test data was also used to establish the fact that a 12-foot chute was the approximate size required to deploy three 100-foot chutes from the vehicle. Hence, a 12-foot chute was used for the first stage of the system. It now became a simple matter of defining the  $h - V$  conditions at which first-stage deployment was required to insure a velocity of 440 fps or less at second-stage deployment. As the trajectory of Figure X-1-4 shows, deployment of the first-stage chute at  $h = 60,000$  feet,  $V = 1250$  fps for a chute  $C_D = 0.35 \rightarrow 0.5$  resulted in  $V = 456$  fps at  $h = 30,000$  feet. For preliminary design purposes, this is felt to be sufficiently close to the 440 fps figure. The  $C_D$  values shown above are for a ribbon-type chute, and since first-stage deployment occurs in the supersonic region, (at  $M > 2$ ), a ribbon chute is a logical choice for the first stage of

~~CONFIDENTIAL~~

the system. Shock loads for the ribbon chute deployment are of the order of 8500 pounds, and this is within tolerable levels. The total weight of System I as described here and shown in Table X-1-1 is about 650 pounds or 6.5 percent of the total recovered weight. This includes a small pilot chute (for first-stage deployment) and three small stabilization chutes located above the canopies of the fully open 100-foot conical chutes.

Similar analyses were done to establish Systems II and III for a 7000-pound payload and  $V_t = 30$  fps, and Systems IVA and IVB for a 5000 pound payload and  $V_t = 30$  fps. The trajectories for these systems are shown in Figures X-1-5, X-1-6, X-1-7, and X-1-8 respectively, and their description is given in Table X-1-1. The final stage again employs the conical type - 108 gore parachute, but its diameter is now reduced to 77 feet due to the decreased  $C_{DA}$  requirement for 6500 square feet at  $h = 0$ . Note also that an inflatable cone is used as the first stage in System II since deployment was chosen at  $M > 2$ , a region in which parachute operation becomes unreliable in the present "state-of-the-art". A number of interesting observations can be made in examining three- and four-stage systems such as Systems II and III and comparing their relative merits. In the  $h - V$  plot of Figure X-1-9, it can be seen that the addition of the first-stage inflatable cone on System II has no effect on the  $h - V$  characteristics below 50,000 feet and hence provides no additional deceleration for the reefed opening of the final-stage chutes. Its main effect is felt at high altitudes, where a rapid velocity decrease occurs with little altitude loss (Figure X-1-10). In fact, Figure X-1-11 illustrates this in that the first stage of System III can be deployed as low as 21,000 feet, in order to obtain the desired velocity characteristics at the selected second-stage deployment location of 15,000 feet. Hence, deployment of an initial retardation stage at high altitudes does not buy any velocity advantage, with respect to final-stage deployment conditions, but as Figure X-1-12 clearly indicates, load limits will not permit deployment of the System III first stage at altitudes below 24,000 feet for the 9 g limiting case or 46,000 feet for the 8 g limiting case (these g limits are quasi-steady state conditions and opening shock forces could run the transient as high as 12 g's, the desired upper limit). Figure X-1-12 also indicates that, in all probability, neither  $V$  nor  $q$  will limit first stage deployment at  $h < 100,00$  feet for System III. But the g limit problem points to the need for additional stages (e.g. System II) if ribbon chute deployment is desired at  $h > 68,000$  feet or  $h < 24,000$  feet.

~~CONFIDENTIAL~~

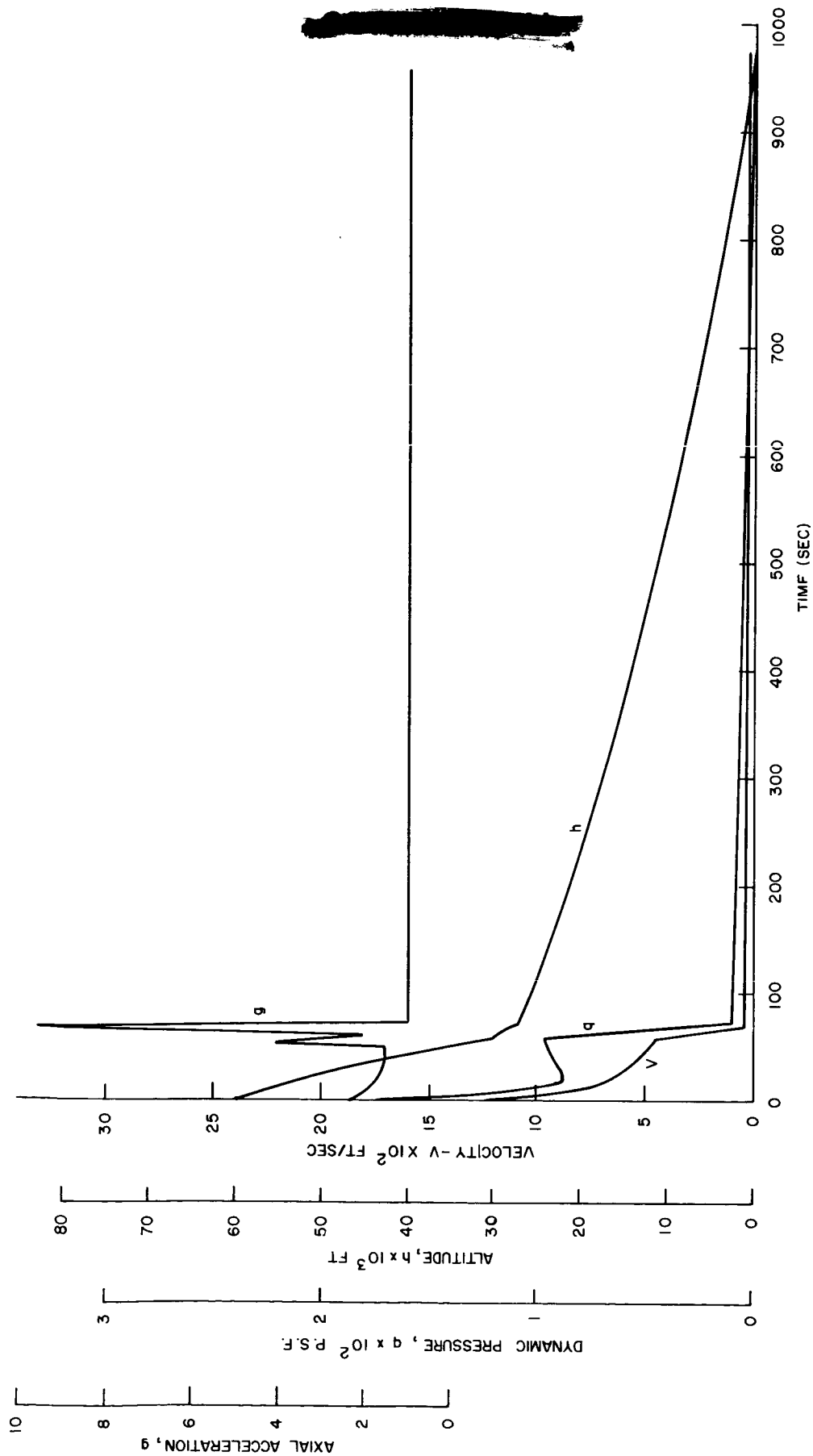


Figure X-1-4. System I—Terminal (retardation trajectory. Payload weight = 10,000 pounds.

~~CONFIDENTIAL~~

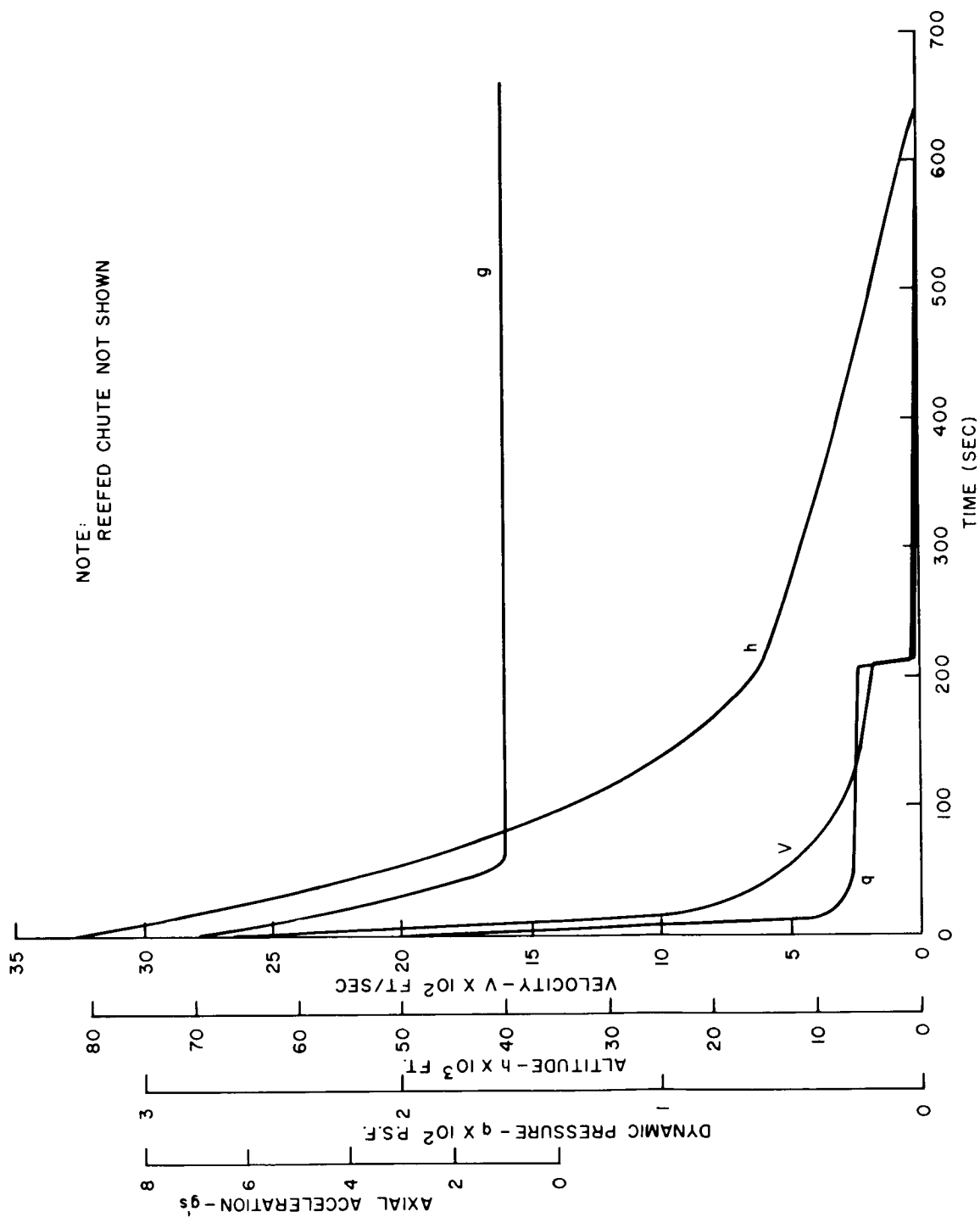


Figure X-1-5. System II—Terminal (retardation) trajectory. Payload weight = 7,000 pounds

~~CONFIDENTIAL~~



NOTE: REEFED CHUTE NOT SHOWN

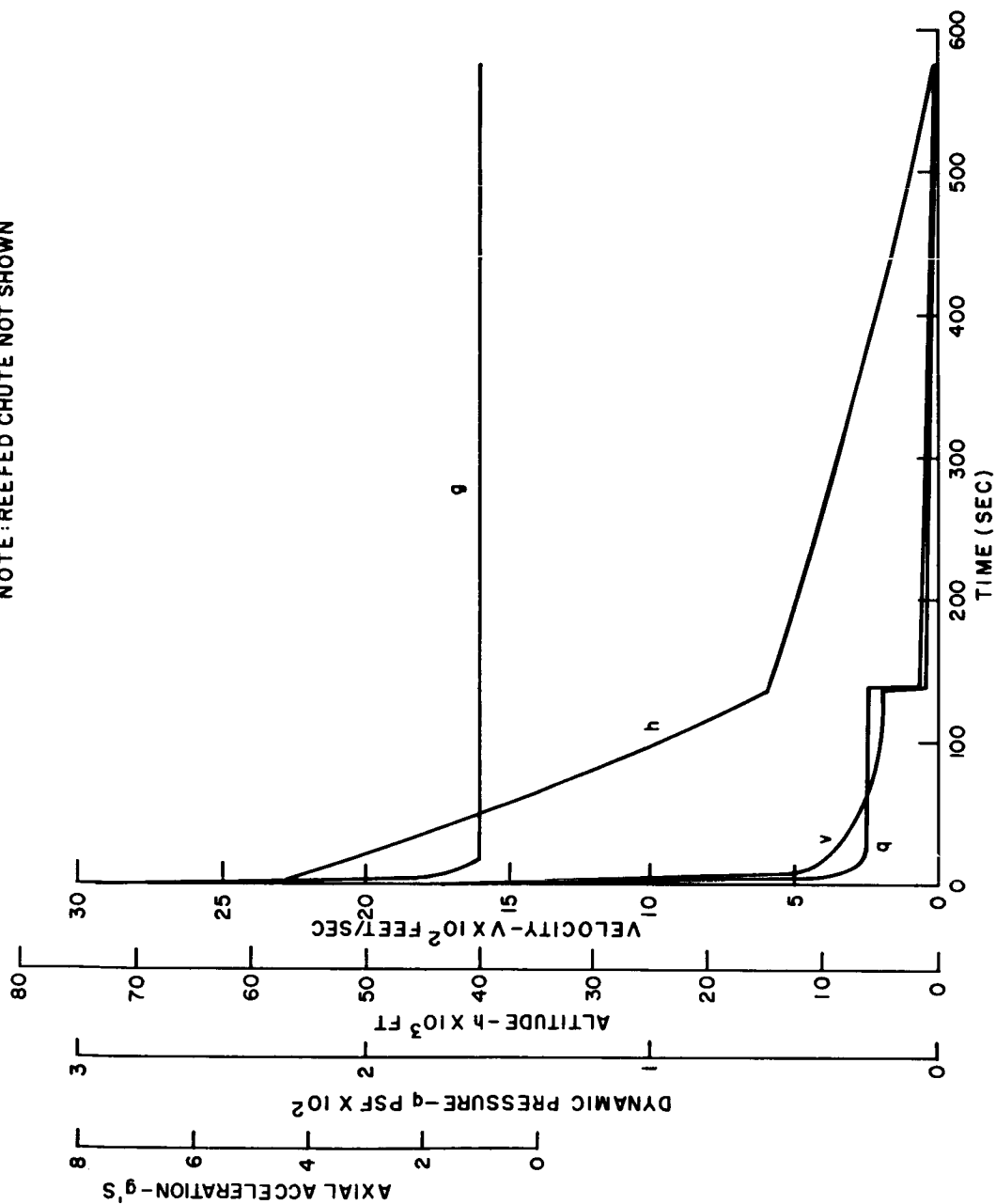


Figure X-1-6. System III—Terminal (retardation) trajectory. Payload weight = 7,000 pounds

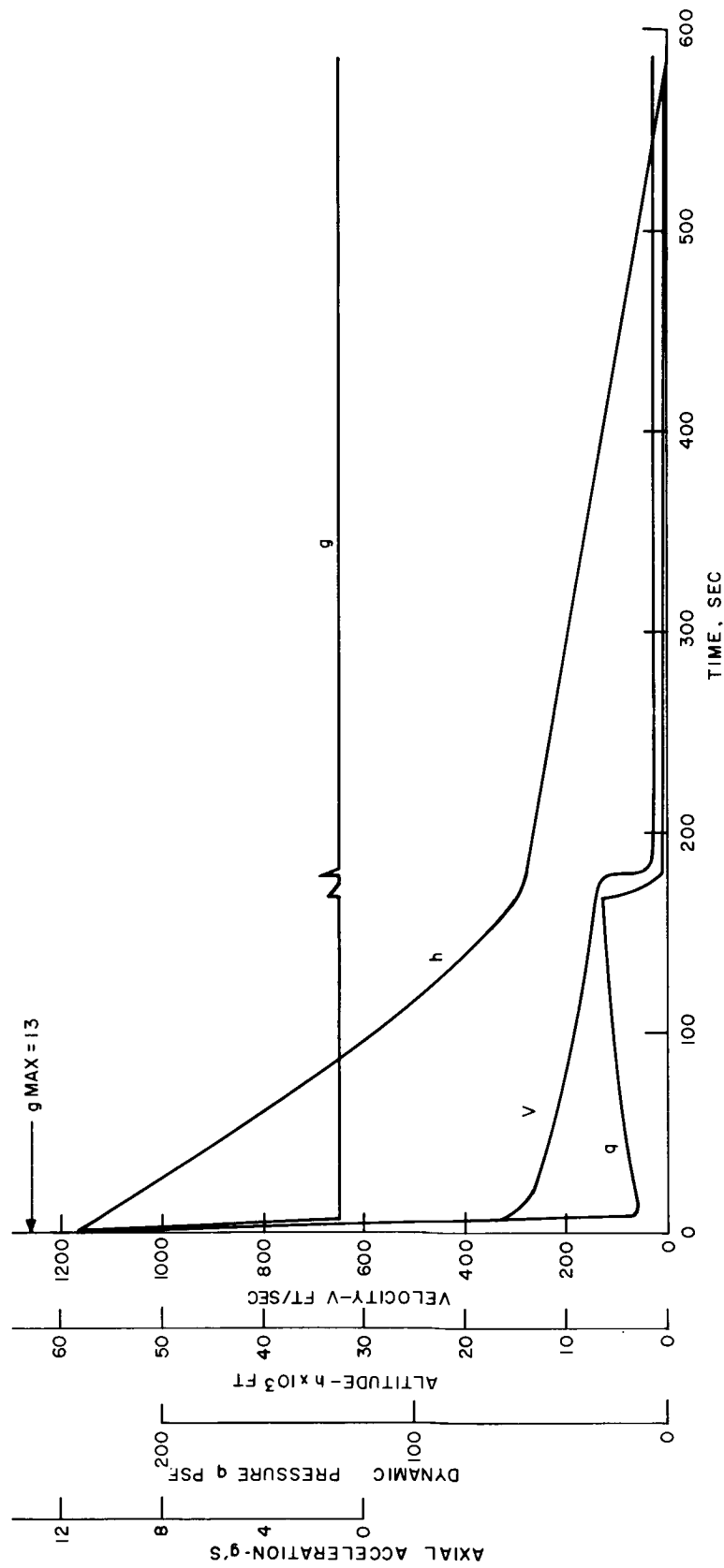


Figure X-1-7. System IVA--Terminal (retardation) trajectory. Payload weight = 5,000 pounds

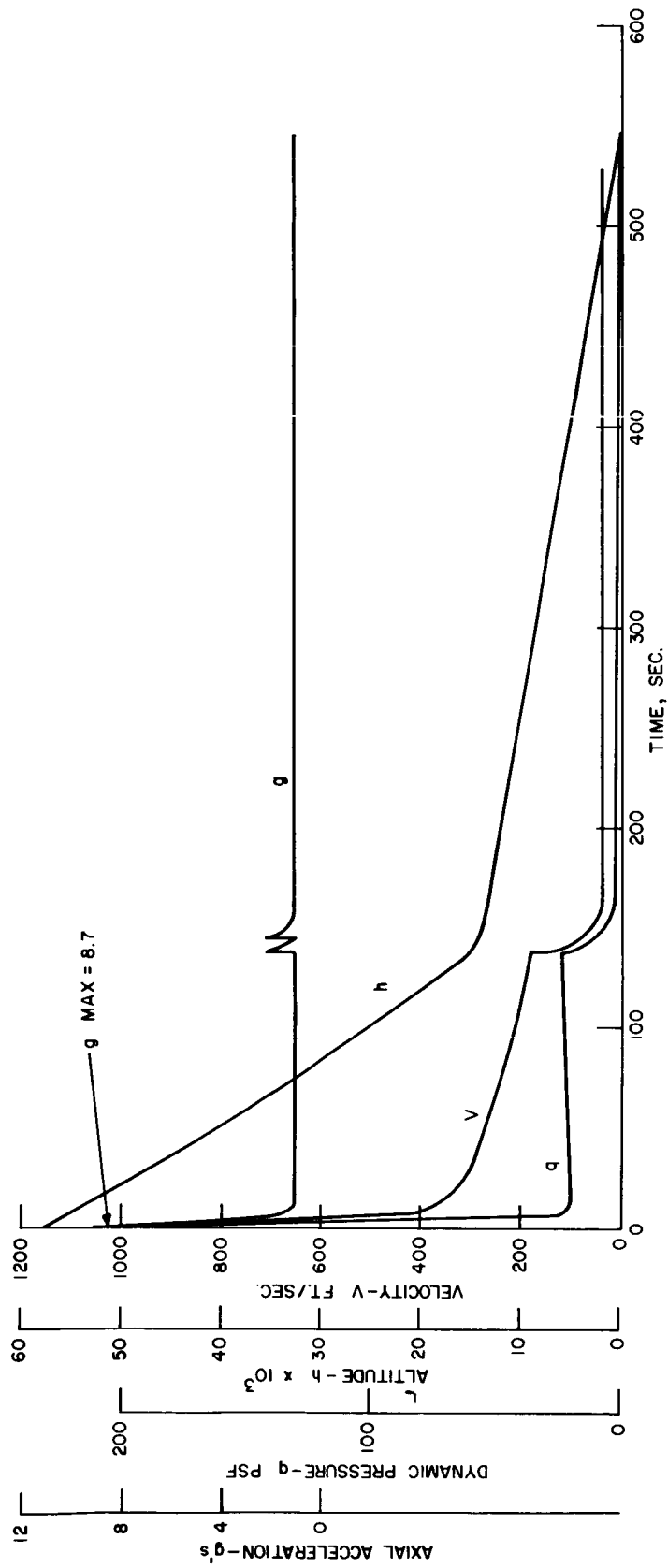


Figure X-1-8. System IVB—Terminal (retardation) trajectory. Payload weight = 5,000 pounds

CONFIDENTIAL

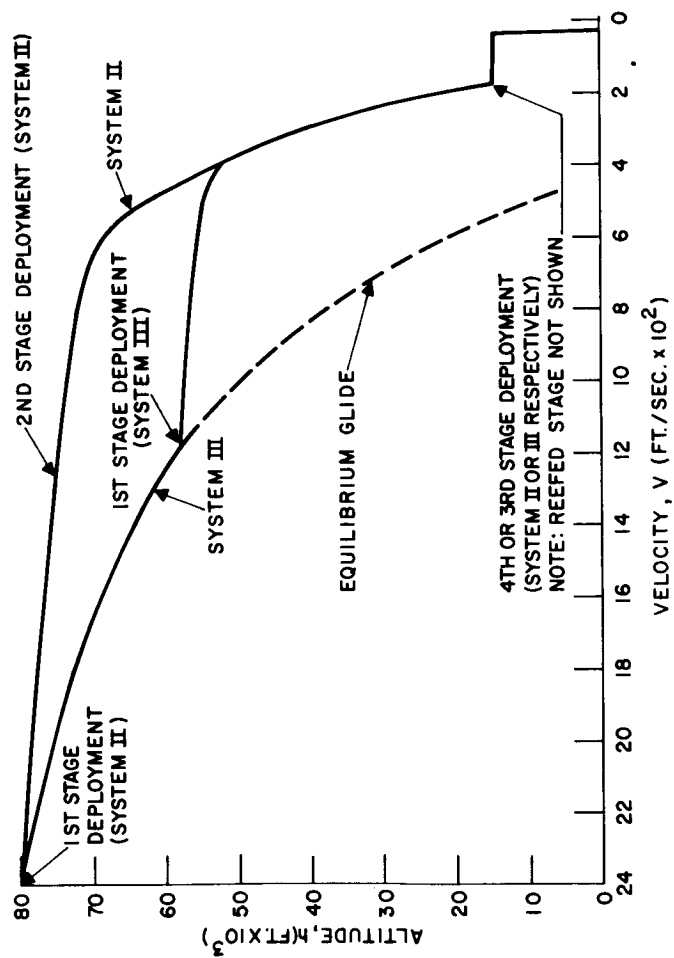


Figure X-1-9. System II and System III—Altitude versus retardation trajectory

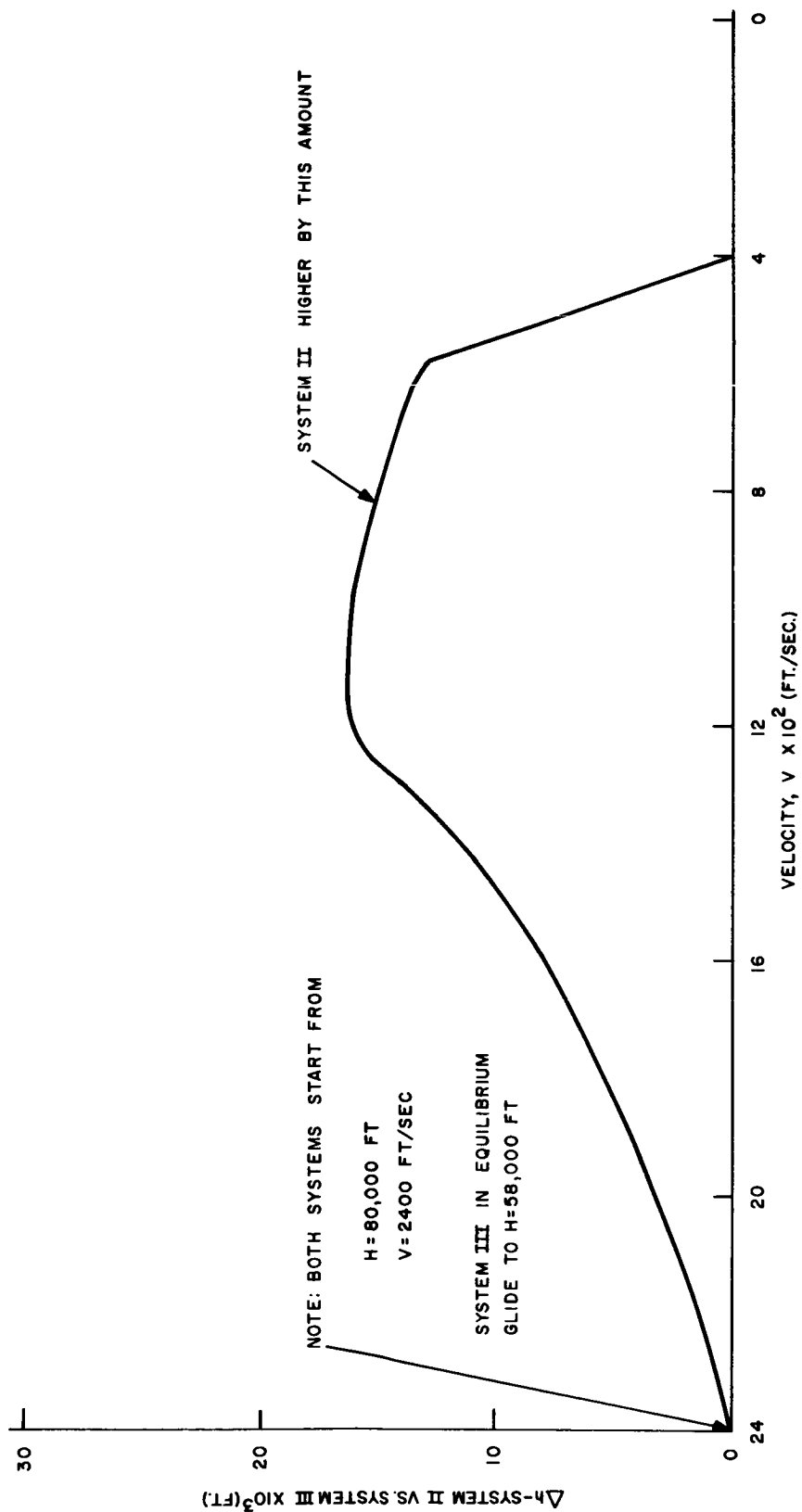


Figure X-1-10. System II versus System III—Comparison of altitude difference versus velocity along the terminal trajectory

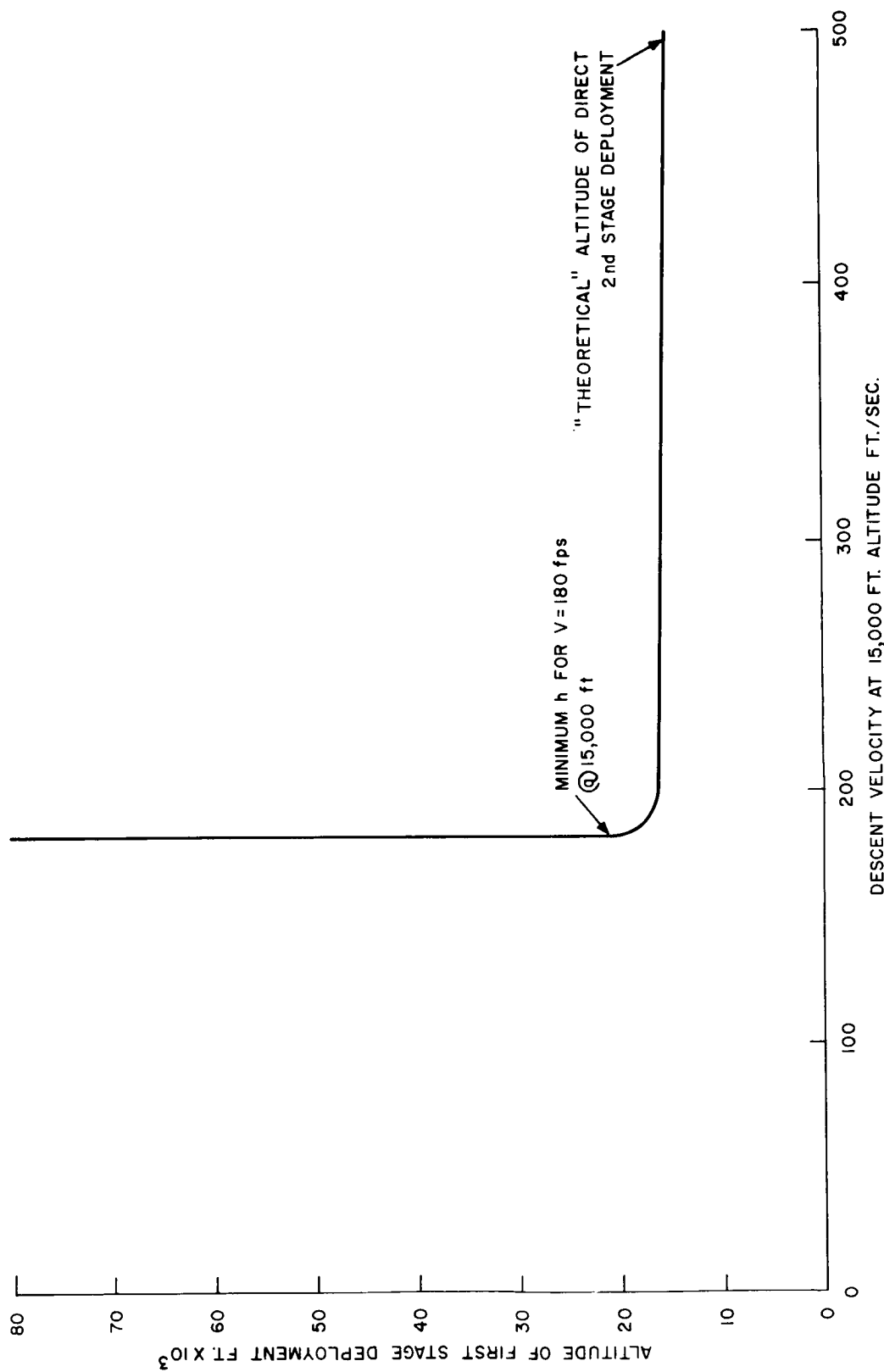


Figure X-1-11. System III—Altitude of first-stage deployment versus descent velocity at 15,000 feet

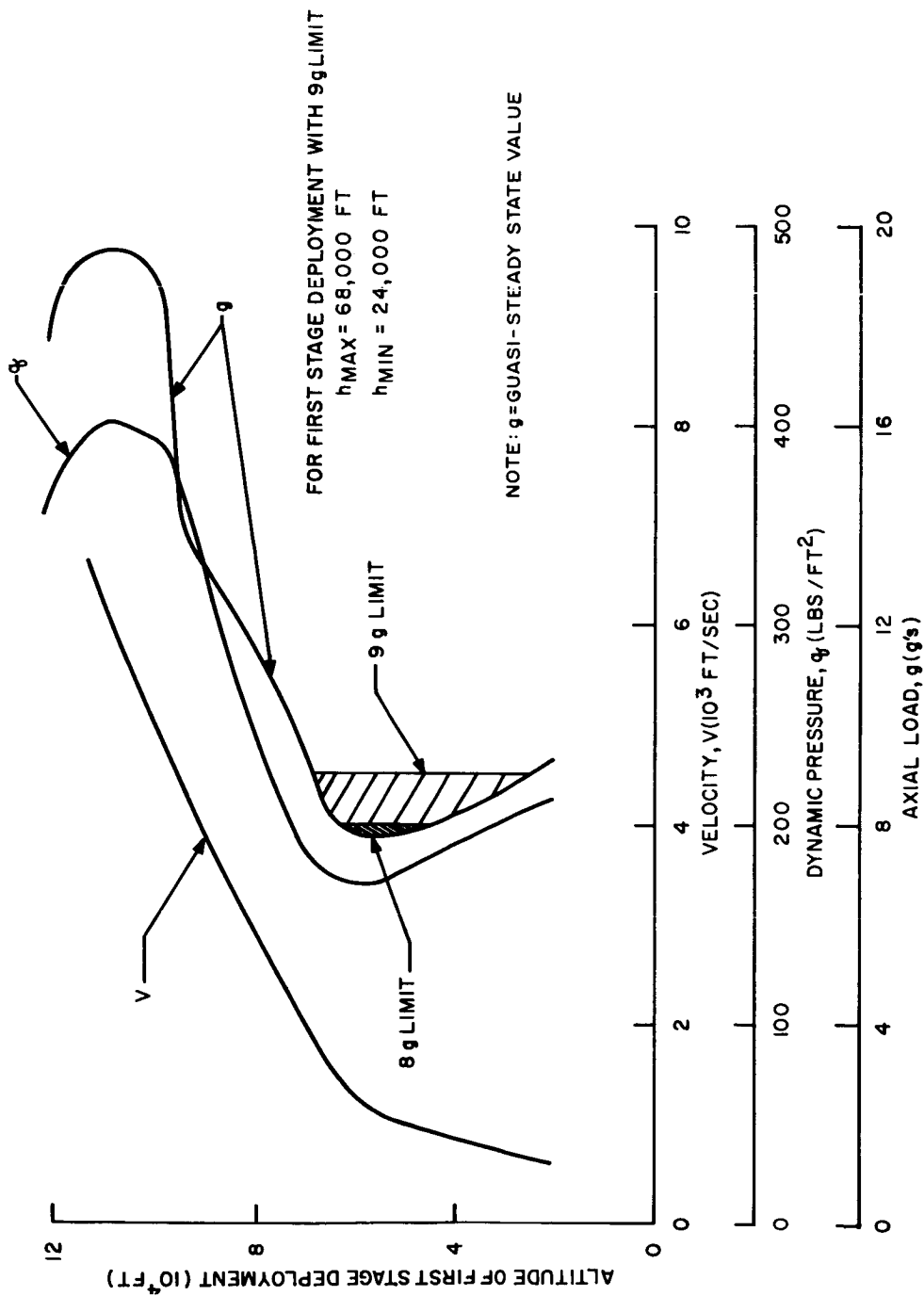


Figure X-1-12. System III—Altitude of first-stage deployment versus terminal trajectory  $V$ ,  $q$ ,  $g$

~~CONFIDENTIAL~~

The diameter of the final-stage chutes for Systems IVA and IVB are reduced to  $D_0 = 65$  feet each in scaling the systems for a payload weight of 5000 pounds. These systems represent a realistic approach for the D-2 configuration.

Noting the total weights for Systems IVA and IVB are 232 pounds and 213 pounds respectively, these weights could possibly be further reduced by two methods. One by the use of one 95 feet diameter main chute instead of two 65 feet chutes. The weight of each system could be reduced by approximately 30 pounds. The second method by which the weight could be reduced is by the use of ring sail chutes, as main chutes. The possible weight reduction could be as much as 55 pounds for each system. The ring sail chute has been tested with weights of the order of the payload. If the ring sail chute were used in System IVB the total weight could be as low as 158 pounds or 3.29 percent of the payload.

In Figure X-1-13, a comparison of range effect is shown, and System III covers a larger "downrange" distance than System II since its retardation system is deployed at a much lower altitude. Figure X-1-13 suggests that the use of selective deployment can, to a certain degree, provide selective downrange impact within the operational limits of the retardation system. One can expand upon this theme and show delta range ( $\Delta R$ ) as a function of altitude of first-stage deployment on System III with deployment at  $h_{\max} = 68,000$  feet as the zero point (Figure X-1-14), and  $\Delta R$  as a function of altitude of first-stage deployment on System III with System II deployment at  $h = 80,000$  as the zero point (Figure X-1-15). Downrange variations up to seven miles are possible through this selective deployment process.

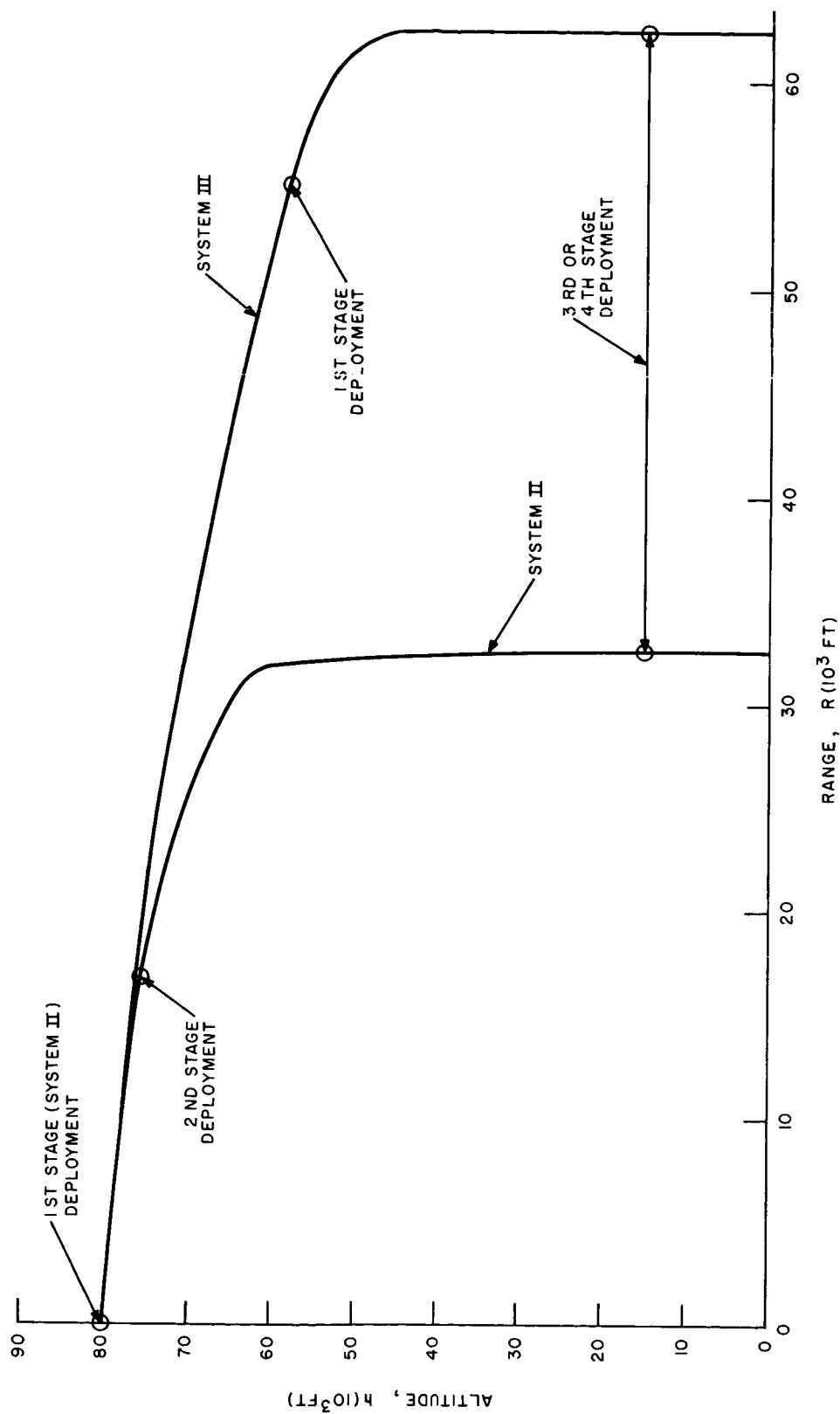
Similarly, a comparison of range effect for Systems IVA and IVB are shown in Figure X-1-16. Using the same R/V weight (5000 pounds) and deployment conditions for the first-stage chute, a range difference of 1800 feet can be recognized by a change in the diameter of the first-stage chute from 25 to 16 feet.

As an additional point of interest,  $\pm$  tolerances on the nominal re-entry trajectory and their resulting effects on the recovery sequence have been investigated in a very preliminary manner. As was previously mentioned, these tolerances have not been fully defined. Thus, an assumption of  $h$  nominal  $\pm 0.2h$  at the deployment conditions for both System II and III was made. The resulting trajectories did not produce any violations

~~CONFIDENTIAL~~



~~CONFIDENTIAL~~



~~CONFIDENTIAL~~

Figure X-1-13. System II and System III—Altitude versus range

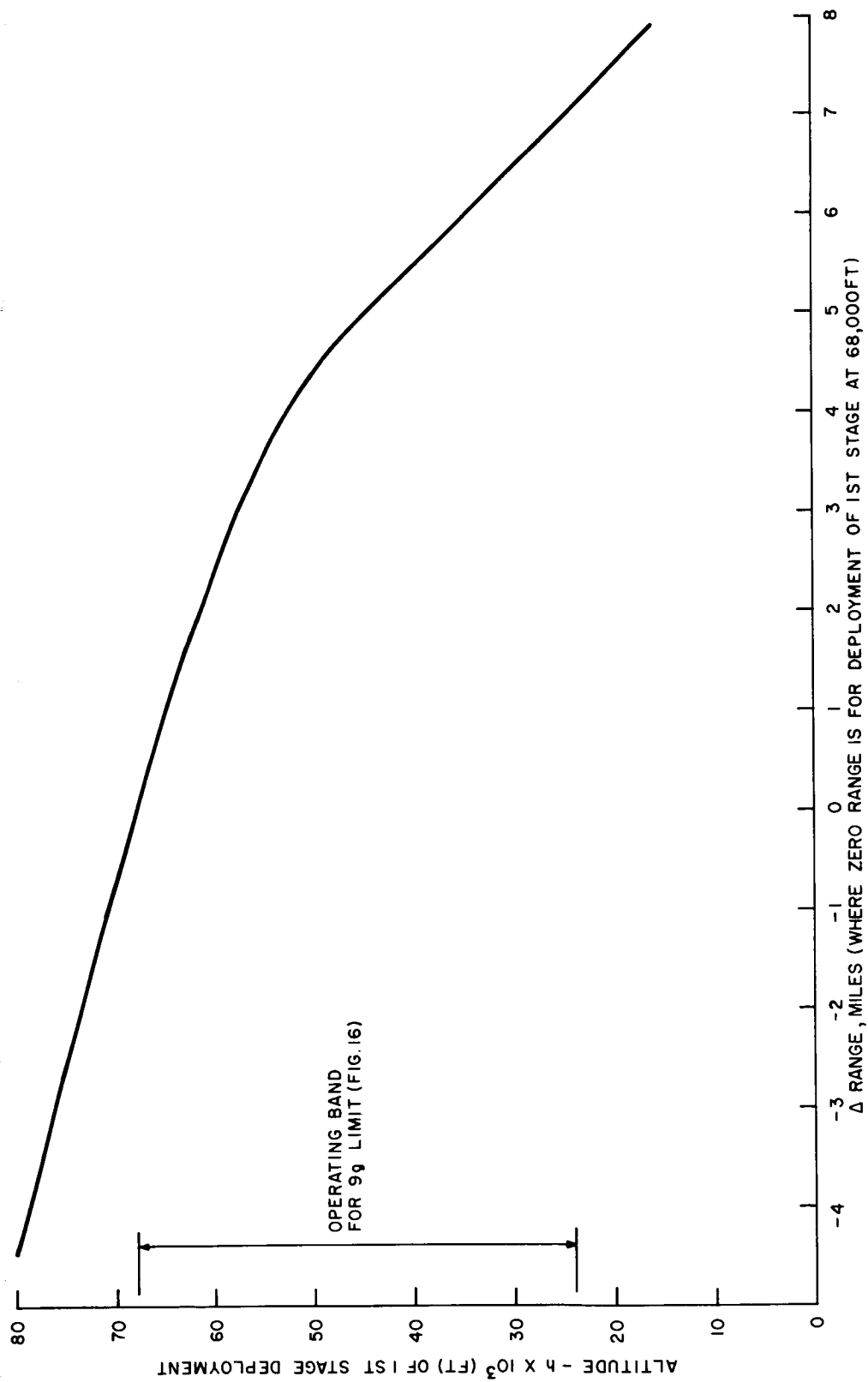


Figure X-1-14. System III--Altitude of first-stage deployment versus  $\Delta$  range (referenced to System III first-stage deployment at  $h_{\max} = 68,000$  feet)

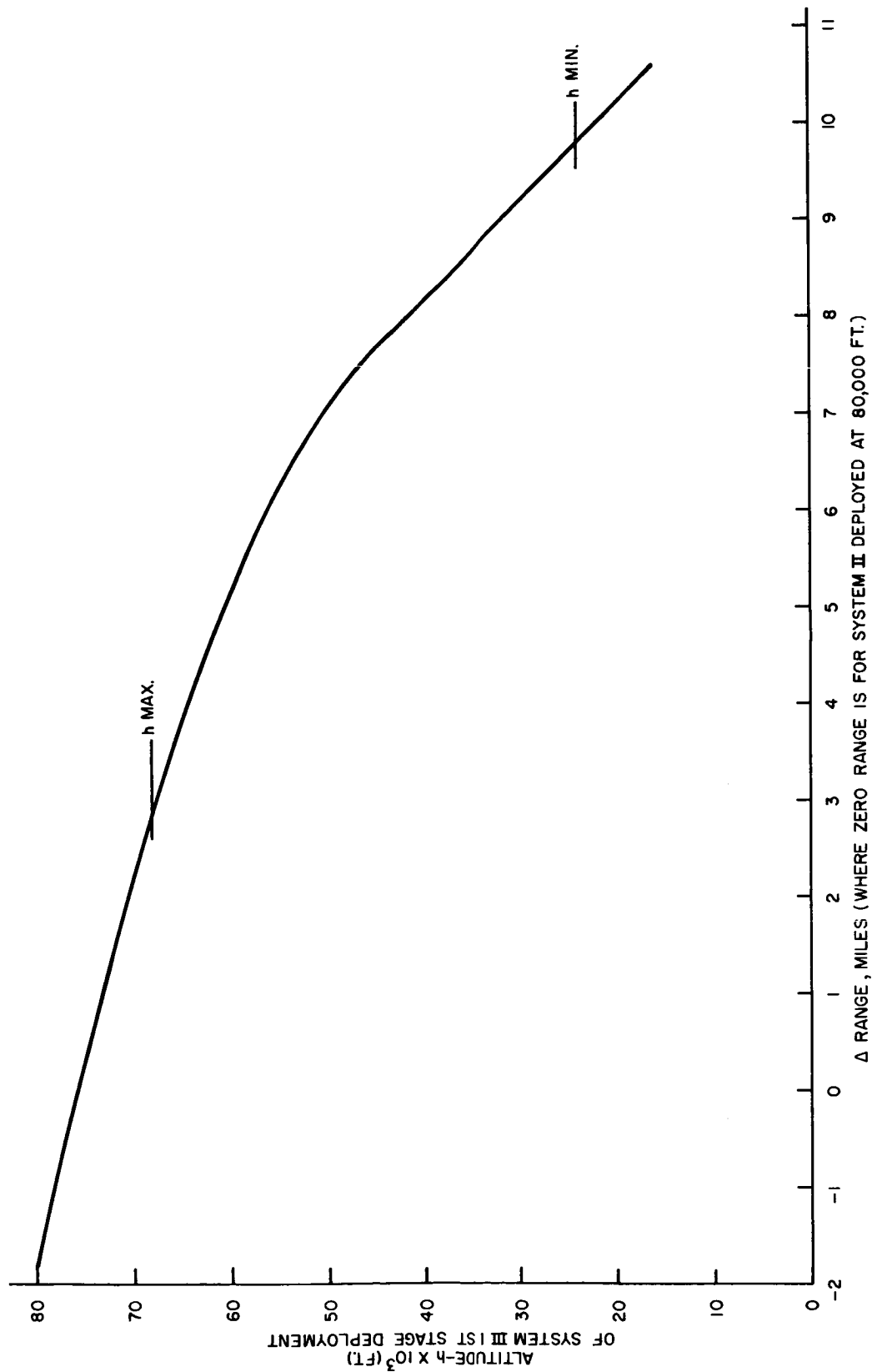


Figure X-1-15. System III--Altitude of first-stage deployment versus  $\Delta$  range (referenced to System II first-stage deployment at  $h = 80,000$  feet)

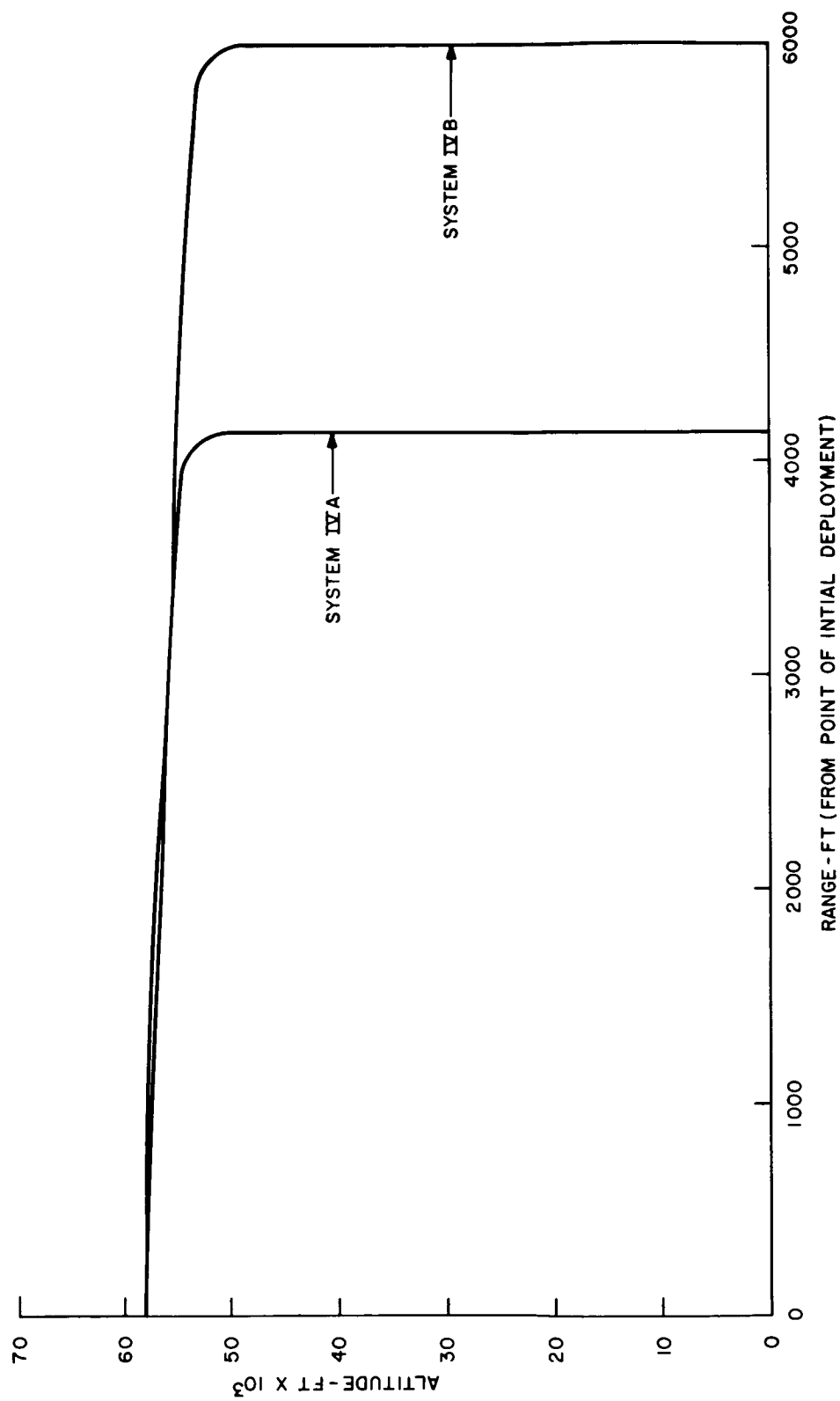


Figure X-1-16. System IVA and System IVB--Altitude versus range

[REDACTED]

on the limits previously established for the nominal case, and the chief point of interest was the delta range encountered. Figure X-1-17 presents the results of the  $h - R$  relationship for these tolerances. It generally can be concluded from these curves that  $\Delta R$  due to re-entry trajectory tolerances of the type assumed can be kept to a minimum by initiating retardation at the lowest possible altitude on the re-entry trajectory.

#### TERMINAL TRAJECTORY WIND EFFECTS

The wind effects on final recovery stages should not be a serious threat to the vehicle, as far as position is concerned, provided that the vehicle is not at the outer perimeter of the landing area with the winds tending to carry it on out of this area. A range error of approximately 5 miles will be induced on a vehicle falling the final 15,000 feet at the vertical equilibrium velocity and being blown parallel to the earth at a velocity equal to a 40-mile-per-hour wind. This error should be tolerable and as calculated above is highly conservative. Even though the wind error on range may not be a problem, the horizontal velocity component induced by this wind may have adverse effects on the landing attenuation system. Consequently, further consideration of the wind problem is necessary.

#### Launch Pad Abort

The absolute necessity for abort capability on Project APOLLO is unquestioned. From the recovery system viewpoint, it has been initially assumed that a "worst case" is the launch pad abort situation. This assumption is based on the fact that  $h = 0$  at abort initiation; and this places upon the escape-rocket system a requirement for attaining a minimum vehicle altitude condition that is compatible with a reliable functioning of the recovery and landing system. A preliminary analysis of the launch pad abort is given in the following paragraphs.

A large number of typical launch pad abort trajectories has been calculated for various escape launch attitudes,  $g$  accelerations and rocket burning times. An attempt has been made to select two of the samples for analyzing the recovery system. The two selected cases are for 10 degree launch, 2 seconds burning time, and 10  $g$  and 20  $g$  accelerations respectively. The recovery system used is System III of the foregoing Section.

~~CONFIDENTIAL~~

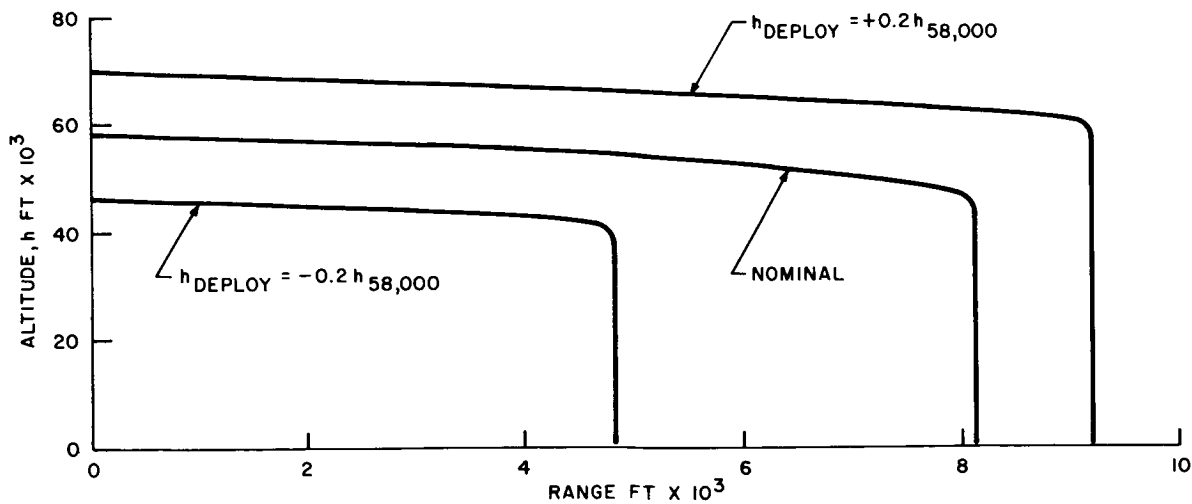
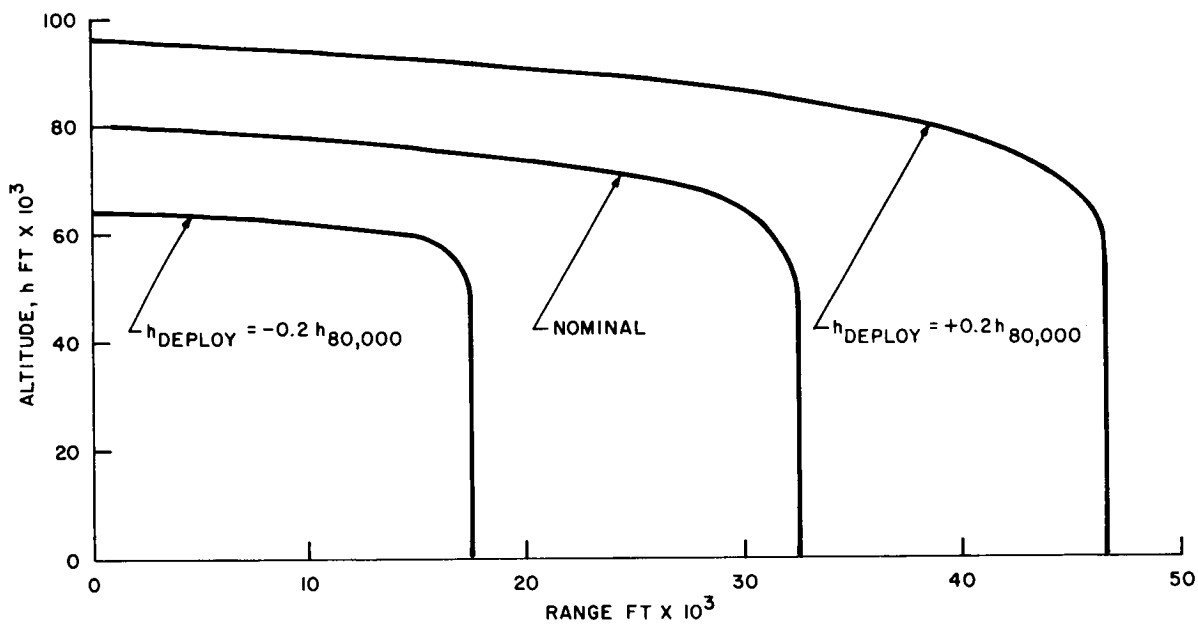


Figure X-1-17. System III—Trajectory tolerance effect, altitude versus range

~~CONFIDENTIAL~~

~~CONFIDENTIAL~~

The critical nature of launch pad abort arises from the fact that it takes time, (hence altitude) to deploy the system in a suitable manner (not to exceed tolerable loads). Based on past experience with deployment and chute opening times, the following time schedule was established for the abort functioning of the system:

- at  $h = h_0, t_0 = 0$  - eject pilot chute
- at  $h = h_1, t_1 = 3$  seconds - pilot chute open, pulling First Stage out.
- at  $h = h_2, t_2 = 5$  seconds - First Stage deployed
- at  $h = h_3, t_3 = 7$  seconds - First Stage open, pulling out main chutes (Second Stage)
- at  $h = h_4, t_4 = 10$  seconds - Second Stage deployed reefed.
- at  $h = h_5, t_5 = 12$  seconds - Second Stage disreefed.
- at  $h = h_6, t_6 = 18$  seconds - Third Stage, fully open.

It was assumed that the deployment process had no effect on the ballistic abort trajectory until  $t_4 = 10$  seconds since all the force was going into deployment of the various stages and nothing remained "connected" to the vehicle to induce an additional force on it. From  $t_4 = 10$  seconds to  $t_5 = 12$  seconds, the reefed  $C_{DA}$  of 232 square feet was used. From  $t_5 = 12$  seconds to  $t_6 = 18$  seconds, a step-wise increase in  $C_{DA}$  was used until at  $t_6$ ,  $C_{DA} = 6500$  square feet was employed. For the two cases studied, it was found that this particular sequencing induced sufficient force on the pilot and First Stage chutes for deployment of subsequent stages and likewise resulted in tolerable deceleration and shock loads.

The resulting trajectories for these two cases are presented in Figures X-1-18, X-1-19 and X-1-20, where  $t_0$  was assumed to occur at apogee. For the 10 g acceleration case, a safe ( $V_t = 30$  fps) landing appears to be marginal since  $V_t = 30$  fps occurs only some 75 feet prior to impact. To alleviate this marginality, deployment of the retardation could be initiated prior to trajectory apogee, but care would be required not to initiate the sequence too pre-maturely and induce excessive rotational g's on the capsule at the opening of the second (reefed) stage. For the 20 g case, a higher apogee is realized, and equilibrium descent is accomplished at altitudes approaching 1400 feet.

Additional analyses are being performed in an attempt to specify, in a parametric manner, the minimum  $h - V$  combinations that are required for a safe launch pad abort.

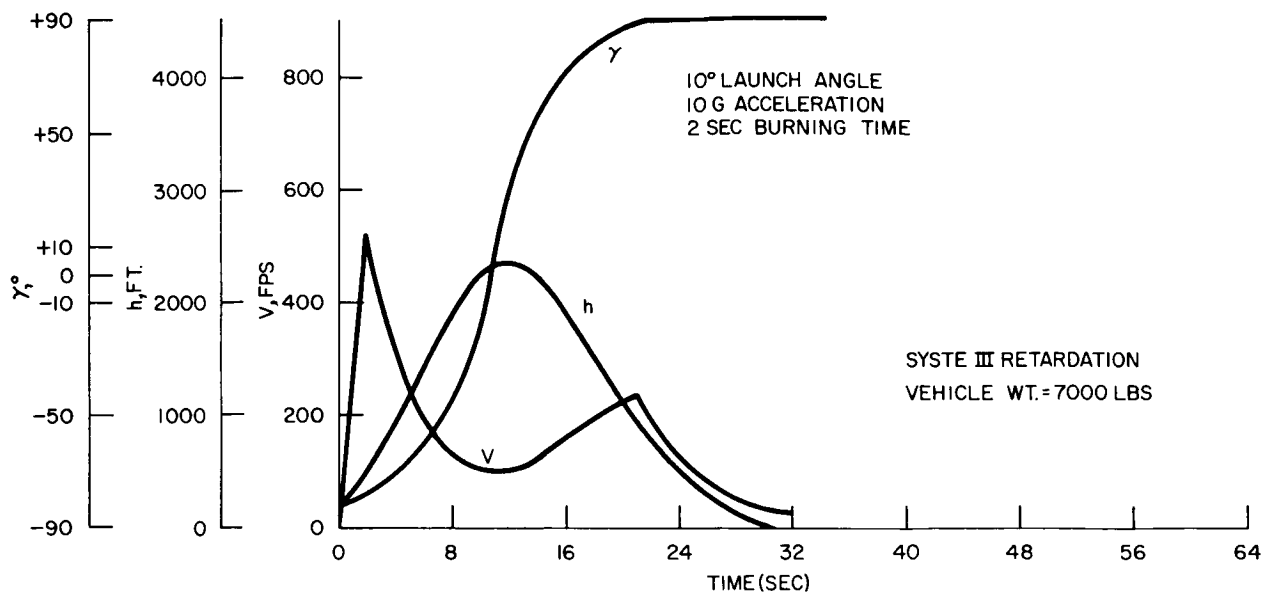


Figure X-1-18. Typical abort trajectory for parachute study

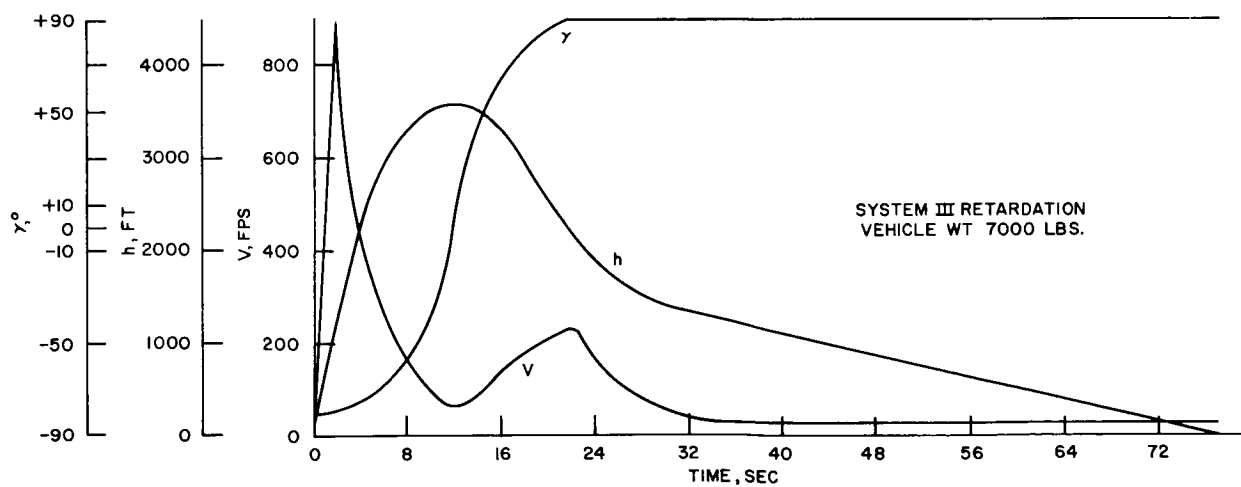


Figure X-1-19. Typical abort trajectory for parachute study



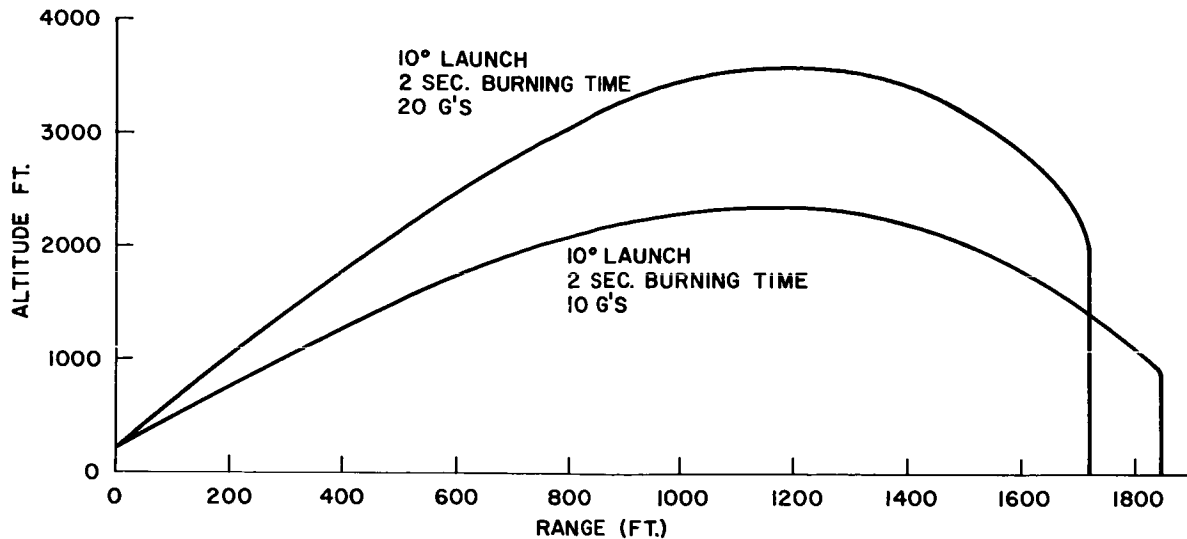


Figure X-1-20. Typical abort trajectory range including retardation

## The Paraglider for Maneuver During Retardation

### HIGH ALTITUDE GLIDE MANEUVERING

In a previous Section, various systems utilizing a drag retardation scheme for recovering the APOLLO ballistic-type re-entry vehicle are described. These systems are adequate means for recovering the vehicle, but do not allow any large compromises for position error. For the pure retardation systems to place the vehicle within a specified landing area, they must be initiated at a predetermined point in space (i.e., altitude and range from landing site) having certain specified conditions (i.e., initial velocity and flight path angle). This type of system can only tolerate relatively small errors in the above parameters and still place the vehicle within the landing area. If the point for initiating the recovery sequence is not achieved with sufficient repeatability, the negligible amount of lateral maneuverability that may be had from parachutes will not suffice. In order to compensate for these errors, thus indirectly increasing the flexibility of the entire system, some means of augmenting the vehicles' lift-drag ratio ( $L/D$ ) during terminal flight should be provided. The moderately high

~~CONFIDENTIAL~~

L/D, light weight and low packaging volume required of the paraglider make this device attractive for providing maneuvering capability to the ballistic-type APOLLO re-entry vehicle. For example, the paraglider could be deployed immediately after the vehicle is decelerated by a conical retardation stage such as found in System II, discussed earlier. The paraglider will then be used to place the vehicle over the landing area at which time it will be cut away to allow the final three stages of retardation to bring the vehicle to the earth, Figure X-1-21.

In order to evaluate the merits of this scheme, the amount of range correction possible was initially investigated. Figure X-1-22 indicates the amount of range correction available for a specified loss in altitude, a given flight path angle and vehicle velocity. These figures indicate that sufficient range correction is available to make this concept worthwhile. The vehicle with the deployed paraglider was assumed to fly along an equilibrium glide path. Using typical ballistic-type re-entry vehicles that will produce L/D's on the order of 0.25 and 0.50, Figure X-1-23 was developed to indicate the amount of L/D that must be supplied by the paraglider. Utilizing this information paragliders were sized to do the job as shown on Figure X-1-24. A more extensive analysis of this system will be accomplished when better definition of paraglider characteristics are available (e.g., load limitations, packaging and deployment methods and means of control).

### **The Spiral Maneuver**

An interesting means of recovering the APOLLO vehicle is to fly a spiral descent maneuver initiated at some specified point in the vicinity of the landing area. A schematic diagram of this maneuver is depicted in Figure X-1-25. This type of maneuver is initiated at some point distant from the center of the landing area equal in amount to the initial turn radii. As the vehicle decelerates along the spiral path, maintaining a constant load factor, the spiral radius decreases; thus, when the recovery sequence is initiated the vehicles' flight path lies completely within the landing area, Figure X-1-25. For this phase of the study, typical ballistic-type re-entry vehicles developing lift-drag ratios of 0.25 and 0.50 are considered. A maneuvering load factor of 3 g's has been utilized since this is an acceptable limit for long time durations. This

~~CONFIDENTIAL~~

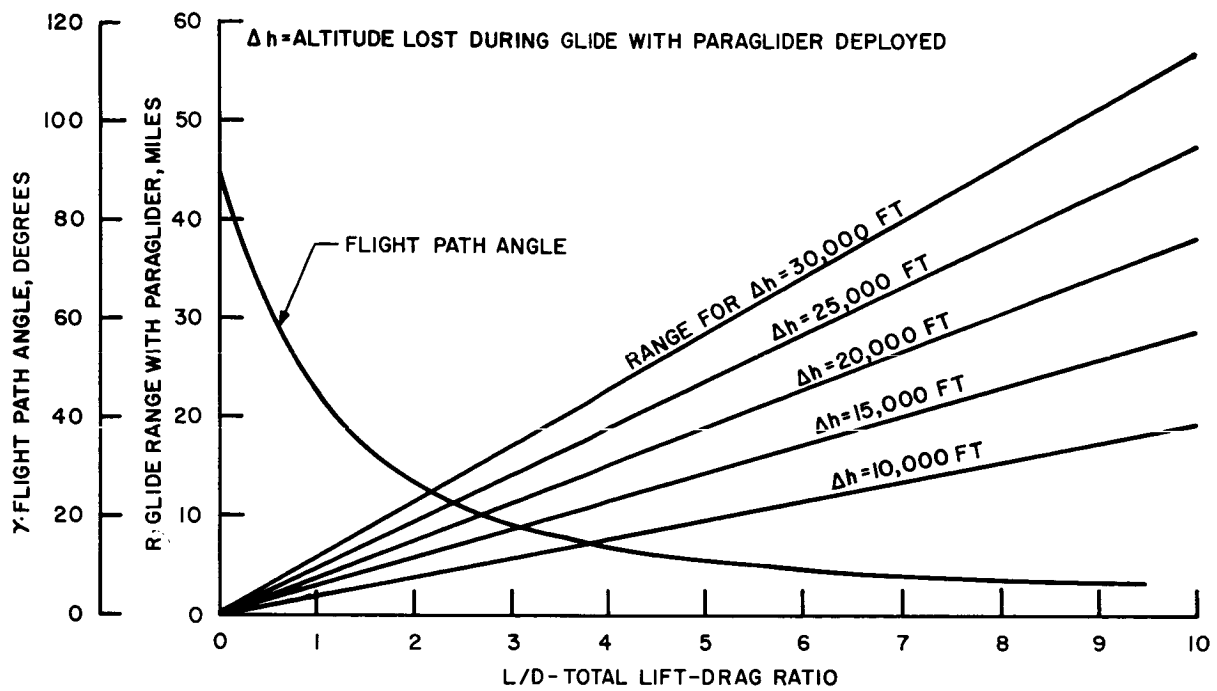


Figure X-1-22. Position corrections available utilizing a paraglider for lift augmentation equilibrium glide

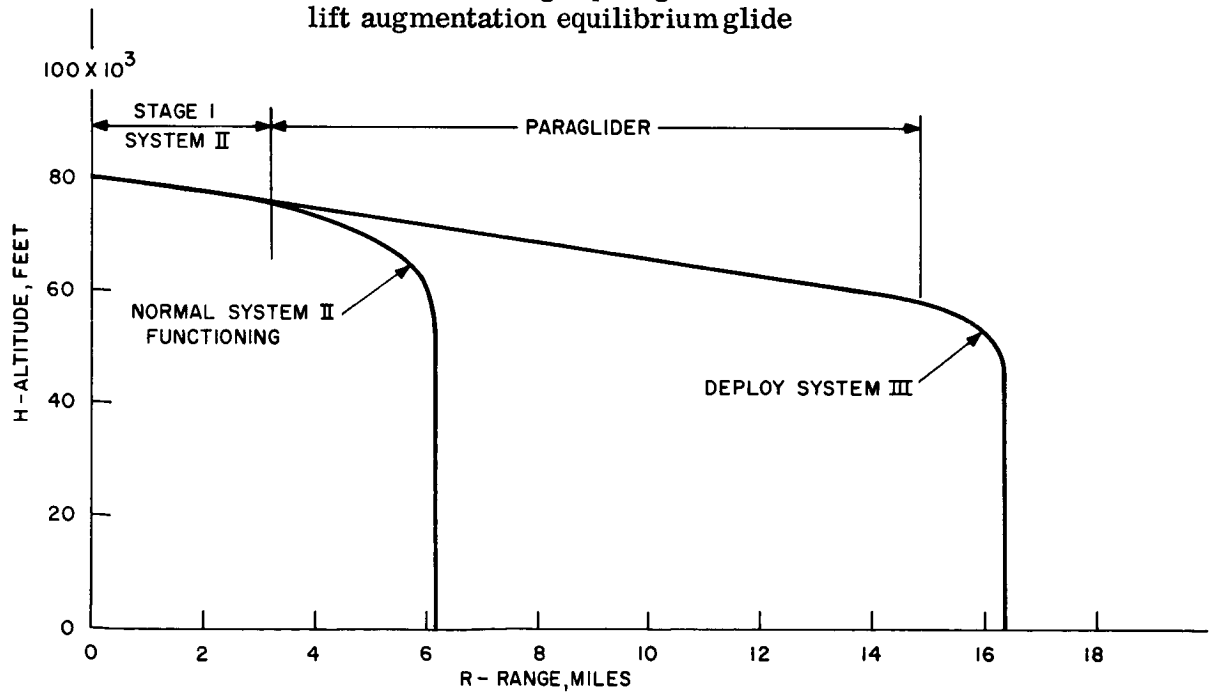


Figure X-1-21. Typical recovery trajectories indicating the effects of a paraglider

~~CONFIDENTIAL~~

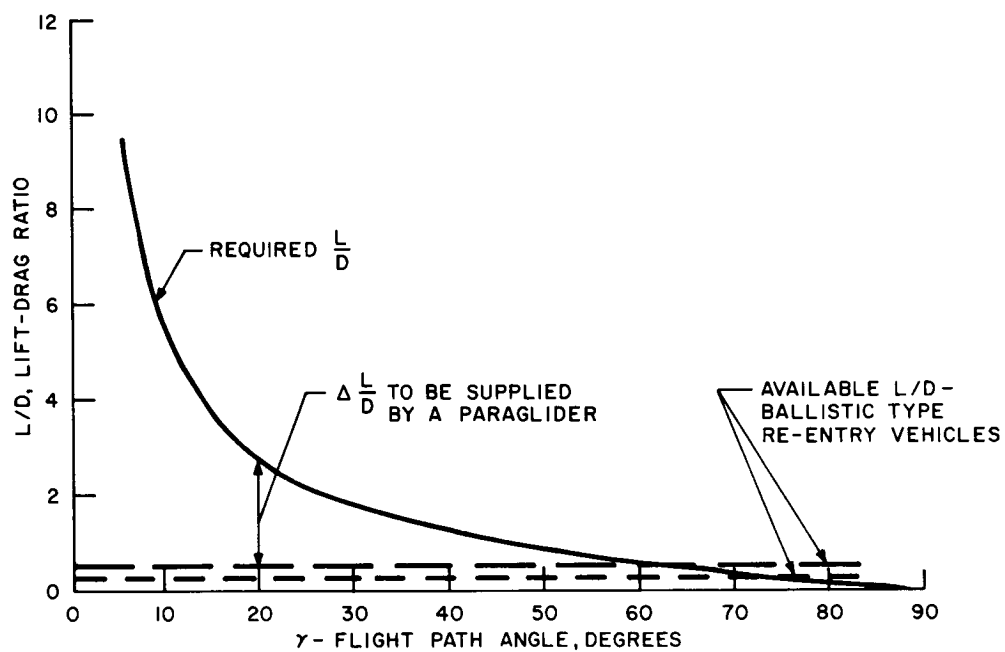


Figure X-1-23. Lift-drag augmentation required for maneuvering a ballistic-type re-entry vehicle

~~CONFIDENTIAL~~

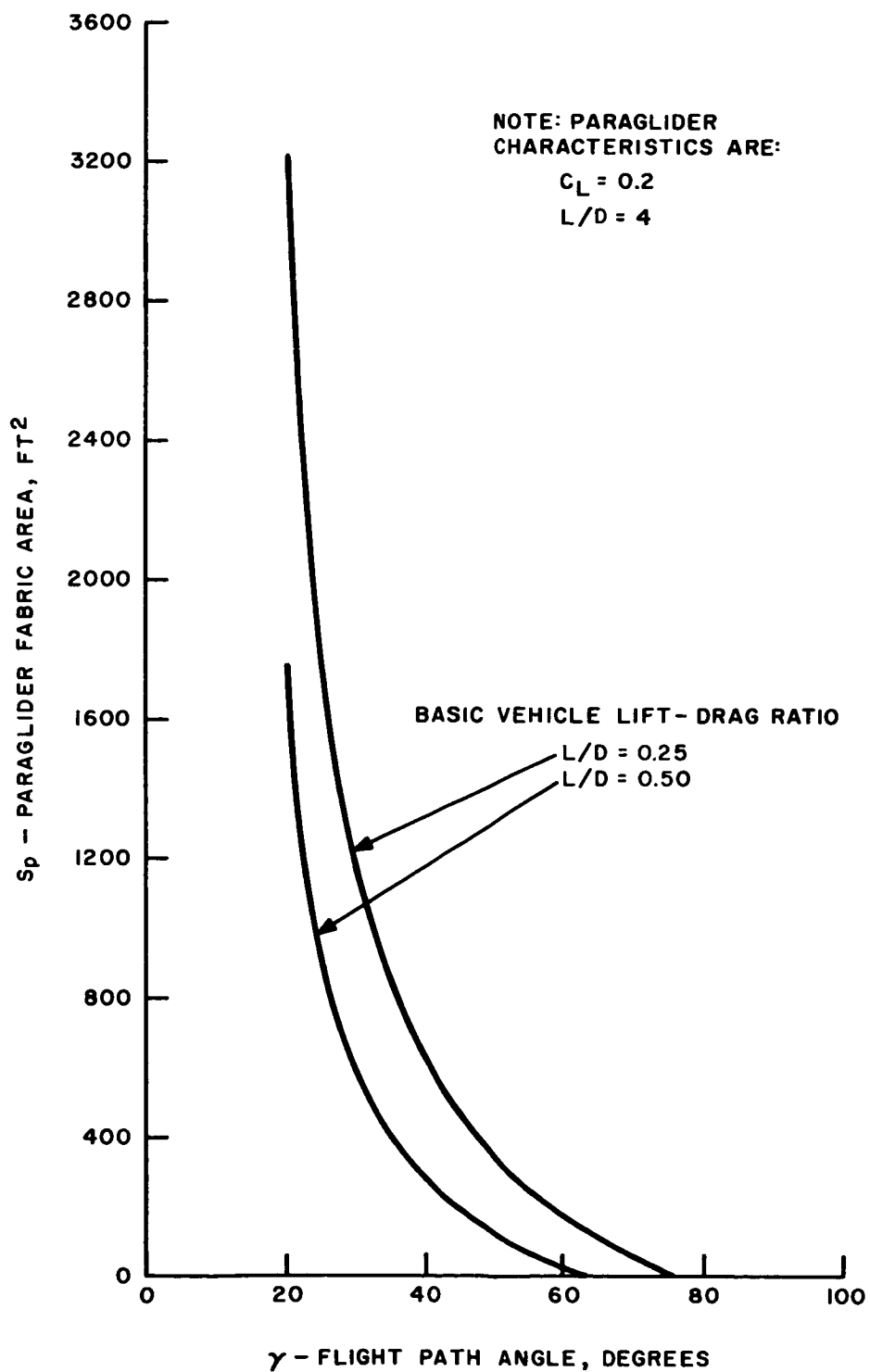
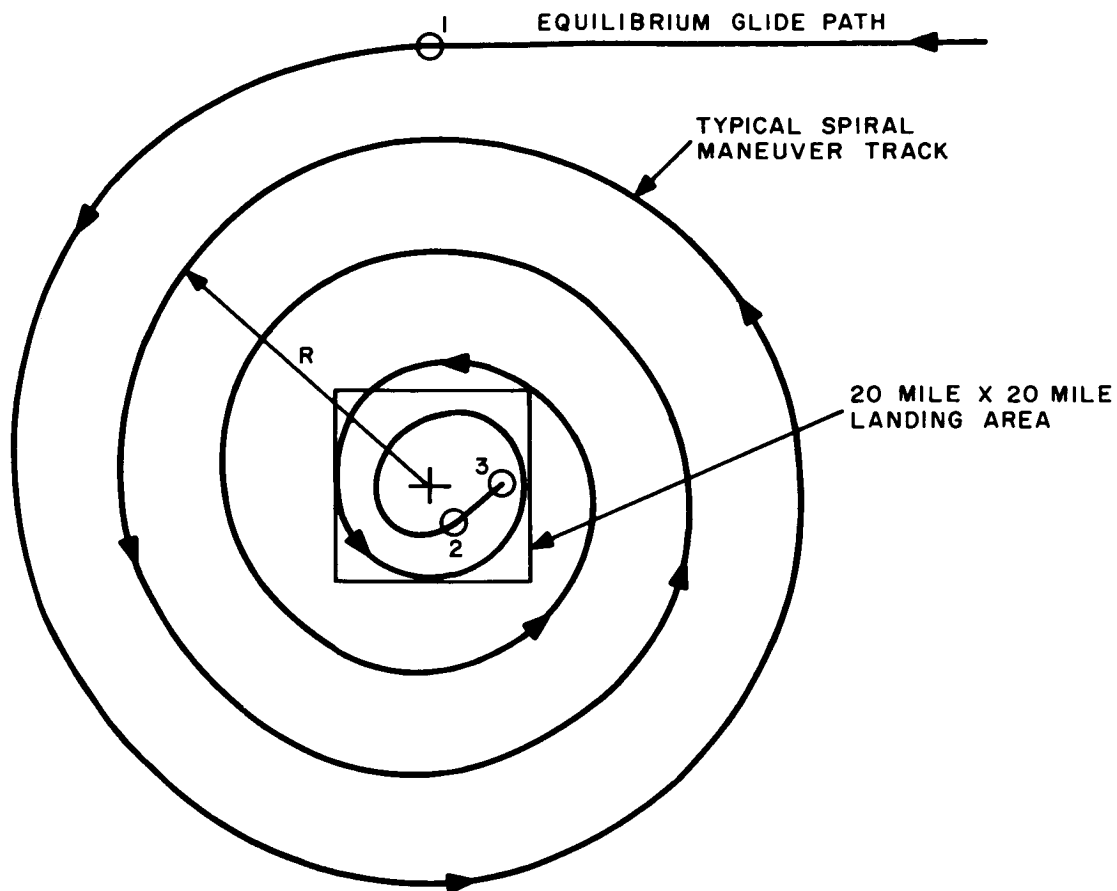


Figure X-1-24. Paraglider area required for terminal maneuverability

**CONFIDENTIAL**

~~CONFIDENTIAL~~



POINT 1 — INITIATE A SPIRAL DESCENT MANEUVER MAINTAINING A CONSTANT LOAD FACTOR. THIS MANEUVER IS INITIATED AT SOME PREDETERMINED ALTITUDE ( $h$ ), VELOCITY ( $V$ ), FLIGHT PATH ANGLE ( $\gamma$ ), AND A RADIAL DISTANCE ( $R$ ) FROM THE CENTER OF THE LANDING AREA.

POINT 2 — INITIATION OF RECOVERY SEQUENCE. THE VELOCITY HAS SUFFICIENTLY REDUCED SO THAT AN ENTIRE 360-DEGREE TURN IS ACCOMPLISHED WITHIN THE CONFINES OF THE LANDING AREA.

POINT 3 — VEHICLE IMPACT

Figure X-1-25. Schematic of spiral descent maneuver

~~CONFIDENTIAL~~

**CONFIDENTIAL**

analysis has been conducted in a parametric manner in the absence of typical spiral descent trajectories, thus, some modification of the results is expected with a more refined analysis.

In the course of this analysis the spiral radius as a function of velocity, lift-drag ratio ( $L/D$ ) and flight path angle were determined, Figures X-1-26 and X-1-27. Utilizing these data the required  $C_L A$  was compared to that available in Figure X-1-28, where it was found that the vehicle does not initially produce sufficient  $C_L A$  to perform the maneuver. This deficiency is further described in Figure X-1-29. Thus, for the vehicle to perform the spiral descent maneuver, lifting area must be augmented in some manner. A means of augmenting the lift lies in the use of a paraglider in conjunction with the vehicle. The paraglider is deployed at the beginning of the spiral maneuver and is released just prior to the recovery sequence. Figure X-1-30 indicates the size of paraglider required to produce the required lifting area specified on Figures X-1-28 and X-1-29.

The various figures of this section were calculated from expressions derived using the standard equations of motion modified to meet the present conditions. Typical paraglider characteristics were compiled from all available reports and papers.

## OTHER ADVANCED RETARDATION DEVICES

### Parachutes

In considering the possible avenues of parachutes optimization that can be followed, it would appear that two possibilities exist; namely, methods of reducing the canopy weight for given load and  $C_D A$  conditions and an extension of the region in which parachute operation can be reliably accomplished.

Reduction of canopy weight appears to be quite feasible. The final stage chute selected for the conventional retardation systems discussed earlier (i.e. the conical type - 108 gore) certainly does not represent an optimum weight selection. In light of available data, however, it represents a very reliable design since it has been tested with payload weights up to 10,000 pounds. As Figure X-1-31 indicates, there are at least

**CONFIDENTIAL**

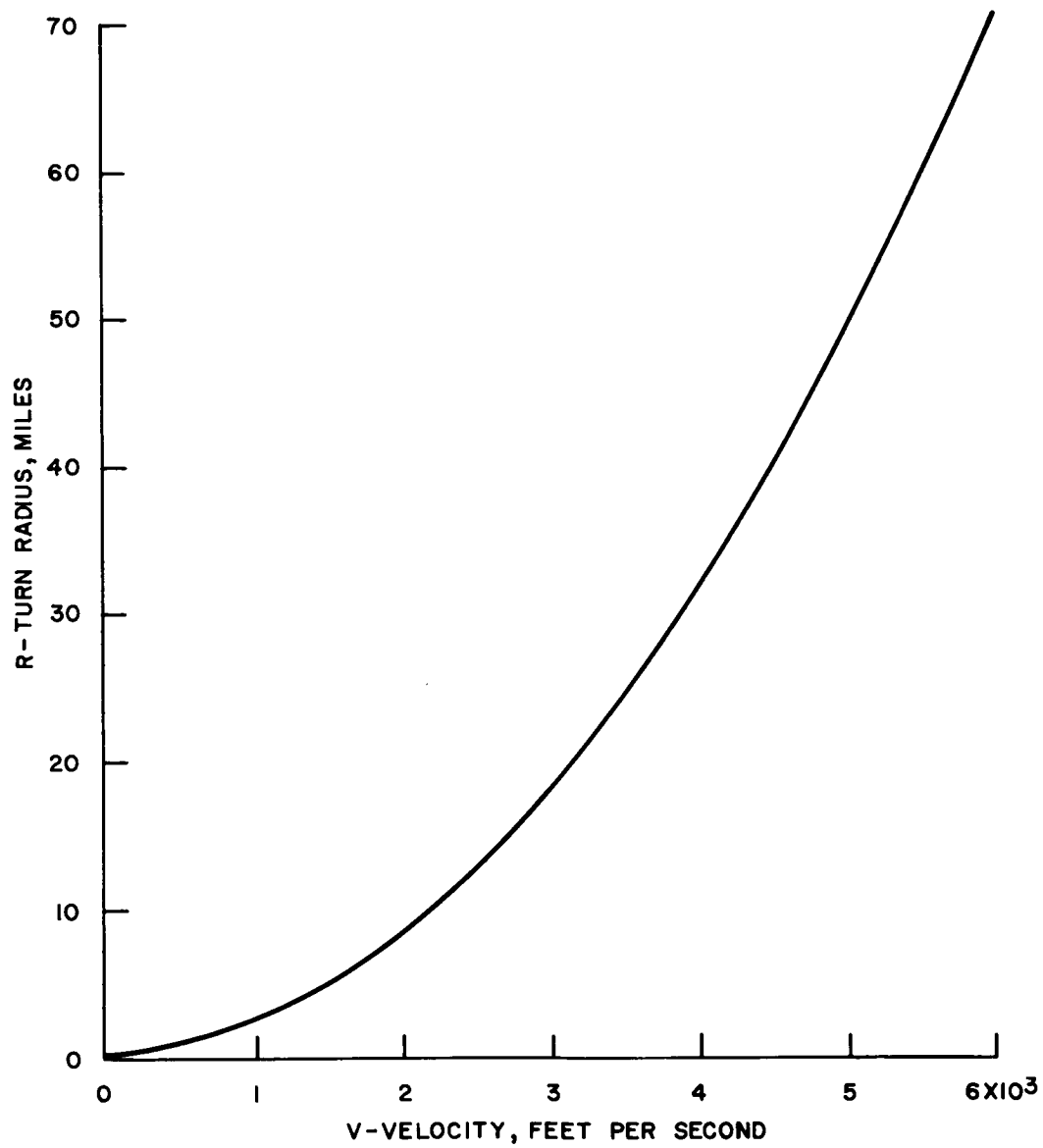


Figure X-1-26. Spiral radius as a function of velocity, load factor = 3 g



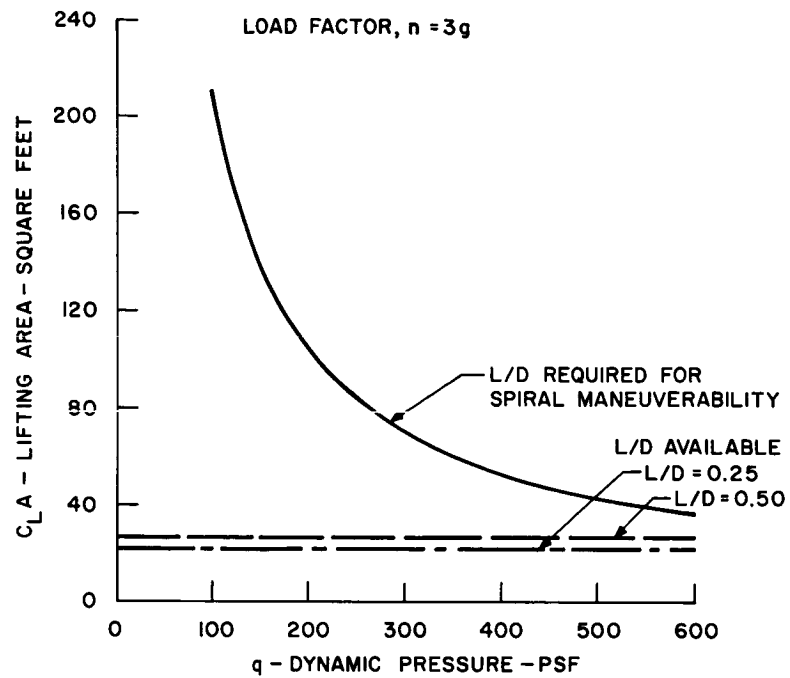


Figure X-1-28. Lift augmentation required to initiate spiral maneuver

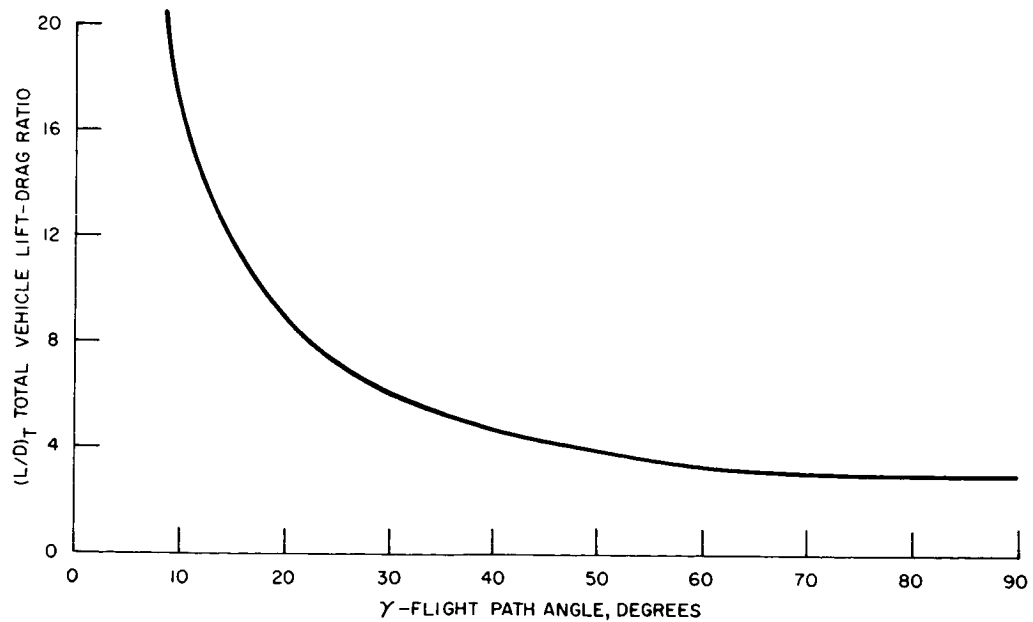


Figure X-1-27. Lift-drag maneuver ratio required for spiral descent; 3g maneuver equilibrium glide

~~CONFIDENTIAL~~

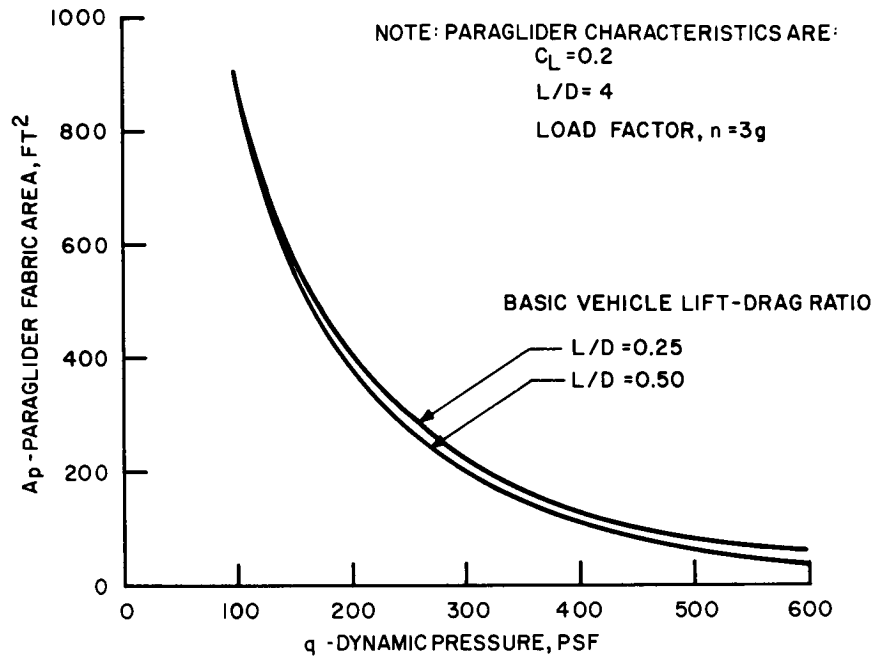


Figure X-1-30. Paraglider area required spiral maneuver

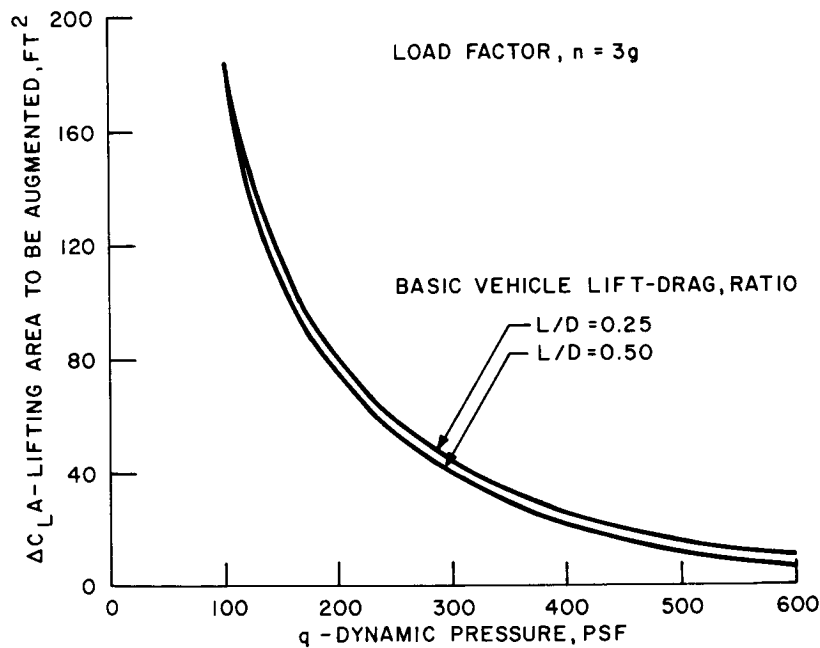


Figure X-1-29. Increment of area to be supplied by paraglider

~~CONFIDENTIAL~~

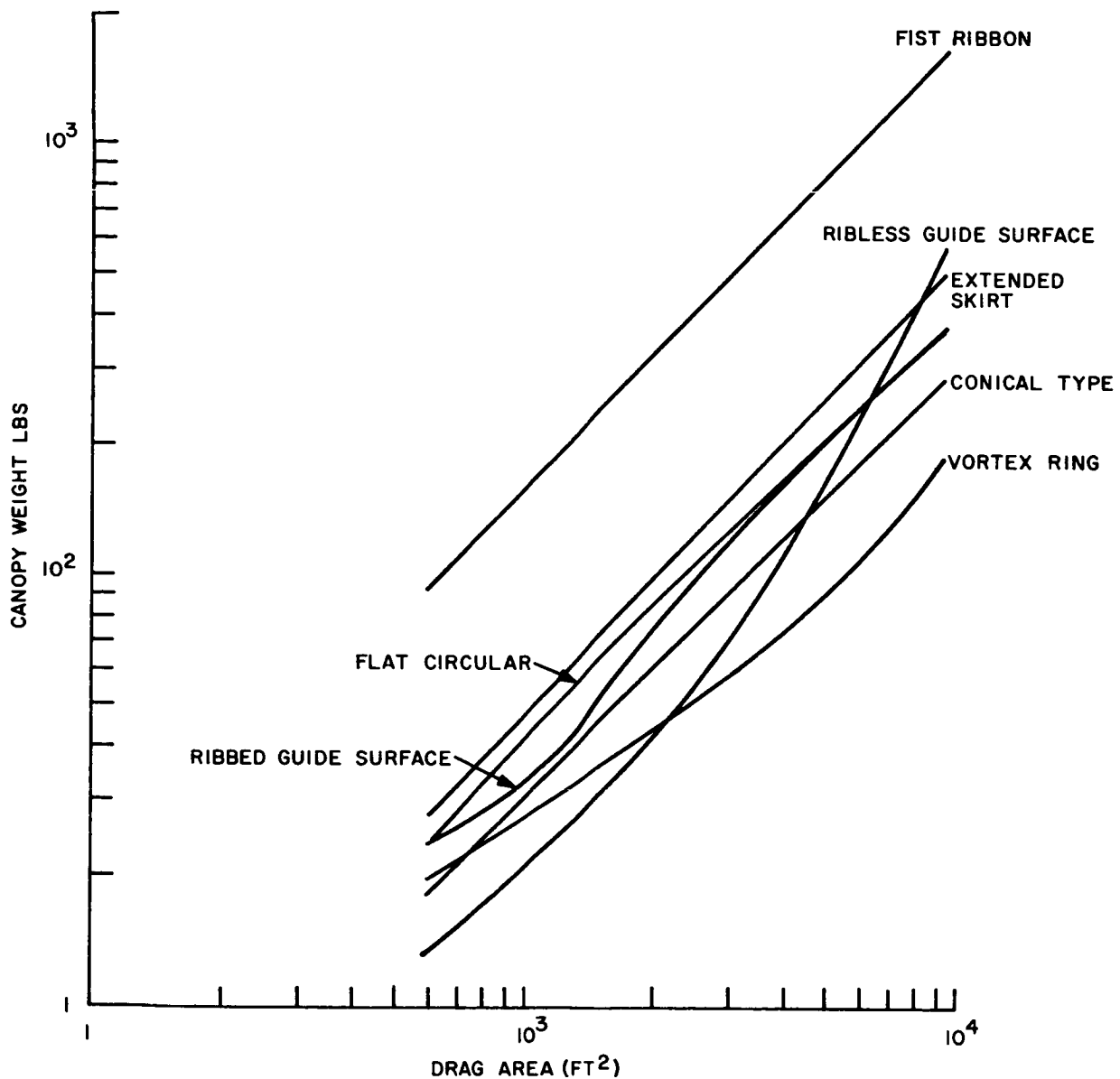


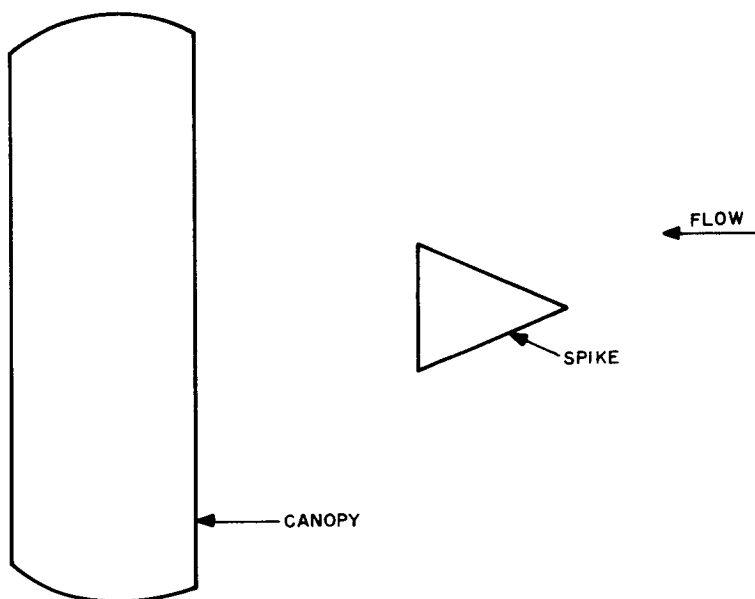
Figure X-1-31. Drag area ( $C_D A$ ) versus final-stage canopy weight, other 'chutes

~~CONFIDENTIAL~~

~~CONFIDENTIAL~~

three other parachutes that have lower weights for certain  $C_D A$  condition; namely, the guide surface, ring sail and vortex ring parachutes. The question is: "What are their operational characteristics, under given environments, with suspended loads on the order of 5,000 to 10,000 pounds." A further examination of available data on these chutes may permit, to some degree, an extrapolation of their performance to the large payload weight situation. But in the final analysis, testing will be required to prove the reliability of these lighter parachutes.

In regard to the extension of operational regions, numerous investigators have concluded that chute operation at  $M > 2$  can be extremely critical; chute opening is unreliable or, if it opens, stability characteristics are poor either in connection with unstable or random oscillations, structural instability and eventual canopy destruction. To alleviate this problem, a supersonic retardation device has been proposed by Dr. H. G. Heinrich of the University of Minnesota, which would increase the static pressure of the captured air in a series of smaller pressure changes, and finally allow the entire air mass to escape through the vent of a parachute-like cup. A sketch of this design, known as a spiked parachute, is shown in Figure X-1-32. Testing of the flow



COURTESY OF UNIVERSITY OF MINNESOTA

Figure X-1-32. Supersonic spiked parachute configuration

~~CONFIDENTIAL~~

~~CONFIDENTIAL~~

details about the configuration has been accomplished with a water table and wind tunnel tests at  $M = 3.0$  have been conducted. To date, the results are very encouraging in that stable conditions have been obtained for reasonable values of drag coefficient (0.28). The continued development of the spike parachute could certainly contribute to an optimization of the APOLLO retardation system in those cases where retardation actuation at  $M > 2$  would be desirable (e.g. with System II).

## **Rotor Systems**

To date, the analysis of advanced retardation devices has, with the exception of the parachutes just mentioned, centered in the pursuit of information on rotor system concepts. This approach has been taken since preliminary investigations have indicated possible performance advantages with this type of system that are highly desirable for the APOLLO mission concept. These include the possible "built-in" terminal maneuvering capability that rotors possess (in addition to retardation) and the ability to flare-out prior to touchdown (thus minimizing or eliminating the impact attenuation system). The introduction of high performance launch pad abort capabilities in terms of minimum "safe" altitude requirements and range maneuvering from the blast area may be possible also in some cases. In order to capitalize on these advantages, two critical questions must be answered:

1. Can critical weight and packaging requirements be met with this type of system?
2. Since the weight will undoubtedly be critical, and preclude the use of any other type of recovery or retardation system in the vehicle, can the rotor system be utilized as the "sole source" system for the entire recovery sequence?

Preliminary information indicates that both of these requirements can be met, but extensive development programs will most likely be required to solve the engineering problems involved in the design of such recovery systems.

Specifically, two rotor-type systems have been investigated. Each utilize the same basic approach, but differ widely in the specifics of the design concept. A review of these systems is presented in the following paragraphs.

## SYSTEM A - ROCKETS ON ROTORS (ROR)

Studies have been initiated to investigate the use of a rotor blade recovery system equipped with liquid-propellant rockets on the tips of the rotors. The concept here calls for the initial deployment of the rotor as a simple drag device using aerodynamic forces for rotation. When the velocity of the vehicle is reduced to approximately 100 ft/sec, cyclic controls are applied and the vehicle is erected to allow conventional helicopter-type autorotation, a condition which can be entered at an altitude of 20,000 feet to 40,000 feet depending on rotor design. Facilitated by a rotor-mounted rocket system, maneuvering to a pre-selected landing spot followed by flare-out can then be accomplished; the maneuvering capability (in terms of range) being a function of the particular design used.

The ROR system design and hardware is based on its use in conjunction with the escape rocket system in that fuel, tankage and certain other hardware components would serve a dual role for both the ROR and abort escape rockets. If abort is not required, certain elements of the escape rocket system can be discarded and the weight of the combined system reduced considerably for normal re-entry flight. Preliminary design calculations have been run for a ROR and escape rocket system and these are shown in Table X-1-2. It should be noted that if the escape system weight is discarded, the ROR system will require 74 pounds of propellant for ground approach and hovering maneuvers for the monopropellant fuel, and 50 pounds of bipropellant fuel for the same maneuvers. Thus, rocket system fuel and hardware would run about 113 pounds and 86 pounds for the mono- versus bi-propellant ROR systems respectively. This would mean that the rotor blades and associated hardware would have to weigh on the order of 550 pounds for a 10,000-pound vehicle in order to make this recovery system "competitive" with the retardation design of System I in the section entitled "The Retardation System". If landing attenuation can be discarded, this "competitive" figure could become as large as 700 pounds.

Additional performance data for the ROR system will be analyzed during the remainder of the study contract in order to obtain a more quantitative evaluation of its feasibility. Investigations on this concept are being pursued in conjunction with the Reaction Motors Division of Thiokol Chemical Corporation.

TABLE X-1-2. PRELIMINARY DATA FOR ROR AND ESCAPE SYSTEM

The results are based on the following assumptions:

1 - Number of Rotors	1
2 - Number of Blades	3
3 - Rotor Radius (ft)	15
4 - Capsule Weight (lb)	10,000
5 - Rotor Tip Velocity (ft/sec)	800
6 - Specific Impulse - Monopropellant (sec)	150
7 - Specific Impulse - Bipropellant (sec)	230
8 - Duration Escape Rocket (sec)	10
9 - Altitude After Escape (ft)	500

Type System	Monopropellant Combined System	Biopropellant Combined System
Total ROR Thrust for Glide Approach and Hover	1,340	1,340
Thrust Each Chamber for Glide Approach and Hover	447	447
Thrust for Escape Rockets Total	13,840	13,840
Weight for 3-ROR Glide and Hover Chambers	21	15
Glide and Hover Chamber Propellant and Tank Weight	*	*
Glide and Hover Chamber Valves, Fittings, and Line Weight	18	21
Escape Rocket Weight	200	140
Escape Propellant Weight	923	600
Escape Tank Weight	93	60
Escape Valve, Fittings, and Line Weight	40	50
Escape Pressurizing System Weight	50	40
WEIGHT TOTALS	1,345	926

\* Propellant required and tank weight are included in escape system propellant and tank weight.  
All values are expressed in pounds unless otherwise noted.

~~CONFIDENTIAL~~

## SYSTEM B - AUTO-ROTATIONAL FLEXI-ROTOR SYSTEM (FRS)

One additional study has been recently initiated to investigate the flexi-rotor system concept. Unlike System A, the blades in this system are of cloth, with suitable weights mounted on the tips. Deployment is accomplished after the blade hub has been pre-spun. The hub can be either a metal device or a rotating parachute. In the latter case, the entire system is essentially made of cloth and represents what may be considered an advanced parachute concept. Figure X-1-33 shows a preliminary weight curve for the FRS as a function of vehicle weight. One point from an experimental system is shown (metal hub), and the other two points represent analytical calculations. These latter two points utilize the rotating parachute as the hub. Tests on this particular design have been recently run in the NASA Langley Vertical Wind Tunnel.

Investigations on this concept are being pursued in conjunction with Barish Associates of New York City.

## LANDING IMPACT ATTENUATION

### Operational Requirements

The basic requirements of a landing impact attenuation system for the APOLLO vehicle are smooth deceleration within safe human tolerances (e.g. 20 g for 0.2 seconds), simplicity and reliability, low weight, minimum packaging volume, and ability to perform adequately under varying and unpredictable conditions of impact. The optimum system will utilize to a maximum degree other existing vehicle parts to perform vital functions during the landing. For instance, the heat shield, which must be strong enough to transmit re-entry aerodynamic forces to the internal vehicle can be used effectively during the initial impact when rugged ground conditions are possible. Hence, the severity of landing on uneven or rocky terrain can be lessened.

### Preliminary Study of Impact Attenuation Devices

Many devices have been recommended and/or used in impact landing such as crushable structures and compliant metal struts, spikes, reverse thrust rockets, and pneumatic bags. An initial insight into the relative efficiencies of several of these approaches is

~~CONFIDENTIAL~~



~~CONFIDENTIAL~~

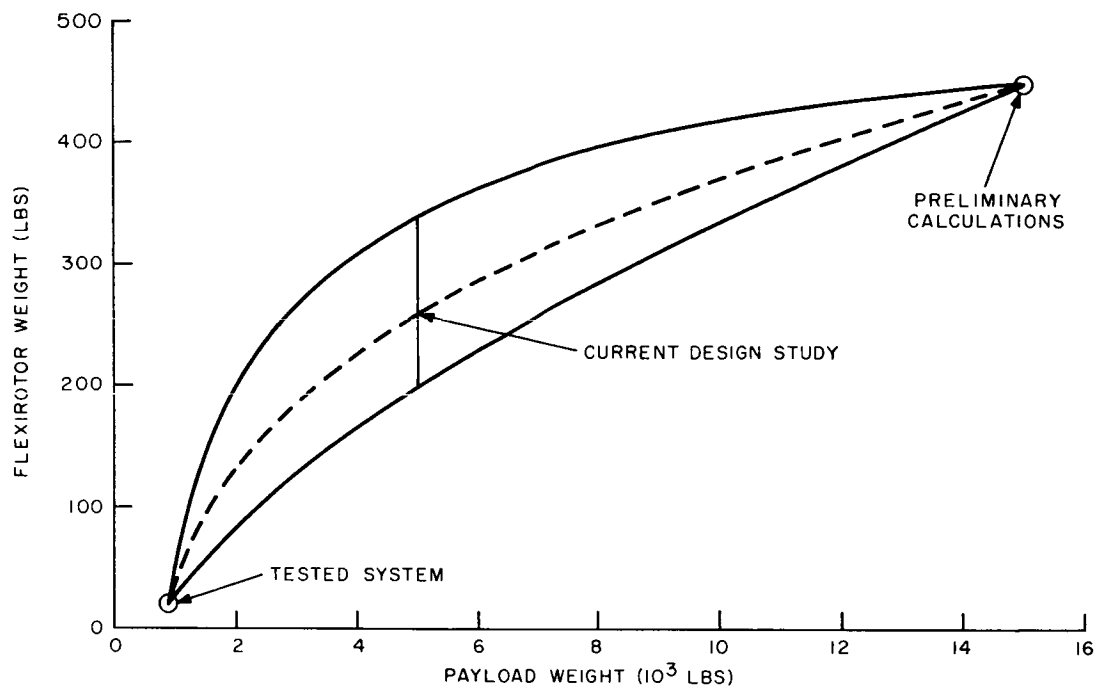


Figure X-1-33. Flexi-rotor weight versus payload weight. Flareout at  $h = 0$ .

~~CONFIDENTIAL~~

~~CONFIDENTIAL~~

given in Figure X-1-34. To discuss briefly the merit of these devices with reference to the above stated operational requirements, it is apparent that spikes, struts, and crushable structures have inherent packaging disadvantages. It may be recalled that the basic function of the impact device is to provide sufficient deceleration length or stroke between the payload and the impact surface. Since the longer the stroke the lower are the deceleration forces, the device naturally requires length in the direction of the vehicle motion and forward of the payload. This property is in conflict with aerodynamic stability, desirable launching configuration, and maximum utilization of internal volume.

Large variations within the groups shown in Figure X-1-34 are due to several factors. The difference between using available rockets and especially developed rockets is particularly obvious. Inflatable landing bags become increasingly more efficient as we proceed from relatively low strength cloth fabric through higher strength cloth fabric to wire fabric. Crushable cylinders also show some variation due mainly to material of construction.

The reasonable efficiencies of the inflatable bag, particularly with the possible use of wire fabric, coupled with the fact that it can be packaged in a small volume and

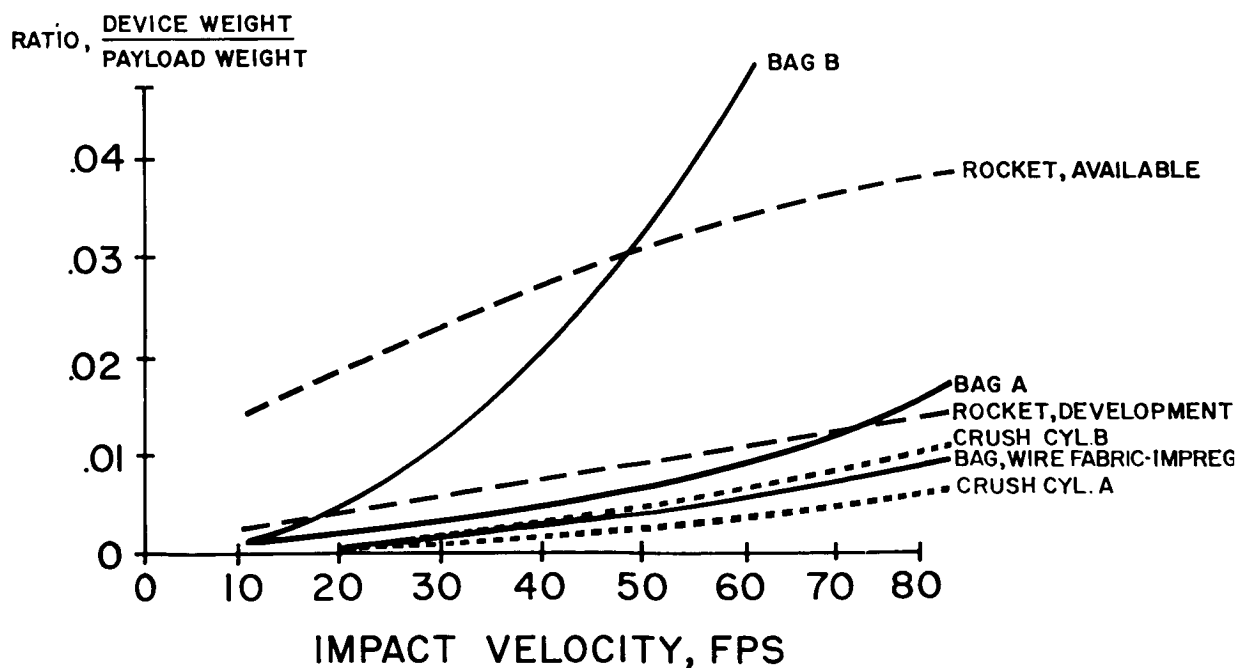


Figure X-1-34. Impact attenuation study

~~CONFIDENTIAL~~

[REDACTED]

expanded into functioning position by relatively simple means have encouraged further study. In addition, it possesses desirable and predictable deceleration characteristics and favorable weight properties.

Of the pneumatic bags, the vertical cylinder possesses the most favorable deceleration characteristics because of its long stroke. Moreover, when the gas within the cylinder is maintained at a constant pressure, at a level which produces stresses below the rupture strength of the bag material, the vertical cylinder is extremely efficient from an over-all performance and weight standpoint. The vertical pneumatic cylinder between the front of the pressurized capsule and the heat shield, therefore, has been selected initially for detailed study as an impact attenuation device for the APOLLO semi-ballistic-type recovery vehicle.

## Performance

The stopping ability of pneumatic cylinder and the maximum corresponding accelerations are given in Figures X-1-35 through X-1-38, inc. The ratio of the bag mass to the payload mass is plotted against impact velocity for several cylinder lengths, 1 = 3, 5, and 10 feet. Each curve corresponds to a specific value of  $\gamma$  which is the ratio of the allowable hoop stress in the bag wall to the mass density of the bag material. The bag mass does not include the mass of internal partitions, mounting flanges, and hardware.

It is obvious that the ratio  $\frac{M_b}{M_p}$  should vary inversely with the internal pressure differential. This is demonstrated in Figures X-1-35 through X-1-38 by the great effect on  $\frac{M_b}{M_p}$  of  $\gamma$ , the higher value of which corresponds to a higher value of internal pressure (see Figure X-1-39). The dashed curves superimposed on the curves of length show the maximum accelerations, which occur at the end of the impact due to the decreased mass of the moving portion of the bag.

Figures X-1-35 through X-1-38 show the great weight saving potential possible through the use of high-strength bag materials. Materials made of wire mesh suitably filled having a  $\gamma = 10^6 \text{ ft}^2/\text{sec}^2$  are presently obtainable. For example, using a material having  $\gamma = 10^6 \text{ ft}^2/\text{sec}^2$ , and limiting the maximum acceleration force to -5g's, a

~~CONFIDENTIAL~~

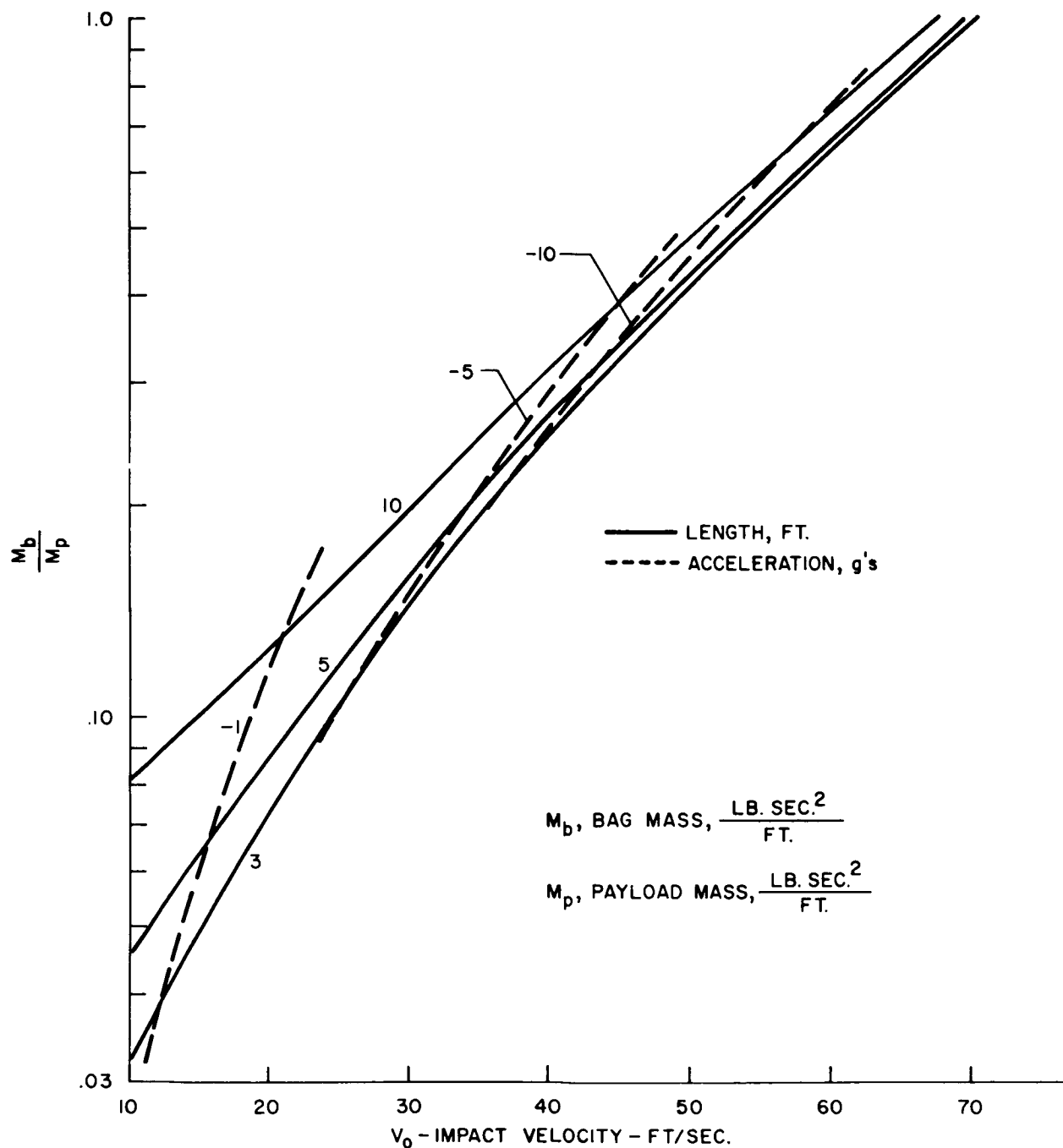


Figure X-1-35. Landing bag performance,  $\gamma = 10^4 \text{ ft}^2/\text{sec}^2$

~~CONFIDENTIAL~~

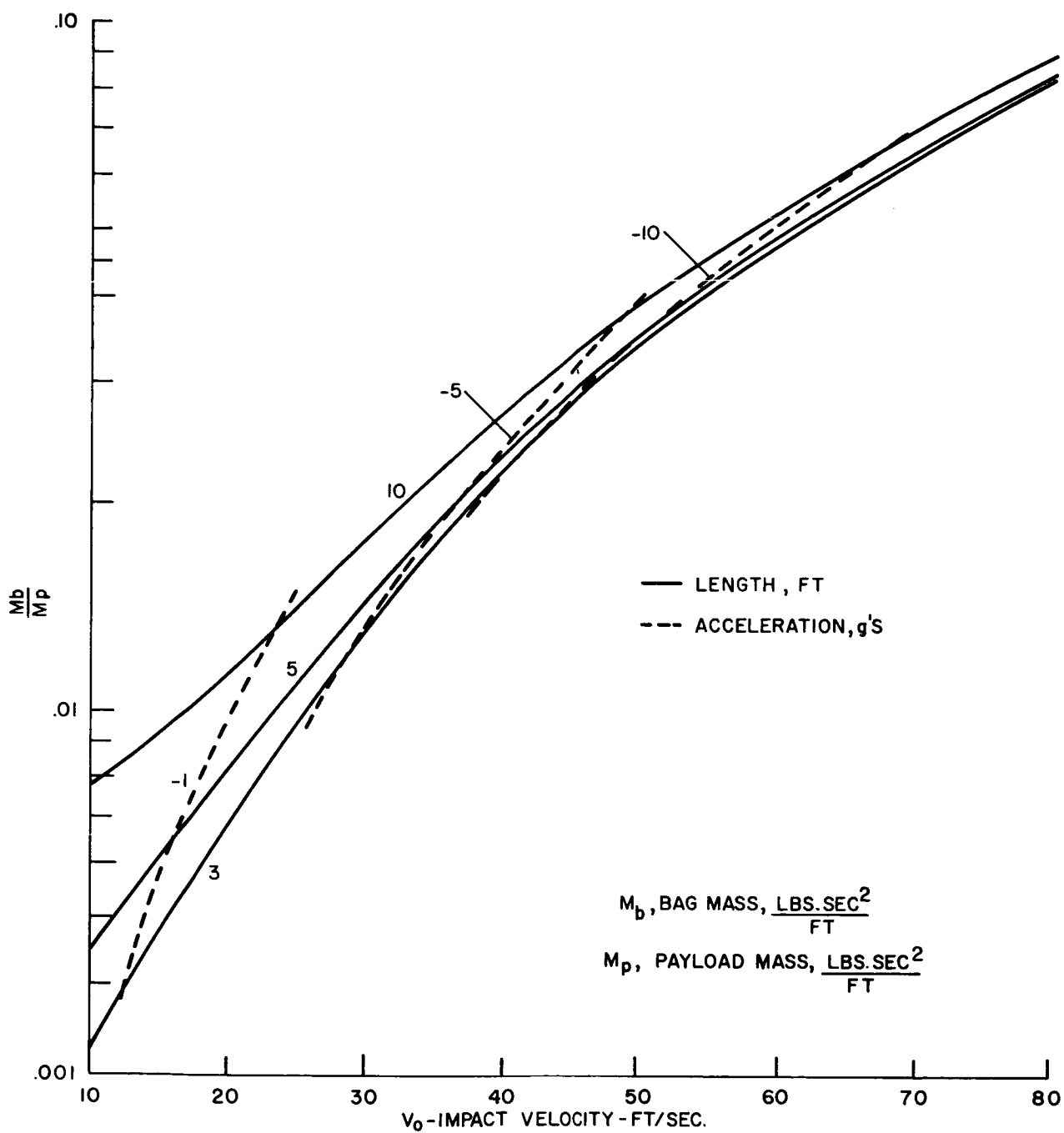


Figure X-1-36. Landing bag performance,  $\gamma = 10^5 \text{ ft}^2/\text{sec}^2$

~~CONFIDENTIAL~~

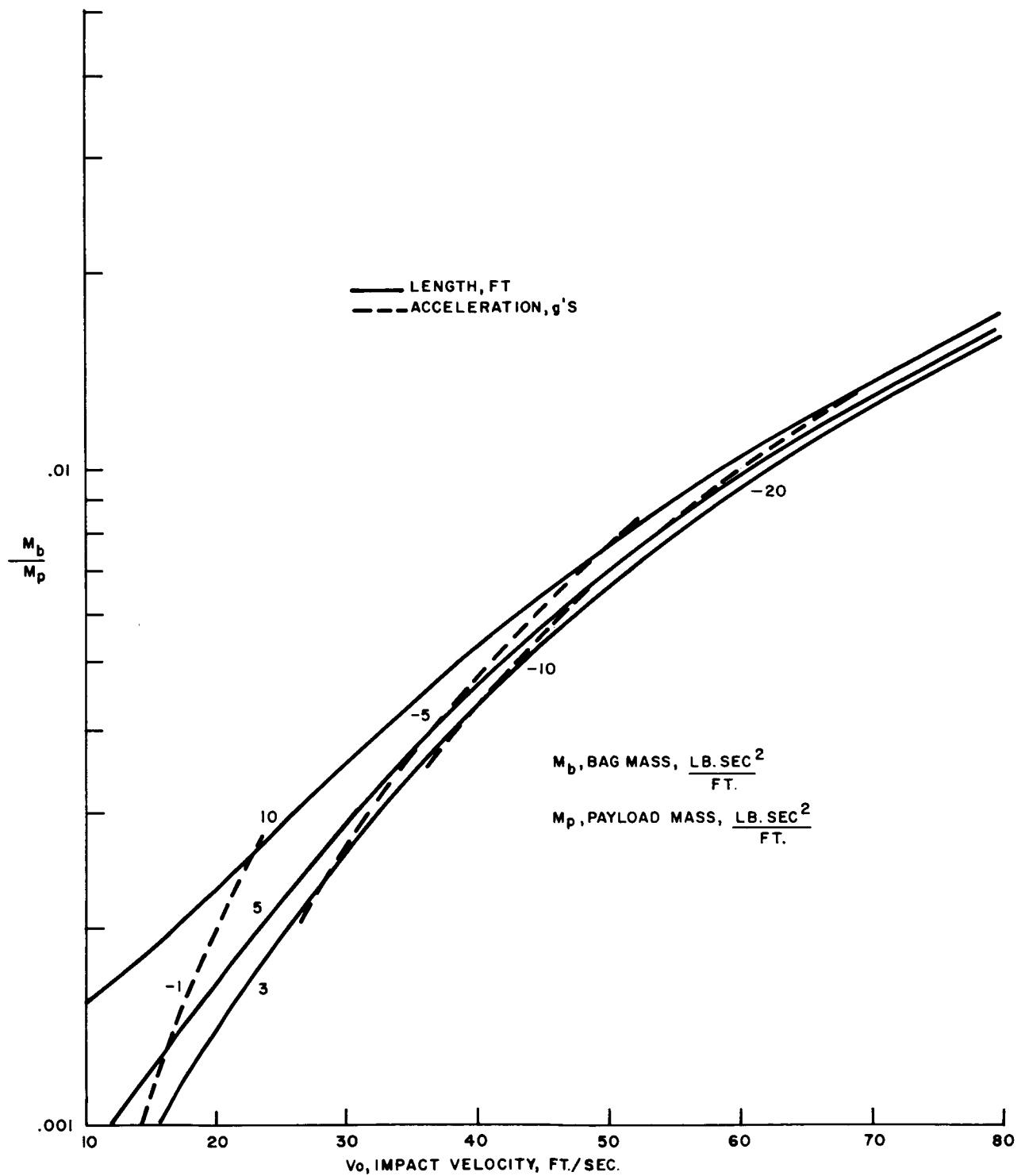


Figure X-1-37. Landing bag performance,  $\gamma = 5 \times 10^5 \text{ ft}^2/\text{sec}^2$

~~CONFIDENTIAL~~

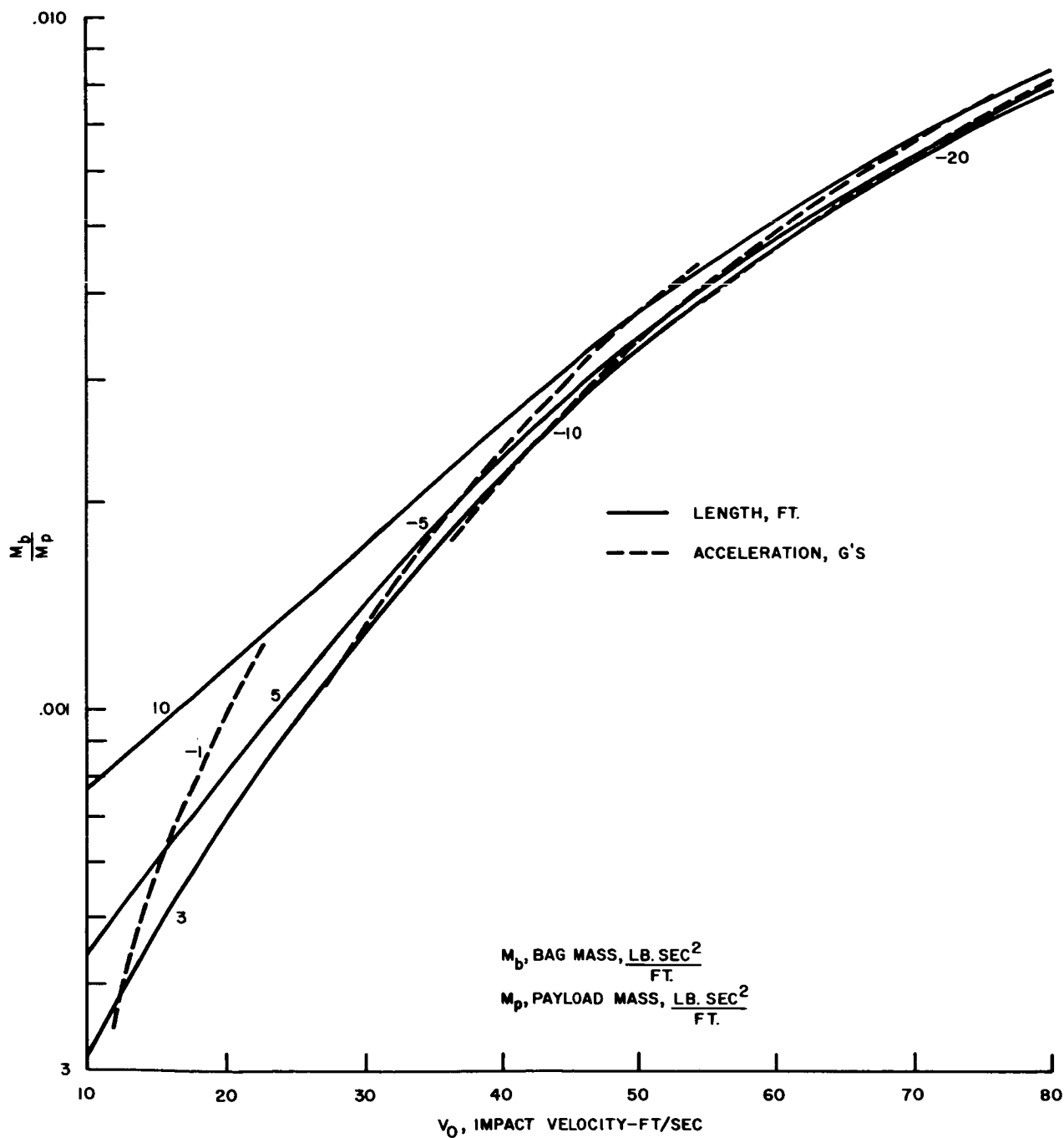


Figure X-1-38. Landing bag performance,  $\gamma = 10^6 \text{ ft}^2/\text{sec}^2$

~~CONFIDENTIAL~~

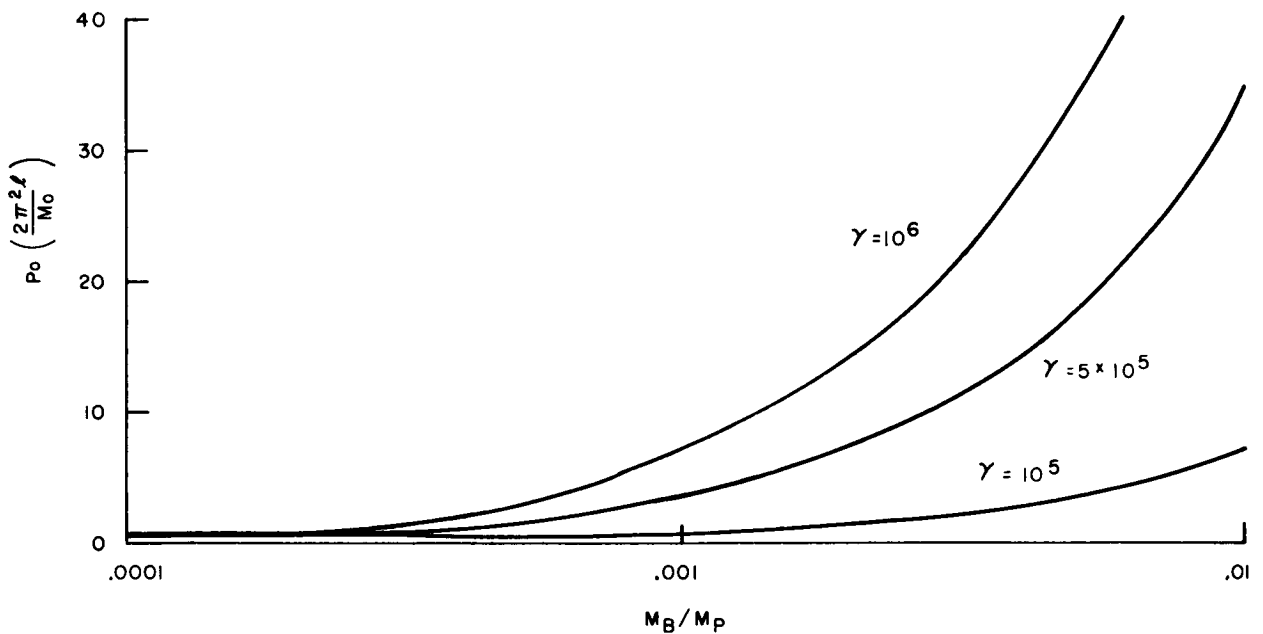


Figure X-1-39. Internal pressure differential across bag wall

bag having a length of 3 feet and whose mass is 0.00115 Mp would accept a  $V_0 = 28$  ft/sec while a bag having a length of 10 ft and whose mass is equal to 0.004 Mp would accept a  $V_0 = 51$  ft/sec.

### Description of the Landing Bag System

Two systems of pressurization of the cylinder are presently under detailed study. The first one utilizes initial pressure supplied by a gas supply and constant pressure bleed through variable area pressure valves. The use of this system enables the use of stronger bag material which in turn results in a lower ratio of bag to payload weight. It also can provide flotation capability since rupture of the bag is not required. Trade-off between the weight of this system and the flotation gear required for a rupture-type system (as discussed below) is indicated. The other system utilizes ambient internal pressure introduced through open orifices as the heat shield expands the cylinder (as in the Mercury recovery capsule). As the cylinder is collapsed and the internal pressure rises to an appropriate level, rupture discs burst and the gas is released through orifices, thereby maintaining a desirable internal pressure during a considerable portion of the remaining stroke. This system of course will not require a

~~CONFIDENTIAL~~



gas supply but will require additional flotation gear and not utilize as efficient materials as in the system previously mentioned.

### Landing Impact Attenuation Operational Concept

A sketch of the basic landing system is shown in Figure X-1-40. The bag is mounted to a flange on the capsule wall and at the forward end to a flange on the heat shield liner. Prior to expansion the bag is folded in an inextensional manner. This allows a minimum of strain in the bag material, a minimum of package volume, and a cylindrical arrangement of the folded wall. The cylinder is itself compartmented by radially positioned membranes, as shown in Figure X-1-41. This is to allow pressure to build up in a local circumferential region in the event of a non-axisymmetric impact. The bag is extended prior to impact by the combined action of internal pressure and the weight of the heat shield after it is released, and is pressurized to a pressure,  $P_0$ . This pressure, which produces stresses in the bag material within a safe factor of the ultimate strength of the bag material, is maintained at a practically constant level during

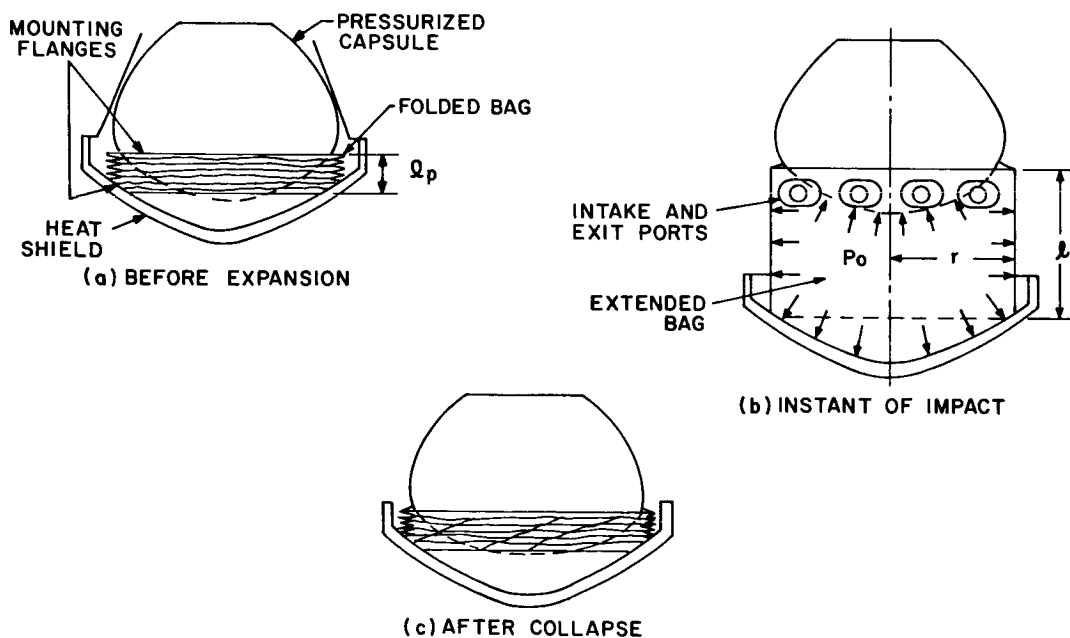


Figure X-1-40. Landing bag impact attenuation system, B-2 configuration

~~CONFIDENTIAL~~

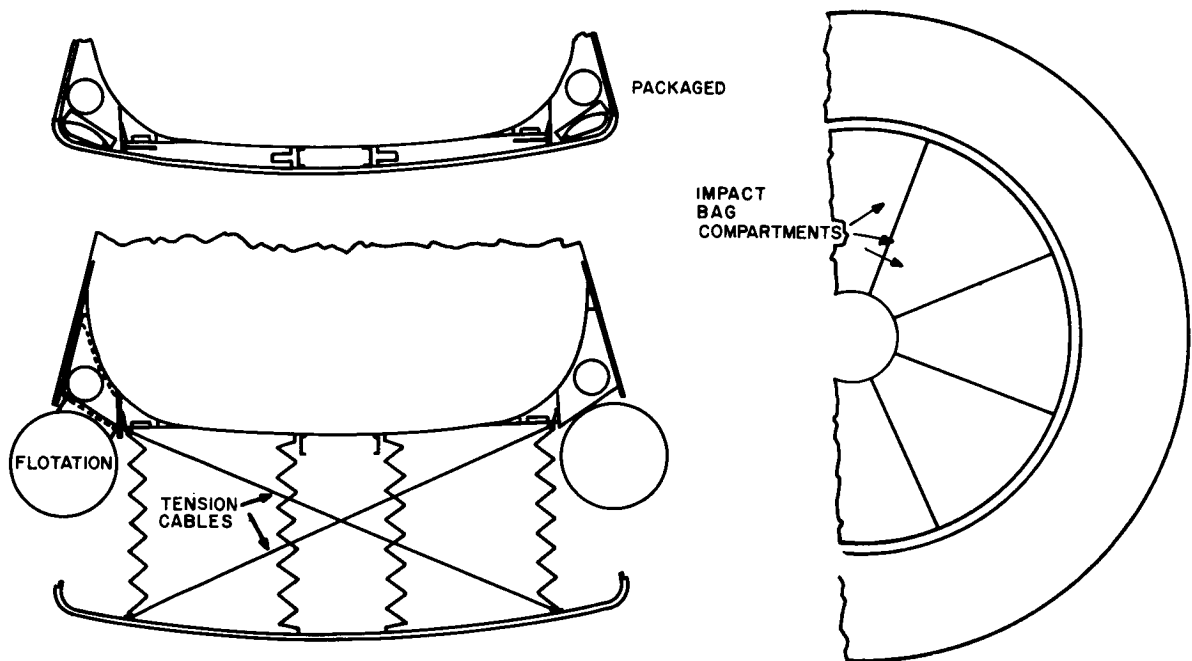


Figure X-1-41. Landing bag impact attenuation and flotation

the collapse of the bag by allowing the air to exit through pressure actuated valves. In this manner, the decelerating force on the capsule during the collapse of the bag is close to rectangular (i.e. constant with time) throughout the stroke.

The gas ports are situated in the upper part of the bag near the upper mounting flange. As shown in Figure X-1-40, during collapse, the capsule moves forward with respect to the heat shield a distance equal to  $l - l_p$ . In the performance curves the value of  $l - l_p$  used is 0.80, but generally  $l_p$  depends on the thickness of the bag material and is smaller than the employed value of  $l_p = 0.20$ , thereby allowing a larger stroke.

The heat shield serves to reduce the high onset  $g$  rate associated with a vertical cylindrical configuration by penetrating the water impact surface. It also minimizes the danger of bag puncture by rugged ground conditions.

A feature incorporated in this design is the use of tension cables cross-connected between the shield and the R/V structure. These are shown in Figure X-1-41. Non-vertical forces induced in the landing structure by a horizontal component of landing velocity are taken up in tension in these cables, thus minimizing further the danger of

~~CONFIDENTIAL~~

~~CONFIDENTIAL~~

rupturing the bags. Detailed study of landing surface conditions as they limit the "planing" capability of this system are, at present, under study. Note that the heat shield of blunt semi-ballistic shapes is nearly ideal for such "planing" or sliding.

Current plans are to further investigate this landing system for evaluating the effect of the heat shield on lowering the on-set g rate, and to determine the reproducibility of the deceleration characteristics of the constant pressure system for impacts in water and on concrete. Additional studies will also be conducted to ascertain the proper design and applicability of the pressure valves for use in this system.

### Optimization Study

Now, one may inquire as to what the optimum impact velocity may be on the basis of the combined weight of the retardation system and impact attenuation system. This answer can be obtained for a typical recovery vehicle through the combination of the data on Figures X-1-42 and X-1-43. In Figure X-1-42, various recovery system weights have been established as a function of  $V_t$ . Here, it is assumed that all parachute stages prior to the final stage have a total weight of 50 pounds and that the final-stage parachute bags weigh 30 pounds each. Then, for various final-stage canopy and line weights, a total retardation system weight is established. The evolution of the impact attenuation system weight versus  $V_t$  (Figure X-1-43) is described in more detail in the previous Section. Using the curve from Figure X-1-42 for the conical type - 108 gore parachute system, and the data of Figure X-1-43, it can be seen that the system becomes optimized, on a weight basis, at  $V_t = 35$  fps (Figure X-1-44).

~~CONFIDENTIAL~~

**CONFIDENTIAL**

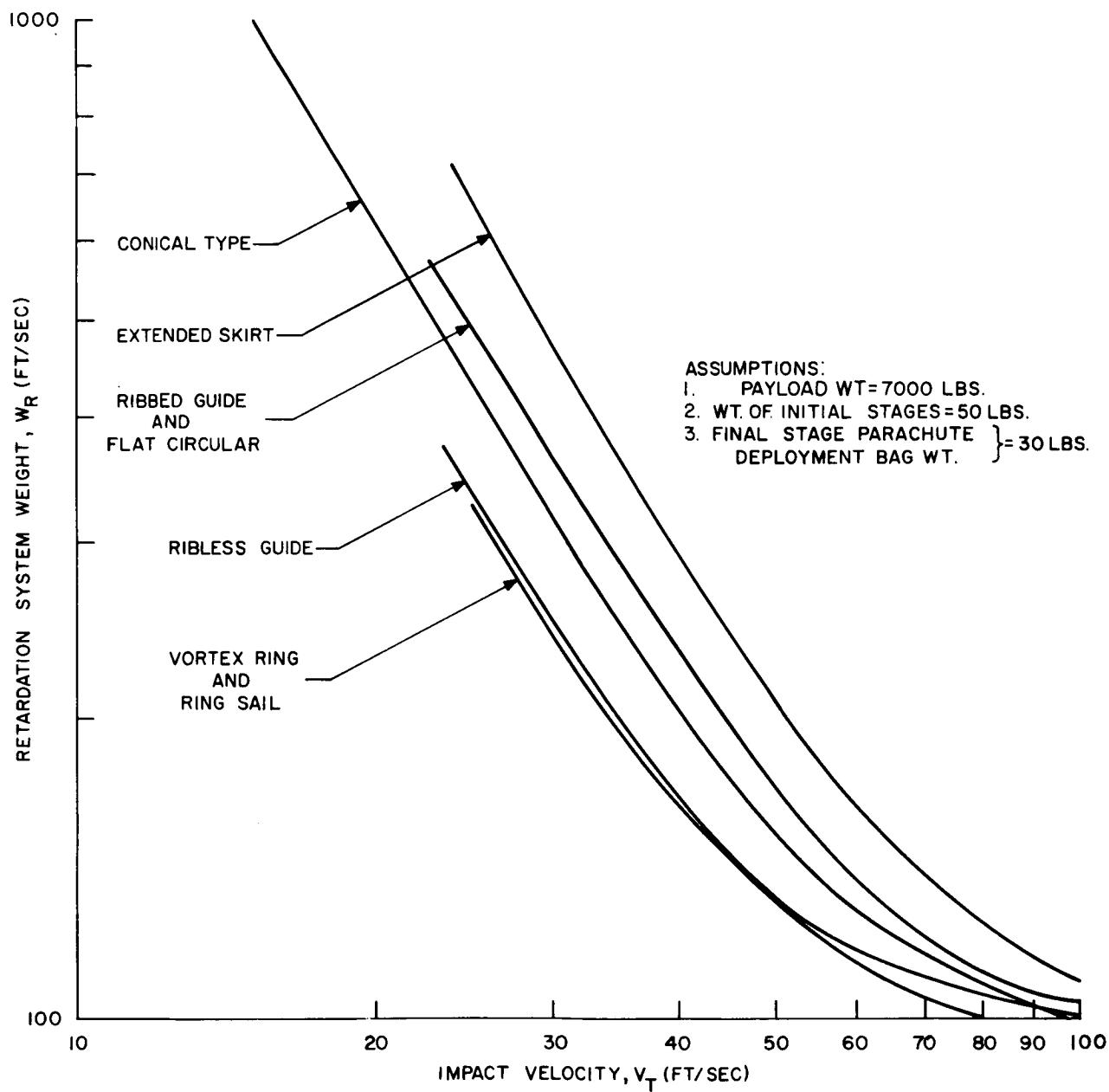


Figure X-1-42. Retardation system weight versus impact velocity

**CONFIDENTIAL**

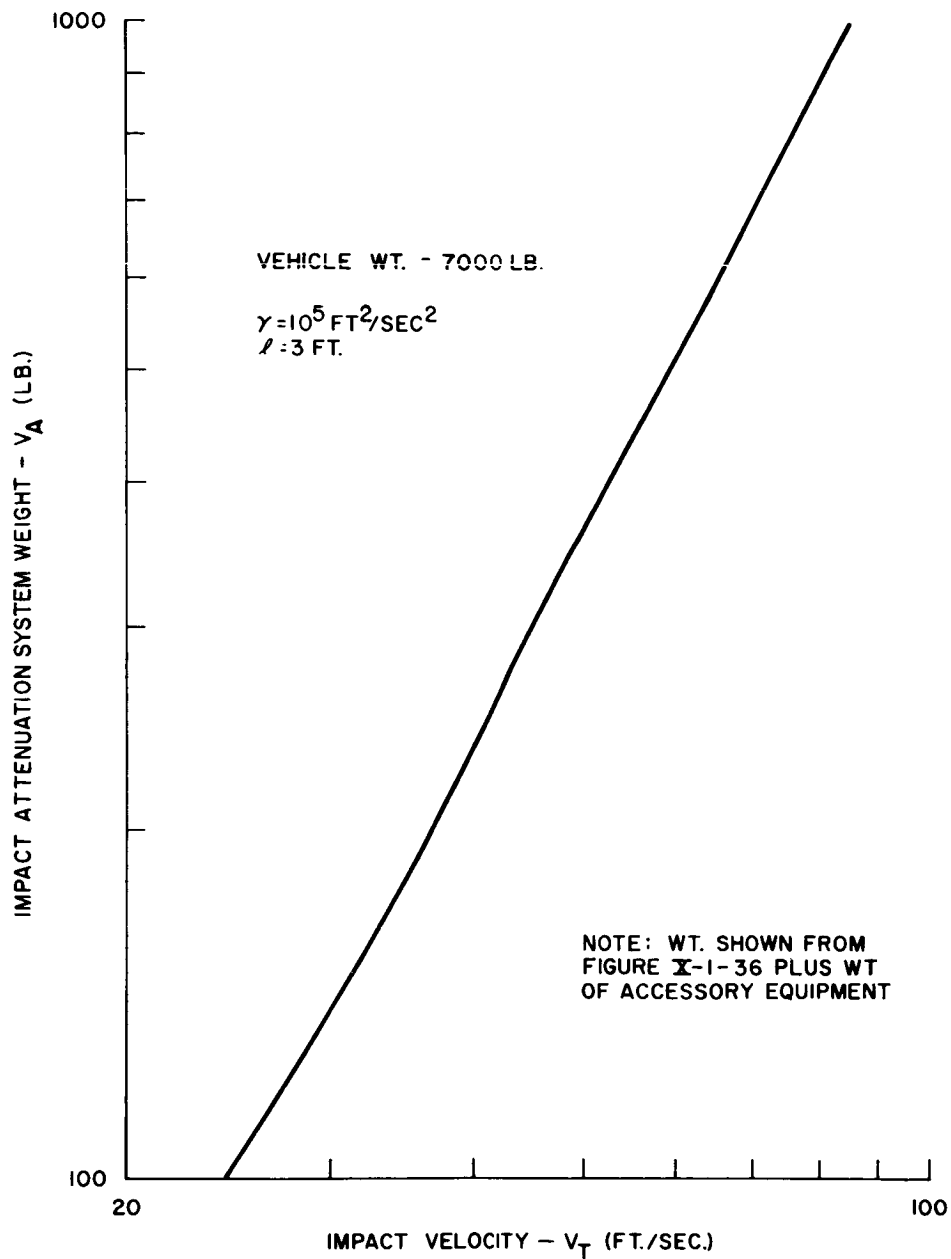


Figure X-1-43. Impact attenuation system weight versus impact velocities

~~CONFIDENTIAL~~

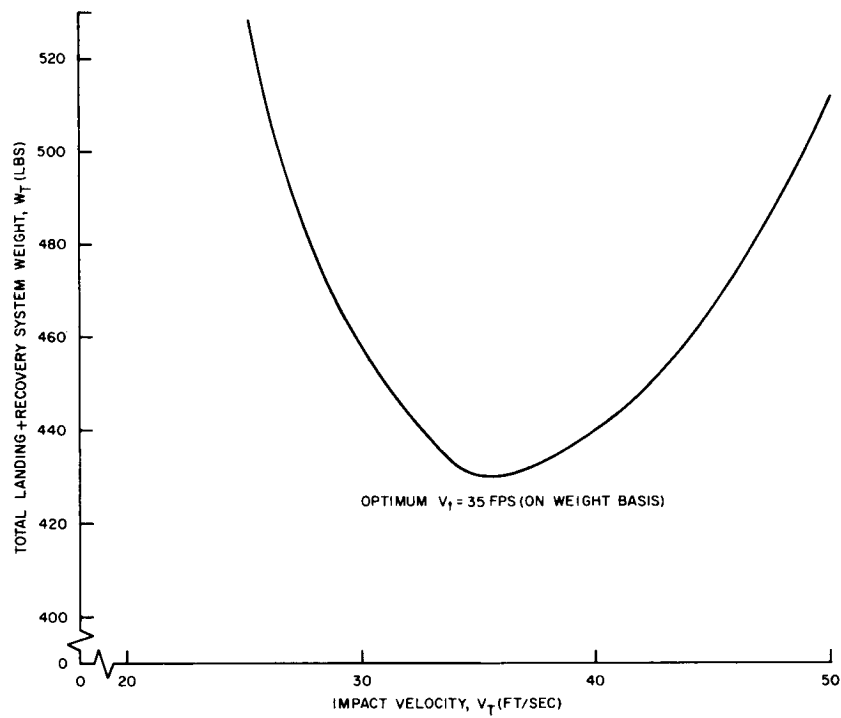


Figure X-1-44. Total landing plus recovery system weight versus impact velocity

~~CONFIDENTIAL~~

~~CONFIDENTIAL~~

## GENERAL LIST OF REFERENCES EMPLOYED

1. Heinrich, H. G. et al, "Theoretical Parachute Investigations", Progress Reports 1-15, University of Minnesota, 1957-1960.
2. "Atmospheric Model, December, 1951", GE-MSVD PIBA-2.
3. United States Air Force Parachute Handbook, December, 1956.
4. Maynard, Julian D., "Aerodynamics of Decelerators at Supersonic Speeds", Recovery of Space Vehicles Proceedings, 1960.
5. Smith, Anthony M., "Some Aerodynamic Considerations in the Recovery of Re-entry Vehicles", GE-MSVD TIS R60SD423, Secret.
6. Kane, M. T., "A Guided Parachute System", Recovery of Space Vehicles Proceedings, 1960.
7. Ewing, E. G., "A Minimum Weight Landing System for Interplanetary Spacecraft", Recovery of Space Vehicles Proceedings, 1960.
8. Gimalouski, Edward G., "Development of a Final Stage Recovery System for a 10,000 Pound Weight", WADC TR 59-109, December, 1958.
9. Howell, R., "Parachute Recovery System, Bomb Drop Tests", The Martin Company Engineering Report No. 10197, June, 1958.
10. Engstrom, B. A. and Meyer, R. A., "Performance of Trailing Aerodynamic Decelerators at High Dynamic Pressures", WADC TR 58-284, Parts I, II, III, 1959.
11. Wiant, Harry W. and Fredette, Raymond O., "A Study of High Drag Configurations As First Stage Decelerators", WADC TN 56-320, July, 1956.
12. Cilmi, P., "Results of Wind Tunnel Tests to Determine the Forces and Moments on the Discoverer Mark 2 and 4 Heat Cover Configurations", GE-MSVD Aero. Data Report 60SD665 Revised, 1960.
13. Bondurant, Stuart et al, "Human Tolerance to Some of the Accelerations Anticipated in Space Flight", WADC TR 58-156, April, 1958.

~~CONFIDENTIAL~~

~~CONFIDENTIAL~~

14. Lysdale, C. A., "Launch Vehicle Recovery Techniques", IAS Paper #61-51.
15. Penland, Jim A. and Fitterman, David E., Jr., "The Effects at a Mach Number of 6.88 of Drag Brakes on the Lift, Drag and Pitching Moment of an Ogive Cylinder", NACA RM L 55K23, 1956.
16. Kurbjun, Max C., "High-Altitude Performance of a 64 Foot Diameter Ring Sail Parachute", NASA TM X-232, 1959.
17. Musil, Ray L., "Requirements and Considerations For Testing Hypersonic Retardation Devices For Re-entry Vehicle Recovery", AFFTC TR 59-4, March, 1959.
18. Heinrich, H. G. and Riabokin, Toma, "Analytical and Experimental Considerations of the Velocity Distribution in the Wake of a Body of Revolution", WADC TR 60-257, December, 1959.
19. Rogallo, F. M. and Lowry, J. G., "Flexible Re-entry Gliders", Presented at the SAE National Aeronautics Meeting, N.Y., 1960.
20. Naeseth, Rodger L., "An Exploratory Study of a Parawing As a High-Lift Device For Aircraft", NASA TN D-629, November, 1960.
21. Rogallo, Francis M., Lowry, John G., Croom, Delwin R., Taylor, Robert T., "Preliminary Investigation of a Paraglider", NASA TN D-443, August, 1960.
22. Taylor, Robert N., Judd, Joseph H., Hewes, Donald E., "Flexible Gliders", AF/NASA Joint Conference on Lifting Manned Hypervelocity and Re-entry Vehicles, April, 1960.
23. Fisher, Lloyd J., Jr., "Landing Energy Dissipation for Manned Re-entry Vehicles", NASA TN D-453, September, 1960.
24. Esgar, Jack B., and Morgan, William C., "Analytical Study of Soft Landings on Gas Filled Bags", NASA TR R-75, 1960.
25. General Electric Proposal No. GE 290-533 "Investigation of Dynamic Buckling of Shell Structures Subject to Impact", June, 1960.

~~CONFIDENTIAL~~



- [REDACTED]
26. Coppa, A. P., "On the Mechanism of Buckling of a Circular Cylindrical Shell under Longitudinal Impact", General Electric Co. TIS Report R60SD494, Proceedings of the 10th International Congress of Applied Mechanics, September, 1960.

[REDACTED]

~~CONFIDENTIAL~~

## 2. LANDING STUDY FOR GLIDE-TYPE RE-ENTRY VEHICLE

To establish the subsonic L/D requirements for satisfactory landing characteristics of hypervelocity glide vehicles, the results of two approaches to a quality rating were reviewed. These were based on the results of X-15 flight tests and flight tests of an F-104A and an F-102 which were simulating low L/D aircraft landings. The L/D and approach velocity boundaries within which the landing characteristics are deemed acceptable differ in each approach although there is a considerable overlap of acceptable area. They differ partly because one approach apparently uses only flight test data while the other included additional calculations and assumptions relating to hypervelocity vehicles. Further differences were undoubtedly introduced in the analysis of flight tests and pilot opinion both of which offer considerable data "scatter". Both approaches appear sound and are presented here with the recommendation that the APOLLO vehicle be designed with subsonic characteristics that would be acceptable to either rating system.

The first approach is one which was used as comparative criteria for the Dyna-Soar Phase Alpha Study and is presented in Figure X-2-1. The figure consists of a background of lines of constant approach velocity plotted on ordinates of Rate-of-Sink and L/D. It is divided into five areas, each of which has a "quality" rating of the capability to make a tangential landing. The background curves are calculated by the following equations evaluated at sea level.

$$\tan \gamma = \frac{1}{L/D \left( 1 + \frac{V}{g} \frac{dv}{dh} \right)}$$

$$\text{Rate of Sink} = V \sin \gamma$$

The expression  $\frac{V}{g} \frac{dv}{dh}$  is a correction to the flight path angle to account for the kinetic energy change in gliding-flight.

To use the figure, the characteristics of the configuration in question should be used to determine the minimum velocity from which the flare and touchdown can be accomplished

~~CONFIDENTIAL~~

~~CONFIDENTIAL~~

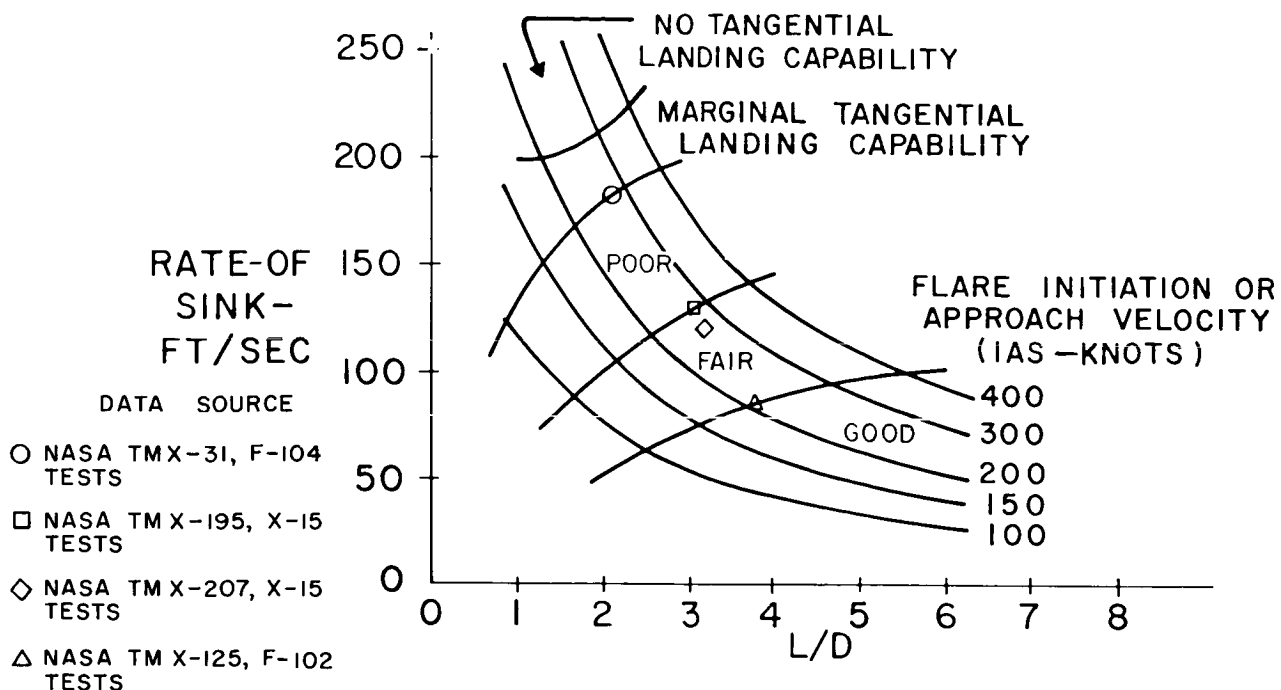


Figure X-2-1. Rate-of-sink criteria

with touchdown occurring at the velocity calculated by the equation

$$V = \sqrt{\frac{2W}{\rho S C_L}}$$

where the coefficient is for the touchdown angle of attack and includes ground effects (which for Dyna-Soar amounted to about 25 percent  $C_L$  increase). When the minimum begin-flare velocity has been determined, it should be increased by 25 percent to allow for flare and maneuver margins. This velocity is then plotted on Figure X-2-1 to determine the quality index.

Rather than determine the approach velocity in the above manner, it is suggested that for preliminary studies the landing velocity be calculated and added to an estimate of the velocity loss from flare initiation to touchdown obtained from Figure X-2-2 which is based on actual flight tests from References 1 and 2. Spotted on Figure X-2-1 are points obtained from the results of tests reported in these references.

~~CONFIDENTIAL~~

~~CONFIDENTIAL~~

The second approach is an analytical approach based on the same test data as discussed above and is presented in Reference 3. Results which were calculated in Reference 3 for configurations fairly representative of the landable glider approach to APOLLO are presented in Figure X-2-3. These show that for a highly swept delta wing configuration with a wing loading on the order of 35 pounds-per-square foot, the  $(L/D)_{\max}$  must be at least 2.5. It further shows the range of allowable flare-initiation speeds for  $(L/D)_{\max}$  values up to 5. The range of acceptable flare-initiation speeds is bounded on the high-speed side by the flight path angle of -35 to -45 degrees and is defined on the low-speed side by a minimum time of approximately 5 seconds to terminate the landing following completion of the flare. The range of allowable flare-initiation speeds may be used as a measure of the "quality" rating of the configuration. The wider the range of speeds, the greater the flexibility of landing techniques and the greater the allowance for flare and maneuver margins. From Figure X-2-3 it may be seen that with an  $L/D$  of 2.5, the flare must be initiated at 248 knots in order to have an initial flight path no greater than -45 degrees and to have the minimum time of 5 seconds to land following completion of the flare. Thus an  $L/D$  of 2.5 could be rated acceptable but poor. An  $L/D$  of 3.5 or higher should provide fair to good landing characteristics with minimum and maximum flare-initiation speeds of about 200 and 325 knots respectively. Figure X-2-3 was obtained by starting at various velocities and calculating the flares and landings of several configurations which varied in  $(L/D)_{\max}$  from 2.5 to 4.5. Assumptions which were used were a maximum normal acceleration of 2 g in the flare and a maximum angle of attack of 13 degrees. Although the exact lift coefficients used are not known, the landing speeds indicate them to be representative. The effects of wing loading are not shown and it is felt that if it should vary greatly from 35 pounds-per-square foot, Figure X-2-3 should be recalculated.

A summary chart which is a composite of the results of both of the above types of analysis is presented in Figure X-2-4. It shows the  $L/D$  ratios and corresponding limits of flare-initiation speeds which will permit acceptable landings to be made and the minimum  $L/D$  for good landing capability is indicated. From this composite plot, the minimum acceptable  $L/D$  is 2.8 and for good landing capability the minimum  $L/D$  is 3.75.

~~CONFIDENTIAL~~

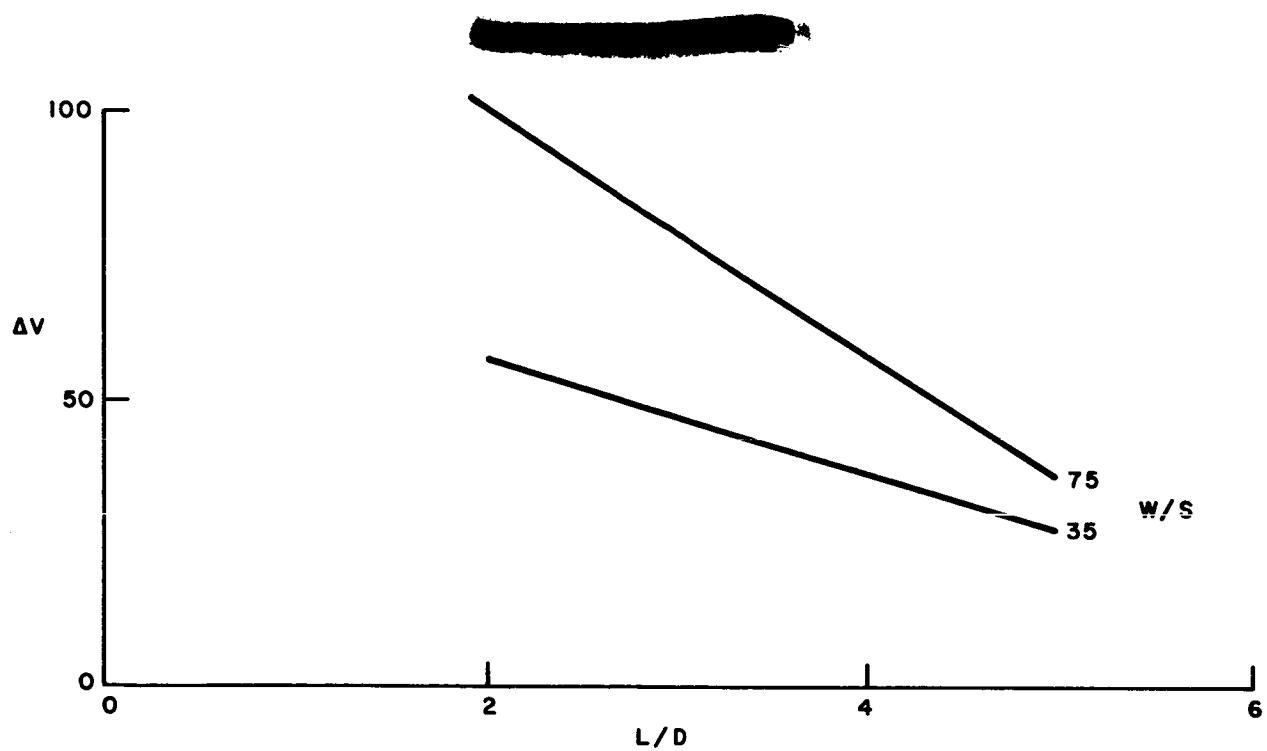


Figure X-2-2. Velocity loss from flare initiation to touchdown

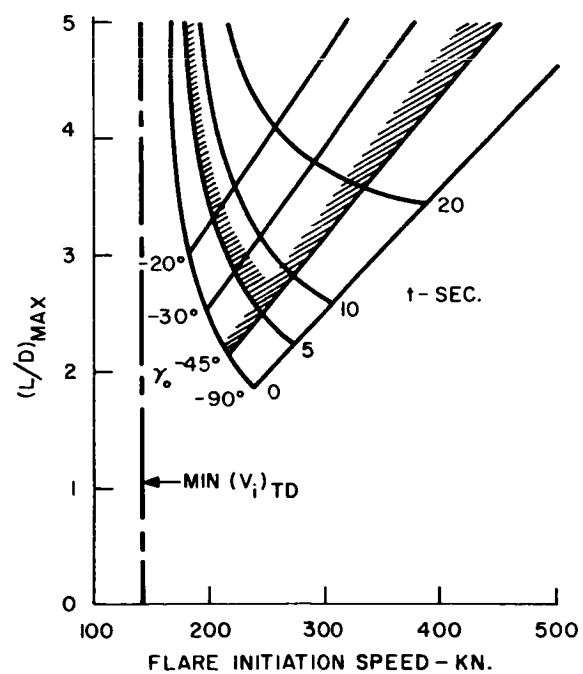


Figure X-2-3. Low  $L/D$  landing analysis

FLARE  
INITIATION  
SPEED-KNOTS

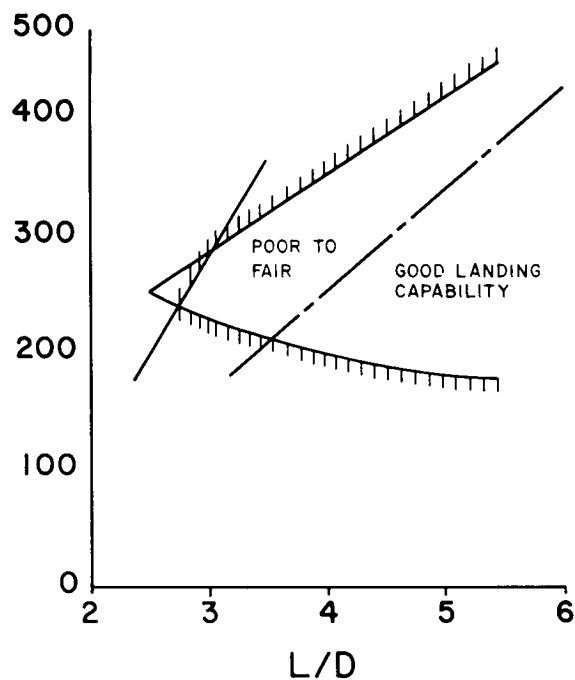


Figure X-2-4. L/D and approach speeds for acceptable landing characteristics

#### LIST OF REFERENCES

1. Matranga, G. J. and Armstrong, N. A., "Approach and Landing Investigation at Lift-Drag Ratios of 2 to 4 Utilizing a Straight-Wing Fighter Airplane". NASA TM X-31, August, 1959.
2. Matranga, G. J. and Armstrong, N. A., "Approach and Landing Investigation at Lift-Drag Ratios of 3 to 4 Utilizing a Delta-Wing Interceptor Airplane", NASA TM X-125, October, 1959.
3. Matranga, G. J. and Weil, J., "Review of Techniques Applicable to the Recovery of Lifting Hypervelocity Vehicles", NASA TM X-334, September, 1960.

~~CONFIDENTIAL~~

### 3. FLOTATION SYSTEM

#### GENERAL DESCRIPTION

A flotation system is proposed for the recovery vehicle to supplement the inherent buoyancy of the vehicle itself. In the event of damage to the normally sealed R/V module, such a system would assure buoyancy for the 72-hour search period even though water tight integrity of the R/V was lost.

The system will consist of the following basic items.

1. Buoyancy bag
2. Pressurized gas supply
3. Sensing circuit
4. Plumbing and valve equipment

The anticipated design configuration of the buoyancy bag is that of the torus packaged near the outer periphery of the R/V between the ablation shield and the internal R/V structure. After inflation, the torus shape will offer resistance to capsizing in rough seas and will contribute to system stability on the water surface.

It is proposed to construct the flotation bag with a flexible nylon outer casing with neoprene bladder. Dual-flotation capability can be incorporated into the design by fabricating the bladder with a flexible membrane dividing the circular section into two torus compartments. Pressurizing each compartment will permit loss of gas in either compartment (due to possible damage at impact or during the flotation period) without greatly effecting the displacement volume or stability of the floating mass.

Rapid inflation of the buoyancy bag will be accomplished by opening an explosive actuated valve from the pressurized gas supply to the bag. Dry air or nitrogen are being considered as the working medium. Carbon dioxide offers the advantage of reduced weight in the pressurized supply system due to its high free to compressed volume

~~CONFIDENTIAL~~

ratio (gas to solid) but the possibility of solid material carry over and valve freezing precludes its use toward a reliable system design. Considering a service pressure of approximately 2500 psi, these problems are not as pronounced with either air or nitrogen.

The system will be activated on contact with the sea water. A sensing circuit independent of the recovery system programmer will be provided to initiate the inflation process. On contact with the sea water, a pyrotechnic-time-delay switching unit will be activated which will, after a predetermined time limit, complete an electrical circuit from the power supply to the explosive valve. Selection of the timing interval shall be based on the time required for the recovery vehicle to stabilize on the water surface. This time delay will prevent bag rupture due to hydrodynamic pressure build-up during initial penetration and will minimize damage from collision with the shield during the compression stroke of the impact shock absorption bag. A sketch of the proposed system for the D-2 R/V configuration is shown on Figure X-3-1.

~~CONFIDENTIAL~~



~~CONFIDENTIAL~~

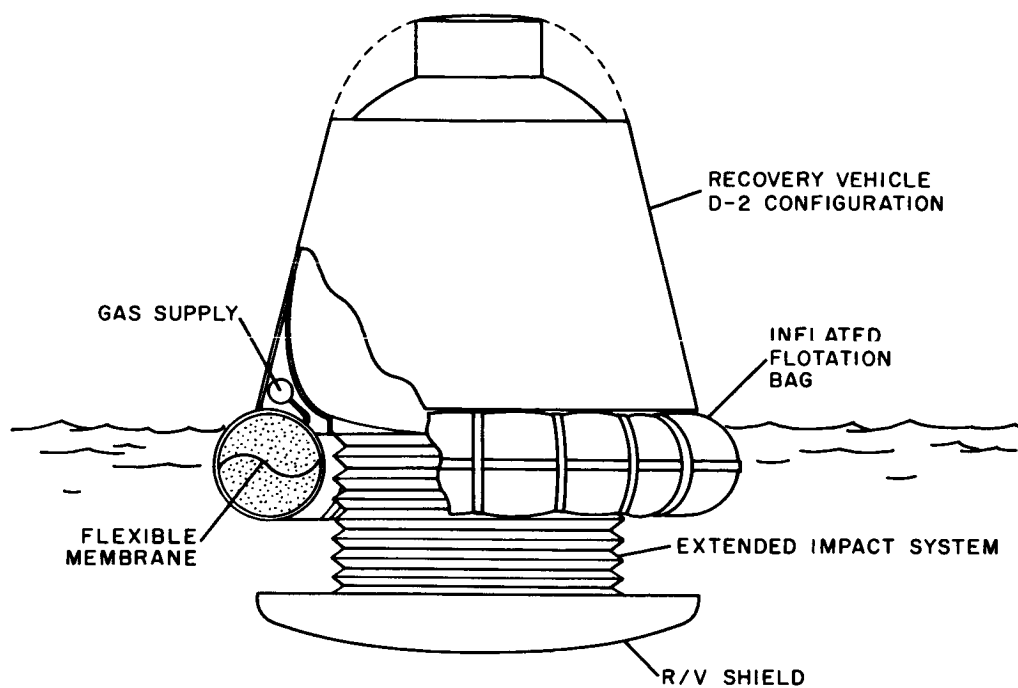


Figure X-3-1. APOLLO flotation system

~~CONFIDENTIAL~~

~~CONFIDENTIAL~~

#### 4. RECOVERY AID SYSTEM

##### GENERAL DESCRIPTION

The recovery aid system will perform the function of locating the vehicle and occupants for subsequent retrieval. To calculate adequately the location of the vehicle at the final impact, a nominal tracking capability must be provided to ground observers for impact area prediction. This data is then provided to alert recovery forces available in the specific area and direct the search efforts (if required) to the point of actual recovery. Location aids are provided to assist the recovery team in location determination after flight termination.

These capabilities for tracking and locating the vehicle must insure adequate performance under a variety of atmospheric conditions, climatic conditions and physical environments associated with landing in land or water, rugged or flat terrain.

##### BASIC ASSUMPTIONS

The system design is predicated on the most catastrophic failures conceivable and the most severe environments. This insures that location under ideal conditions will be more than adequate. This assumption is based on the following considerations:

1. Retrieval of the occupants is of primary consideration irrespective of vehicle performance.
2. Localized weather disturbances are not predictable on a long-term basis.
3. Under emergency conditions, the landing site might not be selected by the occupants.
4. Vehicle failure data is of extreme importance in the successful completion of the program.

~~CONFIDENTIAL~~

**CONFIDENTIAL**

The specific equipment developments as conceived should not require extensive modifications to the ground equipment (both airborne and land based) presently in existence or currently in the planning stage for future installation. Future efforts for development should be directed toward improvement in performance capabilities of the airborne system rather than gross modifications of equipment existing and planned at various tracking sites. Some additional tracking site locations might be recommended.

Operation of the system must be programmed for automatic operation, in the event of incapacity of the occupant or prior occupation of the crew with more important functions such as attitude control. Overrides must be included for human manipulation for optimization under the various conditions that may exist during the flight termination phase. Programming functions would also include logical circuitry to provide for optimization of the system performance under such influencing factors as

1. Climatic conditions
2. Marginal performance of equipment
3. Power supply residual capacity.

## **SYSTEM SYNTHESIS**

The system requirements are dependent on such factors as trajectory parameters, operation time and other external constraints.

For purposing of isolating the various flight modes for analysis of required equipment performance, the following phases are considered (see Figure X-4-1):

1. Near Earth terminal Phase
2. Re-entry/Glide path Phase
3. Retardation Phase
4. Post Impact Phase

**CONFIDENTIAL**

~~CONFIDENTIAL~~

Nominal conditions have been assigned to each of the phases based on a return trajectory. As a result of this data, abort from powered flight or sub-orbital flight imposes less stringent conditions than those established.

### **Near Earth Terminal Phase**

Extending for 400,000 feet outward to approximately 8,000 miles. Since the deep space tracking antennas are incapable of providing 100 percent coverage at altitudes of less than 8000 miles a considerable area exists in which tracking from these locations might be lost. For this reason, it is desirable to maintain contact with the vehicle to establish a nominal trajectory during this final phase with sufficient accuracy to predict the initial point of re-entry. Long range distances are involved, but accuracies of the location of impact of less than tens of miles are not required at this time for recovery.

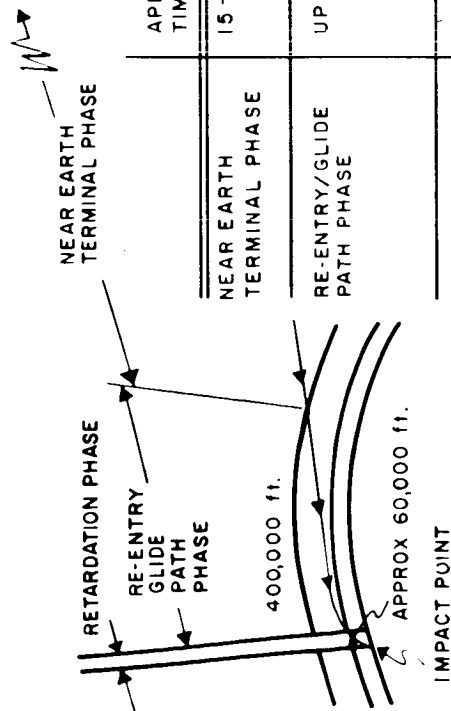
### **Re-entry/Glide Path Phase**

This phase is defined by the start of re-entry at a nominal altitude of 400,000 feet and is characterized by ionization and heating to various degrees. Electronic tracking during this phase is hampered by re-entry ionization but enhanced visually by heating. Tracking during this phase is the most critical for determination of the final impact point, since relatively small dispersions can occur after reaching an altitude of around 60,000 feet.

### **Retardation Phase**

This phase is most desirable for use in determination of the final impact point since the vehicle is stable, either hovering or falling to the final impact point. Electronic search is enhanced by the altitude of the vehicle as compared to the ground elevation after final impact. Location of this phase in the flight will refine the final impact location since gross deviations cannot occur.

~~CONFIDENTIAL~~



	APPROXIMATE TIME DURATION	MAJOR CHARACTERISTICS	EQUIPMENT REQUIREMENTS
NEAR EARTH TERMINAL PHASE	15 - 20 min	VEHICLE AT ESCAPE VELOCITY LARGE DISTANCES INVOLVED	HIGH POWER TRANSMISSIONS
RE-ENTRY/GLIDE PATH PHASE	UP TO 40 min	IONIZATION EXTREME HEATING GRADUAL DECELERATION	1. OPERATE DURING RE-ENTRY 2. MODERATE POWER CONSISTENT WITH GROUND FACILITIES
RETARDATION PHASE	15 minutes	SLOW VELOCITY LATERAL MOVEMENT MINIMIZED	1. PROVIDE FINAL IMPACT AREA DETERMINATION
POST IMPACT PHASE	72 hours	FINAL POSITION FIXED	1. PROVIDE FINAL RECOVERY SITING 2. PROVIDE LONG RANGE DIRECTIONAL DATA

Figure X-4-1. Schematic representation of major recovery phases

~~CONFIDENTIAL~~

## Post Impact Phase

This is the most critical for final recovery. Final contact with the vehicle must be made visually although sufficient recovery aids must be active to direct recovery forces to the immediate area. Since a survival capability of 72 hours is required, the vehicle is equipped for electronic transmission for at least this time interval.

Although the vehicles' location will not be altered, equipment capabilities must be compatible with extremes of local environment. A brief summary of the various flight modes is shown in Figure X-4-1.

Based on the foregoing arbitrary breakdown of the major flight regimes, equipment requirements can be established based on existing tracking equipment, airborne equipment performance, search requirements and previous search and recovery procedures.

Additional consideration is given to the future National Search and Recovery plans as presently conceived by various military and civilian establishments. The matrix shown in Table X-4-1 has been established, based on these parameters.

~~CONFIDENTIAL~~

~~CONFIDENTIAL~~

TABLE X-4-1. PHASE/RECOVERY AID PROGRAM

Requirements can then be correlated to formulate the system requirements.

X - Required  
D - Desirable  
NR - Not Required

<u>Equipment Type</u>	<u>Near Earth Terminal</u>	<u>Re-entry Glide Path</u>	<u>Retardation</u>	<u>Post Impact</u>
RF Propagation				
Radar - Beacon	X	D <sup>2</sup>	D	NR
Chaff	X	D <sup>2</sup>	X	NR
Skin Tracking	D <sup>1</sup>	D <sup>2</sup>	X	NR
Radio - VHF CW	X	D <sup>2</sup>	X	X <sup>4</sup>
VHF Voice	X	NR	X	X <sup>4</sup>
HF CW	NR	D <sup>3</sup>	X	X <sup>5</sup>
HF Voice	NR	D <sup>3</sup>	X	X <sup>5</sup>
Light Propagation				
Visible - Human Sensing	D	X <sup>6</sup>	D	X <sup>7</sup>
Electronic "	D	D <sup>6</sup>	D	D
IR - (Electronic Sensing)	D	D <sup>6</sup>	D	D
Miscellaneous				
Sofar	NR	NR	NR	X <sup>8</sup>
Dye	NR	NR	NR	X <sup>8</sup>

Notes:

1. Desirable, but difficult to achieve at great distances
2. Propagation during re-entry is difficult
3. Feasible during re-entry
4. Primary Source if short range DF (line of sight)
5. Primary Source if long range DF
6. Vehicle radiates in these bands - no equipment requirement
7. Primary Source of location data for recovery
8. Applicable to water impact only

~~CONFIDENTIAL~~

~~CONFIDENTIAL~~

## SYSTEM DESIGN

Analyzing the matrix of Table X-4-1, a system definition can be formulated based on (1) immediate airborne equipment capabilities, (2) existing tracking equipment capabilities and (3) economically and expected feasibility airborne and ground component development.

In order to systematically formulate this system, a functional block diagram has been prepared as shown in Figure X-4-2. This diagram suggests programming methods and serves as a basis for establishing the parametric studies required to determine realistic RF output power levels, compatible power supplies; thus, establishing system requirements compatible with vehicle weight constraints, tracking limitations and mission requirements.

~~CONFIDENTIAL~~



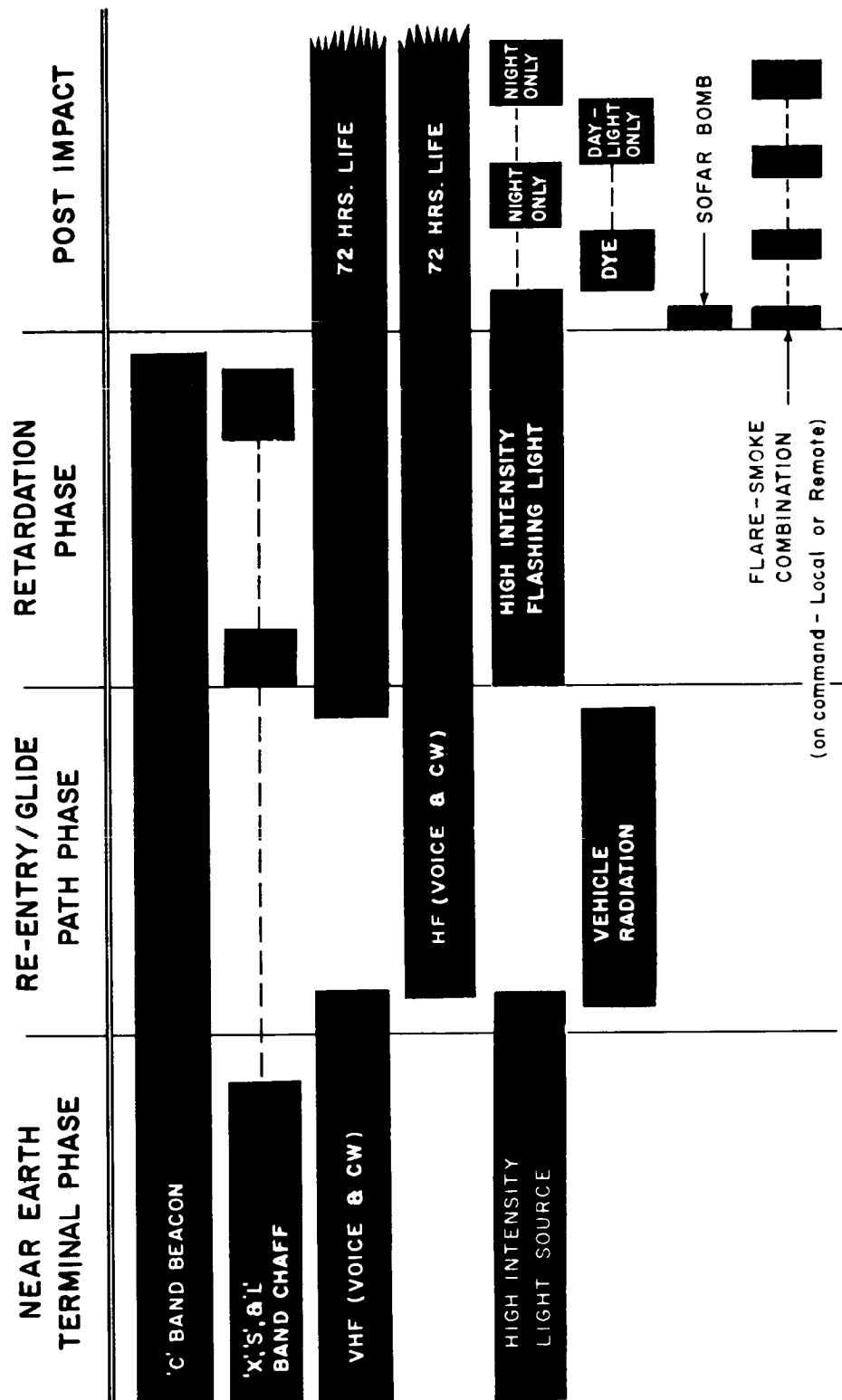


Figure X-4-2. Block diagram of recovery aid system

~~CONFIDENTIAL~~

X-80

~~CONFIDENTIAL~~